

Energy, Mines and Resources • *Yukon Geological Survey*

YUKON

EXPLORATION & GEOLOGY

2009



YUKON
EXPLORATION
& GEOLOGY
2009

Edited by
K.E. MacFarlane, L.H. Weston and
L.R. Blackburn

Yukon Geological Survey
Energy, Mines and Resources
Government of Yukon

Published under the authority of the Minister of Energy, Mines and Resources, Government of Yukon
<http://www.emr.gov.yk.ca>

Printed in Whitehorse, Yukon, 2010.

Publié avec l'autorisation du ministre de l'Énergie, des Mines et des Ressources du gouvernement du Yukon, <http://www.emr.gov.yk.ca>

Imprimé à Whitehorse (Yukon) en 2010.

© Minister of Energy, Mines and Resources, Government of Yukon

ISSN 1718-8326 (on-line version)

This, and other Yukon Geological Survey publications, may be obtained from:

Geoscience Information and Sales

Yukon Geological Survey

102-300 Main Street

Box 2703 (K-102)

Whitehorse, Yukon, Canada Y1A 2C6

phone (867) 667-3201, fax (867) 667-3198, e-mail geosales@gov.yk.ca

Visit the Yukon Geological Survey website at www.geology.gov.yk.ca

In referring to this publication, please use the following citation:

Yukon Exploration and Geology 2009. K.E. MacFarlane, L.H. Weston and L.R. Blackburn (eds.), 2010.

Yukon Geological Survey.

Papers from this document are available in colour on the Yukon Geological Survey website.

Production by K-L Services, Whitehorse, Yukon.

Front cover photograph: Altered limestone. View is to the northwest; Atlin Road in foreground, Marsh Lake in background. Photo by Nicolai Goepfel.

PREFACE

Yukon Exploration and Geology (YEG) continues to be the main publication of the Yukon Geological Survey (Energy, Mines and Resources, Yukon government). This is the 32nd volume of the series and marks the first time that it is only available digitally. Individual YEG papers, with colour images, can be downloaded from our website. The Yukon Exploration and Geology Overview remains a separate volume and is available in print and digital formats. As in previous volumes, YEG 2009 contains up-to-date information on mining and mineral exploration activity, studies by industry, and results of recent geological field studies. Information in this volume comes from prospectors, exploration and government geologists, mining companies and students who are willing to contribute to public geoscience for the benefit of the scientific community, general public, and mineral and petroleum industries of Yukon. Their efforts are appreciated.

Having accepted the position of Head, Technical Services for the Yukon Geological Survey (YGS) in 2009, I also inherited the title of Chief Editor of YEG. It was my first experience with this volume and I must thank Leyla Weston and Lauren Blackburn for their patience and assistance as co-editors. Their commitment and hard work in ensuring that this volume can be delivered to you speaks volumes to their abilities to work gracefully under pressure. Several of our colleagues at the YGS have contributed to this volume, both in preparing and reviewing manuscripts, and deserve a thank you as well.

Wynne Krangle and Peter Long of K-L Services continue to provide excellent service in putting this production together, including editing suggestions, design of diagrams, volume layout, and working under the pressure of a tight deadline. Chera Hunchuk of the Queen's Printer ensured that the publishing process went smoothly.

This year's Yukon Exploration and Geology is dedicated to the geologists, prospectors and colleagues who continue to live on in spirit. May they continue to inspire.

We welcome any input or suggestions that you may have to improve future YEG publications. Please contact me at (867) 667-8519, or by e-mail at karen.macfarlane@gov.yk.ca.

Karen MacFarlane



TABLE OF CONTENTS

Field notes on the Upper Devonian Imperial Formation (NTS map sheet 106L), Tetlit Creek, east Richardson Mountains, Yukon T.L. Allen	1
Deconstructing complex Au-Ag-Cu mineralization, Sonora Gulch project, Dawson Range: A Late Cretaceous evolution to the epithermal environment V. Bennett, C. Schulze, D. Ouellette and B. Pollries.....	23
U-Pb isotopic age dating by LAM ICP-MS, INCO Innovation Centre, Memorial University: Sample preparation methodology and analytical techniques V. Bennett and M. Tubrett.....	47
New U-Pb age constraints at Freegold Mountain: Evidence for multiple phases of polymetallic mid- to Late Cretaceous mineralization T. Bineli Betsi and V. Bennett.....	57
High-sulphidation epithermal Au-Ag-Cu mineralization at the McKay Hill property – a revised deposit model L.R. Blackburn	85
Pre-Reid surficial geology investigations in southwest J. Bond and P. Lipovsky.....	103
Preliminary description and slope stability analyses of the 2008 Little Salmon Lake and 2007 Mt. Steele landslides, Yukon M.-A. Brideau, D. Stead, P. Lipovsky, M. Jaboyedoff, C. Hopkinson, M. Demuth, J. Barlow, S. Evans and K. Delaney	119
Particle-size distribution of gold within the Sulphur and Dominion creek drainages, Klondike District, Yukon, and implications for gold winning and the formation of distal placers containing fine gold R.J. Chapman, D.P.G. Bond and W.LeBarge.....	135
The Duke River fault, southwest Yukon: Preliminary examination of the relationships between Wrangellia and the Alexander terrane R. Cobbett, S. Israel and J. Mortensen.....	143
Bedrock geology of southwest McQuesten (NTS 115P) and part of northern Carmacks (NTS 115I) map area M. Colpron and J.J. Ryan.....	159
Major- and trace-element composition of platinum group minerals and their inclusions from several Yukon placers Y. Fedortchouk, W. LeBarge, A.Y. Barkov, L. Fedele and R.J. Bodnar.....	185
Preliminary Quaternary geology of Coal River area (NTS 95D), Yukon K. Kennedy.....	197
Ar-Ar geochronology and Pb isotopic constraints on the origin of the Rau gold-rich carbonate replacement deposit, central Yukon S. Kingston, J.K. Mortensen, J. Gabites and M. Dumala.....	213

continued

Evaluation of titanite as an indicator mineral for tungsten-skarn mineralization R. Linnen and X. Che.....	223
Pressure-depth relationships of the Roop Lakes Stock and Keno Hill Ag-Pb-Zn veins G. Lynch.....	229
Upper Fifteenmile Group in the Ogilvie Mountains and correlations of early Neoproterozoic strata in the northern Cordillera F.A. Macdonald and C.F. Roots	237
Structural controls on hydrothermal gold mineralization in the White River area, Yukon D. MacKenzie and D. Craw	253
The Proterozoic Pinguicula Group: Stratigraphy, contact relationships and possible correlations K.P.R. Medig, D.J. Thorkelson and R.L. Dunlop.....	265
Preliminary O-S isotopic compositions of Cretaceous granitoids in the Cassiar Platform and Selwyn Basin, Yukon and Northwest Territories K.L. Rasmussen and G.B. Arehart	279
Soil reconnaissance of the Fort Selkirk volcanic field, Yukon (115I/13 and 14) P. Sanborn	293
Observations of polymetallic Ag-Pb-Zn (\pm Au \pm In) mineralization at the Eagle and Fisher vein-faults, airborne total field magnetics and identification of Tombstone age-equivalent aplite dykes in the Galena Hill area, Keno City, Yukon D. Tupper and V. Bennett.....	305

Field notes on the Upper Devonian Imperial Formation (NTS map sheet 106L), Tetlit Creek, east Richardson Mountains, Yukon

Tammy L. Allen¹
Yukon Geological Survey

Allen, T.L., 2010. Field notes on the Upper Devonian Imperial Formation (NTS map sheet 106L), Tetlit Creek, east Richardson Mountains, Yukon. *In: Yukon Exploration and Geology 2009*, K.E. MacFarlane, L.H. Weston and L.R. Blackburn (eds.), Yukon Geological Survey, p. 1-21.

ABSTRACT

Although the Upper Devonian Imperial Formation is widespread across northern Yukon and Northwest Territories, its geology is poorly understood in northern Yukon. The Imperial Formation is well exposed in outcrop along the eastern flank of the Richardson Mountains, notably on Tetlit Creek and Trail River (NTS map sheet 106L). During the summer of 2008, detailed partial stratigraphic sections were measured on Tetlit Creek to record lithologic variation within the formation. In addition, samples were collected to establish the age of the strata and its source rock potential by means of palynological, geochemical and vitrinite reflectance analyses.

In the east Richardson Mountains, Imperial Formation strata can be informally subdivided into two parts. The lower is predominantly mudstone and siltstone while the upper part comprises sandstone and fine-grained siliciclastic rocks. Palynological analyses for this region have established that the Imperial Formation is late Frasnian to Famennian in age. Accompanying thermal alteration indices (T.A.I.), as well as vitrinite reflectance data, suggest that the strata are overmature with respect to hydrocarbon generation. Based on Rock Eval/TOC results from surface, most of the organic matter present within the strata are not favourable for source rock potential.

¹tammy.allen@gov.yk.ca

INTRODUCTION

Fine-grained siliciclastic rocks and sandstone successions characterize Upper Paleozoic and Cretaceous strata of the Richardson anticlinorium and adjacent Peel Plateau and Eagle Plain regions. The Imperial Formation is a thick sequence of predominantly mudstone and shale in its basal portion with an increase in sandstone higher in the succession. Although in outcrop there does not appear to be abundant organic-rich strata, the Imperial Formation is potentially an important source rock attaining a thickness of up to 1909 m on the east flank of the northern Richardson Mountains (A.W. Norris, 1997). Osadetz *et al.* (2005) suggest that the slope and shelf sandstone of the Imperial Formation may represent significant opportunities for the structural entrapment of petroleum. Little is known about the Imperial Formation including its hydrocarbon source rock potential and thermal maturity in the study area, which includes the eastern Richardson Mountains and adjacent Peel Plateau. To more fully document the character, age, hydrocarbon source rock potential and related thermal maturity of the Imperial Formation, detailed studies were undertaken. Stratigraphic sections were measured and samples collected with the results presented herein.

STUDY AREA AND LOCATION

Upper Devonian Imperial Formation exposures occur along both the western and eastern flanks of the Richardson Mountains and extend to the west under Eagle Plain and east under Peel Plateau and Plain. This paper focuses on Imperial Formation strata along the eastern flank of the Richardson Mountains that are continuously exposed over tens of kilometres on Tetlit Creek (NTS map sheets 106L/11 and 12), a tributary of the Road River, northeast Yukon (Fig. 1). Strata dip slightly to the east (010° to 020°) over much of the area. Parts of exposures were easily accessible via gravel bars along the Tetlit Creek, however deep rushing waters of Tetlit Creek often prohibited closer examination of the outcrop.

PREVIOUS WORK

A summary of Imperial Formation nomenclature and previous work is outlined in publications by Pugh (1983), A.W. Norris (1985; 1997) and Hadlari *et al.* (2009). Previous geological work on Tetlit Creek is limited to 1:250 000-scale bedrock mapping of the Trail River map sheet (NTS 106L) as part of Operation Porcupine (Norris,

1981b). During this mapping exercise, Norris separated the Imperial Formation into two parts including a lower part comprising “shale, dark grey, rusty-weathering; siltstone, dark grey” and an upper part comprising “sandstone, fine-grained, lithic, dark grey; siltstone, dark grey” (Norris, 1981a; b). The author has used these two designations in this paper.

A regional summary addressing the hydrocarbon potential of the Imperial Formation in the Peel Plateau is a petroleum resource assessment of the Peel Plateau and Plain by Osadetz *et al.* (2005), in which the Imperial Formation is identified as contributing to three conceptual natural gas plays, however little data were available for this assessment. Recommendations made by Osadetz *et al.* (2005) were followed up in the collaborative Regional Geoscience Studies and Petroleum Potential, Peel Plateau and Plain, Northwest Territories and Yukon project (“Peel Project”) by GSC, Northwest Territories Geoscience Office and the Yukon Geological Survey. Data collected and compiled on the Imperial Formation as part of this project are presented in Allen and Fraser (2008) as well as Chapters 7 and 10 of Pyle and Jones (2009). Supplementary follow-up work, including results of Rock-Eval/total organic carbon (TOC) analyses for all Yukon’s exploration oil and gas wells, is presented in Allen *et al.* (2008).

METHODOLOGY

Objectives of this study include outlining and integrating stratigraphy, as well as palynological and source rock geochemical information acquired through both reconnaissance and detailed sampling of Imperial Formation sections. Data originate from four well-exposed stratigraphic sections, ranging from 20 to 450 m thick, measured on Tetlit Creek, Yukon (NTS map sheets 106L/11 and 12; Fig. 2). The results presented here stem from field research conducted in 2008 and follow-up analysis. This research involved measuring, describing and sampling partial sections of the Imperial Formation in detail to document its occurrence, sedimentology and variability in this region, and to assess its source rock potential. This included documenting the abundance of sandstone and its relationship to adjacent fine-grained strata. Mudstone, siltstone and shale were analysed for source rock potential including quality and quantity of organic matter, as well as thermal maturity.

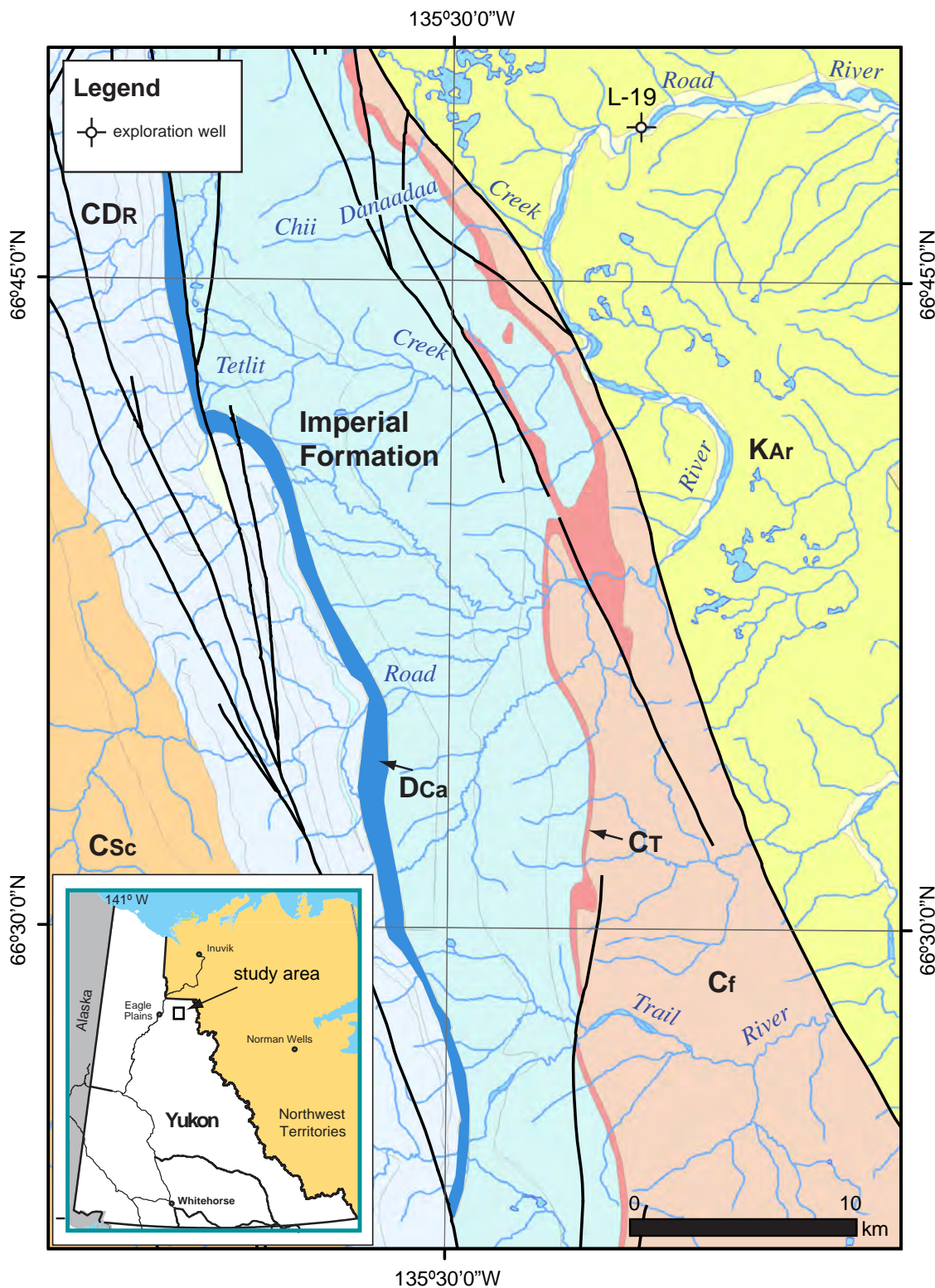


Figure 1. Location map including Tetlit Creek, Road River, Trail River and borehole Peel River Y.T. L-19. KAr = Lower Cretaceous Arctic Red Formation, Cf = Upper Devonian Ford Lake Shale, CT = Upper Devonian Tuttle Formation, DCa = Upper Devonian Canol Formation, CDR = Cambrian to Devonian Road River Group, CSc = Cambrian Slats Creek Formation. Geology from Gordey and Makepeace (2001).

MEASURED SECTIONS

Stratigraphic section 08TLA-TET-01 records lithologies of the top 50 m of the Upper Devonian Canol Formation as well as the basal 400 m of the Imperial Formation (Fig. 3). Two concise stratigraphic sections, 08TLA-TET-02 and 08TLA-TET-04 (each approximately 20 m thick), were measured in the upper part of the Imperial Formation and demonstrate the difference in the percentage of sandstone compared to the lower member (Figs. 4, 5). A fourth section, 08TLA-TET-09, of the Tuttle Formation on Tetlit Creek is included for comparison purposes (Fig. 6).

This Tuttle section was previously published in Allen *et al.* (2009).

SAMPLES

A variety of analyses were conducted on samples collected from the Imperial Formation. Seventeen samples were submitted to the Palynology Laboratory of the Geological Survey of Canada (GSC), Calgary to provide new constraints on age and thermal maturation. Thirty-four samples were submitted to the Organic Geochemistry Laboratory of the GSC, Calgary to assess hydrocarbon source rock potential and provide new

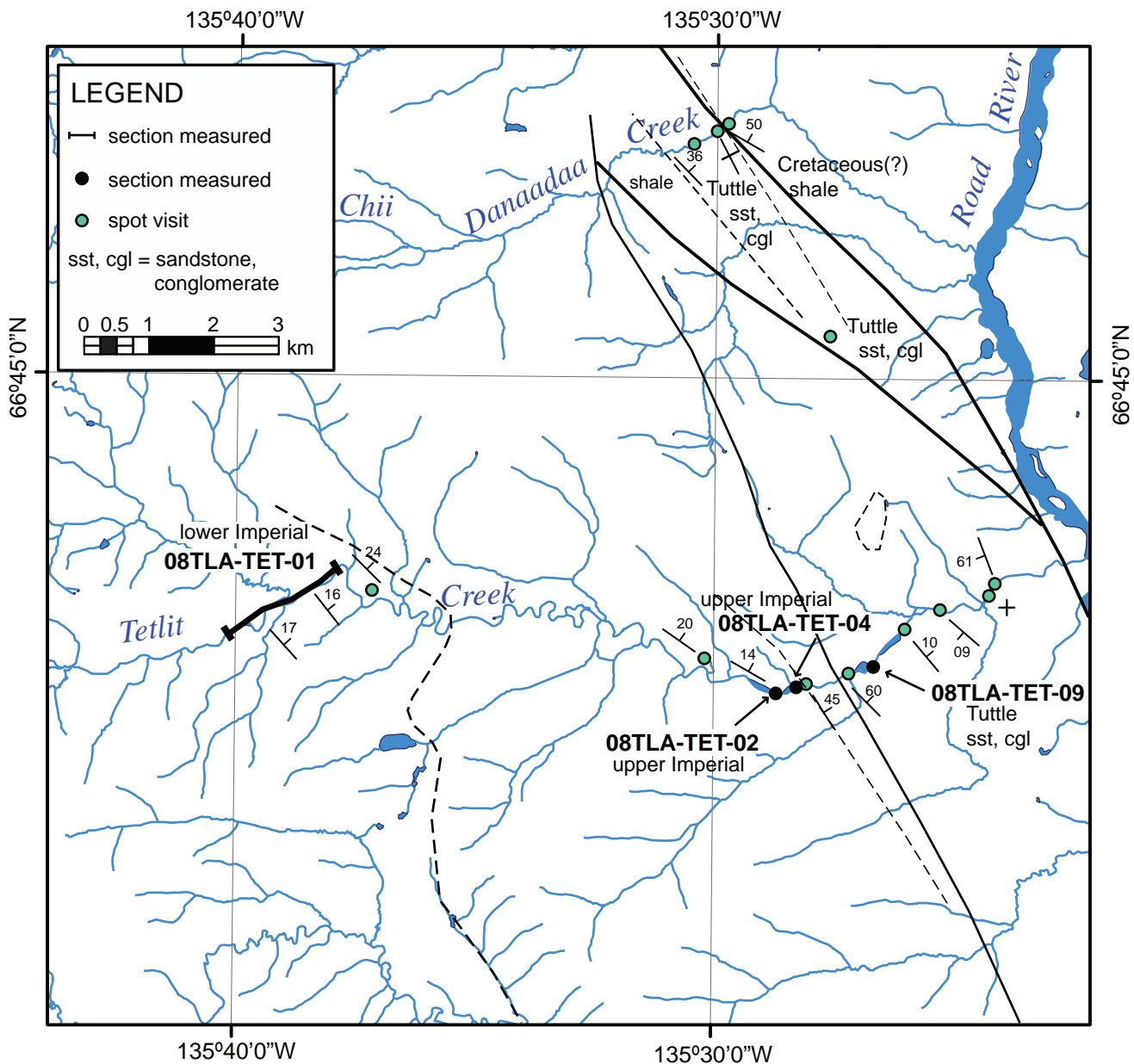


Figure 2. Map illustrating location of measured sections on Tetlit Creek.

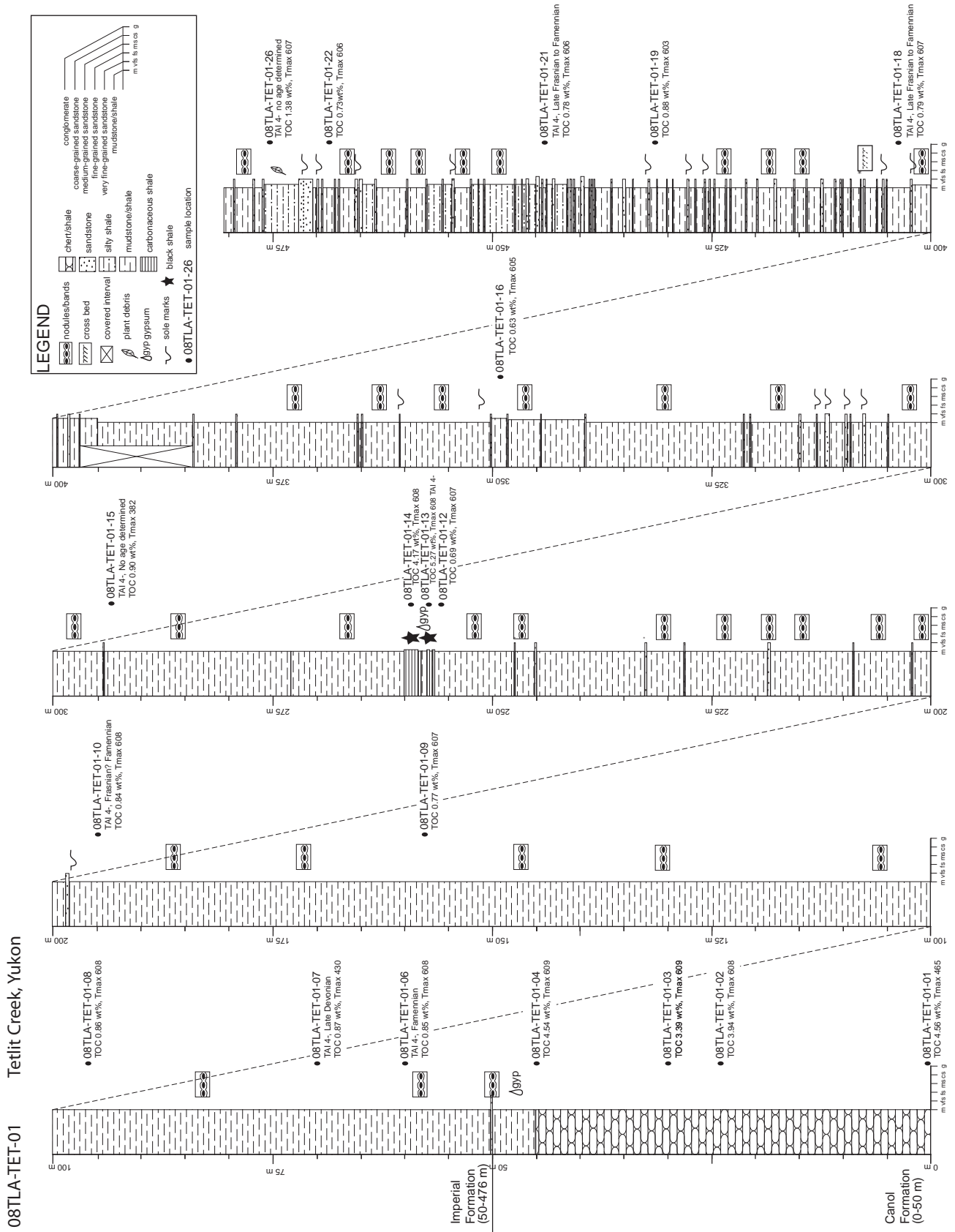


Figure 3. Measured section 08TLA-TET-01 of Canol Formation and lower Imperial Formation on Tetlit Creek, starting at UTM 470501, 7399711 (NAD83, Zone 8). The entire section was measured on the north side of Tetlit Creek (NTS map sheet 106L/12) over approximately a 2 km distance.

08TLA-TET-02 Tetlit Creek, Yukon

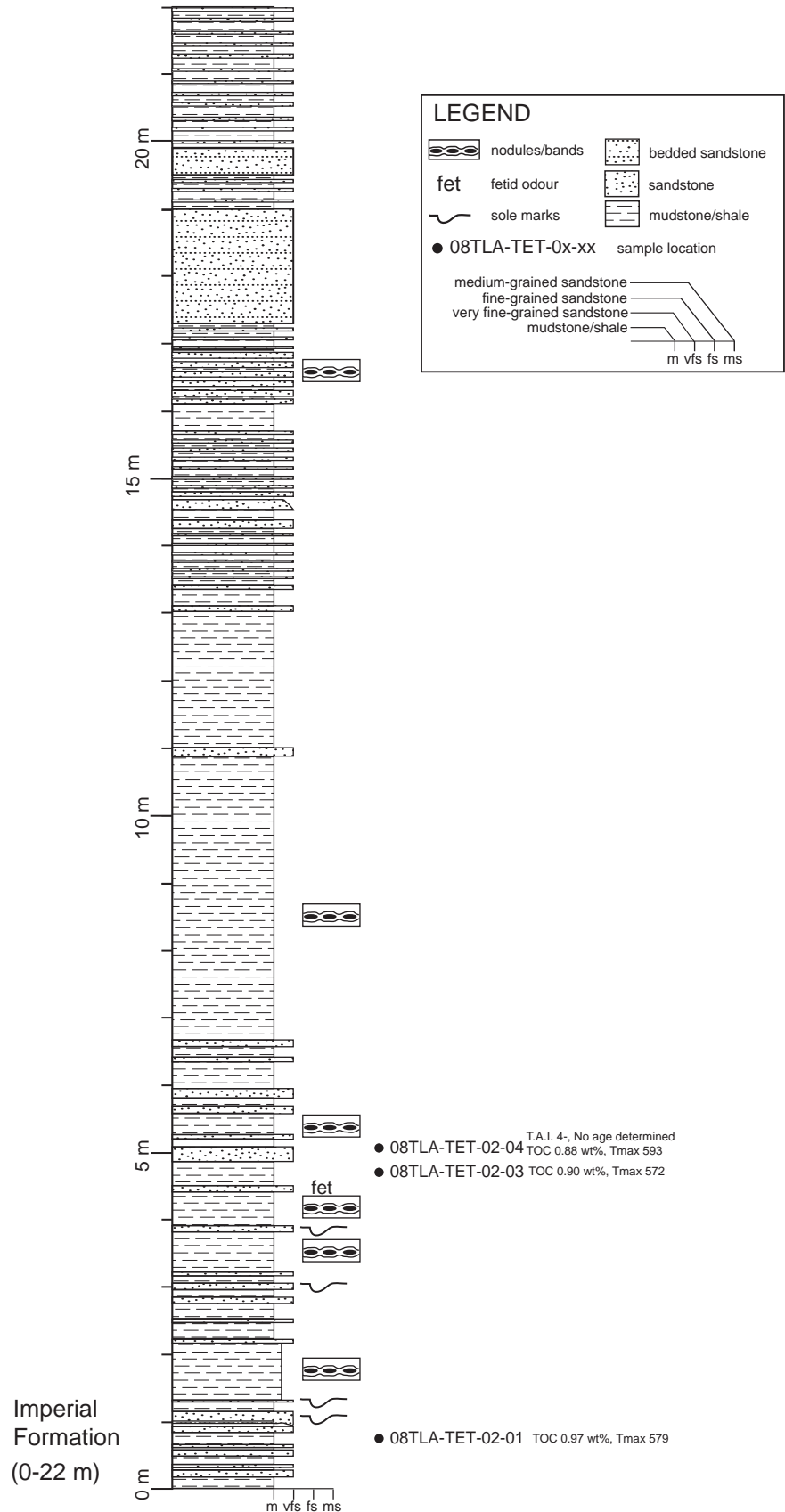


Figure 4. Measured section 08TLA-TET-02 of upper Imperial Formation on Tetlit Creek, starting at UTM 478859, 7398783 (NAD83, Zone 8). The entire section occurs on the south side of Tetlit Creek (NTS map sheet 106L/11), approximately 7 km downstream from section 08TLA-TET-01.

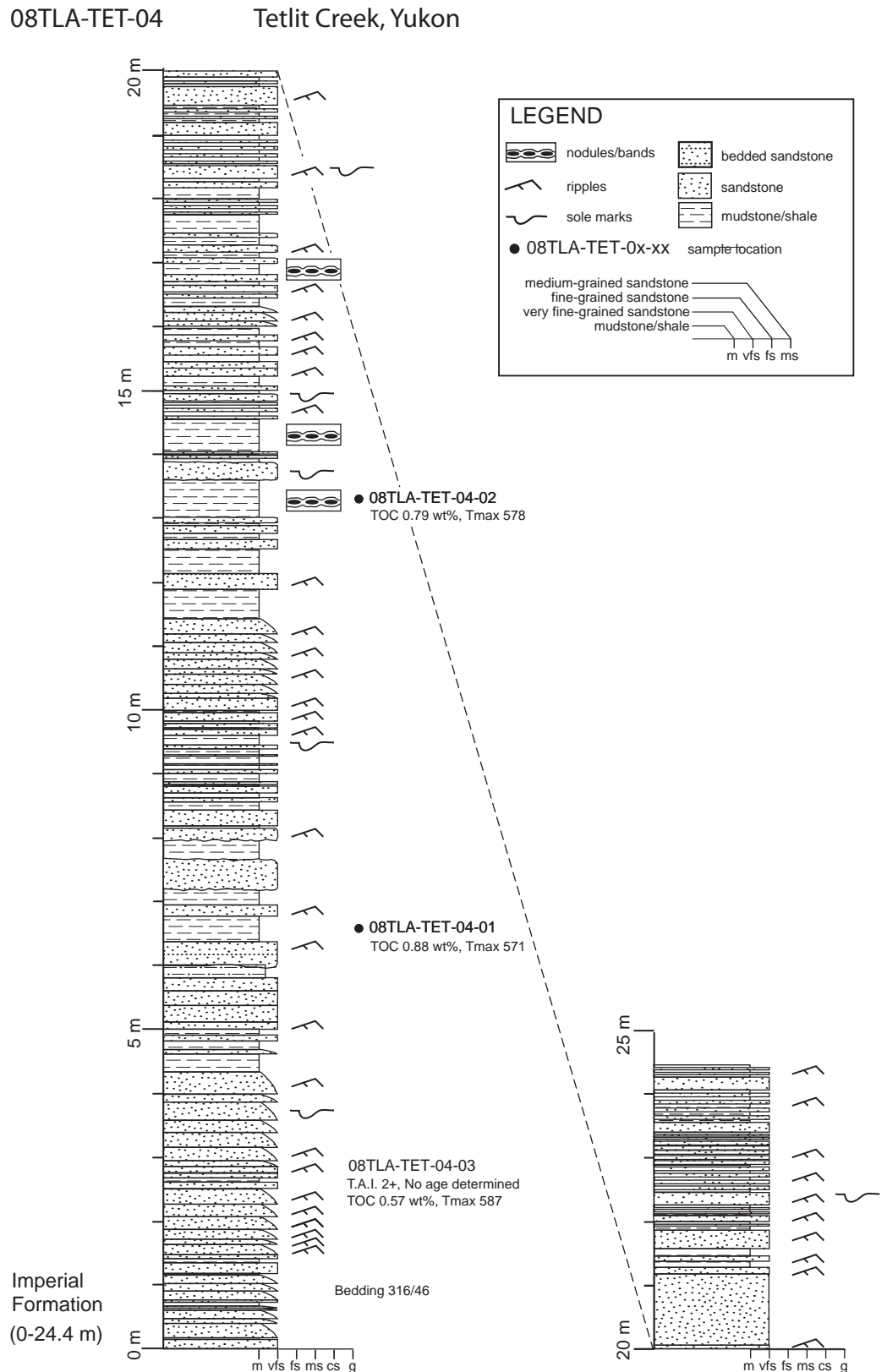


Figure 5. Measured section 08TLA-TET-04 of upper Imperial Formation on Tetlit Creek, starting at UTM 479213, 7398847 (NAD83, Zone 8). The entire section was measured on the south side of Tetlit Creek (NTS map sheet 106L/11), approximately 335 m east of section 08TLA-TET-02.

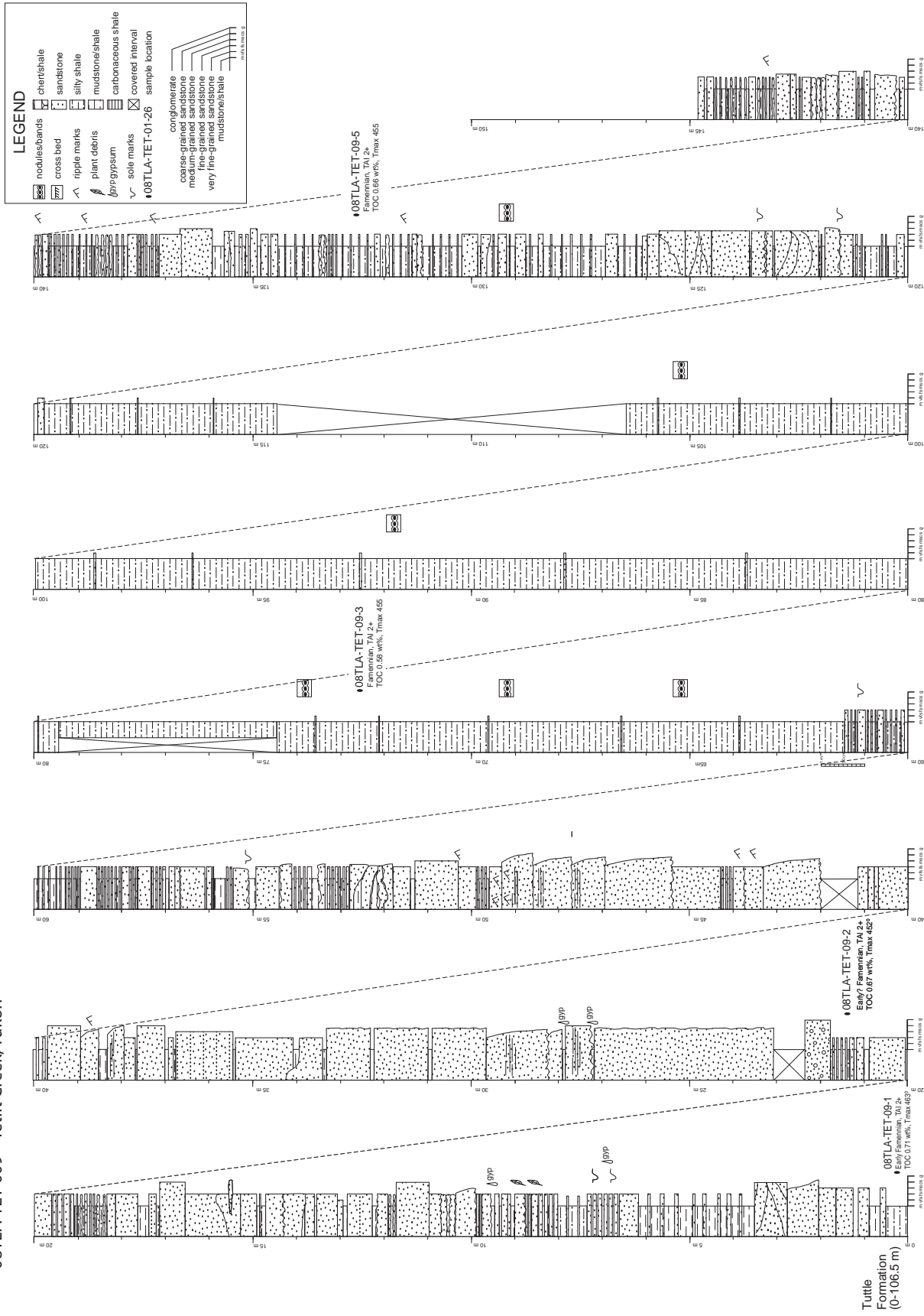


Figure 6. Measured section 08TLA-TET-09 of Tuttle Formation on Tetlit Creek, starting at UTM 480401, 7399167 (NAD83, Zone 8). The entire section was measured on the south side of Tetlit Creek (NTS map sheet 106L/11), approximately 1.2 km down stream from section 08TLA-TET-04. This section was previously published in Allen et al. (2009) and is included here for quick reference.

information on organic matter quantity, type and thermal maturity. These rock samples were pyrolyzed using Rock-Eval 6/TOC at the Organic Geochemistry Labs on a Delsi Rock-Eval 6 unit equipped with a total organic carbon (TOC) content analysis module. Peters (1986) provides a summary of interpretive guidelines for Rock-Eval data. Rock-Eval/TOC results of three mudstone samples collected on Tetlit Creek in 2007 as part of reconnaissance work during the multi-agency “Peel Project” are included here as well. Two Imperial Formation samples were submitted to the Organic Geochemistry and Organic petrology Laboratory of the GSC, Calgary to determine thermal maturity using vitrinite reflectance.

STRATIGRAPHY

Paleozoic strata, ranging from Cambrian to Early Carboniferous, flank the Richardson Mountains and underlie large areas in the Eagle Plain basin and Peel Plateau and Plain. The Imperial Formation records deposition of a clastic wedge into a foreland basin of Yukon and Ellesmerian fold belts associated with uplift during the Frasnian to Tournaisian Ellesmerian Orogeny (Pugh, 1983; Richards *et al.*, 1997). Basinal mudstone and shale with turbiditic sandstone characterize the Late Devonian Imperial Formation in this region (Braman and Hills, 1992). The Imperial Formation is conformably

underlain by the black, marine shale and chert of the Upper Devonian Canol Formation and in turn, overlain conformably by Upper Devonian to Early Carboniferous Tuttle Formation or unconformably by Cretaceous strata (Fig. 7).

CANOL FORMATION

The Upper Devonian Canol Formation (Bassett, 1961) is a marine unit characterized by black chert and siliceous shale coated in a light yellow to pale green weathering patina. Beds are predominantly hard, platy, planar and up to 10 cm thick (Fig. 8). Due to the resistant nature of the



Figure 8. Close-up of Canol Formation, Tetlit Creek. Scale card is 9 cm long.

Figure 7. Stratigraphic correlation chart of Upper Paleozoic strata illustrating the stratigraphic position of the Imperial Formation in the Richardson Mountains and Peel Plateau. The stratigraphic position for the Imperial Formation, Tuttle Formation and Ford Lake Shale (and equivalent ‘Cf’) has been modified based on new palynological data (Utting, 2008; 2009). ¹Modified from Morrow *et al.* (2006), ²modified from Pigage (2007). Time scale after Gradstein *et al.* (2004).

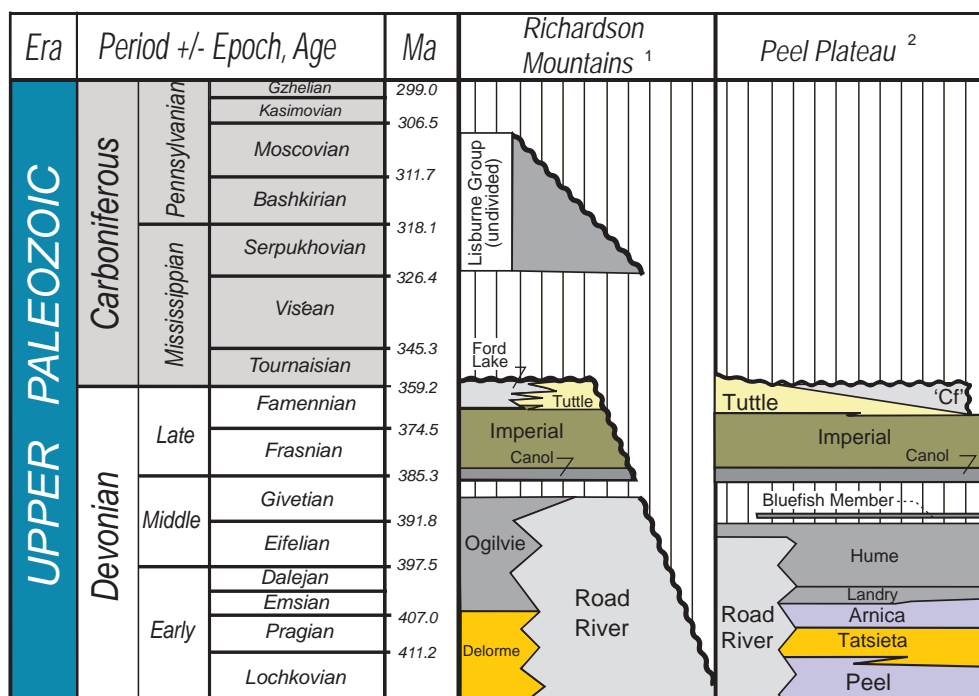




Figure 9. Photo of Canol and Imperial formations as noted on Tetlit Creek. Note the resistant nature of the Canol shale and chert in the foreground versus the recessive weathering of the Imperial Formation mudstone.

strata, the Canol Formation forms narrow canyons. On Tetlit Creek, the Canol Formation forms a canyon with rushing water that is partly inaccessible except in its upper part, which is included in section 08TLA-TET-01 (Fig. 3). Mineralization is common in the Canol Formation in the form of small, scattered pyrite nodules (up to 25 cm across) and stringers (noted by author in 2007 in exposures on Road River). Water pooling at the base of the formation is generally bright orange or rusty due to its high iron content.

The base of the Imperial Formation is partially exposed adjacent to the Upper Devonian Canol Formation on Tetlit Creek (Fig. 9). The contact between the Canol and Imperial formations, although sharp, appears to be conformable (A.W. Norris, 1997). Palynomorphs indicate a late Givetian or more probably an early Frasnian age as identified by D.C. McGregor from the Canol Formation on Trail River (Norris, 1985).

IMPERIAL FORMATION

The Imperial Formation, originally defined by Hume and Link (1945) and later modified by Bassett (1961), applies to the sequence of Upper Devonian marine to marginal marine clastic rocks and minor interbedded limestone that overlie the Canol Formation and unconformably underlie Cretaceous strata throughout a large part of the Mackenzie River area (Norris, 1985). A.W. Norris (1968) measured approximately 1816.6 m of Imperial Formation

on Trail River, which included Tuttle equivalent strata in the top 134.1 m (Norris, 1985).

The Imperial Formation has been informally subdivided into lower and upper parts, originally designated by Tassonyi (1969), later modified by Norris (1981a; b) and then Pugh (1983) who separated the conglomerate, conglomeratic sandstone and shale out of the upper Imperial Formation and assigned them to the Tuttle Formation. The usage in this paper follows Norris (1981a, b) where the lower part includes “shale, dark grey, rusty-weathering; siltstone, dark grey” and the upper part “sandstone, fine-grained, lithic, dark grey; siltstone, dark grey”.

Lower Imperial Formation

In the study area, rocks assigned to the lower member crop out mainly along Tetlit Creek, Trail River and Road River (Fig. 1). The lower member consists predominantly of non-fissile mudstone, siltstone and shale (Fig. 10). Rusty weathered nodules and continuous bands of clay and siltstone ironstone are common in the lower part of the Imperial Formation (Fig. 11). The lower part of the Imperial Formation contains little to no sandstone. The sandstone that is present is very fine grained and occurs in beds averaging 10 to 20 cm thick. On both Trail River (Allen and Fraser, field notes, 2006) and Tetlit Creek, thin organic-rich, black shale intervals were identified (Fig. 12).



Figure 10. View of section 08TLA-TET-01 of the Imperial Formation on north side of Tetlit Creek, Yukon. Here the Imperial Formation is largely grey shale and mudstone. Rusty weathered fracture surfaces give the outcrop an overall reddish hue. The thin resistant bands (<10 cm thick) are nodular layers of ironstone. Person circled for scale.



Figure 11. Close-up of lower Imperial Formation (08TLA-TET-01). The presence of clay ironstone nodules and nodular bands are ubiquitous in this unit. Pencil circled for scale.

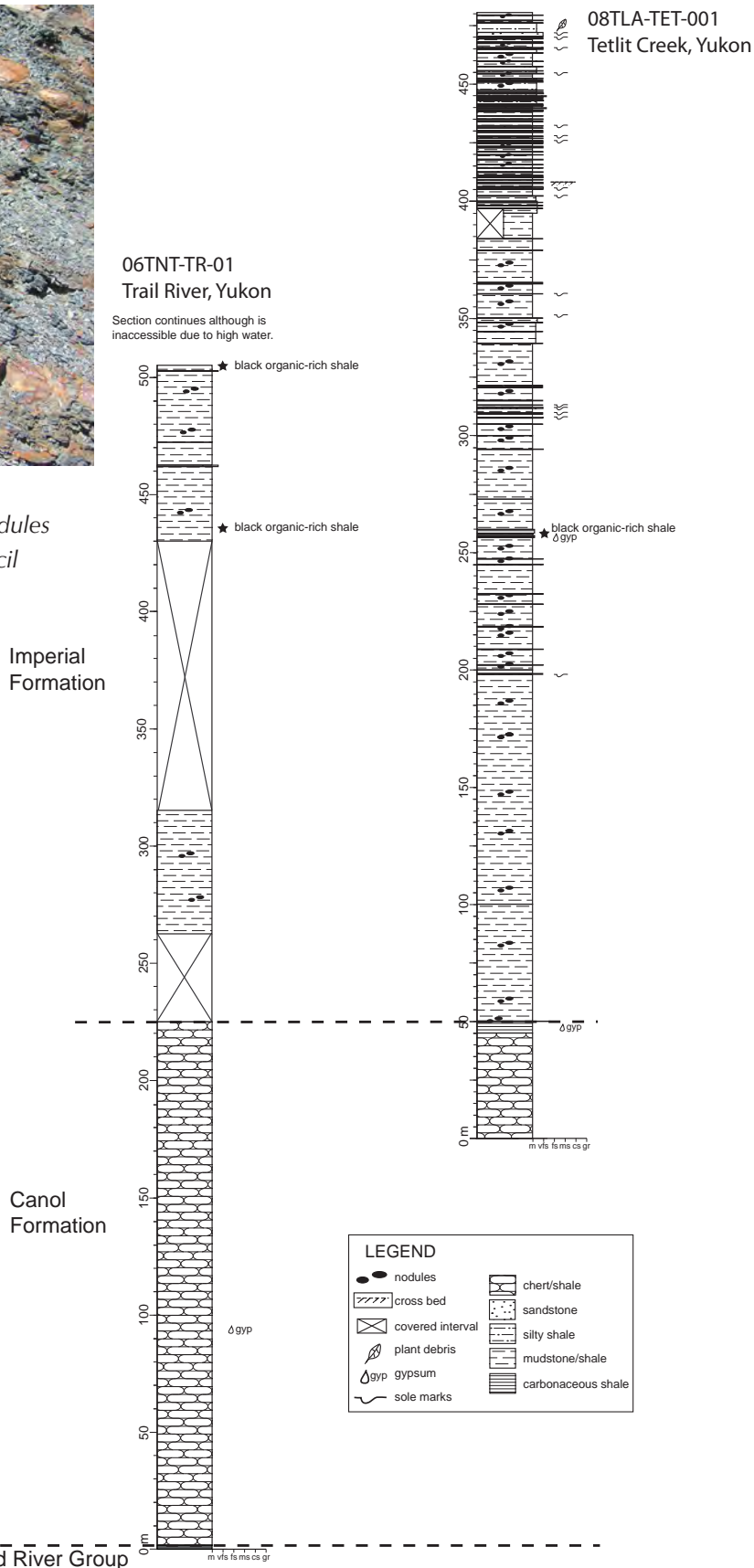


Figure 12. Correlation of Canol and lower Imperial formations on Trail River and Tetlit Creek. The Trail River section is approximately 14.5 km due south-southeast of the Tetlit Creek section. Note the occurrence of organic-rich shale at approximately the same stratigraphic level in both sections. The location of the Canol/Imperial contact on Trail River is estimated.

Mudstone

The dominant lithology in the lower member of the Imperial Formation is a combination of mudstone, shale and less commonly, siltstone. The lithology lacks fissility and commonly breaks into small irregular blocks or shards (≤ 1 cm across; Fig. 13). The mudstone and shale are medium dark grey to dark grey on the fresh surface and rusty weathered on their fracture surfaces, giving the outcrop an overall reddish or purplish hue. Locally, white to yellow popcorn-like precipitate coats the mudstone and sandstone.



Figure 13. Close-up of lower Imperial Formation on Tetlit Creek, Yukon. The unit is predominantly dark grey shale and mudstone that breaks into small irregular blocks or shards as shown here.



Figure 14. Close-up of black, organic-rich shale of the lower Imperial Formation. Hammer for scale is 28 cm long.

Nodules and laterally continuous to discontinuous bands of medium to dark grey clay and siltstone ironstone are ubiquitous throughout the lower part of the Imperial Formation. The individual nodules occur as various shapes, generally 2 to 4 cm thick, but may be up to 10 cm thick, in discrete discontinuous layers that can be traced along bedding. Faint laminae are commonly visible in these layers. These resistant and very well-indurated ironstone bands form continuous marker beds that are useful to follow when measuring sections in mudstone-dominated sections.

Black, organic-rich shale

Within the lower Imperial Formation (section 08TLA-TET-01), four bands of fissile, black, organic-rich shale were recorded over a 3.7-m interval within grey mudstone (Fig. 14). These beds are 30, 25, 35 and 165 cm thick and occur approximately 200 m above the base of the Imperial Formation. Their contacts are abrupt with the underlying and overlying mudstone. From afar, these bands may be easily mistaken with sandstone intervals due to their brown rusty weathering and resistant nature (Fig. 15).

Thin-bedded sandstone

Sandstone in the lower Imperial Formation weathers yellowish grey and is dark grey on the fresh surface. The sandstone is very fine grained, quartz-rich with lesser chert and finely micaceous. Some sandstone beds show a fining upward with an abrupt massive base, grading up into parallel laminated sandstone and siltstone, passing



Figure 15. Outcrop of black, organic-rich shale interval, approximately 200 m above the base of the Imperial Formation on Tetlit Creek. This interval is 165 cm thick.

upward into mudstone. The basal contacts of the sandstone beds are typically abrupt with underlying units, and are planar to undulating with local scours apparent with up to 3 cm of relief. Tool and flute marks were also observed and measurable. Plant impressions on top of sandstone beds were observed, though are not common. Utting (2009) identified abundant woody and coaly fragments in samples of both the lower and upper Imperial Formation mudstone.

The sandstone forms continuous resistant ledges within the more recessive mudstone and siltstone of the formation, notably above 350 m stratigraphic thickness. The sandstone beds range in thickness from 3 cm to 55 cm but are generally 10 to 20 cm thick. The thickest sandstone package noted was 170 cm thick at approximately 420 m above the base of the Imperial Formation (08TLA-TET-01). This sandstone, comprises two large beds separated by 10 cm of shale, is fine grained, dark grey and has a scoured base with flute marks as well as coalified plant debris. The upper part of this sandstone package is parallel laminated and fines upward into siltstone.

Upper Imperial Formation

Concise stratigraphic sections (08TLA-TET-02 and 08TLA-TET-04) were measured of the upper Imperial Formation (Figs. 4, 5). In these sections, it is apparent that sandstone is much more common than in the lower Imperial Formation, with sandstone comprising more than 50 percent of the strata. Mudstone and siltstone intervals, 1 to 50 cm thick, are interstratified with sandstone intervals of similar thickness.

Sandstone

Sandstone in the upper Imperial Formation is very fine grained, moderately to poorly sorted and quartz-rich. It weathers from moderate reddish brown to yellowish grey and is medium dark grey to dark grey on the fresh surface. In hand specimen, the sandstone appears to be similar in composition to the lower Imperial Formation. The sandstone is well indurated with little to no apparent porosity. Allen and Fraser (2008) reported negligible porosity and permeability for the Imperial Formation based on standard porosity and permeability procedures by AGAT Laboratories, and on thin section analyses of representative samples of the formation collected from Trail River. The sandstone beds are variable in thickness, ranging from 2 to 54 cm thick and averaging 12 to 20 cm. The sandstone beds are generally tabular and ledge-

forming amongst the finer grained siliciclastic rocks in which they occur (Fig. 16). Individual bed thicknesses commonly vary laterally, giving sandstone beds a lensoidal appearance. The bases of the beds are sharp (Fig. 17) and commonly undulating, due to scouring into underlying fines by as much as 15 cm. Bases of sandstone beds commonly exhibit flute and/or tool marks indicating flow directions. The tops of the sandstone beds are either in sharp contact with overlying mudstone or demonstrate a fining-upward succession in which the sandstone grades



Figure 16. Typical exposure of the upper Imperial Formation on Tetlit Creek characterized by sandstone beds (5 to 10 cm thick) separated by mudstone and shale intervals of similar thickness.



Figure 17. Close-up of sandstone in upper Imperial Formation on Tetlit Creek showing abrupt undulating basal contact over shale and visible sole marks. Circled pencil for scale.

Figure 18. Thick sandstone and conglomerate beds of Tuttle Formation exposed on south side of Tetlit Creek. Person circled for scale.



up into siltstone and finally mudstone. The top parts of these graded beds are often rippled or parallel laminated.

Higher in the stratigraphic succession, the relative abundance of sandstone to mudrock continues to increase. The percentage of sandstone, individual bed thickness and grain size gradually increases up section, presumably grading into the Tuttle Formation. Approximately 850 m due east of section 08TLA-TET-04, the sandstone is light grey, medium to coarse grained, poorly sorted, rich in quartz and multi-coloured chert grains (white, green, black, grey) with a white chalky infill between the grains. This lithology is very similar to the Tuttle Formation observed on Trail and Road rivers (Fraser and Allen, 2007).

Along the Richardson Mountains, the top of the Imperial Formation is marked by the occurrence of either the sandstone and/or conglomerate or silty shale of the Tuttle Formation or the Dus map unit of Norris (1981b) and A.W. Norris (1997). In the northern part of the Trail River map sheet, Norris (1981b) mapped Upper Jurassic to Lower Cretaceous North Branch Formation on top of the Imperial Formation, with the unconformable contact representing the sub-Cretaceous unconformity.

TUTTLE FORMATION

Norris (1981a; b) mapped the Upper Devonian to Lower Carboniferous sandstone and conglomerate of the Peel and Eagle Plain region as the Tuttle Formation, which was later formally designated by Pugh (1983). The sandstone in this unit is lithologically distinct from the Imperial

Formation due to its bed thickness (Fig. 18), light grey colouring, coarser grain size, poor sorting, abundance of visible quartz and multi-coloured (grey, green, black and white) chert grains within a kaolin-filled matrix (Fig. 19). The conglomerate in this unit ranges from granule to pebble conglomerate and tends to be more commonly observed in the northern part of the Trail River map sheet (106L; Fraser and Allen, 2007). The Tuttle Formation is resistant and crops out in the drainages making it a good marker unit. Figure 6 illustrates the Tuttle Formation section measured on Tetlit Creek (08TLA-TET-09).

The contact between the Imperial and Tuttle formations appears to be gradational but diachronous and likely intertongues (Pugh, 1983). Pugh (1983) states that the base of the Tuttle Formation can be distinguished from the underlying Imperial Formation by the first occurrence of conglomerate, silicified beds or brownish-black shale. On Tetlit Creek, there is a break in exposure between the Imperial Formation and the Tuttle Formation and therefore the contact relationship has not been included in a measured section. This may be related to the recessive nature of fine-grained packages in the Imperial, or to the north-trending fault mapped by Norris (1981b).

PALYNOLOGY AND PROBABLE AGE

Fossils were uncommon in the components of the Imperial Formation examined for this study, with the exception of scattered coalified plant debris and palynomorphs. Pollen and spores identified from the Imperial Formation on Tetlit Creek sections have been

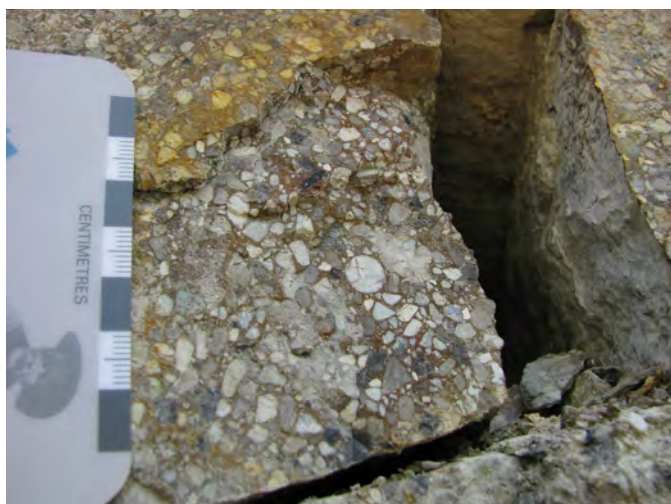


Figure 19. Close-up of Tuttle Formation chert granule to pebble conglomerate, Tetlit Creek.

assigned a Frasnian to Famennian (Late Devonian) age (Utting, 2008; 2009). This age range is consistent with palynomorphs identified in Imperial Formation on Trail River, also assigned to Frasnian to early Famennian(?)

(14.5 km to the south; Utting, 2007). In 6 of 13 samples submitted from Tetlit Creek, the preservation of spores was too poor for identification and thus, no age was determined.

In 3 of 6 samples from correlative Imperial Formation strata on Trail River, spores are common but preservation is very poor due to sulphide pseudomorphs and high thermal maturity (Utting, 2007). The high thermal maturity in some samples has resulted in a large number of specimens being too dark to be confidently identified. Exceptions include species of *Hystricosporites* and *Ancyrospora* that have a distinctive ornament of grapnel tipped spines that are recognizable even on specimens that are black (Utting, 2007).

Recent palynological studies of Tuttle Formation strata on Trail River indicate that the formation is late Frasnian to Strunian (latest Famennian) in age (Utting, 2007; 2008). Palynomorphs identified from the six samples collected from Tuttle Formation strata on Tetlit Creek are assigned an early to late Famennian age (Utting, 2008; 2009; Table 1), which is consistent with the results from Trail River.

Table 1. Summary of palynological data including probable age and thermal alteration index (T.A.I.) for the Imperial and Tuttle formations.

Sample	GSC C-Nos.	Probable age	Formation	T.A.I.	NAD83, Zone 8		Reference
					UTME	UTMN	
08TLA-TET-01-06	532919	Famennian, Late Devonian	Imperial	4-	470627	7399851	Utting, 2009
08TLA-TET-01-07	532920	Late Devonian	Imperial	4-	470654	7399864	Utting, 2009
08TLA-TET-01-10	532921	Frasnian(?), Famennian, Late Devonian	Imperial	4-	471144	7400102	Utting, 2009
08TLA-TET-01-13	481986	none	Imperial	4-	471356	7400236	Utting, 2009
08TLA-TET-01-15	532922	none	Imperial	4-	471555	7400282	Utting, 2009
08TLA-TET-01-18	532923	late Frasnian to Famennian, Late Devonian	Imperial	4-	471933	7400370	Utting, 2009
08TLA-TET-01-21	532924	late Frasnian to Famennian, Late Devonian	Imperial	4-	472097	7400445	Utting, 2009
08TLA-TET-01-26	532925	not determined	Imperial	4-	472162	7400584	Utting, 2009
<i>07TNT-TET-22A</i>	<i>473141</i>	<i>Devonian</i>	<i>Imperial</i>	<i>4-</i>	<i>477777</i>	<i>7399240</i>	<i>Utting, 2008</i>
<i>07TNT-TET-23A</i>	<i>473142</i>	<i>Famennian(?), Late Devonian</i>	<i>Imperial</i>	<i>4-</i>	<i>472740</i>	<i>7400219</i>	<i>Utting, 2008</i>
08TLA-TET-02-04	532926	not determined	Imperial	4	478836	7398794	Utting, 2009
08TLA-TET-04-03	532927	not determined	Imperial	2	479213	7398847	Utting, 2009
08TLA-TET-06-03	532928	not determined	Imperial	4-	479913	7399032	Utting, 2009
08TLA-TET-09-01	532929	early Famennian, Late Devonian	Tuttle	2+	480401	7399167	Utting, 2009
08TLA-TET-09-02	532930	early(?) Famennian, Late Devonian	Tuttle	2+	480471	7399267	Utting, 2009
08TLA-TET-09-03	532931	Famennian, Late Devonian	Tuttle	2+	480499	7399314	Utting, 2009
08TLA-TET-09-05	532932	Famennian, Late Devonian	Tuttle	2+	480534	7399371	Utting, 2009
<i>07TNT-TET-21A</i>	<i>473139</i>	<i>Late Devonian</i>	<i>Tuttle</i>	<i>2</i>	<i>482352</i>	<i>7400500</i>	<i>Utting, 2008</i>
<i>07TNT-TET-21B</i>	<i>473140</i>	<i>late(?) Famennian, Late Devonian</i>	<i>Tuttle</i>	<i>2</i>	<i>482286</i>	<i>7400408</i>	<i>Utting, 2008</i>

Italics previously published in Allen and Fraser (2008).

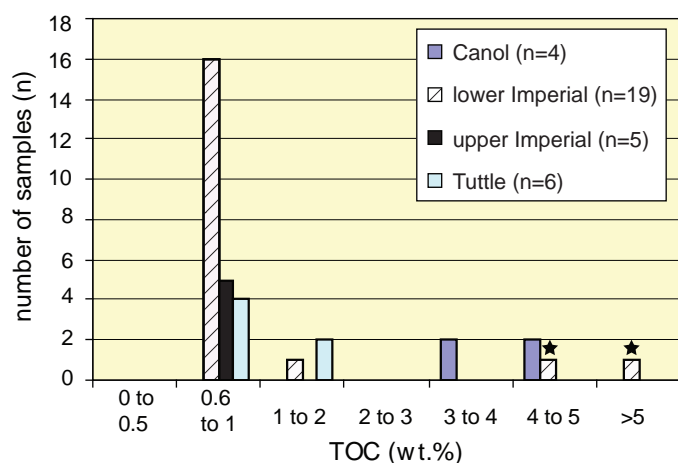


Figure 20. Histogram summarizing total organic carbon (TOC), expressed in weight percent (wt%), from samples collected during this study of the Canol, Imperial and Tuttle formations. Note that the two black, organic-rich shale samples (stars) had TOC values similar to the Canol Formation.

SOURCE ROCK POTENTIAL

Thirty-four samples collected from Tetlit Creek were analysed for source rock determination using Rock-Eval pyrolysis/TOC analysis. These analyses provide implications for source rock distribution and quality, thermal maturation and hydrocarbon potential. Table 2 summarizes Rock-Eval/TOC results. Figure 20 illustrates the distribution of the number of samples by formation, and the corresponding weight percent (wt%) of total organic carbon (TOC). TOC values for the Imperial Formation on Tetlit Creek range from 0.57 to 1.38 wt%, with the exception of two samples collected from black, organic-rich shale intervals (25 and 165 cm thick) which measured 5.27 and 4.17 wt%, respectively. With the exception of these two black shale intervals, TOC values suggest that the Imperial Formation is generally not a favourable source rock. These TOC values are consistent with values reported for Imperial Formation strata in Peel Plateau subsurface (*i.e.*, boreholes C-60, G-72, F-37, H-71 and H-37), which generally have TOC values <1 wt%. Subsurface S₂ values, however, measure >0.2 mg HC/g rock suggesting thermal maturities are within the “oil window” (Allen *et al.*, 2008).

The Canol and Imperial formation samples are all overmature and the original kerogen type cannot reliably be determined from geochemical data. The type of organic matter in the Canol Formation could not be determined using the pseudo-van Krevelen diagram due to high thermal maturities which result in values plotting too low to be meaningful (Peters, 1986). Plotting the Imperial Formation hydrogen and oxygen indices on a pseudo-van Krevelen diagram (Fig. 21a) suggests that types III (gas-prone) and IV (inert or dry-gas prone) kerogen are present in the rocks. Type IV kerogen can originate from other kerogen types that were reworked or oxidized (Peters *et al.*, 2005). Outcrop samples commonly show depletion in S₁ and S₂ due to weathering (Peters, 1986). Caution should be used with samples that have S₂ values below 0.2 mg HC/g rock, as they are unreliable due to the broad nature of their S₂ peak (Peters, 1986). Rock-Eval and TOC results from outcrop suggest that the Imperial Formation has little to no hydrocarbon-generating potential. This is misleading due to the very low S₂ values and related high thermal maturities which can make source rocks appear less like a source rock (Dembicki, 2009). Results for the Tuttle Formation plot along the base of the type II and III kerogen evolutionary pathways suggesting the organic matter is likely gas-prone.

Thermal maturity levels of stratigraphic successions can be estimated using T_{max} values derived from Rock-Eval pyrolysis, thermal alteration indices and vitrinite reflectance. Most samples analysed from the Canol and Imperial formations have very low S₂ values, less than 0.2 mg HC/g rock, and are therefore unreliable predictors of thermal maturity and production index (S₁/(S₁+S₂)). T.A.I. corresponds to maturity-induced colour changes noted in miospores under the microscope in transmitted light (Staplin, 1969). T.A.I. values estimated by Utting (2008; 2009) also indicate that the Imperial Formation is thermally mature (Tables 1, 2). Vitrinite reflectance (%Ro_R), a key measurement used to assess petroleum source rocks, was performed on selected samples. Collectively, the high thermal maturity values imply that, at surface, the Canol and Imperial formations are thermally overmature. This is consistent with results for the Imperial Formation on Trail River, reported in Allen and Fraser (2008) and by Norris (1985) who reported that D.C. McGregor determined that all of the unoxidized spores from the Imperial Formation on Trail River are dark brown to black indicating severe thermal maturation.

Table 2. Summary of Rock-Eval/TOC outcrop data, as well as thermal maturity indicators, thermal alteration index (T.A.I.) and vitrinite reflectance (%Ro_R) (OGOPet Lab, 2009; Coal Maceral and Vitrinite Reflectance) from Tetlit Creek. Parameters measured and derived from Rock-Eval pyrolysis include TOC = total organic carbon as percent weight of whole rock; S1 = mg hydrocarbons per gram of rock; S2 = mg hydrocarbons/g rock; S3 = mg CO₂/g rock; PI = Production Index (S1/S1+S2); HI = Hydrogen Index (100 x (S2/TOC)); OI = Oxygen Index (100 x (S3/TOC)); T_{max} = maximum temperature (°C) at top of S2 peak. Note where S2 values are less than 0.2 mg HC/g rock, the PI and T_{max} values are unreliable (values in italics). T.A.I. 3+/4- and T.A.I. 4- indicate strata are overmature or within the dry gas zone, while T.A.I. 2 and T.A.I. 2+ correspond to the “oil window” (Utting et al., 1989). *Organic-rich, black shale of lower Imperial Formation.

Sample	TOC	S1	S2	S3	PI	HI	OI	T _{max} (°C)	T.A.I.	VR %Ro _R	NAD83, Zone 8		
											UTME	UTMN	Formation
08TLA-TET-01-1	4.56	0.02	0.05	0.32	0.24	1	7	465			470502	7399710	Canol
08TLA-TET-01-2	3.94	0.01	0.02	0.32	0.35	1	8	608			470541	7399760	Canol
08TLA-TET-01-3	3.39	0.01	0.04	1.65	0.20	1	49	609			470577	7399768	Canol
08TLA-TET-01-4	4.54	0.01	0.03	0.64	0.19	1	14	609			470611	7399814	Canol
08TLA-TET-01-6	0.85	0.01	0.04	0.18	0.12	5	21	608	4-		470627	7399851	lower Imperial
08TLA-TET-01-7	0.87	0.01	0.04	0.28	0.12	5	32	430	4-		470654	7399864	lower Imperial
08TLA-TET-01-8	0.86	0.00	0.03	0.19	0.13	3	22	608			470852	7399826	lower Imperial
08TLA-TET-01-9	0.77	0.01	0.03	0.48	0.17	4	62	607			470981	7399934	lower Imperial
08TLA-TET-01-10	0.84	0.00	0.02	0.54	0.21	2	64	608	4-		471144	7400102	lower Imperial
08TLA-TET-01-12	0.69	0.00	0.03	0.27	0.12	4	39	607			471356	7400236	lower Imperial
*08TLA-TET-01-13	5.27	0.01	0.04	0.65	0.26	1	12	608	4-	2.27	471356	7400236	lower Imperial
*08TLA-TET-01-14	4.17	0.01	0.04	0.53	0.20	1	13	608			471356	7400236	lower Imperial
08TLA-TET-01-15	0.90	0.03	0.09	0.27	0.23	10	30	382	4-		471555	7400282	lower Imperial
08TLA-TET-01-16	0.63	0.01	0.05	0.21	0.13	8	33	605			471768	7400272	lower Imperial
08TLA-TET-01-18	0.79	0.00	0.03	1.27	0.10	4	161	607	4-		471933	7400370	lower Imperial
08TLA-TET-01-19	0.88	0.01	0.05	0.82	0.11	6	93	603			472015	7400465	lower Imperial
08TLA-TET-01-21	0.78	0.01	0.05	0.21	0.13	6	27	606	4-		472097	7400445	lower Imperial
08TLA-TET-01-22	0.73	0.00	0.03	0.20	0.11	4	27	606			472160	7400544	lower Imperial
08TLA-TET-01-26	1.38	0.01	0.03	0.80	0.18	2	58	607	4-	2.36	472162	7400584	lower Imperial
07TNT-TET-23A	0.57	0.00	0.02	0.23	0.12	4	40	605	4-		472740	7400219	lower Imperial
08TLA-TET-02-1	0.97	0.00	0.10	0.28	0.04	10	29	579			478900	7398756	lower Imperial
08TLA-TET-02-3	0.90	0.00	0.09	0.21	0.04	10	23	572			478836	7398794	lower Imperial
08TLA-TET-02-4	0.88	0.01	0.07	0.41	0.07	8	47	593	4		478836	7398794	lower Imperial
07TNT-TET-22A	0.86	0.01	0.10	0.17	0.06	12	20	581	4-		477777	7399240	upper Imperial
08TLA-TET-04-1	0.88	0.01	0.12	0.36	0.05	14	41	571			479213	7398847	upper Imperial
08TLA-TET-04-2	0.79	0.01	0.09	0.43	0.06	11	54	578			479213	7398847	upper Imperial
08TLA-TET-04-3	0.57	0.01	0.10	0.15	0.06	18	26	547	2		479213	7398847	upper Imperial
08TLA-TET-06-3	0.69	0.01	0.21	0.16	0.06	30	23	484	4-		479913	7399032	upper Imperial
08TLA-TET-09-1	0.71	0.03	0.27	0.24	0.11	38	34	463	2+		480401	7399167	Tuttle
08TLA-TET-09-2	0.67	0.01	0.29	0.41	0.04	43	61	452	2+		480471	7399267	Tuttle
08TLA-TET-09-3	0.58	0.03	0.19	0.13	0.13	33	22	455	2+		480499	7399314	Tuttle
08TLA-TET-09-5	0.66	0.01	0.32	0.34	0.04	48	52	455	2+		480534	7399371	Tuttle
07TNT-TET-21A	1.31	0.06	1.21	0.20	0.05	92	15	437	2		482352	7400500	Tuttle
07TNT-TET-21B	1.29	0.04	1.29	0.18	0.03	100	14	447	2		482286	7400408	Tuttle

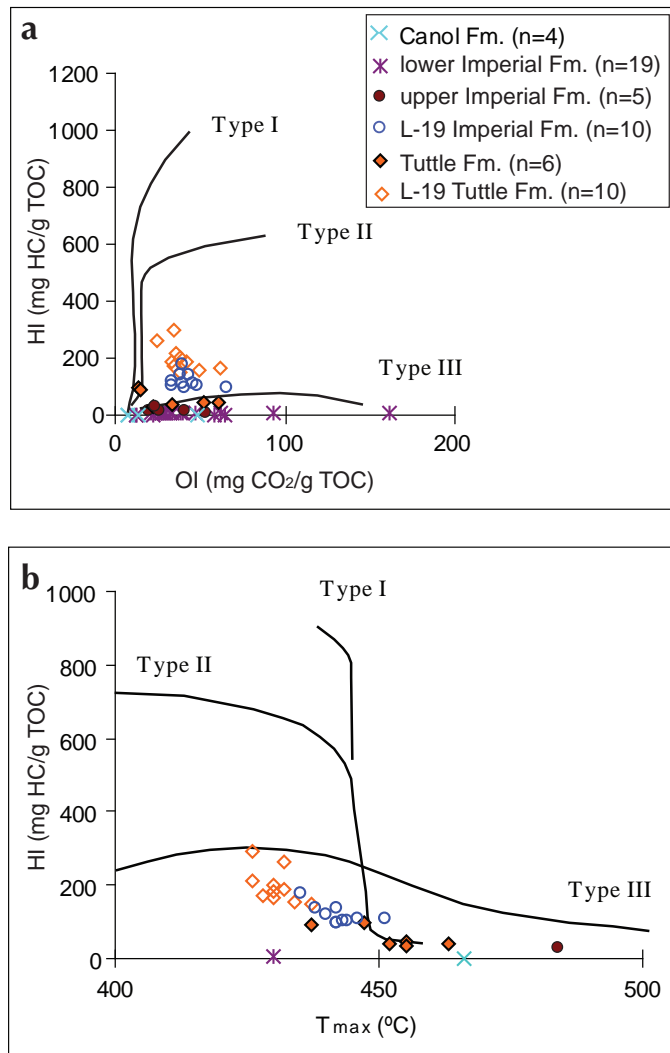


Figure 21. Cross plots of Rock-Eval and TOC data; n = number of samples. (a) Oxygen indices (OI) and hydrogen indices (HI) plotted on a pseudo van Krevelen diagram. Due to low S_2 values and very high thermal maturities, most values plot too low on the diagram to be meaningful (Peters, 1986). Imperial samples plot along the type III evolutionary pathway, while Tuttle samples plot on both the type II and III. Borehole L-19 data from Allen *et al.* (2008). (b) The T_{max} versus HI cross plot indicates that the Tuttle Formation contains types II and III kerogen. Due to the unreliable T_{max} data for most of the dataset, most values from surface samples do not plot on this cross plot. Borehole L-19 data from Allen *et al.* (2008).

Borehole Peel River Y.T. L-19 (U.W.I. 300L196650135150) is the closest oil and gas exploration well to Tetlit Creek that penetrated the Imperial Formation. In this well, T_{max} values for the Imperial Formation range from 435° to 451°C (Table 3), showing a gradual increase in maturity with increasing depth (Allen *et al.*, 2008). These thermal maturity results for L-19 and for exploration wells to the east (e.g., C-60, F-37, G-72, H-37 and I-21) indicate that Imperial Formation strata are within the “oil window” (Allen *et al.*, 2008). These results show a discrepancy from outcrop sample results that typically indicate that Imperial strata are overmature with respect to hydrocarbon generation. Organic matter within the Imperial Formation subsurface comprises type II, oil- and gas-prone kerogen, and type III, gas-prone kerogen (Allen *et al.*, 2008; Figure 21). A possible explanation for the discrepancy in the thermal maturation between the surface and subsurface may be proximity to the Richardson Mountains and related structural histories that resulted in higher thermal maturity levels for outcrop samples.

CONCLUSIONS

The lower part of the Imperial Formation is distinct from the upper part, most notably in the abundance of sandstone. The lower Imperial Formation is predominantly non-fissile mudstone and shale with lesser siltstone and sandstone. Rusty weathered clay ironstone bands and nodules are very common in the lower Imperial Formation. Thin, organic-rich, black shale intervals with high TOC values were documented in the lower Imperial Formation on Tetlit Creek. Similar shale documented on Trail River occurs at approximately the same stratigraphic level. The geographic extent and thickness of this organic-rich shale interval is uncertain.

The upper Imperial Formation contains at least 50% sandstone. The sandstone is very fine grained, well indurated, with no visible porosity. The abundance of sandstone beds, bed thickness and grain size increases up section, until it grades into the Tuttle Formation. The sandstones are characterized by their very fine grain size and sharp basal contacts that commonly exhibit sole marks. Fossils are uncommon although some coalified plant debris was observed. Other sedimentary structures noted associated with the sandstone beds include graded beds, parallel- to cross-laminae and scours.

Palynology results indicate that the Imperial Formation is Frasnian to Famennian (Late Devonian) in age. Associated T.A.I. values indicate that the Imperial Formation strata are

overmature with respect to hydrocarbon generation at surface. Due to high thermal maturities, spore and pollen identification was prohibitive in some samples. Corresponding vitrinite reflectance values also indicate high thermal maturation for the strata.

Rock-Eval/TOC pyrolysis results indicate that kerogen within the Imperial Formation strata are possibly type III or terrestrially-derived organic matter (gas-prone). TOC values suggest that the Imperial Formation has overall low total organic carbon contents (0.57 to 1.38 wt%), with the exception of thin organic-rich, black shale intervals noted in the lower Imperial Formation (4.17 and 5.27 wt%). Combined Rock-Eval/TOC results from surface suggest that the Imperial Formation is not a favourable source rock. Rock-Eval/TOC results from subsurface samples east of the Richardson Mountains indicate that the Imperial Formation strata are within the “oil window” and contain types II and III kerogen (oil- to gas-prone) indicating much better prospects of being a suitable petroleum source rock.

ACKNOWLEDGEMENTS

I would like to thank Bailey Staffen for providing excellent field assistance. Trans North Helicopters provided safe and reliable helicopter support. This manuscript benefited from review by Tiffani Fraser and editorial comments by Lauren Blackburn.

REFERENCES

Allen, T.L. and Fraser, T.A., 2008. Hydrocarbon potential of Upper Paleozoic strata, eastern Richardson Mountains, northern Mackenzie Mountains and Peel Plateau, Yukon. *In: Yukon Exploration and Geology 2007*, D.S. Emond, L.R. Blackburn, R.P. Hill and L.H. Weston (eds.), Yukon Geological Survey, p. 91-114.

Table 3. Summary of Rock-Eval/TOC data for borehole Peel River Y.T. L-19 (U.W.I. 300L196650135150), previously published in Allen et al. (2008). Location of well is UTM 486115E, 7410232N, Zone 8, NAD83.

Sample depth from (F)	Sample depth from (F)	TOC (wt%)	S1 (mg HC/g rock)	S2 (mg HC/g rock)	S3 (mg CO ₂ /g rock)	Production index (S1/(S1+S2))	Hydrogen index (mg HC/ g TOC)	Oxygen index (mg CO ₂ /g rock)	T _{max} (°C)	Formation
160	190	2.94	0.36	6.23	1.07	0.05	212	36	426	Tuttle
510	540	1.50	0.36	4.40	0.52	0.08	293	35	426	Tuttle
810	840	0.83	0.22	1.42	0.29	0.13	171	35	428	Tuttle
1400	1440	1.33	0.49	3.49	0.33	0.12	262	25	432	Tuttle
1680	1720	0.75	0.29	1.37	0.25	0.18	183	33	430	Tuttle
2010	2040	0.67	0.26	1.26	0.28	0.17	188	42	432	Tuttle
2350	2380	0.72	0.31	1.45	0.27	0.18	201	38	430	Tuttle
2660	2690	0.74	0.25	1.21	0.46	0.17	164	62	430	Tuttle
2970	3000	0.66	0.23	0.97	0.26	0.19	147	39	437	Tuttle
3200	3230	0.54	0.18	0.85	0.27	0.18	157	50	434	Tuttle
3440	3470	0.58	0.28	1.02	0.23	0.22	176	40	435	Imperial
3750	3780	0.55	0.16	0.76	0.24	0.18	138	44	438	Imperial
4100	4130	0.62	0.21	0.86	0.24	0.19	139	39	442	Imperial
4380	4410	0.86	0.29	1.04	0.28	0.22	121	33	440	Imperial
4710	4740	0.64	0.14	0.65	0.31	0.18	102	48	443	Imperial
5010	5040	0.65	0.18	0.67	0.22	0.21	103	34	444	Imperial
5330	5360	0.65	0.17	0.63	0.43	0.21	97	66	442	Imperial
5670	5700	0.66	0.23	0.66	0.27	0.26	100	41	442	Imperial
5980	6010	0.67	0.22	0.73	0.31	0.23	109	46	446	Imperial
6280	6310	0.65	0.20	0.71	0.26	0.22	109	40	451	Imperial

- Allen, T.L., Fraser, T.A. and Osadetz, K.G., 2008. Rock-Eval/TOC data for 18 wells, Peel Plateau and Plain, Yukon Territory (65°50' to 67°00'N; 133°45' to 135°15'W). Yukon Geological Survey, Open File 2008-1, 14 p. plus spreadsheets.
- Allen, T.L., Fraser, T.A. and Utting, J., 2009. Chapter 8 – Upper Devonian to Carboniferous Strata II – Tuttle Formation Play. *In: Regional Geoscience Studies and Petroleum Potential, Peel Plateau and Plain, Northwest Territories and Yukon: Project Volume*, L.J. Pyle and A.L. Jones (eds.), Northwest Territories Geoscience Office and Yukon Geological Survey, NWT Open File 2009-02; YGS Open File 2009-25, p. 365-409.
- Bassett, H.G., 1961. Devonian stratigraphy, central Mackenzie River region, Northwest Territories, Canada. *In: Proceedings of the First International Symposium on Arctic Geology*, vol. 1, G.O. Raasch (ed.), University of Toronto Press, p. 481-498.
- Braman, D.R. and Hills, L.V., 1992. Upper Devonian and Lower Carboniferous miospores, western District of Mackenzie and Yukon Territory, Canada. *Palaeontographica Canadiana*, no. 8, 97 p.
- Dembicki, H., Jr., 2009. Three common source rock evaluation errors made by geologists during prospect or play appraisals. *AAPG Bulletin*, vol. 93, no. 3 (March, 2009), p. 341-356.
- Fraser, T. and Allen, T., 2007. Field investigations of the Upper Devonian to Lower Carboniferous Tuttle Formation, eastern Richardson Mountains, Yukon. *In: Yukon Exploration and Geology 2006*, D.S. Emond, L.L. Lewis and L.H. Weston (eds.), Yukon Geological Survey, p. 157-173.
- Gordey, S.P. and Makepeace, A.J. (compilers), 2001. *Bedrock Geology, Yukon Territory*. Geological Survey of Canada, Open File 3754 and Exploration and Geological Services Division, Yukon Region, Indian and Northern Affairs Canada, Open File 2001-1, scale 1:1 000 000.
- Gradstein, F., Ogg, S. and Smith, A., 2004. *A geologic time scale 2004*. Cambridge University Press, Cambridge, United Kingdom, 589 p.
- Hadlari, T., Tylosky, S.A., Lemieux, Y., Zantvoort, W.G. and Catuneanu, O., 2009. Slope and submarine fan turbidite facies of the Upper Devonian Imperial Formation, Northern Mackenzie Mountains, NWT. *Bulletin of Canadian Petroleum Geology*, vol. 57, no. 2, p. 192-208.
- Hume, G.S. and Link, T.A., 1945. *Canol geological investigations in the MacKenzie River area, Northwest Territories and Yukon*. Geological Survey of Canada, Paper 45-16, 87 p.
- Morrow, D.W., Jones, A.L. and Dixon, J., 2006. *Infrastructure and resources of the Northern Canadian Mainland Sedimentary Basin*. Geological Survey of Canada, Open File 5152, 59 p.
- Norris, A.W., 1968. Reconnaissance Devonian stratigraphy of northern Yukon Territory and northwestern District of Mackenzie. Geological Survey of Canada, Paper 67-53, 287 p.
- Norris, A.W., 1985. Stratigraphy of Devonian outcrop belts in northern Yukon Territory and Northwest Territories, District of Mackenzie (Operation Porcupine Area). Geological Survey of Canada, Memoir 410, 81 p.
- Norris, A.W., 1997. Devonian. *In: The geology, mineral and hydrocarbon potential of northern Yukon Territory and northwestern District of Mackenzie*, D.K. Norris (ed.), Geological Survey of Canada, Bulletin 422, p. 163-200.
- Norris, D.K., 1981a. *Geology: Eagle River, Yukon-Northwest Territories*. Geological Survey of Canada, Map 1523A, scale 1:250 000.
- Norris, D.K., 1981b. *Geology: Trail River, Yukon-Northwest Territories*. Geological Survey of Canada, Map 1524A, scale 1:250 000.
- Norris, D.K. (ed.), 1997. *Geology and mineral and hydrocarbon potential of Northern Yukon Territory and Northwestern District of Mackenzie*. Geological Survey of Canada, Bulletin 422, 401 p.
- Osadetz, K.G., MacLean, B.C., Morrow, D.W., Dixon, J. and Hannigan, P.K., 2005. *Petroleum Resource Assessment, Peel Plateau and Plain, Yukon Territory, Canada*. Yukon Geological Survey, Open File 2005-3, Geological Survey of Canada, Open File 4841, 76 p.
- Peters, K.E., 1986. Guidelines for evaluating petroleum source rock using programmed pyrolysis. *American Association of Petroleum Geologists Bulletin*, vol. 70, no. 3, p. 318-329.
- Peters, K.E., Walters, C.C. and Moldowan, J.M., 2005. *The Biomarker Guide, Volume 1. Biomarkers and Isotopes in the Environment and Human History*. Cambridge University Press, New York, 471 p.

- Pigage, L., 2007. Yukon Stratigraphic Correlation Chart, version 3.0. Yukon Geological Survey and Oil and Gas Management Branch, Yukon Geological Survey, Open File 2007-2.
- Pugh, D.C., 1983. Pre-Mesozoic geology in the subsurface of Peel River map area, Yukon Territory and District of Mackenzie. Geological Survey of Canada, Memoir 401, 61 p.
- Pyle, L.J. and Jones, A.L. (eds.), 2009. Regional Geoscience Studies and Petroleum Potential, Peel Plateau and Plain, Northwest Territories and Yukon: Project Volume. Northwest Territories Geoscience Office and Yukon Geological Survey, NWT Open File 2009-02; YGS Open File 2009-25, 549 p.
- Richards, B.C., Bamber, E.W. and Utting, J., 1997. Upper Devonian to Permian. *In: Geology and Mineral and Hydrocarbon Potential of Northern Yukon Territory and Northwestern District of Mackenzie*, D.K. Norris (ed.), Geological Survey of Canada, Bulletin 422, p. 201-251.
- Staplin, F.L., 1969. Sedimentary organic matter, organic metamorphism and oil and gas occurrence. *Bulletin of Canadian Petroleum Geology*, vol. 17, no. 1, p. 47-66.
- Tassonyi, E.J., 1969. Subsurface Geology, Lower Mackenzie River and Anderson River area, District of Mackenzie. Geological Survey of Canada, Paper 68-25.
- Utting, J., 2007. Palynological investigation of 25 outcrop samples and 8 core samples from the Upper Paleozoic, Yukon Territory. Submitted by T. Allen and T. Fraser, Yukon Geological Survey (NTS 106E/15, 16 and NTS 106L/1,2,6,8,9,10,11). Geological Survey of Canada, unpublished report 02-JU-2007, 14 p.
- Utting, J., 2008. Palynological investigation of 40 outcrop samples, western District of Mackenzie, submitted by T. Allen and T. Fraser, Yukon Geological Survey (NTS 106F/11, 12 and 106L/1, 2, 6, 11, 12, 14). Geological Survey of Canada, Paleontological Report 04-JU-2008, 19 p.
- Utting, J., 2009. Palynological investigation of 28 outcrop samples, Yukon Territory, submitted by T. Allen and T. Fraser, Yukon Geological Survey (NTS 106L/1, 2, 3, 6, 11, 12, 14). Geological Survey of Canada, Paleontological Report JU-2009-04, 14 p.
- Utting, J., Goodarzi, F., Dougherty, B.C. and Henderson, C.M., 1989. Thermal maturity of Carboniferous and Permian rocks of the Sverdrup Basin, Canadian Arctic Archipelago. Geological Survey of Canada, Paper 89-19, 20 p.

Deconstructing complex Au-Ag-Cu mineralization, Sonora Gulch project, Dawson Range: A Late Cretaceous evolution to the epithermal environment

Venessa Bennett¹

Yukon Geological Survey

Carl Schulze²

All-Terrane Mineral Exploration Services

Dennis Ouellette³ and Bonnie Pollries⁴

Northern Tiger Resources

Bennett, V., Schulze, C., Ouellette, D. and Pollries, B., 2010. Deconstructing complex Au-Ag-Cu mineralization, Sonora Gulch project, Dawson Range: A Late Cretaceous evolution to the epithermal environment. *In: Yukon Exploration and Geology 2009*, K.E. MacFarlane, L.H. Weston and L.R. Blackburn (eds.), Yukon Geological Survey, p. 23-45.

ABSTRACT

We present new field and U-Pb analytical data from the Sonora Gulch Project that demonstrate a protracted history of polymetallic mineralization (Au-Ag-Cu-Zn ± Mo) associated with several pulses of Cretaceous magmatism. Recent exploration on the Sonora Gulch Project has highlighted the presence of two important mineralized zones: the Nightmusic zone, a mesothermal Au-enriched base metal skarn, and the Amadeus zone, an epithermal Au-Ag system. Four U-Pb age dates determined from each of two feldspar porphyry dykes (ca. 74 Ma), a weakly mineralized quartz porphyry stock (ca. 75 Ma) within the Nightmusic zone and the Au-Ag mineralized Amadeus stock (ca. 75 Ma), demonstrate the widespread occurrence of Late Cretaceous magmatism. The age determinations indicate that mineralization occurring within the Sonora Gulch project area are temporally equivalent to the Casino Cu-Au-Mo deposit, located roughly 40 km to the west-northwest. These new data extend the currently known eastern limit of Late Cretaceous magmatism and associated mineralization.

¹venessa.bennett@gov.yk.ca

²allterrane@northwestel.net

³douellette@firestoneventures.com

⁴bpollries@northern-tiger.com

INTRODUCTION

The Sonora Gulch property, which is wholly owned by Northern Tiger Resources Inc., is located in the central Dawson Range, west-central Yukon where it forms part of a regionally extensive, northwest-trending polymetallic mineral belt associated with Early Jurassic (e.g., Minto deposit) to latest Cretaceous magmatism (e.g., Casino deposit; Figs. 1, 2). An important characteristic of metal concentration occurring throughout the belt is the superposition of mineralizing events upon pre-existing ores, such that early phase mineralization can be significantly enriched and/or remobilized along active structural corridors to be subsequently re-deposited at structurally and chemically favourable sites (e.g., Mortensen *et al.*, 2002; Bineli Betsi and Bennett, this

volume). Importantly, the Sonora Gulch property occurs where a major regional northwest-trending structure, the Big Creek fault, intersects both mid- and Late Cretaceous magmatism and hence represents a highly desirable location to explore for economically important concentrations of metals. Placer gold mines have operated on streams draining the Sonora Gulch property since the turn of the 20th century, recovering angular nuggets of gold, commonly with tetradymite (a bismuth telluride).

Historical exploration conducted on the property identified two main mineralized zones including: (i) a kilometre-scale zone of anomalous Cu-Au mineralization hosted by a pyritic quartz-feldspar porphyritic intrusion; and (ii) a zone of gold-tetradymite quartz vein-hosted

Figure 1. Terrane map of Yukon illustrating the location of Northern Tiger Resources' Sonora Gulch Project, located west of the Teslin fault within the Yukon-Tanana terrane.

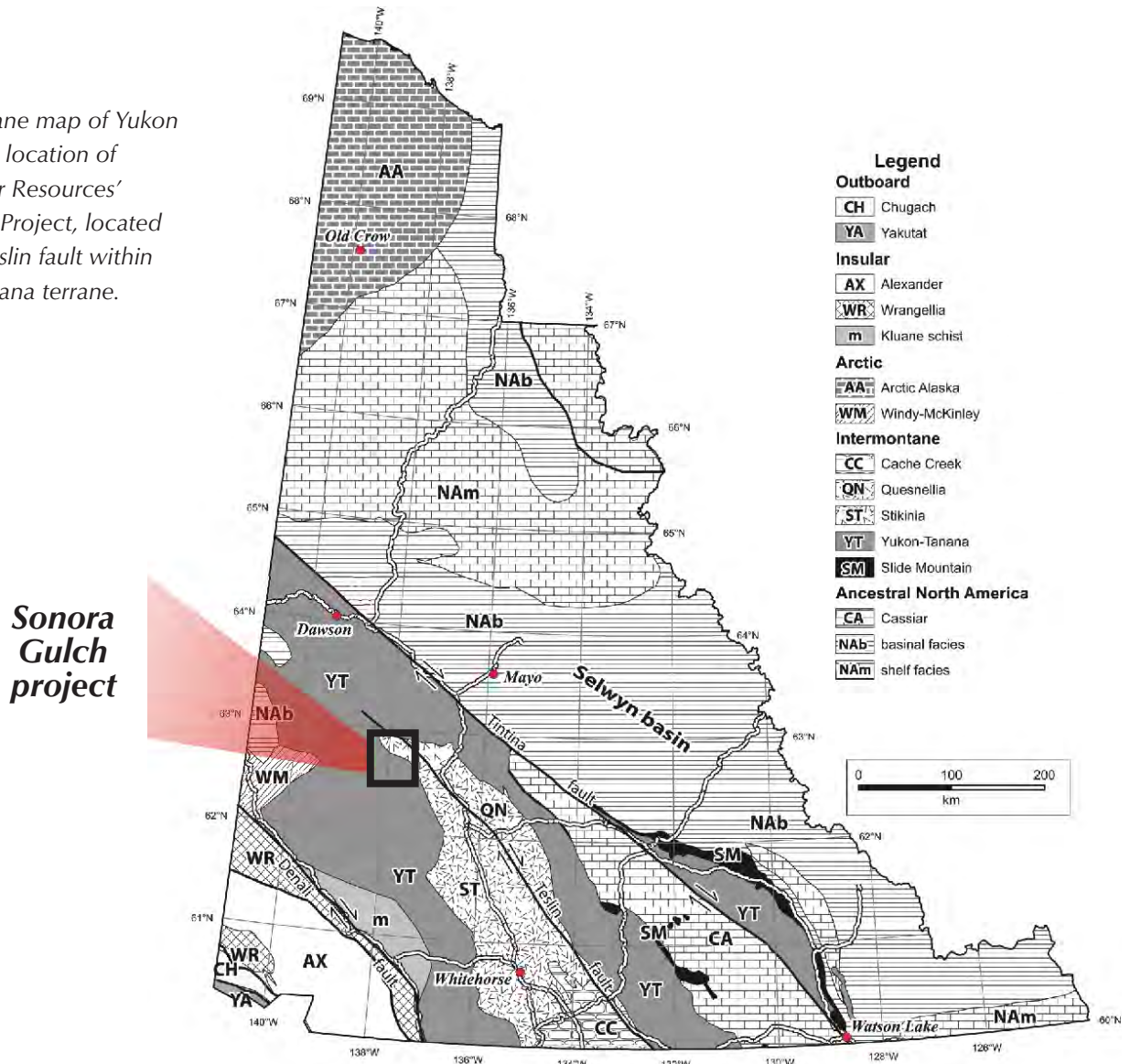
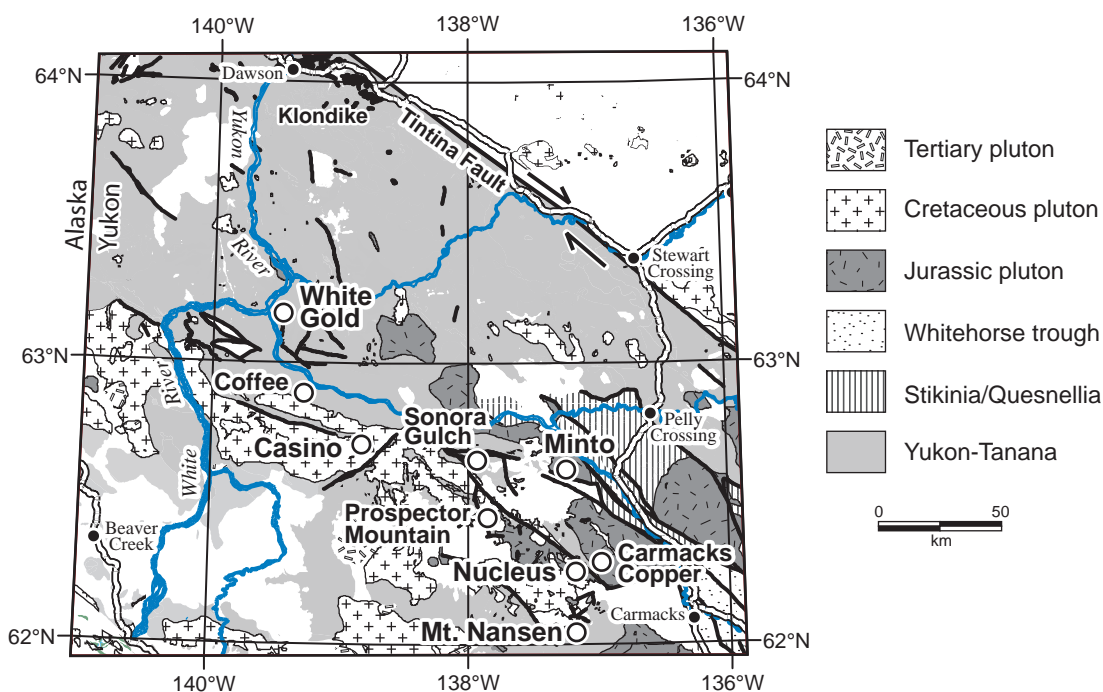


Figure 2. Regional geological map illustrating distribution of main mineral occurrences and deposits within the Dawson Range (courtesy of M. Colpron). Location of Sonora Gulch camp marked.



mineralization oriented northwest, approximately along the interpreted trace of the Big Creek fault. In addition to these historical zones, recent exploration on the Sonora Gulch project has highlighted the presence of several zones of important Au-Ag ± Cu ± Zn ± Mo mineralization, the most advanced being the Nightmusic (mesothermal skarn/replacement) and Amadeus zones (epithermal stock; Fig. 3; Schulze, 2004, 2007a,b). In this contribution, we present new field and U-Pb analytical data from the Nightmusic and Amadeus zones that demonstrate a protracted history of polymetallic mineralization associated with discrete pulses of Cretaceous magmatism.

DISTRICT GEOLOGY

The Sonora Gulch property lies entirely within the Yukon-Tanana terrane, an accreted terrane locally separated from strata of the ancestral North American margin by the northwest-trending Tintina fault. The Yukon-Tanana terrane consists of a belt of Late Devonian to Late Permian metamorphic rocks, including various metasedimentary and metavolcanic assemblages, and up to four distinct suites of calc-alkaline metaplutonic rocks (Mortensen, 1992; Colpron *et al.*, 2006). The northwest-trending Denali (Shakwak) fault, located approximately 140 km to the southwest, forms the southwestern boundary of the Yukon-Tanana terrane (Gordey and Makepeace, 1999; Davidson, 2000).

In the Dawson Range, the Yukon-Tanana terrane typically includes metasedimentary and metavolcanic sequences of quartz-mica schist and diorite gneiss. Plutonic rocks of the mid-Cretaceous Dawson Range batholith intrude the Yukon-Tanana terrane over vast areas and consist of large bodies of granodiorite and quartz monzonite, and smaller high-level felsic porphyry plugs and sills. Locally, narrow ultramafic units of unknown age have been emplaced along major structures within the Yukon-Tanana terrane. A suite of quartz-eye feldspar ± biotite porphyritic monzonite to granite intrusions, including felsic dykes, was previously interpreted as part of the mid-Late Cretaceous Prospector Mountain suite (Davidson, 2000). Late volcanic rocks in the district consist of sills, dykes and flows of the Late Cretaceous Mount Nansen Group, and mafic flows and pyroclastic volcanic rocks of the Late Cretaceous Carmacks Group (Templeman-Kluit, 1984, Davidson, 2000).

Two regional-scale faults crosscut the region: the northwest-trending Big Creek fault and an east-trending fault. The Big Creek fault, which extends northwest approximately 80 km from the Freegold Mountain property of Northern Freegold Resources Ltd., intersects the east fault, west of the junction of Selkirk and Hayes creeks. From this intersection, the Big Creek fault projects more westerly in orientation. Importantly, the Big Creek fault and related northwest-trending faults are considered to represent the locus of an important mineralizing belt,

extending possibly as far as the Casino deposit of Western Copper Inc. Copper porphyry and structurally hosted gold deposits occur ubiquitously along these northwest to north-northwest-trending fault systems, and associated placer gold deposits occur within watersheds draining these mineralized zones.

GEOLOGY OF SONORA GULCH PROPERTY

The Sonora Gulch property is underlain by polydeformed and metamorphosed Devonian to Mississippian metagranitic, metavolcanic and subordinate metasedimentary rocks assigned to the Wolverine Creek metamorphic suite of the Yukon Tanana terrane (Johnston and Hachey, 1993). Several ultramafic sills and numerous mid- and Late Cretaceous monzonitic – granitic magmatic units intrude the Wolverine Creek assemblage within the property area (Fig. 3). West of Hayes Creek, several

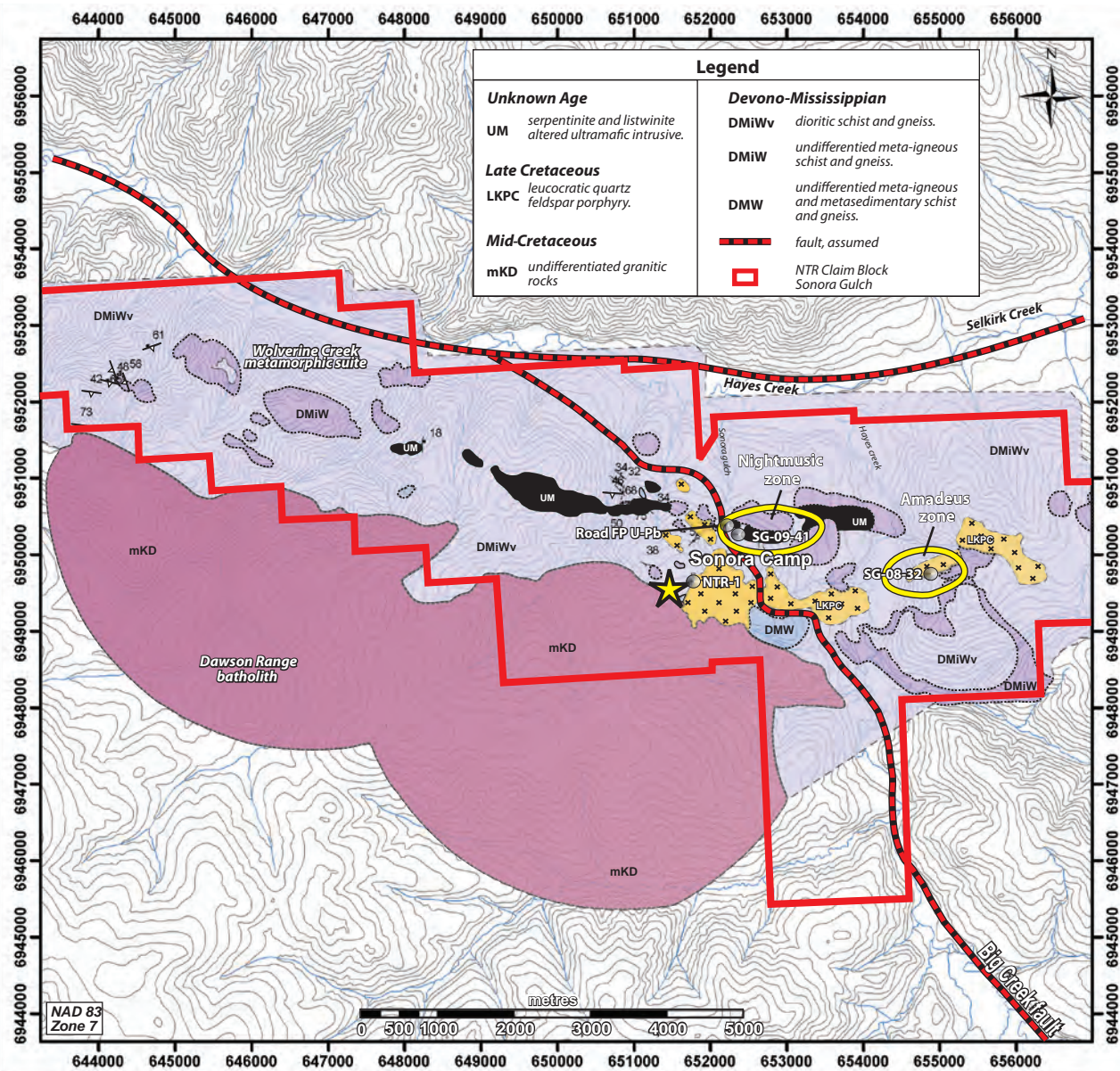


Figure 3. Property geology map, Sonora Gulch project, 2009, Northern Tiger Resources. Location of the Nightmusic and Amadeus zones and sampling localities for U-Pb geochronology marked. Star indicates position of camp.

ultramafic lenses are intercalated within the west-northwest striking Wolverine Creek units. Importantly, these ultramafic bodies are spatially associated with mineralization occurring in the Nightmusic zone. The mid-Cretaceous east-southeast-trending Dawson Range batholith occurs along the southwest margin of the Sonora Gulch property, west of the Big Creek fault (Fig. 3). Late Cretaceous quartz-feldspar porphyritic monzonite of the Prospector Mountain suite intrudes the Wolverine Creek sequence along the northern boundary of the Dawson Range batholith, east of the Sonora camp. Furthermore, this monzonitic stock is crosscut by the Big Creek fault (Fig. 3). East of Hayes Creek, a small stock of strongly pyritic feldspar porphyritic monzonite, called the Amadeus stock, occurs in association with significant Au-Ag mineralization.

WOLVERINE CREEK METAMORPHIC SUITE

Metabasaltic rocks represent the most aerially extensive member of the Wolverine Creek suite within the Sonora Gulch property area. They are typically strongly foliated and characterized by a well-developed gneissic fabric. Metabasaltic rocks have a weak to moderate calcareous composition and are commonly host to replacement-style and skarn mineralization within the Nightmusic zone. Granitic gneiss underlies much of the Sonora Gulch property and most commonly occurs as augen gneiss characterized by quartz and feldspar augen porphyroclasts up to 0.5 cm in length. Granitic gneiss hosts a greater proportion of foliation-parallel quartz veining than metabasalts, as well as more pervasive sericite alteration and weak pyrite mineralization. Metasedimentary rocks of the Wolverine Creek suite, which underlie most of the northeastern part of the property, consist of phyllite, siltstone and mudstone, with lesser sandstone. They are variably calcareous, and include minor limestone horizons. Metasedimentary rocks exhibit a prominent schistose foliation, with variable and locally intense sericite and/or phlogopite alteration.

ULTRAMAFIC UNITS

Discontinuous lenses and irregular bodies of a strongly serpentized and listwanite-altered ultramafic body occur in an east-trending structural corridor immediately east and west of the Big Creek fault. Where not completely altered, the composition of the ultramafic unit is primarily pyroxenitic. Pervasive secondary carbonate-silica alteration has resulted in destructive listwanite-alteration of the body, particularly proximal to the southern hanging

wall contacts. The ultramafic lens has undergone significant deflection (ca. 500 m) related to dextral motion along the Big Creek fault (Fig. 4). Additionally, three separate ultramafic horizons have been identified west of the Big Creek fault.

CRETACEOUS MAGMATIC UNITS

Within the Sonora Gulch property, the mid-Cretaceous Dawson Range batholith varies from quartz-hornblende-biotite granodiorite, quartz monzonite and quartz diorite to granite. Textures are typically coarse grained and equigranular. A Late Cretaceous intrusive unit, which abuts the northern contact of the Dawson Range batholith is a massive quartz-feldspar porphyritic monzonite characterized by 35 to 40% evenly distributed feldspar grains approximately 2-3 mm in length and hosted in an aphanitic groundmass. The Late Cretaceous Amadeus stock varies from 50 m to 250 m in width and is monzonitic in composition. The stock is strongly leached and has undergone moderate to strong argillic and moderate phyllic alteration that largely masks primary textures.

MINERALIZATION

Two zones of historical mineralization occur on the Sonora Gulch property: a kilometre-scale zone of anomalous copper-gold mineralization, called the 'Gold Vein System', located towards the western end of a Late Cretaceous quartz-feldspar porphyritic monzonite stock; and a gold-tetradymite vein system, known as the 'Tetradymite Vein System', occurring several hundred metres to the north of the 'Gold Vein System' and paralleling the approximate surface trace of the Big Creek fault for approximately 1.3 km. The 'Gold Vein System' consists of disseminated pyrite and minor chalcopyrite with total sulphide concentrations approaching 10%. Gold and copper mineralization occurs both in the interior of the monzonitic stock and also along northwest-trending shear zones and fractures. Locally, the underlying unoxidized zone contains gold-bearing quartz-arsenopyrite veins with sphalerite, galena and stibnite. Precious metal content within the 'Gold Vein System' appears to be directly associated with depth, sulphide content and quartz vein density. A sample of the monzonitic stock from the 'Gold Vein System' was sampled for U-Pb age dating (sample NTR-1). Mineralization within the 'Tetradymite Vein System' is

confined to narrow, high-grade quartz-arsenopyrite veins of limited strike length.

Recent exploration on the Sonora Gulch property has defined the presence of several zones of anomalous gold including the Nightmusic and Amadeus zones, and the Sonata, Jupiter, Wolfgang and Concerto anomalies. The Nightmusic and Amadeus zones represent the most advanced of the anomalies thus far identified. The two zones are marked by distinct mineralization styles and metal suites. Mineralization in the Nightmusic zone is complex and consists of: (i) mesothermal Au-enriched base-metal skarns (Cu-Zn-Pb), (ii) replacement zones hosted by calcareous metaclastic and metavolcanic rocks, (iii) bonanza-style lode gold associated with listwanitic ultramafic rocks, and (iv) structurally controlled veins and stockwork. In contrast, the Amadeus zone represents a high-level epithermal Au-Ag mineralizing system. Importantly, the two mineralized zones occur along that portion of an east-trending structural corridor located east of the northwest-trending Big Creek fault. Farther south within the Freegold Mountain Project area, similar east-trending mineralizing structures occur to the west of the Big Creek fault, suggesting the fault system may represent a significant mineralizing conduit of regional extent.

The Nightmusic zone was initially identified through re-interpretation of historical diamond drilling results, and from a single 2007 drillhole designed to target the east-trending ultramafic horizon (Figs. 3, 4). The zone was further delineated during drill testing in 2008 and 2009. Replacement and skarn-style mineralization hosting significant gold and base-metal concentrations occur along the southern hanging wall side of the east-trending ultramafic body. Mineralized zones also occur adjacent to, or within, listwanitic ultramafic horizons, with visible gold identified at one location within the ultramafic unit. Replacement-style gold mineralization, which occurs more commonly in the western Nightmusic zone (Fig. 5a,b), appears to contain the highest grades of gold recognized thus far. In contrast, skarn mineralization and associated calc-silicate alteration that occurs at the eastern end of the Nightmusic zone hosts greater concentrations of base metals (Zn-Cu-Pb) with subordinate gold (Fig. 5e-h). The lateral variation in metal suites within the Nightmusic zone, ranging from gold-enrichment in the west to base-metal enrichment in the east, may indicate lateral zoning in a mesothermal skarn mineralizing system. The magmatic source for the Nightmusic skarn zone has yet to be located.

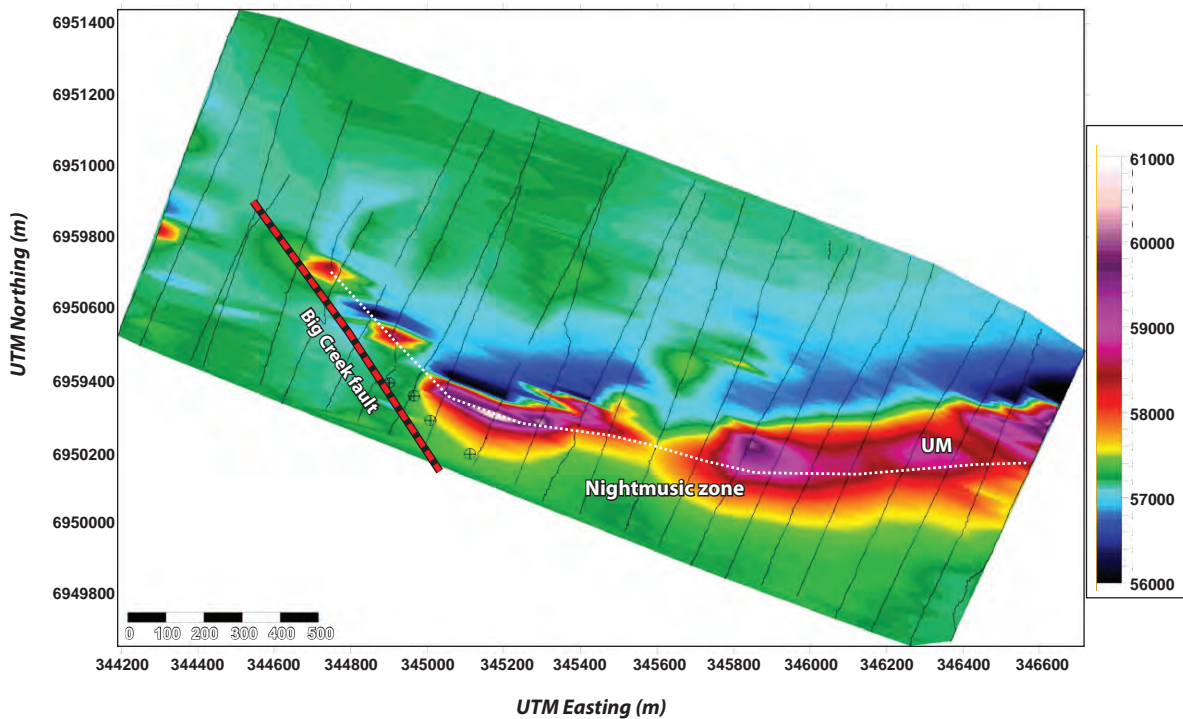


Figure 4. Ground magnetic survey across the Nightmusic zone. The dataset highlights the location of the ultramafic unit (UM) and its deformation associated with dextral movement along the Big Creek fault. White dotted line represents the trend of the ultramafic body.



Figure 5. Replacement-style and skarn mineralization occurring in the Nightmusic zone; (a) to (d) replacement-style Au-Cu mineralization (DDH SG-08-27). Note: (b) and (d) show chalcopyrite (Cp) replaced by later pyrite (Py) + pyrrhotite (Po); (c) and (d) show epithermal veins crosscutting replacement-style Au mineralization. Scale bars represent 1 cm.

Sulphide paragenesis in both replacement and skarn-style mineralized zones indicates early phase chalcopyrite \pm sphalerite partially to completely overprinted by pyrite + pyrrhotite, with pyrrhotite recognized as the latest sulphide phase (Fig. 5b, e-i). Accessory molybdenite occurs in association with the Cu-Zn skarn of the eastern Nightmusic zone (Fig. 5i). Late-stage overprinting veining with epithermal textures is ubiquitous throughout the Nightmusic zone, where they are observed to crosscut both replacement and skarn mineralization (Fig. 5c,d,j).

The epithermal veins indicate the occurrence of multiple fluid and mineralizing events within the Nightmusic zone. Feldspar porphyry dykes, that are interpreted to postdate replacement and skarn mineralization, also intrude the Nightmusic zone (Fig. 6). The dykes are commonly limonite \pm hematite-altered and do not host appreciable mineralization. Two feldspar porphyry dykes from the Nightmusic zone were sampled for U-Pb geochronology, one of which is crosscut by the Big Creek fault (sample SG-09-41). Brecciation and fracturing of the porphyry

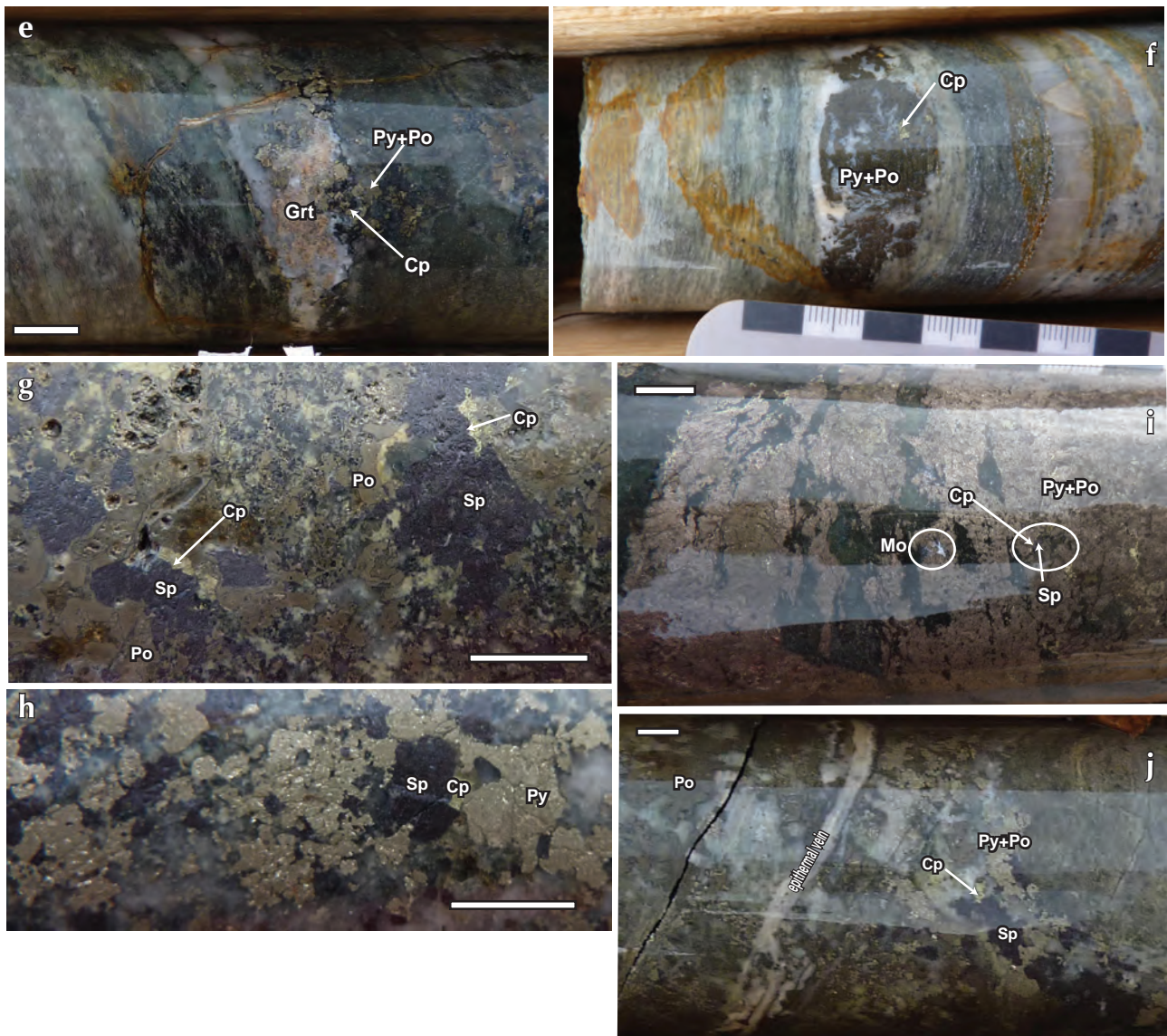


Figure 5. continued. (e) Garnet + chalcopyrite replaced by pyrite + pyrrhotite in skarn zone, SG-09-43. (f) Sulphide vein replacement mineralization in skarn-altered gneissic host rock, Nightmusic zone, SG-09-43. Figures 5 (g) and (h) sphalerite - chalcopyrite skarn mineralization overprinted by pyrite + pyrrhotite, Nightmusic zone, SG-09-43. (i) Sphalerite-chalcopyrite and rare molybdenite replaced by pyrite + pyrrhotite. (j) Late, overprinting epithermal vein crosscutting Cu-Zn skarn mineralization, SG-09-43, Nightmusic zone. Scale bars represent 1 cm. Cp = chalcopyrite, Py = pyrite, Po = pyrrhotite, Grt = garnet, Sp = Sphalerite.

indicates that deformation and movement associated with the Big Creek fault post-dated dyke emplacement.

The Amadeus zone (Fig. 3) is hosted by a high-level, epithermal quartz-feldspar porphyritic stock, which is strongly leached and has undergone moderate to strong pervasive argillic alteration and lesser silicification. Gold and silver mineralization occurs both in the Yukon-Tanana terrane host rocks immediately above the intrusive contact of the stock and within the stock itself. Immediately above the intrusion, granitic gneiss hosts multiple phases of pyrite \pm chalcopyrite vein and fracture

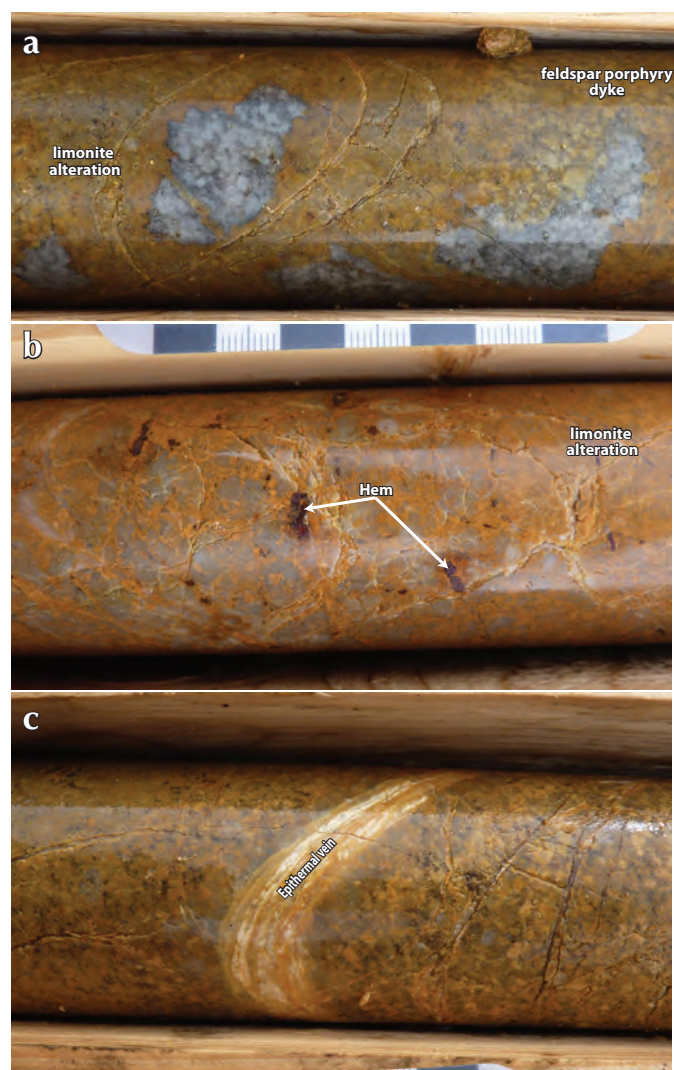


Figure 6. Altered feldspar porphyry dykes intruding Nightmusic zone (DDH SG-09-43). (a) Near-complete fracture-controlled limonite alteration of feldspar porphyry dyke. (b) Hematite-limonite alteration of feldspar porphyry dyke. (c) Late-stage epithermal vein crosscutting limonite-altered feldspar porphyry dyke. Hem = hematite.

mineralization (Fig. 7a,b). Gold and silver mineralization also occurs at the brecciated intrusive contact of the Amadeus stock and the Yukon-Tanana terrane, where pyrite \pm Au and Ag mineralization occur as matrix minerals of the intrusive clast-supported breccia (Figs. 7c and 8). Within the Amadeus stock, gold and silver show a correlation with depth; gold occurs at higher levels, while appreciable silver concentrations occur at depth (Fig. 8). Gold is typically associated with fine-grained disseminated euhedral pyrite (Fig. 7d) and shows a correlation with clay alteration assemblages. Intervals of higher grade gold are typically associated with low to background arsenic values, suggesting a more evolved epithermal nature of gold mineralization. Silver mineralization within the stock is associated with occurrences of quartz and/or pyrite veining occurring at lowermost levels (Fig. 7e). Notably, late stage epithermal-style veining and feldspar porphyry dykes were not observed to crosscut the Amadeus stock, suggesting stock emplacement was coeval with, or post-dated, the epithermal and dyking events observed in the Nightmusic zone. A sample of the Amadeus stock was collected for U-Pb geochronology.

GEOCHRONOLOGY

Four intrusive samples were collected from the Sonora Gulch property in order to place maximum and minimum age constraints on magmatism and related mineralization within both the Nightmusic and Amadeus zones. Sample preparation and U-Pb Laser Ablation Microprobe Inductively Coupled Plasma Mass Spectrometry (LAM ICP-MS) geochronology was completed at the Earth Sciences Department and the INCO Innovation Centre, Memorial University, St John's, Newfoundland. A detailed outline of the methodology is given in Bennett and Tubrett (this volume). Analytical techniques used to characterize the zircon populations included standard optical microscopy and backscattered electron imaging (BSE) and cathodoluminescence (CL) image analysis in order to permit greater understanding of zircon zoning and growth history. Image analysis was completed on all zircon grains selected ($n = 20-80$, depending on yield). Field relationships and zircon zonation styles are briefly described for each sample before reporting the U-Pb isotopic results. Final interpreted crystallization ages are based on calculation of concordia ages from individual U-Pb isotopic analyses that have a probability of concordance greater than 0.20 (see Bennett and Tubrett, this volume). Weighted mean $^{206}\text{Pb}/^{238}\text{U}$ ages are also reported, to remain consistent with current U-Pb

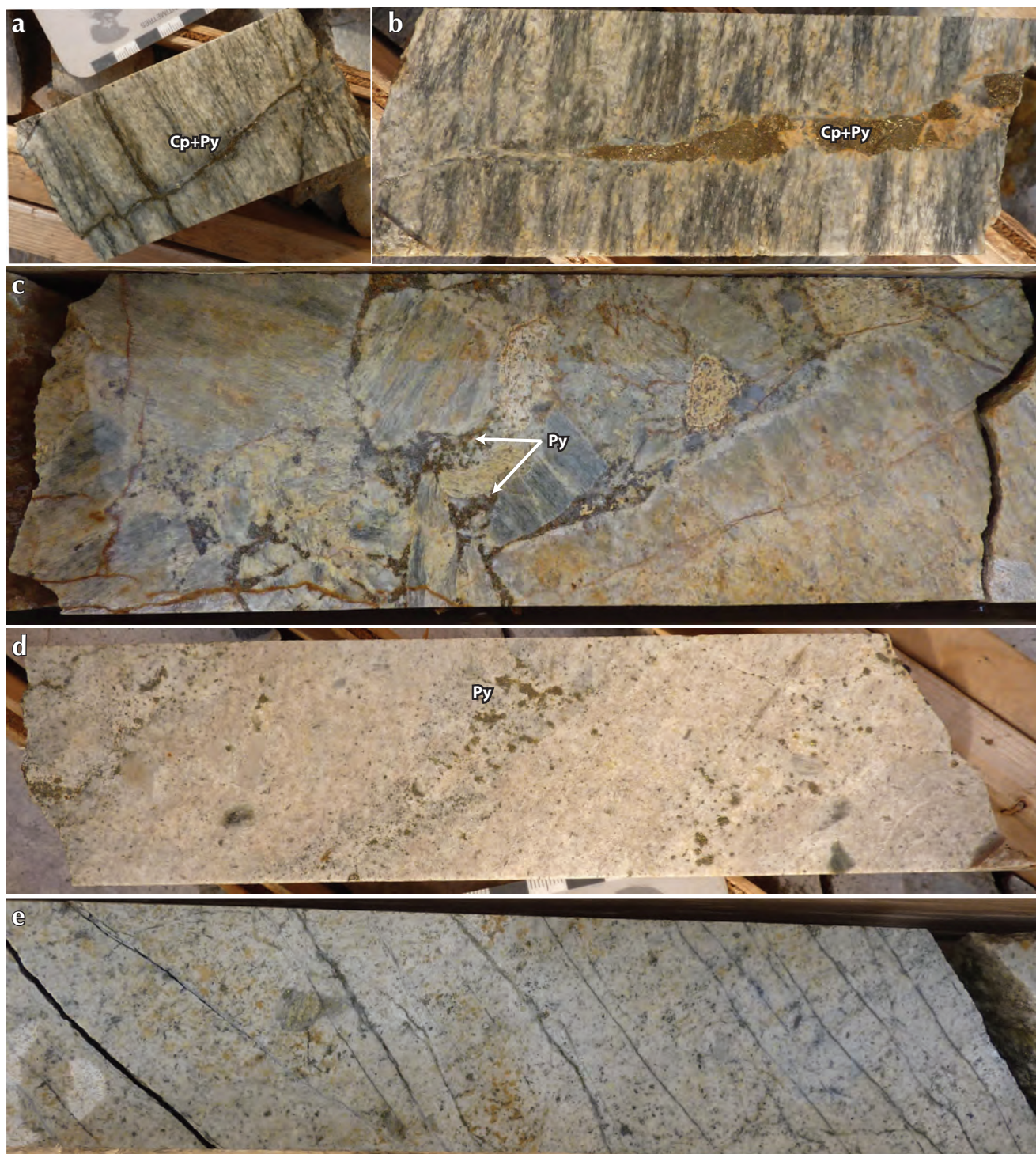


Figure 7. Styles of mineralization occurring in the Amadeus stock, Amadeus zone (SG-08-31). **(a)** and **(b)** vein-hosted pyrite + chalcopyrite mineralization in basement granitic gneisses immediately above contact with Amadeus stock. **(c)** Intrusive breccia texture, contact zone, Amadeus stock. **(d)** Example of high-level Au mineralized zone in feldspar porphyry stock, Amadeus zone. **(e)** Example of lower level Ag mineralized zone, Amadeus stock. Cp = chalcopyrite, Py = pyrite.

geochronology reporting trends. Two sigma uncertainty levels are reported for all calculated ages and plotted on concordia and weighted mean diagrams, unless stated otherwise. Final age calculations include U decay constant uncertainties, which are plotted graphically on concordia plots. Concordia and weighted mean $^{206}\text{Pb}/^{238}\text{U}$ ages were calculated using Ludwig (1999). The concordia age that includes U decay constant uncertainties is considered the best estimate of the crystallization age of a sample (see Bennett and Tubrett, this volume). Where a concordia age has a mean square of weighted deviates (MSWD) >1.5, the weighted mean $^{206}\text{Pb}/^{238}\text{U}$ age is considered the best estimate of the crystallization age. Uranium and thorium concentration

data and Th/U ratios were also calculated for each sample.

NIGHTMUSIC ZONE

Three magmatic samples were collected from the Nightmusic zone, including a weakly mineralized, quartz feldspar granitic porphyry stock (NTR-1) sampled from the historical gold vein system, and two feldspar porphyry dykes sampled from both drill core (DDH SG-09-41) and from surface within Nightmusic zone (Road FP dyke).

Sample NTR-1, QFP Stock (UTM 651779E 6949756N, NAD 83 Zone 7)

Weak to moderately pyritic quartz-feldspar granite was sampled approximately 300 m north of the current site of Northern Tiger Resources' Sonora Gulch summer exploration camp, within the historical gold vein system for which the Sonora Gulch area was initially staked in 1965. The stock has a porphyritic texture with smoky to clear quartz eyes, feldspar phenocrysts and lesser biotite (Davidson, 2000; Fig. 9a-c). Argillic and propylitic alteration and abundant quartz veining occur in mineralized portions of the stock. The U-Pb sample site was located in a relatively unaltered part of the stock (Fig. 9a).

The U-Pb sample yielded abundant zircon grains of poor to moderate quality. Two morphologically distinct populations are present: subordinate, clear to turbid prisms (Fig. 9d) and abundant elongate bipyramidal prisms with colourless, translucent overgrowths (Fig. 9e). Backscattered electron and CL imaging of both zircon populations demonstrate magmatic zircon occurs as both entire grains, and as rims of partially resorbed xenocrystic cores. In either case, magmatic zircon growth is characterized by sharp oscillatory growth zoning. Clear truncation of xenocrystic cores is a striking feature characterizing zircon within the NTR-1 sample (Fig. 10).

Twenty-three analyses were collected from 18 magmatic rims and 5 xenocrystic cores (Fig. 11, Appendix 1). A concordia age calculated from 18 rim analyses yielded an age of 75.73 ± 0.93 Ma (MSWD = 0.0020) and a weighted mean $^{206}\text{Pb}/^{238}\text{U}$ age of 75.75 ± 0.96 Ma (MSWD = 0.27; Fig. 11a,b). Xenocrystic core analyses yielded 3 different age populations including ca. 85 Ma, 104 Ma and 410 Ma (Appendix 1). Concentration data calculated from magmatic zircon varies from 223-2250 ppm U and 75-427 ppm Th (Appendix 1); Th/U ratios calculated for all zircon analyses highlight the

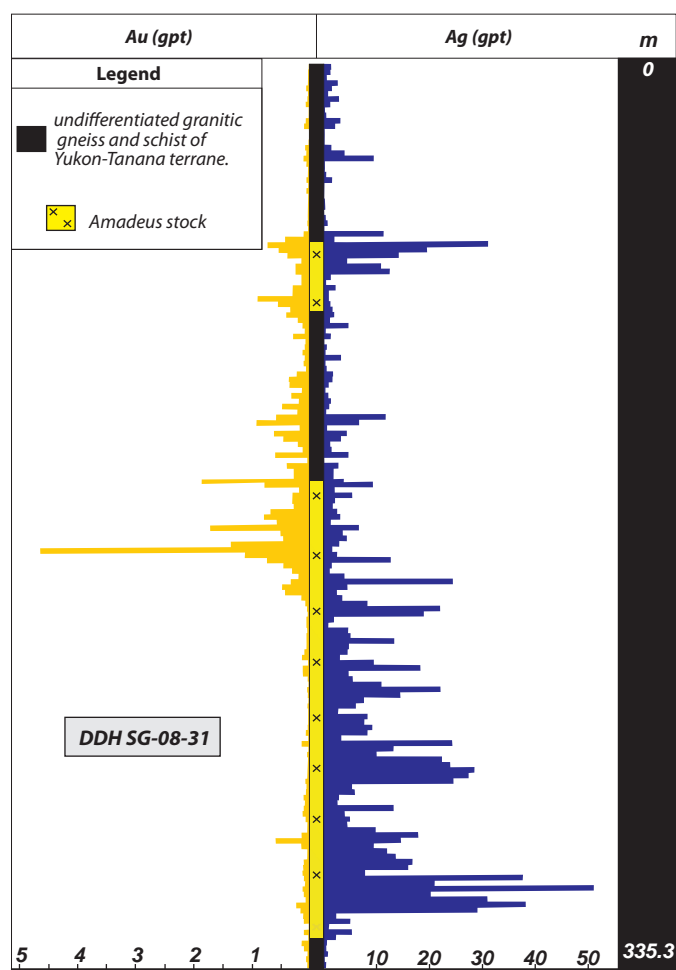


Figure 8. Schematic drill log of DDH SG-08-31, illustrating vertical zonation trends in Au and Ag mineralization (gpt) within the high-level Amadeus stock. Economic concentrations of Au occur at higher levels of the intrusion and Ag increases in concentration at lowermost levels. Modified after Northern Tiger Resources 2008 assessment report, drill log DDH SG-08-31.

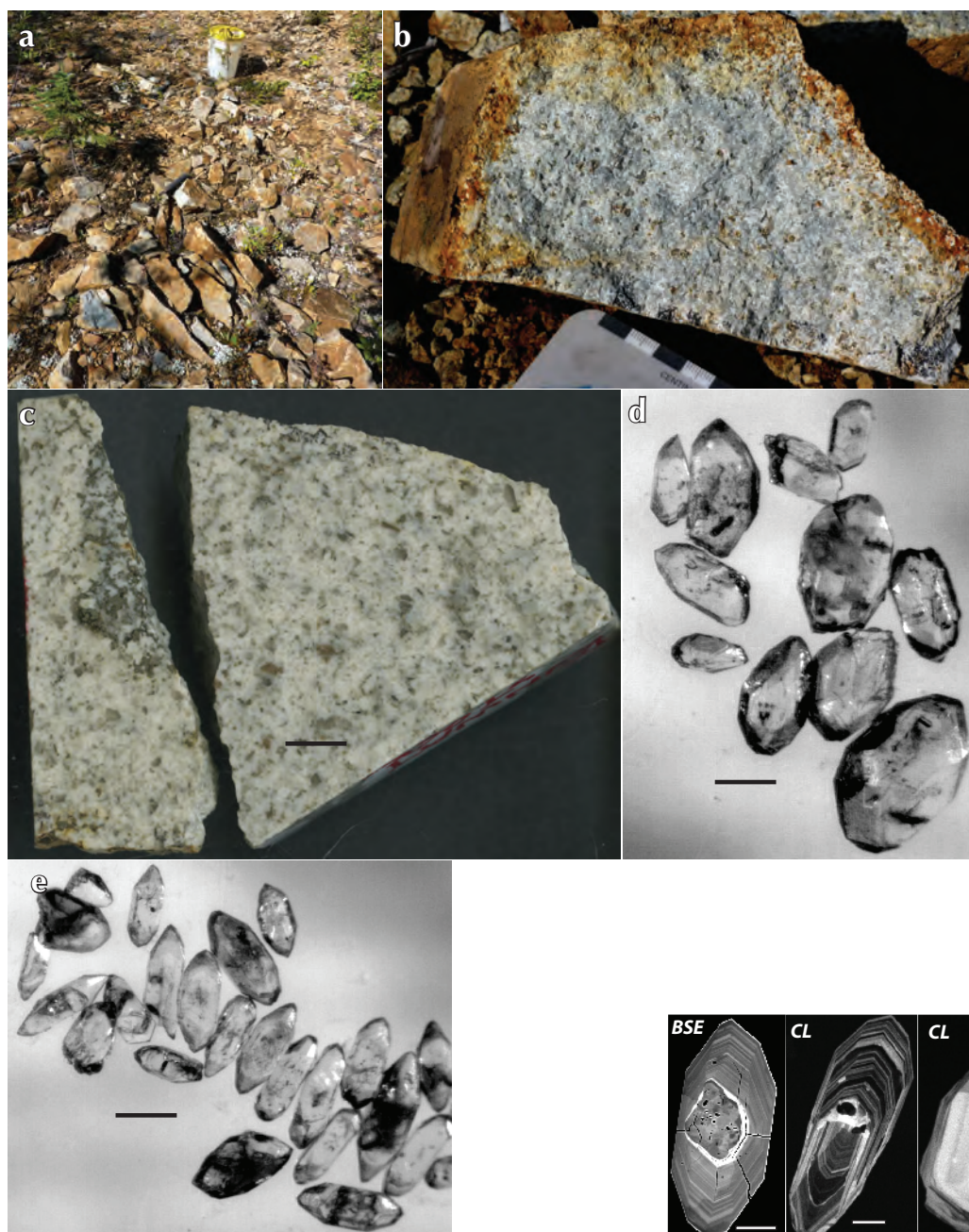


Figure 9. (a) U-Pb sampling locality for NTR-1, QFP stock. (b) Weakly mineralized (Py ± Po) QFP stock adjacent to sampling locality. (c) Slab image of U-Pb sample, NTR-1. Scale bar represents 1 cm. Transmitted light images of (d) zircon prism population and (e) zircon overgrowth, bipyramid population from NTR-1, QFP stock. Scale bars in d and e represent 50 μm.

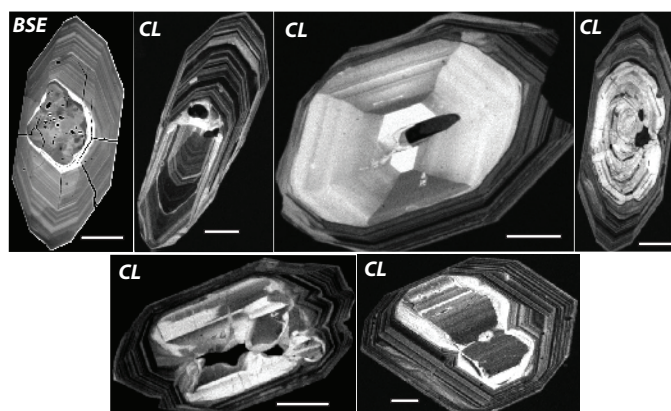


Figure 10. Representative BSE and CL images (denoted on image) of analysed zircon grains from NTR-1, QFP stock. Images demonstrate complex xenocrystic core and magmatic rim relationships. Magmatic rims exhibit fine, well defined, oscillatory zones enclosing partially resorbed xenocrystic cores. Scale bars represent 50 μm. BSE = backscattered electron, CL = cathodoluminescence.

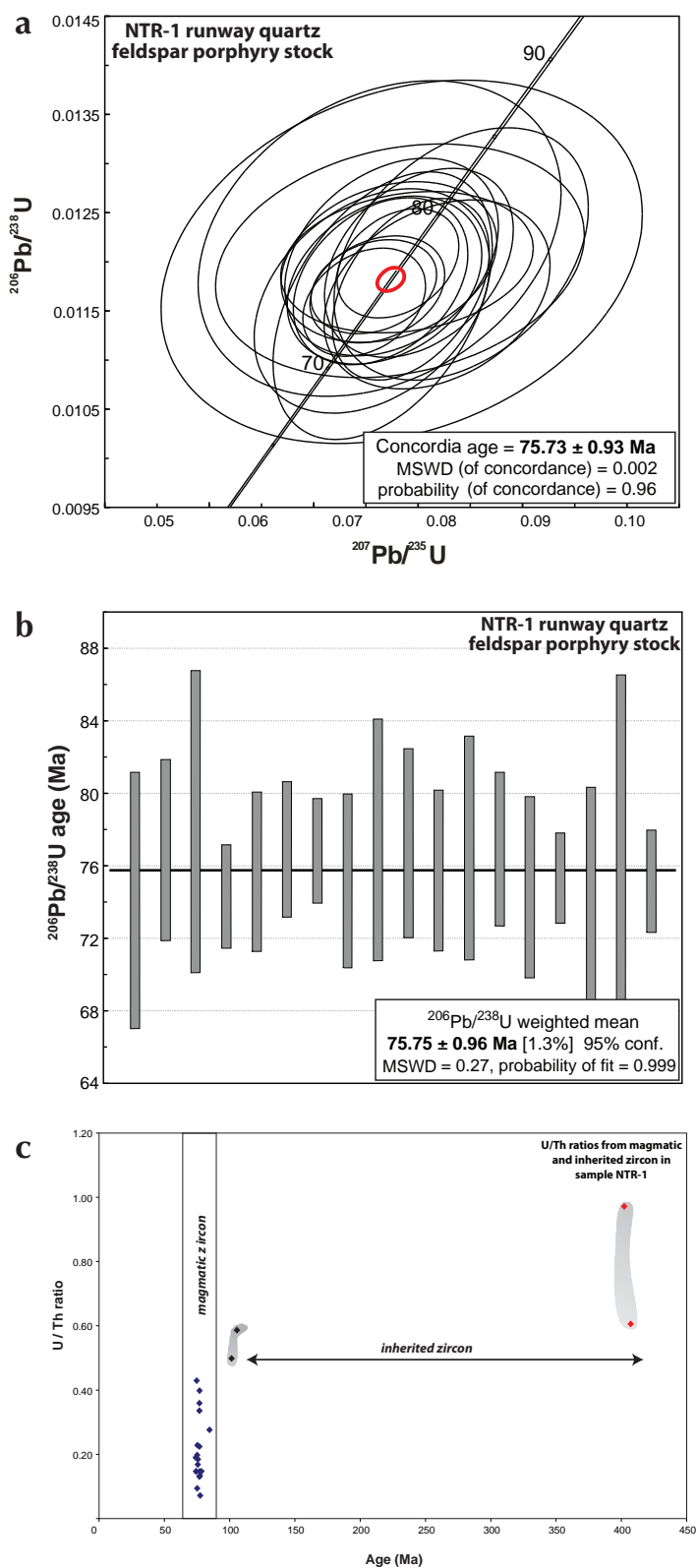
difference in zircon chemistry between xenocrystic cores and magmatic rims, notably due to the higher U content associated with magmatic zircon (Fig. 11c).

Feldspar porphyry dykes

Several feldspar porphyry dykes occur in both drill core and at surface within the Nightmusic zone. The dykes are typically weakly mineralized (Py) and commonly associated with pervasive limonite alteration and vein halo potassic alteration (Figs. 6 and 12). Minor late-stage chalcidonic veining exhibiting open space-filling epithermal textures, overprint the porphyry dykes (Fig. 6c). A series of feldspar porphyry dykes were intersected in DDH SG-09-41 at a depth that intersected the Big Creek fault. A single dyke was sampled between the interval 152.8-153.3 m (Fig. 12a,b). A second feldspar porphyry dyke was sampled on surface at the western margin of the Nightmusic zone, immediately adjacent to the surface trace of the Big Creek fault (Figure 12e; 652238E 6950372N, NAD 83 Zone 7).

Nineteen zircon grains were extracted from the porphyry dyke sampled from DDH SG-09-41. Zircon populations consisted of: (i) elongate needles and prisms with small, well-faceted overgrowths; and (ii) a subordinate population of large broken and fractured grains with indistinct crystal terminations (Fig. 12c,d). The porphyry dyke sampled at surface yielded abundant zircon grains of moderate to high quality that were subdivided into three morphologically distinct populations: (i) minor translucent, well-faceted, elongate to equidimensional prisms; (ii) abundant elongate prisms with optically distinct core and rim relationships; and (iii) elongate bipyramidal prisms with thin colourless and

Figure 11. (a) Concordia diagram for U-Pb analyses of magmatic zircon from NTR-1, QFP stock. Analyses included in age calculation have a probability of concordance greater than 0.20. (b) Plot of weighted mean $^{206}\text{Pb}/^{238}\text{U}$ ages with probability of concordance greater than 0.20. (c) Plot of U/Th ratio for magmatic and inherited zircon illustrating chemical variation between magmatic zircon and xenocrystic cores. Notes: 1. On all diagrams, MSWD = mean square of the weighted deviates; 2. On all U-Pb concordia diagrams, data point error ellipses represent 2σ error and 2σ uranium decay constant errors are included in final age calculation; 3. On all weighted mean $^{206}\text{Pb}/^{238}\text{U}$ diagrams, box heights represent 2σ .



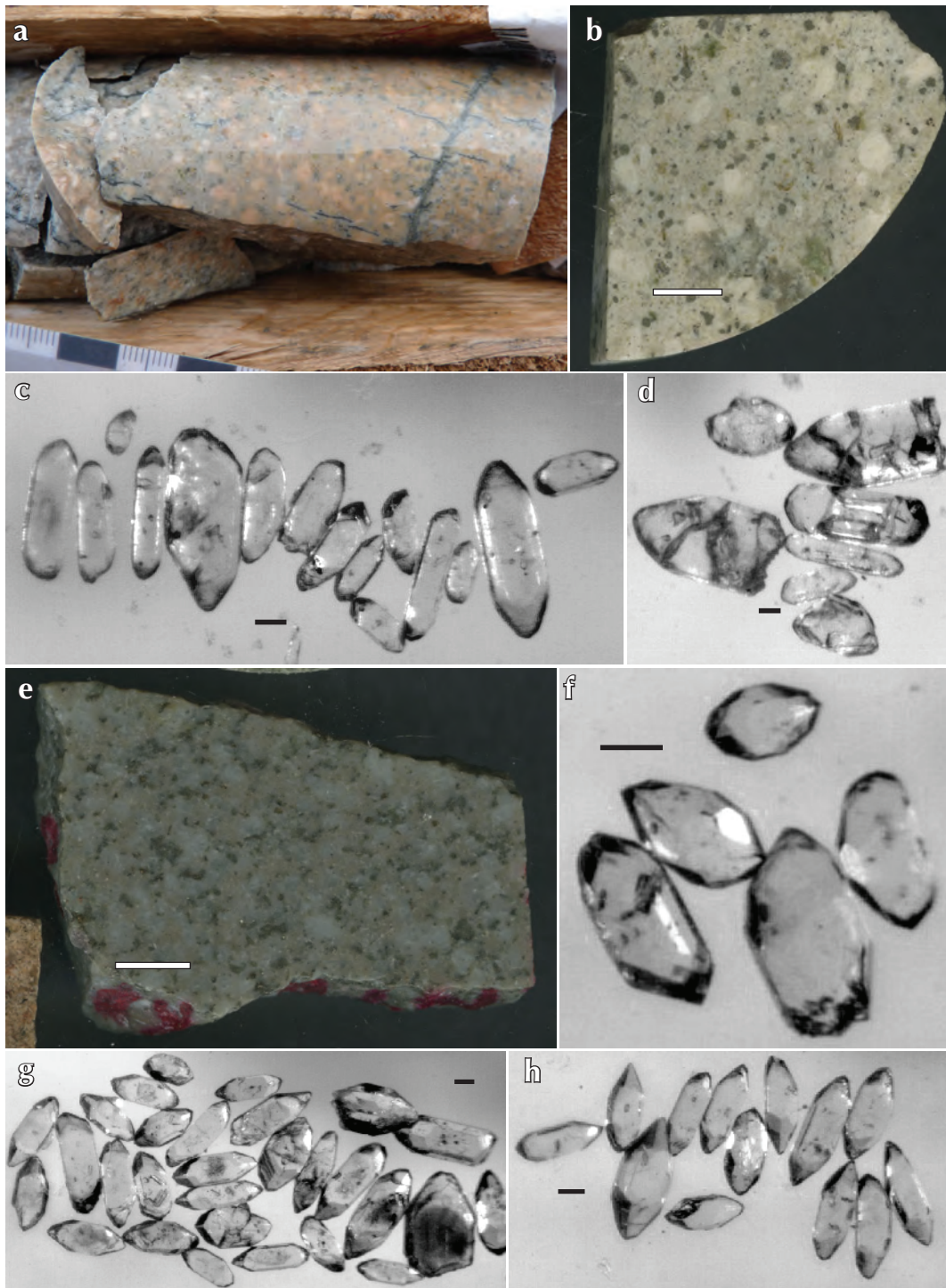


Figure 12. (a) Core photo illustrating vein-hosted sulphide mineralization and associated alteration halo within feldspar porphyry dyke, DDH SG-09-41. (b) Slab image of feldspar porphyry dyke, U-Pb sample. Scale bar represents 1 cm. Transmitted light images of (c) needle and elongate zircon prism population with overgrowths and (d) irregular large fractured grains. Scale bar represents 50 μm . (e) Slab image of feldspar porphyry dyke, U-Pb sample occurring at surface in Nightmusic zone. Scale bar represents 1 cm. Transmitted light images of (f) large, equidimensional prism zircon population, (g) complex core-rim zircon grains, and (h) prismatic bipyramidal zircon population. Scale bar represents 50 μm .

translucent overgrowths (Fig. 12f-h). Backscattered electron and CL imaging of zircon grains in feldspar porphyry dyke samples demonstrates magmatic zircon occurs as entire grains and as rims mantling xenocrystic cores (Fig. 13). Magmatic zircon in both samples is characterized by well-defined, sharp oscillatory growth zoning.

Twenty-four analyses were acquired from 15 zircon grains exhibiting magmatic growth zoning from the feldspar porphyry dyke sampled from DDH SG-09-41, (Fig. 14a; Appendix 2). A concordia age calculated from 22 analyses yielded an age of 74.64 ± 0.61 Ma (MSWD = 1.6) and a weighted mean $^{206}\text{Pb}/^{238}\text{U}$ age of 74.79 ± 0.61 Ma (MSWD = 0.47; Figure 14a,b). Concentration data calculated for magmatic zircon ranges from 162-1637 U ppm and 50-242 ppm Th (Appendix 2).

For the feldspar porphyry sampled at surface from the Nightmusic zone, 24 analyses were collected from 19 grains (Fig. 14c; Appendix 3). A concordia age calculated from 17 analyses yielded an age of 74.42 ± 0.75 Ma (MSWD = 2.4) and a weighted mean $^{206}\text{Pb}/^{238}\text{U}$ age of 73.91 ± 0.81 Ma (MSWD = 0.5; Fig. 14c,d). Concentration data calculated for magmatic zircon vary from 170-2772 ppm U and 29-323 ppm Th (Appendix 3).

AMADEUS ZONE

Amadeus stock (DDH SG-08-32)

The Amadeus stock represents an epithermal quartz-feldspar porphyry intrusion and hosts significant Au-Ag mineralization. The stock is characterized by pervasive bleaching and primary zoned plagioclase phenocrysts

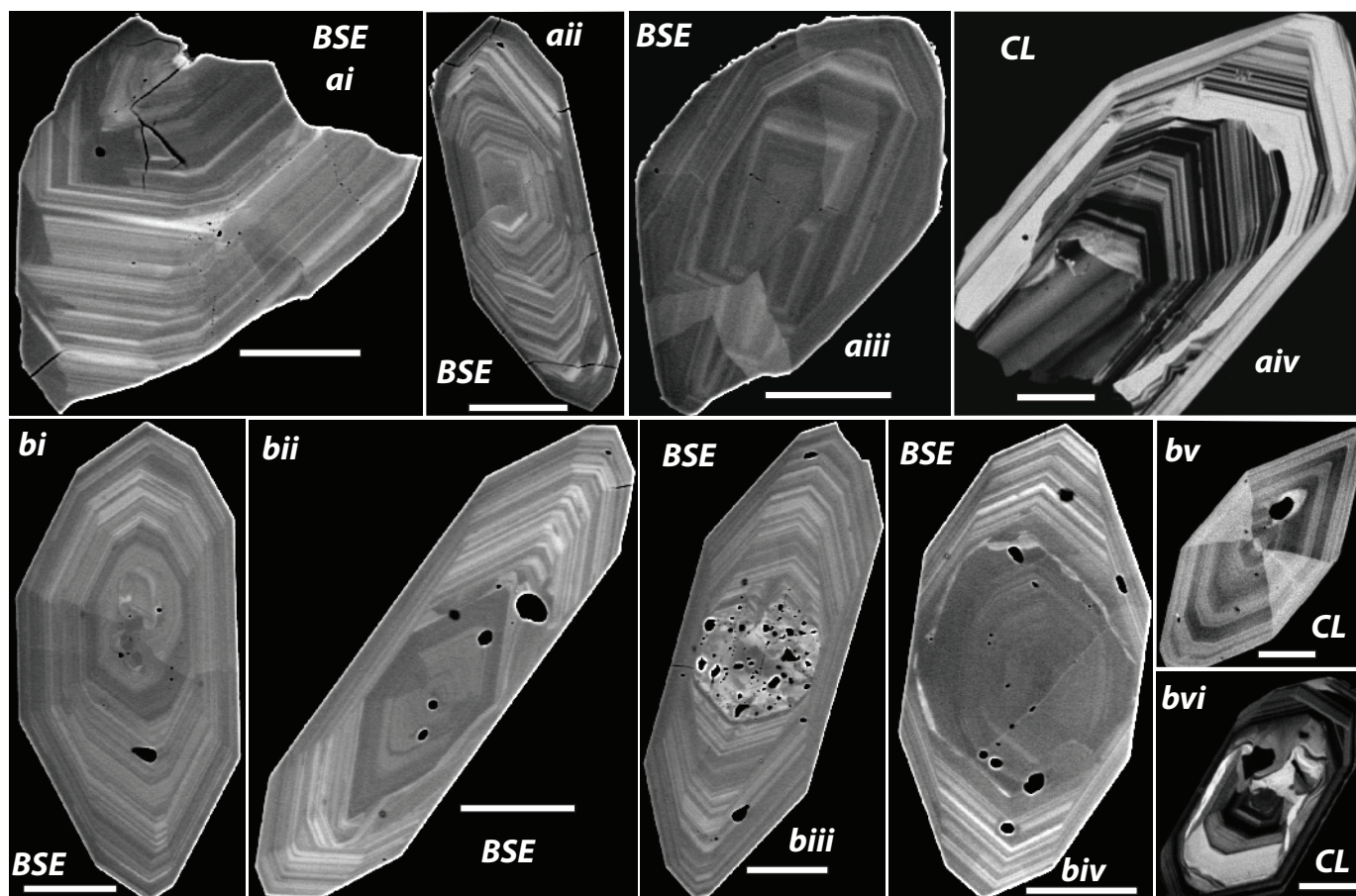


Figure 13. (ai-aiv) Representative BSE and CL images (denoted on image) of analysed zircon grains from feldspar porphyry dyke sampled from SG-09-41. Zircon grain in image 13(aiv) exhibits prominent oscillatory-zoned magmatic rims enclosing a partially resorbed xenocrystic core. (bi-bvi) Representative BSE and CL images (denoted on image) of analysed zircon grains from feldspar porphyry dyke sampled at surface within Nightmusic zone. Magmatic zircon is characterized by oscillatory zoning occurring either as rims on xenocrystic cores or as entire grains. Scale bars represent 50 μm . BSE = backscattered electron, CL = cathodoluminescence.

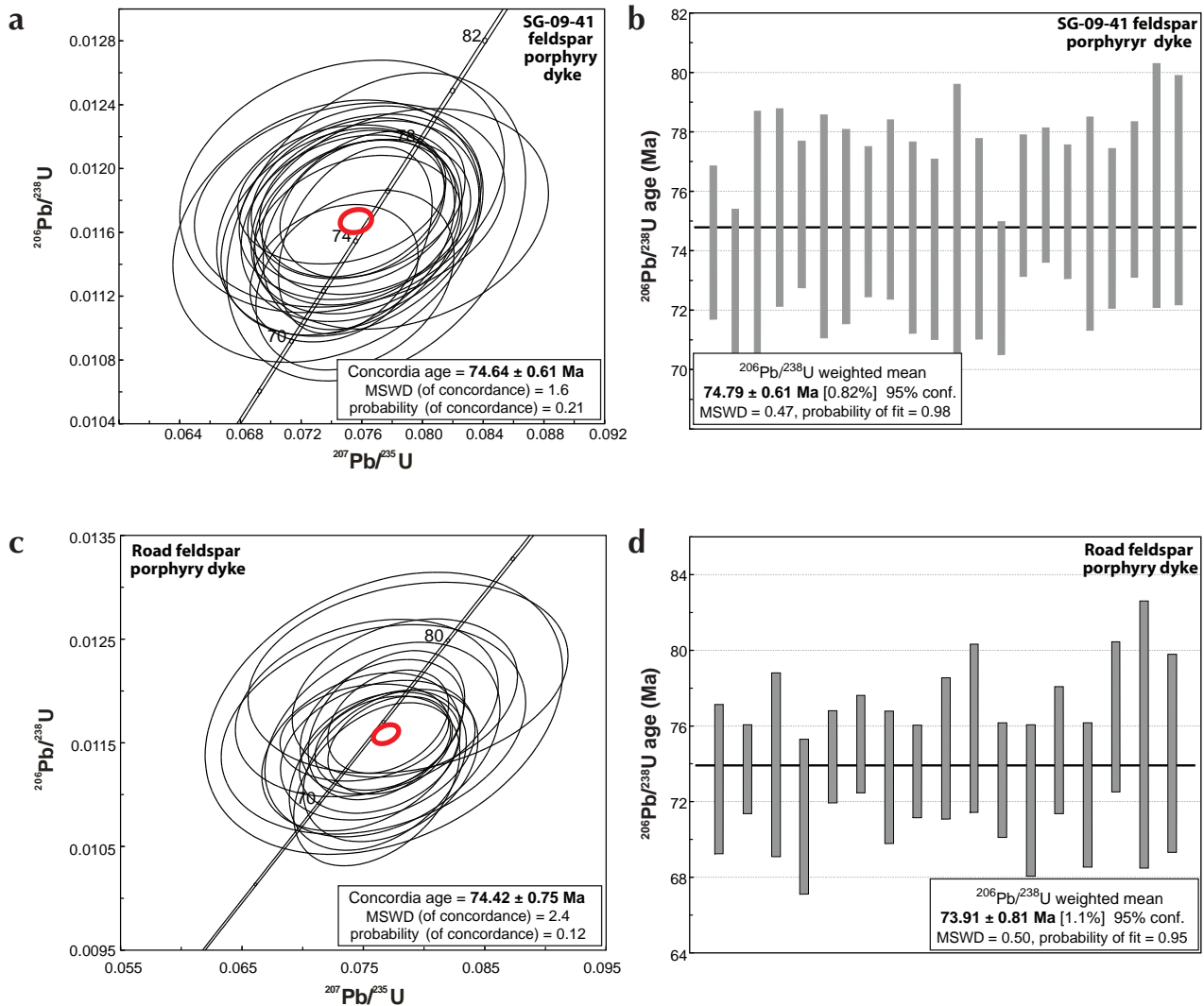


Figure 14. (a) Concordia diagram illustrating U-Pb analyses of magmatic zircon from feldspar porphyry dyke sampled from DDH SG-09-41 (ca. 152.8-153.3 m). Analyses included in age calculation have a probability of concordance greater than 0.20. Decay constant uncertainties of concordia are indicated. (b) Plot of weighted mean $^{206}\text{Pb}/^{238}\text{U}$ ages with probability of concordance greater than 0.20 for feldspar porphyry dyke, DDH SG-09-41. (c) Concordia diagram illustrating U-Pb analyses of magmatic zircon from feldspar porphyry dyke sampled at surface within the Nightmusic zone. Analyses included in age calculation have a probability of concordance greater than 0.20. (d) Plot of weighted mean $^{206}\text{Pb}/^{238}\text{U}$ ages with probability of concordance greater than 0.20 for surface sample of feldspar porphyry dyke, Nightmusic zone.

that have been completely replaced by secondary clay minerals, particularly in Au-enriched portions of the intrusion (Fig. 15a,b). Xenoliths of metasedimentary and meta-igneous gneiss occur sporadically throughout the body, and are particularly abundant along upper and lower contacts, which are typically brecciated (Fig. 15c,d). Sampling for U-Pb geochronology was restricted to xenolith-free portions of the stock that displayed clear magmatic textures from DDH SG-08-32 (272.2-300.4 m; Fig. 15b).

Abundant zircon of moderate quality was extracted from the sample of the Amadeus stock. Two morphologically

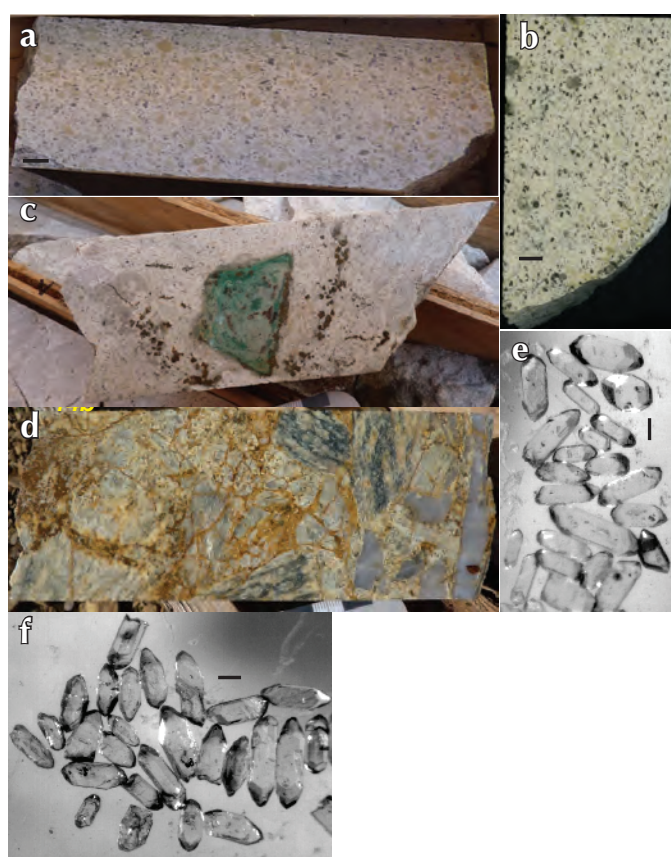


Figure 15. (a) Core photo illustrating feldspar porphyritic texture of medium to coarse-grained feldspar porphyry stock (Amadeus stock) sampled from DDH SG-08-32 (272.2-300.4 m). Scale bar represents 1 cm. (b) Slab image of U-Pb sample. Scale bar represents 1 cm. (c) Listwanite-altered ultramafic inclusion within Amadeus stock. (d) Brecciated upper contact of Amadeus stock with basement gneiss of Yukon-Tanana terrane. Transmitted light images of (e) faceted to prismatic zircon population, and (f) overgrowth zircon population. Scale bars represent 50 μm .

distinct populations are present in subequal amounts, including (i) clear, well-faceted elongate prisms and needles (Fig. 15c), and (ii) elongate prisms with core and rim relationships (Fig. 15f). Backscattered electron and CL imaging of both zircon populations demonstrate magmatic zircon occurs both as entire grains and as thick magmatic rims. Magmatic zircon is characterized by sharp oscillatory zoning (Fig. 16).

Twenty-seven analyses were acquired from 25 grains that were interpreted as magmatic zircon (Appendix 3). A concordia age calculated from 18 analyses yielded an age of 75.5 ± 0.79 Ma (MSWD = 1.07) and a weighted mean $^{206}\text{Pb}/^{238}\text{U}$ age of 75.53 ± 0.89 Ma (MSWD = 0.48; Figure 17a,b). Concentration data calculated from magmatic zircon ranges from 718-2608 ppm U and 92-796 ppm Th (Appendix 3).

DISCUSSION AND CONCLUSIONS

New geological, geophysical and U-Pb analytical data from the Sonora Gulch project indicate the occurrence of multiple overprinting events that can be correlated to different mineralizing environments (mesothermal vs. epithermal) and metal associations. Important vectoring criteria for the Nightmusic zone include proximity to the

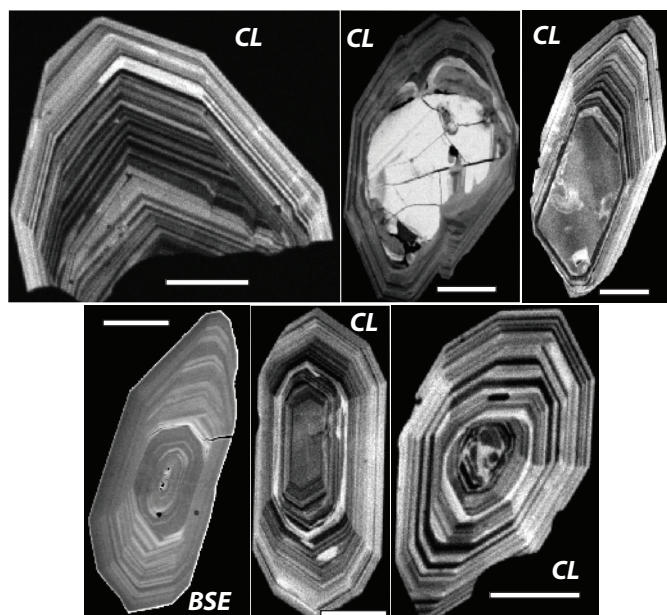


Figure 16. Representative BSE and CL images (denoted on image) of analysed zircon grains from Amadeus stock. Magmatic rims exhibit oscillatory enclosing partially resorbed xenocrystic cores. Scale bars represent 50 μm .

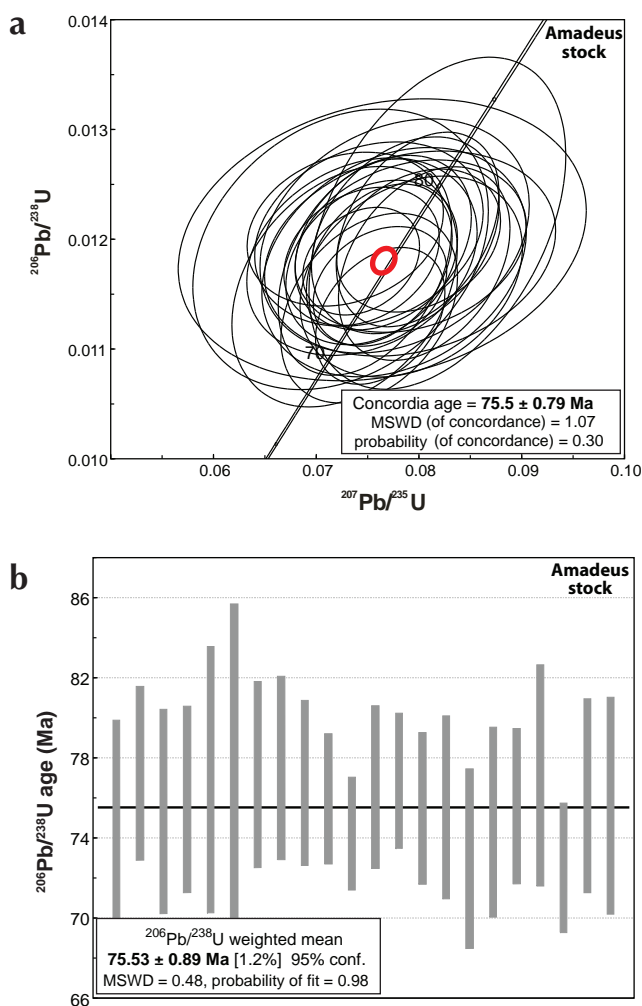


Figure 17. (a) Concordia diagram illustrating U-Pb analyses of magmatic zircon from Amadeus stock. Analyses included in age calculation have a probability of concordance greater than 0.20. Decay constant uncertainties of concordia are indicated. **(b)** Plot of weighted mean $^{206}\text{Pb}/^{238}\text{U}$ ages with probability of concordance greater than 0.20 for Amadeus stock.

northwest-trending Big Creek fault zone and recognition of an associated second-order, east-trending structural corridor. Serpentinized and listwanite-altered ultramafic lenses provide useful lithologies to focus on important target areas in this structural setting. Gold-enriched mesothermal base-metal skarn and replacement-style mineralization in the Nightmusic zone is overprinted by post-skarn fluid and magmatic events, including ubiquitous epithermal veining, feldspar porphyry dyke suite intrusion. Additionally, skarn sulphide paragenesis indicates replacement of sphalerite-galena-chalcopyrite (\pm Au)

mineralization by secondary pyrite and pyrrhotite, which may represent either the latest stage of skarn fluid evolution, or a discretely different fluid event that remobilized the pre-existing ore. Gold and silver mineralization occurring in the Amadeus stock show vertical zonation with appreciable concentrations of gold occurring at higher levels and silver at lower levels. Intervals of higher grade gold are typically associated with low to background arsenic values, suggesting a more evolved epithermal nature of gold mineralization.

The new U-Pb age data determined from each of two feldspar porphyry dykes (74.79 ± 0.61 Ma and 73.91 ± 0.81 Ma), a weakly mineralized quartz porphyry stock (75.73 ± 0.93 Ma) within the Nightmusic zone, and the gold-silver mineralized Amadeus stock (75.5 ± 0.79 Ma) demonstrate the widespread occurrence of Late Cretaceous magmatism within the property. This magmatism is coeval with the Late Cretaceous Carmacks Group rather than the mid-Late Cretaceous Prospector Mountain suite as previously interpreted. Age dating of a feldspar porphyry dyke located in the Nightmusic zone and occurring within the Big Creek fault zone, indicates that brittle deformation and movement along the Big Creek fault post-dated dyke emplacement (ca. 74 Ma). The age data also indicate that mineralization styles evolved from early mesothermal replacement and skarn type (Nightmusic zone), to a younger epithermal mineralizing environment, with the most economic concentrations currently recognized as occurring within the Amadeus zone. The lack of late-stage epithermal-style veining or feldspar porphyry dyke emplacement within the Amadeus stock is consistent with U-Pb age data that indicate that stock and dyke emplacement were contemporaneous.

Importantly, the new age dates indicate that magmatic-associated mineralization occurring within the Sonora Gulch property area are temporally equivalent to Western Copper Corporation's Casino Cu-Au-Mo deposit, located roughly 40 km to the west-northwest. Hence, these new datasets extend the currently known eastern limit of Late Cretaceous magmatism and associated polymetallic mineralization.

ACKNOWLEDGEMENTS

We thank Pam King, Earth Sciences Department, and Michael Tubrett and Michael Schaeffer for access and assistance in the MafIIC analytical facility, Memorial University. An earlier draft of this paper was reviewed and improved by Maurice Colpron.

REFERENCES

- Bennett, V. and Tubrett, M., 2010. U-Pb Isotopic Age dating by LAM ICP-MS, INCO Innovation Centre, Memorial University: Sample preparation methodology and analytical techniques. *In: Yukon Exploration and Geology 2009*, K.E. MacFarlane, L.H. Weston and L.R. Blackburn (eds.), Yukon Geological Survey, p. 47-55.
- Bineli Betsi, T. and Bennett, V., 2010. New U-Pb age constraints at Freegold Mountain: evidence for multiple phases of polymetallic mid- to Late Cretaceous Mineralization. *In: Yukon Exploration and Geology 2009*, K.E. MacFarlane, L.H. Weston and L.R. Blackburn (eds.), Yukon Geological Survey, p. 57-84.
- Colpron, M., Nelson, J.L. and Murphy, D.C., 2006. A tectonostratigraphic framework for the pericratonic terranes of the northern Cordillera. *In: Paleozoic Evolution and Metallogeny of Pericratonic Terranes at the Ancient Pacific Margin of North America*, M. Colpron and J.L. Nelson (eds.), Geological Association of Canada, Special Paper 45, p. 1-23.
- Davidson, G.S., 2000. Summary Report on the Sonora Gulch Property. Private report for Engineer Mining Corporation.
- Gordy, S.P. and Makepeace, A.J., 1999. Yukon Digital Geology. Geological Survey of Canada, Open File D3826. Exploration and Geological Services Division, Yukon, Indian and Northern Affairs Canada, Open File 1999-1(D).
- Johnston, S.T. and Hachey, N., 1993. Preliminary Results of 1:50 000 Scale Geologic Mapping in Wolverine Creek Map Area (1151-12), Dawson Range, Southwest Yukon. *In: Yukon Exploration and Geology 1992*, Exploration and Geological Services Division, Yukon Region, Indian and Northern Affairs Canada, p. 49-60.
- Ludwig, K.R., 1999. User's manual for Isoplot/Ex, version 2.06: a geochronological toolkit for Microsoft Excel. Berkeley Geochronological Center, Special Publication No. 1a, 49 p.
- Mortensen, J.K., 1992. Pre-mid-Mesozoic tectonic evolution of the Yukon-Tanana terrane, Yukon and Alaska. *Tectonics*, vol. 11, p. 836-853.
- Mortensen, J.K., Appel, V.L. and Hart, C.J.R., 2003. Geological and U-Pb age constraints on base and precious metal vein systems in the Mount Nansen area, eastern Dawson Range, Yukon. *In: Yukon Exploration and Geology 2002*, D.S. Emond and L.L. Lewis (eds.), Exploration and Geological Services Division, Yukon Region, Indian and Northern Affairs Canada, p. 165-174.
- Schulze, C. 2004: Summary and Preliminary Exploration Report on the Sonora Gulch Property, Dawson Range, Yukon; NI 43-101 Compatible Report for Firestone Ventures Inc. Effective date of report completion, April 14, 2004. Downloaded from SEDAR <<http://www.sedar.com>>, December, 2009.
- Schulze, C., 2007a: Assessment Report, 2006 Geological, Geophysical and Diamond Drilling Programs on the Sonora Gold Project, Carmacks area, Yukon Territory, Canada. Ministry of Energy, Mines and Resources, Government of Yukon.
- Schulze, C. 2007b. NI 43-101 technical report on the 2006 and 2007 exploration programs, Sonora Property, Dawson Range, Yukon, 279 p. Effective date of report completion, October 15, 2007. Downloaded from SEDAR <<http://www.sedar.com>>, July, 2009.
- Tempelman-Kluit, D.J., 1984. Geology of the Laberge (105E) and Carmacks (1151) map areas. Geological Survey of Canada, Open File 1101, 1:250 000 scale.

Appendix 1. LAM ICP-MS U-Pb analytical data for magmatic and inherited zircon from NTR-1, runway stock.

Analysis	Measured isotopic ratios				Calculated ages						U ppm	Ratio Th/U						
	$^{207}\text{Pb}/^{235}\text{U}$ 1 σ err.	$^{206}\text{Pb}/^{238}\text{U}$ 1 σ err.	Rho	$^{207}\text{Pb}/^{206}\text{Pb}$ 1 σ err.	$^{207}\text{Pb}/^{235}\text{U}$ 1 σ err. Ma	$^{206}\text{Pb}/^{238}\text{U}$ 1 σ err. Ma	Conc. age (Ma)	2 σ err. Ma	MSWD of conc.	Prob. of conc.			Th ppm					
Magmatic zircon																		
oc15B92	0.0766	0.0043	0.0116	0.0006	0.4303	0.0487	0.0004	75	4	74	4	74	6	0.05	0.82	427	2250	0.19
oc15B93	0.0801	0.0037	0.0120	0.0004	0.3551	0.0491	0.0007	78	3	77	3	77	5	0.16	0.69	119	530	0.22
oc15B94	0.0763	0.0071	0.0122	0.0007	0.2883	0.0467	0.0009	75	7	78	4	78	8	0.30	0.58	198	1342	0.15
oc15B96	0.0748	0.0024	0.0116	0.0002	0.3025	0.0477	0.0005	73	2	74	1	74	3	0.19	0.66	245	1666	0.15
oc15B97	0.0764	0.0034	0.0118	0.0003	0.3291	0.0482	0.0007	75	3	76	2	75	4	0.07	0.79	143	852	0.17
oc15B98	0.0789	0.0049	0.0120	0.0003	0.1958	0.0508	0.0013	77	5	77	2	77	4	0.00	0.95	75	223	0.34
oc15B99	0.0781	0.0024	0.0120	0.0002	0.3105	0.0480	0.0005	76	2	77	1	77	3	0.04	0.84	126	968	0.13
oc15B100	0.0793	0.0031	0.0117	0.0004	0.4163	0.0494	0.0005	77	3	75	2	76	4	0.67	0.41	279	1408	0.20
oc15B101	0.0841	0.0050	0.0121	0.0005	0.3672	0.0497	0.0007	82	5	77	3	79	6	0.99	0.32	122	1708	0.07
oc15B106	0.0775	0.0042	0.0120	0.0004	0.3162	0.0478	0.0006	76	4	77	3	77	5	0.13	0.72	114	852	0.13
oc15B107	0.0768	0.0038	0.0118	0.0003	0.2979	0.0488	0.0005	75	4	76	2	76	4	0.03	0.87	226	1225	0.18
oc15B108	0.0783	0.0072	0.0120	0.0005	0.2194	0.0521	0.0011	77	7	77	3	77	6	0.00	0.95	170	427	0.40
oc15B111	0.0772	0.0042	0.0120	0.0003	0.2549	0.0470	0.0008	76	4	77	2	77	4	0.12	0.73	160	446	0.36
oc15B112	0.0818	0.0044	0.0117	0.0004	0.3116	0.0510	0.0007	80	4	75	3	76	5	1.51	0.22	233	543	0.43
oc15B114	0.0758	0.0025	0.0117	0.0002	0.2564	0.0493	0.0005	74	2	75	1	75	2	0.23	0.63	283	1239	0.23
oc15B116	0.0756	0.0046	0.0116	0.0005	0.3299	0.0488	0.0006	74	4	74	3	74	6	0.01	0.93	133	909	0.15
oc15B117	0.0784	0.0094	0.0120	0.0008	0.2622	0.0515	0.0007	77	9	77	5	77	9	0.00	0.98	192	1306	0.15
oc15B118	0.0761	0.0026	0.0117	0.0002	0.2738	0.0472	0.0007	74	2	75	1	75	3	0.06	0.80	93	994	0.09
Inherited zircon																		
oc15B95	0.5017	0.0163	0.0652	0.0013	0.2962	0.0559	0.0007	413	11	407	8	409	14	0.25	0.61	101	167	0.61
oc15B109	0.1046	0.0056	0.0165	0.0005	0.2858	0.0473	0.0007	101	5	106	3	105	6	0.76	0.38	339	578	0.59
oc15B110	0.0872	0.0070	0.0132	0.0004	0.2045	0.0484	0.0010	85	7	85	3	85	5	0.00	0.96	101	365	0.28
oc15B113	0.1056	0.0065	0.0159	0.0007	0.3463	0.0485	0.0007	102	6	102	4	102	8	0.00	0.95	346	694	0.50
oc15B115	0.5349	0.1798	0.0644	0.0093	0.2144	0.0577	0.0010	435	119	402	56	406	109	0.07	0.79	413	425	0.97

Appendix 2. LAM ICP-MS U-Pb analytical data for magmatic zircon from diamond drillhole SG-09-41 feldspar porphyry dyke and Road feldspar porphyry dyke.

Analysis	Measured isotopic ratios				Calculated ages							U ppm	Ratio Th/U					
	$^{207}\text{Pb}/^{235}\text{U}$ 1 σ err.	$^{206}\text{Pb}/^{238}\text{U}$ 1 σ err.	Rho	$^{207}\text{Pb}/^{206}\text{Pb}$ 1 σ err.	$^{207}\text{Pb}/^{235}\text{U}$ 1 σ err. Ma	$^{206}\text{Pb}/^{238}\text{U}$ 1 σ err. Ma	Conc. age (Ma)	2 σ err. Ma	MSWD of conc.	Prob. of conc.	Th ppm							
SG-09-41 - FP																		
oc15c166	0.07575	0.00281	0.01159	0.00020	0.23652	0.04926	0.00058	74	3	74	1	74	3	0.00	0.97	219	1371	0.16
oc15c167	0.07555	0.00267	0.01130	0.00023	0.28854	0.04959	0.00062	74	3	72	1	73	3	0.36	0.55	177	1113	0.16
oc15c168	0.07369	0.00414	0.01161	0.00034	0.25760	0.04567	0.00076	72	4	74	2	74	4	0.31	0.58	120	535	0.22
oc15c169	0.07520	0.00418	0.01177	0.00026	0.19989	0.05036	0.00084	74	4	75	2	75	3	0.21	0.65	100	482	0.21
oc15c170	0.07534	0.00280	0.01173	0.00019	0.22275	0.04916	0.00077	74	3	75	1	75	2	0.29	0.59	162	666	0.24
oc15c172	0.07522	0.00359	0.01167	0.00029	0.26497	0.04709	0.00086	74	3	75	2	75	4	0.12	0.73	71	398	0.18
oc15c173	0.07588	0.00320	0.01167	0.00026	0.26101	0.04890	0.00060	74	3	75	2	75	3	0.03	0.86	75	893	0.08
oc15c174	0.07630	0.00281	0.01170	0.00020	0.23063	0.04945	0.00056	75	3	75	1	75	2	0.01	0.91	112	1405	0.08
oc15c175	0.07589	0.00326	0.01176	0.00024	0.23501	0.04882	0.00073	74	3	75	2	75	3	0.12	0.72	189	859	0.22
oc15c176	0.07605	0.00268	0.01161	0.00025	0.31043	0.04700	0.00062	74	3	74	2	74	3	0.00	1.00	148	920	0.16
oc15c177	0.07557	0.00207	0.01155	0.00024	0.37819	0.04733	0.00041	74	2	74	2	74	3	0.00	0.98	83	1637	0.05
oc15c187	0.07695	0.00402	0.01163	0.00039	0.32438	0.04774	0.00071	75	4	75	3	75	5	0.03	0.85	113	669	0.17
oc15c188	0.07407	0.00273	0.01192	0.00020	0.22676	0.04756	0.00060	73	3	76	1	76	2	2.16	0.14	242	788	0.31
oc15c190	0.07442	0.00314	0.01160	0.00027	0.27042	0.04775	0.00064	73	3	74	2	74	3	0.25	0.62	89	710	0.13
oc15c191	0.07417	0.00227	0.01134	0.00018	0.25389	0.04846	0.00055	73	2	73	1	73	2	0.00	0.98	111	1305	0.09
oc15c194	0.07535	0.00249	0.01178	0.00019	0.24120	0.04780	0.00059	74	2	75	1	75	2	0.54	0.46	245	928	0.26
oc15c195	0.07469	0.00280	0.01184	0.00018	0.20055	0.04893	0.00077	73	3	76	1	76	2	1.05	0.31	112	743	0.15
oc15c196	0.07605	0.00222	0.01175	0.00018	0.25802	0.04794	0.00051	74	2	75	1	75	2	0.17	0.68	298	1473	0.20
oc15c197	0.07850	0.00400	0.01168	0.00028	0.23697	0.04996	0.00071	77	4	75	2	75	3	0.24	0.62	196	698	0.28
oc15c198	0.07819	0.00230	0.01206	0.00020	0.27975	0.04678	0.00059	76	2	77	1	77	2	0.14	0.71	174	672	0.26
oc15c204	0.07570	0.00276	0.01166	0.00021	0.24812	0.04701	0.00067	74	3	75	1	75	3	0.06	0.80	128	617	0.21
oc15c205	0.07576	0.00288	0.01181	0.00021	0.22938	0.04934	0.00066	74	3	76	1	76	3	0.32	0.57	108	613	0.18
oc15c206	0.07470	0.00437	0.01189	0.00032	0.23236	0.04819	0.00118	73	4	76	2	76	4	0.53	0.47	50	162	0.31
oc15c207	0.07513	0.00462	0.01186	0.00030	0.20810	0.04922	0.00084	74	4	76	2	76	4	0.32	0.57	75	557	0.14

continued on next page

Appendix 2. continued

Analysis	Measured isotopic ratios					Calculated ages								
	$^{207}\text{Pb}/^{235}\text{U}$ 1 σ err.	$^{206}\text{Pb}/^{238}\text{U}$ 1 σ err.	Rho	$^{207}\text{Pb}/^{206}\text{Pb}$ 1 σ err.	$^{207}\text{Pb}/^{235}\text{U}$ 1 σ err. Ma	$^{206}\text{Pb}/^{238}\text{U}$ Ma	1 σ err. Ma	Conc. age (Ma)	2 σ err. Ma	MSWD of conc.	Prob. of conc.	Th ppm	U ppm	Ratio Th/U
Road - FP Dyke														
oc15B59	0.0748	0.0033	0.3057	0.0490	0.0006	73	3	73	4	0.00	0.97	195	1160	0.17
oc15B62	0.0787	0.0054	0.2368	0.0484	0.0008	77	5	78	5	0.02	0.88	156	1113	0.14
oc15B63	0.0766	0.0023	0.2708	0.0477	0.0005	75	2	74	2	0.34	0.56	295	1549	0.19
oc15B64	0.0766	0.0040	0.3214	0.0498	0.0006	75	4	74	5	0.07	0.79	121	973	0.12
oc15B65	0.0761	0.0028	0.3939	0.0494	0.0005	74	3	71	4	1.59	0.21	194	2772	0.07
oc15B66	0.0803	0.0027	0.3152	0.0494	0.0006	78	3	78	3	0.10	0.75	105	779	0.13
oc15B68	0.0751	0.0028	0.2182	0.0499	0.0007	74	3	74	2	0.09	0.76	154	1117	0.14
oc15B73	0.0771	0.0020	0.3286	0.0467	0.0005	75	2	75	2	0.03	0.85	318	1632	0.19
oc15B75	0.0762	0.0033	0.2799	0.0502	0.0007	75	3	73	3	0.18	0.67	177	1079	0.16
oc15B76	0.0772	0.0021	0.3091	0.0487	0.0005	76	2	74	2	0.98	0.32	284	1789	0.16
oc15B77	0.0769	0.0026	0.3673	0.0469	0.0006	75	2	75	3	0.03	0.86	78	1119	0.07
oc15B78	0.0753	0.0044	0.2512	0.0496	0.0009	74	4	76	4	0.26	0.61	46	526	0.09
oc15B80	0.0763	0.0027	0.2957	0.0494	0.0006	75	3	73	3	0.39	0.53	323	1680	0.19
oc15B81	0.0762	0.0030	0.3589	0.0496	0.0005	75	3	72	4	0.82	0.37	317	2246	0.14
oc15B82	0.0765	0.0028	0.3160	0.0486	0.0005	75	3	75	3	0.00	0.94	137	1411	0.10
oc15B83	0.0773	0.0029	0.3493	0.0496	0.0007	76	3	72	4	1.37	0.24	154	1106	0.14
oc15B84	0.0784	0.0038	0.2704	0.0484	0.0008	77	4	76	4	0.00	0.95	124	449	0.28
oc15B85	0.0767	0.0060	0.3005	0.0501	0.0007	75	6	76	7	0.01	0.93	183	491	0.37
oc15B86	0.0758	0.0051	0.2625	0.0499	0.0012	74	5	75	5	0.00	0.95	54	259	0.21
oc15B86	0.0847	0.0056	0.2448	0.0482	0.0006	83	5	85	5	0.16	0.69	298	1388	0.21
oc15B61	0.5102	0.0686	0.4148	0.0551	0.0009	419	46	423	77	0.01	0.92	90	170	0.53
oc15B69	0.0834	0.0300	0.1305	0.0561	0.0014	81	28	75	14	0.05	0.82	156	1311	0.12
oc15B74	0.0938	0.0083	0.2126	0.0539	0.0011	91	8	94	7	0.11	0.74	29	227	0.13
oc15B79	0.2904	0.0440	0.3370	0.0582	0.0008	259	35	262	48	0.01	0.94	166	212	0.78

Appendix 3. LAM ICP-MS U-Pb analytical data for magmatic zircon from Amadeus stock.

Analysis	Measured isotopic ratios					Calculated ages										
	$^{207}\text{Pb}/^{235}\text{U}$ 1 σ err.	$^{206}\text{Pb}/^{238}\text{U}$ 1 σ err.	Rho	$^{207}\text{Pb}/^{206}\text{Pb}$ 1 σ err.	$^{207}\text{Pb}/^{235}\text{U}$ 1 σ err. Ma	$^{206}\text{Pb}/^{238}\text{U}$ 1 σ err. Ma	Conc. age (Ma)	2 σ err. Ma	MSWD of conc.	Prob. of conc.	Th ppm	U ppm	Ratio Th/U			
oc15B21	0.07276	0.00448	0.31412	0.04766	0.00069	71	4	74	3	73	5	0.43	0.51	247	1247	0.20
oc15B23	0.07513	0.00454	0.23537	0.04730	0.00063	74	4	77	2	77	4	0.71	0.40	378	1130	0.33
oc15B24	0.07474	0.00345	0.37173	0.04713	0.00060	73	3	75	3	75	5	0.40	0.53	183	718	0.26
oc15B25	0.07445	0.00458	0.25223	0.04811	0.00077	73	4	76	2	75	4	0.46	0.50	181	761	0.24
oc15B26	0.07642	0.00811	0.20606	0.05105	0.00079	75	8	77	3	77	7	0.07	0.79	258	1022	0.25
oc15B27	0.08179	0.00510	0.40771	0.04946	0.00064	80	5	78	4	79	7	0.17	0.68	92	1272	0.07
oc15B28	0.07868	0.00373	0.32069	0.04744	0.00066	77	4	77	2	77	4	0.00	0.95	241	1093	0.22
oc15B29	0.07987	0.00324	0.36970	0.04698	0.00068	78	3	77	2	78	4	0.03	0.85	252	1050	0.24
oc15B30	0.07652	0.00350	0.29629	0.04774	0.00055	75	3	77	2	76	4	0.30	0.58	233	1156	0.20
oc15B31	0.07441	0.00309	0.26163	0.04802	0.00052	73	3	76	2	75	3	1.05	0.31	436	1520	0.29
oc15B36	0.07620	0.00265	0.27629	0.04983	0.00064	75	3	74	1	74	3	0.03	0.87	518	1326	0.39
oc15B37	0.07920	0.00459	0.23172	0.04958	0.00086	77	4	76	2	77	4	0.04	0.84	163	736	0.22
oc15B38	0.07997	0.00326	0.27264	0.04873	0.00080	78	3	77	2	77	3	0.18	0.67	302	922	0.33
oc15B39	0.07613	0.00290	0.33385	0.04805	0.00059	75	3	75	2	75	4	0.11	0.74	472	1236	0.38
oc15B40	0.08051	0.00341	0.36148	0.04924	0.00067	79	3	75	2	76	4	0.97	0.33	193	829	0.23
oc15B41	0.07515	0.00351	0.33211	0.04834	0.00068	74	3	73	2	73	4	0.04	0.84	194	1061	0.18
oc15B42	0.07925	0.00442	0.28732	0.04939	0.00082	77	4	75	2	75	5	0.42	0.52	270	1133	0.24
oc15B43	0.07540	0.00341	0.28655	0.04758	0.00064	74	3	76	2	75	4	0.29	0.59	234	1179	0.20
oc15B44	0.07763	0.00535	0.26259	0.04848	0.00074	76	5	77	3	77	5	0.05	0.82	347	868	0.40
oc15B46	0.07622	0.00257	0.33352	0.04876	0.00058	75	2	72	2	73	3	0.78	0.38	330	1542	0.21
oc15B50	0.07914	0.00578	0.21988	0.04997	0.00083	77	5	76	2	76	5	0.05	0.82	291	986	0.30
oc15B51	0.07758	0.00526	0.26690	0.05000	0.00079	76	5	76	3	76	5	0.00	0.95	179	765	0.23
oc15B53	0.07283	0.00390	0.22094	0.04539	0.00075	71	4	77	2	77	4	2.68	0.10	345	899	0.38
oc15B54	0.07238	0.00588	0.26988	0.04644	0.00067	71	6	76	3	75	6	0.90	0.34	349	1091	0.32
oc15B55	0.07437	0.00232	0.27170	0.04677	0.00058	73	2	76	1	75	2	1.57	0.21	233	1386	0.17
oc15B20	0.08081	0.00311	0.26420	0.05685	0.00056	79	3	71	1	71	3	8.25	0.00	796	2608	0.31
oc15B22	0.06773	0.00790	0.08599	0.06018	0.00141	67	8	76	2	76	3	1.55	0.21	289	1045	0.28

U-Pb isotopic age dating by LAM ICP-MS, INCO Innovation Centre, Memorial University: Sample preparation methodology and analytical techniques

Venessa Bennett¹

Yukon Geological Survey

Michael Tubrett

CREAIT Network, Microanalysis Facility, INCO Innovation Centre, Memorial University

Bennett, V. and Tubrett, M., 2010. U-Pb isotopic age dating by LAM ICP-MS, INCO Innovation Centre, Memorial University: Sample preparation methodology and analytical techniques. *In: Yukon Exploration and Geology 2009*, K.E. MacFarlane, L.H. Weston and L.R. Blackburn (eds.), Yukon Geological Survey, p. 47-55.

ABSTRACT

This contribution reports on sample preparation methods and Laser Ablation Microprobe Inductively Coupled Plasma Mass Spectrometry (LAM ICP-MS) analytical techniques routinely used to acquire U-Pb isotopic age data at the INCO Innovation Centre, Memorial University. Four concordant zircon reference materials that span from Miocene to Archean in age (9.52 Ma, 337.15 Ma, 1066.3 Ma and 2674.3 Ma) were recently analysed during a data collection session in which U-Pb isotopic data for 11 suspected Cretaceous plutonic rocks were being acquired. Final U-Pb age calculations determined for the four zircon reference materials are in excellent agreement with the corresponding known and/or published ID TIMS ages and demonstrate the reproducibility, accuracy and precision of the LAM ICP-MS technique. Furthermore, data collected for sample GP-09-02 demonstrate the applicability of the LAM ICP-MS technique for dating zircon populations as young as Miocene.

¹venessa.bennett@gov.yk.ca

INTRODUCTION

The intent of this contribution is to outline the sample preparation and analytical methodology employed during the recent acquisition of U-Pb isotopic datasets on Cretaceous-age plutonic rocks through Laser Ablation Microprobe Inductively Coupled Plasma Mass Spectrometry (LAM ICP-MS). The LAM ICP-MS instrumentation used comprises part of the Micro Analytical Facility within the INCO Innovation Centre at Memorial University. Geochronology using ICP-MS techniques has been carried at Memorial University since at least 1993, when initial experiments indicated that analysis of $^{206}\text{Pb}/^{207}\text{Pb}$ ratios could be performed *in situ* on zircon grains when the ICP-MS was coupled to a laser ablation sample introduction system (Fryer *et al.*, 1993; Jackson *et al.*, 2004.). Since the initial experiments, the methodology has consistently evolved and improved, such that data currently produced are sufficiently accurate and precise to unravel complex geological histories from at least the Miocene onwards. We report the analytical conditions and sample preparation techniques that were employed to complete U-Pb dating of 11 Cretaceous plutonic rocks collected throughout Yukon during the summer of 2009 (presented elsewhere in this volume). Additionally, we present U-Pb isotopic data for four zircon reference materials that were routinely analysed during data collection.

ANALYTICAL METHODS

Zircon separates were extracted using standard crushing techniques, and heavy mineral concentrates were produced using a WilfleyTM table, heavy liquids and a FrantzTM isodynamic separator before hand-picking in ethanol under a binocular microscope. All extraction and analyses were conducted at Memorial University, Department of Earth Sciences and INCO Innovation Centre.

Subdivision of zircon populations was initially carried out using a binocular microscope and standard optical criteria (*i.e.*, colour, morphology and inclusion characteristics). A subset (average of $n = 20\text{-}30$ per population) of grains selected from each zircon population identified using optical criteria were isolated, photographed in transmitted light and subsequently mounted in epoxy resin and polished to expose grain cores. Grain mounts were then carbon coated and imaged using backscattered electron (BSE) and cathodoluminescence (CL) image analysis. The number of zircon grains imaged per sample ranged

between 60 and 100 depending on the complexity of the zircon populations. Thorough characterization of the magmatic zircon populations is crucial for correct selection of grains that will yield the most accurate estimate of the crystallization age. Additionally, a clear understanding of zircon epitaxial relationships (core vs. rim) occurring within an unknown population assists intragrain placement of the laser beam, which ensures analysis of single discrete age domains rather than overlapping age domains. Analysis of multiple age domains within a single zircon grain produces isotopically heterogeneous data which, typically, is a significant contributor to U-Pb discordance using the LAM ICP-MS technique.

Zircon unknowns and reference materials were polished to a $0.25\ \mu\text{m}$ finish using an automated Struers TegrasytemTM polisher. Grain mounts were washed in ethyl alcohol and placed in an ultrasonic bath of deionized water for 2-5 minutes between polishing steps and after the final $0.25\ \mu\text{m}$ polish was attained. Immediately prior to loading grain mounts into the laser sample cell, unknowns and reference materials were repolished for 3 minutes to $0.25\ \mu\text{m}$, washed in ethyl alcohol and placed in an ultrasonic bath of deionized water for 2-5 minutes. Grain mounts were then dried and transferred to a reflected-light microscope, where a cotton swab soaked in acetone was used to gently scrub grain surfaces and remove any dirt or other particles. Each grain mount was viewed under the reflected light microscope to ensure the sample surface was clean of particles and free of scratches.

U/Pb and Pb/Pb isotopic ratios of the unknown samples and four zircon reference materials analysed for data quality control purposes were measured using a Finnigan ELEMENT XR double focusing magnetic sector field ICP-MS coupled to Geolas 193 nm excimer laser. Zircon grains previously imaged by BSE and CL techniques were ablated using two ablation methods:

Method 1: a $10\ \mu\text{m}$ laser beam was rastered over the sample surface at a velocity of $10\ \mu\text{m}/\text{s}^{-1}$ to create a $40 \times 40\ \mu\text{m}$ square spot (Fig. 1a,b). Laser energy was set at $5\ \text{J}/\text{cm}^2$ with a laser repetition rate of 10 Hz.

Method 2: $10\ \mu\text{m}$ and $20\ \mu\text{m}$ diameter line rasters were employed (Fig. 1c-f) where either zircon epitaxial relationships required sampling of thin magmatic rims ($10\ \mu\text{m}$ lines) or, where increased precision was required ($20\ \mu\text{m}$ lines). In each situation, the laser beam was programmed to create a linear ablation within

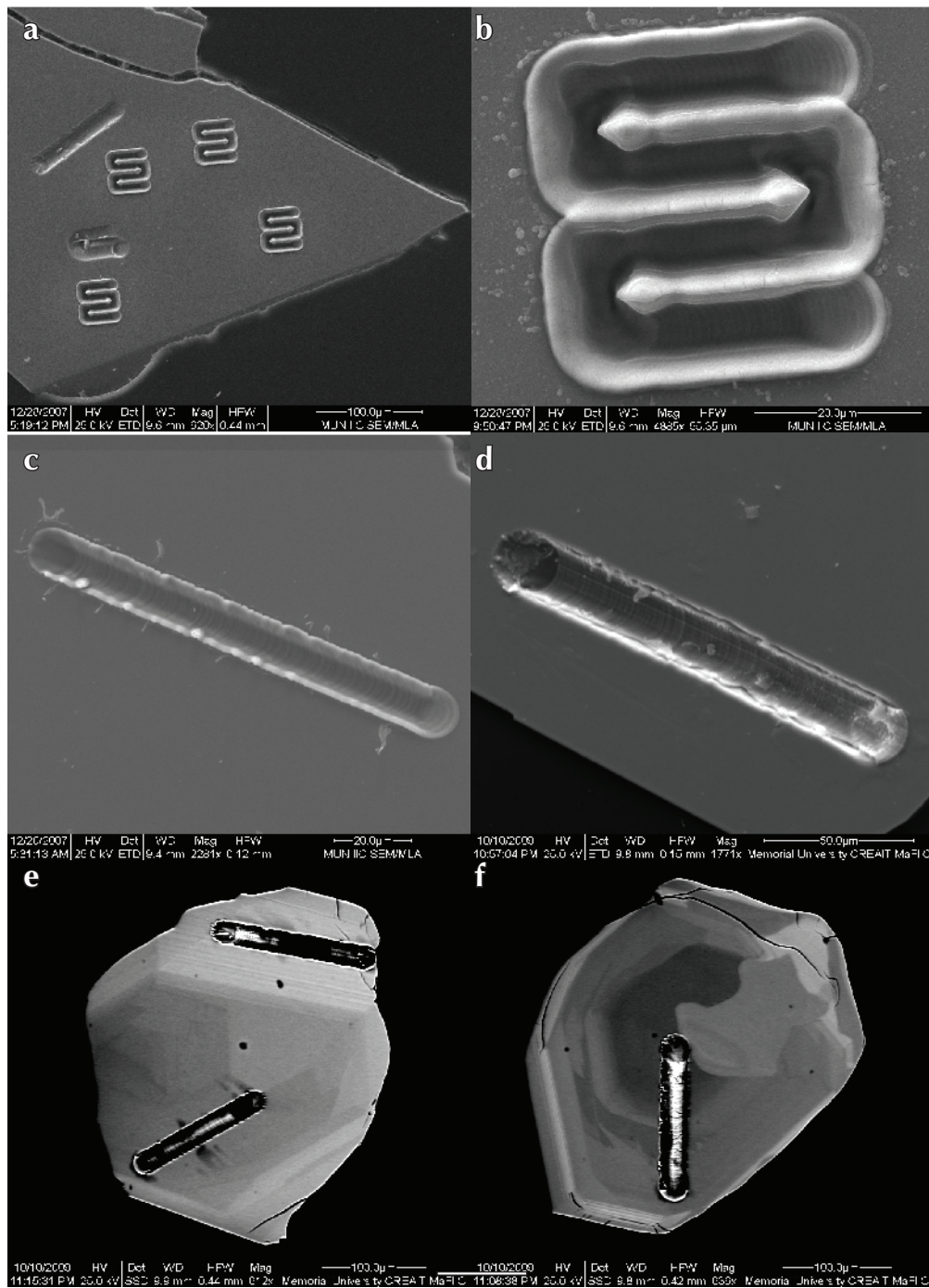


Figure 1. Representative LAM ICP-MS pit images of ablated zircon. **(a)** Secondary electron (SE) image enlargement of 40 x 40 μm raster ablation pit in Plešovice zircon. **(b)** SE image of 40 x 40 μm raster ablation pit morphology. **(c)** Secondary electron image illustrating pit morphology of 10 μm line raster. **(d)** SE image illustrating pit morphology of 20 μm line raster. **(e)** and **(f)** Representative backscattered electron images illustrating location of 20 μm pits associated with core and rim analysis performed on complex zircon populations.

zones of interest. Laser energy was set at 5 J/cm² with a laser repetition rate of 5 Hz and the stage was moved along the desired path at 1 μm/s⁻¹. Prior to data collection using linear ablation, the grain was pre-ablated by firing 5-10 shots of the laser beam (60-100 μm diameter; 5 J/cm² energy) onto the grain surface to remove surface contamination.

The sample introduction system enabled simultaneous nebulization of an internal standard tracer solution and laser ablation of the solid sample. The tracer solution, consisting of a mixture of natural Tl (²⁰⁵Tl/²⁰³Tl = 2.3871), ²⁰⁹Bi and enriched ²³³U, and ²³⁷Np (concentrations of ~1 ppb per isotope) transported in a mixed Ar-He carrier gas, was employed to correct for instrumental mass bias. The various isotopic compositions of the aspirated solution were calibrated against a variety of well-characterized zircon reference materials. These zircons have a wide range of ages and U and Pb concentrations and hence, provide enough variation in isotopic ratios to cover the isotopic range of unknown zircons analysed.

Time-resolved data acquisitions (120-205 s experiments) consisted of N 20-30 s measurement of the Ar-He gas blank and aspirated tracer solution prior to introduction of ablated material.

Data were collected on unknown zircon samples and four zircon reference materials, GP-09-02 (ca. 9.52 Ma), Plešovice (ca. 337 Ma), 91500 (ca. 1065 Ma) and VB165 (ca. 2674 Ma), whose U-Pb and Pb-Pb ages had been previously determined by Isotope Dilution Thermal Ionization Mass Spectrometry (ID TIMS). Typically 10 unknowns were collected for every 6-8 analyses of the reference materials. Analysis and treatment of zircon reference materials as unknowns is a robust quality control procedure that allows assessment of the accuracy and precision of the technique during an analytical session. This approach ensures the efficiency of the mass bias correction as well as the correction for laser-induced fractionation. Additionally, the choice of zircon reference materials that encompass a range of geological time (Miocene to Archean) ensures that the accuracy of all three measured isotopic ratios, ²⁰⁷Pb/²³⁵U, ²⁰⁶Pb/²³⁸U and ²⁰⁷Pb/²⁰⁷Pb are monitored. Typically Archean material produces precise ²⁰⁷Pb/²⁰⁷Pb ages and less precise ²⁰⁷Pb/²³⁵U and ²⁰⁶Pb/²³⁸U ages. In contrast, analysis of Phanerozoic material results in precise ²⁰⁷Pb/²³⁵U and ²⁰⁶Pb/²³⁸U ages, but generally imprecise ²⁰⁷Pb/²⁰⁷Pb ages. This is particularly useful when analysing inherited or detrital zircon populations, which are typically characterized by a wide range of ages.

During ablation, U and Pb isotopes and tracer solution signals were acquired in time-resolved peak-jumping, pulse-counting mode with one point measured per peak. The range of masses measured for each analysis was: ²⁰²(Hg) (flyback or settling mass), ²⁰⁴(Hg), ²⁰³(Tl), ²⁰⁵(Tl), ²⁰⁶(Pb), ²⁰⁷(Pb), ²⁰⁹(Bi), ²³²(Th), ²³³(U), ²³⁷(Np) and ²³⁸(U). Three oxide masses ²⁴⁹(²³³U¹⁶O), ²⁵³(²³⁷Np¹⁶O) and ²⁵⁴(²³⁸U¹⁶O) were measured to correct for oxide formation by adding signal intensities at masses 249, 253 and 254 to the intensities at masses 233, 237 and 238, respectively. Raw data were corrected for dead time (20 ns) of the electron multiplier and processed off line in an Excel spreadsheet-based program (LAMdate - Košler *et al.*, 2002). For detailed description of the technique, see Košler *et al.* (2002) and Cox *et al.* (2003). Data reduction for ablation method 1 included correction for gas blank, laser-induced elemental fractionation of Pb and U via the intercept method after Sylvester and Ghaderi (1997) and instrument mass bias. The mass bias correction utilized the power law and the ratio measurements of the isotopic tracer solution (Horn *et al.*, 2000; Košler *et al.*, 2002).

The intercept method of Sylvester and Ghaderi (1997) was not readily applicable to the line raster analyses performed with ablation method 2 due to the minimization of elemental fractionation at the ablation site when utilizing a 1 μm/s⁻¹ raster speed. In these cases, average isotopic ratios were used rather than intercept ratios.

No common Pb correction was applied to the data, however, mass 204 was monitored as an indirect assessment of common Pb concentrations. For any individual analysis, where 204 levels exceeded acceptable background levels, the data were rejected from the final dataset. Th and U concentrations for the unknown zircons were calibrated against analyses of zircon 91500. Isoplot vs. 2.06 of Ludwig (1999), in conjunction with the LAMdate Excel spreadsheet program was used to calculate final U-Pb ages of unknowns, and present data in graphical format (Košler *et al.*, 2002).

Final interpreted crystallization ages of both unknown and reference materials are based on calculation of concordia ages from individual U-Pb isotopic analyses that have a probability of concordance greater than 0.20. Age calculations include U decay constant uncertainties, which are plotted graphically on concordia plots. A concordia age that includes U decay constant uncertainties is considered the best estimate of the crystallization age of a sample.

ANALYSES OF REFERENCE MATERIALS AND TREATMENT OF DATA

Routine analysis of four zircon reference materials was carried out during a recent session of U-Pb isotopic data collection (October 14-19, 2009). As mentioned above, reference material analysis is a necessary quality control procedure that ensures production of geologically accurate and precise isotopic data. In addition to the two internationally recognized zircon reference materials, Plešovice (weighted mean $^{206}\text{Pb}/^{238}\text{U} = 337.13 \pm 0.37$ Ma; Slama *et al.*, 2008) and 91500 (weighted mean $^{207}\text{Pb}/^{206}\text{Pb} = 1066.4 \pm 0.3$ Ma; Schoene *et al.*, 2006), we used two internal reference materials with ID TIMS ages, GP-09-02 and VB165. GP-09-02 has a weighted mean $^{206}\text{Pb}/^{238}\text{U}$ date of 9.520 Ma ($n = 7$, MSWD = 0.5) with a total combined error (internal, tracer solution calibration

and decay constant error) of ± 0.022 Ma (unpublished data, Boise State University Isotope Geology Laboratory). This age was corrected for initial Th/U disequilibrium. A Th/U ratio for the melt of 3 was used in the correction and resulted in increasing the $^{206}\text{Pb}/^{238}\text{U}$ date by ca. 70 ka. VB165 has a weighted mean $^{207}\text{Pb}/^{206}\text{Pb}$ age of 2674.3 ± 0.8 Ma (not including decay constant errors; $n = 4$, MSWD = 0.42; Bennett *et al.*, 2005) and a concordia age of 2671 ± 3 Ma (U decay constant uncertainties included).

Representative CL and BSE images, U-Pb concordia and weighted mean plots for LAM ICP-MS analyses collected for the four reference materials are shown in Figures 2-5. Table 1 summarizes the final calculated LAM ICP-MS ages for each sample and the accepted ID TIMS age for each zircon reference material. Uncertainties reported for all

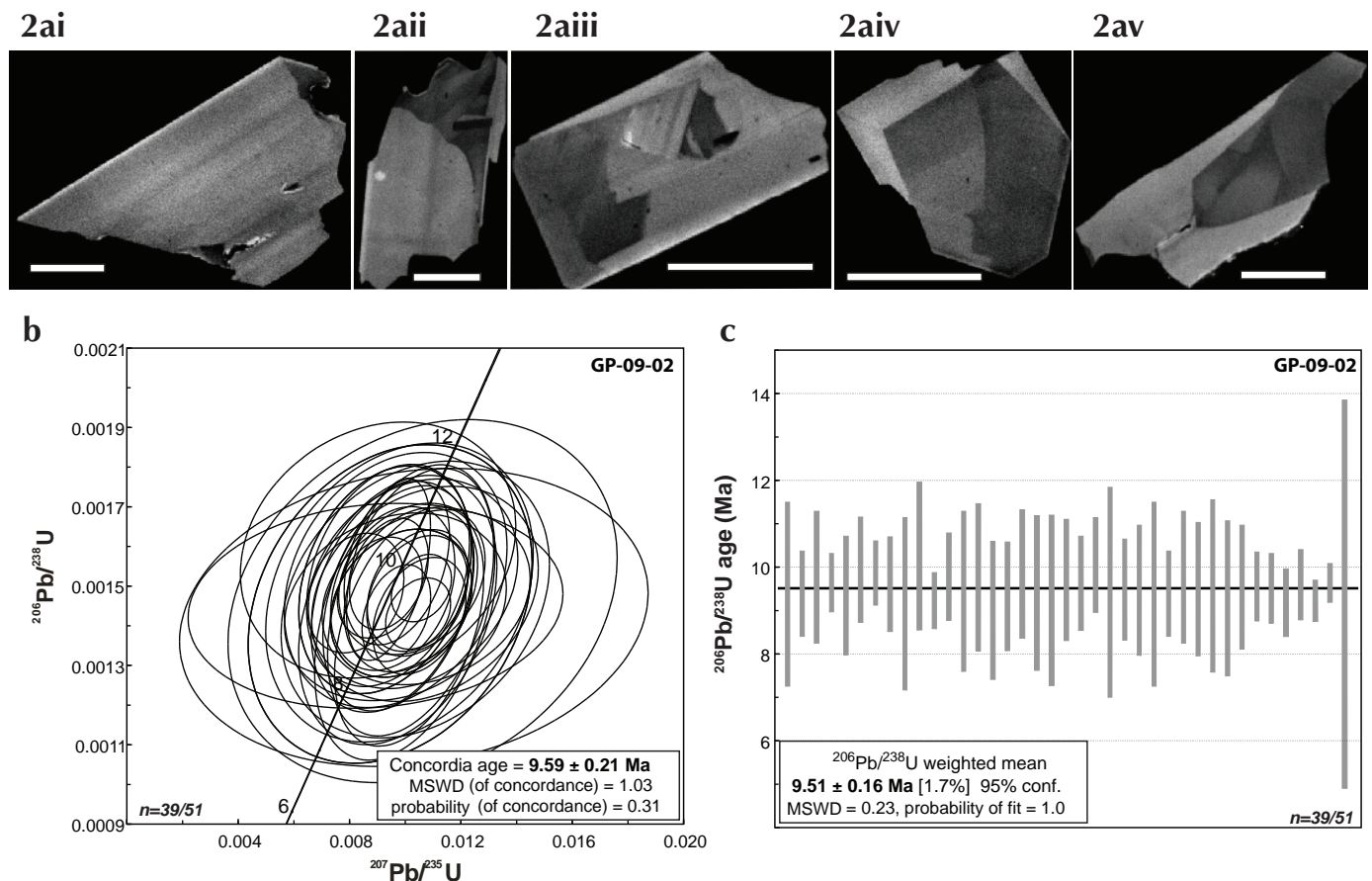


Figure 2. (a) Representative CL images of zircon grains from reference material GP-09-02. Scale bar represents 50 μm. (b) Concordia diagram for U-Pb analyses from reference material GP-09-02. (c) Plot of weighted mean $^{206}\text{Pb}/^{238}\text{U}$ ages from GP-09-02. A total of 51 analyses of GP-09-02 were collected during data acquisition. Of the total dataset, 39 analyses have a probability of concordance greater than 0.2 and only these are used to calculate final concordia and weighted mean $^{206}\text{Pb}/^{238}\text{U}$ ages.

calculated ages given in Table 1 and plotted on associated concordia and weighted mean diagrams are at the 2σ uncertainty level unless stated otherwise. Final age calculations include U decay constant uncertainties. Decay constant uncertainties are plotted graphically on concordia plots. The concordia age that includes U decay constant uncertainties is considered the best estimate of the crystallization age of a sample when analysed by ICP-MS. Initial filtering of data involves discarding analyses where data have been affected by instrument drift, surface contamination, ablation irregularities or high common Pb contents (e.g., inclusion phases). Final age calculations involve a second filtering of data to include analyses with a probability of concordance greater than 0.20. This subset of data are then used to calculate weighted mean $^{206}\text{Pb}/^{238}\text{U}$ and $^{207}\text{Pb}/^{206}\text{Pb}$ ages (which do not include U decay constant uncertainties).

concordia and the weighted mean age calculations for all four reference materials analysed during this study are in excellent agreement with the corresponding ID TIMS ages (Table 1). Importantly, LAM ICP-MS isotopic data collected for sample GP-09-02 demonstrate the applicability of the technique to zircon populations as young as Miocene. A final concordia age of 9.59 ± 0.21 Ma (decay constant uncertainties included) and a $^{206}\text{Pb}/^{238}\text{U}$ weighted mean age of 9.51 ± 0.16 Ma (decay constant uncertainties not included) are in excellent agreement with the highly precise ID TIMS age of 9.520 ± 0.022 Ma. Concentration data calculated from GP-09-02 show a variation in U concentrations from 141-1325 ppm for zircon grains from sample GP-09-02. The excellent agreement between datasets for zircon reference materials of widely varying geological age, demonstrate that the LAM ICP-MS results are both precise and accurate.

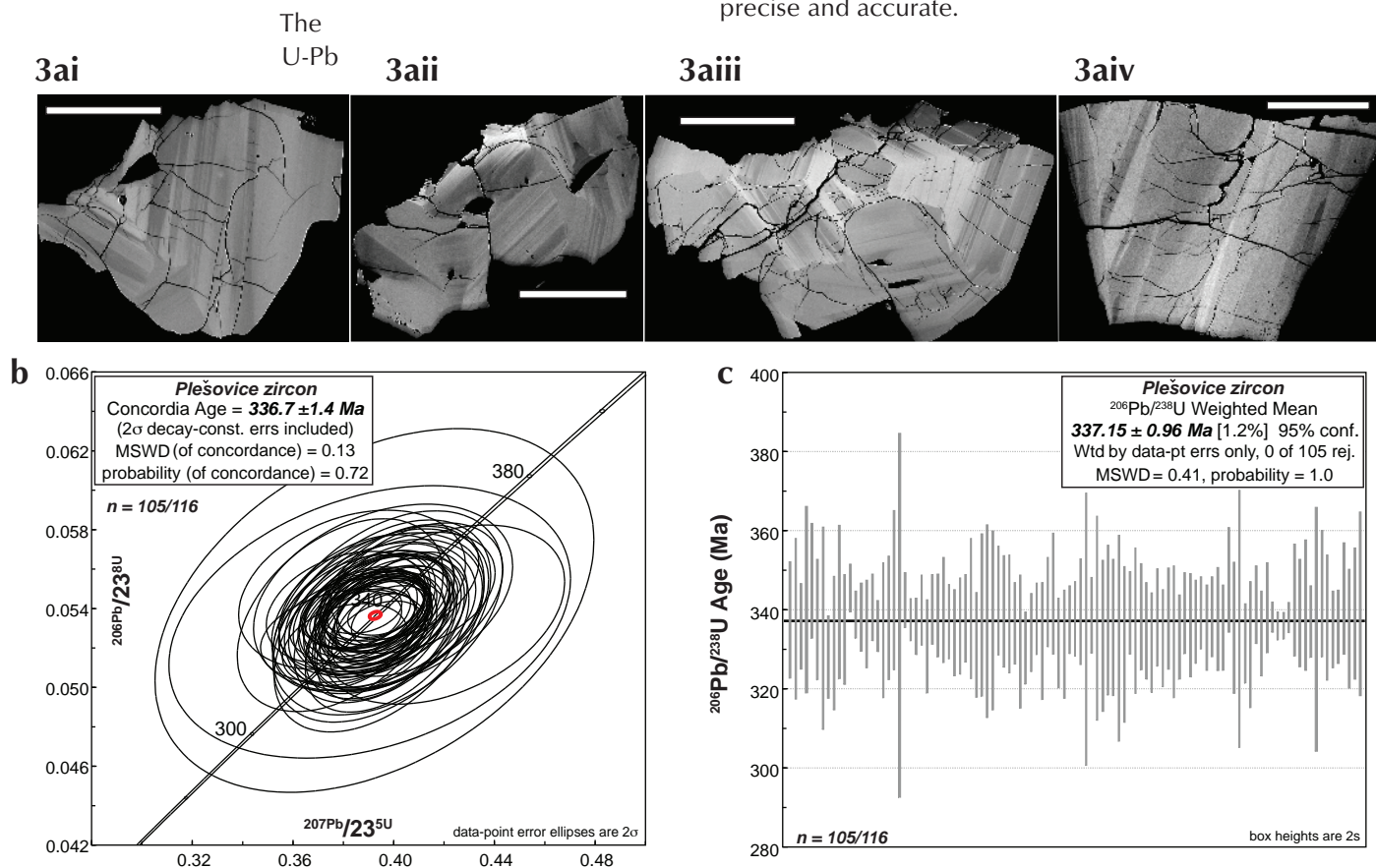


Figure 3. (a) Representative BSE images of Plešovice zircon reference material. Scale bar represents $500 \mu\text{m}$.

(b) Concordia diagram for U-Pb analyses from Plešovice zircon reference material. **(c)** Plot of weighted mean $^{206}\text{Pb}/^{238}\text{U}$ ages from Plešovice zircon standard. A total of 116 analyses of the Plešovice zircon reference material were collected during data acquisition. Of the total dataset, 105 analyses had a probability of concordance greater than 0.2 and only these are used to calculate final concordia and weighted mean $^{206}\text{Pb}/^{238}\text{U}$ ages.

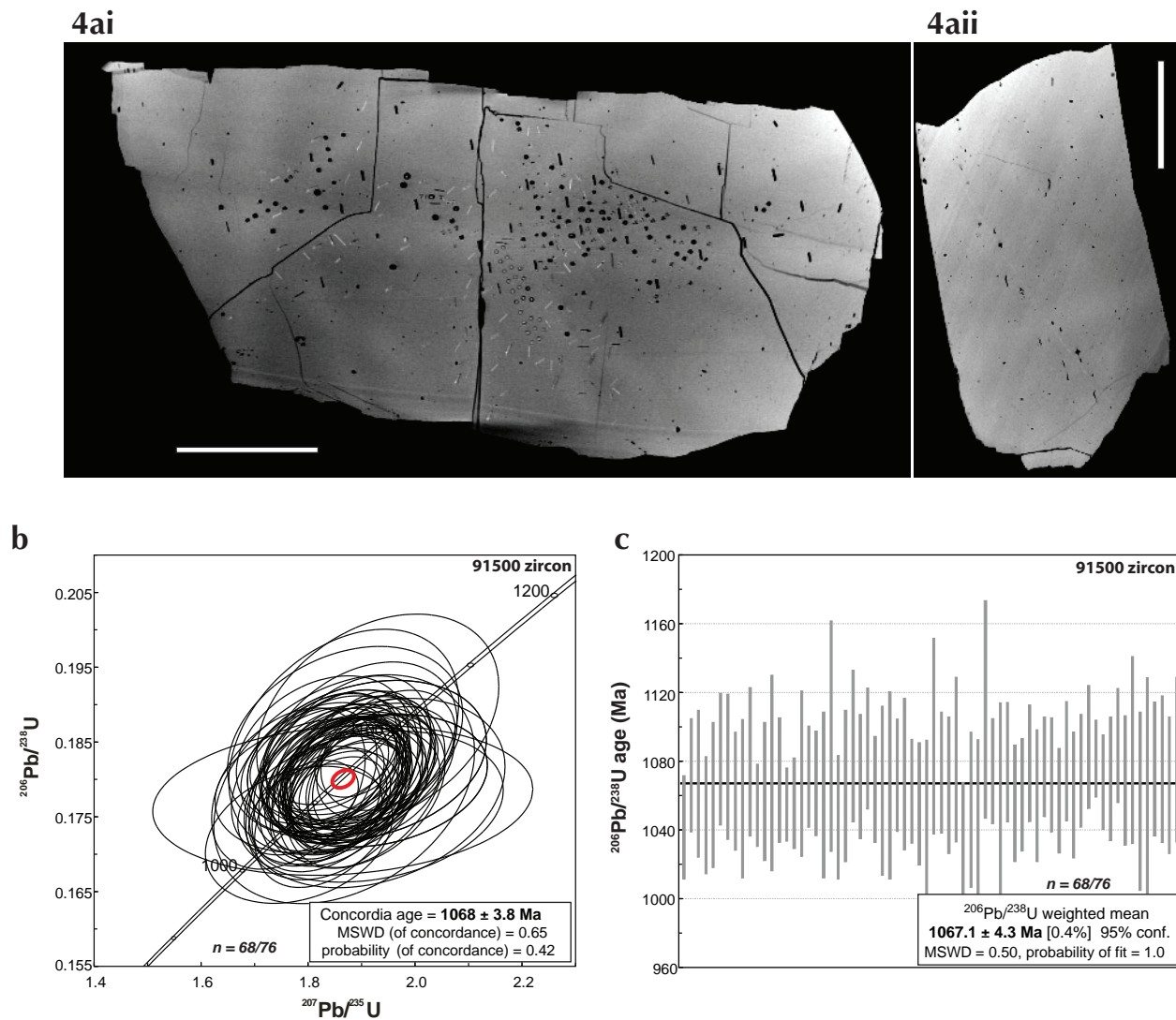


Figure 4. (a) Representative BSE images of 91500 zircon reference material. Scale bar represents 2 mm. (b) Concordia diagram for U-Pb analyses from 91500 zircon reference material. (c) Plot of weighted mean $^{206}\text{Pb}/^{238}\text{U}$ ages from 91500 zircon reference material. A total of 76 analyses of the 91500 zircon reference material were collected during data acquisition. Of the total dataset, 68 analyses have a probability of concordance greater than 0.2 and only these are used to calculate final concordia and weighted mean $^{206}\text{Pb}/^{238}\text{U}$ ages.

Table 1. Summary calculated ages.

	LAM ICP-MS		ID TIMS
	Concordia Age (2σ)	Weighted $^{206}\text{Pb}/^{238}\text{U}$ (2σ)	Weighted $^{206}\text{Pb}/^{238}\text{U}$ (2σ)
GP-09-02	9.59 ± 0.21 Ma	9.51 ± 0.16 Ma	9.520 ± 0.022 Ma
Plešovice	336.7 ± 1.4 Ma	337.15 ± 0.96 Ma	337.13 ± 0.37 Ma
91500	1068.0 ± 3.8 Ma	1067.1 ± 4.3 Ma	$1065.x \pm 0.4$ Ma

	Concordia Age	Weighted $^{207}\text{Pb}/^{206}\text{Pb}$
vb165	2676.2 ± 5.7 Ma	2672.8 ± 2.3 Ma

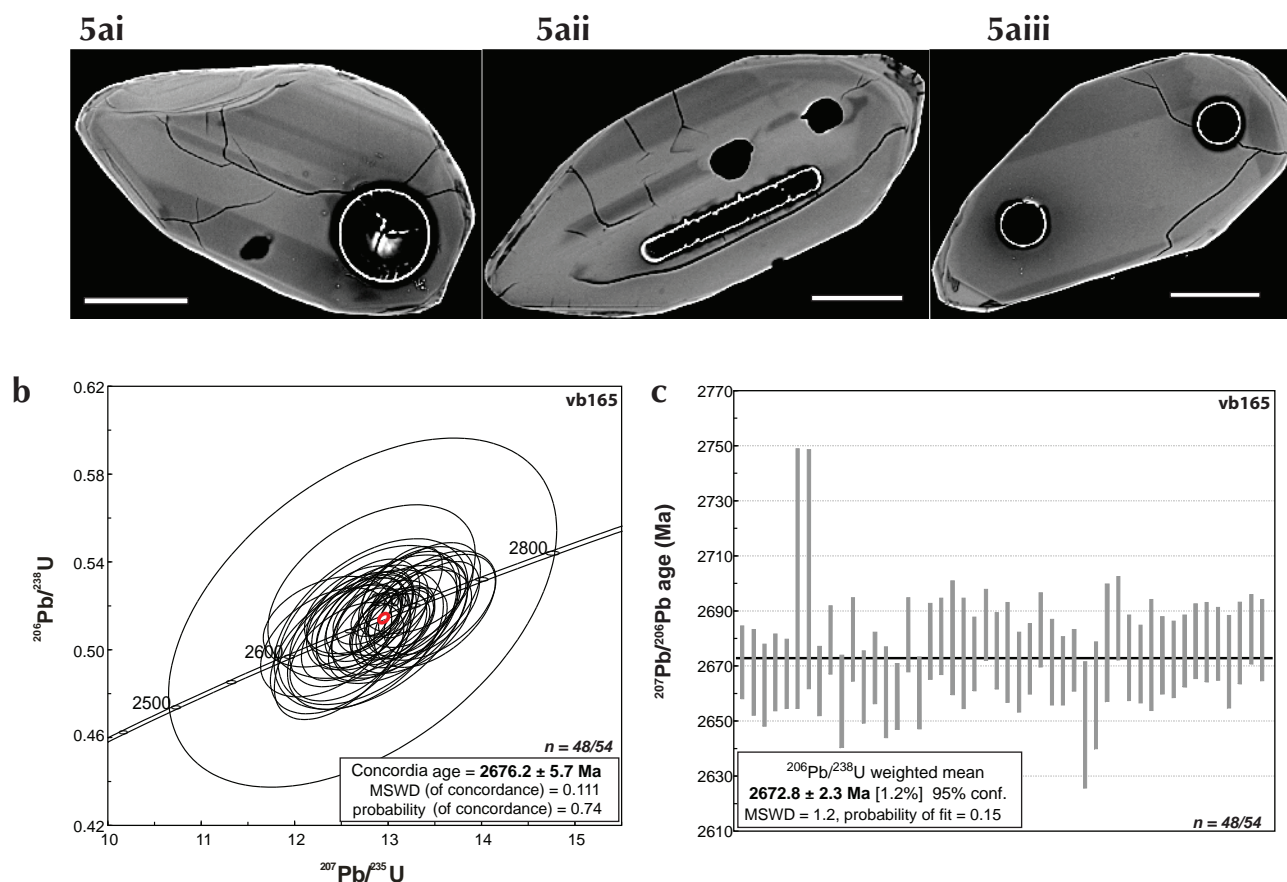


Figure 5. (a) Representative BSE images of zircon grains from reference material vb165. Scale bar represents 50 μm . (b) Concordia diagram for U-Pb analyses from reference material, vb165. (c) Plot of weighted mean $^{207}\text{Pb}/^{206}\text{Pb}$ ages from reference material, vb165. A total of 54 analyses of the vb165 zircon reference material were collected during data acquisition. Of the total dataset, 48 analyses have a probability of concordance greater than 0.2 and only these are used to calculate final concordia and weighted mean $^{206}\text{Pb}/^{238}\text{U}$ ages.

ACKNOWLEDGEMENTS

Thank you to Pam King, Earth Sciences Department, Memorial University and Michael Schaffer for access and assistance in the MaflIC SEM facility. We thank Jim Crowley of Boise State University Isotope Geology Laboratory for providing us the GP-09-02 sample. Helpful reviews by Jim Crowley and Jim Mortensen improved early versions of this manuscript.

REFERENCES

- Bennett, V., Jackson, V.A., Rivers, T., Relf, C., Horan, P. and Tubrett, M., 2005. Geology and U-Pb geochronology of the Neoproterozoic Snare River terrane: tracking evolving tectonic regimes and crustal growth mechanisms. *Canadian Journal of Earth Sciences*, vol. 42, no. 6, p. 895-934.
- Cox, R.A., Wilton, D.H.C. and Košler, J., 2003. Laser ablation U-Th-Pb *in situ* dating of zircon and allanite: An example from the October Harbour granite, central coastal Labrador, Canada. *The Canadian Mineralogist*, vol. 41, no. 2, p. 273-291.

- Fryer, B.J., Jackson, S.E. and Longerich, H.P., 1993. The application of laser ablation-inductively coupled plasma-mass spectrometry to *in situ* zircon geochronology. *Chemical Geology*, vol. 211, p. 47-49.
- Horn, I., Rudnick, R.L. and McDonough, W.F., 2000. Precise elemental and isotope ratio determination by simultaneous solution nebulization and laser ablation-ICP-MS: application to U-Pb geochronology. *Chemical Geology*, vol. 164, no. 3-4, p. 281-301.
- Jackson, S.E., Pearson, N.J., Griffin, W.L. and Belousova, E.A., 2004. The application of laser ablation microprobe-inductively coupled plasma-mass spectrometry (LAM ICP-MS) to *in situ* (U) - Pb geochronology. *Chemical Geology*, vol. 109, p. 1-8.
- Košler, J., Fonneland, H., Sylvester, P.J., Tubrett, M. and Pedersen, R., 2002. U-Pb dating of detrital zircons for sediment provenance studies - a comparison of laser ablation ICP-MS and SIMS technique. *Chemical Geology*, vol. 182, p. 605-618.
- Ludwig, K.R. 1999. User's manual for Isoplot/Ex, version 2.06: a geochronological toolkit for Microsoft Excel. Berkeley Geochronological Center, Special Publication No. 1a, 49 p.
- Slama, J., Košler, J., Condon, D.J., Crowley, J.L., Gerdes, A., Hanchar, J.M., Horstwood, M.S.A., Morris, G.A., Nasdala, L., Norberg, N., Schaltegger, U., Schoene, B., Tubrett, M.N. and Whitehouse, M.J., 2008. Plešovice zircon: A new natural reference material for U-Pb and Hf isotopic microanalysis. *Chemical Geology*, vol. 249, no. 1-2, p. 1-35.
- Schoene B., Crowley J.L., Condon D.J., Schmitz M.D. and Bowring S.A., 2006. Reassessing the uranium decay constraints for geochronology using ID-TIMS U-Pb data. *Geochimica et Cosmochimica Acta*, vol. 70, p. 426-445.
- Sylvester, P.J. and Ghaderi, M., 1997. Trace element analysis of scheelite by excimer laser ablation-inductively coupled plasma-mass spectrometry (ELA-ICP-MS) using a synthetic silicate glass standard. *Chemical Geology*, vol. 141, p. 49-65.
- Wiedenbeck, M., Alle, P., Corfu, F., Griffin, W.L., Meier, M., Oberli, F., von Quadt, A., Roddick, J.C. and Spiegel, W., 1995. Three natural zircon standards for U-Th-Pb, Lu-Hf, trace element and REE analyses. *Geostandards and Geoanalytical Research*, vol. 19, p. 1-23.

New U-Pb age constraints at Freegold Mountain: Evidence for multiple phases of polymetallic mid- to Late Cretaceous mineralization

Thierry Bineli Betsi¹

University of New Brunswick

Venessa Bennett²

Yukon Geological Survey

Bineli Betsi, T. and Bennett, V., 2010. New U-Pb age constraints at Freegold Mountain: Evidence for multiple phases of polymetallic mid- to Late Cretaceous mineralization. *In: Yukon Exploration and Geology 2009*, K.E. MacFarlane, L.H. Weston and L.R. Blackburn (eds.), Yukon Geological Survey, p. 57-84.

ABSTRACT

In this contribution, we present new U-Pb age data for ten intrusive units that bracket the timing of polymetallic mineralization occurring within the Northern Freegold Resources Ltd. (NFR), Freegold Mountain project area. Polymetallic mineralization occurring in the Tinta zone predates trachytic dykes (~109 Ma) and represents the earliest phase of mineralization recognized on the Freegold Mountain property thus far. Feldspar porphyry dykes that intrude the Revenue zone are correlative to the Nucleus zone feldspar porphyry dykes, and yield ages of ~105-104 Ma, indicating that the structural corridor in which Au mineralization occurred was active from at least this time. Furthermore, monzodiorite was emplaced at ~107 Ma within the Revenue zone. An ~97 Ma aplitic dyke that intrudes porphyritic granite of the Stoddart intrusion predates ~94 Ma Mo-Cu-W mineralization. Andesitic dykes (~77 Ma) that crosscut the Stoddart porphyry and rhyolitic dykes (~75 Ma) intruding the Revenue zone, represent Carmacks-age volcanism in the region. These new age data indicate that economically important mineralizing events took place over a period of at least 40 Ma.

¹thierry.binel@unb.ca

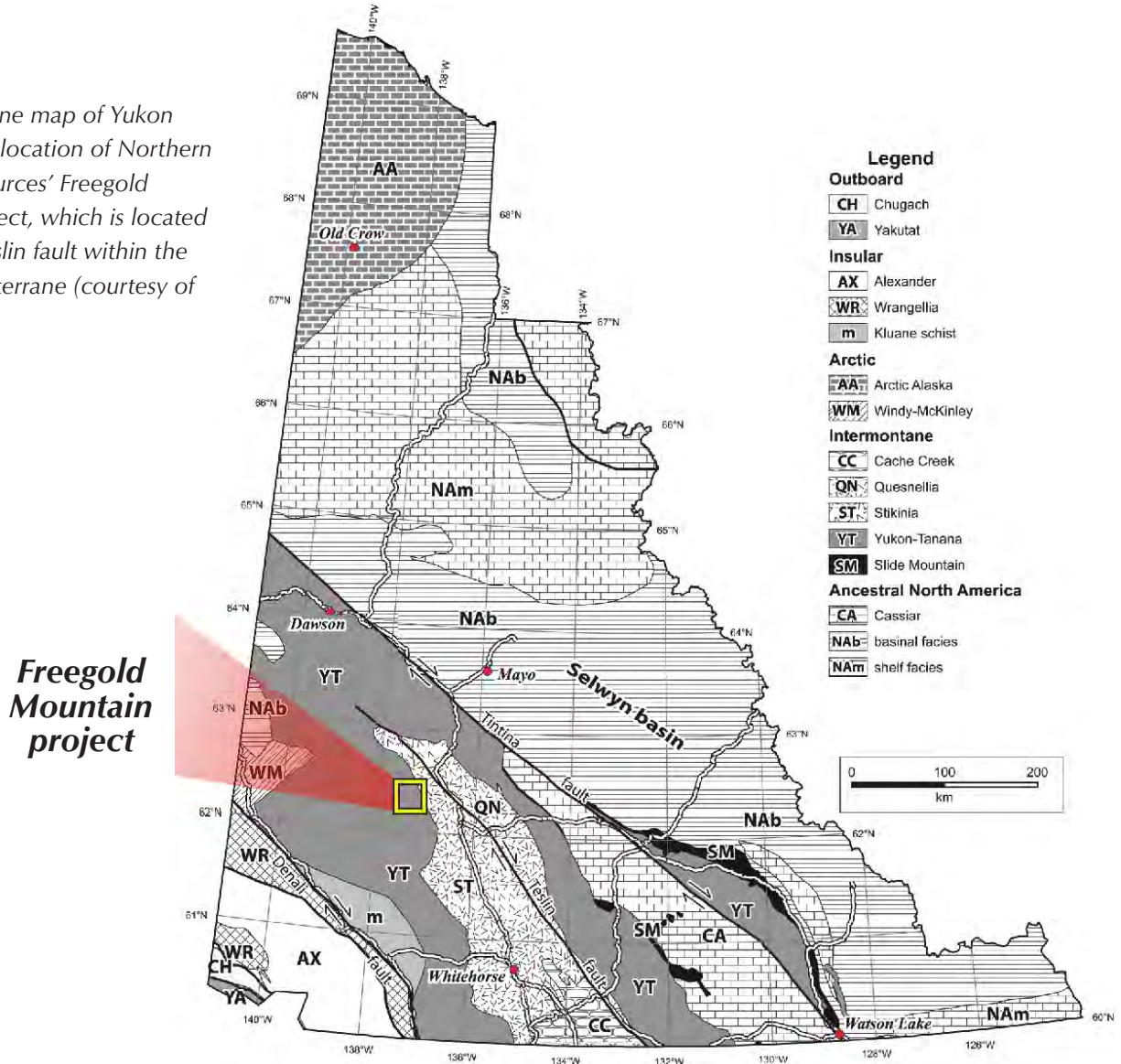
²venessa.bennett@gov.yk.ca

INTRODUCTION

The Freegold Mountain project, owned and operated by Northern Freegold Resources Ltd., is located in the central Dawson Range, west central Yukon. The property is situated at the southern end of a regionally extensive, northwest-trending polymetallic mineral belt associated with Jurassic to latest Cretaceous magmatic events (Figs. 1, 2). The Freegold Mountain property represents a large land parcel exceeding 12 000 hectares and is host to numerous important mineralized zones, including two with NI 43-101 resources, *i.e.*, the Tinta deposit (*Au-Ag-Cu-Pb-Zn*) and the Nucleus Au deposit. Significant zones of mineralization currently recognized across the property include, from northwest to southeast, Nitro, Big, Nucleus,

Revenue, Castle, Discovery (Ridge and Stoddart), Goldy and Tinta (Fig. 3). Each mineralized zone is associated with a different metal suite of interest, and corresponding style and setting of mineralization. The density of such diverse styles of mineralization in a relatively small area suggests a complex interplay of long-lived structural conduits and multiphase fertile magmatism. The following report presents new U-Pb age data from the Tinta, Revenue, Stoddart and Ridge mineralized zones that demonstrate a protracted history of polymetallic mineralization extending for over 40 Ma that was associated with discrete pulses of Cretaceous magmatism. Importantly, these new age data place maximum and minimum age constraints on the timing of mineralization occurring across the Freegold Mountain project area.

Figure 1. Terrane map of Yukon illustrating the location of Northern Freegold Resources' Freegold Mountain project, which is located west of the Teslin fault within the Yukon-Tanana terrane (courtesy of M. Colpron).



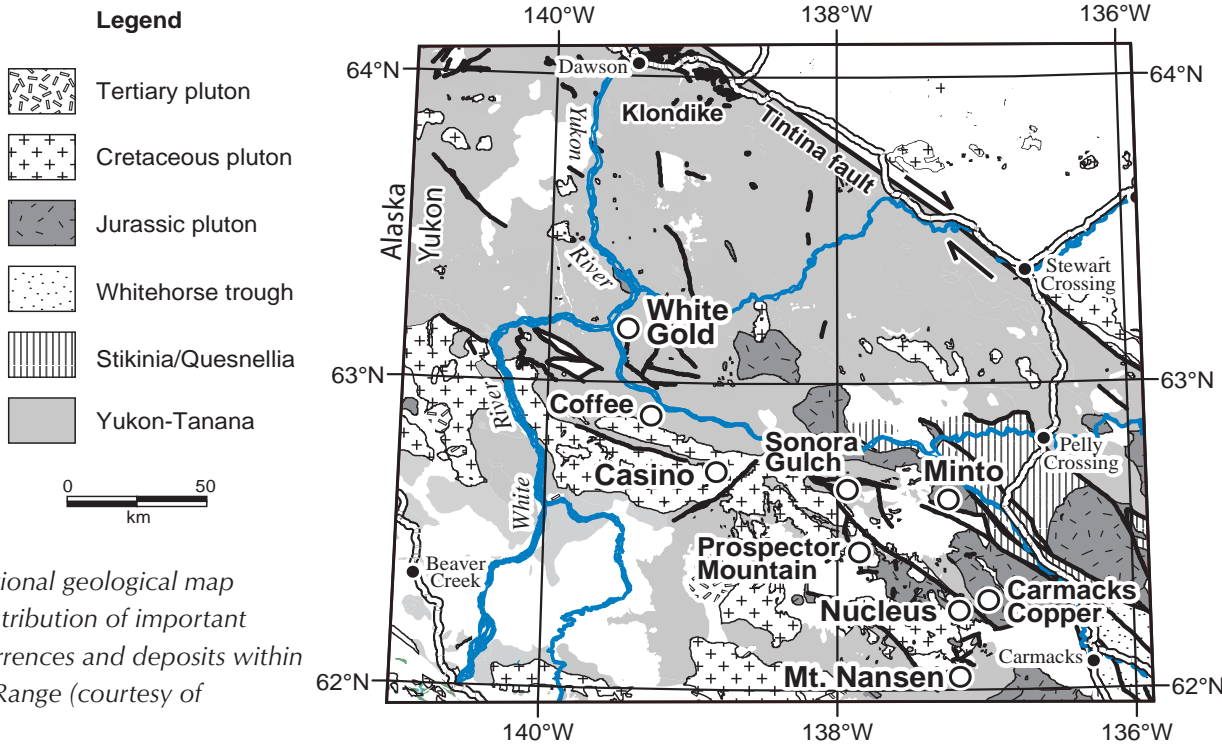


Figure 2. Regional geological map illustrating distribution of important mineral occurrences and deposits within the Dawson Range (courtesy of M. Colpron).

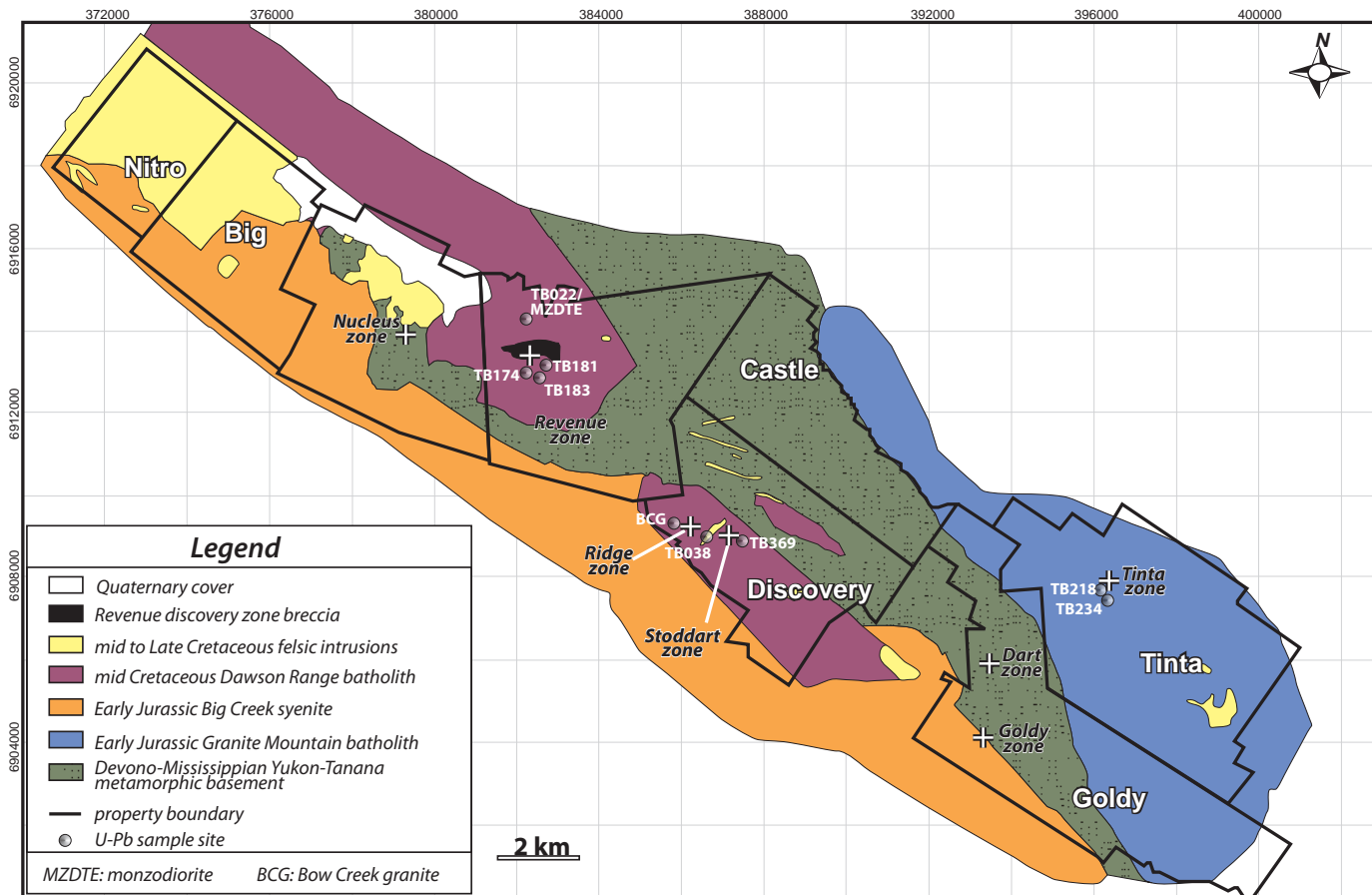


Figure 3. Property geology map of Freegold Mountain project, 2009 (Northern Freegold Resources Ltd.); location of U-Pb sampling sites are noted.

REGIONAL GEOLOGY

The Freegold Mountain project is located within the Dawson Range (Fig. 2), which is bounded primarily by the Yukon River to the north and the Nisling River to the south. It extends west-northwesterly from the town of Carmacks to the White River. The Dawson Range is underlain, in part, by Paleozoic metasedimentary and metaplutonic rocks of the pericratonic Yukon-Tanana terrane (YTT), which represents a composite of terranes that were accreted to the North American continent during early Mesozoic time (Colpron *et al.*, 2006). Regional metamorphic grade varies from greenschist to lower amphibolite facies (Payne *et al.*, 1987). The YTT has been intruded by several different phases of plutonic rocks of at least three different ages. More than one terminology has been introduced in the literature for some of the different suites and specific intrusions in the Dawson Range. The following nomenclature is recommended.

1. Early Jurassic Aishihik and Long Lakes suites (Johnston, 1995)

- Big Creek Metaplutonic Suite (Carlson, 1987) or Big Creek syenite (Tempelman-Kluit, 1984): orthoclase-hornblende porphyritic syenite, plagioclase-hornblende monzonite, and hornblendite
- Granite Mountain batholith (Tempelman-Kluit, 1984; Carlson, 1987): foliated coarse-grained hornblende-biotite granodiorite and leucogranodiorite

2. Mid-Cretaceous Whitehorse Plutonic Suite (Gordey and Makepeace, 2000)

- Dawson Range batholith (Tempelman-Kluit, 1974): hornblende-biotite-quartz diorite, hornblende-biotite diorite, and biotite-hornblende granodiorite
- Coffee Creek granite (Carlson, 1987): granite to quartz monzonite
- Casino granodiorite (Gordey and Makepeace, 2001)

3. Late Cretaceous Prospector Mountain Suite (Johnston, 1995)

- Casino Plutonic Suite (Johnston, 1995): leucocratic granite, quartz monzonite and alaskite with associated aplite phases
- Bow Creek granite (Carlson, 1987): biotite granite and related quartz-feldspar porphyry dykes

- Seymour Creek stock (McCausland *et al.*, 2001): biotite-hornblende granodiorite to quartz monzonite
- Middle and Late Cretaceous volcanic sequences and associated hypabyssal dykes belong to the Mount Nansen and Carmacks groups respectively (Carlson, 1987)

Late Cretaceous plutons in the Dawson Range are thought to have been derived through subduction processes and melt generation within the mantle, whereas mid-Cretaceous intrusions were generated through partial melting of the YTT basement (Selby *et al.*, 1999). The Big Creek fault is a prominent northwest-trending topographic and aeromagnetic feature of regional extent that extends across the Freegold Mountain project area. Importantly, the Big Creek fault zone is the locus of numerous copper porphyry and structurally hosted gold deposits, as well as associated placer gold. Mid and Late Cretaceous pluton emplacement may have been localized by the presence of these major northwest-trending structures.

FREGOLD MOUNTAIN PROJECT - PROPERTY GEOLOGY

Poly-deformed and metamorphosed metagranitic, metavolcanic, and subordinate metasedimentary rocks of probable Devonian to Mississippian and older ages comprise the YTT basement that underlies the Freegold Mountain project area. The metamorphic assemblage has been intruded by four regional magmatic suites including, (i) the early Jurassic Granite Mountain batholith, located in the southeast margin of the property; (ii) the early Jurassic Big Creek syenite, which parallels the southwest property boundary and locally occurs in the south-central region of the property; (iii) the mid to Late Cretaceous Dawson Range batholith that underlies Revenue, and parts of the Nucleus and Discovery zones; and (iv) mid and Late Cretaceous intrusions and volcanic rocks of the Mount Nansen volcanic suite that partly underlie the Nitro and Big zones. The Big Creek lineament parallels Big Creek, which anastomoses in a general west-northwest trend across the Freegold Mountain property. The Big Creek lineament is interpreted to represent an important structure for controlling pluton emplacement and associated mineralization. Here, we provide more details on the geological setting for the Tinta, Revenue, Stoddart and Ridge mineralized zones for which U-Pb geochronology samples were collected.

TINTA ZONE

The Tinta zone is underlain by early Jurassic granodiorite, quartz monzonite and minor hornblendite of the Granite Mountain batholith and, locally, small lenses of amphibolites of the YTT basement (Fig. 3). Early Jurassic plutonic rocks within the Tinta zone are crosscut by two phases of dykes including pink, equigranular aplite dykes and dark green to black, quartz-feldspar porphyry dykes of trachytic composition. Samples of both dyke suites were collected to constrain maximum and minimum ages of mineralization within the Tinta zone. Tinta zone mineralization represents a structurally controlled, northwest-trending polymetallic (Cu-Zn-Pb-As-Ag-Au) vein system. Mineralization occurs as quartz-pyrite-rich, base-metal-bearing Au-Ag vein systems (Fig. 4). Sulphide phases include chalcopyrite, galena and sphalerite (Fig. 4). Silver-bearing minerals include tennantite and/or tetrahedrite, in addition to galena. The mineralized vein is typically zoned and composed of a marginal pyritic zone, and a central zone comprising mostly base metals and

rare sulfosalts (Fig. 4b). Locally, base-metal mineralization is zoned into a peripheral chalcopyrite zone, and an interior galena-sphalerite zone (Fig. 4b). Alteration mineral assemblages that include quartz-sericite-adularia-carbonate and open-space colloform and comb quartz textures are indicative of a high-level vein emplacement; this is consistent with an epithermal designation for the Tinta deposit.

REVENUE AND NUCLEUS ZONES

Historically, the Revenue and Nucleus mineralized zones were considered as a single property, termed Golden Revenue (Eaton, 1984), but are now recognized as discrete and different mineralized zones that include the NI 43-101 Nucleus Au Deposit (Inferred resource of 1,082,000 ounces of gold at 0.50 g/t Au with a cutoff of 0.3 g/t) and the Au ± Cu prospect of the Revenue zone (Fig. 3). We describe the geology and mineralization of the Nucleus and Revenue zones together in this study due to the likely continuation of the structural corridor hosting



Figure 4. (a) Massive quartz-pyrite-chalcopyrite vein crosscut by later crustiform quartz-carbonate vein, Tinta Hill (drillhole TH07-11, ~329 m depth). (b) Massive quartz-pyrite-chalcopyrite-sphalerite-galena vein exhibiting zonation from pyrite zone (upper; Py) to galena-sphalerite-chalcopyrite zone (lower; Gn-Sp-Cp); field of view is 6 cm. Py = pyrite, Cp = chalcopyrite, Gn = galena.

Nucleus-style mineralization into the Revenue zone, as well as the occurrence of Nucleus-style feldspar porphyry dykes within the Revenue zone.

Basement rocks of the Nucleus and Revenue zones consist predominantly of strongly deformed, locally mylonitic, metasedimentary and meta-igneous schistose and gneissose rocks of the YTT that are intruded by early Jurassic, mid and Late Cretaceous intrusive bodies.

Intrusive units intruding the Nucleus and Revenue zones are compositionally diverse and consist of the following:

- i. medium-grained, unfoliated and equigranular leucogranite (Nucleus and Revenue);
- ii. fine-grained, foliated and unfoliated, locally porphyritic leucomicrogranite (Nucleus and Revenue);
- iii. medium to coarse-grained, locally porphyritic alkali leucogranite (Revenue);
- iv. white-brown weathering, equigranular and pervasively chloritized biotite-hornblende granite and homogeneous, locally foliated biotite granite (Revenue);
- v. mesocratic, medium-grained hornblende-biotite monzonite to quartz monzonite (Revenue); and
- vi. weakly deformed monzodiorite-monzogabbro (Revenue).

The youngest intrusions identified through observation of overprinting relationships in both the Revenue and Nucleus zones include aplitic and dacitic to rhyolitic porphyry dyke swarms. In addition, a high-level intrusive breccia, referred to as tuffisite, has also intruded the composite plutonic basement, described above, that underlies the Revenue zone. The tuffisite consists of angular to subrounded lithic clasts of quartz-feldspar porphyry and subordinate, variably altered granitic and metasedimentary clasts hosted in a crystal-rich quartz-feldspar matrix. Four trachydacitic to rhyolitic porphyry dykes from the Revenue zone were sampled to determine a crystallization age.

Despite the initial classification as a porphyry Cu-Mo-Au target, the Nucleus Deposit has been reinterpreted on the basis of detailed drilling as a structurally controlled, telescoped magmatic hydrothermal system. Mineralization styles include Au-enriched, mesothermal sulphide-calc-silicate replacement bodies (Fig. 5a); Au-Cu quartz stockworks and associated veining (Fig. 5b); sheeted veins and breccias (Fig. 5c and d respectively); and epithermal crustiform veins in addition to mineralized feldspar

porphyry dykes (Fig.5d). Oriented diamond drilling indicates that Nucleus mineralization is oriented east-west, as defined by geometry of both the feldspar porphyry dyke swarm and vein-hosted styles of mineralization. Overprinting relationships in the Nucleus Au Deposit demonstrate a progression from deeper level, early-formed porphyry, skarn and replacement styles of mineralization, to higher level, likely epithermal mineralization, that are inferred to be associated with both the Mt. Nansen and Carmacks magmatic events.

Significant mineralization currently recognized in the Revenue zone consists of the initial Revenue discovery zone breccia pipe (tuffisite) that has significant supergene copper mineralization (malachite-azurite-gypsum/anhydrite; Fonseca, 2009; Fig. 5e and f). Sulphide copper mineralization is observed in both the clasts and the matrix of the intrusive breccia. Preferential mineralization occurs in Fe-bearing clasts by the process of sulfidation reactions, and by pyrite \pm chalcopyrite formation within the crystal-rich matrix.

DISCOVERY ZONE – STODDART AND RIDGE

The polymetallic Ridge and Stoddart porphyry mineralized deposits represent the two main targets occurring within the Discovery zone, which is comprised of several intrusive bodies including a series of dyke swarms of basaltic-andesitic (Ridge) and aplitic (Stoddart) compositions. Four main intrusive bodies are recognized within the Discovery zone including an equigranular, medium-grained, hornblende-biotite-magnetite granite; a strongly magnetic alkali feldspar porphyritic granite; a pink, medium-grained granite with distinctive hornblende-biotite aggregates (Bow Creek granite); and a medium-grained, melanocratic biotite monzonite.

Porphyry-style Cu-Mo-W mineralization at the Stoddart zone occurs as both quartz-chalcopyrite-molybdenite-scheelite veins and microstockwork, as well as a sub-parallel set of veins, or as chalcopyrite-molybdenite-scheelite disseminations (Fig. 6a and c). Additionally, mineralization is observed to be associated with either phyllic (quartz-sericite), or potassic (K-feldspar-biotite-magnetite after primary biotite) alteration. A Re-Os isotopic age date of molybdenite sampled from the Stoddart zone mineralization yielded a model age of 93.6 ± 1.5 Ma (Geospec Consultants Ltd., 2008).

Polymetallic Au-Ag-Pb-Cu mineralization occurring within the Ridge zone is hosted by a northwest-trending shear zone approximately 5 m to 10 m wide (apparent), located

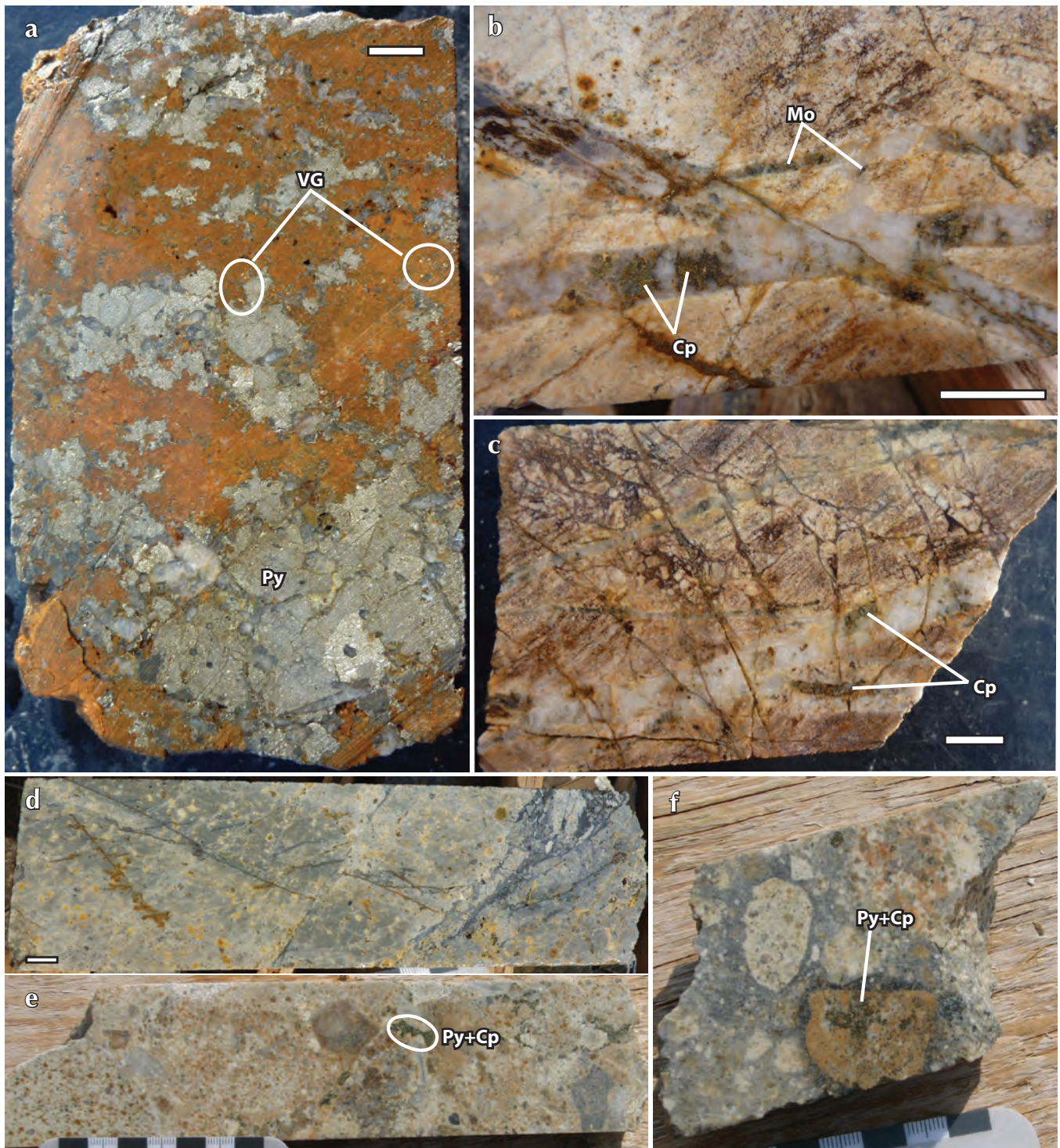


Figure 5. (a) High-grade, gold-copper skarn, Nucleus zone. Visible gold (VG) occurs in early phase assemblage (quartz-feldspar-biotite) and is overprinted by pyrrhotite-chalcopyrite-pyrite. (b) Quartz-chalcopyrite-molybdenite stockwork mineralization, Nucleus zone. (c) Quartz stockwork mineralization overprinted by late-stage brittle veining and brecciation, Nucleus zone. (d) Example of silicified feldspar porphyry dyke with overprinting brittle deformation and brecciation, Nucleus zone. (e) Matrix mineralization of pyrite and chalcopyrite (Py + Cp) occurring within tuffisite unit, Revenue zone. (f) Clast-hosted sulphide mineralization (Py + Cp), tuffisite, Revenue zone. Scale card increments and scale bars in Figures 5 a-f represent 1 cm. Py = pyrite, Mo = molybdenite, Cp = chalcopyrite.

at, or near, the contact of a strongly foliated biotite granodiorite and the Bow Creek granite. Early-phase copper and gold mineralization occurs as malachite, azurite, chalcocite, and/or telluride, with gold. Dolomitic veining represents late-stage overprinting and exhibits crustiform textures that locally host galena mineralization (Fig. 7a-d). Dolomite veining parallels the southeast-trend of the shear zone, and crosscuts the biotite monzonite (Fig. 7a) and Bow Creek granite.

GEOCHRONOLOGY

Ten magmatic samples were collected from surface and drill core from the Tinta, Revenue, Stoddart and Ridge mineralized zones for U-Pb dating. Sampling was restricted to magmatic phases, which were either directly associated with mineralization, or were observed to postdate it. Dating was completed using both U-Pb Isotope Dilution Thermal Ionization Mass Spectrometry (ID-TIMS; 7 samples) and Laser Ablation Microprobe Inductively Coupled Plasma-Mass Spectrometry (LAM ICP-MS; 3 samples) techniques. The samples are reported

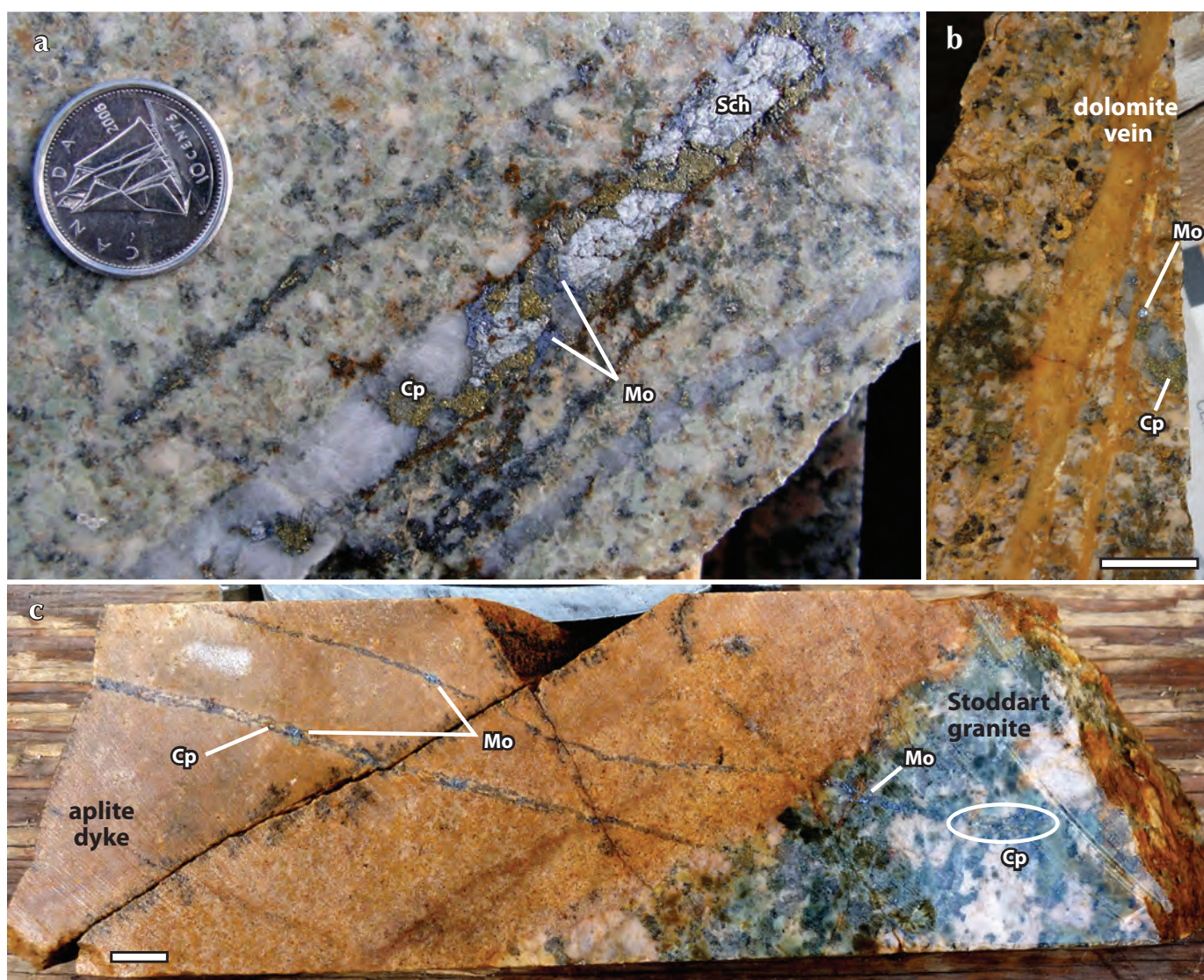


Figure 6. (a) Quartz-scheelite-chalcopyrite-molybdenite vein crosscutting granite and overprinted by phyllic (sericite-quartz) alteration (drillhole 08 ST07, at 180 m). (b) Quartz-chalcopyrite-molybdenite mineralization within Stoddart zone granite overprinted by late-stage dolomitic veining. (c) Quartz-chalcopyrite-molybdenite veins crosscutting aplite dyke that intrudes Stoddart pluton. Aplite dyke is equivalent to TB369 sampled for U-Pb age dating. Scale bars represent 1 cm. Cp = chalcopyrite, Mo = molybdenite, Sch = scheelite.

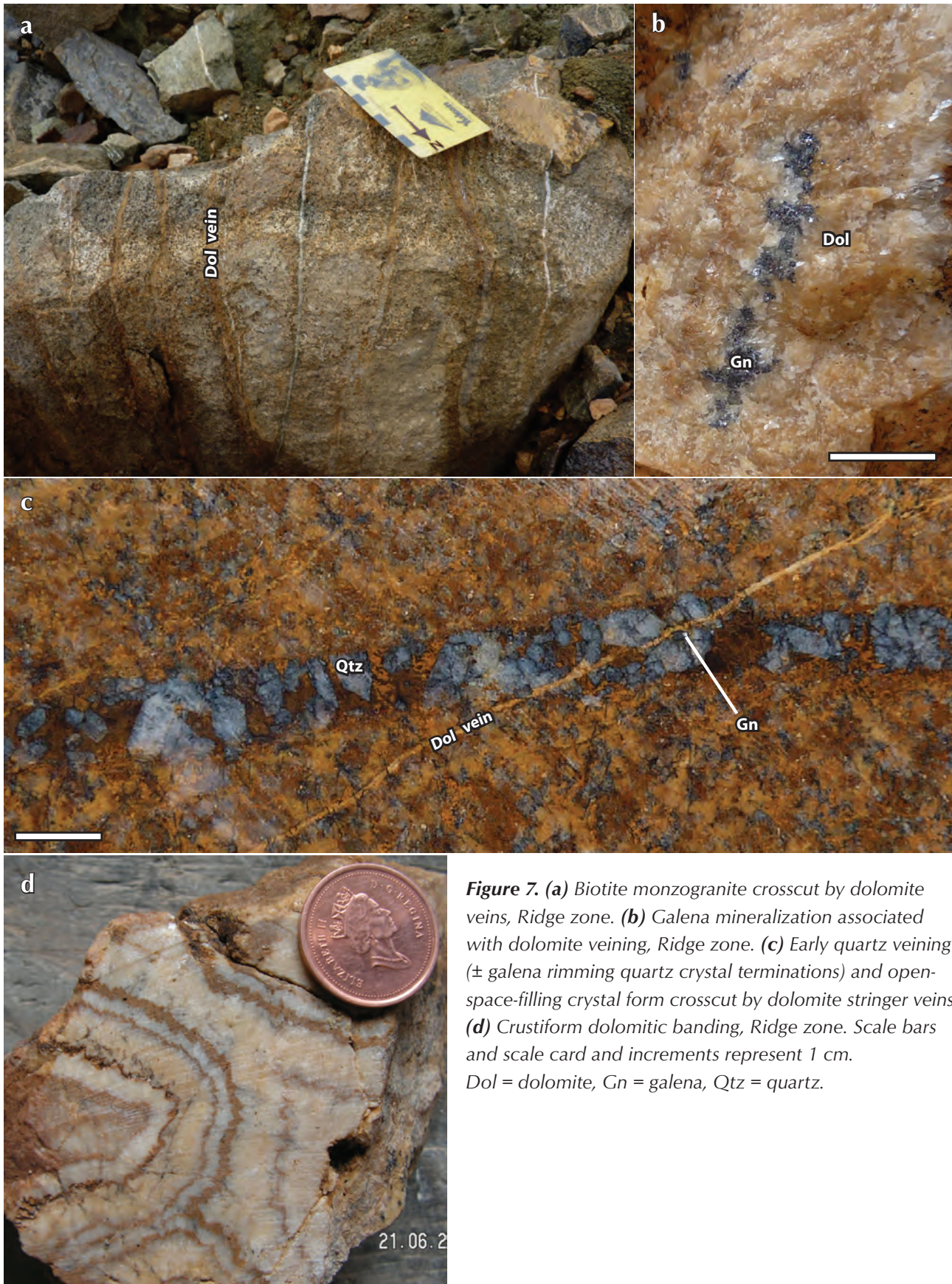


Figure 7. (a) Biotite monzogranite crosscut by dolomite veins, Ridge zone. (b) Galena mineralization associated with dolomite veining, Ridge zone. (c) Early quartz veining (\pm galena rimming quartz crystal terminations) and open-space-filling crystal form crosscut by dolomite stringer veins. (d) Crustiform dolomitic banding, Ridge zone. Scale bars and scale card and increments represent 1 cm. Dol = dolomite, Gn = galena, Qtz = quartz.

Table 1. Summary of crystallization ages, Freegold Mountain project.

Zone	Sample	$^{206}\text{Pb}/^{238}\text{U}$ weighted mean age
Tinta	TB234	unresolved
	TB218	108.7 ± 0.4 Ma
Revenue	TB183	105.7 ± 0.2 Ma
	TB022	105.5 ± 0.2 Ma
	TB174	104.4 ± 0.1 Ma
	TB181	75.2 ± 0.2 Ma
	Revenue Creek granite	107.1 ± 0.6 Ma
Stoddart Re-Os Mo (94Ma)	TB369 (Concordia age)	97.9 ± 0.4 Ma
	TB038	76.9 ± 0.9 Ma
Ridge	Bow Creek granite	68.4 ± 0.9 Ma

according to the mineralized zone in which they were sampled and, where possible, sequentially presented from oldest to youngest. Final calculated ages are reported in Table 1.

Conventional and chemical abrasion ID-TIMS zircon U-Pb dating was performed at the Pacific Centre for Isotope and Geochemical Research (PCIGR) of the University of British Columbia. Analytical techniques for U-Pb dating studies by ID-TIMS at the PCIGR are as described by Mortensen *et al.* (1995). Interpreted crystallization ages are based on a weighted average of the $^{206}\text{Pb}/^{238}\text{U}$ ages calculated for at least two overlapping concordant points. Errors for the calculated concordia and weighted mean $^{206}\text{Pb}/^{238}\text{U}$ ages are given at the 2 sigma level. Field relationships are briefly described for each sample before reporting the U-Pb IDTIMS isotopic results.

Three samples from the Freegold Mountain property were dated using U-Pb LAM ICP-MS techniques at the INCO Innovation Centre at Memorial University, St. Johns, Newfoundland. A detailed outline of the methodology is given in Bennett and Tubrett (this volume). Analytical techniques to characterize the zircon populations included standard optical microscopy and backscattered electron imaging (BSE) and cathodoluminescence (CL) image analysis in order to permit greater understanding of zircon zoning and growth history. Image analysis was completed on all zircon grains selected ($n = 20$ to 80, dependent on yield). Field relationships and zircon zonation styles are briefly described for each sample before reporting the U-Pb isotopic results. Uncertainties

reported for all calculated ages and plotted on associated concordia and weighted mean diagrams are at the 2σ uncertainty level, unless stated otherwise. Final age calculations include U-decay constant uncertainties, which are plotted graphically on concordia plots. Concordia and weighted mean $^{206}\text{Pb}/^{238}\text{U}$ ages were calculated using Ludwig (1999). The concordia age that includes U-decay constant uncertainties is considered the best estimate of the crystallization age of a sample (see Bennett and Tubrett, this volume). Where a concordia age has a mean square of weighted deviates (MSWD) >1.5 , the weighted mean $^{206}\text{Pb}/^{238}\text{U}$ age is considered the best estimate of the crystallization age. Uranium and Th concentration data and Th/U ratios were also calculated for each sample.

TINTA ZONE

One porphyry dyke and one aplite dyke were sampled from the Tinta mineralized zone, TB218 and TB234, respectively. The porphyry dyke was observed to crosscut polymetallic mineralization, whereas the aplite dyke hosts mineralization.

Sample TB218 is a dark green to black feldspar porphyritic dyke of trachytic composition sampled from DDH TH 07-08 between intervals 38.45 m and 38.65 m. The dyke has strong pervasive chlorite-epidote alteration of both phenocrysts and groundmass. The sample TB218 dyke intrudes hornblende-granodiorite of assumed Jurassic age, and is possibly associated with the Granite Mountain batholith. Additionally, carbonate veining is observed crosscutting the dyke, and represents a later overprinting fluid system.

Three single-grain zircon fractions were analysed from sample TB218 by conventional ID-TIMS (Table 2; Fig. 8a). Three overlapping concordant data points yielded a concordia age of 108.7 ± 0.17 Ma (MSWD = 0.25) and a weighted mean $^{206}\text{Pb}/^{238}\text{U}$ age of 108.7 ± 0.36 , which is interpreted to be the crystallization age of TB218 (Fig. 8b).

Sample TB234 is a pink, equigranular aplitic dyke sampled from DDH TH 07-11, at 188.1 m. The dyke intrudes granodiorite of the Granite Mountain batholith and is comprised dominantly of feldspars (~80 vol. %) exhibiting poikilitic textures and subordinate quartz (~20 vol. %). Locally, feldspar is altered to saussurite, carbonate and clay minerals. Five single-grain zircon fractions were analysed from TB234 (Table 2; Fig. 8c). No overlapping concordant points occur in the dataset, and calculated $^{206}\text{Pb}/^{238}\text{U}$ ages range from ca. 188 Ma to 216 Ma. The

most reasonable interpretation of the isotopic variability in the dataset is that the zircon fractions analysed represent inherited populations. Further work is required to establish the crystallization age of this sample.

REVENUE ZONE

Four feldspar porphyry dykes (TB022, TB174, TB183, TB181) and one monzodiorite intrusion (Revenue Creek monzodiorite) were sampled in the Revenue zone. The porphyry dykes are interpreted to be correlative to the mineralizing porphyry dykes that occur in the Nucleus zone. The porphyry dykes were analysed using

conventional ID-TIMS, whilst U-Pb dating of the Revenue Creek monzodiorite was done using LAM ICP-MS.

Sample TB022 was collected in Revenue Creek, immediately adjacent to Revenue Camp (382254E, 6914428N). The dyke is rhyolitic in composition and contains approximately 5% modal quartz and feldspar phenocrysts set in an aphanitic groundmass composed almost entirely of quartz. Strong pervasive silicification and weak to moderate pyrite \pm chalcopyrite mineralization is also associated with TB022. Importantly, the feldspar porphyry dyke crosscuts the Revenue Creek monzodiorite. Immediately proximal to the dyke contacts, strong biotite alteration is observed, which is associated

Table 2. Conventional U-Pb ID-TIMS data for zircon fractions from porphyritic dykes from Tinta and Revenue zones.

sample/ fraction	$^{207}\text{Pb}/$ ^{235}U ratio	$\pm 1\sigma,$ %	$^{206}\text{Pb}/$ ^{238}U ratio	$\pm 1\sigma,$ %	rho	$^{206}\text{Pb}/$ ^{238}U age	$\pm 2\sigma,$ Ma	$^{207}\text{Pb}/$ ^{235}U age	$\pm 2\sigma,$ Ma	$^{207}\text{Pb}/$ ^{206}Pb age	$\pm 2\sigma,$ Ma
TB234 Tinta											
A	0.2212	0.1700	0.0314	0.0920	0.8025	199.3	0.4	202.9	0.6	244.5	5.1/5.1
B	0.2343	0.1980	0.0332	0.0720	0.6243	210.4	0.3	213.7	0.8	250.4	7.5/7.5
C	0.2033	0.2390	0.0296	0.0810	0.6012	188.0	0.3	187.9	0.8	187.8	9.3/9.4
D	0.2372	0.2560	0.0338	0.0950	0.5224	214.1	0.4	216.2	1.0	238.7	10.2/10.2
E	0.2197	1.5250	0.0315	0.1530	0.6047	199.7	0.6	201.7	5.6	224.9	65.1/67.8
TB218 Tinta											
A	0.1130	0.3500	0.0170	0.1130	0.4963	108.6	0.2	108.7	0.7	111.3	14.6/14.7
B	0.1132	0.1630	0.0170	0.0810	0.6510	108.8	0.2	108.9	0.3	111.8	5.9/6.0
C	0.1127	0.2430	0.0170	0.1400	0.4494	108.5	0.3	108.4	0.5	108.1	10.3/10.4
TB183 Revenue											
A	0.1090	1.1720	0.0165	0.1420	0.5589	105.6	0.3	105.0	2.3	92.8	51.3/52.9
B	0.1100	1.0710	0.0165	0.1900	0.4424	105.8	0.4	106.0	2.2	110.6	46.6/48.0
C	0.1104	0.8830	0.0166	0.1690	0.4619	105.8	0.4	106.3	1.8	117.6	38.2/39.1
D	0.1049	1.8080	0.0160	0.1980	0.6360	102.1	0.4	101.3	3.5	80.6	78.3/82.2
E	0.1046	2.9410	0.0157	0.2350	0.5813	100.4	0.5	101.0	5.7	116.1	127.5/138.2
TB022 Revenue											
A	0.1098	0.3520	0.0165	0.1300	0.5438	105.5	0.3	105.8	0.7	113.2	14.2/14.3
B	0.7554	0.1460	0.0574	0.1070	0.6663	360.1	0.8	571.4	1.3	1535.6	4.1/4.1
C	0.5838	0.1640	0.0531	0.0980	0.6961	333.8	0.6	466.9	1.2	1189.1	4.7/4.7
D	0.1098	0.3180	0.0165	0.1110	0.5499	105.4	0.2	105.7	0.6	112.7	12.9/12.9
E	0.1095	0.5030	0.0165	0.2690	0.6666	105.5	0.6	105.5	1.0	104.4	17.9/18.1
TB174 Revenue											
A	0.1077	0.2050	0.0161	0.0940	0.6889	103.2	0.2	103.9	0.4	119.3	7.3/7.4
B	0.1085	0.2060	0.0163	0.1240	0.7131	104.5	0.3	104.6	0.4	106.2	6.9/6.9
C	0.1182	0.2290	0.0174	0.1680	0.7988	111.4	0.4	113.4	0.5	156.0	6.5/6.5
D	0.1085	0.2170	0.0164	0.1200	0.6932	104.6	0.3	104.6	0.4	104.2	7.5/7.6
E	0.1082	0.1810	0.0163	0.0900	0.7277	104.4	0.2	104.4	0.4	102.9	6.2/6.2
TB181 Revenue											
A	0.0756	0.4180	0.0116	0.0770	0.4999	74.2	0.1	74.1	0.6	69.2	18.3/18.5
B	0.0768	3.3320	0.0117	0.2960	0.6417	75.1	0.4	75.1	4.8	75.5	143.3/156.9
C	0.2041	0.1610	0.0280	0.1110	0.7951	178.3	0.4	188.6	0.6	319.6	4.5/4.5
D	0.0770	0.4070	0.0117	0.1740	0.4770	75.2	0.3	75.3	0.6	79.6	16.9/17.1

Note: A, B etc. are labels for fractions composed of single zircon grains or fragments.

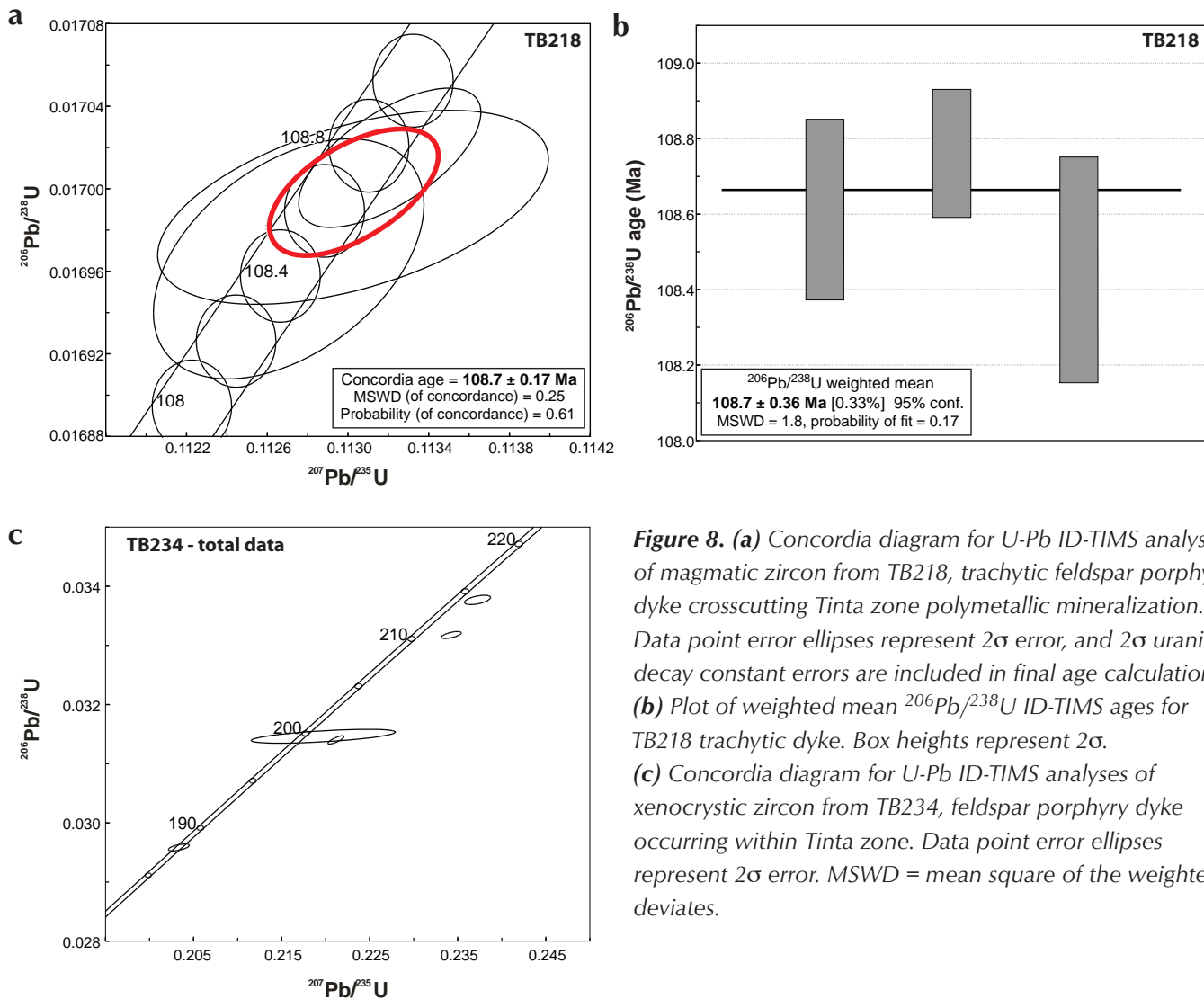


Figure 8. (a) Concordia diagram for U-Pb ID-TIMS analyses of magmatic zircon from TB218, trachytic feldspar porphyry dyke crosscutting Tinta zone polymetallic mineralization. Data point error ellipses represent 2σ error, and 2σ uranium-decay constant errors are included in final age calculation. **(b)** Plot of weighted mean $^{206}\text{Pb}/^{238}\text{U}$ ID-TIMS ages for TB218 trachytic dyke. Box heights represent 2σ . **(c)** Concordia diagram for U-Pb ID-TIMS analyses of xenocrystic zircon from TB234, feldspar porphyry dyke occurring within Tinta zone. Data point error ellipses represent 2σ error. MSWD = mean square of the weighted deviates.

with (i) destruction of primary plutonic textures in the monzodiorite, and (ii) local pyrite \pm chalcopyrite mineralization hosted in the alteration selvage. Five single-grain zircon fractions were analysed from TB022 (Table 2). Of the five fractions, three resulted in overlapping concordant analyses from which a concordia age of 105.5 ± 0.20 Ma and a weighted mean $^{206}\text{Pb}/^{238}\text{U}$ age of 105.5 ± 0.16 Ma were calculated (Fig. 9a and b). The two remaining fractions resulted in strongly discordant data, interpreted as inherited (Table 2).

Sample TB174 is a yellowish brown to pink feldspar porphyry dyke of trachydacitic composition that intrudes a strongly altered plutonic rock in Revenue zone (382613E, 6913285N). The dyke is strongly mineralized (chalcopyrite-pyrite-malachite-manganese oxides). Five single-grain zircon fractions were analysed from TB174 (Table 2). Of the five fractions, three resulted in

overlapping concordant analyses from which a concordia age of 104.5 ± 0.17 Ma and a weighted mean $^{206}\text{Pb}/^{238}\text{U}$ age of 104.5 ± 0.13 Ma were calculated (Fig. 9c and d). The two remaining fractions resulted in discordant data and were not used in the age calculation (Table 2).

Sample TB183 (382690E 6912989N) is a fine-grained, equigranular monzonic dyke comprised of predominantly feldspar, subordinate quartz (<10%) and rare biotite. Where sampled, the dyke intrudes a coarse-grained granitic pluton of similar mineralogy. Five single-grain zircon fractions were analysed from TB183 (Table 2). Of the five fractions, three resulted in overlapping concordant analyses from which a concordia age of 105.7 ± 0.22 Ma and a weighted mean $^{206}\text{Pb}/^{238}\text{U}$ age of 105.7 ± 0.19 Ma were calculated (Fig. 9e and f). The two remaining fractions also resulted in concordant data at

ca. 102 and 100 Ma, and are interpreted to be reset ages due to overprinting thermal events (Table 2).

Sample TB181 is a purple porphyritic dyke of rhyolitic composition and is comprised of distinctive ‘quartz-eye’ and feldspar phenocrysts hosted in an aphanitic, quartz-dominant groundmass. The dyke is weak to moderately sericite-saussurite-altered, and additionally, has notable malachite staining at the margins of the dyke when in

contact with the country rock, which is an altered granitoid of unknown composition. Four single-grain zircon fractions were analysed from TB181 (Table 2). Of the four fractions, two resulted in overlapping concordant analyses from which a concordia age of 75.15 ± 0.23 Ma and a weighted mean $^{206}\text{Pb}/^{238}\text{U}$ age of 75.16 ± 0.22 Ma were calculated (Fig. 9g and h). The two remaining fractions also resulted in one strongly discordant older analysis interpreted as inherited, and one concordant

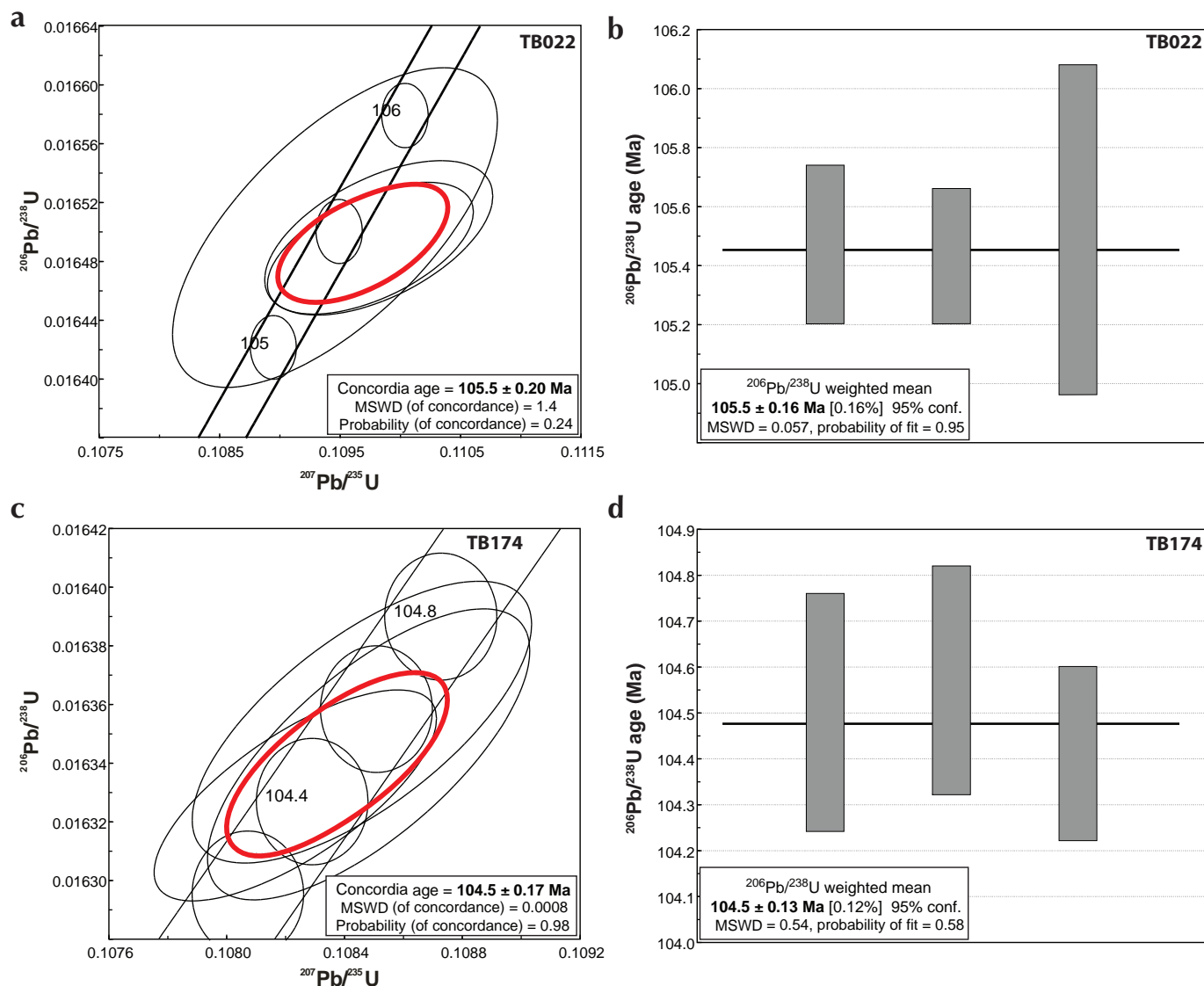


Figure 9. (a) Concordia diagram for U-Pb ID-TIMS analyses of magmatic zircon from TB022; silicified feldspar porphyry dyke crosscutting Revenue Creek monzodiorite, Revenue zone. Data point error ellipses represent 2σ error, and 2σ uranium-decay constant errors are included in final age calculation. (b) Plot of weighted mean $^{206}\text{Pb}/^{238}\text{U}$ ID-TIMS ages for TB022; feldspar porphyry dyke, Revenue zone. Box heights represent 2σ . (c) Concordia diagram for U-Pb ID-TIMS analyses of magmatic zircon from TB174; feldspar porphyry dyke, Revenue zone. (d) Plot of weighted mean $^{206}\text{Pb}/^{238}\text{U}$ ID-TIMS ages for TB174; feldspar porphyry dyke, Revenue zone. Box heights represent 2σ . MSWD = mean square of the weighted deviates. (Figure 9e,f,g,h continued on next page.)

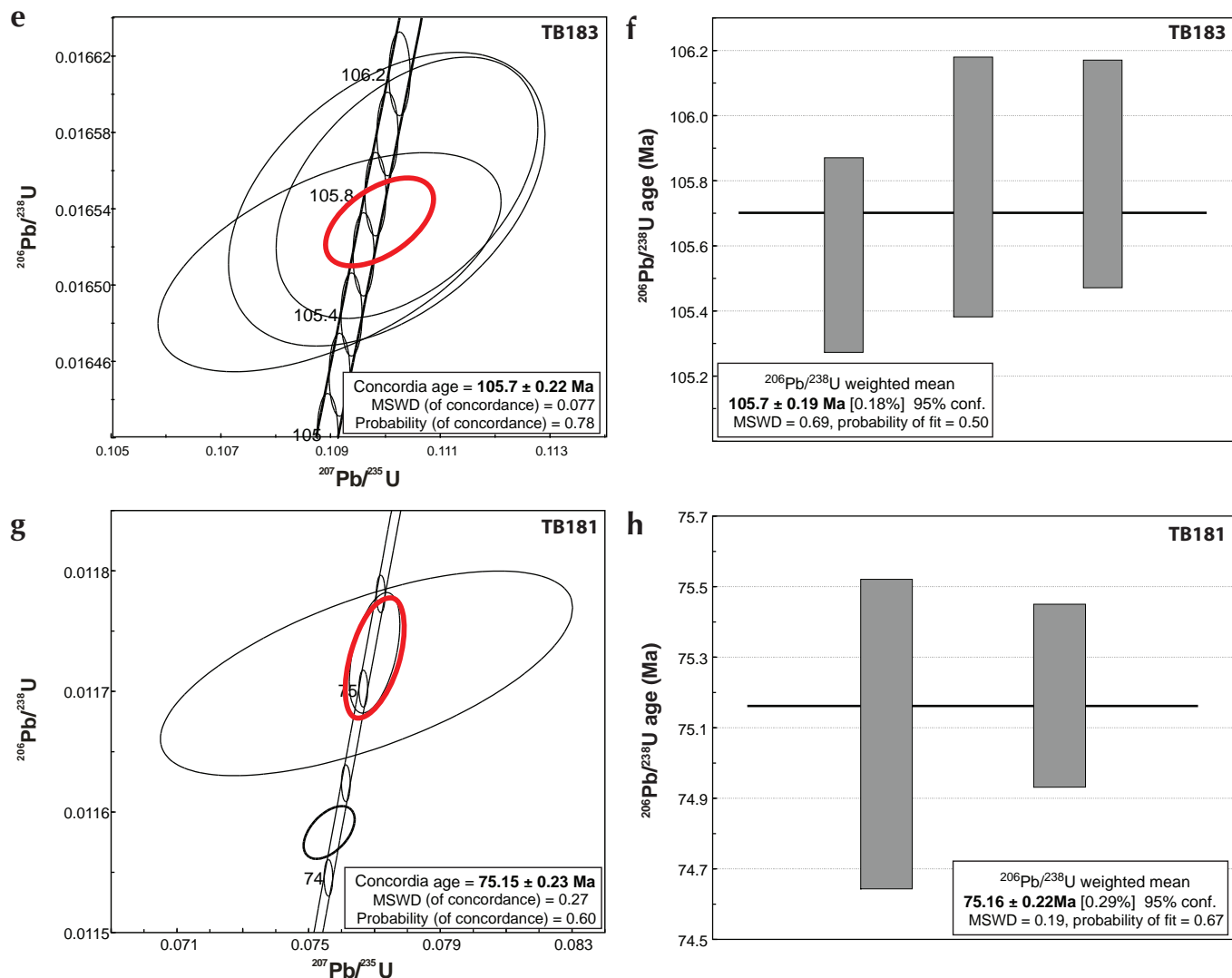


Figure 9. continued **(e)** Concordia diagram for U-Pb ID-TIMS analyses of magmatic zircon from TB183; feldspar porphyry dyke, Revenue zone. Data point error ellipses represent 2σ error, and 2σ uranium-decay constant errors are included in final age calculation. **(f)** Plot of weighted mean $^{206}\text{Pb}/^{238}\text{U}$ ID-TIMS ages for TB183; feldspar porphyry dyke, Revenue zone. Box heights represent 2σ . **(g)** Concordia diagram for U-Pb ID-TIMS analyses of magmatic zircon from TB181; rhyolite dyke, Revenue zone. Data point error ellipses represent 2σ error, and 2σ uranium-decay constant errors are included in final age calculation. **(h)** Plot of weighted mean $^{206}\text{Pb}/^{238}\text{U}$ ID-TIMS ages for TB181; rhyolite dyke, Revenue zone. Box heights represent 2σ . MSWD = mean square of the weighted deviates.

analysis at ca. 74 Ma, which is interpreted as resetting ages (Table 2).

A sample of the Revenue Creek monzodiorite was collected at the feldspar porphyry dyke U-Pb locality (sample TB022; Fig. 10) in order to better constrain the age of plutonism into which the Revenue feldspar dykes intrude. The site relationships are described above and illustrated in Figure 10c.

Abundant zircon of moderate quality was extracted from the sample of the Revenue Creek monzodiorite. Two morphologically distinct populations are present in subequal amounts: (i) clear, well-faceted equidimensional prisms (Fig. 11a), and (ii) elongate to irregular prisms with core and rim zircon growth (Fig. 11b). BSE and CL imaging of both zircon populations demonstrates that magmatic zircon occurs as both entire grains and as thick magmatic

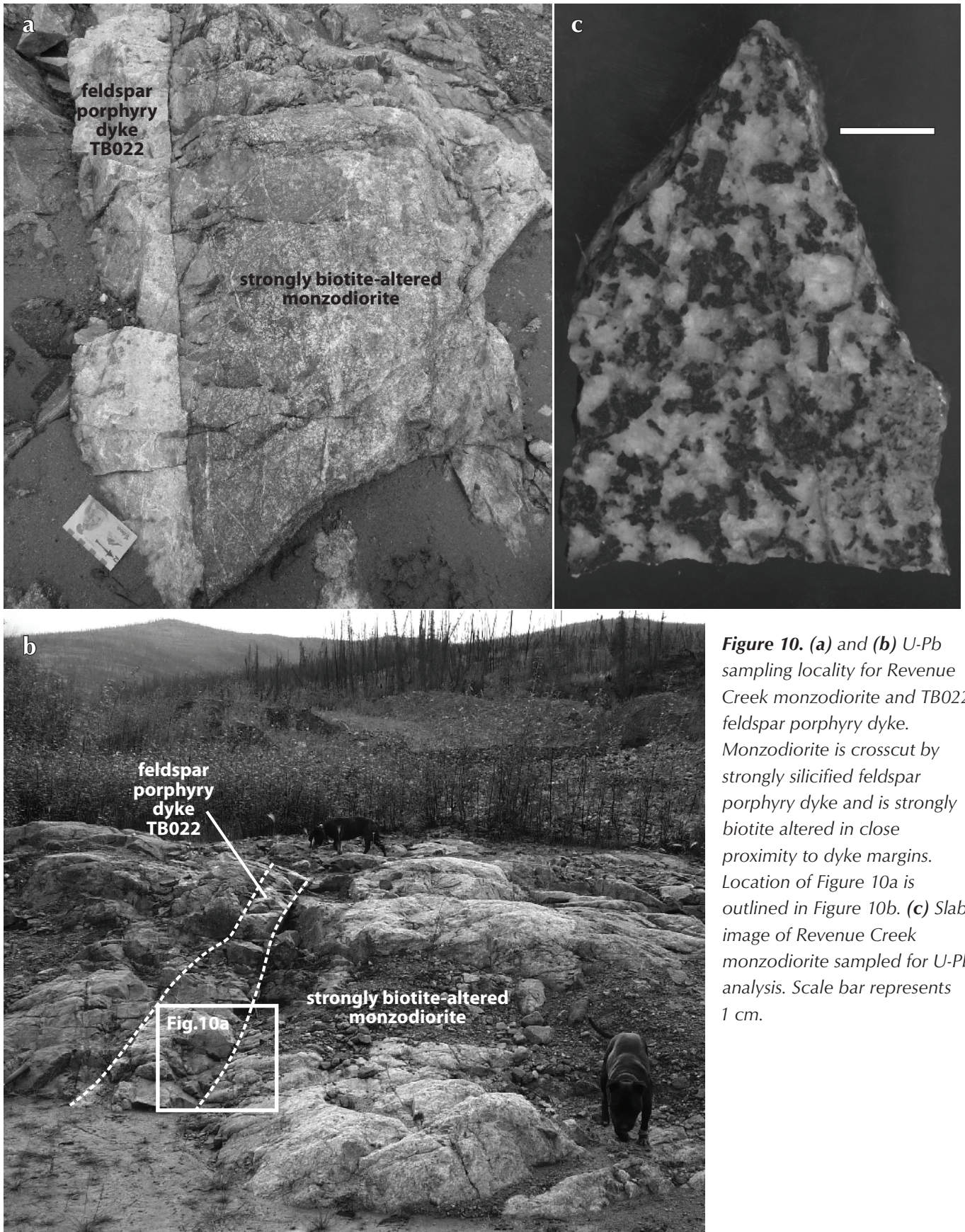


Figure 10. (a) and (b) U-Pb sampling locality for Revenue Creek monzodiorite and TB022 feldspar porphyry dyke. Monzodiorite is crosscut by strongly silicified feldspar porphyry dyke and is strongly biotite altered in close proximity to dyke margins. Location of Figure 10a is outlined in Figure 10b. (c) Slab image of Revenue Creek monzodiorite sampled for U-Pb analysis. Scale bar represents 1 cm.

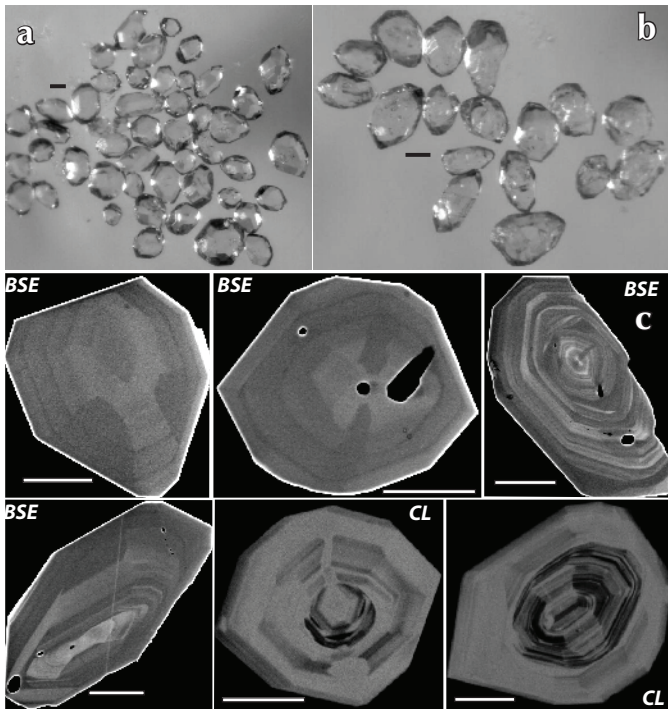


Figure 11. Transmitted light images of (a) stubby, equidimensional zircon prism population, and (b) overgrowth population of zircons from Revenue Creek monzodiorite. Scale bars represent 50 μm . (c) BSE and CL images (denoted on image) of magmatic zircon occurring as entire grains and magmatic overgrowths on xenocrystic cores (CL images). Scale bars represent 50 μm . BSE = backscattered electron, CL = cathodoluminescence.

rims, and that magmatic zircon is characterized by more diffuse oscillatory zoning (Fig. 11c).

Thirty-one analyses were collected from both magmatic zircon grains and magmatic rims (Appendix 1). Twenty micron-diameter line rasters were employed to analyze zircon rims, whereas 40 x 40 μm box rasters were used to analyze magmatic zircon grains. A concordia age calculated from 31 analyses yielded an age of 107.06 ± 0.68 Ma (MSWD = 0.0014) and a weighted mean $^{206}\text{Pb}/^{238}\text{U}$ age of 107.05 ± 0.649 Ma (MSWD = 0.91; Fig. 12a and b). Concentration data calculated from magmatic zircon varies from 128 ppm U, and 54 ppm to 301 ppm Th (Appendix 1).

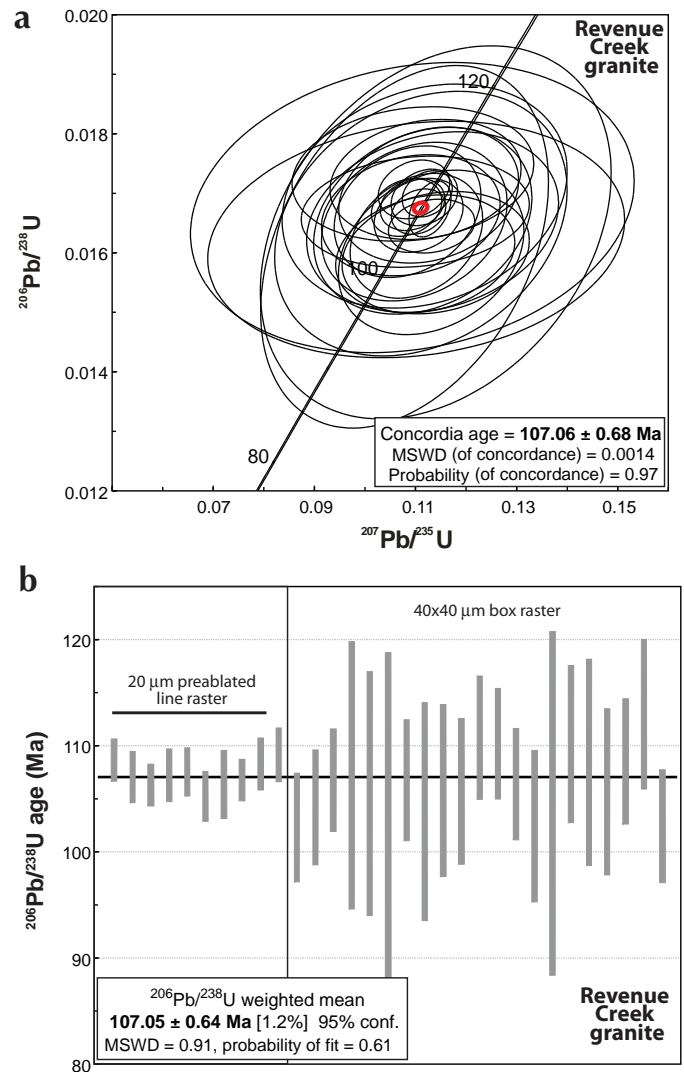


Figure 12. (a) Concordia diagram for U-Pb LAM ICP-MS analyses of magmatic zircon from Revenue Creek monzodiorite. Individual analyses with probability of concordance less than 0.2 are not included in final data calculations. Data point error ellipses represent 2σ error, and 2σ uranium-decay constant errors are included in final age calculation. (b) Plot of weighted mean $^{206}\text{Pb}/^{238}\text{U}$ ages with probability of concordance greater than 0.20. Box heights represent 2σ . MSWD = mean square of the weighted deviates.

STODDART ZONE

Two intrusive rocks were sampled from the Stoddart zone including an aplitic dyke (TB369) and a porphyritic andesitic dyke (TB038). Both dykes are observed to crosscut the Stoddart granite. The aplitic dyke was dated using ID-TIMS, whilst U-Pb dating of the andesitic dyke was done using LAM ICP-MS.

Sample TB369 is one of a suite of aplitic dykes that crosscut the Stoddart porphyry. Additionally, the aplite dykes are observed to be overprinted by quartz-chalcopyrite-molybdenite \pm scheelite mineralized veins for which the molybdenite has a Re-Os age of ca. 94 Ma (Fig. 6c). Four single-grain zircon fractions were analysed from TB369 (Appendix 2) and four concordant analyses of widely different ages (ca. 162 Ma, 102 Ma, 97 Ma and 78 Ma; Fig. 13a) were obtained. The spread in concordant U-Pb age data can only be interpreted by taking into consideration the age of molybdenite mineralization at Stoddart (ca. 94 Ma) and the age of TB038 (ca. 77 Ma, outlined below). The fractions yielding concordant ages of ca. 162 Ma and 102 Ma are considered to represent inheritance. The concordant analysis yielding an age of ca. 78 Ma is consistent with the age of crystallization of TB038 and is thus interpreted as a reset age. If the age of molybdenite mineralization is constrained to ca. 94 Ma, then the third fraction, which has a concordia age of 97.9 ± 0.40 Ma (Fig. 13b), is considered the best estimate of the crystallization age of the aplitic dyke and is

consistent with the overprinting chalcopyrite-molybdenite \pm scheelite mineralized veins observed in core.

TB038 was sampled from the Stoddart zone where a weakly mineralized porphyritic andesitic dyke crosscuts an equigranular phase of the Stoddart granitic intrusion (Fig. 14). The andesite dyke consists of coarse-grained plagioclase, hornblende, biotite and quartz phenocrysts with weak to moderate flow alignment in a fine-grained groundmass of similar mineralogy. Malachite staining was observed at the margins of the andesitic dyke, similar to that observed for TB181 within the Revenue zone.

The sample yielded abundant zircons of moderate to good quality, from which three morphologically distinct populations could be recognized, including: (i) elongate to irregular prisms with core and rim zircon growth (Fig. 15a), (ii) clear, well-faceted equidimensional prisms (Fig. 15b), and (iii) elongate prisms transitional to needle-shaped populations (Fig. 15c). BSE and CL imaging of the zircon populations demonstrates that magmatic zircon occurs as both entire grains and as magmatic rims and that the magmatic zircon is characterized by more diffuse to sharp oscillatory zoning (Fig. 15d).

Twenty-six analyses were collected from both magmatic zircon grains and magmatic rims (Appendix 3). A concordia age calculated from 22 analyses yielded an age of 76.86 ± 0.86 Ma (MSWD = 0.0023) and a weighted mean $^{206}\text{Pb}/^{238}\text{U}$ age of 76.89 ± 0.86 Ma (MSWD = 0.57; Fig. 16a and b). Concentration data calculated from

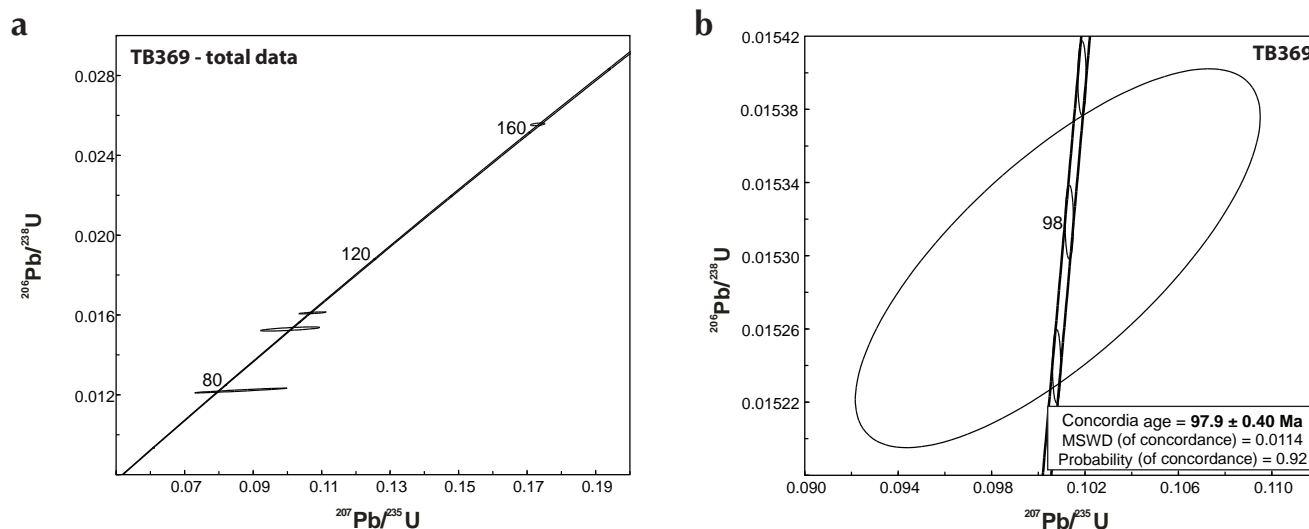


Figure 13. (a) Concordia diagram for U-Pb ID-TIMS analyses of magmatic zircon from TB369; aplitic dyke crosscutting Stoddart zone Cu-Mo-W mineralization. (b) Plot of weighted mean $^{206}\text{Pb}/^{238}\text{U}$ ID-TIMS ages for TB369; aplitic dyke crosscutting Stoddart zone granite. Box heights represent 2σ . MSWD = mean square of the weighted deviates.

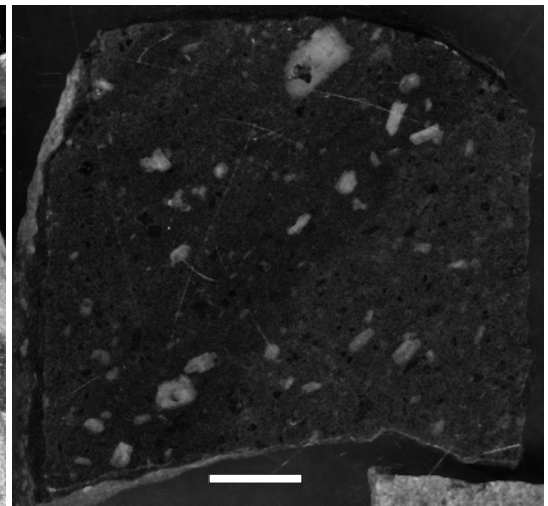
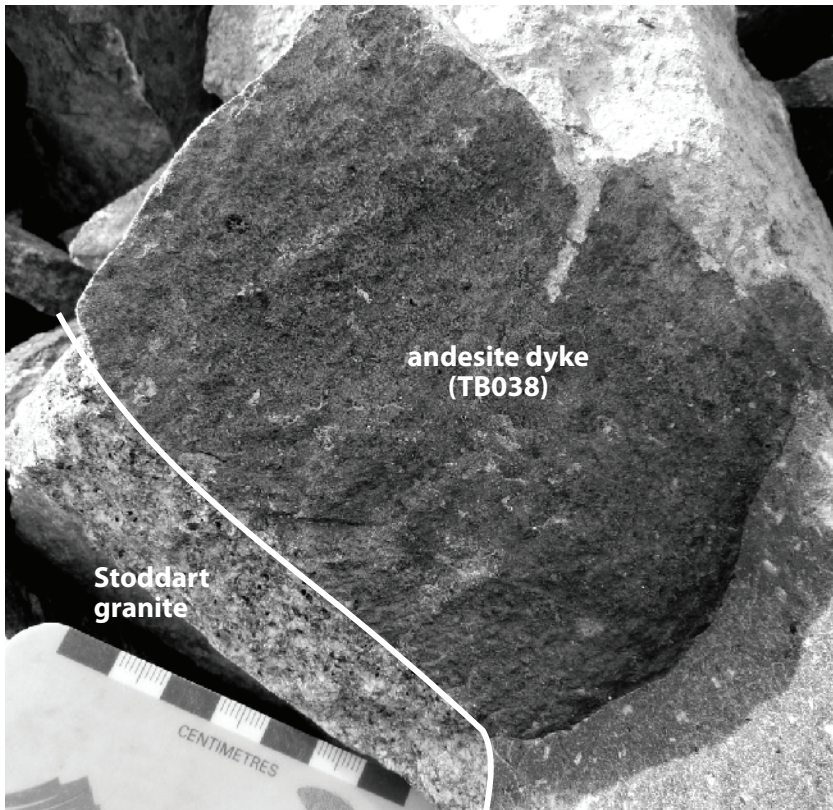
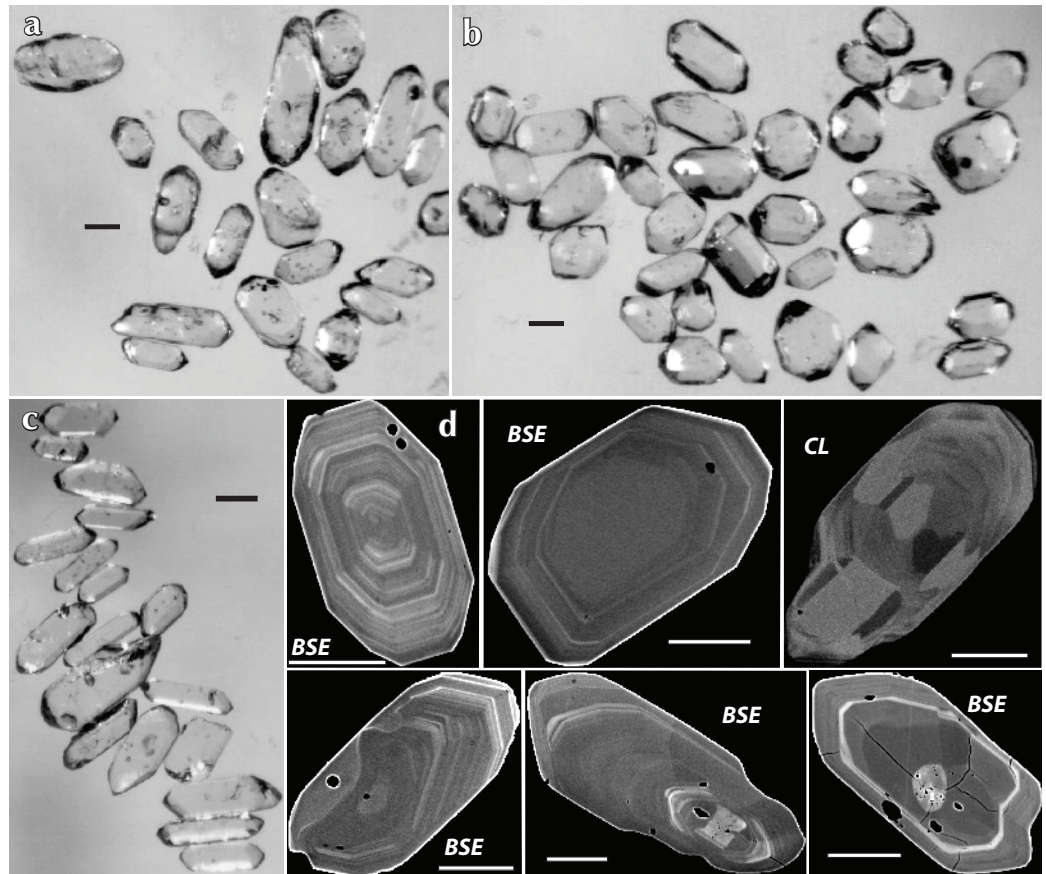


Figure 14. (a) Porphyritic andesitic dyke (TB038) crosscutting Stoddart zone granite. (b) Slab image of andesitic dyke (TB038) sampled for U-Pb analysis. Scale bar represents 1 cm.

Figure 15. Transmitted light images of (a) overgrowth zircon population, (b) well-faceted, stubby zircon prism population, and (c) zircon needle and elongate prism population (with some overgrowth tips) of zircons from andesitic dyke (TB038). Scale bars represent 50 μm . (d) BSE and CL images (denoted on image) of magmatic zircon from andesitic dyke (TB038) occurring as entire grains and magmatic overgrowths on xenocrystic cores. All scale bars represent 50 μm . BSE = backscattered electron, CL = cathodoluminescence.



magmatic zircon varies from 105 ppm to 2118 ppm U, and 44 ppm to 1588 ppm Th (Appendix 3).

RIDGE ZONE

Observations from the Ridge zone trench and drill core indicate that mineralization in this zone postdates the intrusion of the Bow Creek granite (Fig. 17a). A sample of the Bow Creek granite from the Ridge zone mineralized trench was collected to place a maximum age constraint on the timing of mineralization associated with dolomitic alteration within this zone (Fig. 17b and c).

The sample yielded abundant zircon of good quality from which three morphologically distinct populations could be recognized, including: (i) translucent, well-faceted, equidimensional prisms (Fig. 18a), (ii) elongate to irregular prisms with core and rim zircon growth (Fig. 18b), and (iii) subordinate, large needle and needle fragment population (Fig. 18c). BSE and CL imaging of the zircon populations demonstrates magmatic zircon occurs as entire grains and as magmatic rims, and that magmatic zircon is characterized by diffuse to sharp oscillatory and sector zoning (Fig. 18d).

Thirty analyses were collected from both magmatic zircon grains and magmatic rims (Appendix 4). A concordia age calculated from 23 analyses yielded an age of 68.25 ± 0.90 Ma (MSWD = 1.6) and a weighted mean $^{206}\text{Pb}/^{238}\text{U}$ age of 68.43 ± 0.91 Ma (MSWD = 0.37; Fig. 19a and b). Concentration data calculated from magmatic zircon varies from 148 ppm to 1380 ppm U, and 37 ppm to 1057 ppm Th (Appendix 4).

DISCUSSION AND CONCLUSIONS

The NFR Freegold Mountain project is host to several discrete mineralized zones, including two with NI 43-101 resources, e.g., the Tinta Deposit (Au-Ag-Cu-Pb-Zn) and the Nucleus (Au) Deposit. Each mineralized zone is associated with a different metal suite of interest and corresponding style and setting of mineralization indicative of a tectonic setting involving a complex interplay of long-lived structural conduits and multiphase fertile magmatism.

Quartz-feldspar porphyry dyke relationships within the Tinta zone indicate that structurally controlled, polymetallic mineralization took place prior to 108.7 ± 0.4 Ma (zircon). A U-Pb age from hornblende-biotite monzodiorite, which is crosscut by Nucleus-style Au-Cu mineralized dykes in Revenue Creek

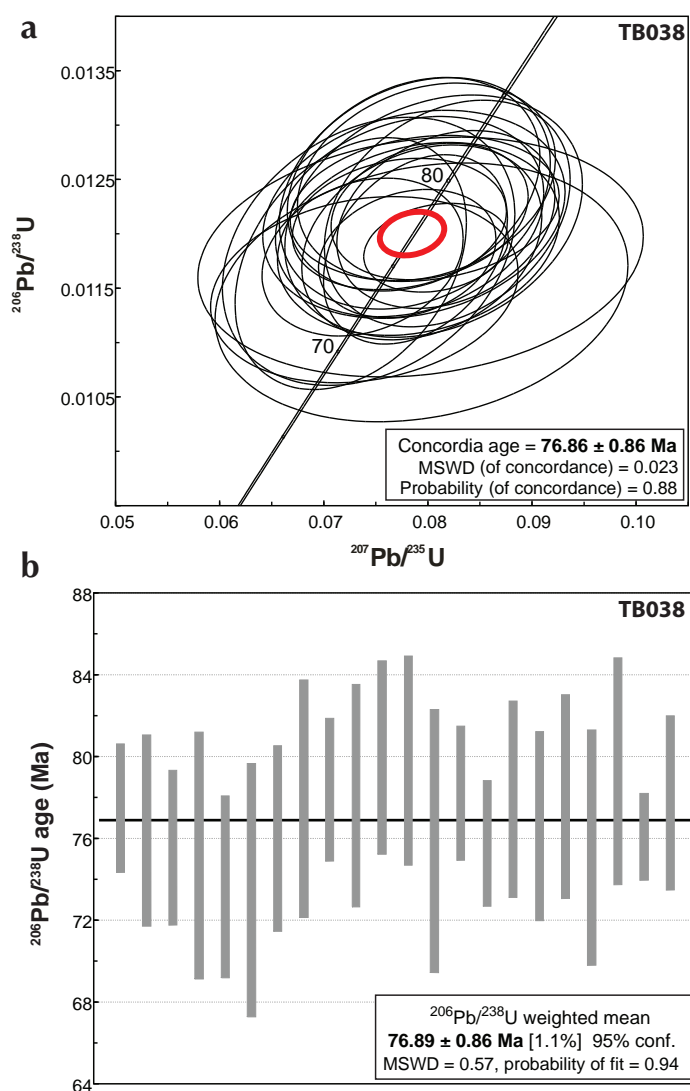


Figure 16. (a) Concordia diagram for U-Pb LAM ICP-MS analyses of magmatic zircon from andesitic dyke, TB038. Individual analyses with probability of concordance less than 0.2 are not included in final data calculations. Data point error ellipses represent 2σ error, and 2σ uranium-decay constant errors are included in final age calculation. **(b)** Plot of weighted mean $^{206}\text{Pb}/^{238}\text{U}$ ages with probability of concordance greater than 0.20 for magmatic zircon from andesitic dyke, TB038. Box heights represent 2σ . MSWD = mean square of the weighted deviates.



Figure 17. (a) Core photo of epithermal dolomite vein crosscutting Bow Creek granite, Ridge zone. Location of 17b marked. (b) Rotated enlargement of dolomite vein exhibiting epithermal veining textures. (c) Slab image of Bow Creek granite sampled from Ridge zone for U-Pb analysis. Scale bars represent 1 cm.

Figure 18. Transmitted light images of (a) well-faceted, equidimensional zircon prism population, (b) overgrowth population, and (c) zircon needle population (with some overgrowth tips) from Bow Creek granite. Scale bars represent 50 μm . (d) BSE and CL images (denoted on image) of magmatic zircon from Bow Creek granite. All scale bars represent 50 μm .

BSE = backscattered electron, CL = cathodoluminescence.

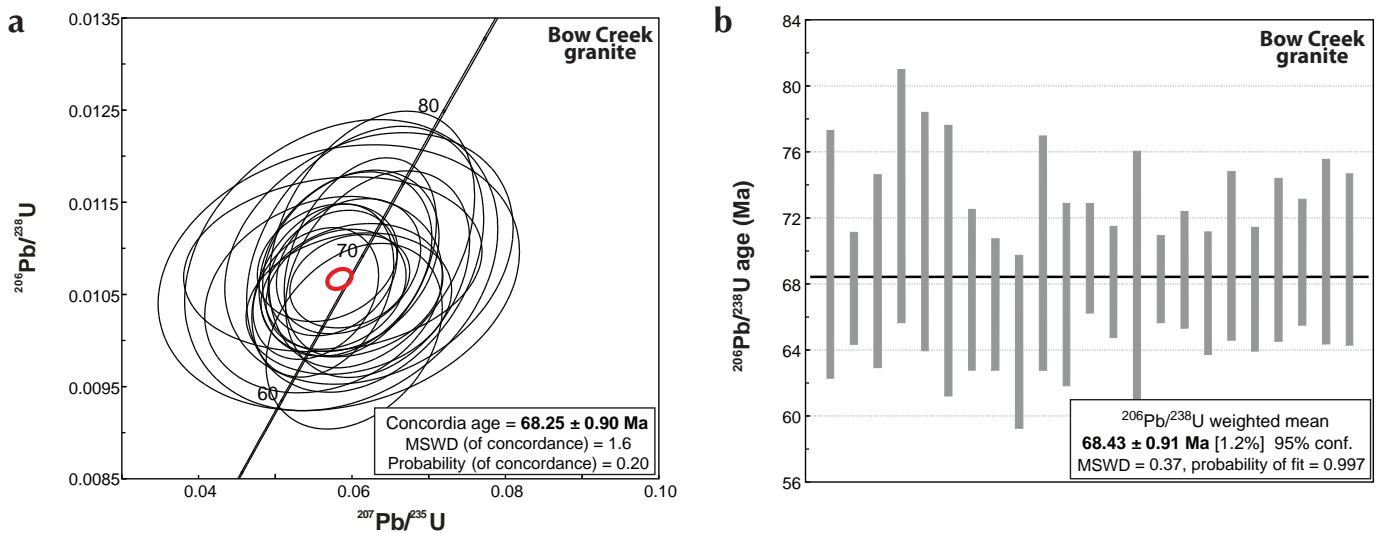
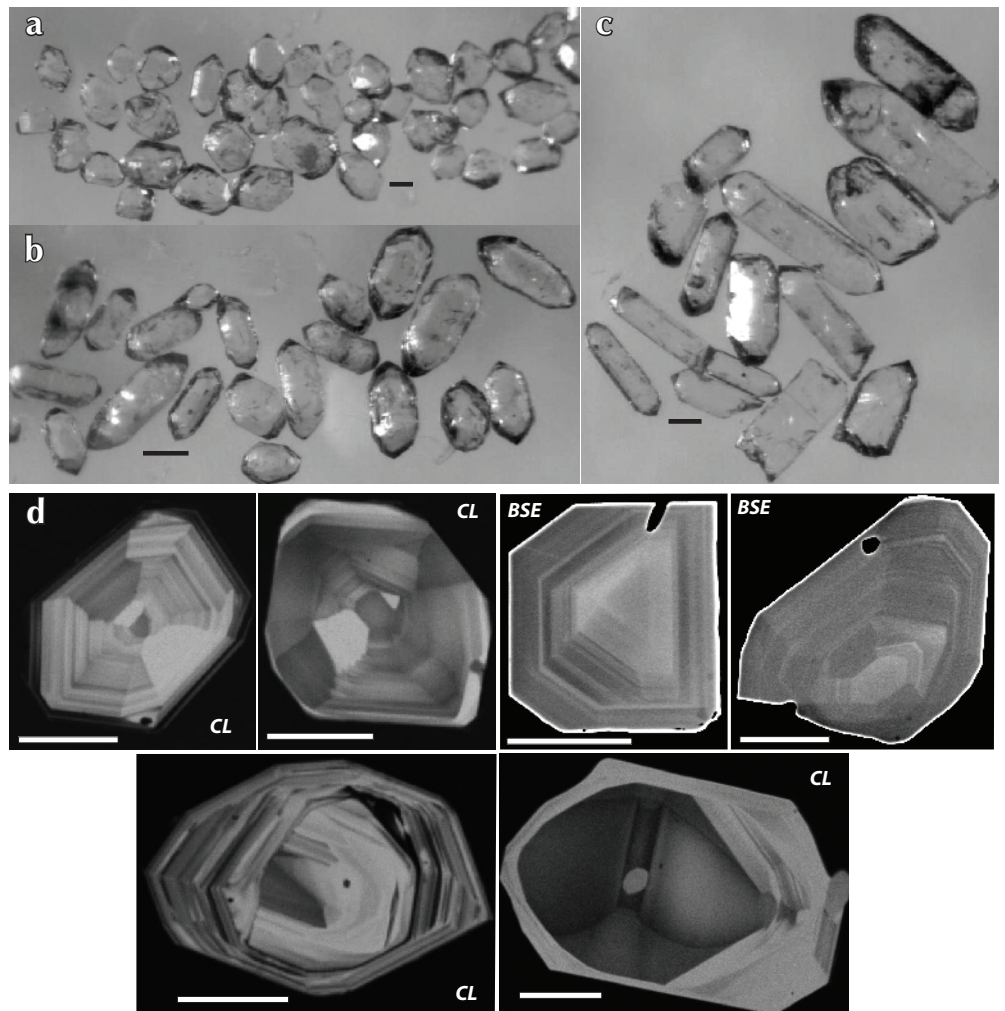


Figure 19. (a) Concordia diagram for U-Pb LAM ICP-MS analyses, Bow Creek granite. Individual analyses with probability of concordance less than 0.2 are not included in final data calculations. Data point error ellipses represent 2σ error, and 2σ uranium-decay constant errors are included in final age calculation. (b) Plot of weighted mean $^{206}\text{Pb}/^{238}\text{U}$ ages with probability of concordance greater than 0.20 for magmatic zircon from Bow Creek granite. Box heights represent 2σ . MSWD = mean square of the weighted deviates.

(105.7 ± 0.2 Ma, 105.5 ± 0.2 Ma and 104.4 ± 0.1 Ma; U-Pb zircon), yields an age of 107.1 ± 0.6 Ma (U-Pb zircon), demonstrating a broadly synchronous relationship. The Stoddart Cu-Mo-W porphyry is crosscut by several dyke suites ranging from aplitic to andesitic and basaltic in composition. A U-Pb zircon age from an aplitic dyke that crosscuts the Stoddart porphyry, but is itself crosscut by Cu-Mo-W vein mineralization, yields an age of 97.9 ± 0.4 Ma, consistent with the younger Re-Os molybdenite model age of 93.7 ± 1.5 Ma. An andesitic dyke that locally hosts Cu mineralization, and which crosscuts the Stoddart biotite granite, yielded an age of 76.9 ± 0.9 Ma (U-Pb zircon). This age and style of mineralization has also been recorded from a rhyolitic dyke that intrudes the Revenue zone (75.2 ± 0.2 Ma; U-Pb zircon). Shear-hosted, polymetallic Au-Ag-Pb-Cu mineralization occurring at the Ridge zone, which occurs at or near the contact between the Casino granodiorite

and the Bow Creek granite, is characterized by both base-metal-bearing silica and dolomitic fluids. Importantly, galena-rich dolomitic veins are observed to crosscut the Bow Creek granite, which yielded a U-Pb zircon date of 68.4 ± 0.9 Ma, indicating that dolomitic fluids associated with the Ridge zone post date the intrusion of the Bow Creek granite.

Collectively, the new age data determined from Cretaceous magmatic units that intrude the Tinta, Revenue, Stoddart and Ridge mineralized zones demonstrate that a protracted history of economically important, polymetallic mineralization extended for more than 40 Ma (Fig. 20). Importantly, these new age data place maximum and minimum age constraints on the timing of mineralization occurring across the Freegold Mountain project area.

	Age (Ma)	Magmatic event	Mineralization event
Late Cretaceous	<i>Post 68 Ma</i>	<i>Ridge zone polymetallic mineralization, base-metal mineralization associated with epithermal dolomite veins crosscuts Bow Creek granite</i>	Ridge zone (polymetallic)
	<i>68 Ma (U-Pb)</i>	<i>Intrusion of Bow Creek granite</i>	Revenue late-stage Cu-Au
	<i>75 Ma (U-Pb)</i>	<i>Rhyolitic Revenue dyke emplacement</i>	
	<i>77 Ma (U-Pb)</i>	<i>Andesitic dyke crosscutting Stoddart zone granite</i>	
Mid Cretaceous	<i>~94 Ma (Re-Os)</i>	<i>Cu-Mo-W mineralization, Stoddart porphyry</i>	Stoddart zone (Cu-Mo-W)
	<i>~98 Ma (U-Pb)</i>	<i>Intrusion of aplite dykes crosscutting Stoddart granite</i>	Nucleus and Revenue (Au-Cu) skarn and later dyke and structurally hosted Au-Cu mineralization
	<i>106 - 104 Ma (U-Pb)</i>	<i>Intrusion of Nucleus and Revenue dykes</i>	
	<i>107 Ma (U-Pb)</i>	<i>Intrusion of Revenue Creek granite</i>	
	<i>Pre 109 Ma</i>	<i>Chlorite-altered trachytic dyke crosscuts polymetallic mineralization, Tinta zone</i>	
	<i>Pre 109 Ma(?)</i>	<i>Tinta zone mineralization crosscutting Jurassic(?) granite</i>	Tinta zone (polymetallic)

Figure 20. Summary diagram illustrating the distribution through time of important magmatic and mineralizing events known to occur throughout the Freegold Mountain project area.

ACKNOWLEDGEMENTS

We thank the Yukon Geological Survey (YGS), Northern Freegold Resources (NFR), and NSERC for funding and logistical support. We are also grateful to David Lentz from University of New Brunswick, for supervising the PhD thesis of Thierry Bineli Betsi and for pre-reviewing this manuscript. We acknowledge Fabrizio Colombo, Wade Barnes, Roger Hulstein and Emily Miller, all from NFR, for their assistance during field work. Thank you to Pam King, Earth Sciences Department, Memorial University and Michael Tubrett and Michael Schaeffer for access and assistance in the MaFLIC analytical facility. Grant Abbott provided clarity on terminology and the regional geology section. Roger Hulstein and Wade Barnes are thanked for comments on an earlier draft of the manuscript.

REFERENCES

- Bennett, V. and Tubrett, M., 2010 (this volume). U-Pb isotopic age dating by LAM ICP-MS, INCO Innovation Centre, Memorial University: Sample preparation, methodology and analytical techniques. *In: Yukon Exploration and Geology 2009*, K.E. MacFarlane, L.H. Weston and L.R. Blackburn (eds.), Yukon Geological Survey, p. 47-55.
- Carlson, G.G., 1987. Geology of Mount Nansen (115-1/3) and Stoddart Creek (115-1/6) map areas Dawson Range, Central Yukon. Exploration and Geological Services Division, Yukon Region, Indian and Northern Affairs Canada, Open File 1987-2, 181 p.
- Colpron, M.N., Nelson, J.L. and Murphy, D.C., 2006. A tectonostratigraphic framework for the Pericratonic terranes of the northern Canadian Cordillera. *In: Paleozoic evolution and metallogeny of Pericratonic Terranes at the ancient pacific margin of North America, Canadian and Alaskan Cordillera*. M. Colpron and J.L. Nelson (eds.), Geological Association of Canada, Special Paper 45, p. 1-23.
- Crowley, J.L., Schoene B. and Bowring S.A., 2007. U-Pb dating of zircon in the Bishop Tuff at the millennial scale. *Geology*, vol. 35, p. 1123-1126.
- Eaton, W.D., 1984. Geological, geochemical, and geophysical report for bulldozer trenching and diamond drilling program at Nat Joint Venture Nucleus 1-141 claims. Archer, Cathro & Associates, Assessment Report #091600.
- Fonseca, A., 2009. NI 43-101 technical report on the Freegold Mountain property, Dawson Range, Yukon. <<http://www.sedar.com>>, 167 p., {Sept 9, 2009}.
- Geospec Consultants Ltd., 2008. Re-Os isotopic analyses and age dating of Molybdenite for Northern Freegold Resources Ltd.
- Gordey, S.P. and Makepeace, A.J. (comps.), 2000. Bedrock geology, Yukon Territory. Geological Survey of Canada, Open File 3754, and Exploration and Geological Services Division, Yukon Region, Indian and Northern Affairs Canada, Open File 2001-1, 1:1 000 000 scale.
- Jaffey, A.H., Flynn, K.F., Glendenin, L.E., Bentley, W.C. and Essling, A.M., 1971. Precision measurements of half-lives and specific activities of ^{235}U and ^{238}U . *Physical Review C*, vol. 4, p. 1889-1906.
- Johnston, S.T., 1995. Geological compilation with interpretation from geophysical surveys of the northern Dawson Range, central Yukon (115-J/9 and 115- J/10, 115-J/12, 1: 100 000-scale map). Exploration and Geological Services Division, Yukon Region, Indian and Northern Affairs Canada, Open File 1995-2 (G), 171 p.
- Johnston, S.T., Mortensen, J.K. and Erdmer, P., 1996. Igneous and metaigneous age constraints for the Aishihik metamorphic suite, southwest Yukon. *National Research Council of Canada, Canadian Journal of Earth Sciences*, vol. 33, no. 11, p. 1543-1555.
- Ludwig, K.R., 1999. User's manual for Isoplot/Ex, version 2.06: a geochronological toolkit for Microsoft Excel. Berkeley Geochronological Center, Special Publication No. 1a.
- Mattinson, J.M., 2005. Zircon U-Pb chemical abrasion (CA – TIMS) method: combined annealing and multi-step dissolution analysis for improved precision and accuracy of zircon ages. *Chemical Geology*, vol. 220, p. 47-56.
- McCausland, P.J.A., Symons, D.T.A., Hart, C.J.R. and Blackburn, W.H., 2001. Paleomagnetic study of the Late Cretaceous Seymour Creek stock, Yukon: Minimal geotectonic motion of the Yukon-Tanana Terrane, *In: Yukon Exploration and Geology 2000*, D.S. Emond and L.H. Weston (eds.), Exploration and Geological Services Division, Yukon Region, Indian and Northern Affairs Canada, p. 207-216.

- Mortensen, J.K., Ghosh, D. and Ferri, F., 1995. U-Pb age constraints on intrusive rocks associated with copper-gold porphyry deposits in the Canadian Cordillera. *In: Porphyry Deposits of the Northwestern Cordillera of North America*, T.G. Schroeter (ed.), CIM Special Volume 46, p. 142-158.
- Payne, J.G., Gonzalez, R.A., Akhurst, K. and Sisson W.G., 1987. Geology of Colorado Creek (115-J/10), Selwyn River (115-J/9), and Prospector Mountain (115-1/5) map areas, western Dawson Range, west-central Yukon. Exploration and Geological Services Division, Yukon Region, Indian and Northern Affairs Canada, Open File 1987-3, 141 p.
- Schmitz, M.D. and B. Schoene, 2007. Derivation of isotope ratios, errors, and error correlations for U-Pb geochronology using ^{205}Pb - ^{235}U -(^{233}U)-spiked isotope dilution thermal ionization mass spectrometric data. *Geochemistry, Geophysics, Geosystems*, vol. 8, Q08006, doi:10.1029/2006GC001492.
- Selby, D., Creaser, R.A. and Nesbit, E.B., 1999. Major and trace element compositions and Sr-Nd-Pb systematics of crystalline rocks from the Dawson Range, Yukon, Canada. *Canadian Journal of Earth Sciences*, vol. 36, p. 1463-1481.
- Tempelman-Kluit, D.J., 1974. Reconnaissance geology of Aishihik Lake, Snag and part of Stewart River map-areas, west-central Yukon (115A, 115F, 115G and 115K). Geological Survey of Canada, Paper 73-41, 97 p.
- Tempelman-Kluit, D.J., 1984. Geology, Laberge (105E) and Carmacks (105I), Yukon Territory. Geological Survey of Canada, Open File 1101, maps with legends, 1:250 000 scale.

Appendix 1. LAM ICP-MS U-Pb isotopic analyses of magmatic zircons from Revenue Creek granite.

Analysis	Measured isotopic ratios				Calculated ages											
	$^{207}\text{Pb}/^{235}\text{U}$ 1 σ err.	$^{206}\text{Pb}/^{238}\text{U}$ 1 σ err.	Rho	$^{207}\text{Pb}/^{206}\text{Pb}$ 1 σ err.	$^{207}\text{Pb}/^{235}\text{U}$ Ma	1 σ err. Ma	$^{206}\text{Pb}/^{238}\text{U}$ Ma	1 σ err. Ma	Conc. age (Ma)	2 σ err. Ma	MSWD of conc.	Prob. of conc.	Th (ppm)	U (ppm)	Ratio Th/U	
oc19c15	0.1123	0.0020	0.2591	0.0479	0.0009	108.1	1.8	108.6	1.0	108.5	2	0.08	0.78	104	405	0.26
oc19c16	0.1129	0.0017	0.3807	0.0487	0.0007	108.6	1.5	107.0	1.2	107.5	2	1.05	0.31	301	791	0.38
oc19c17	0.1139	0.0020	0.2665	0.0497	0.0011	109.6	1.8	106.2	1.0	106.7	2	3.26	0.07	186	451	0.41
oc19c18	0.1082	0.0028	0.2244	0.0464	0.0011	104.4	2.6	107.2	1.3	106.8	2	1.14	0.29	249	550	0.45
oc19c19	0.1094	0.0026	0.2239	0.0473	0.0011	105.4	2.4	107.5	1.1	107.2	2	0.74	0.39	199	400	0.50
oc19c20	0.1132	0.0035	0.1822	0.0493	0.0015	108.9	3.2	105.2	1.2	105.4	2	1.34	0.25	81	259	0.31
oc19c21	0.1106	0.0036	0.2351	0.0484	0.0019	106.5	3.3	106.3	1.6	106.3	3	0.00	0.95	71	216	0.33
oc19c22	0.1106	0.0022	0.2344	0.0477	0.0010	106.5	2.0	106.7	1.0	106.7	2	0.01	0.93	137	317	0.43
oc19c23	0.1118	0.0027	0.2376	0.0478	0.0013	107.6	2.5	108.2	1.2	108.1	2	0.07	0.79	86	234	0.37
oc19c24	0.1097	0.0029	0.2243	0.0466	0.0013	105.7	2.6	109.1	1.3	108.7	2	1.63	0.20	83	259	0.32
oc14B40	0.1119	0.0072	0.1960	0.0456	0.0016	107.7	6.6	102.2	2.6	102.6	5	0.69	0.41	84	270	0.31
oc14B47	0.1102	0.0054	0.2706	0.0491	0.0009	106.1	4.9	104.1	2.7	104.4	5	0.16	0.69	212	555	0.38
oc14B48	0.1100	0.0092	0.1363	0.0463	0.0024	105.9	8.4	106.7	2.4	106.7	5	0.01	0.93	219	518	0.42
oc14B49	0.1094	0.0179	0.1812	0.0555	0.0023	105.4	16.4	107.1	6.3	107.0	12	0.01	0.92	138	396	0.35
oc14B50	0.1111	0.0118	0.2589	0.0525	0.0013	106.9	10.8	105.4	5.8	105.7	11	0.02	0.89	100	343	0.29
oc14B51	0.1078	0.0116	0.3583	0.0493	0.0013	104.0	10.7	103.0	7.9	103.3	15	0.01	0.92	80	264	0.30
oc14B52	0.1084	0.0059	0.2473	0.0463	0.0010	104.5	5.4	106.7	2.9	106.4	5	0.16	0.69	228	478	0.48
oc14B53	0.1101	0.0168	0.1635	0.0563	0.0028	106.1	15.4	103.7	5.1	103.9	10	0.02	0.88	104	238	0.44
oc14B54	0.1114	0.0088	0.2449	0.0492	0.0012	107.3	8.1	105.7	4.1	105.9	8	0.04	0.85	123	366	0.34
oc14a41	0.1098	0.0075	0.2409	0.0499	0.0014	105.7	6.9	105.6	3.5	105.7	7	0.0	0.99	60	175	0.340
oc14a42	0.1095	0.0098	0.1493	0.0557	0.0015	105.5	8.9	110.7	2.9	110.4	6	0.3	0.56	73	189	0.387
oc14a59	0.1120	0.0077	0.1735	0.0512	0.0012	107.8	7.1	110.1	2.6	110.0	5	0.1	0.74	106	308	0.344
oc14a60	0.1091	0.0072	0.1888	0.0520	0.0012	105.1	6.6	106.3	2.6	106.2	5	0.0	0.85	169	352	0.479
oc14a61	0.1131	0.0075	0.2660	0.0503	0.0016	108.8	6.8	102.4	3.6	103.2	7	0.9	0.35	92	185	0.498
oc14a62	0.1140	0.0142	0.3151	0.0522	0.0013	109.6	12.9	104.5	8.1	105.5	15	0.2	0.69	82	221	0.373
oc14a63	0.1041	0.0079	0.2252	0.0485	0.0011	100.5	7.2	110.1	3.7	108.7	7	1.7	0.19	81	249	0.325
oc14a64	0.1118	0.0115	0.2201	0.0511	0.0013	107.6	10.5	108.4	4.9	108.3	9	0.0	0.94	72	163	0.444
oc14a65	0.1134	0.0102	0.2088	0.0563	0.0013	109.1	9.3	105.6	3.9	105.9	8	0.1	0.71	102	224	0.456
oc14a66	0.1126	0.0073	0.2131	0.0499	0.0012	108.4	6.6	108.5	3.0	108.5	6	0.0	0.99	92	258	0.357
oc14a67	0.1043	0.0089	0.1857	0.0521	0.0015	100.7	8.1	112.9	3.5	111.6	7	2.2	0.14	60	128	0.470
oc14a68	0.1140	0.0076	0.1976	0.0569	0.0017	109.6	6.9	102.3	2.7	102.9	5	1.1	0.29	54	185	0.294

Appendix 2. Chemical abrasion U-Th-Pb ID-TIMS data for zircon fractions from TB369, aplite dyke crosscutting Stoddart porphyry, Stoddart zone.

Sample (a)	Compositional parameters					Radiogenic isotope ratios					Isotopic ages												
	Wt. mg (b)	U ppm (c)	Th U ppm (d)	Pb ppm (c)	$^{206}\text{Pb}^*$ mol $\times 10^{-13}$ mol (e)	mol % $^{206}\text{Pb}^*$ (e)	Pb* (e)	Pb _c (pg) (e)	$^{206}\text{Pb}/^{204}\text{Pb}$ (f)	$^{208}\text{Pb}/^{206}\text{Pb}$ (g)	$^{207}\text{Pb}/^{206}\text{Pb}$ (g)	% err (h)	$^{206}\text{Pb}/^{238}\text{U}$ (g)	% err (h)	$^{207}\text{Pb}/^{235}\text{U}$ (i)	% err (h)	$^{206}\text{Pb}/^{238}\text{U}$ (i)	\pm (h)					
TB369																							
TB369 A	0.002	940	0.459	26.8	2.0032	97.46%	12	4.29	728	0.146	0.049126	0.921	0.173084	1.013	0.025553	0.212	0.521	153.86	21.56	162.09	1.52	162.66	0.34
TB369 C	0.002	176	0.301	4.9	0.1793	72.82%	1	5.50	68	0.104	0.051318	11.988	0.086446	12.754	0.012217	0.801	0.960	255.13	275.47	84.19	10.30	78.28	0.62
TB369 D	0.002	319	0.402	6.6	0.4281	92.46%	4	2.87	245	0.129	0.048343	2.848	0.107350	3.033	0.016105	0.253	0.752	116.11	67.13	103.54	2.99	102.99	0.26
TB369 E	0.002	48	0.262	1.2	0.0618	84.34%	2	0.94	118	0.083	0.047803	6.622	0.100835	7.024	0.015299	0.553	0.746	89.55	156.88	97.55	6.53	97.87	0.54

(a) A, B etc. are labels for fractions composed of single zircon grains or fragments; all fractions annealed and chemically abraded after Mattinson (2005).
 (b) Nominal fraction weights estimated from photomicrographic grain dimensions, adjusted for partial dissolution during chemical abrasion.
 (c) Nominal U and total Pb concentrations subject to uncertainty in photomicrographic estimation of weight and partial dissolution during chemical abrasion.
 (d) Model Th/U ratio calculated from radiogenic $^{208}\text{Pb}/^{206}\text{Pb}$ ratio and $^{207}\text{Pb}/^{235}\text{U}$ age.
 (e) Pb* and Pb_c represent radiogenic and common Pb, respectively; mol. % $^{206}\text{Pb}^*$ with respect to radiogenic, blank and initial common Pb.
 (f) Measured ratio corrected for spike and fractionation only. Daly analyses, based on analysis of NBS-982.
 (g) Corrected for fractionation, spike and common Pb; up to 1 pg of common Pb was assumed to be procedural blank: $^{206}\text{Pb}/^{204}\text{Pb} = 18.50 \pm 1.0\%$; $^{207}\text{Pb}/^{204}\text{Pb} = 15.50 \pm 1.0\%$; $^{208}\text{Pb}/^{204}\text{Pb} = 38.40 \pm 1.0\%$ (all uncertainties 1-sigma). Excess over blank was assigned to initial common Pb.
 (h) Errors are 2-sigma, propagated using the algorithms of Schmitz and Schoene (2007) and Crowley et al. (2007).
 (i) Calculations are based on the decay constants of Jaffey et al. (1971). $^{206}\text{Pb}/^{238}\text{U}$ and $^{207}\text{Pb}/^{235}\text{U}$ ages corrected for initial disequilibrium in $^{230}\text{Th}/^{238}\text{U}$ using Th/U [magma] = 3.
 (j) Corrected for fractionation, spike and blank Pb only.

Appendix 3. LAM ICP-MS U-Pb isotopic analyses of magmatic zircon from andesitic dyke, TB038.

Analysis	measured isotopic ratios					Calculated ages								
	$^{207}\text{Pb}/^{235}\text{U}$ 1 σ err.	$^{206}\text{Pb}/^{238}\text{U}$ 1 σ err.	Rho	$^{207}\text{Pb}/^{206}\text{Pb}$ 1 σ err.	$^{207}\text{Pb}/^{235}\text{U}$ Ma	$^{206}\text{Pb}/^{238}\text{U}$ Ma	1 σ err. Ma	Conc. age (Ma)	2 σ err. Ma	MSWD of conc.	Prob. of conc.	Th (ppm)	U (ppm)	Ratio Th/U
oc15a54	0.07726	0.00420	0.18770	0.04786	0.00098	76	4	77	3	0.23	0.63	184	357	0.52
oc15a56	0.07942	0.00471	0.25910	0.04826	0.00087	78	4	76	4	0.07	0.79	1588	2118	0.75
oc15a58	0.07373	0.00395	0.23491	0.04764	0.00074	72	4	76	4	0.77	0.38	403	828	0.49
oc15a76	0.07259	0.00454	0.32263	0.04379	0.00133	71	4	75	6	0.84	0.36	91	140	0.65
oc15a80	0.07390	0.00604	0.19634	0.05551	0.00139	72	6	74	4	0.05	0.83	77	156	0.49
oc15a81	0.07939	0.00810	0.20786	0.05622	0.00144	78	8	73	6	0.29	0.59	51	184	0.28
oc15a82	0.07880	0.00361	0.32732	0.04758	0.00086	77	3	76	4	0.09	0.76	116	269	0.43
oc15a84	0.08055	0.00584	0.25793	0.04969	0.00159	79	5	78	6	0.02	0.89	81	145	0.56
oc15a85	0.07969	0.00528	0.16918	0.05219	0.00131	78	5	78	3	0.01	0.92	315	522	0.60
oc15a86	0.08186	0.00482	0.29643	0.04740	0.00099	80	5	78	5	0.16	0.69	202	373	0.54
oc15a87	0.07987	0.00506	0.23485	0.04830	0.00123	78	5	80	5	0.16	0.69	81	198	0.41
oc15a92	0.07863	0.00496	0.25542	0.04747	0.00122	77	5	80	5	0.39	0.53	77	128	0.60
oc15a93	0.07431	0.00574	0.27551	0.04417	0.00123	73	5	76	6	0.32	0.57	57	128	0.44
oc15a95	0.08016	0.00387	0.21782	0.04999	0.00080	78	4	78	3	0.00	0.98	189	455	0.42
oc15a96	0.07802	0.00348	0.22845	0.04771	0.00090	76	3	76	3	0.03	0.87	107	271	0.39
oc15a97	0.07825	0.00526	0.22987	0.05071	0.00132	76	5	78	5	0.08	0.78	62	145	0.43
oc15a98	0.07909	0.00553	0.21683	0.05244	0.00125	77	5	77	4	0.02	0.90	100	225	0.44
oc15a99	0.07866	0.00593	0.21275	0.04723	0.00135	77	6	78	5	0.04	0.84	65	166	0.39
oc15c101	0.07930	0.00874	0.17331	0.05171	0.00143	77	8	76	6	0.06	0.81	132	247	0.53
oc15c102	0.07875	0.00532	0.26020	0.04953	0.00131	77	5	79	5	0.21	0.65	44	105	0.42
oc15c103	0.08078	0.00284	0.20002	0.04840	0.00167	79	3	76	2	1.10	0.29	500	995	0.50
oc15c104	0.08174	0.00428	0.26297	0.05190	0.00118	80	4	78	4	0.26	0.61	137	254	0.54
oc15a55	0.08245	0.01881	0.69473	0.04899	0.00176	80	18	81	35	0.00	0.97	947	1493	0.63
oc15a78	0.08089	0.01302	0.18540	0.04675	0.00102	79	12	75	9	0.11	0.74	495	807	0.61
oc15a79	0.07492	0.00434	0.24760	0.04390	0.00114	73	4	79	4	1.71	0.19	76	150	0.50
oc15a83	0.07509	0.00530	0.23983	0.04457	0.00133	74	5	83	5	3.20	0.07	77	146	0.53

Appendix 4. LAM ICP-MS U-Pb isotopic analyses of magmatic zircons from Bow Creek granite, Ridge Zone.

Analysis	Measured isotopic ratios					Calculated ages								
	$^{207}\text{Pb}/^{235}\text{U}$ 1 σ err.	$^{206}\text{Pb}/^{238}\text{U}$ 1 σ err.	Rho	$^{207}\text{Pb}/^{206}\text{Pb}$ 1 σ err.	$^{207}\text{Pb}/^{235}\text{U}$ 1 σ err. Ma	$^{206}\text{Pb}/^{238}\text{U}$ Ma	1 σ err. Ma	Conc. age (Ma)	2 σ err. Ma	MSWD of conc.	Prob. of conc.	Th (ppm)	U (ppm)	Ratio Th/U
oc14B55	0.0717	0.0063	0.3078	0.0485	0.0014	70	6	70	7	0.01	0.93	276	619	0.44
oc14B58	0.0679	0.0037	0.2299	0.0479	0.0010	67	4	68	3	0.07	0.79	694	1082	0.64
oc14B59	0.0733	0.0049	0.3195	0.0506	0.0013	72	5	69	6	0.46	0.50	221	501	0.44
oc14B70	0.0772	0.0078	0.2624	0.0502	0.0015	76	7	73	4	0.09	0.76	398	741	0.54
oc14B71	0.0726	0.0055	0.3399	0.0498	0.0013	71	5	71	7	0.00	1.00	171	381	0.45
oc14B73	0.0686	0.0083	0.2454	0.0537	0.0022	67	8	69	8	0.06	0.80	71	207	0.34
oc14B74	0.0662	0.0038	0.3186	0.0463	0.0008	65	4	68	5	0.48	0.49	1057	1295	0.82
oc14B77	0.0696	0.0055	0.1916	0.0499	0.0015	68	5	67	4	0.10	0.76	365	684	0.53
oc14B78	0.0703	0.0047	0.3068	0.0522	0.0013	69	4	64	5	1.04	0.31	338	591	0.57
oc14B79	0.0722	0.0077	0.2407	0.0517	0.0014	71	7	70	7	0.02	0.89	129	332	0.39
oc14B80	0.0663	0.0063	0.2171	0.0519	0.0014	65	6	67	5	0.13	0.72	177	409	0.43
oc15a14	0.0668	0.0037	0.2149	0.0472	0.0011	66	4	70	3	1.16	0.28	158	367	0.43
oc15a15	0.0624	0.0036	0.2158	0.0470	0.0010	61	3	68	3	3.60	0.06	135	335	0.40
oc15a16	0.0683	0.0096	0.1957	0.0517	0.0012	67	9	68	7	0.02	0.88	174	378	0.46
oc15a17	0.0697	0.0032	0.2122	0.0497	0.0009	68	3	68	3	0.00	0.95	1045	1169	0.89
oc15a18	0.0675	0.0034	0.2543	0.0458	0.0009	66	3	69	3	0.59	0.44	209	408	0.51
oc15a19	0.0653	0.0033	0.2709	0.0456	0.0011	64	3	67	4	0.98	0.32	139	273	0.51
oc15a21	0.0698	0.0047	0.2749	0.0496	0.0012	69	4	70	5	0.06	0.80	123	273	0.45
oc15a22	0.0700	0.0048	0.2026	0.0483	0.0013	69	5	68	4	0.05	0.82	338	827	0.41
oc15a35	0.0675	0.0079	0.1519	0.0548	0.0012	66	8	69	5	0.17	0.68	264	531	0.50
oc15a36	0.0695	0.0038	0.2510	0.0489	0.0008	68	4	69	4	0.08	0.78	429	758	0.57
oc15a37	0.0711	0.0041	0.3534	0.0449	0.0010	70	4	70	5	0.00	0.96	195	420	0.46
oc15a38	0.0691	0.0046	0.2832	0.0475	0.0008	68	4	69	5	0.12	0.73	153	802	0.19
oc15a39	0.0889	0.0037	0.3432	0.0531	0.0008	86	3	73	4	15.73	0.00	780	624	1.25
oc15a40	0.0878	0.0115	0.2098	0.0680	0.0019	85	11	72	8	1.46	0.23	37	148	0.25
oc15a41	0.0779	0.0031	0.2133	0.0508	0.0006	76	3	75	2	0.32	0.57	79	1380	0.06
oc15a43	0.0725	0.0037	0.2055	0.0463	0.0008	71	4	73	3	0.23	0.63	353	560	0.63
oc15a44	0.0727	0.0043	0.1884	0.0517	0.0010	71	4	74	3	0.51	0.47	214	426	0.50
oc15a20	0.0937	0.0060	0.3549	0.0602	0.0013	91	6	73	6	11.00	0.00	168	357	0.47
oc15a23	0.0657	0.0399	0.1328	0.0486	0.0019	65	38	71	23	0.03	0.86	224	426	0.53

High-sulphidation epithermal Au-Ag-Cu mineralization at the McKay Hill property – a revised deposit model

*Lauren R. Blackburn*¹
*Monster Mining Corporation*²

Blackburn, L.R., 2010. High-sulphidation epithermal Au-Ag-Cu mineralization at the McKay Hill property – a revised deposit model. *In: Yukon Exploration and Geology 2009*, K.E. MacFarlane, L.H. Weston and L.R. Blackburn (eds.), Yukon Geological Survey, p. 85-101.

ABSTRACT

The past-producing McKay Hill property on NTS map sheet 106D/6 (Nash Creek) has previously been described as polymetallic Ag-Pb-Zn ± Au-style mineralization. During the 2009 YMIP-funded exploration program the central claims on the property were mapped and numerous distinct differences from the proposed polymetallic model became apparent. Unlike Keno Hill, veins on the McKay Hill property lack siderite gangue and are not present as vein-faults. Propylitic alteration halos surrounding vertically zoned ore shoots (high-level Au-Cu and deeper level Ag-Cu-Pb) were observed within consistently north-northwest-striking, near vertical, siliciclastic and hypabyssal-volcanic rocks. The Ag-Pb-Zn veins in the Keno Hill Camp were emplaced in discrete dilational fault structures within polydeformed clastic metasediments and are not associated with extensive alteration. Host rock competency in both areas is vital in controlling mineralization. Re-evaluating the regional framework could potentially illustrate the area's metallogenic potential for different types of mineral occurrences.

¹*lauren.monstermining@gmail.com*

²*Suite 916-925 W Georgia Street, Vancouver, British Columbia, Canada, V6C 3L2*

INTRODUCTION

Bedrock mapping was completed during Monster Mining Corporation's 2009, YMIP-funded target evaluation exploration program over a 700 m² area on the southern flank of Horseshoe Hill in central Yukon. This area is 2 km north of the Beaver River on the Nash Creek 1:50 000-scale map sheet (NTS 106D/6; Fig. 1). The area is located approximately 50 km north-northwest of Keno City and is centered at 64° 20' North Latitude, 135° 22' West Longitude.

The Keno Hill camp is a historic mining camp that has been producing silver, lead and zinc ore for 95 years. The mineralogy of Keno Hill veins is a highly varied mix of sulphides (argentiferous galena and tetrahedrite) and sulphosalts (pyragerite and stephanite). An earlier stage of Au-As-Sn vein mineralization is found within the district; this stage is associated with significantly less silver, lead and zinc. From 1914 to 1989, total silver production exceeded 200 million ounces (J. McFaul, pers. comm., 2009).

The ATAC Resources Ltd. 540 km² Rau gold property (Yukon MINFILE 106D 098), located 2.6 km to the northeast of the McKay Hill property, is hosted in dolomitized or decalcified limestone and is proposed as the northern part of the *Carlin Trend* (ATAC Resources Ltd., web page accessed November 3, 2009). Potential for deeper level Carlin-style mineralization at the McKay Hill property has not been tested to date.

Monster Mining Corporation's 2009 exploration program included detailed mapping of a 450 m X 600 m area; collection and petrographic analysis of 10 thin sections and 7 polished sections; collection of 140 soil samples; and geochemical characterization and analysis of 8 rocks obtained from various veins at different levels. The recently staked White Hill occurrence (Yukon MINFILE 106D 038) situated on the western side of the claim block was located and prospected by M. Bindig.

Previous knowledge of bedrock geology of the 'Nash Creek' area was based on J.A. Roddick's 1972 Geological Survey of Canada (GSC) 1:250 000-scale map 1282A. It is this author's hope that findings at the Rau and McKay Hill properties will prompt the government to complete 1:50 000-scale mapping of the 106D/6 and 106D/7 map sheets.

PROPERTY HISTORY

The McKay Hill property (Yukon MINFILE 106D 037 and 038) history extends back to 1922 during the early days of the Keno Hill district staking rush. Extensive trenching and underground development work was completed on the property in these early years, and in the late 1940s, 143 tonnes of silver-ore grading 390 g/t Ag were produced by East Bay Gold Ltd. from Vein No. 6. In 1929, 832 m of diamond drilling was completed by Cominco Resources International Ltd. on the Carrie claim (quartz claim Snoose 7), the drilling was intended to intersect mineralization of Vein No. 6. Unfortunately, geological mapping of the property was limited, and talus slides were mapped as southwest trending which is roughly perpendicular to the actual bedrock orientation, therefore, attempts at drilling short horizontal holes did not intersect any appreciable mineralization. Falconbridge Limited held the property from 1972 to 1998 but no work was recorded in this period. In 2007, Monster Mining optioned the recently staked McKay Hill property from M. Bindig.

In contrast to the mineralization found in the Keno Hill camp, veins on the property contain relatively low-grade silver and high-grade lead; additionally the property is relatively distal from Keno City and was therefore deemed non-economic in the early years. For the last eighty years the mineralization found in the McKay Hill area was considered to be the northern extension of Keno Hill-style mineralization, and therefore prior to Monster Mining Corporation's (previously Northex Minerals Corp.) 2007 exploration program, no known geochemical analysis for gold or copper had been completed.

GEOLOGY OF THE NASH CREEK AREA

REGIONAL FRAMEWORK

The most recent mapping of the area was completed by the GSC in 1961 by L.J. Green and J.A. Roddick (Roddick, 1972). The south-central portion of NTS 106D (1:50 000 map sheets 6 and 7) has never been mapped at a scale of 1:50 000 and, to date, is relatively poorly understood.

The property is within the northwestern Omineca Belt in a band of regional-scale thrust faults — the Robert Service, Dawson and Tombstone thrusts imbricate rocks of the Selwyn Basin and MacKenzie Platform. McKay Hill is at the centre of the Dawson Thrust sheet, which is bound by

the Dawson thrust to the northeast and the Tombstone thrust to the southwest. The Robert Service thrust occurs between grey quartzite and carbonaceous phyllite of the Keno Hill Quartzite and the muscovite-chlorite phyllite and gritty psammite of the Hyland Group (Roots, 1997).

In the McKay Hill area, the Dawson thrust sheet is currently mapped as underlain by the Yusezyu Formation of the Upper Proterozoic to Lower Cambrian Hyland Group (PCH; Table 1). Approximately 7 km to the southwest, the Hyland Group rocks are overlain by the Earn Group (DME) metasediments, which host the Keno Hill mineral occurrences (Table 1; Fig. 2). The Hyland

Group consists of, from oldest to youngest, coarse turbiditic clastics, limestone and fine clastic rocks typified by maroon and green shale and may include younger scattered mafic volcanic rocks (Gordey and Makepeace, 2003). The Hyland Group is divided into two formations – the Late Proterozoic to Cambrian Narchilla Formation (PCn) and the Late Proterozoic Yusezyu Formation (PY). The McKay Hill area is represented by the more widespread, older Yusezyu Formation which is described by Roots (1997) as consisting of metamorphosed sandstone, grit, black slate, minor limestone, chlorite schist and conglomerate.

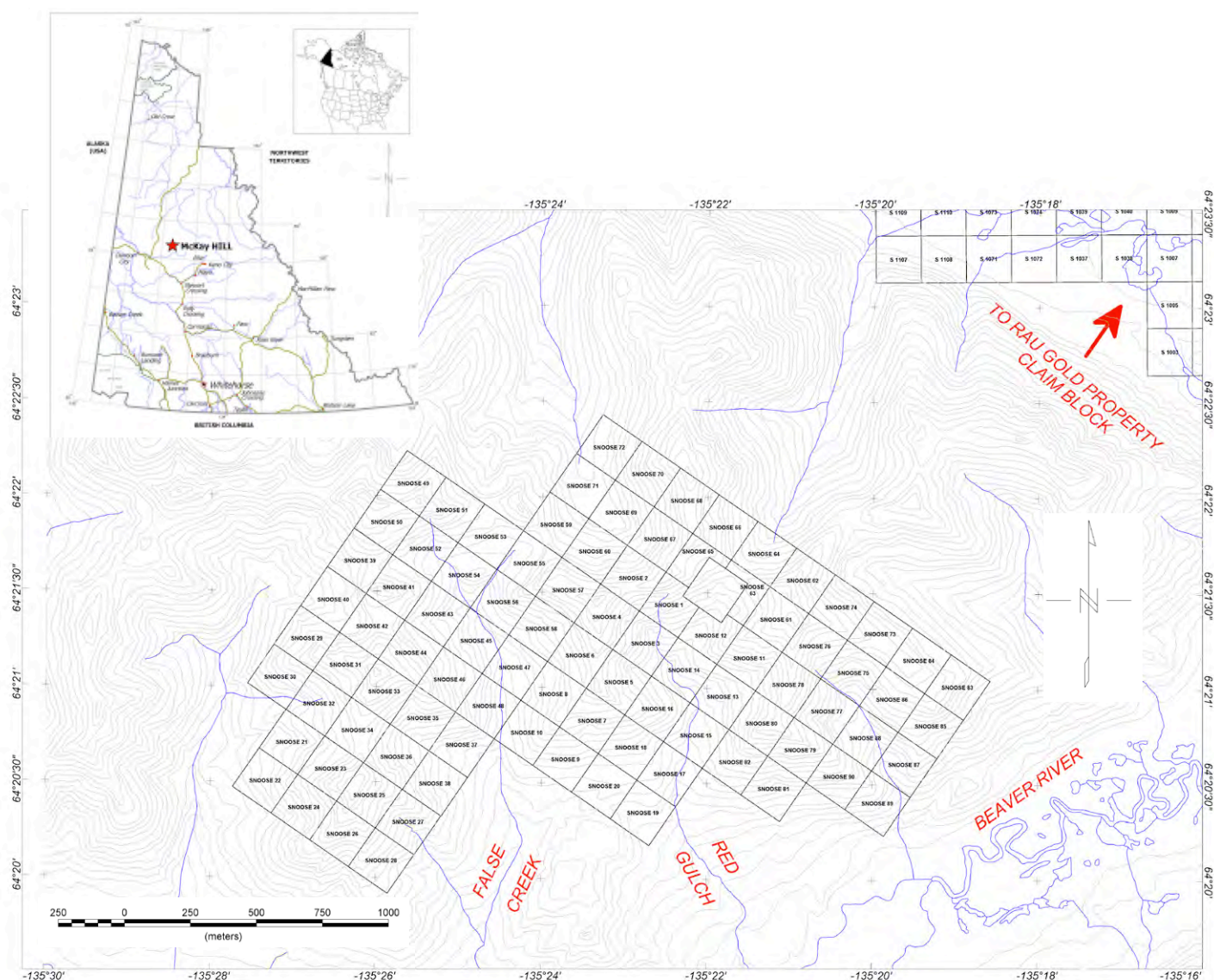


Figure 1. McKay Hill property location map. Note ATAC Resources Ltd. Rau gold property to the northeast and the Beaver River to the south.

Yusezyu Formation stratigraphy comprises shale-siltstone, sandstone-quartzite with younger lesser grits (Fig. 3). The extensive hypabyssal volcanic rocks found at McKay Hill are not incorporated into the geological models proposed for the formation. Conglomerate within the Yusezyu Formation are described as containing strained quartz and feldspar sedimentary clasts surrounded by little matrix

material. However, on the McKay Hill property, the majority of clasts found within the conglomerate are undeformed and volcanic in origin. These findings suggest that the McKay Hill area is, in fact, not underlain by the Hyland Group Yusezyu Formation as currently interpreted.

Mapping completed by Abbott (1997) targeted the eastern Ogilvie Mountains on NTS map sheets 116A/10

Table 1. Regional geological units (Gordey and Makepeace, 2003).

Unit	Age	Rock Type
Hyland Group (PCH)	Upper Proterozoic to Lower Cambrian	greenschist facies metamorphosed coarse turbiditic clastics, limestone and fine clastic rocks typified by maroon and green shale and may include younger scattered mafic volcanic rocks
Earn Group (DME)	Devonian to Mississippian	graphitic shale, chert, siltstone, sandstone, greywacke and conglomerate; minor felsic to intermediate volcanic rocks

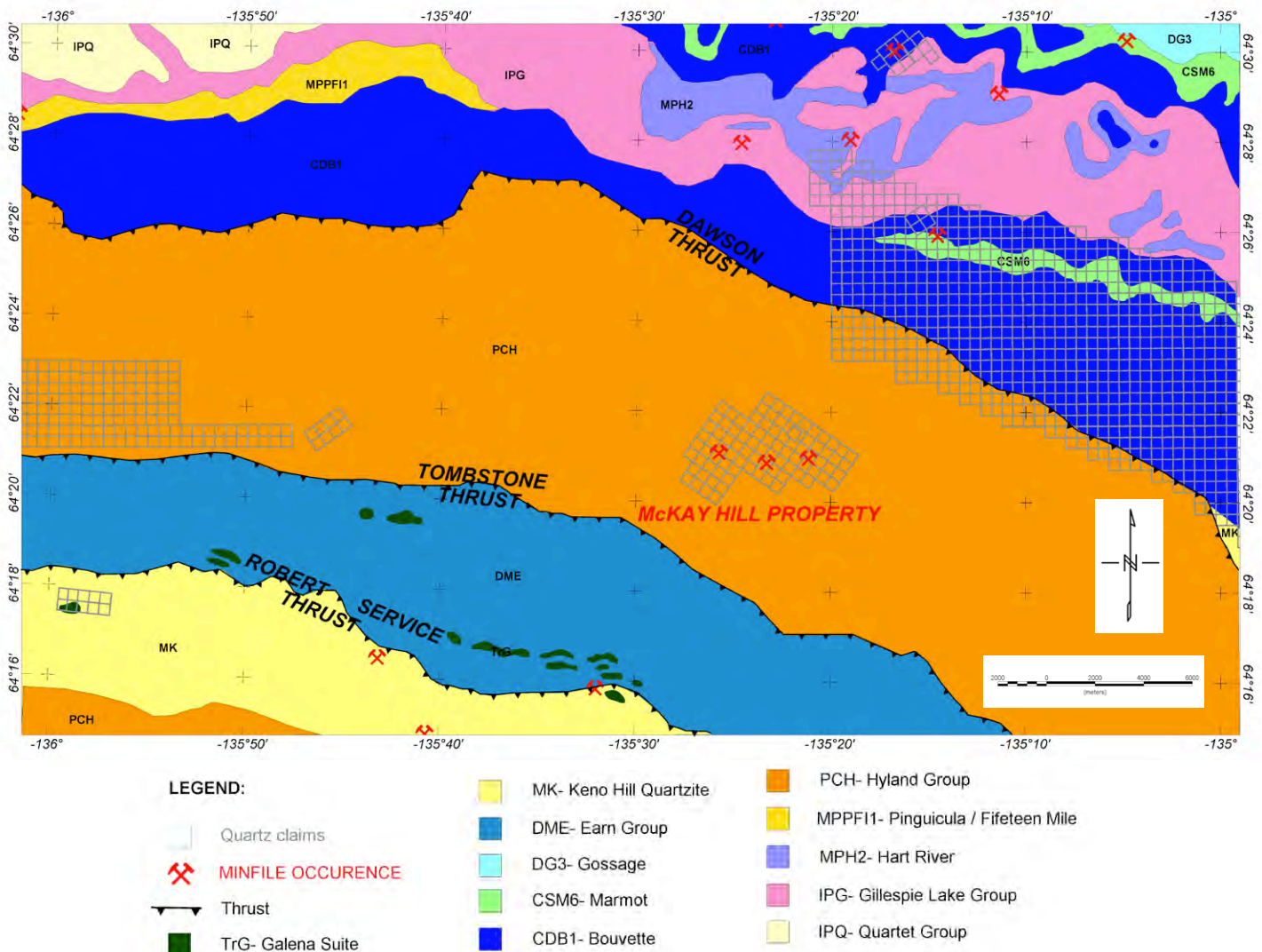


Figure 2. Regional geological framework (Gordey and Makepeace 2003).

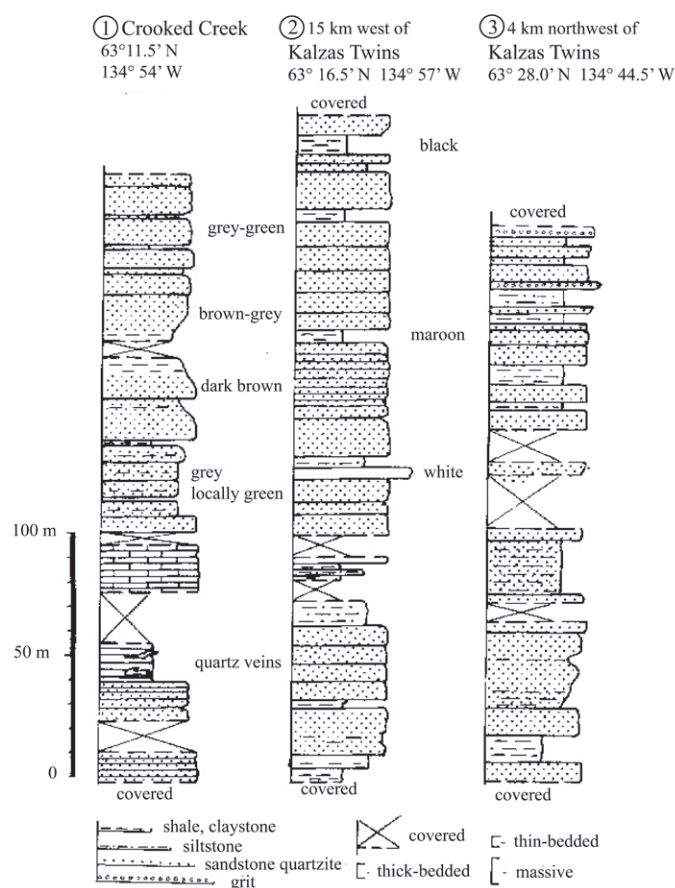


Figure 3. Stratigraphic sections from parts of the Yusezyu Formation from three locations south-southwest of Mayo (Roots, 1997).

and 116A/11, which straddle the boundary between the Foreland and the Omineca belts of the Cordilleran Orogen. In the region immediately south of the Dawson thrust on NTS 116A/11, Abbott (1997) mapped slivers of Middle (?) Cambrian to Early (?) Ordovician volcanic rocks. Goodfellow *et al.* (1995) introduced the name “Dempster volcanics” (COV) for this assemblage but it has never been formally defined. The volcanic rocks form weathering-resistant sequences 10 to 100 m thick, consisting mainly of flow breccias, hyaloclastic breccias, agglomerates and massive or pillowed flows (Abbott, 1997). Mafic volcanic rocks continue west into the Dawson map area where they form thick, extensive accumulations above the Hyland Group south of the Dawson Fault (Roots, 1988). Stratigraphic relationships between the volcanic rocks and the underlying strata are not well understood, but most of the rocks sharply overlie

the Narchilla Formation of the Hyland Group (Abbott, 1997). These volcanic rocks are present south of the Dawson thrust and may be correlative to the hypabyssal volcanic rocks mapped on the McKay Hill property during the 2009 program.

LOCAL GEOLOGY

Previous mapping completed in the area by Cockfield (1924; 1925a,b) recognized two units within the siliciclastic sequence: sedimentary and breccia/volcanic rocks. In 2009, these units were broken up and described more specifically as: sedimentary rocks comprising slate, conglomerate and sandstone grit, and hypabyssal volcanic rocks comprising basalt (amygdaloidal, vesicular and pillowed), andesite, volcanic tuff and their brecciated equivalents (Figs. 4, 5, 6).

Extensive fine-grained grey-blue slate and matrix-supported, polymictic, cobble-conglomerate (diamictite) are present as a steeply dipping, near-vertical succession striking roughly northwest. Slate bedding appears to be consistently parallel to foliation in the mapped area, less a few localized pockets where it was observed as an argillic-altered slate breccia related to brittle deformation along discrete topographic depressions presumed to be faults. Layers of fining-upwards, poorly bedded conglomerate are characterized by very fine to fine-grained, immature matrix material, enveloping poorly sorted subangular to subrounded clasts (Fig. 5a). The diamictite unit is one of the more favourable hosts for deep-level Ag-Cu-Pb mineralization. Clasts (≤ 15 cm) of primarily volcanic (and lesser sedimentary) origin appear to float in the finer grained detrital clay-rich matrix. A thin bed of poorly sorted sandstone grit overlies the conglomerate and is penetratively weathered a distinct rusty-orange colour.

The interior of the succession comprises thickening upward intercalations of volcanic rocks, most notably andesite and basaltic units with extensive local variation. Amygdaloidal, vesicular and pillowed basalts were observed on the property, illustrating the local variation along strike. Calcite (\pm quartz) circular to oblong amygdules (≤ 3 mm) comprise $\leq 35\%$ of the amygdaloidal basalt. This unit was noted to almost always exhibit a weak to well-developed penetrative planar fabric and hosts numerous high-level siliceous veins. Two small, hillside outcrops of pillowed basalt were mapped on the southwest end of the map area on the west margin of the thick conglomerate layer. These pillows were distinctly concentric with a northeasterly younging direction and

locally were brecciated and generally vesicular (Fig. 5b). Highly porous basalts with abundant vesicles were noted on the property as small, but prolific, localized lenses on the west end of the map area. This unit appears to be a particularly favourable host for mineralization at depth. Volcanic tuff is a favourable host for deep-level base-metal mineralization at the Snowdrift Vein, where its groundmass is replaced with galena ± copper carbonate minerals (namely azurite, malachite ± chrysocolla). Outcrops of volcanic tuff, surrounded by resistant andesite, were noted to exhibit extensive iron-carbonate and propylitic alteration (Fig. 5c). At the centre of the map area, a resistant knob of massive (locally foliated), dark green hornblende-porphyritic to nearly aphanitic, locally

propylitic-altered (clay ± pyrite) andesite forms the top of McKay Hill (Fig. 5d).

MINERALIZATION

High-sulphidation epithermal Au-Ag deposits are commonly irregularly shaped, a result of host rock permeability and geometry of ore-controlling structures (Fonseca and Bradshaw, 2005). Primary commodities include Au, Ag and Cu, subordinate As and Sb and highly variable mineralogy. Similar to Keno Hill mineralization, high-sulphidation epithermal veins typically contain galena, tetrahedrite/tennantite, sphalerite and silver sulphosalts.

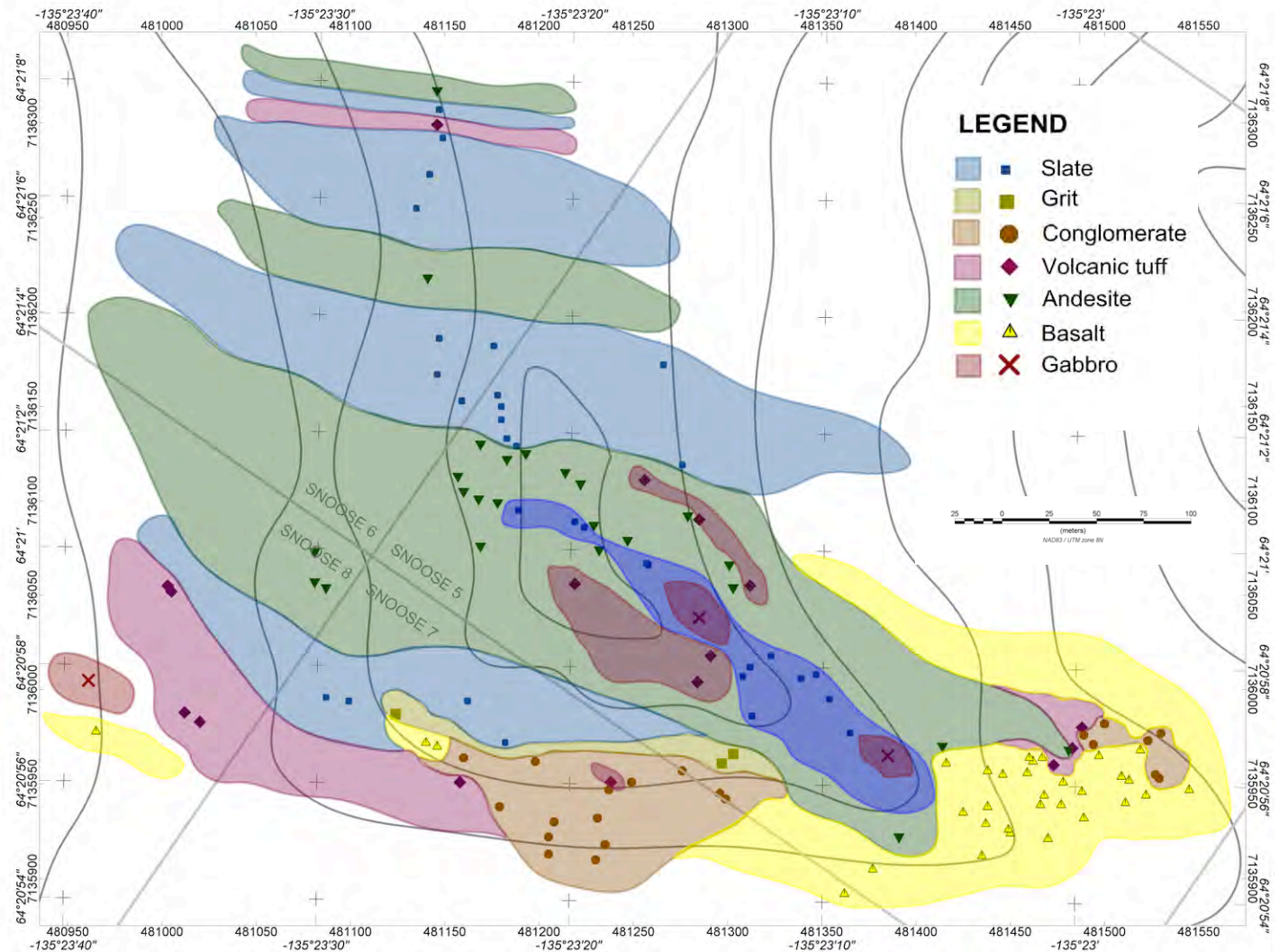


Figure 4. Property geology on Snoose quartz claims numbers 5 to 8; symbols represent outcrop; shaded areas denote interpreted geology.



Figure 5. McKay Hill country rocks: (a) conglomerate, (b) pillow basalt, (c) volcanic tuff, and (d) andesite (locally hornblende-phyric).

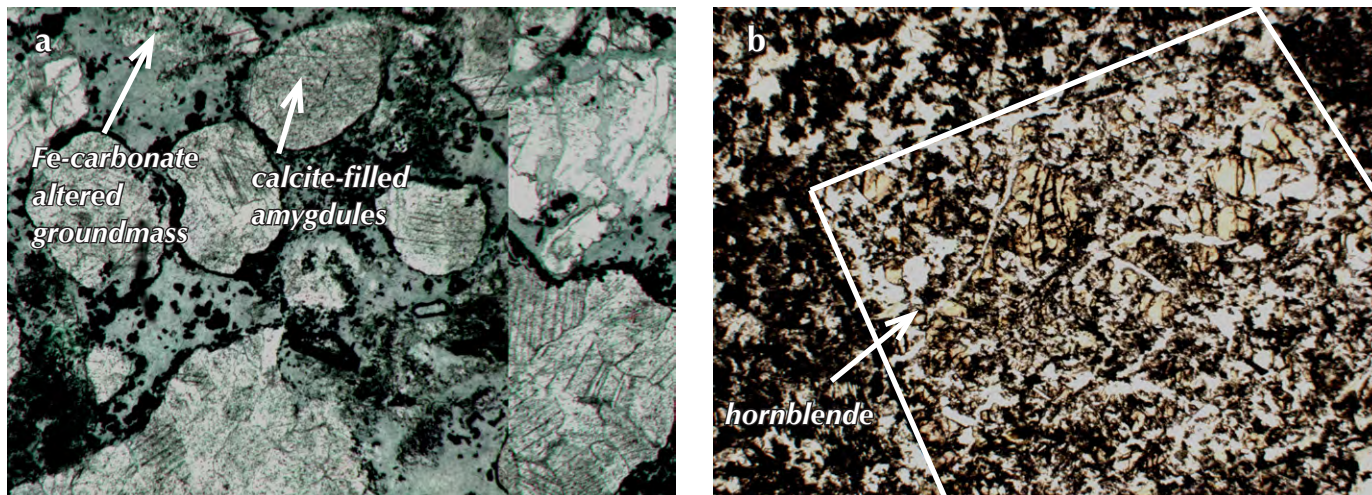


Figure 6. McKay Hill country rocks in thin and polarized sections (field of view (FOV) = 7.2 mm): (a) amygdaloidal basalt, and (b) andesite (locally hornblende-phyric).

The Keno Hill district mineralization is in the form of relatively large but isolated polymetallic Ag-Pb-Zn veins. The Ag-Pb-Zn veins in the Keno Hill camp were emplaced in discrete dilational (tensional stress) fault structures within polydeformed clastic metasediments and are not associated with extensive alteration. Conversely, the McKay Hill property has prolific veination in a localized area. Fifteen high-level Au-Cu and deeper level Ag-Cu-Pb veins are surficially exposed within a 450 x 600 m area (Figs. 4, 7).

Historically, workers in the Keno Hill camp recognized that some mineral associations were characteristic of certain veins and the following paragenetic sequence is generally accepted: quartz, pyrite, arsenopyrite and sulphosalts; siderite, galena, sphalerite, pyrite and freiburgite (with additional fracturing); and cerussite, anglesite, native silver and argentiferous jarosite (by supergene oxidation of sulphides and sulphosalts), and pyrargyrite (Fig. 8; Roots, 1997). Similarly, vein ore mineralogy appears to be both spatially and temporally zoned at the McKay Hill property. The mineralization at McKay Hill appears to evolve from a high-level silica-rich system ($\text{SiO}_2 + \text{Cu} + \text{As} \pm \text{Au}$) to a $\text{Pb} + \text{Ag} \pm \text{Cu}$ system (massive galena) at the lowermost exposed levels of the veins. This vertical zonation is evident as high-level quartz-rich Au-Cu mineralization in competent hypabyssal volcanic rocks to deeper level

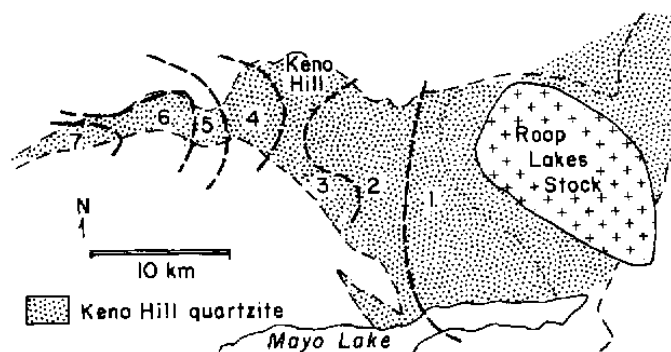


Figure 7. View looking northwest illustrating 3 of 20 known mineralized sites on the central Snoose claims (distance viewed is approximately 200 m in length). Note Fe-carbonate (orange) alteration surrounding mineralized sites (photo courtesy of M. Bindig).

massive galena (Ag-Cu-Pb) mineralization in less competent sedimentary (\pm highly vesicular volcanic) rocks (Fig. 9). Although both properties exhibit spatial zonation, the zonation in the Keno Hill district is present laterally and on a much larger scale.

HIGH-LEVEL QUARTZ-CARBONATE – AU MINERALIZATION

High-level mineralization exposed on the ridgeline is present as distinct, milky-white quartz veins with azurite and malachite-lined fractures (Fig. 10). These veins precipitate along early structures or at lithologic boundaries. Locally, the veins are surrounded by an extensive propylitic alteration zone characterized by intense alteration forming a distinct bright orange-brown, iron-carbonate (Fe-chlorite and calcite) halo. Anhedral, coarse-grained milky-white quartz crystals lined by anhedral coatings and euhedral vug-filling crystals of copper carbonate minerals, namely azurite and malachite, were noted at this level. These siliceous veins are exposed on the ridge as distinct resistant tabular bodies and as



1. FELDSPAR ZONE: K-feldspar, plagioclase, quartz, epidote, \pm tourmaline, apatite, pyrite, arsenopyrite, ilmenite, cassiterite, muscovite
2. CALCITE ZONE: calcite, quartz, epidote \pm pyrite, chalcopyrite, arsenopyrite, galena
3. JAMESONITE ZONE: jamesonite, boulangierite, arsenopyrite, sphalerite, chalcopyrite, tetrahedrite, quartz, calcite, native Au (overlaps with zone 4)
4. SIDERITE-CALCITE ZONE: siderite, quartz, calcite, galena, sphalerite, tetrahedrite, arsenopyrite, pyrite
5. PYRRHOTITE ZONE: siderite, quartz, calcite, galena, sphalerite, tetrahedrite, pyrrhotite, arsenopyrite, pyrite (same as zone 4 with pyrrhotite)
6. SIDERITE ZONE: siderite, quartz, galena, sphalerite, tetrahedrite, pyrite (similar to zones 4 and 5, but without calcite, arsenopyrite, pyrrhotite)
7. EPITHERMAL ZONE: quartz, pyrargyrite, acanthite, polybasite, stephanite, native Ag, pyrite, kaolinite \pm marcasite, chalcopyrite, stibnite, barite (overlaps with zone 6)

Figure 8. Schematic map of lateral mineral zonation in the Keno Hill camp. Contours are drawn according to the appearance or disappearance of specific vein minerals away from the Roop lakes pluton (Roots, 1997).

linear float trains on sides slopes. Replacement and incorporation of country rocks in these high-level siliceous systems was not noted. The high-level veins have reported values up to 16.8 g/t Au, 668 g/t Ag and 3.9% Cu from grab and chip samples collected by Monster Mining Corp. (Table 2).

QUARTZ-CARBONATE-AU-GALENA-PB MINERALIZATION TRANSITION ZONE

A quartz-carbonate-gold to galena-lead transition zone is exposed at mid-level at the Snowdrift and Vein No. 6 sites. The Snowdrift Vein exposes the high-level quartz-carbonate-Au mineralization as a massive, white, siliceous vein evolving towards galena-lead-rich mineralization at

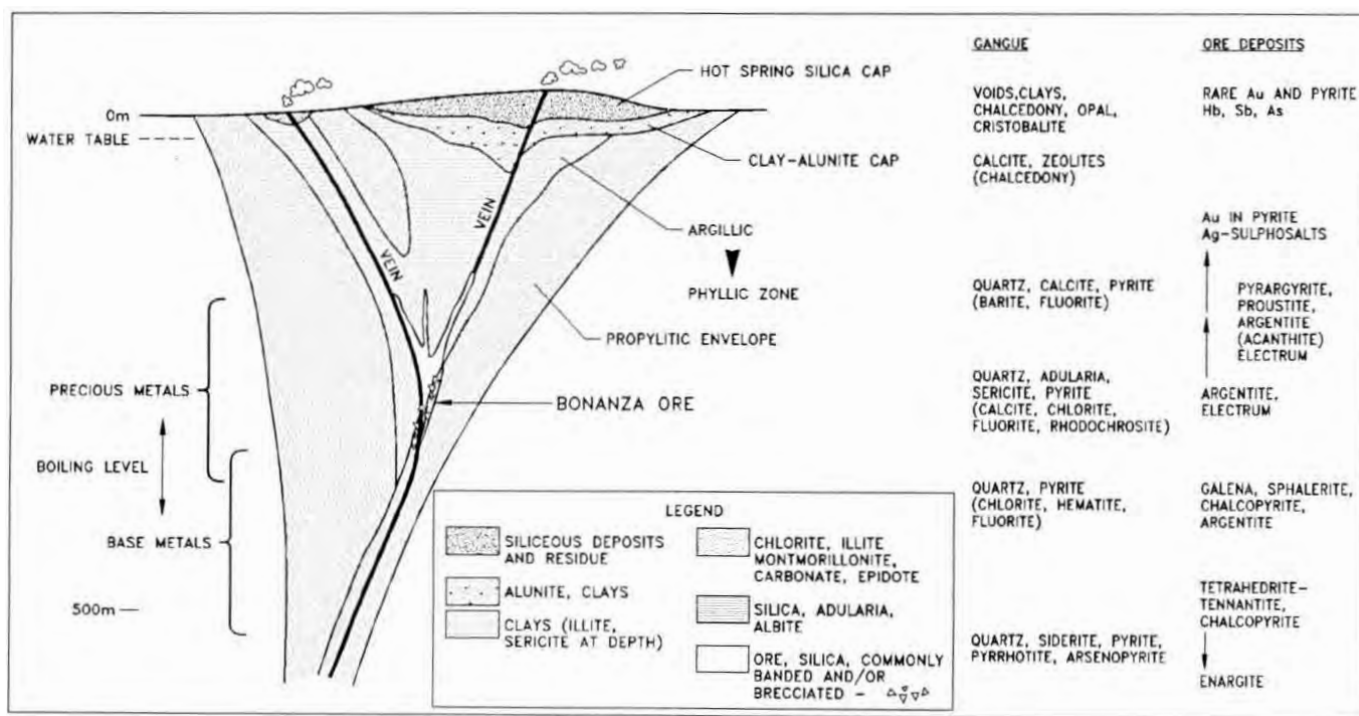


Figure 9. Vertical mineral zonation of high-sulphidation epithermal veins (Panteleyev, 1991). Note high-level precious metal mineralization is associated with siliceous gangue and low-level mineralization is base metal in origin. Also note the propylitic envelope surrounding the ore shoot.

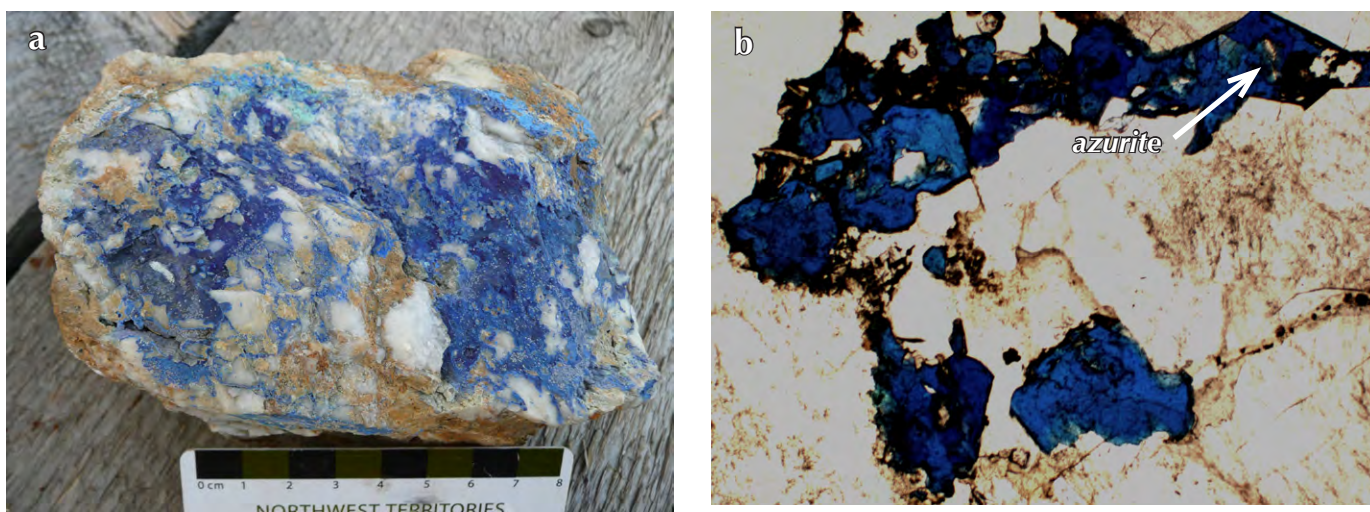


Figure 10. Examples of high-level, siliceous Au-Cu mineralization at the McKay Hill property: (a) hand sample, and (b) thin section (FOV= 7.2 mm).

lower levels within partially to wholly replaced diamictite and vesicular basaltic country rock material. In the transition zone, the copper-carbonate minerals (azurite, malachite \pm scorodite) appeared to be associated with minor epidotization (Fig. 11). Late, translucent 6-sided, pyramidal quartz crystals are noted at this level and appear to be associated with brecciation and healing.

Presence of this 'clean quartz' continues down to lower levels and appears to represent relatively mid to late fluidization. Grab and chip samples collected from this transition zone by Monster Mining Corp. have reported values up to 0.9 g/t Au, 550 g/t Ag, 2.2% Cu and 8.8% Zn (Table 2). Au-Ag-Cu values within this zone tend to be relatively lower and there appears to be an

Table 2. McKay Hill selected 2007 and 2008 geochemical results (Pautler, 2009).

Zone	Vein	Sample	Width (m)	Au (g/t)	Ag (g/t)	Cu (%)	Zn (%)	Pb (%)
High-level	Snowdrift	MK-06	Grab	15.6	668	3.9	0.94	2.4
	Snowdrift	526150	Grab	2.61	174	0.69	0.13	0.42
	Snowdrift	526196	1.5	1.37	57.2	0.63	4.7	1.51
	Blackhawk W	526244	Grab	1.14	100	1.46	0.17	0.27
	No. 8	MK-02	Grab	16.8	646	0.64	0.14	33
	No. 1 W	29887	Grab	0.765	502	2.4	0.47	46.4
Transition	Snowdrift	29885	Grab	0.085	470	0.595	0.29	46.5
	Blackhawk	29890	Grab	0.51	551	0.51	1.16	47.3
	Blackhawk	29889	Grab	0.9	484	0.53	8.33	54.6
	No. 9	29896	Grab	0.59	132	2.24	2.31	5.14
Low-level	North?	526241	Grab	1.84	372	1.96	7.01	22.74
	No. 6	526239	Grab	0.565	528	1.52	8.66	50.55
	No. 6	526238	1.1	0.83	683	0.78	0.4	40.5
	Snowdrift	29886	Grab	2.49	534	2.16	0.46	47

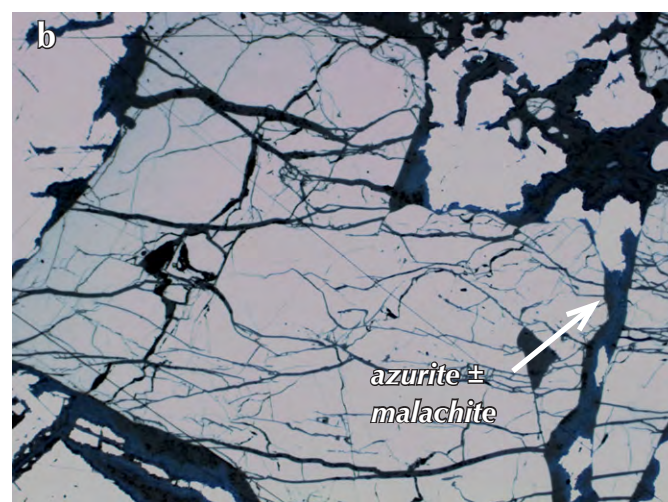


Figure 11. Examples of mineralization within the transition zone at the McKay Hill Property: (a) hand sample, and (b) thin section (note brecciated texture; FOV= 3.6 mm).

enrichment of zinc; rocks within this ‘transition zone’ typically contained up to 8% zinc.

LOW-LEVEL GALENA-PB MINERALIZATION

Fluids continue to evolve and are found at depth as prolific base-metal mineralization. Low-level mineralization exposed on the hillsides of the property is found as extensive galena ± malachite, azurite, scorodite mineralization (Fig. 12). These veins have reported values up to 2.5 g/t Au, 700 g/t Ag and 2.2% Cu from grab and chip samples collected by Monster Mining Corp. (Table 2). Mineralization at this level depends extensively on the lithologic permeability and competency of the country rocks and shows variation property-wide in its mineralization style. Mineralization may be present as vein breccias (North vein?), matrix-replacing flow-banded/layered galena within diamictite (Vein No. 6), to nearly whole-rock replacement in the vesicular basalts found at lower levels in the Snowdrift Vein system. Ore was mined from the property at Vein No. 6 within partially to wholly matrix-replaced diamictite; flow-banded galena characterizes the current matrix-material which envelops rotten, soft clasts that exhibit extensive iron-carbonate alteration (Fig. 13). Locally, brecciated parts of vein material contain clean prismatic quartz gangue; these crystals were observed to contain inclusions of euhedral cubic galena which may be suitable for fluid inclusion geochemical analysis (Fig. 14).



ALTERATION

Propylitic alteration (chlorite, calcite, pyrite, epidote, zeolite) is an early-developed, widespread and district-wide alteration in many epithermal districts (Panteleyev, 1994). Commonly, zoning of hydrothermal alteration in epithermal systems is one of the key exploration guides. Within the broad areas of propylitic alteration are more restricted zones of sericitic alteration or recessive-weathering clay alteration, surrounding central zones of silicification or quartz veining (some parts which may be mineralized; Panteleyev, 1994).

Alteration is minimal within the Keno Hill area. Weak alteration is present within the prolific Triassic ‘greenstone’ (meta-gabbro/diorite) found striping through the district. Locally, alteration of arsenopyrite to scorodite occurs in the early quartz-gold veins that are thought to be associated with Tombstone magmatism (e.g., Homestake Vein No. 1, Yukon MINFILE 105M 011).

The most striking aerial feature of the McKay Hill property is the distinct, bright orange alteration vein halos, which consistently occur at mineralized sites (Fig. 7). The iron-carbonate alteration is evident in thin section as Fe-chlorite and calcite which overprint essentially all primary minerals. These alteration halos surround all mineralized sites with minor variations in intensity but are indiscriminate to the various lithologies. Propylitic alteration appears to be coeval with vein emplacement and is present as clay (illite?), calcite and chlorite close to vein emplacement, and pyrite and epidote distal from vein emplacement.

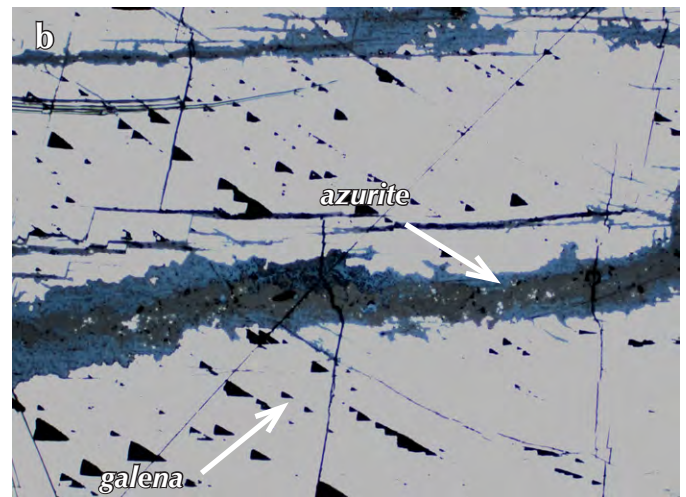


Figure 12. Examples of deep-level, siliceous Au-Cu mineralization at the McKay Hill property: (a) hand sample, and (b) thin section (FOV= 3.6 mm).



Figure 13. Progressive Fe-carbonate alteration and destruction of the conglomerate framework clasts with late-stage matrix replacement of galena.



Figure 14. Euhedral quartz prisms with cubic galena inclusions surrounded in banded base-metal mineralization (galena + malachite \pm scorodite, chrysocolla). mal = malachite, sco = scorodite, chrys = chrysocolla.

STRUCTURAL CONTROLS

Previously, epithermal deposits were closely associated with felsic volcanic rocks related to caldera resurgence; this model has largely been refuted by studies performed in the 1970s and 1980s by the United States Geological Survey (USGS; *i.e.*, Lipan and Steven, 1976; Stack, 1980). Siberman and McKee (1974) completed a radiometric data survey on epithermal deposits in Tertiary volcanic areas of the southwestern United States and found that mineralization was 2 to 17 million years younger than the caldera volcanism, thereby refuting the theory that hydrothermal activity is exclusively related to caldera volcanism. Today, epithermal hydrothermal solutions are largely considered to be meteoric in origin. In addition to meteoric waters, epithermal solutions can contain magmatic fluids, seawater, evaporate and connate waters, deep brines, metamorphic fluids and even far-travelled mesothermal-source fluids (Panteleyev, 1991).

Host rock competency in both Keno Hill and McKay Hill areas has consistently proven vital in controlling mineralization. In the Keno Hill district, almost all veins are hosted in the Keno Hill Quartzite, a very hard, well-indurated rock which exhibits brittle failure when faulted, leaving open space fillings making it an ideal host for the silver ore bodies in the camp. Typically, the veins pinch out or cap when they run into the softer, finer grained

metasedimentary rocks. These veins were emplaced in discrete dilational fault structures associated with late transpressional and transtensional brittle deformation.

At McKay Hill, vein propagation appears to be primarily controlled by competency and lithologic permeability contrasts between units (with localized brecciation of massive volcanic wall rocks; V. Bennett, pers. comm., 2009). Additionally, mineralization present as matrix replacement was found as an irregular body within the thick package of fining-upward conglomerate where the veins propagate as northeast-trending, steeply south-dipping structures within the southeast-trending low-angle slickensides preserved on local, discrete, fault surfaces. Vesicular basalts and volcanic tuffs in the southwest part of the map area are also favourable hosts at depth. Locally, vesicular basalts were wholly replaced and the volcanic tuff unit displayed similar replacement textures to the diamictite unit within its groundmass (e.g., the Snowdrift vein system).

SOURCE OF FLUIDS

The source of fluids for the McKay Hill property is currently unknown. Historically, the Keno Hill district veins have been considered to result from differentiation of magma with the development of a volatile fluid phase that escaped along faults to form the veins (Fonseca and Bradshaw, 2005). Roots (1997) suggests the most likely age of the hydrothermal cell and alteration is during, and immediately following, intrusion of the Roop Lakes pluton. However, recent geochronological work by Bennett (pers. comm., 2009) suggests that Keno Hill mineralization may not be associated with the emplacement of these intrusions but rather may be related to a non-magmatic source.

Epithermal deposits are now considered to form from relatively dilute, near-neutral to weakly-alkaline chloride water (<5 wt% NaCl equivalent) that undergoes boiling or effervescent degassing, fluid mixing and oxidation at temperatures generally between 200 to 230°C and most commonly between 230 and 260°C (Fig. 14; Panteleyev, 1994). Buchanan's (1981) "boiling model" suggests that alteration and coeval mineralization results from boiling and oxidation of the ascending hydrothermal fluids that repeatedly heal ore structures. Episodic refracturing/brecciation along these conduits decreases fluid pressure, thereby cooling the fluids and resulting in precipitation of ore that is commonly banded/layered. At McKay Hill, distinctly layered galena, present as replaced matrix

material within the diamictite and clean quartz that is surrounded by layered base metals within brecciated zones, supports the repetitive temporal refracturing-healing events associated with these deposits.

Possible fluid sources include the high-level Cretaceous granitic stock present at McQuesten Lake (unit mKqS) located ~36 km away on a bearing of 185° (roughly south) to the McKay Hill property. Also, streams in the area surrounding Steamboat Mountain are highly anomalous in thorium, possibly indicating the presence of an unmapped or buried intrusion just to the south of the property, based on a spatial association established in a study by Gleeson and Boyle (1980) between thorium and Tombstone Suite plutons. Plotting the first vertical derivative of the magnetic field using YGS' MapMaker program (<http://maps.gov.yk.ca/imf.jsp?site=YGS>), a small magnetic high appears to be present adjacent to the property, which may represent a small (Tombstone age?) stock.

Alternatively, stratovolcanoes around the Pacific Rim or volcanic dome and dome-flow complexes in continental volcanic settings display volcano-related hydrothermal systems with possible magmatic-hydrothermal, magmatic steam and steam-heated acid sulphate environments (Panteleyev, 1991). Some sites of high-level hydrothermal activity and hot spring deposits have survived over great lengths of time and could provide the steam-heated acid sulphate environments required. Panteleyev (1991) suggests that manifestations of active or extinct geothermal activity at surface are the zones of distinctive hydrothermal alteration that overlie the deeper geothermal systems. Sites of hot spring discharge at the highest structural level are represented at present by the Nash Creek hot springs, located 39.5 km away on a bearing of 055°.

DISCUSSION

To date, mineralization at McKay Hill has been interpreted to be typical of the Keno Hill camp, namely polymetallic Ag-Pb-Zn ± Au shear-hosted vein-style mineralization. During Monster Mining Corporation's 2009 YMIP-funded exploration program, numerous distinct differences became apparent. These findings lead to significant implications in interpreting the geology of the area, potential of the McKay Hill prospect, and potentially, the regional geology.

The McKay Hill area is currently mapped as being underlain by the Yusezyu Formation of the Upper

Proterozoic to Lower Cambrian Hyland Group which comprises metamorphosed sandstone, grit, black slate, minor limestone, chlorite schist and conglomerate. Stratigraphic work completed by Roots (1997) describes the metaconglomerate unit as containing deformed quartz and feldspar clasts that are sedimentary in origin; the clasts within the undeformed conglomerate at McKay Hill are primarily volcanic in origin suggesting that the rocks on the McKay Hill property are not part of the Yusezyu Formation. A thin layer of sandstone grit mapped on McKay Hill may represent the uppermost Yusezyu Formation. However, the predominant hypabyssal volcanic rocks mapped on the property are not present in the stratigraphic sections of Yusezyu Formation mapped by Roots (1997).

Geological mapping completed by Abbott (1997) targeted the Hart River area in the eastern Ogilvie Mountains, the region immediately south of the Dawson thrust on NTS 116A/11. Here, Abbott mapped slivers of Cambrian to Ordovician volcanic rocks (Dempster volcanics (COv)). Roots (1988) found that these mafic volcanic rocks continue west into the Dawson map area, where they form thick, extensive accumulations above the Hyland Group south of the Dawson thrust. Stratigraphic relationships between the volcanic rocks and the underlying strata are not well understood, but most of the

rocks sharply overlie the Narchilla Formation of the Hyland Group (Abbott, 1997). These volcanic rocks are present south of the Dawson thrust (*i.e.*, are part of the Dawson Thrust sheet) and may be correlative to the hypabyssal volcanic rocks mapped on the McKay Hill property during the 2009 program.

Observations made during the 2009 program suggest that the McKay Hill area is not underlain by the Yusezyu Formation of the Upper Proterozoic to Lower Cambrian Hyland Group as currently interpreted, but rather may be correlative to the Cambrian to Ordovician Dempster volcanics (COv) mapped to the northwest on NTS 116A/11. It is crucial to re-evaluate our current interpretations of the regional geology as it could potentially illustrate the area's metallogenic potential for many different types of mineral occurrences.

The siliciclastic-volcanic package present at McKay Hill would have been developed by frontal accretion whereby younger sediments were scraped off near the trench or by underplating of subducted sediments along the shallow parts of the subduction decollement (Fig. 15). If this were the case, the east-facing pillow structures measured indicate an easterly younging direction allowing for creation of a simplified stratigraphic column, whereby frontal accretion over the life of the convergent margin

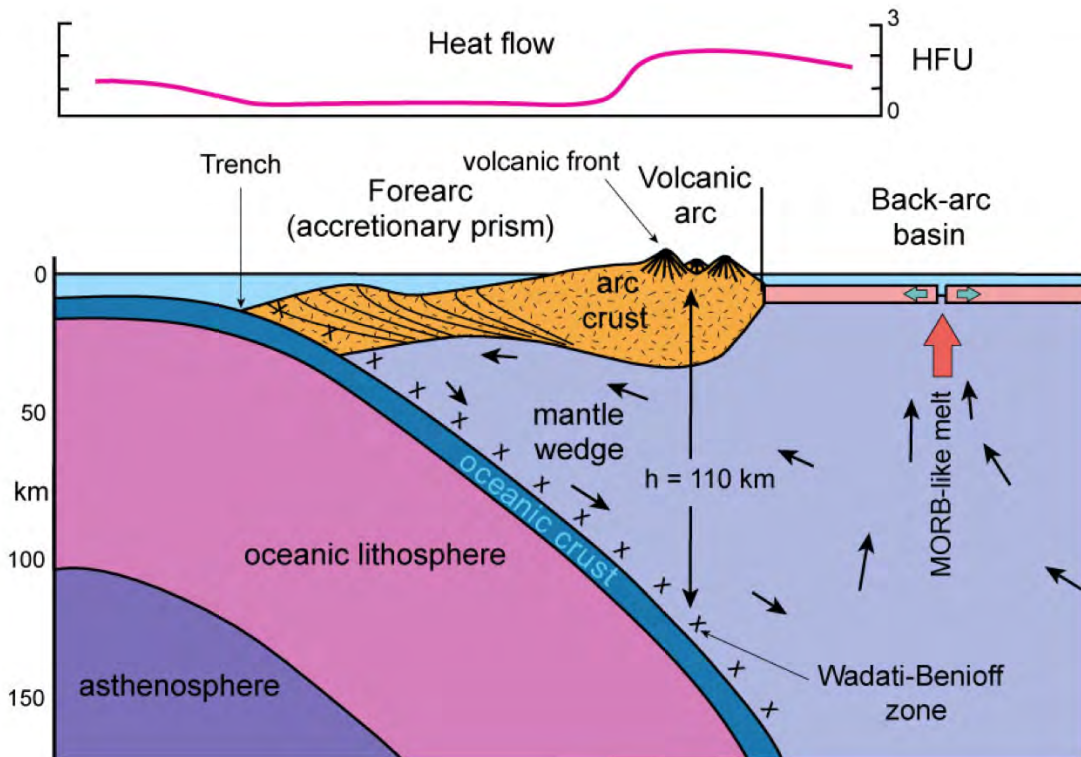


Figure 15. Schematic cross section through a typical island arc (Gill, 1981).

will result in younger sediments defining the outermost margins, leaving an inlier of older volcanic rocks (Winter, 2001). The rocks may represent an arc assemblage, possibly preserved as an accretionary prism. Furthermore, the diamictite-sandstone grit sedimentary interior appears to represent a partially preserved debris-flow sequence syndepositional with convergence. These expansive sedimentary rocks contain intercalations of hypabyssal volcanic rocks that show variation in thickness along strike, from tens to hundreds of feet thick.

In contrasting the polymetallic Ag-Pb-Zn ± Au-style mineralization found in the Keno Hill district, to the high-level Au-Cu and deeper level Ag-Cu-Pb mineralization at the McKay Hill property, numerous differences become evident (Table 3). Namely, (1) mineralization at McKay Hill exhibits distinct local vertical zonation with low-level base-metal mineralization and high-level siliceous precious metal mineralization; (2) ore shoot textures illustrate repetitive brecciation and healing; (3) mineralization is not present as vein faults; (4) gangue mineralogy is exclusively quartz; (5) country rocks are not polydeformed; (6) prolific iron-carbonate alteration associated with mineralization moves outwards into a more extensive propylitic envelope; and, (7) McKay Hill is present at the centre of the Dawson thrust sheet which is separated from the Keno Hill deposits by the Tombstone thrust.

Gold mineralization found as an “acid cap” in high-level siliceous veins is one of the hallmarks of epithermal deposits. This type of mineralization is found within numerous high-level veins on the property. At deeper levels, the neutral to slightly alkaline conditions are favourable sites for silver mineralization and are commonly banded or layered, resulting from the episodic

precipitation of cooler fluids, a feature observed in the matrix-replaced diamictite and the groundmass-replaced volcanic tuff.

At present, there are 24 known high-sulphidation epithermal Yukon MINFILE occurrences in Yukon; three of these are the well-known past producers, the Tally-Ho, the Brown-McDade and the Moosehorn. An epithermal high-sulphidation model appears to most accurately fit the observations made at the McKay Hill property. More specifically, Panteleyev’s (1994) Canadian Cordilleran epithermal model appears to most closely fit the relationships observed (Fig. 16). However, the oldest known favourable host-rocks in the Canadian Cordillera are subaerial andesitic rocks deposited near the end of Early Jurassic island arc volcanism, a significantly later date than the current age for the interpreted geology present at McKay Hill.

Possible fluid sources include: (1) the high-level Cretaceous granitic stock present at McQuesten Lake; (2) potential presence of an un-mapped or buried Tombstone-age (?) intrusion at Steamboat Mountain; (3) small magnetic high adjacent to the property may represent a small (Tombstone-age?) stock; and (4) the Nash Creek hot springs may overlie a deeper geothermal system which could provide the steam-heated acid sulphate environments required.

The Canadian Cordilleran (British Columbia) epithermal model infers a continuum from porphyry copper and skarn deposits, to epithermal veins and hot spring discharge deposits (Panteleyev, 1994). In terms of a fluid source, this model may explain the presence of Mississippi Valley-type (MVT) mineral occurrences resulting from regional-scale fluid migration. MVT

Table 3. *Contrasting Keno Hill and McKay Hill host rocks and mineralization styles.*

Keno Hill camp	McKay Hill property
polymetallic Ag-Pb-An ± Au-style mineralization	high-level Au-Cu and deeper level Ag-Pb ± Cu mineralization
vein faults	veins episodically brecciate and heal
siderite ± quartz gangue	quartz gangue
mineralization present only as veins	mineralization: vein breccias, veins, partial to whole rock replacement
large-scale lateral mineral zonation	local vertical mineral zonation
little to no alteration	extensive propylitic alteration
Keno Hill Quartzite and Carbonaceous Phyllite country rock (Devonian Earn Group)	siliciclastic sediments and hypabyssal volcanic rocks (Upper Proterozoic to Lower Cambrian)
country rocks are intensely folded	country rocks consistently trend NNW, dip nearly vertical

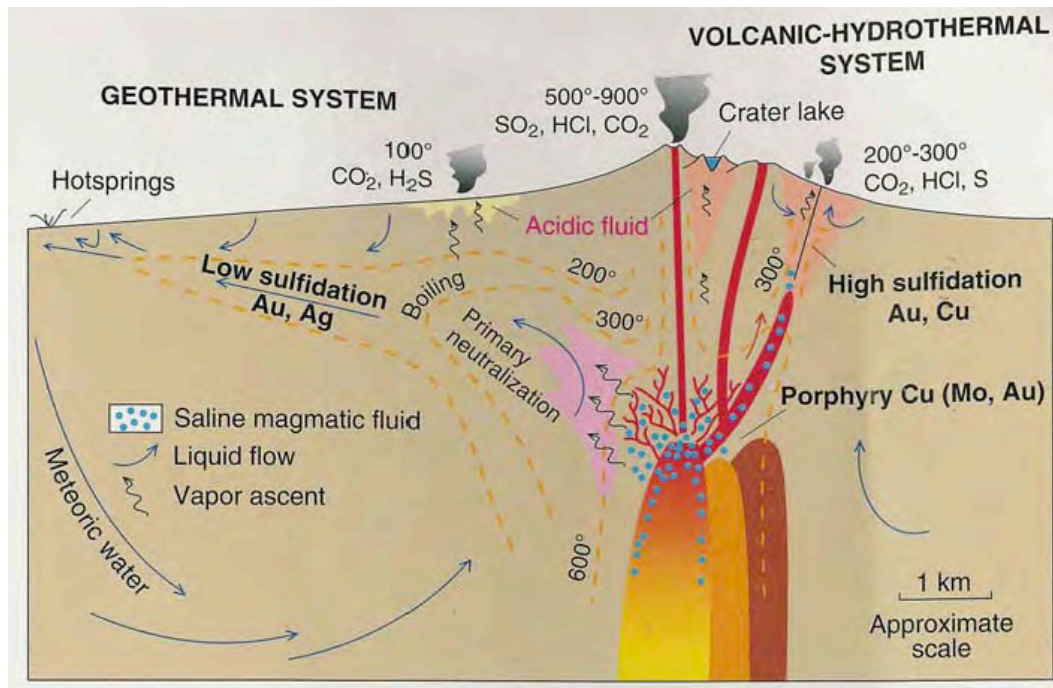


Figure 16. Fluidization in high-sulphidation epithermal deposits (Panteleyev, 1991).

occurrences are found proximal to the McKay Hill area on the opposite side of the Dawson thrust, near the margins of the middle Proterozoic Hart River (mPH2) rocks (Yukon MINFILE 106D 040, 042 and 043).

Accurately understanding the mineralization styles present at McKay Hill is crucial to assessing the full potential of the property.

ACKNOWLEDGEMENTS

The Yukon Geological Survey's Yukon Mining Incentives Program (YMIP) provided funding for this project; this funding is solely responsible for enabling us to perform our 2009 exploration program. Thank you to the YGS for use of their petrographic microscope and particularly to Venessa Bennett for her valuable insights and observations during a property tour she organized which greatly benefitted this project; to Grant Abbott and Charlie Roots for their helpful tips concerning the regional stratigraphy; to Dave Tupper for the countless hours of geological banter during the summer field season and for his valuable comments; to Robert Weicker for his edits and Dave White for his constructive comments and valuable input which greatly improved this paper; to Karen MacFarlane for editing this paper. Last but not least, a special thank you to Monster Mining Corporation for

their open-mindedness towards the re-evaluation of the McKay Hill property and funding of this paper.

REFERENCES

- Abbott, G., 1997. Geology of the Upper Hart River Area, Eastern Ogilvie Mountains, Yukon Territory (116A/10, 116A/11). Exploration and Geological Services Division, Yukon Region, Indian and Northern Affairs Canada, Bulletin 9, 92 p.
- ATAC Resources Ltd., undated: Rau Property; ATAC Resources Ltd., <<http://www.atacresources.com/s/Rau.asp>> [accessed November 3, 2009].
- Buchanan, L.J., 1981. Precious metal deposits associated with volcanic environments in the southwest. *In: Relations of tectonics to ore deposits in the southern Cordillera*, W.R. Dickinson and W.D. Payne (eds.), Arizona Geological Society, Digest, vol. XIV, p. 237-262.
- Cockfield, W.E., 1924a. Upper Beaver River Area, Mayo District, Yukon. *In: Geological Survey of Canada, Summary Report 1924 Part A*, p. 1-18.
- Cockfield, W.E., 1924b. Silver-Lead Deposits of the Beaver River Area, Yukon. *In: Geological Survey of Canada, Summary Report 1923 Part A*, p. 22-28.

- Cockfield, W.E., 1925a. Upper Beaver River Area, Mayo District, Yukon. *In*: Geological Survey of Canada, Summary Report 1924 Part A, p. 1-18.
- Cockfield, W.E., 1925b. Upper Beaver River Area, Mayo District, Yukon. Geological Survey of Canada, Multicoloured Geological Map 2064, 1925.
- Fonseca, A. and Bradshaw, G., 2005. Yukon Mineral Deposit Profiles. Yukon Geological Survey, Open File 2005-5, 163 p.
- Gill, J.B., 1981. Orogenic Andesites and Plate Tectonics. Springer-Verlag, Berlin, Germany, 390 p.
- Gleeson, C.F. and Boyle, R.W., 1980. Minor and trace element distribution in the heavy minerals of the rivers and streams of the Keno Hill District, Yukon Territory. Geological Survey of Canada, Paper 76-31, 9 p.
- Goodfellow, W.D., Cecile, M.P. and Leybourne, M.I., 1995. Geochemistry, petrogenesis and tectonic setting of Lower Paleozoic alkalic and potassic volcanic rocks, northern Canadian Cordilleran Miogeocline. *Canadian Journal of Earth Sciences*, vol. 32, p. 1236-1254.
- Gordey, S.P. and Makepeace, A.J. (compilers), 2003. Yukon Digital Geology. Exploration and Geological Services Division, Yukon Region, Indian and Northern Affairs Canada. Open File 1991-1 (D).
- Lipan, P.W. and Steven, T.A., 1976. Calderas of the San Juan volcanic field, southwestern Colorado. United States Geological Survey, Professional Paper 958, 35 p.
- Panteleyev, A., 1991. Gold in the Canadian Cordillera: A focus on epithermal and deeper environments. *In*: Ore deposits, tectonics and metallogeny in the Canadian Cordillera, Paper 1991-4, Province of British Columbia – Ministry of Energy, Mines and Petroleum Resources, p. 163-212.
- Panteleyev, A., 1994. A Canadian Cordilleran Model for Epithermal Gold-Silver Deposits. *In*: Ore Deposit Models: Geoscience Canada, Reprint Series 3, R.G. Roberts and P.A. Sheahan (eds.), Geological Association of Canada, p. 31-43.
- Pautler, J., 2009. Geological and Geochemical evaluation report on the McKay Hill Project, Assessment Report, 38 p.
- Roddick, J.A., 1972. Geology of Nash Creek, Yukon Territory. Geological Survey of Canada Map 1282A, 1:250 000 scale.
- Roots, C.F., 1988. Cambro-Ordovician volcanic rocks in eastern Dawson map area, Olgilvie Mountains, Yukon. *In*: Yukon Geology, v. 2, Exploration and Geological Services Division, Yukon Region, Indian and Northern Affairs Canada, p. 81-87.
- Roots, C.F., 1997. Geology of the Mayo Map Area, Yukon Territory (105M). Exploration and Geological Services Division, Yukon Region, Indian and Northern Affairs Canada, Bulletin 7, 82 p.
- Siberman, M.L. and McKee, E.H., 1974. Ages of Tertiary volcanic rocks and hydrothermal precious metal deposits in central and western Nevada: Nevada Bureau of Mines, Geology Report 19, p. 67-72.
- Stack, J.F., 1980. Multi-stage vein ores of the Lake City district, western San Juan Mountains, Colorado: *Economic Geology*, vol. 75, p. 963-991.
- Winter, J.D., 2001. An Introduction to Igneous and Metamorphic Petrology. Prentice-Hall, New Jersey, United States of America, 697 p.
- YGS MapMaker Online, 2009. Yukon Geological Survey, <<http://maps.gov.yk.ca/imf.jsp?site=YGS>> [accessed November 15, 2009].
- Yukon MINFILE, 2009. Yukon Minfile - A database of mineral occurrences. Yukon Geological Survey, <http://www.geology.gov.yk.ca/databases_gis.html> [accessed November 1, 2009].

Pre-Reid surficial geology investigations in southwest McQuesten map area (115P)

Jeffrey Bond¹ and Panya Lipovsky²

Yukon Geological Survey

Bond, J. and Lipovsky, P., 2010. Pre-Reid surficial geology investigations in southwest McQuesten map area (115P). *In: Yukon Exploration and Geology 2009*, K.E. MacFarlane, L.H. Weston and L.R. Blackburn (eds.), Yukon Geological Survey, p. 103-117.

ABSTRACT

Recent field investigations have improved our knowledge of the Quaternary surficial geology, stratigraphy and glacial limits in the McQuesten map area. This information has important applications to surficial geochemical and placer exploration. The Quaternary geology of this area is unique because it encompasses early to middle Pleistocene (pre-Reid) glacial surfaces that are preserved beyond the limit of the Illinoian (Reid) glacial limit. These pre-Reid surfaces have been exposed to long periods of weathering and erosion, which have diminished their original distribution and expression. Stratigraphic exposures examined in the map area provide new evidence for a large glacial lake(s) in the Lake Creek basin ('glacial lake Coldspring'); the lake developed when pre-Reid ice dammed outlets in the Willow Hills and lower Lake Creek. In addition, there is evidence that another large glacial lake ('glacial lake Rosebud') formed on the west side of the White Mountains when a pre-Reid glacier dammed Rosebud Creek. Fieldwork in the White Mountains and on Australia Mountain allowed us to delineate the pre-Reid glacial limit at approximately 1000 m (3300-3400 ft) a.s.l. This elevation is lower than the pre-Reid glacial limit previously mapped for the area by Duk-Rodkin (1999) and is consistent with mapping performed in the adjacent Stewart River map sheet by Bostock (1964), Jackson (2005a,b) and Froese and Jackson (2005).

¹jeff.bond@gov.yk.ca

²panya.lipovsky@gov.yk.ca

INTRODUCTION

Surficial geology field investigations were undertaken in July 2009 in the southwest McQuesten map area (NTS 115P) in order to determine the distribution and character of the early to middle Pleistocene (pre-Reid) glacial surficial materials. Stratigraphy and glacial limits were also mapped to improve our understanding of the local Quaternary glacial and interglacial history. The study

area encompasses a large area of pre-Reid drift surfaces (Fig. 1). These deposits are bounded by the Reid (130 ka; Ward *et al.*, 2008; Pewe *et al.*, 2009) glacial limit to the east, and unglaciated terrain to the west. Long periods of weathering and erosion have modified the distribution and expression of the drift surfaces, making air photo interpretation difficult and emphasizing the need for field work in this region. In addition, there are sparse details on ice-flow history since there has been no ground-truthing

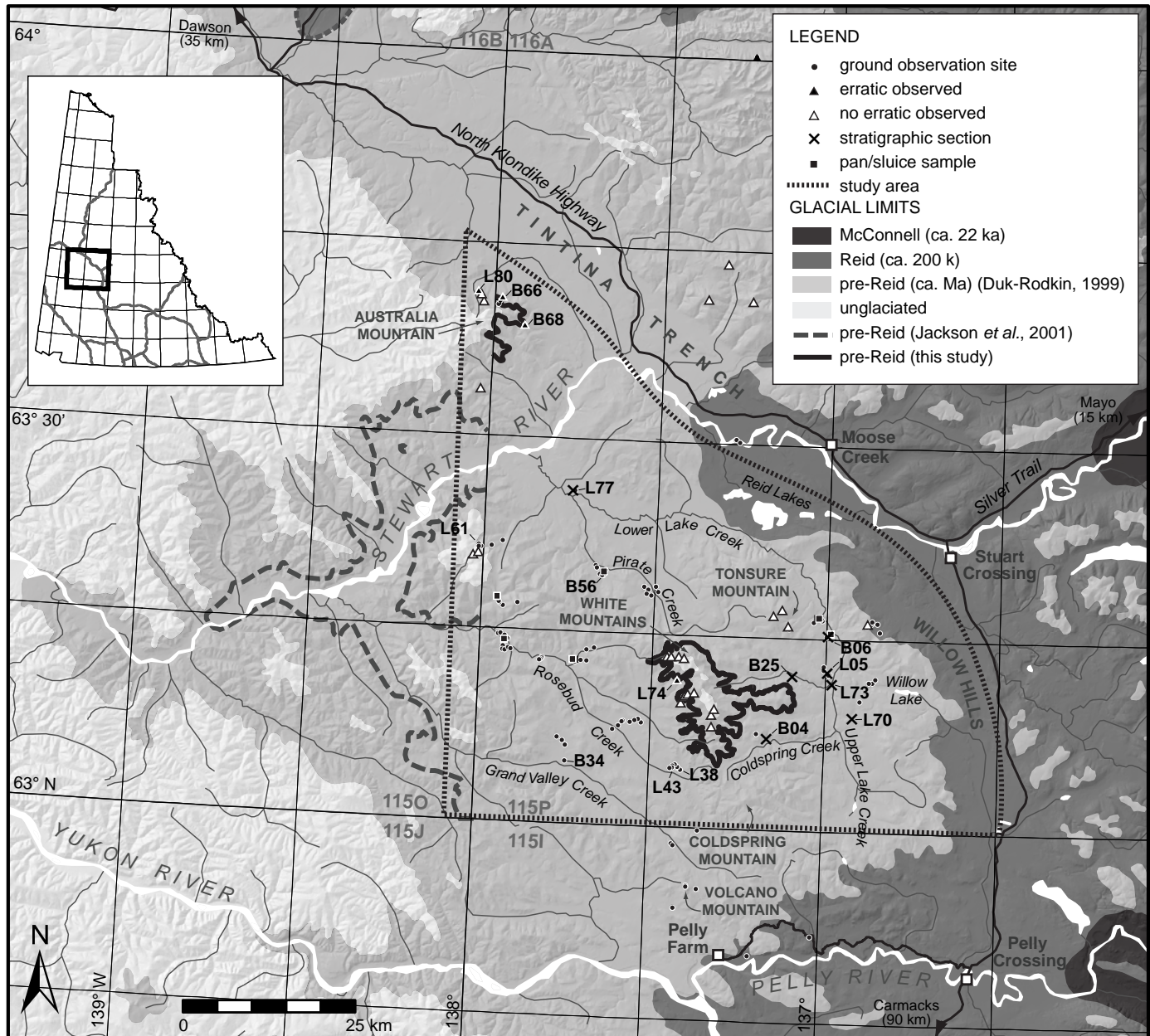


Figure 1. Map illustrating the extent of the study area in southwest McQuesten map area (115P) in relation to glacial limits depicted by various researchers. Inset portrays location within Yukon Territory. Stratigraphic sections, pan/slucice samples, sites where erratics were either observed or not observed, and other ground observation sites are shown. Sites mentioned in text are labeled with site numbers.

of the pre-Reid glacial limit. This paper summarizes our Quaternary geologic observations aimed at addressing these knowledge gaps.

PREVIOUS WORK

The pre-Reid drift surfaces in McQuesten map area have received considerable Quaternary research attention in the past 40 years. Bostock (1948) first recognized that there was evidence for at least two glaciations in the area and later identified four separate glaciations (Nansen, Klaza, Reid and McConnell glaciations; Bostock, 1966). In 1969, Hughes compiled glacial limits and flow patterns for central Yukon and grouped the Nansen and Klaza glaciations into the pre-Reid glaciations due to challenges differentiating the early Pleistocene limits. Hughes also produced a series of surficial geology maps for northeastern McQuesten map sheet (1983, unpublished data). Duk-Rodkin (1999) compiled the first glacial limits map of the Yukon, which included a new limit for the pre-Reid glaciations in Stewart River valley. This area has also been the focus of numerous pedological investigations aimed at differentiating glacial surfaces and identifying past climates (Rutter *et al.*, 1978; Tarnocai *et al.*, 1985; Smith *et al.*, 1986; Tarnocai and Smith, 1989; Tarnocai, 1990; Tarnocai and Schweger, 1991; Dampier *et al.*, 2009). Bond (1997) described the glacial and interglacial stratigraphy along the Stewart River in his MSc thesis and produced an unpublished 1:250 000-scale surficial geology map for the McQuesten map sheet (Bond and Duk-Rodkin, 1996). Part of the rationale for this project included field validation of the 1996 map so that it could be incorporated into the Yukon digital surficial geology compilation (Bond and Lipovsky, 2009). Surficial geology mapping in the adjacent Stewart River (1150) and Carmacks (1151) map areas was completed by Jackson (1997a,b, 2005a,b), and Froese and Jackson (2005). The most recent bedrock geology mapping for the southwest McQuesten map area was carried out by Colpron and Ryan (this volume).

METHODS

Field work was conducted from two base camps, one established south of the study area at the Pelly farm, and a second camp located on the Klondike Highway at Moose Creek Lodge (Fig. 1). Foot traverses were planned using aerial photo interpretation and completed with the assistance of a Hughes 500D helicopter and a Bell 206 Ranger. To improve the accuracy of the interpretation and planning, we acquired high resolution air photo models

from Andrew Neale Digital Mapping. The models were viewed in 3D within ESRI ArcGIS using Purview third party software.

The majority of ground observations were made by examining hand-excavated soil pits, landslide exposures and cut banks. Information recorded at each site consisted of general site characteristics and specific landform and soil material descriptions. Similar information was collected at stratigraphic sections, where detailed sedimentology was also completed. The surficial geology observed at each site was classified using the British Columbia Terrain Classification system which has recently been adopted for surficial geology mapping in Yukon. Glacial limits were mapped by checking flat upland surfaces and frost boils for the presence of erratics, and by determining the upper elevation limit of meltwater channels. Erratics were identified based on lithology and degree of rounding.

SURFICIAL GEOLOGY

A large focus of the 2009 field work in the southwest McQuesten map area was on characterizing pre-Reid surficial material distribution patterns, thicknesses and textures. These findings are summarized in this section, and will be used to update Bond and Duk-Rodkin's 1996 unpublished surficial geology map.

Most surfaces are covered by a veneer of Holocene organic material, or peat, consisting of poorly to partially decomposed fibric and mesic materials, and lesser amounts of well-decomposed humic materials. These deposits are thickest (*i.e.*, generally 10-20 cm) on north-facing slopes where drainage is poor, and are very thin (<5 cm) or absent on dry, south-facing slopes. Thicker blankets of organic materials (>1 m thick) accumulate in bogs and wetlands in valley bottoms, particularly in the the broad, gently sloping valleys of upper Rosebud and Grand Valley creeks. Permafrost is often found within 1 m of the surface where organic materials exist.

A thin veneer of massive eolian silt and/or fine sand (loess) is also widespread either at the ground surface, or just beneath the organic materials. Loess is generally thin (*i.e.*, <5-20 cm thick) on uplands and moderate to steep slopes. Remobilized eolian material commonly accumulates in valley bottoms to thicknesses exceeding 1 m. The loess is typically reworked and mixed into underlying colluvial materials through cryoturbation and mass movement processes.

Modern gravel and sand deposits are found within active floodplains, stream terraces and fluvial fans. Organic-rich sandy and silty fluvial deposits are also found in backchannels and overbank environments (e.g., B06, Fig.1). Where glacial diversions have occurred, for example in Lake and Pirate creeks, the fluvial plain cuts through bedrock uplands and a significant amount of angular material has become incorporated into the alluvium.

Pre-Reid till, glaciolacustrine, and glaciofluvial complexes are predominantly preserved in valley bottoms and obscure the geochemical signature of the underlying bedrock (Fig. 2). Isolated glaciofluvial and till deposits are also preserved on higher level benches on the valley sides east of the White Mountains (Fig. 2a).

Extensive pre-Reid glaciofluvial terraces composed of poorly sorted, stratified sand and gravel are preserved in

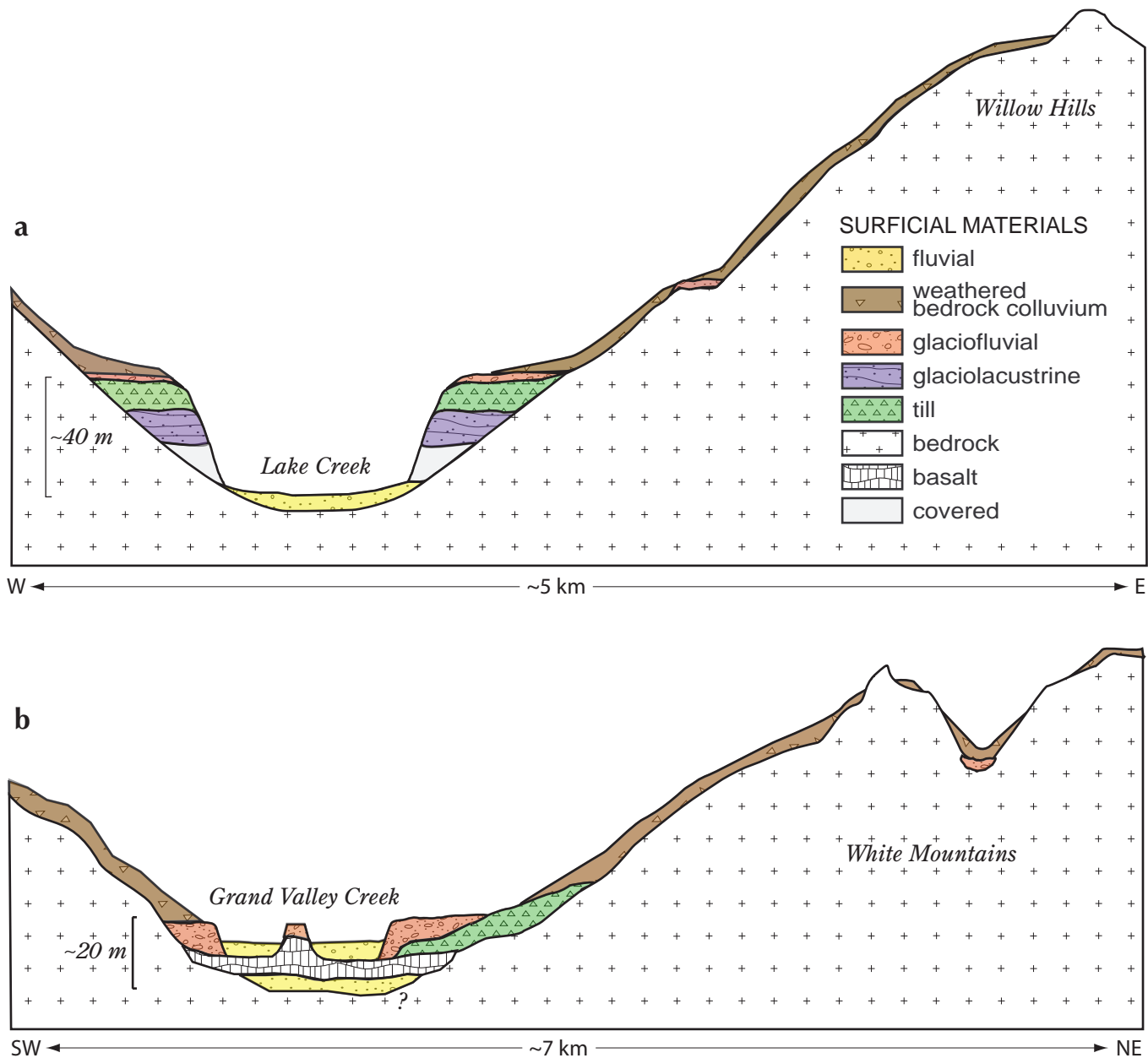


Figure 2. Idealized cross sections illustrating the distribution of surficial materials in the study area. (a) East of the White Mountains, the valley bottoms are covered by thick sequences of pre-Reid drift with alluvium deposited along modern floodplains. (b) Glaciofluvial terraces are the dominant landform in the valley bottoms west of the White Mountains.

Figure 3. Retrogressive slump scars in Willow Hills (scalloped features cutting into upper bench); view is to the south. The upper bench is approximately 70 m above the valley bottom and consists of a glaciofluvial terrace underlain by ice-rich glaciolacustrine sediments. L70 represents a stratigraphic section location.



valley bottoms west of the White Mountains and in lower Lake Creek (Fig. 2b). On the lower slopes of broad valleys, the glaciofluvial deposits overlie and grade into pre-Reid till (Fig. 2b), while in steeper, narrower valleys, the till has been eroded from the hill sides, and the glaciofluvial deposits grade into weathered bedrock colluvium (Fig. 2b). Paleosols formed within these deposits are commonly heavily oxidized and weathered, and contain frost-shattered clasts (e.g., L77, Fig. 1). Where meltwater channels cut across drainage divides, an abundance of angular clasts derived from local bedrock may be incorporated into the glaciofluvial deposits. Drift proximal to the Tintina Trench is typically quite thick as observed at lower Lake Creek (L77, Fig. 1) where pre-Reid glaciofluvial deposits and till are greater than 40 m thick.

Glaciolacustrine sediments are extensive in the Lake Creek and Rosebud Creek valleys, where thick packages of laminated fine sand, silt and clay up to 16 m thick were observed. The presence of several large retrogressive thaw slump scars originating in glaciolacustrine materials in the Willow Hills indicates that these sediments are not only widespread, but are commonly associated with massive ground ice (Fig. 3).

Pre-Reid till is poorly exposed in the map area, but where observed, it consists of a dense, poorly-sorted diamicton with weathered clasts. Matrix texture varied from sandy silt to clay, depending on proximity and relationship to glaciolacustrine units. Thicknesses up to 7 m were observed in Coldspring Creek (B04, Fig. 1) and 4 m in lower Lake Creek (L77, Fig. 1). Morainal sediments have been eroded from steep upland valley sides, leaving a

mixed mantle of weathered bedrock colluvium and eolian deposits on these slopes. In broader valleys west of the White Mountains, till is commonly preserved at the base of slopes (Fig. 2b).

Periglacial activity and permafrost processes are significant mechanisms of weathering and are evident throughout the map area. Physical weathering and subsequent remobilization by periglacial slope processes such as soil creep, slope wash, landslides and solifluction have occurred since the early to middle Pleistocene. This prolonged period of landscape weathering has eroded most of the Pre-Reid glacial materials originally deposited on moderately to steep slopes and uplands, leaving these slopes mantled by weathered bedrock colluvium. On upland sites, weathered bedrock colluvium is generally a thin veneer or blanket of rubbly diamicton with angular clasts and a silty-sand matrix. On slopes, weathered bedrock colluvium is often crudely stratified (Fig. 4). Tors are present above the glacial limit and are most common along the crest of the Willow Hills, and on the White Mountains. Cryoplanation terraces were also identified above the glacial limit near the north end of the White Mountains.

The study area is situated within the extensive discontinuous permafrost zone (Heginbottom *et al.*, 1995). Near-surface permafrost distribution in the study area is primarily controlled by topography, surficial material texture, and drainage. Permafrost was not observed within 1 m of the surface on well-drained colluvial slopes, or within well-drained, coarse or sandy valley bottom materials. Permafrost was observed within 1 m of the



Figure 4. Weathered bedrock colluvium which typically mantles valley sides and uplands. Note angular coarse fragments and stratification resulting from prolonged modification by periglacial processes and mass movement. Loess is commonly incorporated into the near-surface horizons.

surface where thick organic materials covered, or were interbedded with, fine-grained loess, alluvium or glaciolacustrine materials in valley bottoms; shallow permafrost was also observed on north-facing slopes blanketed by silty colluvial diamicton or thick loess. Where frozen ground was observed, the depth to the frost table (in early to mid July) varied between 36 and 174 cm; therefore, active layers in the area likely vary between 0.5 and 2 m thick. At one location (L70, Fig.1), the frost table was observed at 8 m depth in glaciolacustrine materials underlying several metres of glaciofluvial gravel.

Isolated landforms indicating the presence of massive ground ice include retrogressive thaw slump scars (L70, Fig. 1) and active-layer detachment slides (L61, Fig. 1) on valley sides and thermokarst depressions (L43, Fig. 1), as well as ice wedge polygons (B34, Fig. 1) and pingos (B56 and L38, Fig. 1) in valley bottoms. A conical mound approximately 5 m high and 42 m in diameter, and



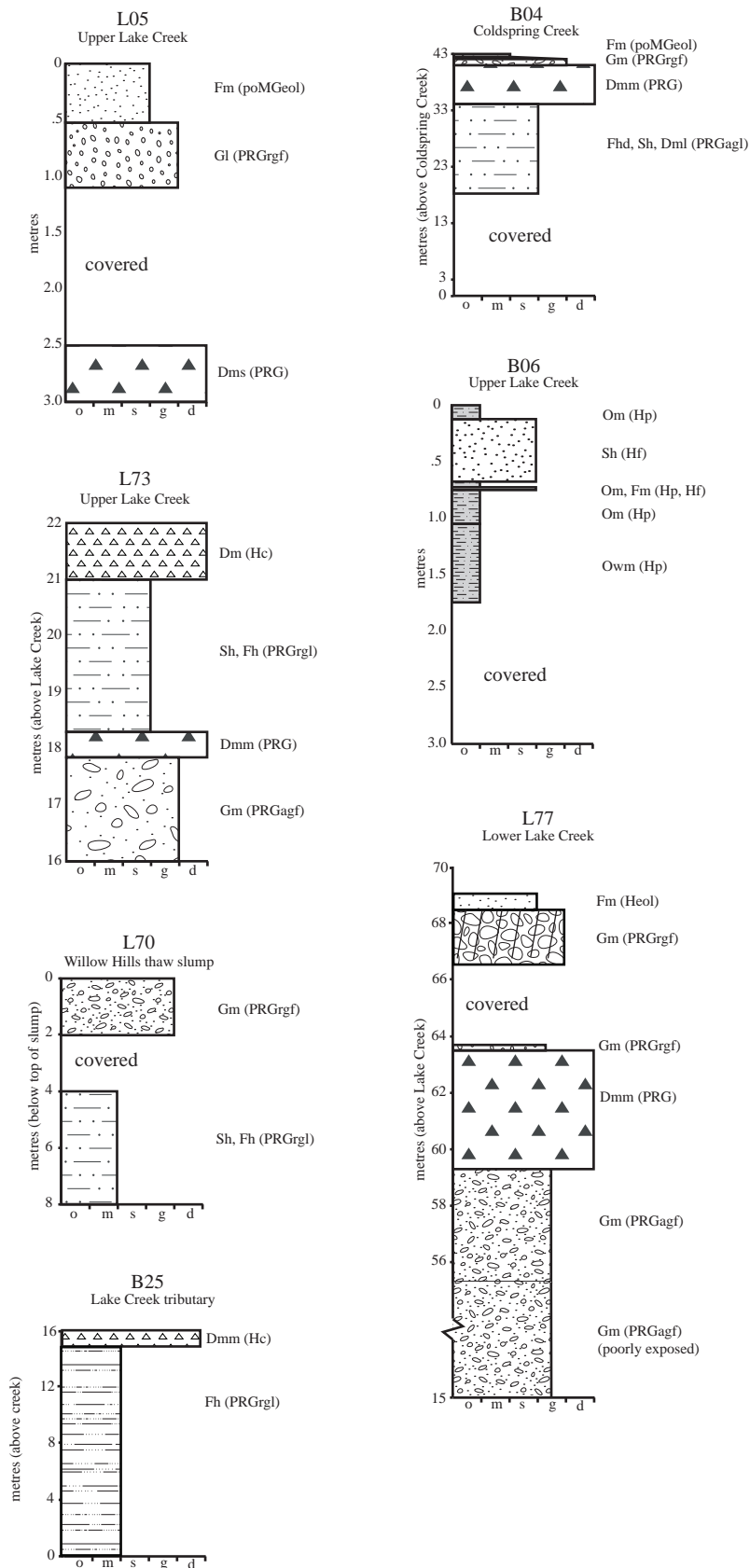
Figure 5. Collapsed rock pingo in upper Rosebud Creek (site L38; Fig. 1). This feature has a diameter of 42 m and developed within granitic bedrock. The largest boulder visible is 2.3 m tall.

composed of granitic angular rock fragments was observed at the toe of a slope in upper Rosebud Creek (L38, Fig. 1). The conical morphology and presence of a collapse crater (2.7 m deep) in the centre of the mound suggests that this feature is the remnant of an open-system rock pingo (Fig. 5).

In Rosebud and Grand Valley creek valleys, glaciofluvial deposits locally overlie basalt flows of the Selkirk volcanic suite (Fig. 2b). Basalt flows underlying pre-Reid glaciofluvial gravel 20 km downstream from the study area in lower Rosebud Creek have been Ar-Ar dated at 2.69 Ma (Jackson, 2005b). Other bedrock exposures in the area include: Mississippian and older metavolcanic rocks of Quesnellia Terrane to the southeast; pristine Mississippian volcanic rocks and coeval granitic plutons in the Reid Lakes area; Permian and older schist, quartzite, amphibolite and orthogneiss of the Yukon-Tanana Terrane; and Triassic metavolcanic rocks of Stikinia Terrane to the southwest (Colpron and Ryan, this volume). Jurassic and Cretaceous plutonic intrusions are also found throughout the study area (Bostock, 1964; Colpron and Ryan, this volume).

STRATIGRAPHY

Most of the stratigraphic sections described in the study area consist of sediments deposited during pre-Reid glaciations (Fig. 6). The oldest sediments were deposited in outwash trains and glacial lakes that formed ahead of



Lithofacies

- Dms - diamicton, matrix-supported resedimented
- Dmm - diamicton, matrix-supported massive
- Dml - diamicton, matrix-supported crudely stratified
- G1 - gravel, crudely bedded
- Gm - gravel, clast-supported
- Sh - sand, horizontally laminated
- Fm - silt, massive
- Fh - silt, horizontally laminated
- Fhd - silt, horizontally laminated, dropstones
- Om - organic, massive
- Owm - organic, woody massive

Interpreted depositional setting

Holocene sediments

- Hp - peat
- Hf - fluvial
- Heol - eolian
- Hc - colluvium

post-McConnell glacial sediments

- poMGeol - eolian

Pre-Reid glacial sediments

- PRGrgf - retreat-phase glaciofluvial
- PRGrgl - retreat-phase glaciolacustrine
- PRG - till
- PRGagf - advance-phase glaciofluvial
- PRGagl - advance-phase glaciolacustrine

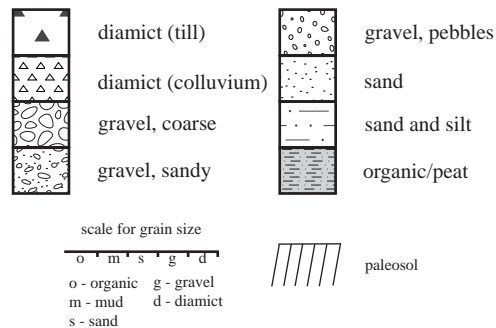


Figure 6. Facies descriptions and interpreted depositional settings for key stratigraphic sections measured in the study area.

the ice front during the advance phase of the pre-Reid glaciation(s). These sediments are overlain by pre-Reid till and retreat-phase glaciofluvial and glaciolacustrine deposits.

ADVANCE-PHASE SEDIMENTS

Advance-phase sediments were observed in the Coldspring Creek and Lake Creek valleys and represent two depositional environments: glaciofluvial (L73, L77) and glaciolacustrine (B04) (Figs. 1, 6). The advance-phase glaciofluvial gravel is typically a poorly sorted, clast-supported gravel that coarsens upward and is crudely to well bedded. Open framework gravel beds are also common, indicating they were deposited in high-energy environments associated with glacier meltwater.

Glaciolacustrine sediments typically consist of horizontally laminated and bedded, well-sorted, silt, clay and fine sand (Fig. 7), and in places contain dropstones and lenses of debris-flow diamict. Loading structures are common near the upper contact with pre-Reid till. The presence of



Figure 7. Glaciolacustrine sediments exposed in lower Rosebud Creek valley.



Figure 8. Flow till deposited above glaciolacustrine sediments (not visible) as pre-Reid ice advanced up Coldspring Creek valley (site B04, Fig. 1). Note beds dipping up-valley and marked by dashed lines.

advance-phase glaciolacustrine sediments indicates that local drainages were dammed by the ice advance.

PRE-REID TILL

Till is sediment deposited directly by glacier ice. Four out of the seven sections that were measured for this study contain diamictons that are interpreted to be pre-Reid till (Figs. 1, 6). The till at sections B04, L73 and L77 consists of a compact, poorly sorted diamicton with pebble to boulder-sized clasts in a silty sand matrix. Striated and polished clasts are present, reflecting the glacial origin of the sediment. In Coldspring Creek (B04), up-valley dipping lenses of stratified silt and sand within the till suggest that the diamict accumulated as a series of flow-tills deposited into a proglacial lake (Fig. 8). Tills at sites L73 and L77 were likely deposited by a combination of ablation and lodgement processes. At each of these three sites (B04, L73 and L77), the lower contact with the advance-phase sediment is sharp or erosional, reflecting warm-based ice conditions. The till described at site L05 (Figs. 1, 6) had a similar texture to the lodgement tills, but was not compacted, which may indicate post-depositional resedimentation in an ablation environment.

RETREAT-PHASE SEDIMENTS

Similar to the advance-phase, the retreat-phase of the pre-Reid glaciations was marked by glaciofluvial and glaciolacustrine sedimentation. Retreat-phase glaciolacustrine sediments are present in the Lake Creek valley (L73), the Willow Hills (L70) and in the valley of an unnamed Lake Creek tributary north of Coldspring Creek



Figure 9. ‘Wounded Moose’ paleosol that developed in pre-Reid retreat outwash exposed at the top of the lower Lake Creek section (site L77; see also Figs. 1, 6). The paleosol shown here is 2.5 m thick and has been heavily weathered and oxidized. Abundant clasts have been shattered by prolonged frost action which has primarily taken place during the glacial periods following the pre-Reid glaciations.

(B25; Figs. 1, 6). These sediments typically consist of laminated fine sand, silt and clay. Retreat-phase glaciofluvial sediments consist of a clast-supported, moderately to well-sorted gravel and clast sizes range from pebble to boulder.

At site L77, the retreat-phase glaciofluvial sediments have a well-developed paleosol preserved in the upper 2.5 m of the deposit (Fig. 9). This soil is similar to the Wounded Moose paleosol, observed on other pre-Reid surfaces in central Yukon. The Wounded Moose paleosol formed over a long period of time under a relatively mild and humid climate during the interglacial(s) between the pre-Reid and Reid glaciations (Tarnocai *et al.*, 1985). Typical Luvisol B horizon thicknesses in pre-Reid outwash can exceed 2 m, which is about 1.8 m thicker than the modern Brunisol B horizon in the study area. This implies that pre-Reid interglacials were considerably warmer and wetter than the present-day climate (Tarnocai *et al.*, 1985).

NONGLACIAL SEDIMENTS

A veneer (generally <1 m) of eolian sediments (loess) caps several sections in the study area (Fig. 6). The loess is typically massive silt and likely originated during

McConnell deglaciation (approximately 15 ka), however, no dating has been conducted to confirm this age. Modern cliff-top eolian sand and silt accumulations were also observed where unconsolidated sediments have been exposed to wind erosion (L77, Fig. 6).

GLACIAL LIMITS

Previous mapping of the pre-Reid glacial limit in the study area was based on air photo interpretation without ground truthing. In the White Mountains, the pre-Reid limit was formerly mapped at 1370 m (4500 ft; Fig. 1; Bond and Duk-Rodkin, 1996; Duk-Rodkin, 1999). This was based on the elevation of potential meltwater channels cutting across the upland. Field-checking of these channels and other flat-lying surfaces immediately below the limit did not reveal any glacial erratics. The highest erratic found during multiple foot traverses was located at 1000 m (3300 ft a.s.l.) on the west side of the White Mountains (Fig. 1, L74). This elevation is similar to that of the highest meltwater channel identified in our re-interpretation of the upland geomorphology, at 1100 m (3650 ft) on the east side of the White Mountains. A similar pre-Reid glacial limit on Australia Mountain was also mapped at 1000 m (3300 ft), based on the highest erratics observed during multiple foot traverses (B66, B68 and L80 in Fig. 1). This elevation is lower than the limit mapped by Duk-Rodkin (1999; Fig. 1), but corresponds with the pre-Reid glacial limit mapped in the adjacent map sheet, which was based on the elevation of the highest meltwater channels (Fig. 1; Froese and Jackson, 2005).

GLACIAL HISTORY

At least 40 periods of high global ice volume can be distinguished in the benthic marine oxygen isotope record spanning the early to middle Pleistocene (Fig. 10). While these periods of high global ice volume are generally correlated with colder climatic periods, it is currently unknown how many of these cold periods produced ice sheets extensive enough to glaciare our study area.

New ages on pre-Reid glaciations were not produced as part of this study but considerable dating has already been completed by previous researchers who have worked near the confluence of the Pelly and Yukon rivers. Through a combination of Ar-Ar, paleomagnetic and fission track dating, an early Pleistocene chronological record has been produced (Westgate *et al.*, 2001; Jackson

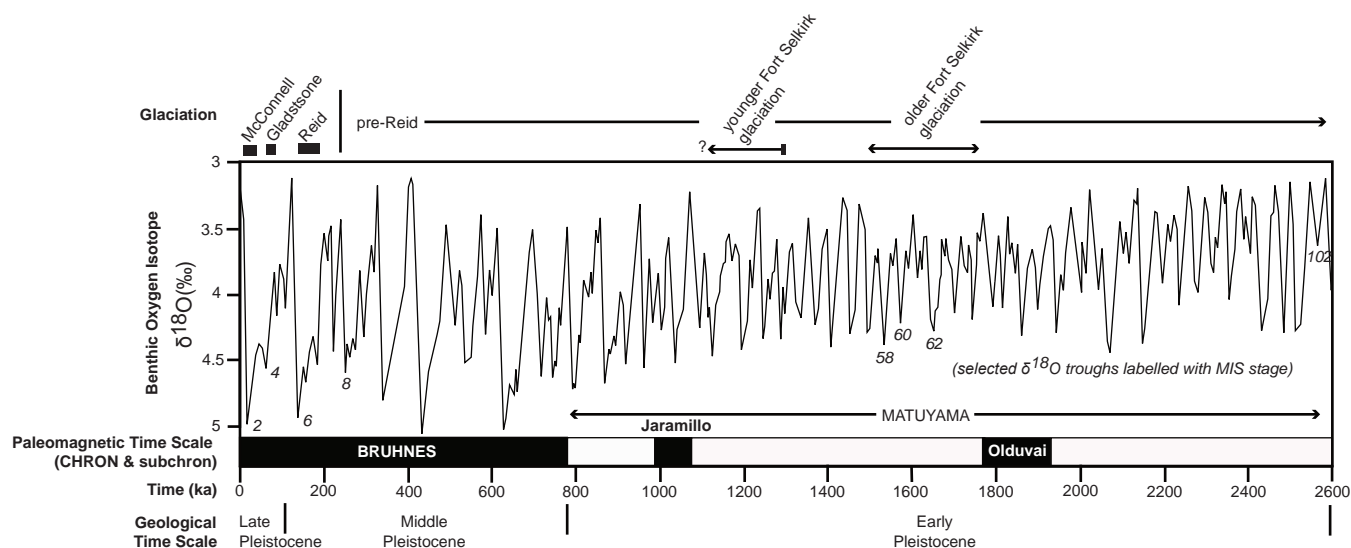


Figure 10. Oxygen isotope ($\delta^{18}\text{O}$) curve for the last 2.6 Ma, constructed by cross-correlating 57 globally distributed benthic marine $\delta^{18}\text{O}$ records (after Lisiecki and Raymo, 2005). The paleomagnetic time scale and local glaciations are also shown for reference (after Nelson et al., 2009). The $\delta^{18}\text{O}$ peaks indicate interglacial stages (low global ice volumes) whereas the troughs denote glacial stages (high global ice volumes). This curve highlights the multitude of global climatic fluctuations in the last 2.6 Ma.

et al., 2003; Nelson et al., 2009). The following conclusions regarding the timing of pre-Reid events can be made from these studies: the oldest pre-Reid glaciation is younger than 2.69 Ma, based on outwash gravel overlying basalt of known age in lower Rosebud Creek (Jackson et al., 2003); the older Fort Selkirk glaciation occurred between 1.77 Ma and 1.5 Ma (Nelson et al., 2009); and the younger Fort Selkirk glaciation occurred after 1.33 Ma (Fig. 10). Surface sediments from the younger Fort Selkirk glaciation are preserved above basalt near Pelly Farm (Jackson et al., 2003). While the limit of the individual pre-Reid glaciations is not known, it is certain they were more extensive than the Reid glaciation and therefore would have glaciated the southwest McQuesten map area. Future Quaternary chronological studies within the map area should focus on the paleomagnetic record preserved within the pre-Reid glaciolacustrine sediments that have been discussed in this study.

A reconstruction of pre-Reid ice flow can be derived from the stratigraphy and geomorphology we documented in the southwest McQuesten map area. The main conduits for the Cordilleran ice sheet entering the study area were the Pelly and Stewart river valleys. The leading edge of the ice sheet would have resembled a system of westwardly

advancing valley glaciers (Fig. 11a). These valley glaciers converged on the eastern side of the Willow Hills and continued to advance around the Willow Hills and through the Willow Lake valley. At this time, the regional eastward drainage off the White Mountains would have been blocked by the ice front, which caused the upper Lake Creek basin to flood, creating glacial lake Coldspring (Fig. 11a). This glacial lake would have developed during each pre-Reid glaciation that advanced into the Willow Hills. Stratigraphic studies also indicate that the lake formed during both ice advance and retreat. At its maximum extent, glacial lake Coldspring was approximately 35 km long and 250 m deep. The main outlet was located south of the White Mountains at an elevation of 900 m (2950 ft) and drained westward into Grand Valley Creek (Fig. 11a). As the ice continued to advance up the eastern flank of the White Mountains, glacial lake Coldspring evolved into a series of separate proglacial lakes occupying the east-west oriented valleys in the Lake Creek drainage. Multiple outlet channels were established at this time as these separate glacial lakes overtopped their divides, or spilled northward into neighbouring valleys. The resulting channels were cut into bedrock and are relatively resistant to weathering and erosion; they therefore provide strong geomorphic

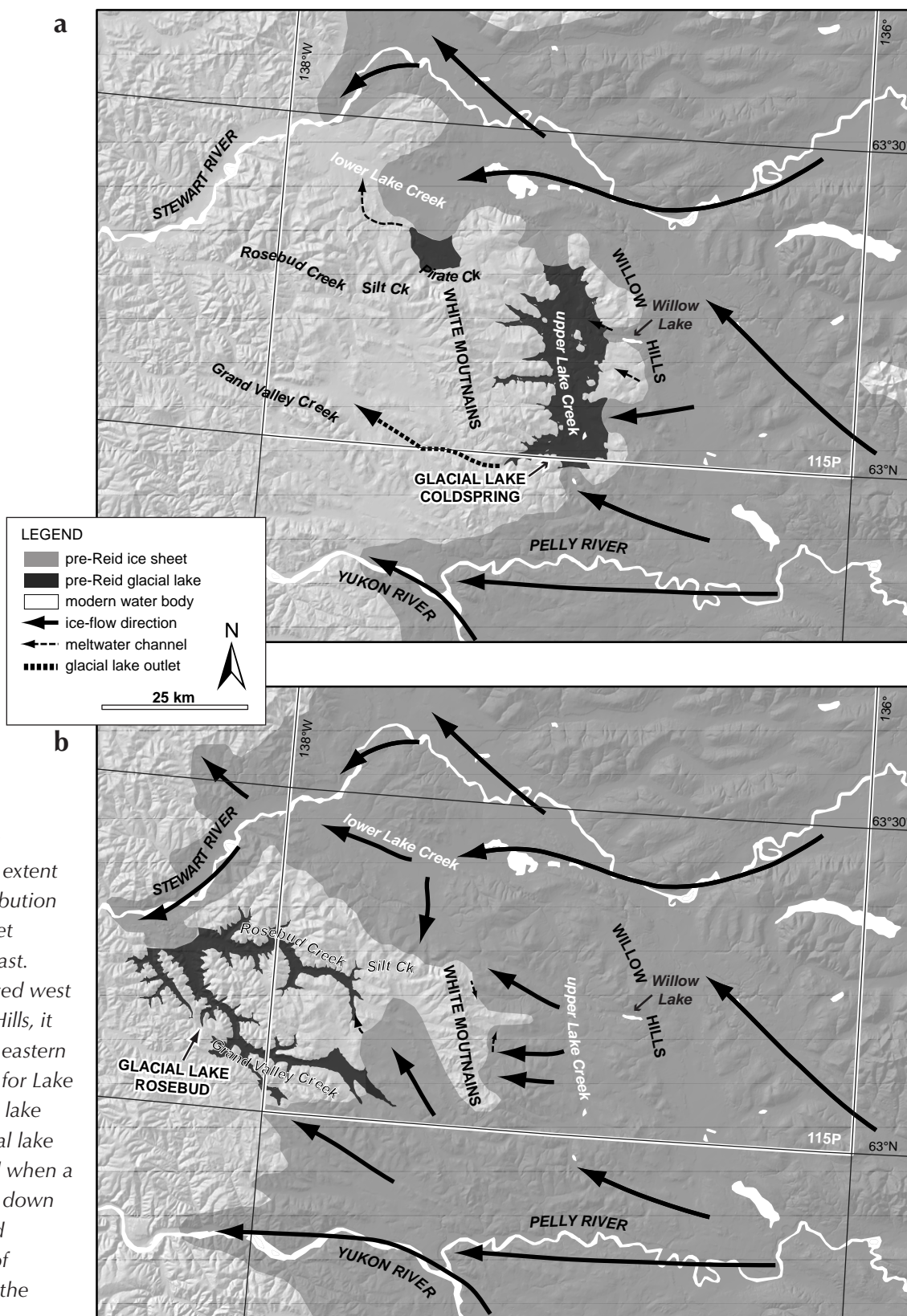


Figure 11. Schematic reconstruction of ice extent and glacial lake distribution as a pre-Reid ice sheet advanced from the east. **(a)** As the ice advanced west through the Willow Hills, it blocked all potential eastern and northern outlets for Lake Creek forming glacial lake Coldspring. **(b)** Glacial lake Rosebud was formed when a lobe of ice extended down the Stewart River and blocked the mouth of Rosebud Creek near the pre-Reid glacial maximum.

evidence for the glacial limit in the area. The up-valley flowing ice on the east side of the White Mountains reached an elevation of 1100 m.

As the ice continued to advance westward, it was bifurcated by the White Mountains (Fig. 11b). Ice flow to the south of the White Mountains advanced down Grand Valley and Rosebud creeks, whereas ice flow to the north of the White Mountains advanced westward down lower Lake Creek and into the Stewart River valley. North-flowing tributaries to Lake Creek, such as Pirate Creek and its unnamed tributaries, were dammed by the southern margin of the glacier occupying lower Lake Creek valley (Fig. 11a). Glaciolacustrine sediment is exposed in one location in a tributary to Pirate Creek and is likely a common material preserved at depth in this area. As the glacier continued to advance down lower Lake Creek, ice and meltwater spilled southwestward across low divides into Rosebud Creek (Fig. 11b). Remnant glaciofluvial terraces documented in Silt Creek support this history.

Meltwater draining pre-Reid ice in lower Lake Creek valley deposited thick glaciofluvial sediments. Terraces preserved on the margin of the valley contain a complete sequence of pre-Reid advance-phase outwash, till and retreat-phase outwash. This section has been unofficially termed the pre-Reid type section within central Yukon (L77; Figs. 1, 6).

Ice advancing down the Stewart River valley eventually blocked the mouth of Rosebud Creek (Fig. 11b). This caused glacial lake Rosebud to flood Rosebud and Grand Valley creeks. Glaciolacustrine sediment related to this lake was observed in Rosebud Creek valley. A significant supply of the meltwater entered the lake from the ice sheet occupying the upper parts of the basin (Fig. 11b).

Paleosols preserved on the drift surfaces of upper Grand Valley Creek are some of the most oxidized in the study area. Typical weathering features include *in situ* clay formation, clay skins and strong brown Munsell colours (7.5YR 4/6). This degree of soil weathering and rubification was not observed to the east of the White Mountains, for example in the Willow Lake channel, where paleosols were also documented on outwash terraces. A likely explanation for this difference is that the surfaces on the west side of the White Mountains are older than those observed on the east side.

The new glacial limit we are proposing for the southwest McQuesten map area also has regional implications for

the ice limits further west in the Stewart River map area. Duk-Rodkin (1999) interpreted the all-time pre-Reid limit reaching the mouth of the Stewart River, whereas Bostock (1966) and Jackson *et al.* (2001) mapped a less extensive all-time limit, which only extended 15 km downstream from the mouth of Rosebud Creek (Fig. 1). The results from this study suggest less-extensive pre-Reid ice flowed into the lower Stewart River valley than what Duk-Rodkin (1999) mapped. Our findings therefore support the previous limits mapped by Bostock (1966) and Jackson *et al.* (2001).

IMPLICATIONS FOR MINERAL AND PLACER EXPLORATION

As outlined in the previous section, field-based glacial-limit mapping confirms that the pre-Reid glacial limit in the southwest McQuesten map area is lower in elevation than previously interpreted by Duk-Rodkin (1999) and Bond and Duk-Rodkin (1996); unglaciated uplands are therefore more extensive than previously interpreted. In addition, upland glaciated slopes have been so heavily weathered and eroded since the early to middle Pleistocene that virtually no glacial deposits remain; these surfaces can essentially be considered unglaciated for surficial geochemical sampling purposes.

Soil geochemistry sampling, and geological interpretation in upland unglaciated regions is generally less complicated than in glaciated regions and valley bottoms because surficial materials are primarily derived from weathered bedrock of local provenance. The main complicating factor in these settings is that any loess present at the surface or mixed into underlying soil horizons will dilute the geochemical signature (Bond and Sanborn, 2006). Loess up to 20 cm thick is present on most upland surfaces in the study area, and is commonly reworked into underlying soil horizons through cryoturbation and mass movement processes, particularly on north-facing slopes (Smith *et al.*, 2009).

In flat and gently-sloping low-lying areas below the glacial limit, abundant eolian, fluvial, glaciofluvial, glaciolacustrine and morainal materials mask the underlying bedrock. In these cases, surficial material genesis and local ice-flow patterns must be carefully considered when planning sampling programs and interpreting both soil and stream geochemistry anomalies. For example, the widespread glaciolacustrine and glaciofluvial materials present in valley bottoms in the

map area would generally be unsuitable for soil geochemistry sampling. Till is a more desirable material to sample, but glacial transport and dispersion must be accounted for. For example, basal till deposited along the eastern flanks of the White Mountains was deposited by ice flowing up-valley, whereas the opposite applies to till deposited on the western flanks.

A rudimentary heavy mineral sampling program was carried out as part of the 2009 field program. Eight samples were collected by portable sluicing and/or panning in tributaries to upper Rosebud Creek, Pirate Creek and upper Lake Creek near locations of former placer exploration activity (Fig. 1; Lipovsky *et al.*, 2001; Caulfield and Ikona, 1986). No significant gold colours were identified in any of the pan concentrates.

Additional placer prospecting is recommended in two locations: in lower Rosebud Creek where basalt bedrock outcrops in the valley bottom and is overlain by fluvial or glaciofluvial gravel; and in the vicinity of a bedrock terrace found on the south side of the Stewart River, west of the fine-gold deposits found in Steamboat Bar (Fig. 12). Both the accessible bedrock surfaces and the relatively thin alluvium at these sites will increase the potential to find placer gold concentrations.

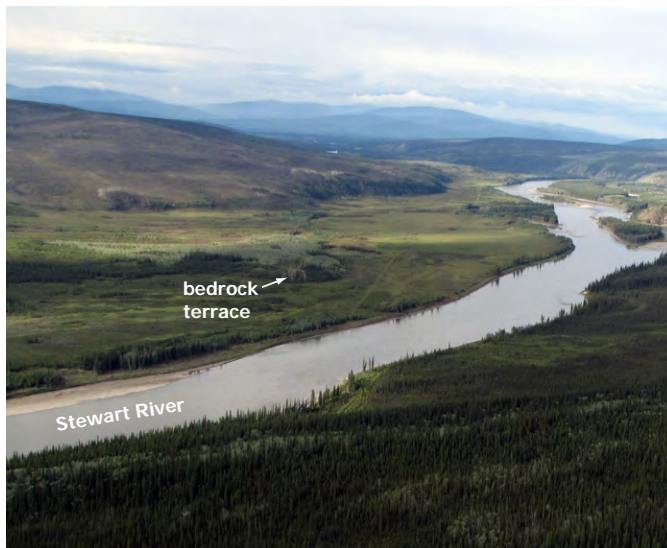


Figure 12. A low bedrock terrace (see arrow) in the Stewart River floodplain, west of Steamboat Bar. Depth to bedrock in adjacent areas of the floodplain may be relatively shallow, which may increase the grade of fine-gold deposits. View is to the southwest.

CONCLUSIONS

Pre-Reid drift surfaces in southwest McQuesten map area are preserved in valley bottoms and on low-angle slopes. The stratigraphy of these sediments indicates that up-valley flowing pre-Reid ice sheets dammed upper Lake Creek which drained the eastern flanks of the White Mountains. The upper Lake Creek basin was then inundated by glacial lake Coldspring, which likely formed numerous times during the early to middle Pleistocene. As ice continued to advance west of the White Mountains, moraine and glaciofluvial sediments were deposited in the valleys of Rosebud and Grand Valley creeks. Glaciolacustrine sediments were also deposited in the Rosebud Creek valley when pre-Reid ice sheets dammed the mouth of Rosebud Creek and created glacial lake Rosebud.

Determining the limit of pre-Reid glaciations on upland surfaces is challenging as prolonged periglacial weathering and colluviation have modified or eroded the glacial deposits. The upper elevation of erratics in the White Mountains and on Australia Mountain was determined to be 1000 m (3300 ft). This elevation correlates with previous mapping by Bostock (1966) and Jackson *et al.* (2001), and is lower than the limit mapped by Bond and Duk-Rodkin (1996) and Duk-Rodkin (1999).

Prospectors using surficial geochemical techniques in southwest McQuesten map area must consider the distribution of surficial materials on the landscape before planning their exploration programs. Upland surfaces and moderate to steep slopes located within the pre-Reid glacial limit have similar surficial material characteristics compared to unglaciated terrain. This also applies to first order drainages with steep gradients. Glacial dispersion and potential dilution must be accounted for in samples taken in valley bottoms and second or third order drainages. Placer prospecting in the study area should target bedrock terraces in Rosebud Creek and on the south side of the Stewart River near Steamboat Bar.

ACKNOWLEDGEMENTS

This project was a success due to the hard work of a number of people. It all started with the construction of a first-rate camp which was organized and managed by Jim Ryan and Maurice Colpron; we sincerely thank them for allowing us the luxury of just showing up and getting straight to work. We also had great field assistance from Riley Gibson, Samantha Darling and Derek Turner, and

their motivation and enthusiasm made all the difference. The skill of our helicopter pilot Yoshio (Prism Helicopters) was outstanding and sold us on using the 500D. A debt of gratitude is owed to all the camp support staff including: the ever-inquisitive and creative Gord (Aurora Geosciences) who kept camp running smoothly; Eileen, who prepared incredible meals and was always positive and pleasant; and the staff at Moose Creek Lodge for their hospitality during our final week of fieldwork. Much appreciated comments and improvements to this paper were provided by Derek Turner and Leyla Weston.

REFERENCES

- Bond, J.D., 1997. Late Cenozoic History of McQuesten (115P), Yukon Territory. Unpublished MSc thesis, University of Alberta, Edmonton, Alberta, 161 p.
- Bond, J.D. and Duk-Rodkin, A., 1996. Surficial geology, McQuesten, Yukon Territory. *In: Late Cenozoic History of McQuesten (115P), Yukon Territory, Unpublished MSc thesis by J.D. Bond, University of Alberta, Edmonton, Alberta, 1:250 000 scale map.*
- Bond, J.D. and Lipovsky, P.S. (compilers), 2009. Yukon digital surficial geology – preliminary data release. Yukon Geological Survey, Open File 2009-42.
- Bond, J.D. and Sanborn, P.T., 2006. Morphology and geochemistry of soils formed on colluviated weathered bedrock: Case studies from unglaciated upland slopes in west-central Yukon. Yukon Geological Survey, Open File 2006-19, 70 p.
- Bostock, H.S., 1948. Physiography of the Canadian Cordillera, with special reference to the area north of the fifty-fifth parallel. Geological Survey of Canada, Memoir 247, 106 p.
- Bostock, H.S., 1964. Geology, McQuesten, Yukon Territory. Geological Survey of Canada, Map 1143A, 1:253 440 scale.
- Bostock, H.S., 1966. Notes on glaciation in central Yukon Territory. Geological Survey of Canada, Paper 65-36, 18 p.
- Caulfield, D.A. and Ikona, C.K., 1986. 1985 summary report on the Pirate mineral claims, McQuesten Gold Project, Stewart Crossing, Yukon Territory. Assessment report prepared by Pamicon Developments Ltd. for Miramar Energy Corporation, 34 p.
- Colpron, M. and Ryan, J.J., 2010 (this volume). Bedrock geology of southwest McQuesten (NTS 115P) and part of northern Carmacks (115I) map area. *In: Yukon Exploration and Geology 2009, K.E. MacFarlane, L.H. Weston and L.R. Blackburn (eds.), Yukon Geological Survey, p. 159-184.*
- Dampier, L., Sanborn, P., Bond, J., Clague, J.J. and Smith, S., 2009. Soil genesis in relation to glacial history in central Yukon. *In: Yukon Exploration and Geology 2008, L.H. Weston, L.R. Blackburn and L.L. Lewis (eds.), Yukon Geological Survey, p. 113-123.*
- Duk-Rodkin, A., 1999. Glacial limits map of Yukon Territory. Geological Survey of Canada, Open File 3694, Exploration and Geological Services Division, Yukon Region, Indian and Northern Affairs Canada, Geoscience Map 1999-2, 1:1 000 000 scale.
- Froese, D.G. and Jackson, L.E., Jr., 2005. Surficial geology, Australia Mountain (105O/09), Yukon Territory. Geological Survey of Canada, Open File 4586, 1:50 000 scale.
- Gordey, S.P., Williams, S.P., Cocking, R. and Ryan, J.J. (compilers), 2006. Digital geology, Stewart River area, Yukon (v. 1, DVD-ROM), Geological Survey of Canada, Open File 5122 (DVD-ROM).
- Heginbottom, J.A., Dubreuil, M.A. and Harker, P.T., 1995. National Atlas of Canada (5th edition), Permafrost, Plate 2.1, (MCR 4177), 1:7 500 000 scale.
- Hughes, O.L., 1969. Glacial map of Yukon Territory, South of 65 Degrees North Latitude. Geological Survey of Canada, Preliminary Map 6-1968, 1:1 000 000 scale.
- Jackson, L.E., Jr., 1997a. Surficial geology, Victoria Rock, Yukon Territory. Geological Survey of Canada, Map 1877A, 1:100 000 scale.
- Jackson, L.E., Jr., 1997b. Surficial geology, Granite Canyon, Yukon Territory. Geological Survey of Canada, Map 1878A, 1:100 000 scale.
- Jackson, L.E., Jr., 2005a. Surficial geology, Ladue Creek (150O/01), Yukon Territory. Geological Survey of Canada, Open File 4573, 1:50 000 scale.
- Jackson, L.E., Jr., 2005b. Surficial geology, Rosebud Creek (105O/08), Yukon Territory. Geological Survey of Canada, Open File 4585, scale 1:50 000.

- Jackson, L.E., Jr., Barendregt, R.W., Baker, J. and Irving, E., 1996. Early Pleistocene volcanism and glaciation in central Yukon: a new chronology from field studies and paleomagnetism. *Canadian Journal of Earth Science*, vol. 33, no. 6, p. 904-916.
- Jackson, L.E., Jr., Shimamura, K. and Huscroft, C.A., 2001. Late Cenozoic geology, Ancient Pacific Margin NATMAP Project, Report 3: A re-evaluation of glacial limits in the Stewart River basin of Stewart River map area, Yukon Territory. Geological Survey of Canada, Current Research 2001-A3, 8 p.
- Jackson, L.E., Jr., Huscroft, C.A., Barendregt, R.W., Froese, D.G. and Villeneuve, M., 2003. A 2.5 Ma chronology of regional glaciation in west-central Yukon, Canada, based on radiometric and paleomagnetic dating of volcanic rocks. *Geological Society of America Abstracts with Programs*, 57-1, p. 175.
- Jackson, L.E., Jr., Froese, D.G., Huscroft, C.A., Nelson, F.E., Westgate, J.A., Telka, A.M., Shimamura, K. and Rotheisler, P.N., 2009. Surficial geology and late Cenozoic history of the Stewart River and northern Stevenson Ridge map areas, west-central Yukon Territory. Geological Survey of Canada, Open File 6059, 414 p.
- Lisiecki, L.E. and Raymo, M.E., 2005. A Pliocene-Pleistocene stack of 57 globally distributed benthic $\delta^{18}\text{O}$ records. *Paleoceanography*, vol. 20, PA 1003, doi: 10.1029/2004PA001071.
- Lipovsky, P., LeBarge, W., Bond, J. and Lowey, G., 2001. Yukon placer activity map (1:1 000 000 scale). Exploration and Geological Services Division, Yukon Region, Indian and Northern Affairs Canada, Open File 2001-34.
- Nelson, F.E., Barendregt, R.W. and Villeneuve, M., 2009. Stratigraphy of the Fort Selkirk Volcanogenic Complex in central Yukon and its paleoclimatic significance: Ar/Ar and paleomagnetic data. *Canadian Journal of Earth Science*, vol. 46, p. 381-401.
- Pewe, T.L., Westgate, J.A., Preece, S.J., Brown, P.M. and Leavitt, S.W., 2009. Late Pliocene Dawson cut forest bed and new tephrochronological findings in the Gold Hill Loess, east central Alaska. *GSA Bulletin*, vol. 121, p. 294-320.
- Rutter, N.W., Foscolos, A.E. and Hughes, O.L., 1978. Climatic trends during the Quaternary in central Yukon based upon pedological and geomorphological evidence. *In: Quaternary Soils*, W.C. Mahaney (ed.), GeoAbstracts, Norwich, England, p. 309-359.
- Smith, C.A.S., Tarnocai, C. and Hughes, O.L., 1986. Pedological Investigations of Pleistocene Glacial Drift Surfaces in the central Yukon. *Géographie physique et Quaternaire*, vol. 40, p. 29-37.
- Smith, C.A.S., Sanborn, P.T., Bond, J.D. and Frank, G., 2009. Genesis of Turbic Cryosols on north-facing slopes in a dissected, unglaciated landscape, west-central Yukon Territory. *Canadian Journal of Soil Science*, vol. 89, p. 611-622.
- Tarnocai, C., 1990. Paleosols of the Interglacial Climates of Canada. *Géographie physique et Quaternaire*, vol. 44, no. 3, p. 363-374.
- Tarnocai, C., Smith, S. and Hughes, O.L., 1985. Soil development on Quaternary deposits of various ages in the central Yukon Territory. *Current Research, Part A*, Geological Survey of Canada, Paper 85-1A, p. 229-238.
- Tarnocai, C. and Smith, C.A.S., 1989. Micromorphology and development of some central Yukon paleosols, Canada. *Geoderma*, vol. 45, p. 145-162.
- Tarnocai, C. and Schweger, C.E., 1991. Late Tertiary and early Pleistocene paleosols in northwestern Canada. *Arctic*, vol. 44, p. 1-11.
- Ward, B.C., Bond, J.D., Froese, D. and Jensen, B., 2008. Old Crow tephra (140 ± 10 ka) constrains penultimate Reid glaciation in central Yukon Territory. *Quaternary Science Reviews*, vol. 27, no. 19-20, p. 1909-1915.
- Westgate, J.A., Preece, S.J., Froese, D.G., Walter, R.C., Sandhu, A.S. and Schweger, C.E., 2001. Dating early and middle (Reid) Pleistocene glaciations in central Yukon by tephrochronology. *Quaternary Research*, vol. 56, no. 3, p. 335-348.

Preliminary description and slope stability analyses of the 2008 Little Salmon Lake and 2007 Mt. Steele landslides, Yukon

Marc-André Brideau¹ and Doug Stead

Earth Science Department, Simon Fraser University, Burnaby, BC

Panya Lipovsky

Yukon Geological Survey, Whitehorse, YT

Michel Jaboyedoff

Université de Lausanne, Lausanne, Switzerland

Christopher Hopkinson

Nova Scotia Community College, Annapolis Valley Campus, NS

Michael Demuth

Geological Survey of Canada, Ottawa, ON

John Barlow

Durham University, Durham, Great Britain

Steve Evans and Keith Delaney

Department of Earth and Environmental Sciences, University of Waterloo, Waterloo, ON

Brideau, M.-A., Stead, D., Lipovsky, P., Jaboyedoff, M., Hopkinson, C., Demuth, M., Barlow, J., Evans, S. and Delaney, K., 2010. Preliminary description and slope stability analyses of the 2008 Little Salmon Lake and 2007 Mt. Steele landslides, Yukon. *In: Yukon Exploration and Geology 2009*, K.E. MacFarlane, L.H. Weston and L.R. Blackburn (eds.), Yukon Geological Survey, p. 119-133.

ABSTRACT

In August 2008, reactivation of the Little Salmon Lake landslide occurred. During this event, hundreds of conical mounds of variable size and composition formed in the deposition zone. The characteristics of these landforms are described and a potential mechanism for their formation is proposed. A preliminary slope stability analysis of the 2007 Mount Steele rock and ice avalanche was also undertaken. The orientation of very high persistence (>20 m long) structural planes (e.g., faults, joints and bedding) within bedrock in the source zone was obtained using an airborne-LiDAR digital elevation model and the software COLTOP-3D. Using these discontinuity orientation measurements, kinematic, surface wedge and simple three-dimensional distinct element slope stability analyses were performed.

¹mbrideau@sfu.ca

THE LITTLE SALMON LAKE LANDSLIDE REACTIVATION

INTRODUCTION

The Little Salmon Lake landslide is located on a moderately steep (15° - 25°) north-facing slope on the south shore of Little Salmon Lake (Figs. 1, 2). The landslide has been previously described by Lyle (Lyle *et al.*, 2005; Lyle, 2006) who suggested that it originated as a deep-seated rotational bedrock slump prior to 1949. In recent years, rockfall activity was observed at the headscarp and the disintegrated slump blocks have moved noticeably since 1989 (Lyle, 2006). The headscarp of an older landslide is located 250 m above the currently active headscarp. Lyle (2006) suggested that the Little Salmon Lake landslide occurs within this larger relict landslide, and noted graphitic layers in the bedrock which may have formed part of the original failure plane.

The former landslide debris was reactivated in a large debris flow/avalanche some time between August 22 and 28, 2008 following a period of higher than normal precipitation. The 2008 reactivation involved little additional material from the headscarp. Instead, bedrock slump blocks and colluvial surficial materials located below the headscarp were mobilized in the debris flow, travelling a horizontal distance of 2050 m and descending 515 m in elevation into Little Salmon Lake, *i.e.*, a $\Delta H/L$ ratio of 0.25. A conservative estimate of the volume of material involved is on the order of 1 Mm^3 , assuming a



Figure 2. View of the Little Salmon Lake landslide.

2 m deposit thickness across a $400\,000 \text{ m}^2$ area. Numerous large trees with trunks up to 50 cm in diameter were pushed over and deposited along the margins of the lower debris flow.

The bedrock material associated with the original slope failure is part of the Snowcap Assemblage, which regionally consists of psammitic schist, quartzite, dark grey carbonaceous schist, calc-silicate rocks, minor amounts of marble, and local amounts of amphibolite, greenstone and ultramafic rocks of Devonian age and older (Colpron *et al.*, 2002; Piercey and Colpron, 2009).

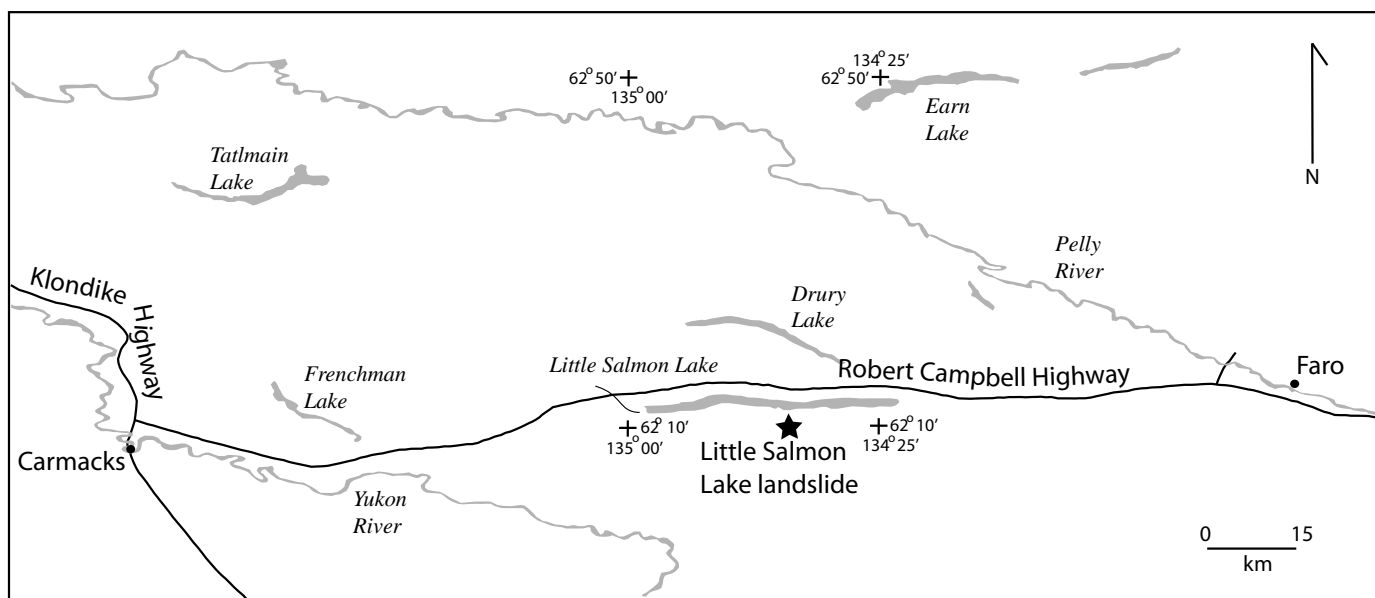


Figure 1. Location of the Little Salmon Lake landslide.

DESCRIPTION OF THE DEPOSIT AND ITS PROPERTIES

The upper part of the landslide deposit consists of tens of large slump blocks, most of which are still vegetated (Fig. 3). The slumped blocks have dimensions on the order of 10 x 10 x 20 m (height x length x width). Two sag ponds were observed behind slumped blocks on the western upper portion of the deposit. Hundreds of conical mounds of distinctly variable colour and varying in height from 0.3 m to 10 m (Fig. 4) comprise the central and lower sections of the deposit. A great majority of the mounds are composed of disintegrated bedrock of unimodal lithology, including yellow quartzite, grey schist and dark grey graphitic schist while others are composed



Figure 3. Slumped block of broken bedrock in the upper section of the landslide deposit.



Figure 4. Conical mounds in the central and lower portion of the landslide deposit. Helicopter circled for scale.

of brown gravel-size surficial material. Where the material in the mounds is derived from two lithologies, the contact between them is sharp (Fig. 5). Some mounds have a thin layer of tephra at their pinnacle. The materials comprising the mounds are generally clast-supported, although occasionally consist of exclusively fine-grained clay-rich material. The clasts primarily consist of medium gravel to small cobbles, with occasional larger cobbles up to 50 cm. The average slope angle of the conical features is between 35° and 37° (Fig. 6a). These values correlate with the angle of repose of gravel which is reported to be between 35° and 40°. Field assessment of the density categories for the conical landforms revealed that they could be excavated with a shovel (S2 and S3) while some needed a pick for excavation (S4) (classification from BC Ministry of Forests, 2002; Fig. 6b).

PERMAFROST AND GROUND ICE

A reconnaissance visit was made at the landslide on September 18, 2008. At that time, frost probing in the undisturbed mature spruce forest adjacent to the lower landslide deposit revealed an active layer that varied in thickness from 51 to 65 cm. Large angular blocks of ice-rich stratified colluvium up to 11 m in height were also noted in the landslide deposit (Fig. 7). Clastic material was actively ravelling from these blocks as they rapidly thawed, which prevented detailed investigations at the time. It was noted that the ravelling fragments were accumulating at the base of the frozen blocks in a conical form. Segregated ice content was visually estimated to be 50% in an approximately 9 m tall block. Frozen blocks were not observed when the site was next visited in July 2009.



Figure 5. Conical mound with bi-modal lithologies (graphitic schist and quartzite).

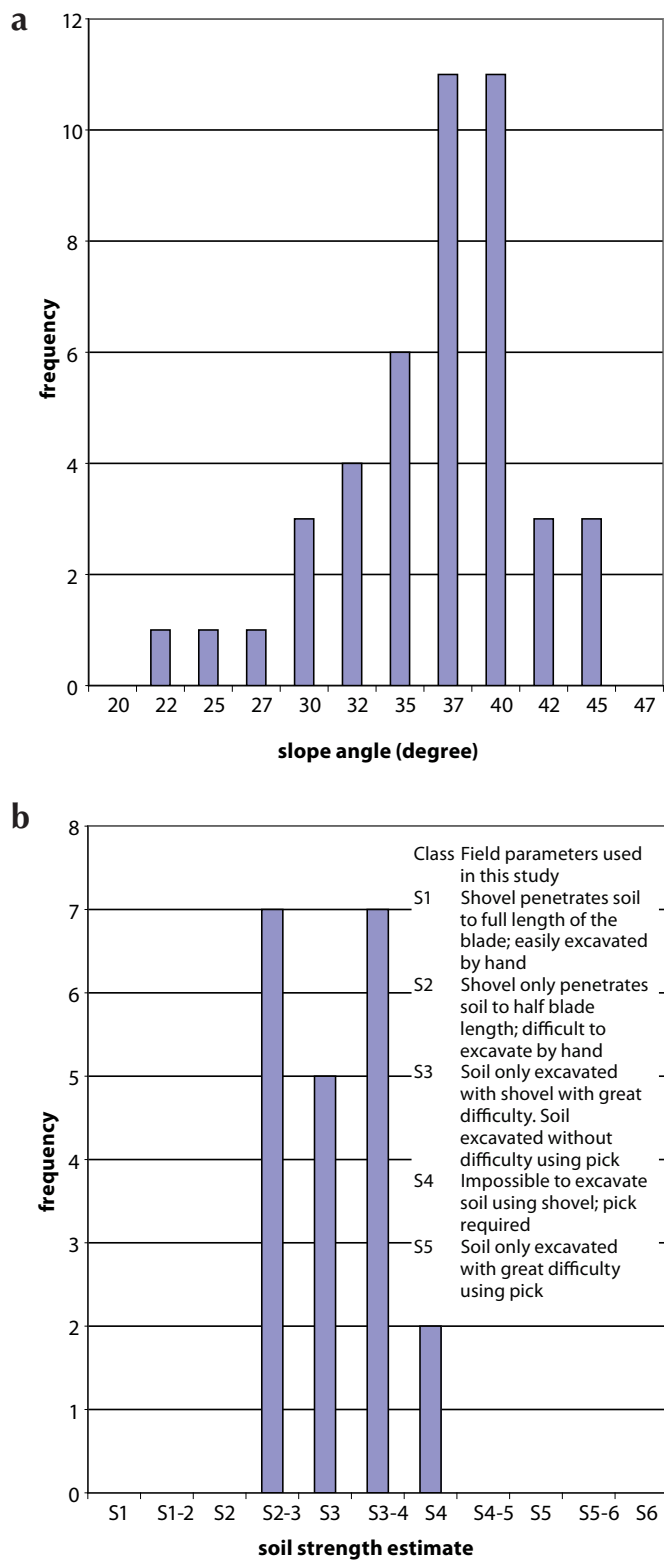


Figure 6. (a) Histogram of the slope angle of the sides of the conical mounds, (b) Material strength categories of the conical mounds.

Ten conical mounds (of varying sizes) were excavated to 0.5 m depth during the week of July 5, 2009 and no ice was observed in them at that time. Soil temperatures were measured (using a household-grade thermometer) at a depth of 0.5 m in these mounds and were found to be 8°C while the ambient air temperature was 23°C. A solid ice lens approximately 10 cm thick was, however, identified in a fractured bedrock slump block found in the upper part of the deposit (Fig. 8).



Figure 7. Frozen angular block of surficial material observed in 2008 in the landslide debris. Person circled for scale.



Figure 8. Ice lens observed at the front of a slumped block of highly broken-up schist.

FORMATION OF CONICAL MOUNDS

The presence of conical mounds in large landslide deposits has long been noted in landslide research, and the features are commonly referred to as molards (McConnell and Brock, 1904; Griggs, 1920; Shreeve, 1966). Several mechanisms for the formation of these landforms have been proposed, as summarized below.

1. Finer debris accumulates around a large boulder core as the landslide comes to rest (Goguel and Pachoud, 1972).
2. The mounds are formed by the vibration of the ground beneath a large landslide (Cassie *et al.*, 1988).
3. Formation of the mounds may be associated with the presence of a cohesive layer between two frictional layers in the original failed material (Shea and van Wyk de Vries, 2008). This heterogeneity leads to a differential deformation rate which in turn results in the formation of hummocks.
4. The mounds form when the velocity of the debris in the flow direction is less than the velocity perpendicular to the flow direction (Dufresne and Davies, 2009).
5. In landslides involving saturated fine-grained material, the mounds are formed from sand or silt boils associated with the release of excess pore pressure (Evans *et al.*, 2009).

The presence of tephra caps on some of the mounds, the dominantly unimodal lithological composition, or sharp contact between lithologies in the case of bimodal mounds and the internal structures (sharp contact between lithologies and stratification in mounds composed of surficial material), all argue against a turbulent or pore pressure release of liquefied material as an emplacement mechanism. The accumulation of surficial material around a boulder core as a formation mechanism is also inconsistent with our field observations. The mechanism we suggest for the formation of the conical mounds at the Little Salmon Lake landslide is that cohesive or frozen blocks of surficial material and fractured rock are mobilized by high pore water pressure in the surrounding saturated sediments. These blocks are rafted downslope in the main body of the landslide and subsequently melted and/or dried to form conical features after they have come to rest in the deposit zone. In this proposed mechanism, the ice would provide the cohesion in a fashion similar to the wet sand in the physical models of Shea and van Wyk de Vries (2008).

ROCK MASS

The rock mass quality was assessed using the Geological Strength Index (GSI) which was originally proposed by Hoek and Brown (1997) and later modified by Marinos and Hoek (2000). The GSI chart provides a quantification of the rock mass quality based on field observations of the structure present in the rock mass and the surface

condition of the discontinuities. The applications and limitations of the GSI approach are discussed in Marinos *et al.* (2005) and Brown (2008). The rock mass quality as observed in the headscarp and sidescarps was low, corresponding to a range between 30 and 45 on the GSI chart (Fig. 9). The rock mass has a persistent and pervasive schistose foliation and four discontinuity sets

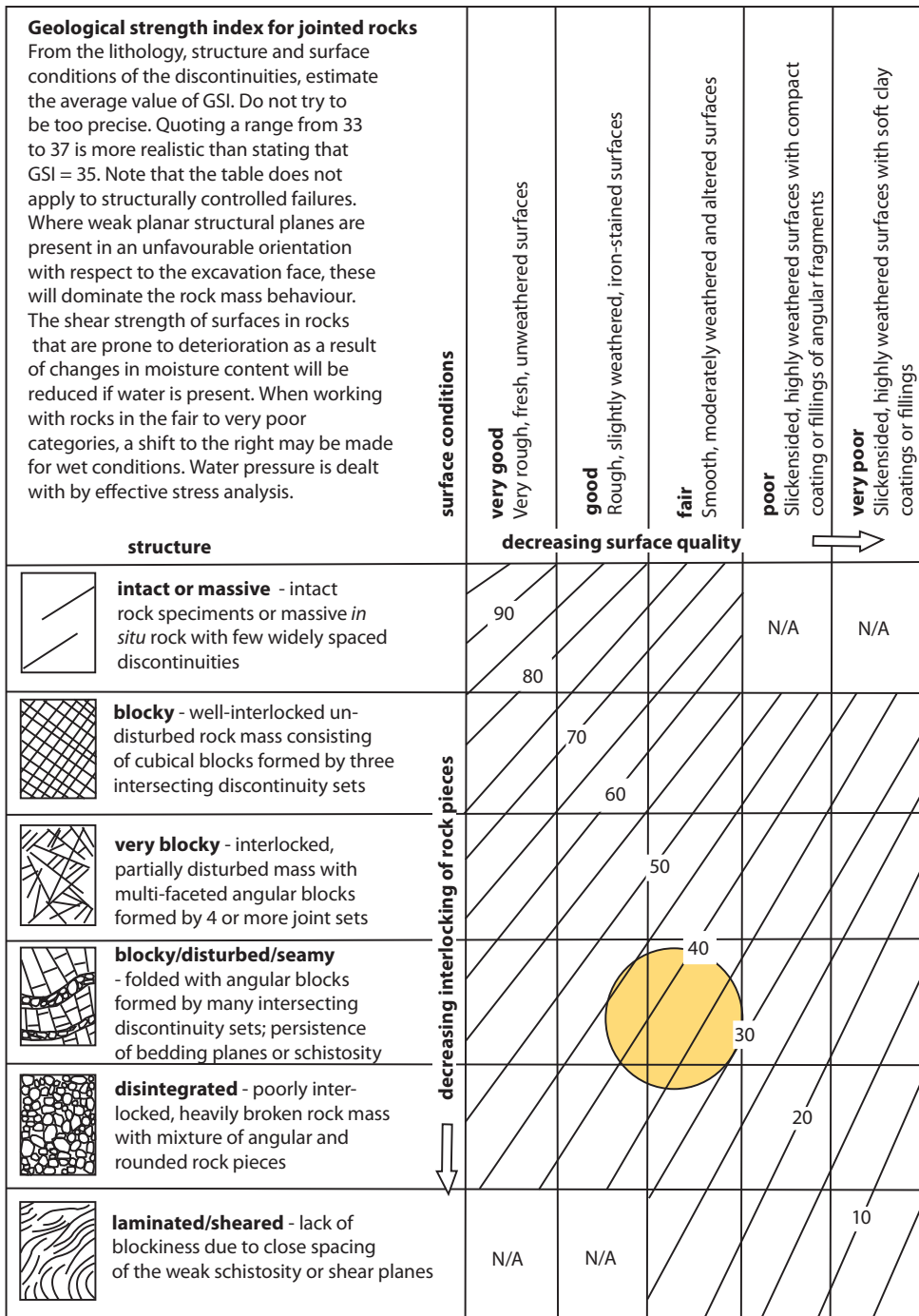


Figure 9. Geological Strength Index chart highlighting the range of rock mass quality observed in the headscarp and sidescarp of the Little Salmon Lake landslide.

which places it at the intersection of the very blocky and blocky/disturbed/seamy rock mass structure categories. Zones of intense weathering often correspond to graphite-rich layers. The discontinuity surface conditions were dominantly fair in the schistose units with some good conditions in the quartzite layers. Such low rock mass qualities are typically associated with zones of tectonic deformation and/or zone of intense alteration and weathering. This could not be rigorously confirmed at the Little Salmon Lake landslide due to the active rockfall activity which restricted access to the headscarp. Groundwater seepage was also observed in various parts of the headscarp and sidescarps. The low rock mass quality suggests that the slope stability is, at least in part, controlled by the rock mass strength.

KINEMATIC ANALYSIS

A limited number ($N = 87$) of discontinuity (foliation and joints) orientation measurements were acquired in the sidescarp of the landslide and used to conduct a kinematic analysis. A kinematic analysis is a geometric test, which uses for the average slope orientation an assumed discontinuity friction angle and the discontinuity measurements to assess the feasibility of simple failure mechanisms (Fig. 10). The stereographic techniques used to kinematically assess the feasibility of the planar, wedge and toppling failure mechanisms are outlined in Wyllie and Mah, 2004. Poles (Figs. 10a and 10c) or intersection of planes (Fig. 10b) which fall within the shaded area of the stereonet indicate a feasible failure mechanism. The results suggest that planar sliding (Fig. 10a) and wedge failures (Fig. 10b) are feasible with an assumed 40° slope angle and a 30° friction angle (angle at which a block would slide along an inclined plane) along the discontinuity surfaces. Only one discontinuity falls within the toppling envelope (Fig. 10c).

SUMMARY

The 2008 reactivation of the Little Salmon Lake landslide primarily involved the mobilization of debris from a previous slope failure at the same location. The surface of

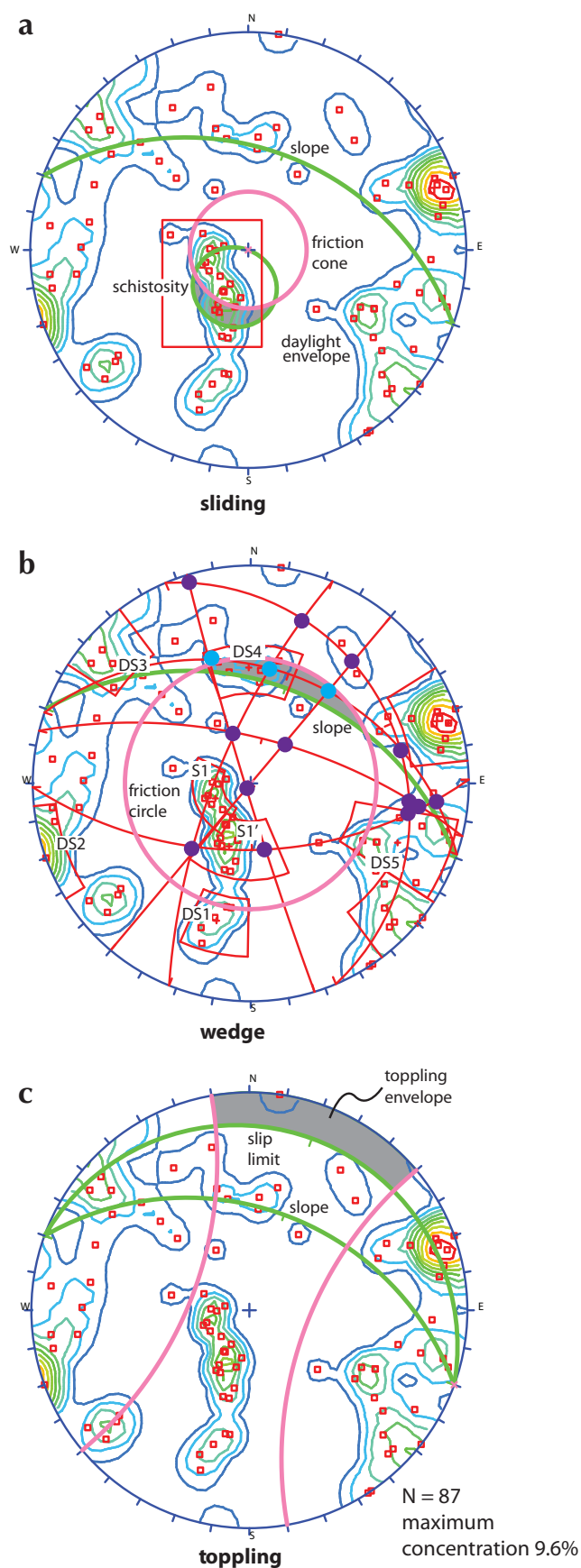


Figure 10. Summary of the kinematic analysis performed on the poles to the discontinuities measured in the sidescarp of the Little Salmon Lake landslide. (a) sliding, (b) wedge, (c) toppling failure mechanism (lower hemisphere projection, equal angle stereonet).

the latest landslide deposit is distinctly characterized by hundreds of conical mounds up to 10 m tall. The most likely mechanism of mound formation is that blocks of frozen colluvium or heavily fractured bedrock moved downslope as coherent masses and subsequently melted into cones with slopes at their angle of repose. The slope stability conditions of the initial Little Salmon Lake landslide were probably controlled by both the rock mass strength (as suggested by the low rock mass quality observed) and by the discontinuities present (suggesting planar sliding and wedge failures).

It is important to note that the geomorphic setting of the Little Salmon Lake landslide is not unique to the area and at least two other large permafrost-related landslides are found within 20 km of this landslide (Lyle, 2006). The fact that pre-existing landslide debris can be reactivated in large destructive landslides has serious implications concerning the location of future development in similar geomorphic settings. The south shore of Little Salmon Lake was intensely burned in a severe forest fire during the summer of 2009 which may significantly affect future slope stability in the area due to altered ground temperature, loss of soil strength associated with the vegetation and soil moisture conditions. A reconnaissance flight on September 25, 2009 revealed that the entire forest surrounding the Little Salmon Lake fire had been completely burned and that numerous shallow landslides had recently occurred on nearby slopes.

MOUNT STEELE 2007 ROCK AND ICE AVALANCHE

INTRODUCTION

On July 24 2007, a large rock and ice avalanche occurred on Mount Steele, located in an uninhabited area of the Kluane National Park in southwestern Yukon (Fig. 11). The mountain lies within the Icefield Ranges of the St. Elias Mountains. The slope failure was on the north face of the mountain (Fig. 12) which has been regionally mapped within a belt of Late Miocene Wrangell Suite granodiorite, diorite and gabbro lithologies (Dodds and Campbell, 1992). Hornblende-biotite-quartz diorite, tonalite and plagioclase-hornblende-biotite porphyry lithologies were observed in rock fragments collected in the deposit zone (Lipovsky *et al.*, 2008a).

Several smaller avalanches were noted in the weeks leading up to the July 24th event. The main and preceding events have been described by Lipovsky *et al.* (2008a,b).

The debris travelled 5.76 km horizontally with a vertical descent of 2160 m for a resultant $\Delta H/L$ ratio of 0.32. The seismic record suggests that the main event lasted approximately 100 seconds and consequently the minimum average velocity of the avalanche was 35 m/s.

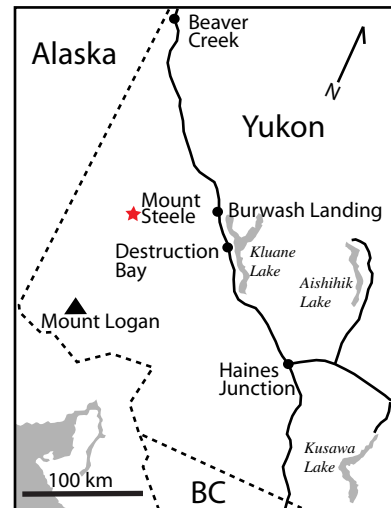


Figure 11. Location of the Mount Steele rock and ice avalanche.

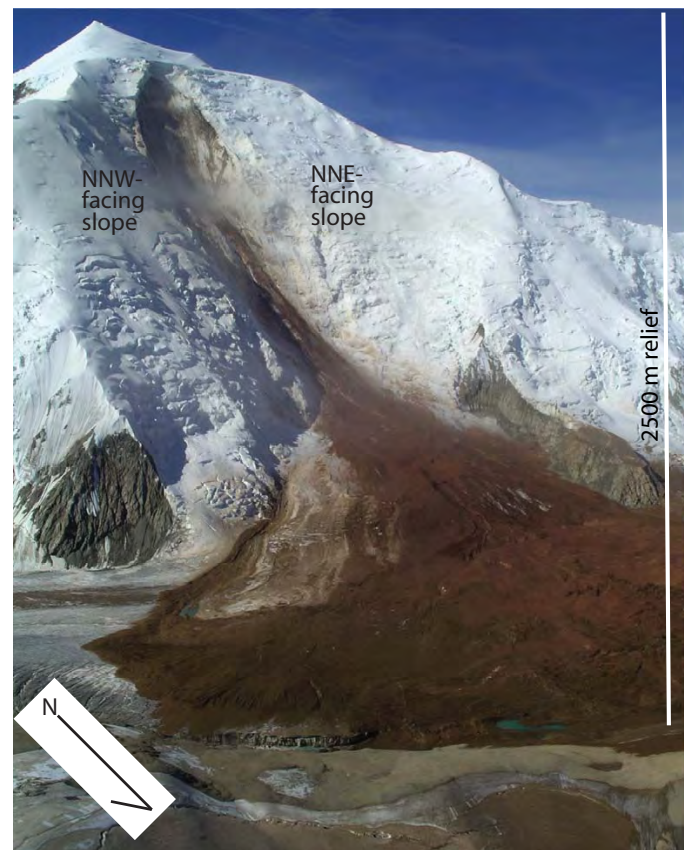


Figure 12. View of the Mount Steele rock and ice avalanche.

The debris covered an area of 3.66 km² with a thickness varying between 4 and 22 m, which suggests a bulked volume between 27.5 and 80.5 Mm³. The failures are not thought to have been triggered by earthquakes or the warmer-than-average, but not abnormally warm temperatures that occurred in the 10 days prior to the main failure.

DISCONTINUITY ANALYSIS USING COLTOP-3D

The software COLTOP-3D (Jaboyedoff *et al.*, 2004) was used to derive surface orientation based on airborne-LiDAR DEM of the Mount Steele area. COLTOP-3D assigns a colour to each cell in the DEM based on the dip and dip direction orientation of its pole. Zones of constant orientation are highlighted and assumed to represent a structural surface in the bedrock such as

bedding, persistent joints and/or faults. These zones of constant orientation are manually identified by the user. COLTOP-3D has been previously used on several rock slope stability case studies (Derron *et al.*, 2005; Pedrazzini *et al.*, 2008; Jaboyedoff *et al.*, 2009; Metzger *et al.*, 2009). Due to the extensive ice cover in the study area, surface orientations could only be obtained from the initiation zone of the landslide and from the east-facing rock wall in the gully that the landslides followed (Fig. 13).

Three discontinuity sets (DS1, DS2, DS3) were identified in the landslide scarp using COLTOP-3D (Fig. 14). They correspond to the discontinuities identified by Lipovsky *et al.* (2008a). DS3 may have a subset with a steeper dip, which is shown as DS3' in Figure 14. Two other discontinuity sets (DS4 and DS5) were also noted in

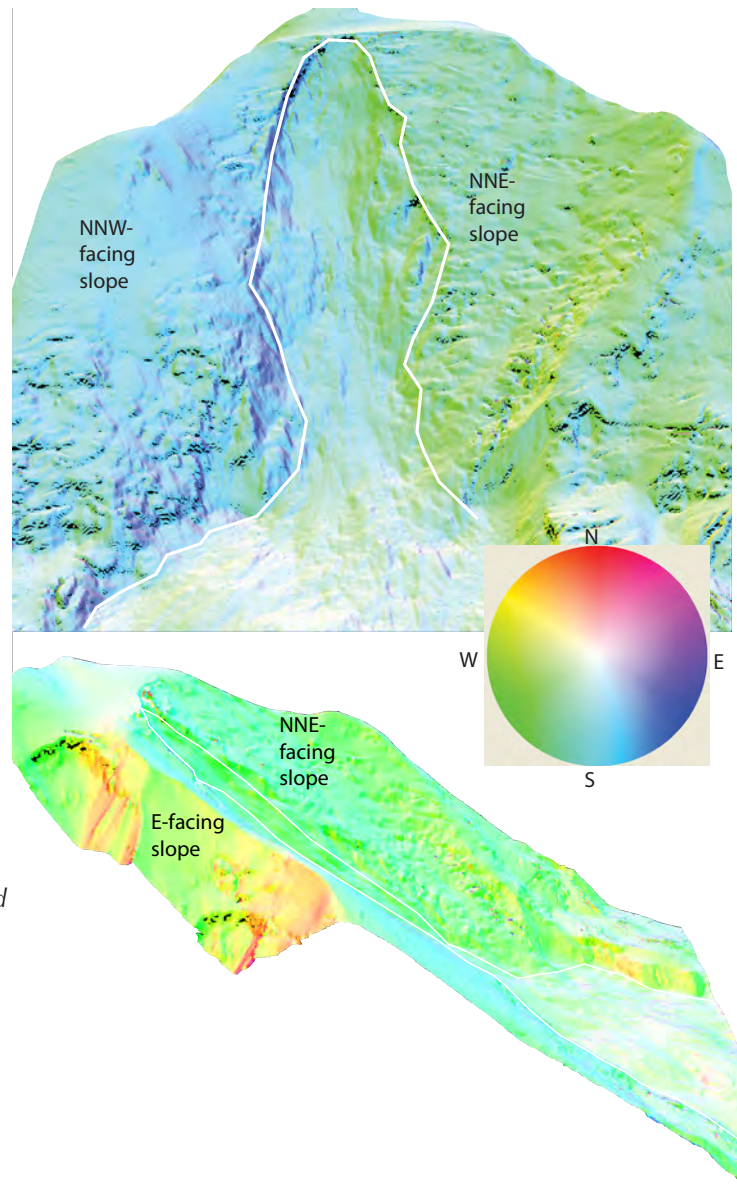


Figure 13. COLTOP-3D rendered view where the digital elevation model is coloured as a function of the dip and dip direction of each cell. The inset stereonet provides the colour coding for the surfaces.

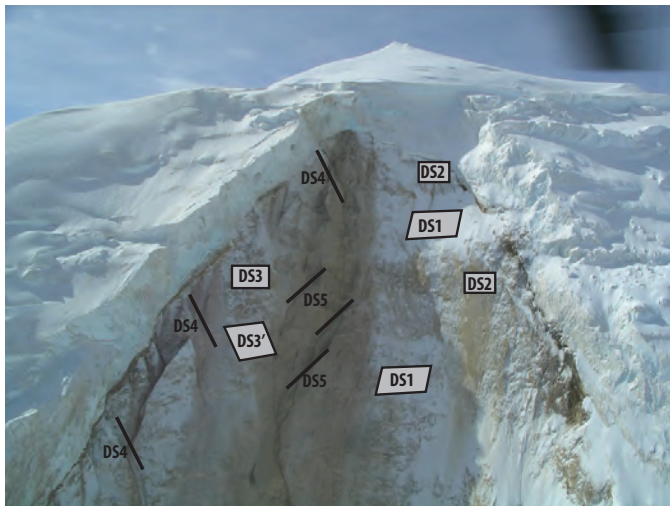


Figure 14. Headscarp of the Mount Steele rock and ice avalanche with the identified discontinuities annotated.

photographs of the headscarp but are dipping into the slope and therefore cannot be resolved in the landslide scar using COLTOP-3D. Upon further investigation of the east-facing gully wall using the LiDAR-derived DEM of Mount Steele, two more surfaces were recognized having orientations consistent with the planes (DS4 and DS5) highlighted in the photograph (Fig. 14).

KINEMATIC ANALYSIS

A preliminary kinematic analysis was performed using a friction angle of 30° along the discontinuity surfaces. Since the failure occurred in a broad gully, two slope surfaces were considered in this analysis. The pre-failure topography was approximated by projecting the orientation of the slope on either side of the landslide source zone into the existing landslide scar. Two such surfaces were defined using COLTOP-3D: a north-northeast wall with dip/direction 42°/018° and a north-northwest wall with dip/direction 45°/340°. The kinematic analysis revealed that sliding failure was feasible on DS1 in the north-northeast wall (Fig. 15a) as suggested by Lipovsky *et al.* (2008a) and that sliding was only marginally feasible on DS1 and DS3 in the north-northwest wall. Wedge failures were feasible along

Figure 15. Summary of the Mount Steele kinematic analysis performed on the poles to the surfaces obtained using COLTOP-3D. (a) sliding, (b) wedge, (c) toppling failure mechanism (lower hemisphere projection, equal angle stereonet).

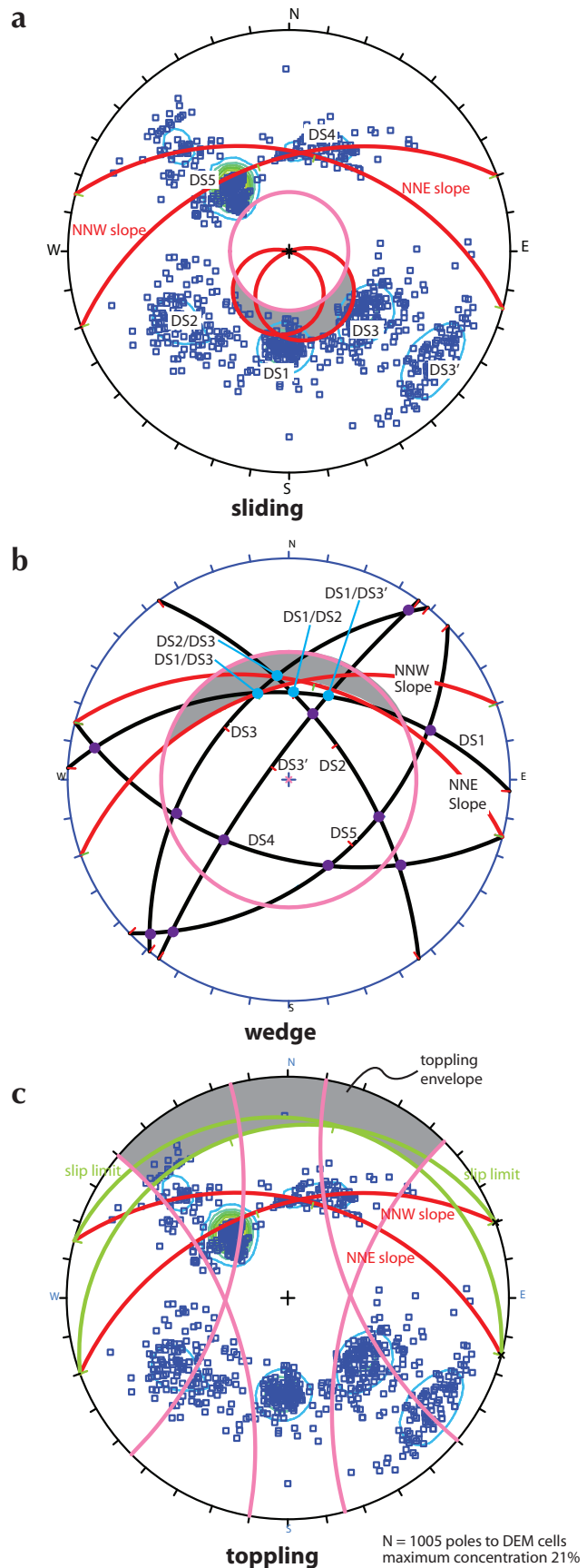


Table 1. Summary of the surface wedge combination analysis conducted using the software Swedge.

	Slope face orientation (dip/dip direction)	
	42°/014° north-northeast	45°/340° north-northwest
Number of combinations	504510	504510
Number of valid wedges	123726	98085
Number of stable wedges	114825 (93%)	77573 (79%)
Number of failed wedges	8901 (7%)	20512 (21%)
Cumulative weight of wedges with FOS<2 (tones)	317E6	429E6

intersections between DS1 and DS3 and DS2 and DS3 in the north-northwest wall; they were only marginally feasible along the intersections between DS1 and DS3' and between DS2 and DS3 in the north-northeast wall and between DS1 and DS2 in the north-northwest wall (Fig. 15b). Toppling was shown to be marginally feasible along discontinuity orientations which represent outliers to DS5 in the north-northwest wall (Fig. 15c).

SURFACE WEDGE ANALYSIS

The limit equilibrium code “Swedge” (Rocscience, 2006) was used to investigate the stability of rock wedges in the various rock slope walls on the northern face of Mount Steele. The combination analysis in Swedge applies a user defined list of discontinuities to calculate the factor of safety (FOS) for each valid wedge intersection for a given slope face. The results of the combination analysis are based on the surface orientations obtained using COLTOP-3D. The analysis was carried out assuming a 30° friction angle on all discontinuity surfaces and a maximum discontinuity persistence of 100 m. The summary of the Swedge combination analyses (Table 1) suggests more wedges and a potentially larger cumulative volume of wedges with a FOS <2 on the north-northwest wall than on the north-northeast wall. The FOS <2 was chosen as a conservative threshold for the calculated stability conditions of the wedges to account for the uncertainty associated with friction angle along the discontinuity surface, discontinuity persistence, the natural variability in the slope face orientation and the pore water pressure conditions in the ice/rock mass.

THREE-DIMENSIONAL DISTINCT ELEMENT ANALYSIS

3DEC (Itasca, 2008) is a three-dimensional distinct element code which represents a rock mass as a collection of blocks bounded by planes (*i.e.*, discontinuities). The constitutive model (rigid, elastic, elasto-plastic), the strength of the material inside the blocks and the shear and tensile strength along the surfaces bounding the blocks can be specified by the user. 3DEC allows for large displacement and rotation of the modelled blocks. More information about 3DEC can be obtained in Cundall (1988) and Hart *et al.* (1988). Preliminary 3DEC models were constructed using rigid blocks and an assumed 30° friction angle along all discontinuities. The geometry of the north face of Mount Steele was modelled as two planes (north-northeast and north-northwest walls) approximating the pre-failure topography of the broad gully as previously described. The spacing of all discontinuity sets in these preliminary models was assumed to be 75 m. The first model assumed that only DS1, DS2, DS3 and DS3' were present, which resulted in a large failure on the north-northwest-facing slope (Fig. 16a). The second model incorporated all six identified discontinuity sets (DS1, DS2, DS3, DS3', DS4 and DS5). As in the previous model a large failure was modelled on the north-northwest-facing slope (Fig. 16b). The results demonstrate that DS1, DS2, DS3 and DS3' play an important role in the stability of the models while DS4 and DS5 appear to be less important. The rock slope failures in both models appear to be restricted to the north-northwest-facing slope.

DISCUSSION

The kinematic, Swedge and 3DEC analyses all suggest that the north-northwest-facing wall (or east side) is the least stable of the two main faces present on the north side of Mount Steele. That is in contrast with the observed failure which occurred at the intersection of the north-northeast and north-northwest-facing walls. This could be due to the fact that the model does not incorporate other factors which may have played an important role in the failure, such as ice cover, groundwater influence and the presence of a large tectonic structure or zone of low rock-mass quality which could not be identified using COLTOP-3D due to the thick ice cover. For example, the Mount Steele landslide may have initiated as an ice avalanche which “plucked” and entrained the underlying rock mass. A large rock and ice avalanche similar to the Mount Steele landslide occurred in 2005 at Mt. Steller in

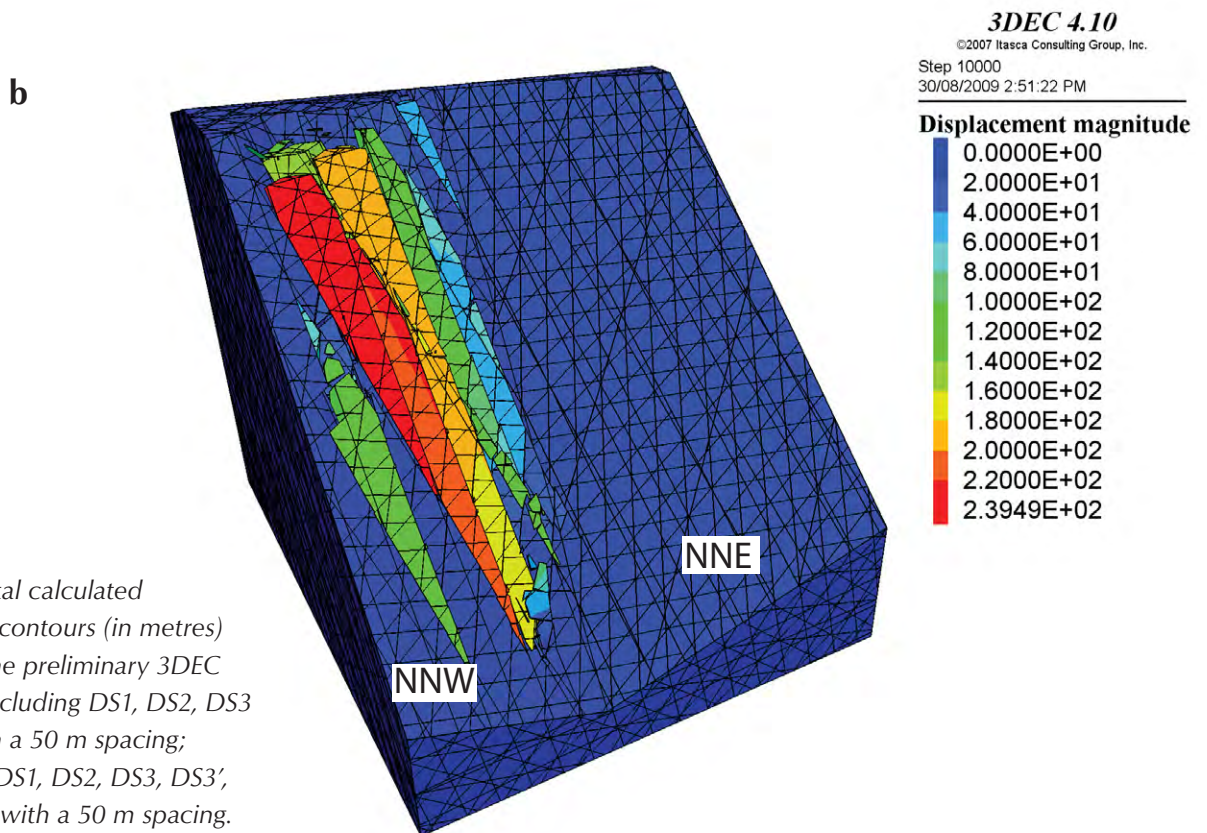
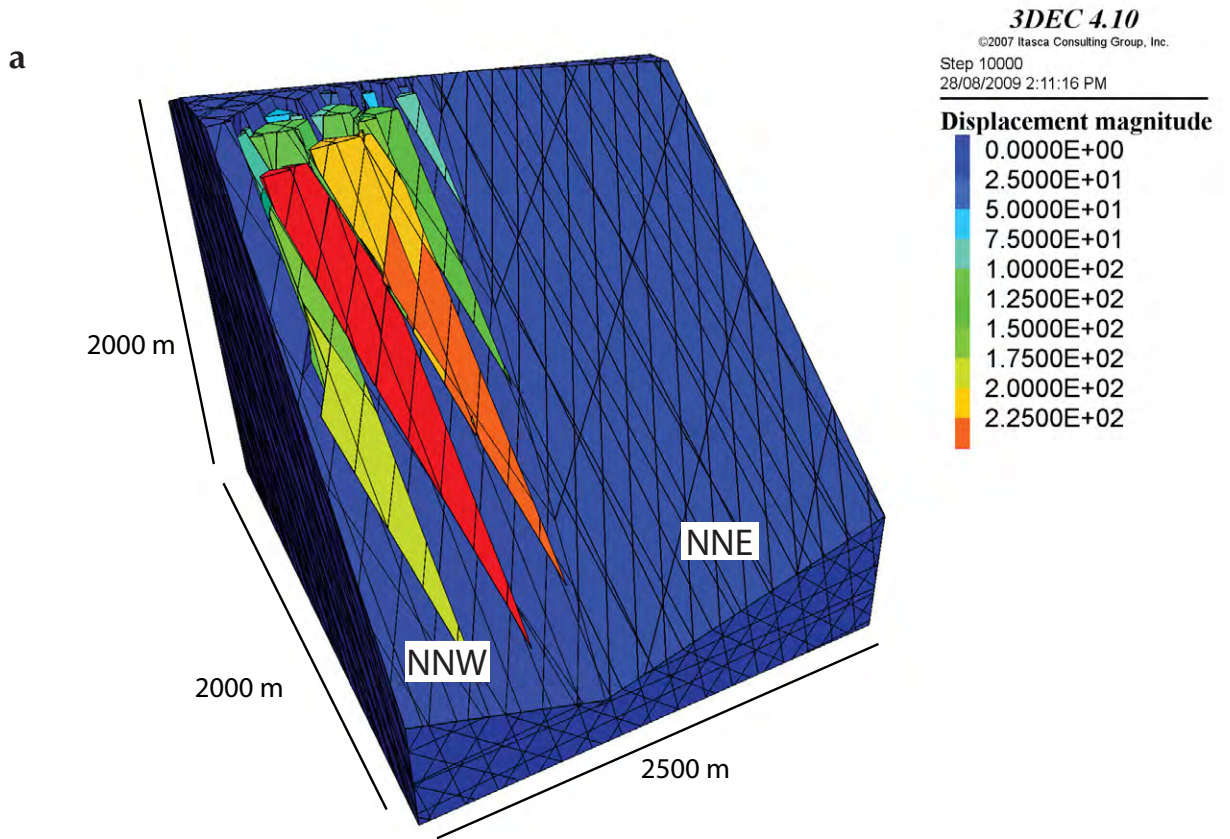


Figure 16. Total calculated displacement contours (in metres) obtained in the preliminary 3DEC models; **(a)** including DS1, DS2, DS3 and DS3' with a 50 m spacing; **(b)** including DS1, DS2, DS3, DS3', DS4 and DS5 with a 50 m spacing.

Alaska (Huggel *et al.*, 2008). Investigators conducted thermal modelling which highlighted that a hanging glacier in the summit area may have promoted warmer ground temperatures and reduced the stability of the underlying permafrost (Huggel *et al.*, 2008). A similar hanging glacier appears to have been present on the north face of Mount Steele and thermal modelling should be included in further slope stability investigations of the site. Finally, it should be highlighted that the quality of the remotely acquired discontinuity orientation data was not verified using other techniques (e.g., ground measurements, photogrammetry or ground-based LiDAR). This introduces a certain degree of uncertainty in the subsequent slope stability analyses, but in remote and inaccessible study sites such as Mount Steele it is not always possible or feasible to obtain alternate data.

SUMMARY

The orientation of very high persistence discontinuity surfaces (>20 m long; ISRM, 1978) in the 2007 Mt. Steele landslide initiation zone were successfully measured from airborne-LiDAR-generated DEM using the software COLTOP-3D. These surface orientations were consistent with discontinuity sets previously identified in photographs of the failure headscarp. The surface orientations were subsequently used to perform a preliminary investigation of slope stability controls at the study area. All analyses suggest that the north-northwest-facing portion of Mount Steele's north face is the least stable. This is inconsistent with the observed failure which occurred at the intersection between north-northeast and north-northwest-facing slopes. This discrepancy highlights that other factors, such as ice cover morphology, groundwater conditions and rock mass strength which were not included in the preliminary slope stability models, may have been more important contributing factors to the 2007 rock and ice avalanches on Mount Steele.

CONCLUSION

This paper presents a preliminary description and slope stability analyses of two recent large landslides in Yukon. The first section of this paper describes some distinctive surface features present in the 2008 Little Salmon Lake landslide deposit. Hundreds of conical mounds in the deposit were found to be dominantly composed of material derived from a unimodal lithology. They varied in height from 0.3 to 10 m and had an average slope angle between 35° and 37°. Field observations suggest that the

mounds were not formed from rapid and turbulent transport or deposition. Rather they suggest that frozen blocks of surficial material and fractured rock were mobilized by surrounding saturated sediments with high pore water pressure. Once the blocks came to rest in the deposit zone, they subsequently melted forming conical mounds shape. The rock mass in the headscarp of the Little Salmon Lake landslide was described using the Geological Strength Index (GSI) and was found to be of low quality.

The second section presents a preliminary slope stability analysis of the June 2007 Mount Steele rock and ice avalanche. An airborne-LiDAR digital elevation model (DEM) was used in conjunction with the software COLTOP-3D to obtain the orientation of very high persistence (>20 m) surfaces. These surfaces were assumed to represent discontinuities in the rock mass and their orientation was subsequently used to conduct slope stability analyses. All the analyses performed suggest that a slope failure was more likely to occur on a different portion of Mount Steele's north face than what actually occurred in 2007. This suggests that external factors not incorporated into the analyses (such as high pore water pressure, the influence of the overlying glacier and/or low rock mass strength resulting from tectonic damage, alteration and weathering), played a greater role in causing the 2007 rock and ice avalanches than the structural characteristics of the local bedrock. All of these scenarios should be considered in future investigations.

ACKNOWLEDGEMENTS

The authors would like to thank Tim Sivak (2009) and Kristen Kennedy (2008) for their assistance in the field at the Little Salmon Lake landslide and Ryan Lyle, Jean Hutchinson and Brent Ward for discussions on slope stability in the Little Salmon Lake area. Funding for this project was provided by the Yukon Geological Survey, Northern Scientific Training Program, NSERC and an SFU graduate fellowship. Matthieu Sturzenegger provided a critical review of the manuscript.

REFERENCES

- BC Ministry of Forests, 2002. Forest Practices Code of British Columbia - Forest Road Engineering Guidebook Second Edition. Government of British Columbia, Victoria, BC, 218 p.

- Brown, E.T., 2008. Estimating the mechanical properties of rock masses. *In*: Southern Hemisphere International Rock Mechanics Symposium 2008, Y. Potvin, J. Carter, A.V. Dyskin and R. Jeffrey (eds.), Perth, Australia, p. 3-22.
- Cassie, J.W., van Gassen, W. and Cruden, D.M., 1988. Laboratory analogue of the formation of molards, cones of rock-avalanche debris. *Geology*, vol. 16, p. 735-738.
- Colpron, M., Murphy, D.C., Nelson, J.L., Roots, C.F., Gladwin, K., Gordey, S.P., Abbott, G. and Lipovsky, P.S., 2002. Preliminary geological map of Glenlyon (105L/1-7, 11-14) and northeast Carmacks (115I/9, 16) areas, Yukon Territory (1:125 000 scale). Indian and Northern Affairs Canada, Exploration and Geological Services Division, Yukon Region, Open File 2002-9, 1:150 000 scale.
- Cundall, P.A., 1988. Formulation of a three-dimensional distinct element model - Part I. A scheme to detect and represent contacts in a system composed of many polyhedral blocks. *International Journal of Rock Mechanics and Mining Sciences & Geomechanics Abstracts*, vol. 25, no. 3, p. 107-116.
- Derron, M.-H., Jaboyedoff, M. and Blikra, L.H., 2005. Preliminary assessment of rockslide and rockfall hazards using a DEM (Oppstadhornet, Norway). *Natural Hazards and Earth System Science*, vol. 5, no. 2, p. 285-292.
- Dodds, C.J. and Campbell, R.B., 1992. Geology of Mount St. Elias map area (115B and C[E1/2]), Yukon Territory. Geological Survey of Canada, Open File 2189, 85 p.
- Dufresne, A. and Davies, T.R., 2009. Longitudinal ridges in mass movement deposits. *Geomorphology*, vol. 105, no. 3-4, p. 171-181.
- Evans, S.G., Roberts, N.J., Ischuk, A., Delaney, K.B., Morozova, G.S. and Tutubalina, O., 2009. Landslides triggered by the 1949 Khait earthquake, Tajikistan and associated loss of life. *Engineering Geology*, vol. 109, no. 3-4, p. 195-212.
- Goguel, J. and Pachoud, A., 1972. Géologie et dynamique de l'écroulement du Mount Granier, dans le Massif de Chartreuse, en novembre 1248, *Bulletin du Bureau de Recherche Géologique et Minière* vol. 1, p. 29-38.
- Griggs, R.F., 1920. The great Mageik landslide. *The Ohio Journal of Science*, vol. 20, no. 8, p. 325-354.
- Hart, R.D., Cundall, P.A. and Lemos, J.V., 1988. Formulation of a three-dimensional distinct element model - part II: Mechanical calculations for motion and interaction of a system composed of many polyhedral blocks. *International Journal of Rock Mechanics and Mining Sciences & Geomechanics Abstracts*, vol. 25, no. 3, p. 117-125.
- Hoek, E. and Brown, E.T., 1997. Practical estimates of rock mass strength. *International Journal of Rock Mechanics and Mining Sciences*, vol. 34, no. 8, p. 1165-1186.
- Huggel, C., Caplan-Auerbach, J., Gruber, S., Molnia, B.F. and Wessels, R.L., 2008. The 2005 Mt. Steller, Alaska, rock-ice avalanche: A large slope failure in cold permafrost. *In*: 9th International Conference on Permafrost, D.L. Kane and K. Hinkel (eds.), Fairbanks, Alaska, p. 747-752.
- ISRM, 1978. Suggested methods for the quantitative description of discontinuities in rock masses. *International Journal of Rock Mechanics, Mining Sciences and Geomechanics Abstract*, vol. 15, p. 319-368.
- Itasca, 2008. 3DEC v. 4.1, Itasca Consulting Group, Minneapolis, Minnesota
- Jaboyedoff, M., Baillifard, F., Couture, R., Locat, J., Locat, P. and Rouiller, J.-D., 2004. New insight of geomorphology and landslide prone area detection using DEM. *In*: 9th International Symposium on Landslides, W.A. Lacerda, M. Ehrlich, A.B. Fontoura and A. Sayo (eds.), Balkema, p. 199-205.
- Jaboyedoff, M., Couture, R. and Locat, J., 2009. Structural analysis of Turtle Mountain (Alberta) using digital elevation model: Toward a progressive failure. *Geomorphology*, vol. 103, no. 1, p. 5-16.
- Lipovsky, P.S., Evans, S.G., Clague, J.J., Hopkinson, C., Couture, R., Bobrowsky, P., Ekström, G., Demuth, M.N., Delaney, K.B., Roberts, N.J., Clarke, G. and Schaeffer, A., 2008a. The July 2007 rock and ice avalanches at Mount Steele, St. Elias Mountains, Yukon, Canada. *Landslides*, vol. 5, no. 4 p. 445-455.

- Lipovsky, P.S., Evans, S.G., Clague, J.J., Hopkinson, C., Couture, R., Bobrowsky, P., Ekström, G., Demuth, M.N., Delaney, K.B., Roberts, N.J., Clarke, G. and Schaeffer, A., 2008b. Reconnaissance observations of the July 24, 2007 rock and ice avalanche at Mount Steele, St. Elias Mountains, Yukon, Canada. *In: 4th Canadian Conference on Geohazards: From Causes to Management*, J. Locat, D. Perret, D. Turmel, D. Demers and S. Leroueil (eds.), Quebec City, p. 323-330.
- Lyle, R.R., Hutchinson, D.J. and Preston, Y., 2005. Landslide processes in discontinuous permafrost, Little Salmon Lake (NTS 105L/1 and 2), South-central Yukon. *In: Yukon and Exploration Geology 2004*, D.S. Emond, L.L. Lewis and G.D. Bradshaw (eds.), p. 193-204.
- Lyle, R.R., 2006. Landslide susceptibility mapping in discontinuous permafrost: Little Salmon Lake, Central Yukon. Unpublished MSc thesis, Department of Geological Sciences and Geological Engineering, Queen's University, Kingston, Ontario, 366 p.
- Marinos, P. and Hoek, E., 2000. GSI: A geologically friendly tool for rock mass strength estimation, *In: GEOENG 2000*, Technomic Publishing Co. Inc., Melbourne, Australia, p. 1422-1440.
- Marinos, V., Marinos, P. and Hoek, E., 2005. The Geological Strength Index: Applications and limitations. *Bulletin of Engineering Geology and the Environment*, vol. 64, no. 1, p. 55-65.
- McConnell, R.G. and Brock, R.W., 1904. Report on the great landslide at Frank, Alberta, 1903. Dominion of Canada, Department of the Interior, Annual report, 1903, part VIII, p. 3-17.
- Metzger, R., Jaboyedoff, M., Oppikofer, T., Viero, A. and Galgaro, A., 2009. COLTOP-3D: A new software for structural analysis with high resolution 3D point clouds and DEM. *In: Frontiers + Innovation: Canadian Society of Petroleum Geologists, Canadian Society of Exploration Geophysicists and Canadian Well Logging Society Joint Convention*, Calgary, Alberta, p. 278-281.
- Pedrazzini, A., Jaboyedoff, M., Froese, C., Langenberg, W. and Moreno, F., 2008. Structures and failure mechanisms analysis of Turtle Mountain. *In: 4th Canadian Conference on Geohazards*, J. Locat, D. Perret, D. Turmel, D. Demers and S. Leroueil (eds.), Quebec City, QC, p. 349-356.
- Piercey, S.J. and Colpron, M., 2009. Composition and provenance of the Snowcap assemblage, basement to the Yukon-Tanana terrane, northern Cordillera: Implication for Cordilleran crustal growth. *Geosphere*, vol. 5 no. 5, p. 439-464.
- Rocscience, 2006. Swedge v5.0, Rocscience Inc. Toronto, Ontario.
- Shea, T. and van Wyk de Vries, B., 2008. Structural analysis and analogue modeling of the kinematics and dynamics of rockslide avalanches. *Geosphere*, vol. 4 no. 4, p. 657-686.
- Shreeve, R.L., 1966. Sherman Landslide, Alaska. *Science*, vol. 154, p. 1639-1643.
- Wyllie, D.C. and Mah, C.W., 2004. *Rock Slope Engineering*, 4th Edition. SponPress, New York, 431 p.

Particle-size distribution of gold within the Sulphur and Dominion creek drainages, Klondike District, Yukon, and implications for gold winning and the formation of distal placers containing fine gold

R.J. Chapman¹ and D.P.G. Bond

School of Earth and Environment, University of Leeds, Leeds, United Kingdom

W. LeBarge²

Yukon Geological Survey

Chapman, R.J, Bond, D.P.G. and LeBarge, W., 2010. Particle-size distribution of gold within the Sulphur and Dominion creek drainages, Klondike District, Yukon, and implications for gold winning and the formation of distal placers containing fine gold. *In: Yukon Exploration and Geology 2009*, K.E. MacFarlane, L.H. Weston and L.R. Blackburn (eds.), Yukon Geological Survey, p. 135-142.

ABSTRACT

A reduced efficiency of gold recovery with decreasing particle size using a sluice box raises the possibility of a very fine gold resource within the Klondike. The grade of fine gold within gravel recovered from the southern Klondike was assessed using a combination of screening and bulk leaching by cyanidation. This approach eliminates the nugget effect and size ranges selected correspond to particle sizes exploitable by different metallurgical methods: <53 µm (cyanidation), 53-125 µm ('enhanced g' concentrators), 125-500 µm (sluice boxes). Colluvium, virgin gravel and tailings from various mining operations were collected from a relatively long drainage where accumulation of fine gold could feasibly occur. In all samples, gold <125 µm was negligible. Despite this negative result, this approach to resource evaluation is straightforward and could be applied advantageously in other areas where source mineralization contains fine gold. A distinction should be made between placer gold grains of fine but equant nature derived from proximal mineralization and gold rendered fine and flaky by fluvial transport.

¹*r.chapman@see.leeds.ac.uk*

²*bill.lebarge@gov.yk.ca*

INTRODUCTION

Although the total gold production from the Klondike District will never be known with any certainty, it is clear that the region hosts one of the world's major placer resources. The vast majority of the gold recovered to date has been separated from the host gravel by basic sluicing techniques, as operated both by small-scale mining operations and larger scale dredging operations. The recovery of fine gold using sluices becomes less efficient with decreasing gold particle size. Consequently, there is potential for a resource of fine gold either remaining in tailings or within virgin gravel.

Recovery of gold particles greater than 250 μm (60 mesh) in size using a simple sluice is usually straightforward, and previous studies on the presence of fine gold within placers and implications for metallurgical efficiency (e.g., Wenquian and Poling, 1983; Subasinghe, 1993; Clarkson, 1994) have focussed on the recovery of gold in the 150-250 μm (100-60 mesh) size fraction. Retention of gold of this size range in a sluice box is influenced by gravel pre-treatment, sluice design and operation. Empirical metallurgical data have shown that the recovery of gold in the 150-250 μm range varies substantially according to the sophistication of the processing circuit (Clarkson, 1989), a factor which has undoubtedly contributed to the successful reworking of some of the main placer areas in the Klondike goldfield. Analysis of the efficiency of gold recovery in Malaysian gold and tin dredges by Fricker (1984) indicates relatively low recoveries of fine gold, with 90% of the gold particles lost being less than 200 μm . Many of the main valleys in the Klondike goldfield were last exploited by dredging and consequently it is possible that a substantial amount of gold recoverable by traditional methods remains in the Klondike goldfield.

An extensive evaluation of metallurgical plant performance of placer operations in the Klondike was reported by Clarkson (1989, 1994). Samples of sluice tailings were collected and upgraded by shaking tables to characterize the efficiency of various processing circuits. On the basis of these tests it was concluded that fine (<140 μm , 100 mesh) gold formed only about 2% of the total gold head grade. However, this figure was based on recoveries in gravity concentration circuits and it could be that a resource of fine gold exists which is too small to be recovered in this way.

Metallurgical approaches to the recovery of fine gold have developed since the last major studies investigating

the recovery performance of placer mines. The advent of the Knelson concentrator and related 'enhanced g' separators has effectively lowered the gold particle size exploitable by gravity concentration circuits (e.g., Laplante *et al.*, 1996; Apling *et al.*, 1997) to a point where gold particles >53 μm in diameter are a valid target. However, recovery of placer gold is not only a function of particle size. Flaky gold grains, formed during fluvial transport, are particularly difficult to recover in conventional sluice circuits as a consequence of their modified settling velocities. Chapman and Houseley (1996) noted that the recovery of placer grains from a particular area may be very high because the gold grains have already been concentrated by hydraulic sorting. The implications of gold shape on recovery, and hence plant performance, have been quantified to some degree (Wenquian and Poling, 1983; Chapman and Houseley, 1996; Apling *et al.*, 1997). Wenquian and Poling (1983) recorded a strong correlation between gold shape and recovery for placer gold from the Fraser River in British Columbia. They noted that the gold lost from the combined jig/sluice processing was much flakier than that recovered, and that this effect was progressively more pronounced in the smaller size ranges. Although this effect can be alleviated to some extent using 'enhanced g' concentrators, their effective operation had more rigorous classification stages than are currently commonly employed within sluice circuits. Consequently it seems unlikely that simple substitution of Knelson concentrators for sluices within existing processing circuits would be of benefit unless a substantial resource of fine gold exists.

For very fine gold grain sizes, hydrometallurgical approaches are the only processing option, and there have been previous attempts to evaluate the suitability of cyanidation to treat White Channel Gravel (Macdonald, 1985). Cyanidation trials were hindered by the high clay content of the solid feed, although the more modern approach of Carbon in Pulp (CIP) or Carbon in Leach (CIL) process could alleviate this problem. Testwork carried out in a leaching column returned gold recoveries of 62%, which is a very low figure for the cyanidation of free gold and possibly reflects the presence of larger gold grains in the feed sample, which were only partially digested during the leaching period.

The potential benefits of applying 'enhanced g' concentrators or a hydrometallurgical approach to auriferous gravel in the Klondike may be assessed by characterization of the particle size of gold within the feed. The widespread belief that there is no fine-gold

resource in the Klondike is largely based on the observations of sluice box performance and the assertions of Clarkson (1989, 1994) that this resource is insignificant. However, recent exploration and associated research has provided two independent lines of evidence which suggests that fine gold could be present in concentrations greater than previously believed.

Klondike Star Mineral Corporation operated a pilot plant facility between 2005 and 2007. Several bulk samples (a total of about 150 tonnes) of ore from various localities on Lone Star Ridge and Hunker Dome (Fig. 1) were treated. Analysis of the gold from these sources indicates compositional consistency with gold from the adjacent placers (Chapman *et al.*, submitted, a,b). Metallurgical testwork in the pilot plant mill indicates an average recovery of 57% for samples from Lone Star Ridge and 44% for samples from Hunker Dome, *i.e.*, around half the gold from the *in situ* source was too small to collect in a simple gravity circuit under carefully controlled conditions. To some extent this low recovery could be ascribed to the generation of fine flaky gold within the mill, which is very difficult to recover by traditional gravity methods (Chapman and Houseley, 1996). However, it could be argued that the milling action of the ball mill is replicated during fluvial transport, so placer gold generated from fine *in situ* gold would also be difficult to recover by conventional gravity separation. If the *in situ* mineralization identified by Klondike Star is representative of the original eroded orebodies, which yielded the Klondike placers, then about half of the original gold remains unrecovered. Also, a recent study of a 5 g nugget from Last Chance Creek revealed a matrix surrounding the nugget impregnated with fine (1-3 μm) gold particles. Where primary gold has been available to study in the Klondike, there is some evidence for the presence of gold particles too small to recover by conventional sluicing.

The present study was designed to generate information concerning the variation in abundance of fine gold within the placer environment. In addition, it aimed to characterize any resource according to the metallurgical technique appropriate for that size range of gold. The data from this investigation could then directly inform subsequent metallurgical evaluations of the resource.

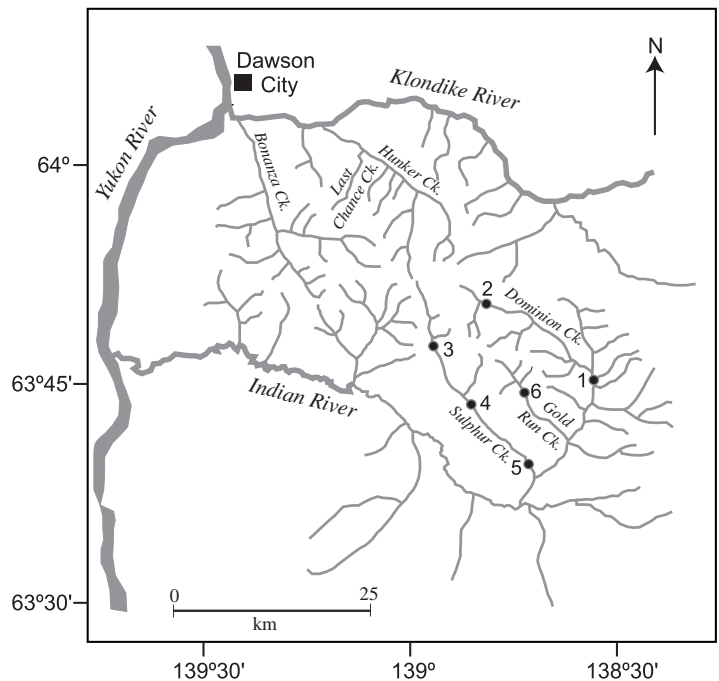


Figure 1. Map of Klondike District showing location of southern Klondike sampling sites. Sites 1 – 6 refer to numbers used in Tables 1 and 2.

1 = lower Dominion Creek, 2 = upper Dominion Creek, 3 = upper Sulphur Creek, 4 = mid Sulphur Creek, 5 = lower Sulphur Creek, 6 = Gold Run Creek.

TESTWORK PROGRAM

CHOICE OF STUDY AREA

The rationale for the study is centred on evidence for the presence of fine gold in the north of the Klondike goldfield, although there were practical barriers to effective sampling in that area. Bonanza and Hunker creeks have both been dredged extensively and only a limited amount of placer mining currently exploits virgin gravel. Collection of samples is greatly facilitated by access to active placer mines, and in their absence, sampling would be largely confined to dredge tailings. Furthermore, the study of Chapman *et al.* (submitted, b) showed the presence of several zones of mineralization in the Lone Star Ridge area. These represent different mineralizing events between which the gold particle size could vary. Sequential influx of gold with different size ranges complicates the process of tracking dispersion of fine gold. In addition, Bonanza Creek is relatively short, whereas other drainages in the Klondike goldfield provide the opportunity for the concentration of fine gold in

placers distal to the source. The placer gold in Dominion Creek and most of the placer gold in Sulphur Creek (Fig. 1) is derived from sources near Hunker Dome (Chapman *et al.*, submitted, a). This part of the Klondike afforded sampling of a variety of materials ranging from virgin gravel to recent and historically produced tailings. Gold Run Creek (Fig. 1) was included in the sample targets because the composition of the placer gold differed from that recorded in Sulphur and Dominion creeks (Chapman *et al.*, submitted, a), which suggests that the gold was derived from a separate source. Thus, a study of the placer gold within the three main southern drainages would permit evaluation of the transport of fine placer gold from different sources constrained by the individual valleys.

SAMPLE COLLECTION

Various types of material were available for sampling, and these have been categorized according to their processing history (Table 1). Colluvium was sampled at the head of Sulphur Creek. Virgin gravel at the bedrock interface was sampled at various locations. Virgin gravel,

2 m above the bedrock contact, was sampled in an active cut in upper Sulphur Creek. Various tailings samples were collected both from modern and historical operations (Fig. 1). Duplicate samples were collected at various sites. Summary data are provided in Table 1. Material was dry sieved at a 2.7 cm size fraction on site, and the undersized fraction was air-dried prior to dry sieving to generate fractions of 1 to 2.7 cm, 1 mm to 1 cm, 0.5 to 1 mm, and <0.5 mm. Sample masses were recorded for each fraction. All fractions, except those <0.5 mm, were panned to recover gold particles. Although the mass of these gold particles was recorded, these data were not used to generate gold grades because of the relatively small sample size and large gold particle size.

RATIONALE FOR SAMPLE TREATMENT

The testwork was designed to establish the distribution of gold by size fractions suited to different methods of gold recovery. The finest size (<53 μm) may contain some gold recoverable by 'enhanced g' separators but also finer gold amenable to cyanidation. Gold particles in the 53-125 μm size range are often difficult to recover in sluicing

Table 1. Description of sample locations.

Sample	Creek	Description	Easting	Northing
1A-i	Lower Dominion	Virgin gravel on bedrock, active cut	621919	7073389
1A-ii		Virgin gravel on bedrock, active cut	621919	7073389
1A-iii		Sluice discharge at 1 m from exit	621919	7073389
1A-iv		Sluice discharge at 10 m from exit	621919	7073389
1B-i		Virgin gravel on bedrock, active cut	620310	7074162
1B-ii		Virgin gravel on bedrock, active cut	620310	7074162
1C-i		Tailings	620503	7073970
1C-ii		Tailings	620477	7073954
2i	Upper Dominion	Colluvium	604358	7082656
2ii		Colluvium	604358	7082656
3A	Upper Sulphur	Virgin gravel on bedrock, active cut	601723	7078831
3B		Virgin gravel, 2 m above bedrock, active cut	601691	7078719
4	Mid Sulphur	Virgin gravel on bedrock	601714	7078820
5	Lower Sulphur	Dredge tailings	613044	7063080
6A	Gold Run	Tailings at sluice box	613294	7071077
6B		Tailings pond (fine fraction)	613318	7071054
6C		Virgin gravel about 30 cm above bedrock, active cut	612722	7071504
6D		Virgin gravel on bedrock, active cut	612722	7071504
6E		Tailings from 1960s operation	613502	7070922

operations, whereas higher recoveries are assured using ‘enhanced g’ separators. Finally, gold in the size range of 125-500 µm is recoverable using sluices, where the gold is not flaky, and the feed has been adequately classified.

The <500 µm (<0.5 mm) material was submitted to ALS Laboratories, Vancouver, for further analysis. Each sample was wet sieved at 125 µm and 53 µm to yield 3 sub samples: <53 µm, 53-125 µm and 125-500 µm, each of which was subsequently dried and weighed. Representative 1 kg samples of each of these size fractions was subjected to bulk leach extractable gold (BLEG) analysis to generate a gold grade. The gold distribution to the various size fractions was calculated from particle-size distributions and gold grade data. In this way, erroneous values from the nugget effect were avoided.

RESULTS

The gold grades of the <500 µm fractions determined by the BLEG analysis are presented in Table 2, together with the gold distribution of the finest two fractions. The <53 µm and 53-125 µm fraction have been combined because of their general very low values in virgin gravel. The high values of distribution of gold to the finest sizes occur only in tailings samples and particularly in those tailings selected specifically for their fine particle size. These values only coincide with very low overall gold grades in the <500 µm material, and most probably reflect the increasing importance of the ultra-fine gold following removal of coarser particles.

VIRGIN GRAVEL

The <53 µm fraction of this gravel comprised less than 10% of the mass for samples from lower Dominion and upper Sulphur creeks. A slightly higher value was recorded for the sample from mid Sulphur Creek, which may reflect the lower energy of the mid reaches of the river system, or a different depositional environment within the ancient meandering river system. The samples from Gold Run Creek consist of around 25% of <53 µm material. In every case, the gold grade of the two finest size ranges was extremely low, which coupled with the small mass fractions of those sizes resulted in a negligible gold distribution to the fine material.

OTHER SAMPLES

The gold content of the colluvium sample was negligible, and this sample is not considered further. The various

Table 2. Gold distribution according to size fraction. Quantitative data applies to the <500 µm material. As the full particle size distribution of the sample is not available, these data cannot be used to generate an overall grade.

Sample	Creek	Gold grade in <500 µm fraction (g/t)	% gold in the <125 µm fraction	
			individual	mean
1A-i	Lower	5.92	0.4	0.35
1A-ii	Dominion	2.46	0.3	
1A		0.16	48	
1A		3.38	2.5	
1B-i		1.67	1.1	1.15
1B-ii		1.76	1.2	
1C-i		0.04	17	32
1C-ii		0.07	47	
2i	Upper	0.03	9	13
2ii	Dominion	0.03	17	
3A	Upper Sulphur	0.58	3.1	
3B		0.04	17.8	
4	Mid Sulphur	4.04	2.3	
5	Lower Sulphur	0.25	2.9	
6A	Gold Run	0.04	24	
6B		0.02	85	
6C		0.49	0.9	
6D		0.65	16	
6E		0.04	9.1	

samples of tailings exhibited a range of size distributions, overall gold grades and gold distributions to the finest sizes. Table 2 shows that the gold grades in the finest two fractions were all extremely low. Tailings samples collected adjacent to the sluice discharge contained more gold than in samples collected a few metres away in the tailings dam.

DISCUSSION

RELIABILITY OF DATA

In general, the testwork program has generated reproducible data, although it is acknowledged that this may be a consequence of the general absence of gold in the fine fractions studied. However, the technique yielded very consistent results for the 125-500 µm fraction, with the only discrepancies appearing in samples with a very low overall gold content.

SAMPLES FROM VIRGIN GRAVEL

In all samples derived from virgin gravel taken from the bedrock interface on Sulphur and Dominion creeks, only 1% of gold present in the >500 µm material was present in the two finest size fractions. The amount is slightly higher for the samples from Gold Run Creek, which may be a consequence of the gold particle size in a different gold source, or reflect the destinations of small equant gold grains derived from very local mineralization, present before transport affected their morphology. The sample of virgin gravel collected 1.5 m above bedrock on upper Sulphur Creek also contained gold predominantly in the 125-500 µm range which suggests that the grade change with depth in gravel is simply a consequence of abundance of gold grains of the same size rather than an indication of increasing gold particle size with depth.

Gold grades in <500 µm fractions of tailings samples were also low and samples collected at the point of sluice discharge returned grades of between 0.6 g/t and 3 g/t, whereas those of samples taken elsewhere in tailings lagoons were negligible. This suggests that fine tuning of sluice boxes could improve overall recovery. A single sample of dredge tailings from lower Sulphur Creek recorded a value of 0.25 g/t (in the <500 µm fraction). This value may be of interest if representative of the huge volume of tailings present in the area.

Even though this study is of a pilot-project scale, it seems evident that there is no resource of fine gold within the southern Klondike. There are two possible explanations for this observation. Firstly, the compositions of the placers remained consistent with the source mineralization, *i.e.*, no fine-gold particles existed originally. Secondly, all fine gold has been completely winnowed from the system. The consistent absence of fine gold in all the different types of material studied from all sample localities suggests the former scenario is more likely.

In light of this result, it is unfortunate that samples were not collected from the Bonanza Creek drainage. At present, it is unclear whether the metallurgical data from Klondike Star indicate a potential resource or an inefficient processing circuit. Wenquian and Poling (1983) allude to the hydrophobicity of gold within milled material. Flaky hydrophobic gold may 'float' and consequently concentrate in the tailings. Although the shaking table was closely monitored during these bulk tests it is not known whether any surfactants were employed to counter the loss of hydrophobic gold.

IMPLICATIONS FOR APPROACHES TO GOLD RECOVERY

This study has shown that it is extremely unlikely that a resource of fine and ultra-fine gold exists in the southern Klondike. Consequently there is no advantage in applying 'enhanced g' separators or cyanidation to either virgin gravel or tailings. However, the higher gold grades recorded in the 125-500 µm size range may translate to a valuable resource, which may currently be incompletely recovered by standard gravity concentration circuits. Previous work has established that gold recovery increases with the degree of pre-screening (Clarkson, 1994). However, although fine equant gold from near the source may be relatively easy to recover (Wenquian and Poling, 1983), this gold grain population becomes more difficult to recover with progressive fluvial transport as the grains become thinner. The progressive flattening of gold will also influence the apparent size of gold as determined by screening. Thus, the recorded values of gold in the 125-500 µm range present in tailings at a sluice discharge from mid-Gold Run Creek (0.6 g/t), may be lower than those for an equivalent sample from lower Dominion Creek (3.38 g/t) because these grains are proximal to source and less flaky.

DEVELOPMENT OF DISTAL PLACERS

During this study changes in the morphology of gold grains were observed between different sites. Placer gold in lower Dominion Creek was particularly flaky and difficult to recover as described above. Much of the fine flat gold could not be separated from the black sand using a gold wheel, and while careful operation of a 'Le Trap' sluice affected a significant concentration of gold within this material at very high recoveries, it was impossible to generate a clean concentrate. The size of this gold was relatively coarse (up to 3 mm) and it could be reasonably expected that progressive transport downstream would further exacerbate the problems generally acknowledged with efficient recovery of flakier gold, which becomes thinner before ultimately splitting into smaller particles.

When considering the development of placers containing well-travelled gold grains, it is appropriate to consider the controls on sedimentation resulting from particle shapes. In his seminal paper, Dietrich (1982) used a large experimental data set to demonstrate that the settling velocity of natural particles increases exponentially with particle size, and that very small particles have very slow settling velocities. In addition, Dietrich (1982) showed that the shape of particles additionally influences their settling

velocity. Particle shapes are frequently characterized using mathematical expressions involving the three dimensions of the particle. The Corey Shape Factor (CSF; Corey, 1949) is commonly employed and is defined as $T/(B \times L)^{1/2}$, where T, B and L are the thickness, breadth and length of the grain. Perfectly spherical grains have a CSF = 1, whereas flatter grains will record a smaller CSF (CSF = 0 for totally flattened particles). Flatter particles, with a low CSF, experience increased drag from the fluid, which further hinders their settling. For all particles, both reduction in size and increased flatness are a hindrance to particle settling (Dietrich, 1982). Dietrich's data were collected in stationary water, and do not account for the high specific gravity of gold, and thus do not replicate settling conditions within Klondike placers. Additionally, although it may be assumed that the effect of reduced settling velocity of smaller, non-spherical particles would be exacerbated in a fast-flowing river (because the effects of turbulence would further hinder settling), preferential collection of fine-gold particles may be favoured by vortices created behind obstacles on the river bed. Clarkson (1994) reported the CSF for fine gold (+100 mesh) from various sites in the Klondike to be between 0.3 – 1.0. However, gold grains recovered in this study, from site 1A (Fig. 1; Table 1), have an average CSF = 0.1, which is interpreted to reflect shape modification during fluvial transport. Wenquian and Poling (1983) concluded that gold particles with a shape factor of less than 0.15 were difficult to recover in gravity circuits. Further transport in the Dominion Creek/Indian River drainage would presumably reduce the CSF further, progressively reducing the likelihood of fluvial concentration of all the gold present in the sediment load into pay streaks.

Studies of the nature of gold within placers are generally considered problematic because of the overall low abundance of gold particles, which necessitates very large sample sizes, (e.g., Clarkson 1994). Various Russian studies have included reference to gold grain shape as a control on placer formation (W. LeBarge, pers. comm.), but these employ qualitative shape descriptors rather than shape factors and hence the data are difficult to compare with those discussed here. The most useful information available to the present study, in the context of placer development, is derived from metallurgical studies which have sought to characterize gold recovery in terms of particle shape. In general, material accumulating in the sluice tailings represents material less likely to be concentrated by fluvial action to form a placer. Clarkson (1994) noted that the action of a sluice was similar to a

centrifugal concentration device due to the formation of vortices downstream of the riffles. Consequently, application of free-settling velocities of particles to the hindered settling/centrifugal-influenced deposition within a sluice box, may be simplistic, but such conditions also exist in the fluvial environment.

Chapman and Houseley (1996) evaluated various methods of shape classification in relation to the destinations of gold grains within a gravity concentration circuit. They showed that indices which include a measurement of gold grain thickness are the most efficient at predicting behaviour in the concentrating circuit, whereas an index utilizing only the length and breadth of the gold particle is far less useful. The implication, for studies of placer development, is that use of sieve aperture as the sole criteria for gold grain characterization is not appropriate, whereas measurement of the third dimension enables prediction on whether the grains could be concentrated by fluvial action. Collection of data, for large populations of gold grains, which describe three-dimensional shape has traditionally been time consuming and labour intensive. However, Crawford (2007) developed image analysis software capable of this task and applied it to relate morphological modification of gold grains to transport distance. This approach could be adapted to predict 'future' morphological change to establish the point downstream beyond which concentration of gold particles by fluvial action is no longer likely.

The consideration of the effect of gold grain shape on placer formation indicates that a distinction should be made between gold made fine (and flat) by fluvial transport and that which consists of equant grains of equivalent sieve aperture. The absence of fine gold in the southern Klondike probably indicates that the original grain size was relatively coarse, and this may be typical for placers derived from orogenic gold. Thus, it may be possible to speculate on the potential for fine placer gold on the basis of the style of source mineralization, with epithermal, porphyry and intrusion-related offering the best prospects for contributing to economically important placers of fine gold.

CONCLUSIONS

This study has established that there is unlikely to be a viable resource of fine gold in the southern Klondike and that this probably reflects the original size distribution of the hypogene gold particles. Similar studies are required

elsewhere in the Klondike goldfield, where placer gold was derived from different source mineralization, to establish whether fine gold is absent throughout the entire area. The methodology developed here avoids spurious results caused by the nugget effect and can establish the resource of gold, within specific size ranges, extractable using different processing options. Field observations of major changes in the shape of gold grains have been correlated with qualitative reports of ease of gold recovery by simple gravity circuits. Metallurgical data describing gold behaviour in gravity concentration circuits can be used as a proxy for predicting placer development. Consequently, the shape indices of gold grains used as a predictive tool in metallurgical research could find application in speculating whether there is potential for fine-gold accumulation. It seems likely that economic concentrations of fine gold could result from those styles of mineralization where the particle size of gold is small within the hypogene source. Thus, equant small particles are more likely to form a placer than fine and thin gold particles generated through prolonged fluvial transport. We propose that screen aperture alone is unsuitable for prediction of fine placer gold accumulation. Recently developed image analysis techniques may permit statistical evaluation of populations of gold grains, and mapping these data onto predicted shape change could prove beneficial for identifying possible targets for further exploration.

ACKNOWLEDGEMENTS

The authors would like to acknowledge funding from the Yukon Geological Survey, without which this study would not have been possible. Various placer miners are thanked for access to their property for sampling collection.

REFERENCES

- Apling, A.C., Chapman, R.J., Houseley, K. and Watson, R.P., 1997. The use of a homogenous feed matrix for shape factor control during milling: effect on gold gravity concentration. *Transactions of the Institution of Mining and Metallurgy, Section C, Mineral Processing and Extractive Metallurgy*, vol. 106, p. 142-145.
- Chapman R.J. and Houseley, K., 1996. The effect of particle geometry on the recovery of gold grains by gravity concentration methods. *Proceedings of the 28th Annual Operator's Conference of the Canadian Mineral Processors, CIM, Ottawa, Canada*, p. 335-357.
- Chapman, R.J., Mortensen, J.K., Crawford, E.C. and LeBarge, W., (submitted a). Orogenic gold mineralization from distinct hydrothermal systems within the Klondike Placer Gold District, Yukon, Canada, identified from compositional studies of lode and placer gold. Submitted to *Economic Geology*, January 2010.
- Chapman, R.J., Mortensen, J.K., Crawford, E.C. and LeBarge, W., (submitted b). Microchemical studies of placer and lode gold in Bonanza and Eldorado creeks, Klondike District, Yukon, Canada: evidence for a small, gold-rich, orogenic hydrothermal system. *Economic Geology*. Submitted to *Economic Geology*, January 2010
- Clarkson, R., 1989. Gold Losses at Klondike Placer Mines: Gold Recovery Project, Phase 1. Report prepared for the Klondike Placer Miners Association, CANMET.
- Clarkson, R., 1994. The use of nuclear tracers to evaluate the gold recovery efficiency of sluicboxes. *CIM Bulletin*, vol. 87, no. 979, p. 29-37.
- Corey, A.T., 1949. Influence of shape on the fall velocity of sand grains. Unpublished MSc thesis, Colorado A & M College, Fort Collins, Colorado, USA.
- Crawford, E.C., 2007. Klondike placer gold: New tools for examining morphology, composition and crystallinity. Unpublished MSc thesis, University of British Columbia, Canada, 151 p.
- Dietrich, W.E., 1982. Settling velocity of natural particles. *Water Resources Research*, vol. 18, no. 6, p. 1615-1626.
- Fricker, A., 1984. Metallurgical efficiency in the recovery of alluvial gold. *Proceedings of the Australian Institute of Mining and Metallurgy*, vol. 289, p. 59-67.
- Laplante, A., Vincent, F. and Luinstra, W., 1996. A laboratory procedure to determine the amount of gravity recoverable gold – a case study at Hemlo Gold Mines. *Proceedings of the 28th Annual Operator's Conference of the Canadian Mineral Processors, CIM, Ottawa, Canada*, p. 69-82.
- Macdonald, C.H., 1985. Summary report on placer research projects. Canada/Yukon Subsidiary Agreement on Mineral Resources Program 3: Placer Mining.
- Subasinghe, G.K.N.S., 1993. Optimal design of sluicboxes for fine gold recovery. *Minerals Engineering*, vol. 6, no. 11, p. 1155-1165.
- Wenquian, W. and Poling, G., 1983. Methods for recovering fine placer gold. *CIM Bulletin*, vol. 76, no. 860, p. 47-56.

The Duke River fault, southwest Yukon: Preliminary examination of the relationships between Wrangellia and the Alexander terrane

Rose Cobbett¹

Department of Earth and Ocean Sciences, University of British Columbia

Steve Israel²

Yukon Geological Survey

James Mortensen

Department of Earth and Ocean Sciences, University of British Columbia

Cobbett, R., Israel, S. and Mortensen, J., 2010. The Duke River Fault, southwest Yukon: Preliminary examination of the relationships between Wrangellia and the Alexander terrane. *In: Yukon Exploration and Geology 2009*, K.E. MacFarlane, L.H. Weston and L.R. Blackburn (eds.), Yukon Geological Survey, p. 143-158.

ABSTRACT

The Duke River fault is a terrane-bounding structure that separates the Alexander terrane from Wrangellia in southwest Yukon. Detailed geological mapping and sampling of three key areas along the fault was completed in August 2009. In these areas, the fault juxtaposes multiply folded, pervasively foliated, greenschist facies rocks of the Alexander terrane against low-grade Wrangellian rocks that record only one phase of folding. Shear bands, fold orientations, rotated grains, lineations, mica fish and fault plane orientations indicate that the Alexander terrane has been thrust over Wrangellia. Preliminary ⁴⁰Ar/³⁹Ar ages from muscovite grains that may have been reset by motions along the Duke River fault or grown during faulting range from 90-104 Ma, suggesting that movement along the fault is at least as old as Cretaceous. Miocene felsic intrusions and Miocene to Pliocene crustal tuffs of the Wrangell lavas have been deformed by the Duke River fault, suggesting movement occurred as recently as the Pliocene.

¹cobbettrosie@gmail.com

²steve.israel@gov.yk.ca

INTRODUCTION

The western margin of the North American Cordillera in western Canada is composed of the Alexander terrane and Wrangellia (Fig. 1). These terranes were amalgamated to form the Insular superterrane (or composite terrane) prior to its accretion to the North American margin in the Middle Jurassic to Early Cretaceous (Monger *et al.*, 1982; van der Heyden, 1992; Wheeler *et al.*, 1991). The tectonic evolution of, and relationships between, the Insular terranes prior to, and after, accretion are not well understood in Yukon. The Duke River fault is a terrane-bounding structure that separates Wrangellia and the Alexander terrane in southwest Yukon and northwestern British Columbia (Fig. 1). The Duke River fault is exposed over much of its strike length and provides an excellent opportunity to study the geological relationships between the Alexander terrane and Wrangellia.

Previous studies suggest the Duke River fault is a post-Triassic dextral strike-slip fault that has accommodated major displacements (Dodds and Campbell, 1992). This contrasts with recent studies that have interpreted seismic and earthquake data along the Duke River fault to indicate reverse oblique movement along the fault (Page *et al.*, 1991; Power, 1988).

The objectives of this study are: 1) to determine the timing and kinematics of movement along the Duke River fault; 2) to restore motion along the Duke River fault and to examine its association with other major faults that have affected Wrangellia and the Alexander terrane; and 3) to establish a pre-Tertiary tectonic framework for the outboard margin of the Cordillera in western Canada and southeast Alaska.

Detailed mapping of the Duke River fault has resulted in six 1:10 000-scale geologic maps of exposures of the fault in southwest Yukon, three of which are presented in this paper. A suite of samples has been collected for petrographic work, and $^{40}\text{Ar}/^{39}\text{Ar}$ and U-Pb geochronology. In this paper, we compare Wrangellian rocks to adjacent rocks of the Alexander terrane, illustrating their contrasting structure and metamorphic character. Microscopic and outcrop-scale structural features from different localities are presented to illustrate the kinematic history of the fault. Preliminary $^{40}\text{Ar}/^{39}\text{Ar}$ ages of mica grains collected within fault fabrics in the Duke River fault and U-Pb ages of intrusive rocks that have been deformed by the fault are also presented.

Preliminary results show that the Duke River fault is dominantly a thrust fault that places multiply deformed greenschist facies Alexander terrane rocks over less deformed, lower-grade rocks of Wrangellia. The fault may be as old as Cretaceous and as young as Miocene.

REGIONAL GEOLOGY

WRANGELLIA

Stratigraphy

Wrangellia is made up of a Paleozoic island arc sequence overlain by a thick package of early Mesozoic flood basalts and sedimentary rocks that were formed outboard of the North American margin. It extends from central Alaska to southern British Columbia (Fig. 1). The Skolai Group is the oldest succession of layered rocks in Wrangellia in southwest Yukon. The Skolai Group consists of Mississippian to Permian volcanic and volcanoclastic rocks of the Station Creek Formation and sedimentary rocks of the Hasen Creek Formation (Smith and MacKevett, 1970; Read and Monger, 1976). The Station Creek Formation includes a lower package of basic to intermediate porphyritic flows with plagioclase and pyroxene phenocrysts and an upper package of volcanoclastic rocks ranging from coarse breccias to fine tuffs (Smith and MacKevett, 1970; Read and Monger, 1976). The Hasen Creek Formation gradationally overlies the Station Creek Formation and consists of chert, black shale, minor conglomerate and limestone that contains Early Permian fossils (Smith and MacKevett, 1970; Read and Monger, 1976). Thin units of Middle Triassic *doenella*-bearing siltstones unconformably overlie the Hasen Creek Formation, and are locally preserved in graben-like structures (Israel *et al.*, 2007; Israel and Cobbett, 2008). Basal conglomerates of the Nikolai Formation normally overlie these siltstones. The basal conglomerate of the Nikolai Formation is overlain by a package of amygdaloidal basalt flows that are up to 3000 m thick (Read and Monger, 1976). Locally, thin-bedded, bioclastic limestone and green and maroon shales are interbedded with flows near the top of the formation. Basalt of the Nikolai Formation has been interpreted as being part of a large igneous province derived from plume-related processes (Greene *et al.*, 2008). The Upper Triassic Chitstone limestone and interbedded limestone and calcareous and carbonaceous sedimentary rocks of the McCarthy Formation conformably overlie the Nikolai Formation (Read and Monger, 1976; Israel and

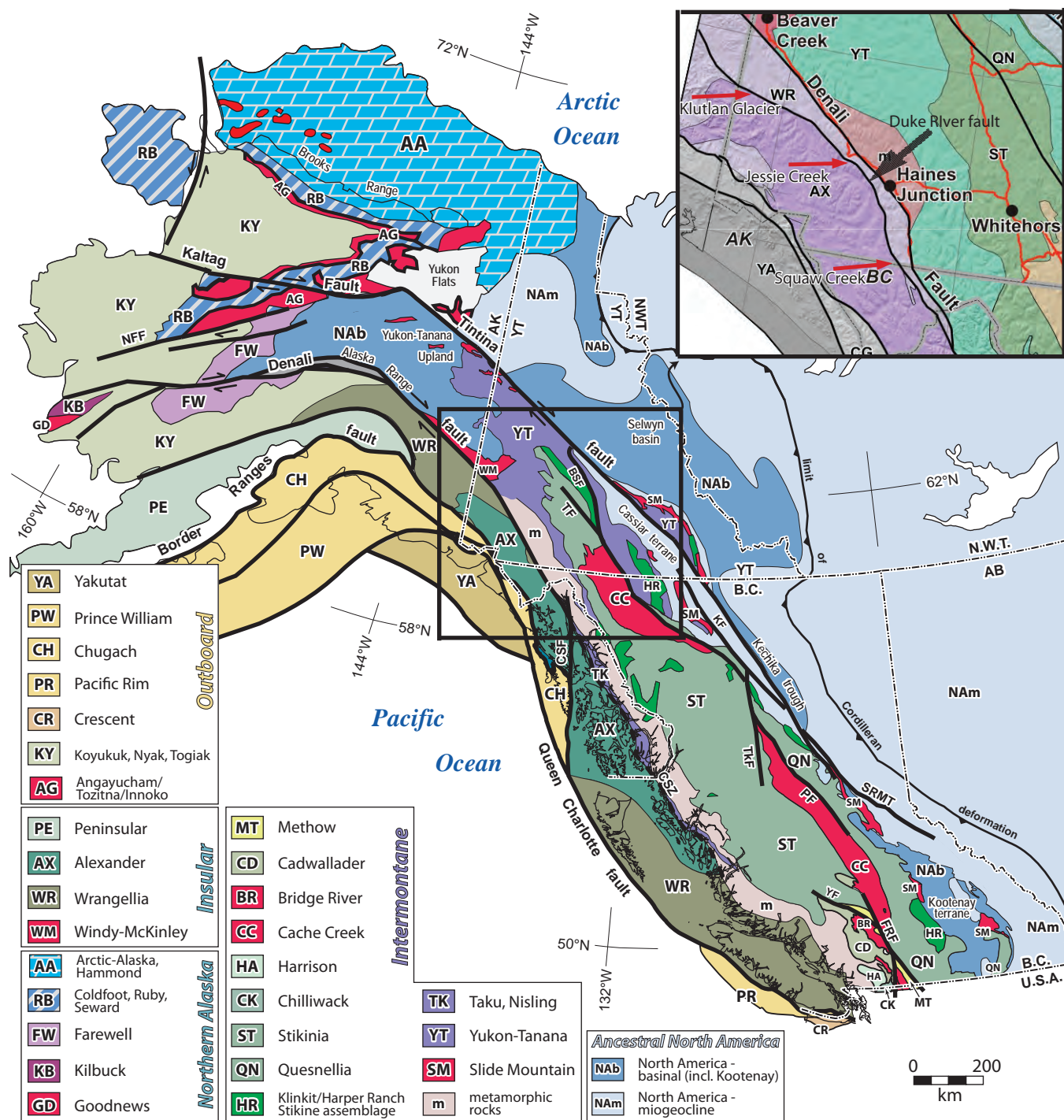


Figure 1. Location of Insular terranes of the Canadian Cordillera (Colpron et al., 2006). The Duke River fault separates Wrangellia from the Alexander terrane as shown in the inset by the black arrow. Locations of maps presented in this paper are indicated by red arrows in the inset.

Cobbett, 2008). Gypsum is found in the lower portions of the Chitistone limestone (Israel *et al.*, 2006; MacKevett, 1971; Read and Monger, 1976). The gypsum varies in thickness from metre-scale deposits to accumulations up to several hundred metres thick.

Intrusive Rocks

Coarse-grained, pyroxene-bearing gabbros of the Steele Creek complex sit unconformably under the Hasen Creek Formation. The gabbros are Latest Devonian in age and are the oldest identified rocks in Wrangellia in southwest Yukon; they likely represent part of the basement that the Skolai Group was deposited upon (Read and Monger, 1976). Plutons ranging in age from Late Triassic to Late Miocene intrude rocks of Wrangellia. Late Triassic mafic and ultramafic intrusive rocks of the Kluane Ultramafic Suite that are inferred to be part of the magmatic system that fed the basalts of the Nikolai formation (Hulbert, 1997) have long been known in the area. Recently, medium to coarse-grained granodiorite to tonalite of Late Triassic age was also recognized (Israel and Cobbett, 2008) having been mapped previously as part of the lithologically similar Early Cretaceous Kluane Ranges Plutonic Suite. The Kluane Ranges Suite is the most abundant intrusive rock in the area. It includes medium to coarse-grained diorite to granodiorite. Locally, medium-grained hornblende-pyroxene gabbro and biotite-hornblende diorite belonging to the Pyroxenite Creek Ultramafic unit have been mapped intruding rocks of Wrangellia. The youngest intrusions are Middle to Late Miocene, felsic to mafic bodies of the Wrangell Plutonic Suite.

Structure

Wrangellia has been affected by several deformation events beginning as early as pre-Middle Triassic and continuing until the present day, as indicated by ongoing seismic activity along faults bounding Wrangellia (Read and Monger, 1976; Power, 1988; Israel and Cobbett, 2008). In southwest Yukon, Wrangellia is characterized by dominantly northwest-trending structures. A pre-Middle Triassic compressional event has been inferred on the basis of folded Paleozoic strata overlain by relatively undeformed Triassic strata, the absence of Early Triassic rocks and the unconformable contact between Triassic and Paleozoic stratigraphy (Read and Monger, 1976; Israel and Cobbett, 2007, 2008). A second, post-Triassic, pre-middle Cretaceous compressional event is characterized by well-documented regionally extensive, tight to isoclinal

folds and accompanying northeast- and southwest-verging thrust faults (Read and Monger, 1976; Israel and van Zeyl, 2005; Israel and Cobbett, 2007). Finally, Wrangellia has been cut by post-Cretaceous strike-slip and associated second-order faults that includes up to 370 km of right-lateral movement along the Denali fault and associated structures as well as an unknown amount of movement along the Duke River fault (Read and Monger, 1976; Lowey, 1998; Israel and van Zeyl, 2005; Israel and Cobbett, 2008). Many of the Cretaceous and older structures were reactivated during this time.

ALEXANDER TERRANE

The Alexander terrane is exposed in southeast Alaska, southwest Yukon and parts of northwestern British Columbia (Fig. 1). It includes intrusive, volcanic and sedimentary rocks that range in age from Cambrian to Late Triassic (Gehrels and Saleeby, 1987).

New studies from Alaska and southwest Yukon suggest that the Alexander terrane as defined by Gehrels and Saleeby (1987) differs from Alexander terrane in peninsular Alaska and from Alexander terrane exposed in southwest Yukon (St. Elias Alexander; S. Karl and C. van Staal, pers. comm., 2009). Gehrels and Saleeby's (1987) work shows that the Alexander terrane in Alaska is made up of a series of amphibolite-grade metamorphic rocks that were affected by an Ordovician orogenic event (The Wales orogeny). These rocks formed the basement to a younger sequence of arc rocks that, together with the older rocks, were deformed by the Klakas orogeny. This tectonic event began in earliest Devonian time, before the deposition of Triassic strata (Gehrels and Saleeby, 1987). In contrast, the St. Elias Alexander terrane consists of an Early Paleozoic carbonate-dominated passive margin that was built on an older arc sequence consisting of basalt and volcanoclastic rocks (Dodds and Campbell, 1992). The St. Elias Alexander terrane rocks have been affected by tectonism of Klakas age, but do not show evidence of the older Wales orogeny. This paper only discusses the St. Elias Alexander rocks and does not consider the Alexander terrane exposed in Alaska and British Columbia.

In Yukon, the Alexander terrane is made up of successions of siliciclastic rocks, carbonates and volcanic rocks of a variety of ages. The oldest exposed rocks are the Cambrian to Ordovician Donjek formation, which consists of greywacke and greenstone with a minor component of carbonate. These rocks are overlain by the Lower Ordovician to Devonian Goatherd formation which comprises dominantly carbonate and clastic rocks. A

similar package of carbonate and clastic rocks of Silurian to Devonian age make up the Bullion formation and are exposed throughout the Alexander terrane in southwest Yukon. The youngest package of layered rocks in the St. Elias Alexander terrane is the Devonian to Upper Triassic Icefield formation. This package consists of pelitic, carbonate and volcanic rocks.

Intrusive Rocks

Two main episodes of plutonism affected St. Elias Alexander rocks. The first of these is the Icefield Ranges Suite which is Pennsylvanian to Permian in age, the second is the Late Jurassic to Early Cretaceous Saint Elias Suite. The Icefield Ranges Suite consists of biotite-hornblende syenite, quartz monzodiorite and diorite and is observed to stitch together rocks of the Alexander terrane and Wrangellia (Gardner *et al.*, 1988). The Saint Elias Suite consists of non-porphyrific to porphyritic (K-feldspar) biotite-hornblende granodiorite. Gabbro and ultramafic bodies found near the Duke River fault intrude rocks of the Alexander terrane and may be part of the Late Triassic and (?) older Klauane Ranges mafic-ultramafic suite that intrudes rocks of Wrangellia. Relatively fresh and undeformed hornblende \pm biotite granodiorite to porphyritic (K-feldspar) hornblende granodiorite of the Miocene Wrangell Suite intrude the Alexander terrane throughout southwest Yukon.

Structure

The Alexander terrane rocks have been metamorphosed to greenschist facies and are pervasively foliated. A northwest structural trend is observed throughout the terrane and includes folds and metamorphic fabrics (Dodds and Campbell, 1992). Two regional-scale phases of folds are found that are pre-Jurassic in age and are likely at least partially contemporaneous with the intrusion of the Pennsylvanian Icefield Ranges Suite (Read and Monger, 1976; Gardner *et al.*, 1988; Dodds and Campbell, 1992). Several phases of faulting affect Alexander terrane rocks in southwest Yukon. These include thrust faults of uncertain age, steeply dipping strike-slip faults related to the Denali and Duke River fault systems, and normal faults that appear to be quite young (Dodds and Campbell, 1992).

OVERLAP ASSEMBLAGES

Several packages of rock are shown to overlie both the Alexander terrane and Wrangellia. The oldest of these are Upper Jurassic to Lower Cretaceous turbidites of the

Dezadeash Formation. The Dezadeash Formation is associated with several similarly aged basins that developed between the Insular and Intermontane terranes during middle Mesozoic time (Smith and MacKevett, 1970; Read and Monger, 1976; McClelland *et al.*, 1992; van der Heyden, 1992). Terrestrially deposited clastic sedimentary rocks of the Oligocene Amphitheatre Formation overlie both the Alexander terrane and significant parts of Wrangellia and were deposited in extensional and compressional basins developed along the Duke River and Denali fault systems (Read and Monger, 1976; Ridgeway *et al.*, 2002). Miocene to Pliocene and (?) younger volcanic rocks of the Wrangell volcanic formation outcrop extensively throughout southwestern Yukon.

DUKE RIVER FAULT, GEOLOGY, STRUCTURE AND METAMORPHISM

Preliminary data from three of the six areas along the Duke River fault that have been mapped for this study are presented and discussed here. These data include lithologic descriptions, petrographic analyses and preliminary geochronology from the southeastern-most, the central and northwestern-most exposures of the Duke River fault.

SQUAW CREEK

The Duke River fault in the Squaw Creek area is exposed in a steep-sided canyon that starts near the Yukon-British Columbia border and extends for about six kilometres to the northwest. In the Squaw Creek area, a deformed gabbro belonging to the Pyroxenite Creek ultramafic suite intrudes tuffs and volcanoclastic rocks of the Station Creek Formation on the north side of the Duke River fault (Fig. 2). Miocene to Pliocene crystal tuff and basalt flows of the Wrangell volcanic formation overlie the Station Creek Formation and the gabbro but are not found on the south side of the fault. Wrangell tuffs near the Duke River fault are foliated (Fig. 3a). Rocks of the Station Creek Formation are deformed by open folds that trend northwest and southeast. The metamorphic grade of these rocks is prehnite/pumpellyite.

In contrast, rocks of the Alexander terrane on the south side of the Duke River fault comprise an assemblage of foliated calcareous and carbonaceous siltstones, phyllitic volcanoclastic rocks, greenschist and massive to layered marbles. The upper walls of the Squaw Creek canyon are dominantly made up of competent marble (Fig. 3b). The main foliation in the Alexander terrane rocks strikes

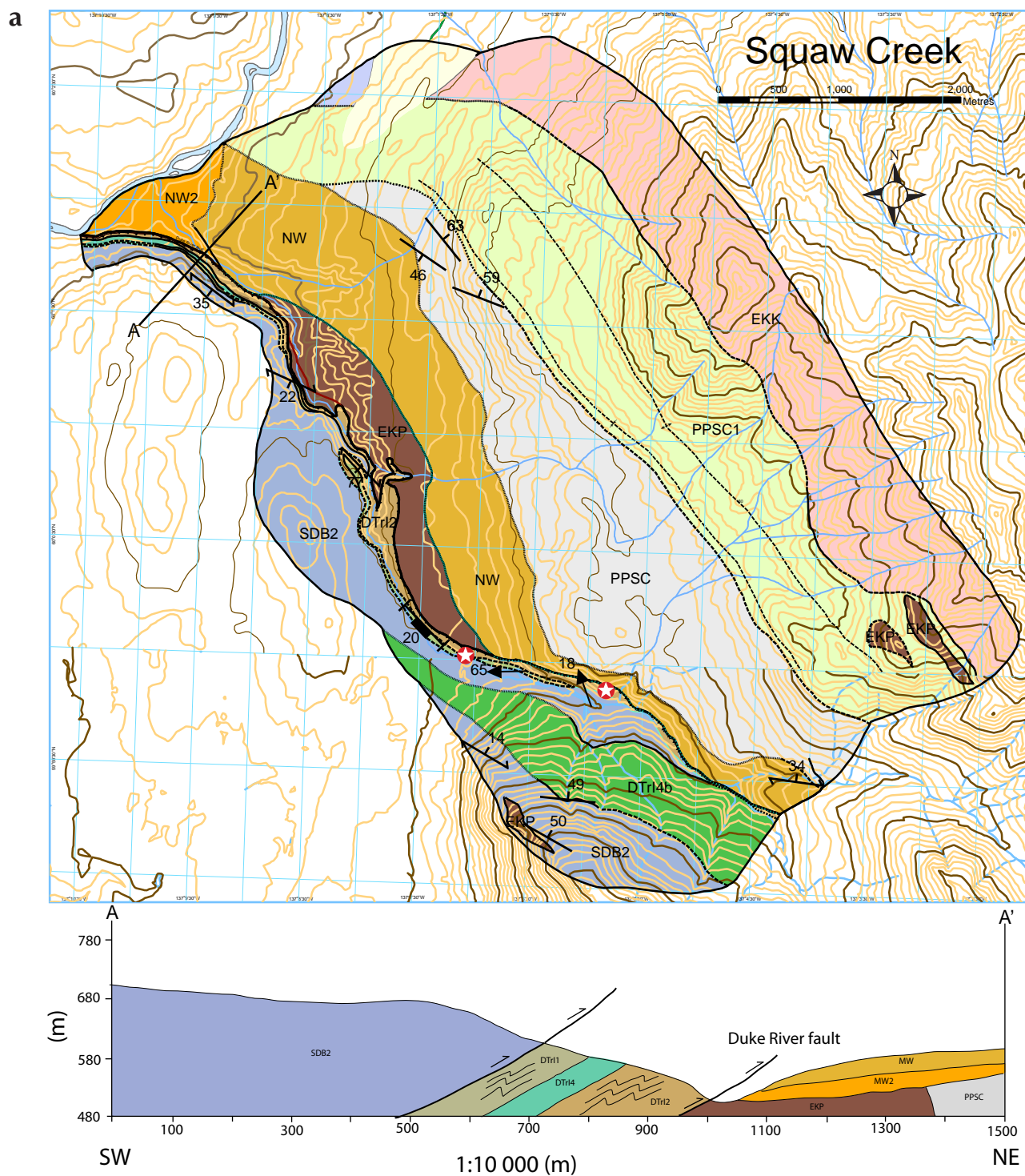


Figure 2. (a) Geologic map and cross section (line A-A') of the Squaw Creek area.

b

LEGEND

MIOCENE TO PIOCENE AND (?) YOUNGER

Wrangell Lavas

- NW Dark grey to black, fine-grained amygdaloidal basalt
- NW2 Beige fresh and weathered, fine-grained crystal lithic tuff

LATE EARLY CRETACEOUS

Pyroxenite Creek Ultramafic

- EKP Green, medium-grained, foliated, plagioclase, clinopyroxene, chlorite and epidote gabbro
- EKK Medium grey, medium to coarse-grained, biotite-hornblende granodiorite, quartz diorite, quartz monzonite, and hornblende diorite

WRANGELLIA

UPPER TRIASSIC

Chitistone

- uTrC Light to dark grey, thinly bedded limestone and limestone breccia

LATE TRIASSIC AND (?) OLDER

Kluane Mafic and Ultramafic Suite

- PTrK Black to dark green, medium-grained pyroxenite
- PTrK2 Green, medium-grained hornblende-actinolite gabbro

PENNSYLVANIAN TO (?) LOWER PERMIAN

Skolai Group: Station Creek Formation

- PPSC1 Laminated to thinly bedded, light grey to light green volcanic tuff and volcanoclastic siltstone; local crystal-rich tufts interbedded with fine-grained volcanic ash
- PPSC Green, fine-grained volcanic breccia and basalt flow

Skolai Group: Hasen Creek Formation

- PHC Interbedded dark grey and brown-weathered siltstone, mudstone and medium to coarse grained sandstones; grey pebble conglomerate and light brown fossilstone; rare thinly bedded black chert

SYMBOLS	geologic contacts (defined, approximate, inferred, covered).....		dyke, vein.....	
	mapping limit.....		bedding (tops known, inclined, vertical).....	
	fault; movement not known (defined, approximate, inferred, covered).....		foliation (dominant, late).....	
	fold axial trace (anticline, overturned-anticline; syncline, overturned-syncline)		fold axis (dominant phase, Z-fold).....	
			intersection lineation.....	
			stretching lineation, mineral lineation.....	
			location of Argon-Argon samples.....	

ALEXANDER

PALEOZOIC, (?) DEVONIAN AND/OR YOUNGER

Steele Creek Suite

- PSC Massive, locally foliated, grey-green, medium to coarse-grained, hornblende pyroxene gabbro; minor medium-grained gabbro diabase and leucocratic gabbro
- DMr Green, fine-grained mafic rock
- MGr Pinkish, fine to medium-grained quartz, feldspar granite

DEVONIAN TO UPPER TRIASSIC (?) AND OLDER

Icefield Formation

- DTr1 Light green, fine to very fine grained, volcanoclastic rock; very fine grained samples could be phyllonites
- DTr12 Dark grey to black, fine grained, carbonaceous phyllite to mica schist; local dark to light grey ribbon chert and occasional fine to medium-grained lithic sandstone
- DTr13 Dark green volcanic breccia with clasts up to 25 cm in diameter having significant reaction rims; local plagioclase-phyric and/or amygdaloidal and vesicular basaltic flows
- DTr14 Grey, thinly bedded limestone and dark grey, bedded calcareous siltstone
- DTr14b Undifferentiated greenschist interfoliated with meta-siltstone and carbonate
- DTr16 White to grey, massive marble; locally brecciated
- DTr17 Interbedded, green, fine-grained volcanoclastic sandstone, maroon and green volcanic conglomerate and basalt flows; occasional very fine-grained tuffaceous horizons; local layers of lithic conglomerate with clasts of chert and siltstone and occasional beds of shale or slate

SULURIAN AND DEVONIAN

Bullion formation

- SDB1 Beige to grey to orange weathered, massive to thinly bedded to brecciated carbonate
- SDB2 Grey to brown, fine-grained, carbonaceous mica schist; local quartzite

Figure 2. continued (b) Map legend for geologic maps of Squaw Creek, Jessie Creek and Klutlan glacier areas.

approximately east and dips moderately to the south. Siltstone and volcanoclastic rocks of the Alexander terrane exhibit three phases of folding. The first phase is manifested as millimetre-scale folded layers in the siltstone and is associated with the dominant foliation (Fig. 3c). This foliation is tightly folded by the second phase of folding which has a well-developed axial-planar cleavage in the hinges (Fig. 3d). The third phase comprises brittle, asymmetric kink folds which refold the first two phases of folding. This late phase commonly occurs in gouge zones, has shallowly dipping hinges that trend eastward, and verge to the north-northeast (Fig. 3d).

The Duke River fault is characterized by a 10 to 20-m-wide cataclastic zone that parallels the dominant foliation in the hanging wall (Fig. 3e). Marble of Alexander terrane is structurally above the cataclastic zone and remains intact. Brittle foliations associated with the fault zone occur within the siltstone or volcanoclastic units, strike southeast and have moderate southwest dips. The gabbro of the Pyroxenite Creek ultramafic suite is more intensely foliated and altered in the bottom of the canyon where it is closest to the cataclastic zone. Thin sections from layered carbonate of the Bullion formation near the fault, show sinistral shear bands in fine-grained muscovite layers. The dominant lineation in the layered carbonate rocks

Figure 3. (a) Foliated crystal tuff of the Wrangell volcanics near Squaw Creek. (b) Marble of Bullion formation sitting structurally above Duke River fault gouge zone. (c) Phase one folds in siltstone near Squaw Creek. (d) Axial-planar cleavage in phase two folds near Squaw Creek. (e) Kink folds in fault gouge near Squaw Creek. These folds strike approximately east and verge to the north-northeast.



plunges approximately 55° towards 200°. Preliminary ⁴⁰Ar/³⁹Ar dating constrains the age of muscovite in the fault zone to the middle Cretaceous (90-104 Ma).

JESSIE CREEK

The Jessie Creek map area is roughly 140 km along strike to the northwest from the Squaw Creek area. At Jessie Creek, the Duke River fault is exposed in a narrow valley between steep-sided mountains of the Klauane Ranges (Fig. 1 inset).

On the north side of the fault, rocks of Wrangellia consist of siltstone and sandstone of the Hasen Creek Formation and the overlying Chitistone limestone. The thinly bedded Chitistone limestone becomes brecciated near the Duke River fault. Both the Chitistone limestone and the rocks of the Hasen Creek Formation have been tightly folded (Fig. 4).

The rocks of the Alexander terrane consist of two distinct assemblages. The first assemblage is found directly adjacent to the Duke River fault and consists of Triassic

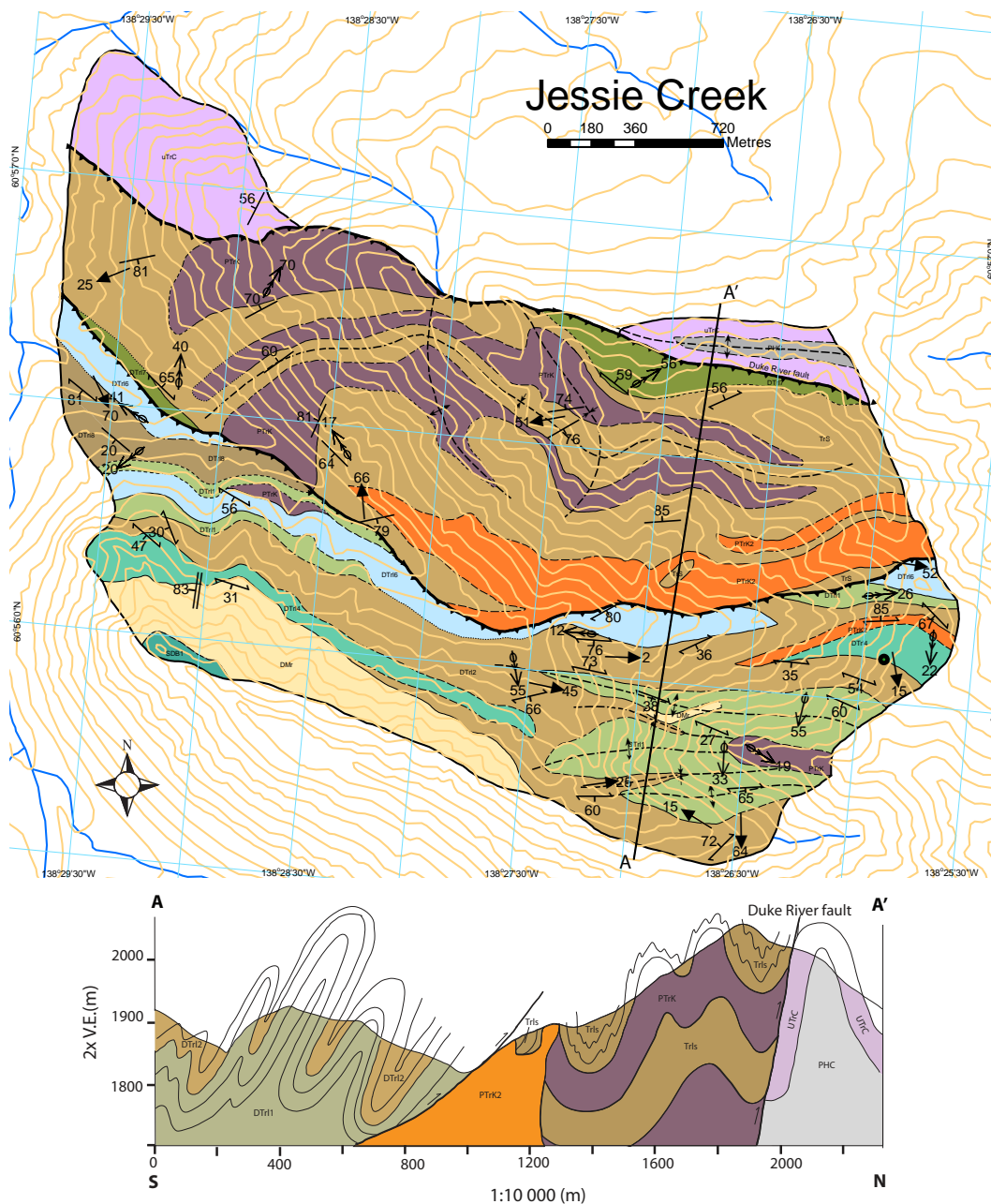


Figure 4. Geologic map and cross section (line A-A') of the Jessie Creek area. Refer to Figure 2b legend for symbol and unit descriptions.



Figure 5. (a) Dome folds created by folding of phase-two folds by phase-three folds in Icefield formation siltstone near Jessie Creek. (b) Isoclinal, rootless phase-one folds within the Icefield formation, near Jessie Creek. (c) Phase-three folds within Alexander terrane rocks, in the Jessie Creek area.

calcareous siltstone interbedded with ribbon chert and volcanic conglomerate. Beds of conglomerate grade upwards into sandstone beds. The whole assemblage is intruded by gabbro and pyroxenite of probable Late Triassic age. The second assemblage of Alexander terrane rocks is in fault contact with the first and includes Devonian volcanoclastic and volcanic rocks, carbonaceous siltstone, banded marbles and locally quartzite.

The two assemblages described above are further distinguished by differences in structural styles. The Triassic rocks are deformed by three phases of folding. The first phase consists of isoclinal folds that are locally preserved in the siltstones. However, the preservation of the folds is not adequate to obtain an orientation. This early phase is folded by a second phase that tightly folds the siltstone unit and more openly folds the cherts. The third phase of folding is hard to characterize because the hinges are nowhere exposed. Its existence is inferred because the phase-two folds regularly change orientations from southeast trending to northeast trending. These third-phase folds openly fold the phase-two folds. The beds of siltstone are deformed by phase-two and phase-

three folds, resulting in complex interference patterns including dome-and-basin (Fig. 5a). The Devonian package of rocks is deformed by up to four phases of folding. The first phase is rarely preserved but locally can be seen as isoclinal, sometimes rootless folds in fine-grained volcanoclastic rocks (Fig. 5b). Phase-one folds have been refolded by a second phase that is responsible for the dominant foliation. The phase-two foliations are tightly folded by asymmetric phase-three folds that have shallowly east-west plunging, curvilinear fold hinges (Fig. 5c). These asymmetric folds verge to the north in some outcrops and to the south in others. A final set of open folds deforms all these rocks. The Triassic package of rocks does not seem to have been affected by the first phase of deformation that folded the Devonian rocks. Phase-one folds in the Triassic rocks are likely equivalent to phase-two folds in the Devonian package. Likewise, phases three and four in the Devonian rocks are most likely equivalent to phases two and three in the Triassic package.

In this area, the Duke River fault is marked by the contact between Chitistone limestone (usually brecciated) and

either gabbros or siltstones belonging to the Alexander terrane. This contact is poorly exposed and kinematic and geometric data for the Duke River fault is interpreted from the rocks exposed on either side of the fault.

KLUTLAN GLACIER

The westernmost exposure of the Duke River fault in Yukon occurs along a ridge near the Klutlan Glacier, a few

kilometres from the Alaska border (Fig. 1). In this area, the Duke River fault juxtaposes rocks of the Station Creek Formation against a variably deformed, medium-grained, hornblende, pyroxene gabbro to leuco-gabbro that has slivers of serpentinized ultramafic rock throughout (Fig. 6).

On the northern side of the Duke River fault, volcanic and volcanoclastic rocks of the Station Creek Formation are deformed into an upright syncline with thinly bedded

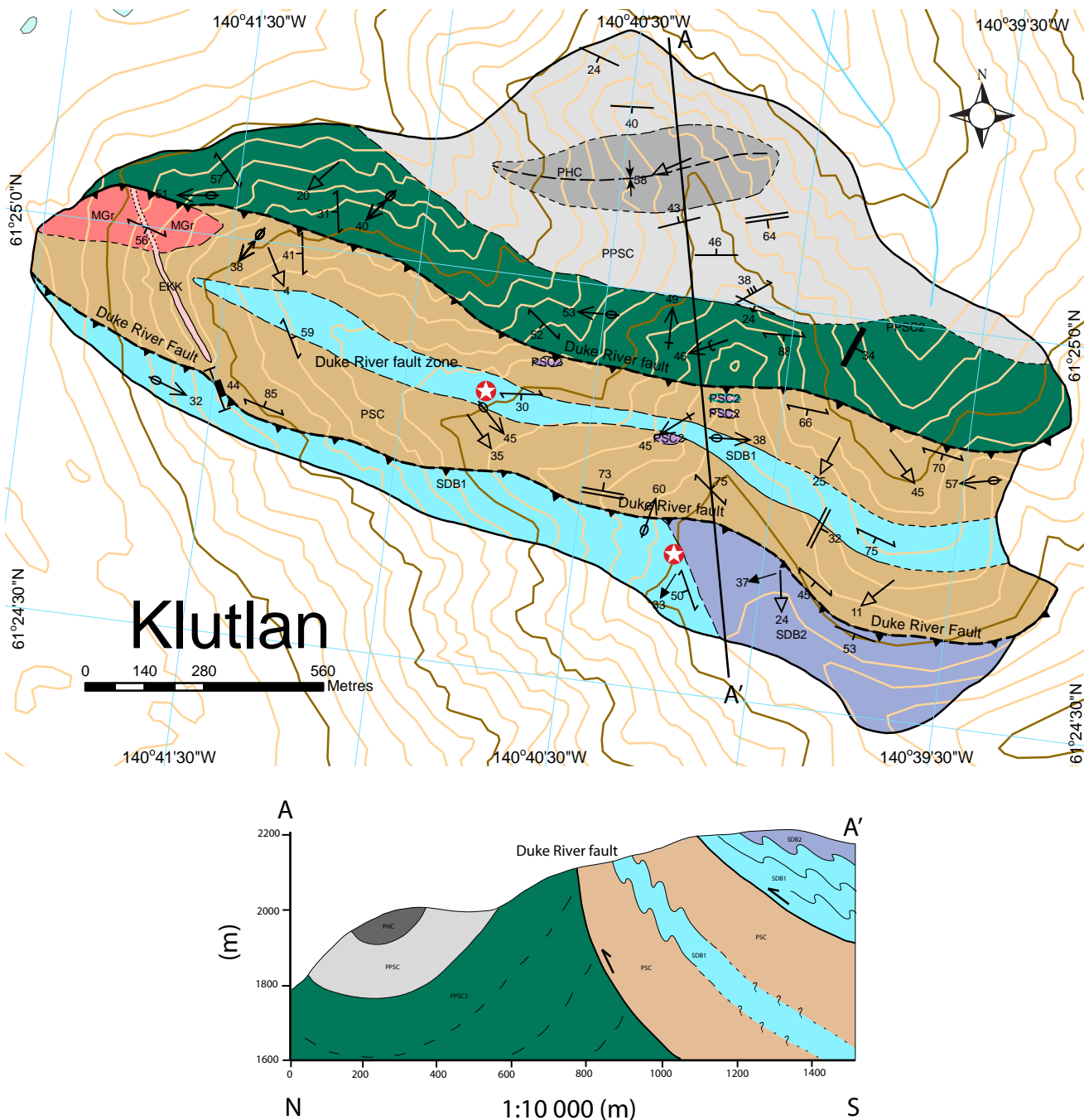


Figure 6. Geologic map and cross section (line A-A') of the Klutlan Glacier area. Refer to Figure 2b legend for symbol and unit descriptions.

sandstones and siltstones of Hasen Creek Formation in its core. This synform trends east and is sub-parallel to the Duke River fault. Locally, the Station Creek Formation is intruded by amygdaloidal fine-grained, dark brown, basaltic dykes.

South of the Duke River fault, the Alexander terrane consists of two assemblages. A deformed gabbro is in fault contact with a Silurian to Devonian limestone, muscovite schist, greenschist and minor quartzite (Fig. 6). A thin sliver of the mica schist is within the gabbro body; however, any evidence of an intrusive contact between the schist and the gabbro has been obscured by complex structures related to the adjacent faults. The gabbro is sheared in most places and locally contains fuchsite. Layers within the quartzite show dynamically recrystallized quartz grains that are inter-foliated with layers of muscovite (Fig. 7a). Foliation in the quartzite is symmetrically and openly folded and the muscovite grains are crenulated. A cataclastic zone approximately 5-10 m wide is between the gabbro and the Bullion formation south of the Duke River fault. Foliation in the gabbro and schists dominantly strike east and mainly dip to the south, although locally these structures dip shallowly to the north. Stretching lineations developed on the main foliation within the schists plunge moderately to the southeast.

The Alexander terrane in this area has been affected by a series of intrusions. An altered, pinkish, fine to medium-grained, quartz, feldspar granitic rock intrudes the Alexander terrane rocks near the Duke River fault and is foliated (Fig. 7b). A purple, fine-grained intermediate dyke crosscuts most structural fabrics and shows minor, brittle offsets in the fault zone (Fig. 7c). This dyke cannot be traced across the contact between the foliated rocks and the Station Creek Formation, suggesting the Duke River fault may have offset it. However, exposure in this area is poor and the dyke may simply disappear under colluvium on the north side of the fault. Crosscutting the gabbro and the Alexander terrane rocks are dark brown to black, fine-grained basaltic to dioritic dykes that do not appear to be deformed by the Duke River fault. Again, these dykes are not seen crosscutting the fault, but may be equivalent to the fine-grained dykes that intrude the Station Creek Formation rocks.

Preliminary age data from the Alexander terrane rocks in this area include $^{40}\text{Ar}/^{39}\text{Ar}$ dates from muscovite grains and a U-Pb age from a felsic intrusion. Preliminary $^{40}\text{Ar}/^{39}\text{Ar}$ dates for muscovite from within the quartzite yield a Permian age (256 Ma). A mineral lineation

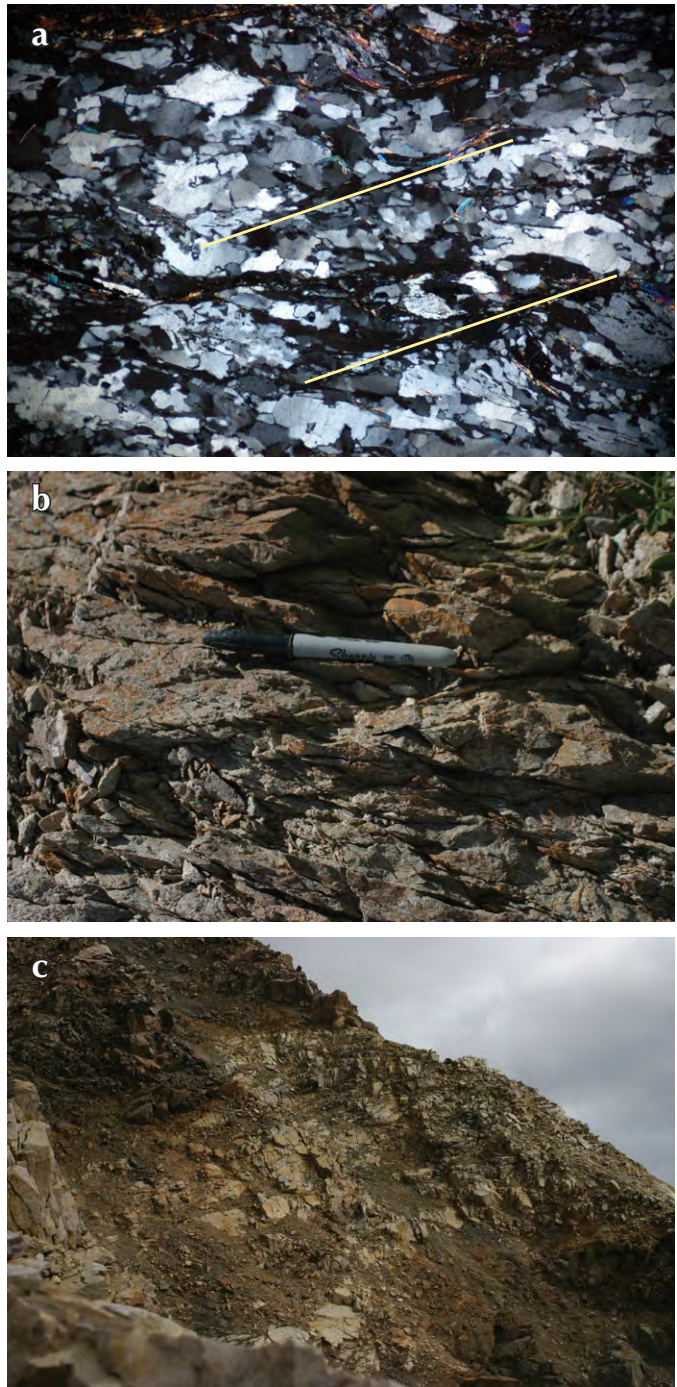


Figure 7. (a) Cross-polar photomicrograph of quartzite from the Bullion formation near Klutlan glacier showing dynamically recrystallized quartz and sinistral shear bands. Width of photograph is ~3.9 mm. (b) Felsic intrusion that has been deformed by the Duke River fault. (c) Felsic to intermediate dyke that crosscuts foliated Alexander terrane rocks and has subsequently been offset by late motion along the fault.

developed along the main foliation within the quartzite plunges moderately to the south-southwest. Muscovite grains from within the schist that occurs as a sliver in the gabbro have returned a preliminary $^{40}\text{Ar}/^{39}\text{Ar}$ Permian age (267 Ma). A preliminary U-Pb age of Early Mississippian (~351 Ma) was obtained from the foliated intrusion.

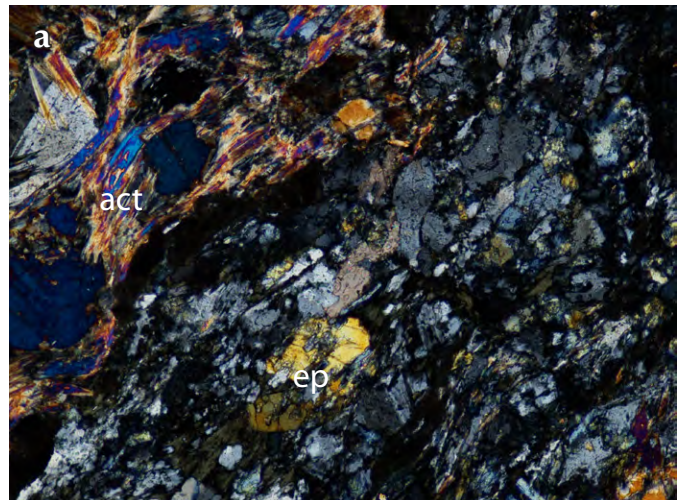
DISCUSSION

In the three mapped areas described above, the Duke River fault separates two very different assemblages of rocks. These differences include stratigraphic relationships, contrasting metamorphic grade and deformation histories. These differences suggest that the Duke River fault has accommodated significant amounts of movement.

Lithologies and the ages of rock units on either side of the Duke River fault are markedly different. For example, near Jessie Creek, a package of Triassic siltstones, ribbon cherts, gabbros and a stretched pebble conglomerate are in fault contact with Chitistone limestone. Although the units are comparable in age, the rocks do not appear to have formed in a similar environment. Further, near the Klutlan Glacier and Squaw Creek areas, the Silurian to Devonian Bullion formation consists of mainly carbonate rocks and is juxtaposed against volcanic and volcanoclastic rocks of the Pennsylvanian to Permian Skolai Group. The contrast in formation ages coupled with the different environments that these packages of rocks formed in, suggests the Duke River fault represents a suture between two terranes that evolved separately in different environments.

The St. Elias Alexander terrane, as suggested by Read and Monger (1976) and confirmed in this study, has been regionally metamorphosed to greenschist facies. This is indicated by the presence of actinolite and epidote within gabbros that intrude the Alexander terrane rocks near Jessie Creek (Fig. 8a). The Alexander terrane rocks have experienced a much higher grade of metamorphism than the relatively unmetamorphosed rocks of Wrangellia,

Figure 8. (a) Photomicrograph of gabbro that intrudes the Alexander terrane. Note the formation of epidote (ep) and actinolite (act) suggesting this rock underwent greenschist grade metamorphism. Width of photograph is ~1.7 mm. (b) Refolded folds within the Donjek formation indicating regional polyphase deformation. (c) Felsic intrusion of the Miocene Wrangell Suite is deformed by the Duke River fault.



suggested by the presence of prehnite found in the Nikolai basalts (Dodds and Campbell, 1992; Read and Monger, 1976; Greene *et al.*, 2009). The contrast in metamorphic grade across the fault suggests either that the Alexander rocks have been uplifted significant distances with respect to Wrangellia along the Duke River fault, or that strike-slip displacement along the Duke River fault has transported the previously uplifted Alexander rocks next to Wrangellia.

The Alexander terrane has undergone more extensive regional deformation than the Wrangellian rocks. Rocks belonging to the Alexander terrane, several tens of kilometres away from the Duke River fault, exhibit fold interference patterns indicative of polyphase deformation (Fig. 8b). In the study areas, only one phase of folding is seen in Wrangellia (Dodds and Campbell, 1992). The difference in number of phases of deformation affecting the two terranes suggests that the Alexander terrane was affected by more than one phase of deformation before it became juxtaposed against Wrangellia.

In general, rocks become progressively more deformed closer to the Duke River fault. For example, outcrops of the Chitistone limestone become brecciated within a few hundred metres of the fault and carbonaceous phyllitic siltstone of the Alexander terrane show up to four phases of folding within one kilometre of the fault.

TIMING OF THE DUKE RIVER FAULT

Motion along the Duke River fault likely occurred over a prolonged period of time. The Permian ages (267 Ma and 265 Ma) from the Klutlan Glacier area, either represent a resetting of muscovite by heat generated during movement on the Duke River fault, or movement along the fault that separates the gabbro from the schist, or date a previously unrecognized regional deformation event that affected the Alexander terrane in Permian time. The crenulated nature of the muscovite could reflect the two phases of regional deformation that were discussed above. Given that the foliation in the dated sample is at a high angle to the fault fabrics and that the lineation trends nearly 90° from lineations near the fault, it seems more likely that these ages date a regional deformation event.

The significance of the Cretaceous ⁴⁰Ar/³⁹Ar ages from the Squaw Creek area are unclear and can be explained by two different processes. The micas could have either formed or been thermally reset during movements along the fault in Cretaceous time, or they may have been thermally reset by the Cretaceous Pyroxenite Creek

ultramafic intrusion. The youngest movement along the Duke River fault is documented by deformation of the Wrangell lavas and associated intrusive rocks. Middle to Late Miocene (?) quartz-feldspar porphyry west of the Jessie Creek area is deformed by the Duke River fault (Fig. 8c) as are Miocene to Pliocene crystal tuffs in the Squaw Creek area. Both of these features demonstrate that the Duke River fault was active after the Miocene and possibly the Pliocene.

KINEMATICS OF THE DUKE RIVER FAULT

The sense of motion along the Duke River fault can be determined from a combination of outcrop and thin-section scale observations. In the Squaw Creek area, kinematic indicators at the outcrop-scale are best observed in the cataclastic zone. Asymmetric kink folds within this zone suggest they formed in a compressional environment. These kink folds verge to the north-northeast which suggest the Alexander terrane has been placed over Wrangellia along the Duke River fault. The foliations within the cataclastic zone dip ~35° to the south which is a favourable orientation for a thrust fault. Shear bands in thin sections cut parallel to lineations formed on the main fault foliation confirm a thrust sense of motion. Movements along the Duke River fault near Jessie Creek are less certain but likely also place the Alexander terrane northwards over Wrangellia along a steeply south-dipping reverse fault (Fig. 4). In the Klutlan area, the Duke River fault dips steeply to the south. Shear bands at outcrop scale suggest the Alexander terrane is being placed over Wrangellia along a reverse fault (Fig. 6). The fault that separates the gabbro from the schistose rocks south of the Duke River fault dips moderately to the south and is characterized by a cataclastic zone 5-10 m thick. Lineations on east-striking foliation planes within this fault, coupled with northwest-verging folds, suggest the Bullion formation is being thrust over the gabbro. The difference in metamorphic grade across all mapped areas of the Duke River fault can also be explained by thrusting, placing higher grade rocks over lower grade rocks. Although a complete kinematic history of the fault cannot be presented at this time it is clear that there has been a large amount of displacement along the Duke River fault.

SUMMARY

The Duke River fault juxtaposes two terranes that contrast in terms of metamorphic grade, degree of deformation and lithologies. On the southwest side of the fault, the Alexander terrane consists of multiply folded, Silurian to Devonian carbonates and clastic rocks and Devonian to Upper Triassic volcanic, pelitic and carbonate rocks. These rocks have been intruded by gabbros, ultramafics, granitoids and basaltic to intermediate dykes. The Alexander terrane rocks have been metamorphosed to greenschist facies and locally show up to four phases of folding.

Across the Duke River fault, Wrangellia consists of Pennsylvanian to Permian volcanic, volcanoclastic and sedimentary rocks and Upper Triassic limestones. Wrangellia has been intruded by gabbros, granitoids and fine-grained basaltic dykes. These rocks have been affected by low-grade metamorphism and one phase of folding.

Shear bands, fold orientations, rotated grains, mica fish and fault-plane orientations indicate that the Alexander terrane has been thrust over Wrangellia along the Duke River fault.

Preliminary $^{40}\text{Ar}/^{39}\text{Ar}$ age dates ranging from 90-104 Ma from muscovite grains that may have been reset by motions along the Duke River fault or grown during faulting suggest that the fault is at least as old as Cretaceous. Miocene felsic intrusions and Miocene to Pliocene crystal tuffs of the Wrangell lavas have been deformed by the Duke River fault suggesting major movement occurred along the fault as recently as the Pliocene.

ACKNOWLEDGEMENTS

Funding for this project was provided by the Yukon Geological Survey, a Geoffrey Bradshaw Memorial Scholarship and the Geological Survey of Canada through the Research Affiliate Program and through Jim Mortensen's National Science and Engineering Research Council grant. Thank you to Steve Israel, Don Murphy and Jim Mortensen for their valuable insights and comments on this paper; and to Shawn O'Connor, Kristy Long, Jenny Haywood and Sydney Van Loon for accompanying me in the field. Lastly, thank you to YGS and UBC for all of their support and contributions to this project.

REFERENCES

- Colpron, M., Nelson, J.L. and Murphy, D.C., 2007. Northern Cordilleran terranes and their interactions through time. *GSA Today*, vol. 17, p. 1-11.
- Dodds, C.J. and Campbell, R.B., 1992. Geology of Mount St. Elias map area (115B and C[E1/2]), Yukon Territory. Geological Survey of Canada, Open File, 2189.
- Gardner, M.C., Bergman, S.C., Cushing, G.W., MacKevett, E.M. Jr., Plafker, G., Campbell, R.B., Dodds, C.J., McClelland, W.C. and Mueller, P.A., 1988. Pennsylvanian pluton stitching of Wrangellia and the Alexander terrane, Wrangell Mountains, Alaska. *Geology*, vol. 16, p. 967-971.
- Gehrels, G.E. and Saleeby, J.B., 1987. Geology of southern Prince of Wales Island, southeastern Alaska. *Geological Society of America Bulletin*, vol. 98, p. 123-137.
- Greene, A.R., Scoates, J.S., Weis, D., 2008. Wrangellia flood basalts in Alaska: A record of plume-lithosphere interaction in a Late Triassic accreted oceanic plateau. *Geochemistry, Geophysics, Geosystems*, vol. 9, Q12004, doi:10.1029/2008GC002092.
- Greene, A.R., Scoates, J.S., Weis, D. and Israel, S., 2009. Geochemistry of Triassic flood basalts from the Yukon (Canada) segment of the accreted Wrangellia oceanic plateau. *Lithos*, vol. 110, p. 1-19.
- Hulbert, L.J., 1997. Geology and metallogeny of the Kluane mafic-ultramafic belt, Yukon Territory, Canada: Eastern Wrangellia - A new Ni-Cu-PGE metallogenic terrane: Geological Survey of Canada, Bulletin 506, p. 265.
- Israel, S. and Cobbett, R., 2008. Kluane Ranges bedrock geology, White River area (Parts of NTS 115F/9, 15 and 16; 115G/12 and 115K/1, 2). *In: Yukon Exploration and Geology 2007*, D.S. Emond, L.R. Blackburn and L.H. Weston (eds.), Yukon Geological Survey, p. 153-167.
- Israel, S., Cobbett, R. and Fozard, C., 2007. Bedrock geology of the Miles Ridge area, Yukon (parts of NTS 115F/15, 16 and 115K/1, 2) (1:50 000 scale), Yukon Geological Survey, Open File 2007-7.
- Israel, S., Tizzard, A. and Major, J., 2006. Bedrock geology of the Duke River area, parts of NTS 115G/2, 3, 4, 6 and 7, southwestern Yukon. *In: Yukon Exploration and Geology 2005*, D.S. Emond, G.D. Bradshaw, L.L. Lewis and L.H. Weston (eds.), Yukon Geological Survey, p. 139-154.

- Israel, S. and Van Zeyl, D.P., 2005. Preliminary geology of the Quill Creek map area, southwest Yukon, parts of NTS 115G/5, 6, 12. *In: Yukon Exploration and Geology 2004*, D.S. Emond, L.L. Lewis and G.D. Bradshaw (eds.), Yukon Geological Survey, p. 129-146.
- Lowey, G.W., 1998. A new estimate of the amount of displacement on the Denali Fault system based on the occurrence of carbonate megaboulders in the Dezadeash Formation (Jura-Cretaceous), Yukon, and the Nutzotin Mountains sequence (Jura-Cretaceous), Alaska. *Bulletin of Canadian Petroleum Geology*, vol. 46, p. 379-386.
- MacKevett, E.M., 1971. Stratigraphy and general geology of the McCarthy C-5 quadrangle, Alaska. *US Geological Survey Bulletin*, B-1323, p. 35.
- McClelland, W.C., Gehrels, G.E. and Saleeby, J.B., 1992. Upper Jurassic-Lower Cretaceous basinal strata along Cordilleran margin: Implications for the accretionary history of the Alexander-Wrangellia-Peninsular terrane. *Tectonics*, vol. 11, p. 823-835.
- Monger, J.W.H., Price, R.A. and Tempelman-Kluit, D.J., 1982. Tectonic accretion and the origin of the two major metamorphic and plutonic welts in the Canadian Cordillera. *Geology*, vol. 10, p. 70-75.
- Page, R.A., Biswas, N.N., Lahr, J.C. and Pulpan, H., 1991. Seismicity of continental Alaska. *In: Neotectonics of North America*, D.B. Slemmons, E.R. Engdahl, M.D. Zoback and D.D. Blackwell (eds.), Boulder, Colorado, Geological Society of America, Decade Map Volume 1.
- Power, M.A., 1988. Mass movement, seismicity, and neotectonics in the northern St. Elias Mountains, Yukon. Unpublished MSc thesis, University of Alberta, Edmonton, Alberta.
- Read, P.B. and Monger, J.W.H., 1976. Pre-Cenozoic volcanic assemblages of the Kluane and Alsek Ranges, southwestern Yukon Territory. *Geological Survey of Canada, Open File 381*, 96 p.
- Ridgway, K.D., Trop, J.M., Nokleberg, W.J., Davidson, C.M. and Eastham, K.R., 2002. Mesozoic and Cenozoic tectonics of the eastern and central Alaska Range: Progressive basin development and deformation in a suture zone. *Geological Society of America Bulletin*, vol. 114, p. 1480-1504.
- Smith, J.G. and MacKevett, E.M., 1970. The Skolai Group in the McCarthy B-4, C-4 and C-5 quadrangles, Wrangell Mountains, Alaska, U.S. Geological Survey, *Bulletin 1274-Q*, p. 1-26.
- van der Heyden, P., 1992. A Middle Jurassic to early Tertiary Andean-Sierran arc model for the Coast Belt of British Columbia. *Tectonics*, vol. 11, p. 82-97.
- Wheeler, J.O., Brookfield, A.J., Gabrielse, H., Monger, J.W.H., Tipper, H.W. and Woodsworth, G.J., 1991. *Terrane Map of the Canadian Cordillera*, Geological Survey of Canada, 1713A.

Bedrock geology of southwest McQuesten (NTS 115P) and part of northern Carmacks (NTS 115I) map area

Maurice Colpron¹
Yukon Geological Survey

James J. Ryan
Geological Survey of Canada

Colpron, M. and Ryan, J.J., 2010. Bedrock geology of southwest McQuesten (NTS 115P) and part of northern Carmacks (NTS 115I) map area. *In: Yukon Exploration and Geology 2009*, K.E. MacFarlane, L.H. Weston and L.R. Blackburn (eds.), Yukon Geological Survey, p. 159-184.

ABSTRACT

The Southwest McQuesten-northern Carmacks area is primarily underlain by rocks of the Yukon-Tanana terrane which is divided into two distinct belts separated by the Willow Creek fault: 1) a central belt of polydeformed, upper greenschist-amphibolite facies metasedimentary and metaplutonic rocks of Permian and older ages; and 2) a northeastern belt of generally undeformed and unmetamorphosed volcano-plutonic rocks of the Early Mississippian Reid Lakes complex. The southern part of the area is underlain mainly by rocks of Quesnellia and Stikinia, including: 1) Paleozoic retrogressed metamorphic rocks of the Boswell assemblage; 2) Upper Triassic augite-phyric volcanic rocks; and 3) Early Jurassic granitoids of the Aishihik plutonic suite. These rocks are dissected by a series of dextral strike-slip faults, probably related to the Teslin fault system. Post-accretion rocks include: 1) mid-Cretaceous biotite monzogranite plutons; 2) dacite and minor basalt of the Upper Cretaceous Carmacks Group; and 3) Quaternary basalt of the Selkirk volcanics. The southwest McQuesten-northern Carmacks area is under-explored, but shares many geological attributes with nearby, highly prospective districts such as the Dawson Range mineral belt, the recently discovered White Gold area and the producing Minto Mine.

¹maurice.colpron@gov.yk.ca

INTRODUCTION

Regional bedrock mapping of the southwest McQuesten and northern Carmacks map areas was carried out between July and early August 2009 (Fig. 1), as part of a joint initiative of the Geological Survey of Canada and Yukon Geological Survey. The project was conducted under the auspices of the Edges project (Multiple Metals Northwest Canadian Cordillera) as part of National Resources Canada's Geomapping for Energy and Minerals

(GEM) program. The area was selected for bedrock mapping because it had not been mapped since reconnaissance mapping by H.S. Bostock in the 1940s (published in 1964), and it was highlighted as a priority area by the Yukon Geological Survey (e.g., Abbott, 2005) due to limited understanding of its mineral prospectivity. Recent mapping of the southwest McQuesten-northern Carmacks area has been the first instalment of a three-year program that will continue westward across the northern Dawson Range (north Stevenson Ridge map

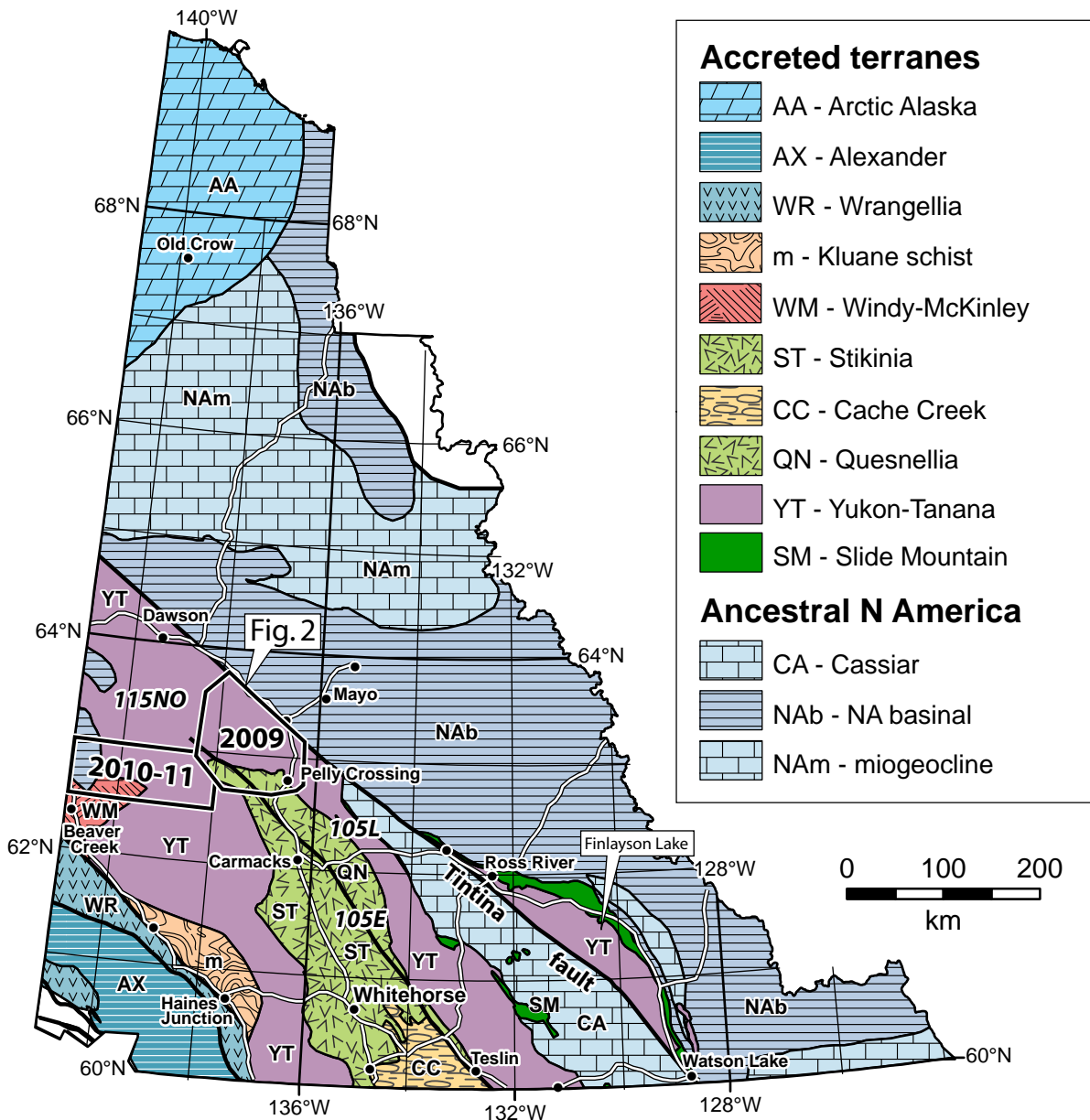


Figure 1. Terrane map of Yukon. Outlines between Pelly Crossing and Beaver Creek illustrate the extent of the area mapped in 2009 (Fig. 2) and the planned mapping area for 2010-2011. They also approximate the area covered by new aeromagnetic surveys (Kiss and Coyle, 2009 a-r, for McQuesten, see Figure 3; and Kiss and Coyle, 2009 s-af, for northern Stevenson Ridge).

sheet - NTS 115J,K) to the Alaska border (see 2010-11 in Fig. 1).

The southwest McQuesten-northern Carmacks area is characterized by rolling hills of the deeply entrenched Yukon Plateau. It is generally covered by dense vegetation and soil, and bedrock is typically poorly exposed. Much of the area was glaciated by the early to middle Pleistocene (pre-Reid) glaciations, and is now bounded by unglaciated terrain to the west and by glacial deposits of the Illinoian glaciation (Reid) to the east. Thick sequences of pre-Reid drift are found in valley bottoms, while slopes are covered in thin colluvium and weathered bedrock (Bond and Lipovsky, this volume). Due to the lack of bedrock exposure, ground-truthing efforts were maximized with the aid of a detailed aeromagnetic survey which was acquired in the previous winter (Kiss and Coyle, 2009a-r).

Access to the southwest McQuesten-northern Carmacks area is limited. It is approximately bounded on the northeast by the North Klondike Highway, which follows in part the Tintina Trench (see Tintina fault, Fig. 1). Near its southern limit, the area can be accessed via a 50 km dirt road extending westward from Pelly Crossing and leading to the Pelly River Ranch, where 2009 field operations were based. The area is also accessible by rivers, namely the Stewart River, along the northwest limit of the map, and the Pelly and Yukon rivers, near the southern limit of the map (Fig. 2). The historical site of Fort Selkirk, a traditional settlement of the Selkirk First Nation, and the first Hudson's Bay Company trading post in Yukon, established by Robert Campbell in 1848, is located near the western apex of the map area. The centre of the map area is mainly accessible by helicopter, although dense vegetation commonly limits the number of possible landing sites. Since the northern area is situated in the semi-arid Yukon Plateau of central Yukon, a region regularly subjected to forest fires, the forest cover is open in many parts of McQuesten, thus facilitating helicopter access. In 2009, forest fires impeded access to parts of the area along its western limit and dense smoke hampered visibility while flying.

Here we present the bedrock geology for southwest McQuesten-northern Carmacks area based primarily on observations made during the 2009 field season, in combination with recently acquired U-Pb geochronological data. This report is to accompany the 1:250 000-scale map of the area which is to be published as an Open File by the Geological Survey of Canada (Ryan *et al.*, in prep.). Continued geochronological,

geochemical and petrographical studies will inevitably provide further constraints that will lead to revisions of the preliminary interpretations presented here.

REGIONAL SETTING AND PREVIOUS WORK

The southwest McQuesten-northern Carmacks area is situated southwest of the Tintina fault and is predominantly underlain by metamorphic rocks of the Yukon-Tanana terrane (Figs. 1, 2). The Carmacks and McQuesten map sheets were first mapped at a scale of 1:253,440 by H.S. Bostock, who accessed these areas with horse pack parties in the mid-1930s and 1940s (Bostock, 1936; 1964), respectively. With the exception of an area that was mapped in some detail around the White Mountains (Erdmer, 1982), the McQuesten area has received little attention since the work of H.S. Bostock. The Carmacks area was remapped at 1:250 000 scale by Tempelman-Kluit (1984; 2009). The southwest McQuesten-northern Carmacks area is between two areas that were recently mapped under the auspices of the Ancient Pacific margin NATMAP project and include: i) Stewart River (115N,O) to the northwest (Ryan and Gordey, 2004; Gordey and Ryan, 2005); and ii) Glenlyon (105L) to the southeast (Colpron *et al.*, 2002; 2003; 2006b). These and other Ancient Pacific margin NATMAP projects (*cf.* Colpron and Nelson, 2006) have contributed to a significant improvement in our knowledge and understanding of the Yukon-Tanana terrane that has resulted in the development of its regional stratigraphic framework (Colpron, 2006; Colpron *et al.*, 2006a). The Yukon-Tanana terrane comprises a basement complex of metasedimentary origin (Snowcap assemblage) overlain by three unconformity-bounded, volcano-sedimentary sequences of predominantly arc affinity: the Finlayson (Upper Devonian to Lower Mississippian), Klinkit (Upper Mississippian to Lower Permian) and Klondike (Middle to Upper Permian) assemblages. Plutonic suites associated with these arc sequences include the Grass Lakes suite (ca. 365-357 Ma), the Simpson Range suite (ca. 355-345 Ma), the Tatlain suite (ca. 342-336 Ma) and the Sulphur Creek suite (ca. 264-252 Ma). Rocks of the Yukon-Tanana terrane experienced at least two phases of penetrative deformation and metamorphism in the Late Permian and Early Jurassic, and show evidence for older, less pervasive events in the Late Devonian and mid-Mississippian (Murphy *et al.*, 2006; Colpron *et al.*, 2006a; 2006b; Berman *et al.*, 2007).

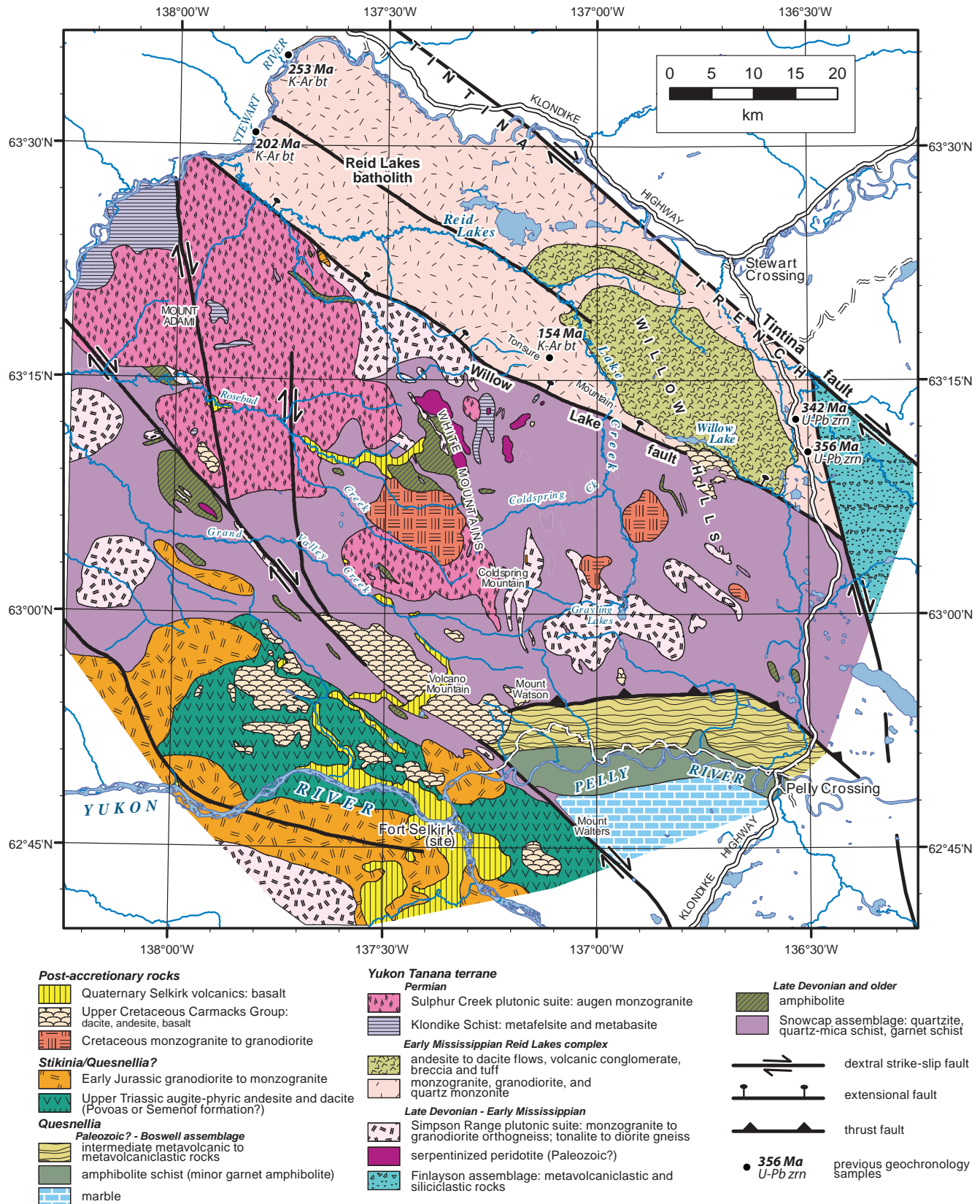


Figure 2. Simplified geological map of southwest McQuesten-northern Carmacks area (after J.J. Ryan, M. Colpron and N. Hayward, in prep.).

The southern edge of the map area is underlain by rocks assigned to Quesnellia and Stikinia (Fig. 2), two major mid-Paleozoic to early Mesozoic arc terranes that are distinguished in British Columbia by their occurrence on either side of the oceanic Cache Creek terrane. The McQuesten project area is situated at the northern apex of these two arc terranes (Fig. 1). Both Quesnellia and Stikinia are primarily characterized by Upper Triassic augite (\pm plagioclase)-phyric andesite and basaltic andesite, locally overlying mid- to upper Paleozoic volcano-sedimentary sequences. In Yukon, Late Triassic to Early Jurassic granite plutons intrude the Stikinia, Quesnellia and Yukon-Tanana terranes. Plutons of this suite occupy the southwestern corner of the map area (Fig. 2), and are of particular metallogenic importance as they host many significant porphyry Cu-Au (\pm Mo) deposits in British Columbia, as well as the Yukon's high-grade Cu-Au Minto Mine and Carmacks Copper (Williams Creek) deposit (Schroeter, 1995; Nelson and Colpron, 2007).

The area is locally underlain by younger, post-accretion, mid-Cretaceous plutonic rocks; volcanic rocks of the Upper Cretaceous Carmacks Group; and Tertiary to recent lavas of the Selkirk volcanics. We have found all of these units to be less extensive than what was previously mapped (*cf.* Gordey and Makepeace, 1999).

MCQUESTEN AEROMAGNETIC SURVEY

In the winter prior to the 2009 field season, a GEM-funded aeromagnetic survey was flown to support bedrock mapping of the poorly exposed McQuesten project area (Kiss and Coyle, 2009a-r). The new survey covered approximately 23 000 line-kilometres at a spacing of 400 m, and 150-m-nominal terrain clearance (Kiss and Coyle, 2009a-r). This new survey was an improvement on the 800 m line-spacing of the previously available regional coverage. Results of the survey are available for download from the GSC's Geoscience Data Repository website (<http://gdr.nrcan.gc.ca/aeromag/>).

In general, the new survey offers an increased resolution that sharpens major anomalies and highlights subtle magnetic features that were not obvious in the older data. In particular, the latest aeromagnetic data highlights a number of prominent anomalies that may represent major structures or lithological features in the area (Fig. 3). The data proved useful in extrapolating limited ground observations across areas with poor bedrock exposure, and was beneficial to strategic planning of ground traverses.

Figure 3 is an image of the first vertical derivative of the magnetic data, which enhances the signal from near-surface sources, and is most useful for bedrock mapping. The most intense anomalies reflect highly magnetic ultramafic bodies in the centre of the map area, the Selkirk volcanic flows in the west, and the Carmacks volcanic flows in the south and east (Figs. 2, 3). Major faults are outlined by magnetic lows and truncation of the magnetic fabric (Fig. 3). Further processing and filtering of the data will likely outline additional structures in the area. For the mineral exploration industry, recent exploration successes in the Stewart River and Dawson Range areas have relied, in part, on detailed geophysical surveys, thus the recent McQuesten dataset will likely prove useful for guiding exploration in this under-explored, poorly exposed area.

YUKON-TANANA TERRANE

The Yukon-Tanana terrane in the McQuesten area occurs in two distinct northwest-trending belts that are separated by the Willow Lake fault (Fig. 2). Southwest of the fault, rocks that typify the terrane are variably deformed, metamorphosed (up to amphibolite facies) and include: siliciclastic, pelitic (commonly carbonaceous) and carbonate sedimentary rocks; mafic, intermediate and felsic volcanic rocks; and a wide variety of plutonic rocks ranging from ultramafic to felsic in composition (*e.g.*, Colpron *et al.*, 2006a). In contrast, rocks exposed on the northeast side of the Willow Lake fault are generally undeformed and only weakly altered (essentially unmetamorphosed). They comprise primarily intrusive rocks of intermediate to felsic composition and, near the eastern limit of our map area, a sequence of intermediate to felsic volcanic and volcanoclastic rocks coeval with the main plutonic body, the Reid Lakes batholith (Fig. 2).

We describe below the metamorphic rocks exposed on the southwest side of the Willow Lake fault, followed by a description of the volcano-plutonic complex that is northeast of the fault. Together with preliminary U-Pb data (not presented here) and past experience in mapping of the Yukon-Tanana terrane, we propose initial correlations with regional stratigraphic units. It is recommended that the reader remain aware of the preliminary nature of our conclusions. As new geochronological and geochemical data become available, correlations presented here will likely be revised.

LAYERED ROCKS SOUTHWEST OF THE WILLOW LAKE FAULT

Based on composition and field relationships, the rocks exposed southwest of the Willow Lake fault are tentatively assigned to regional tectonostratigraphic units of the

Yukon-Tanana terrane (cf. Colpron *et al.*, 2006a). These rocks preserve at least two penetrative foliations and show evidence for metamorphism at upper greenschist to middle amphibolite facies conditions. Metasedimentary rocks in the area have been assigned to the Snowcap assemblage (Fig. 2) while associated metabasites have

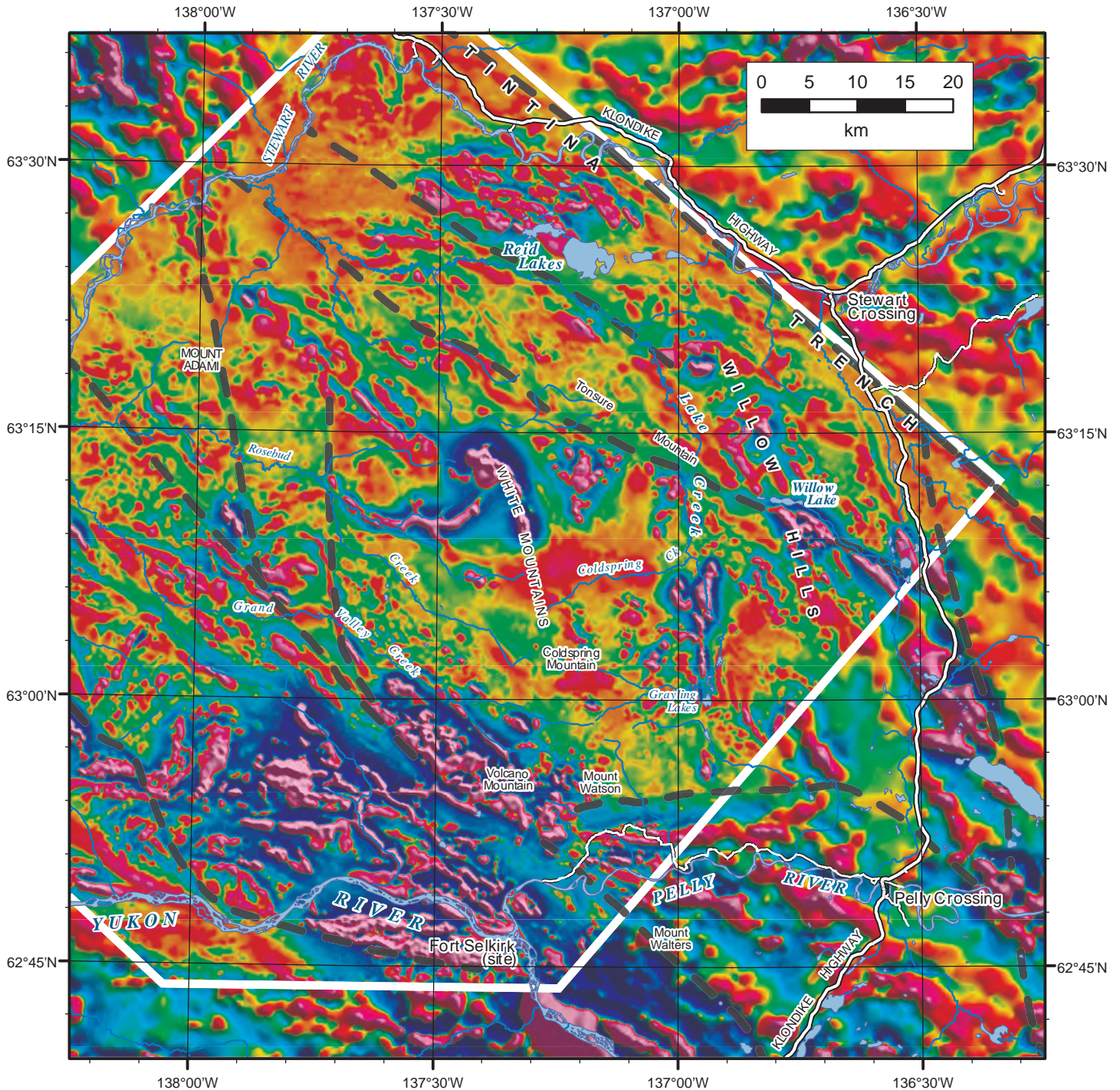


Figure 3. First vertical derivative of aeromagnetic data; 2009 detailed data (outlined in white; 400 m line-spacing) fused with regional archived data (800 m line-spacing). Grey dashed lines are major faults from Figure 2.

been classified as either the Snowcap assemblage, or the overlying Finlayson assemblage. Intermediate to felsic metavolcanic rocks have been assigned to the Klondike assemblage.

Snowcap assemblage

The Snowcap assemblage comprises quartzite, micaceous quartzite and psammitic quartz-muscovite-biotite (\pm garnet) schist. The quartzite is generally fine grained, banded to massive, grey to white in colour (Fig. 4a), and most commonly intercalated (on a centimetre-scale) with garnet-bearing pelitic schist. Locally, pebble metaconglomerate horizons occur within the quartzite (Fig. 4b). In places, the quartzite and intercalated pelitic schist are dark grey in colour, carbonaceous, and locally graphitic (Fig. 4c). It is unclear whether the carbonaceous rocks are a variation of the Snowcap assemblage as described near its type locality in the Glenlyon area to the southeast (Colpron *et al.*, 2003; Piercey and Colpron,

2009), or if they might be equivalent to carbonaceous rocks of the Nasina quartzite in the Stewart River area to the northwest (Gordey and Ryan, 2005). In the Stewart River area, the Nasina quartzite is a regionally extensive unit of the Finlayson assemblage that is not typically associated with metavolcanic rocks or intercalated with Snowcap assemblage rocks (Gordey and Ryan, 2005; Colpron *et al.*, 2006a). In the McQuesten area, carbonaceous meta-siliciclastic rocks are rare and generally associated with metabasic rocks (see following section). They occur as 10 to 100-m-thick horizons within the Snowcap assemblage and may be indicative of compositional variations within the siliciclastic assemblage.

Marble and calc-silicate schist are minor constituents of the metasedimentary belt that occupies the centre of the McQuesten map area. Marble is present in isolated lenses up to tens of metres in thickness. In outcrop, these rocks appear massive and light grey in colour (Fig. 4d), with little obvious compositional variation.

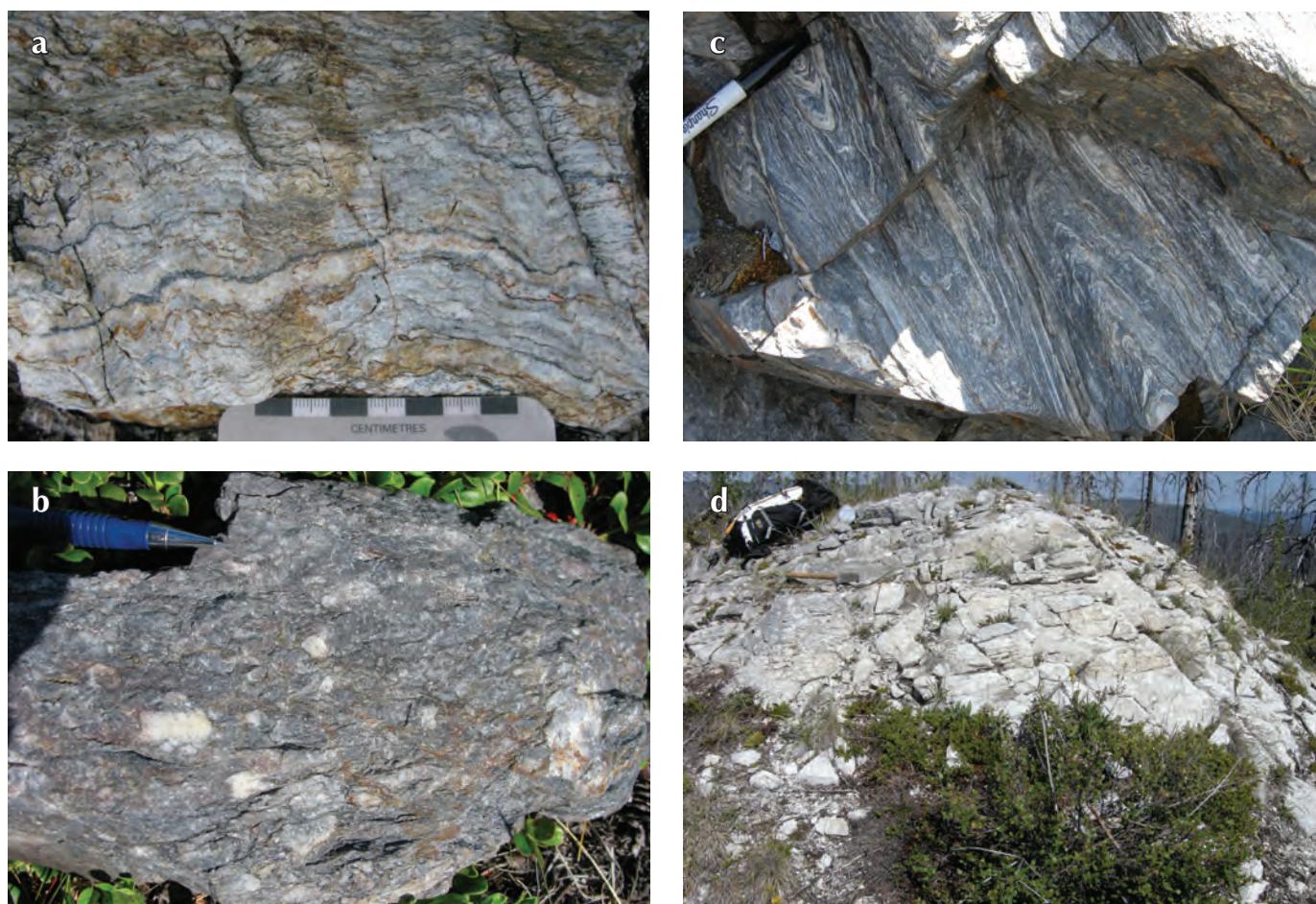


Figure 4. Representative lithologies of the Snowcap assemblage in southwest McQuesten map area: (a) banded quartzite; (b) pebble metaconglomerate; (c) tightly folded carbonaceous quartzite; and (d) marble.

Regionally, the Snowcap assemblage is constrained to be Late Devonian and older by cross-cutting plutons and overlying metasedimentary rocks (Colpron *et al.*, 2006a, 2006b). Detrital zircon profiles and geochemistry of the assemblage are consistent with derivation of protoliths from late Proterozoic to early Paleozoic continental margin similar to the northwest Laurentian miogeocline (Piercey and Colpron, 2009).

Metabasites

Amphibolite and greenstone are locally associated with metasedimentary rocks of the Snowcap assemblage throughout southwestern McQuesten map area (Fig. 2). Amphibolites are most prominent near the White Mountains. They are typically fine to medium-grained and composed of hornblende-plagioclase (\pm garnet)-bearing, massive to schistose rock (Fig. 5a). Coarser grained, homogeneous (Fig. 5b) varieties also occur and may reflect an intrusive origin for some amphibolites. Garnet porphyroblasts (≤ 1 cm) are common to most occurrences (Fig. 5b). Occasionally, amphibolites are retrogressed to chlorite-biotite schist, but most often are characterized by heterogeneous layering and local preservation of volcanic and/or volcanoclastic textures that provide clues to their protolith.

Greenstone is less common; its main exposures occur near Coldspring Mountain (Fig. 2). The greenstone is characterized by a chlorite-actinolite assemblage typical of greenschist facies metamorphism. It is commonly medium green and fine grained, locally preserving relict volcanic and volcanoclastic textures that are evident when viewed down the stretching lineation. The greenstone may represent a lower grade equivalent of the amphibolites mapped to the north, or may be a distinct volcanic sequence that records lower peak metamorphic conditions. It could also represent an isolated occurrence of the Permian Klondike assemblage, rather than the Mississippian or older metabasites.

We do not know with which unit(s) of the Yukon-Tanana terrane the amphibolite and greenstone are most closely affiliated. Garnet amphibolite occurrences are a common constituent of the Snowcap assemblage at its type locality in central Yukon (Piercey and Colpron, 2009) and in the correlative Dorsey complex of northern British Columbia (Nelson and Friedman, 2004). In both regions, Snowcap assemblage amphibolites are characterized by enriched mid-ocean ridge basalt (E-MORB) and/or ocean island basalt (OIB) geochemical signatures. In contrast, garnet amphibolites intercalated with metasedimentary rocks

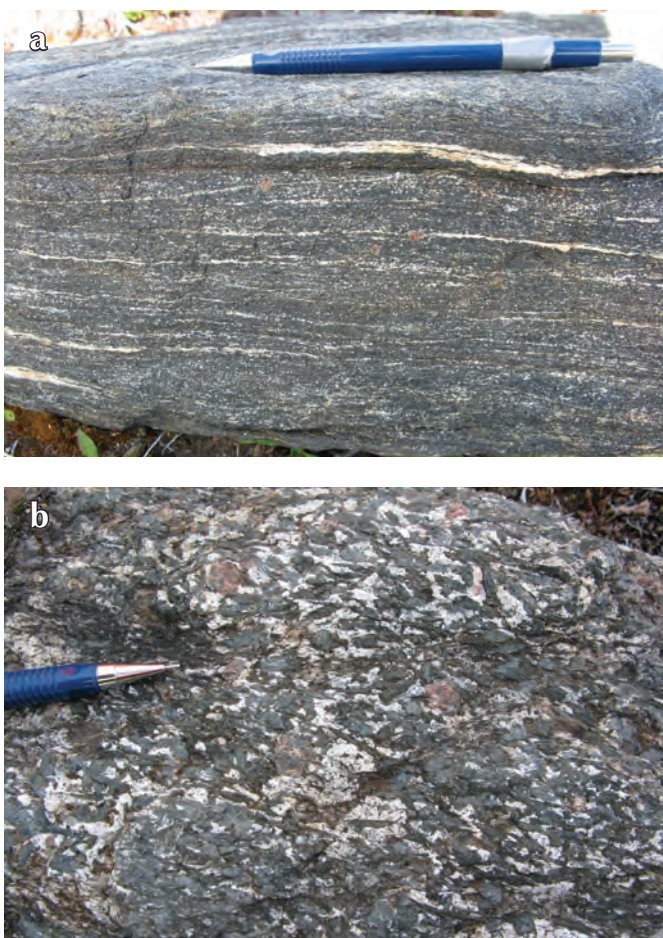


Figure 5. Metabasite of Devono-Mississippian Yukon-Tanana terrane: (a) fine-grained garnet amphibolite; and (b) coarse-grained garnet amphibolite (metagabbro?).

that may be correlative with the Snowcap assemblage in the Stewart River area have geochemical signatures more typical of island arc tholeiites (IAT; S.J. Piercey and J.J. Ryan, unpublished data) and thus are correlated with arc sequences of the Finlayson assemblage of Yukon-Tanana terrane (Piercey *et al.*, 2006). Whole-rock geochemical data for similar rocks in southwest McQuesten area are critical to establishing the setting in which they were emplaced, and ultimately their stratigraphic position within the terrane.

Klondike assemblage

Intermediate chlorite- and quartz-feldspar augen muscovite schists exposed mainly in the northwestern part of the map area are assigned to the Middle to Late Permian Klondike assemblage (Fig. 2). These rocks are typically spatially associated with quartz and K-feldspar

augen granite of the Permian Sulphur Creek plutonic suite (see below). Felsic to intermediate schists of the Klondike assemblage are characterized by a sericite and quartz matrix with more altered and/or metamorphosed examples preserving decussate hornblende (Fig. 6a) and locally coarse (>1 cm) garnet porphyroblasts (Fig. 6b). Hornblende porphyroblasts are in places pseudomorphed by chlorite and biotite. The felsic to intermediate schists are likely derived from volcanic or hypabyssal intrusive protoliths. Locally, the distinction between volcanic rocks of the Klondike assemblage and plutonic rocks of the Sulphur Creek suite is difficult to make. It can be demonstrated in places that the felsic Klondike schist is a highly strained equivalent of the Sulphur Creek suite.

Chlorite schist exposed northwest of Mount Adami is thought to represent intermediate to mafic metavolcanic rocks of the Klondike assemblage. They commonly have pitted weathering surfaces resulting from oxidation of pyrite crystals (Fig. 6c), and locally preserve relict volcanic textures. These rocks are typical of the intermediate to mafic compositions mapped in the Klondike assemblage of the Stewart River area to the west (Gordey and Ryan, 2005).

INTRUSIVE ROCKS SOUTHWEST OF WILLOW LAKE FAULT

Metaplutonic rocks in the Yukon-Tanana terrane exposed southwest of the Willow Lake fault are assigned to two distinct plutonic suites, based primarily on composition and field characteristics: 1) the Early Mississippian Simpson Range suite; and 2) the Middle to Late Permian Sulphur Creek suite (Fig. 2). Akin to the metasedimentary and metavolcanic rocks described above, metaplutonic rocks southwest of the Willow Lake fault also preserve at least two penetrative foliations and metamorphism at greenschist to amphibolite facies conditions.

Simpson Range plutonic suite

The Simpson Range plutonic suite encompasses rocks of widely varying composition, from monzogranite to diorite. The rocks are generally fine to medium grained, equigranular, and weakly to strongly foliated; they commonly are gneissic. Monzogranite to granodiorite are most common. In outcrop, rocks of this suite are typically biotite bearing and pink to orange in colour (Fig. 7a). Locally, monzogranite and granodiorite are porphyritic with K-feldspar phenocrysts (or augens) up to 1 cm long (Fig. 7b). The porphyritic phase resembles the Permian augen granite of the Sulphur Creek suite (see below), but

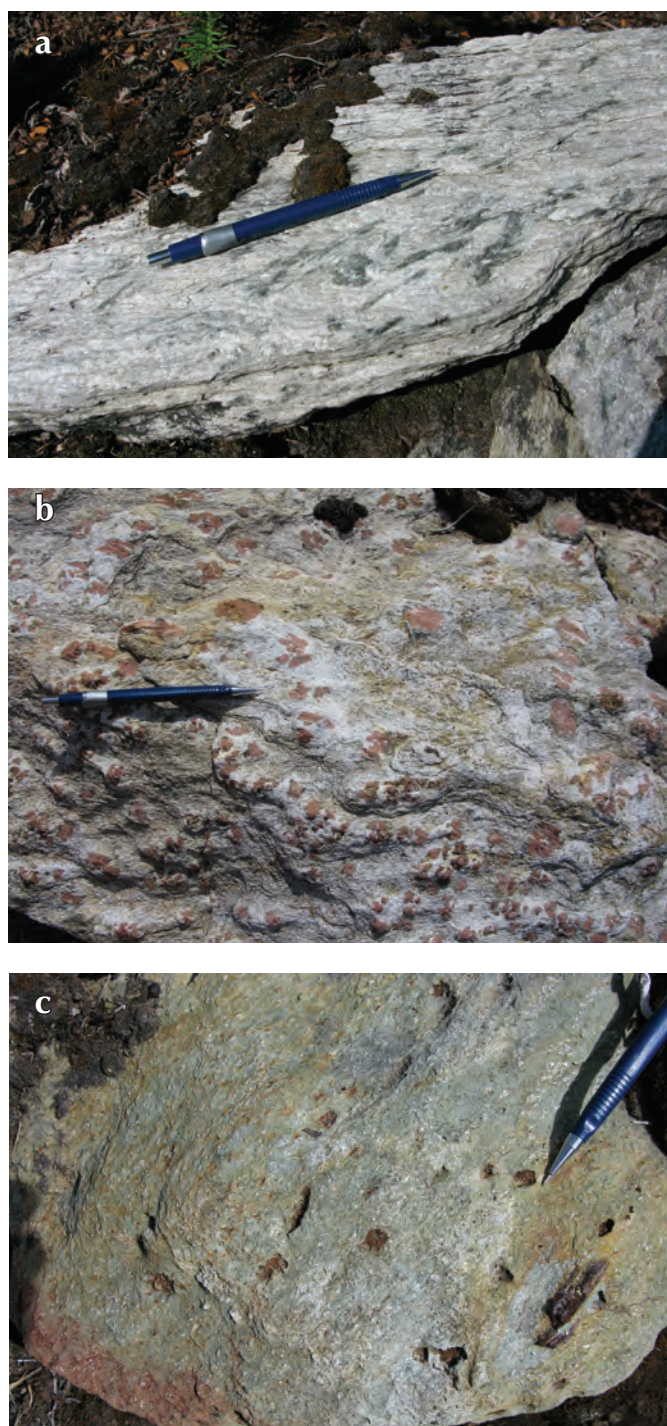


Figure 6. Representative lithologies of the Klondike assemblage: (a) felsic schist with decussate hornblende porphyroblasts; (b) garnet-muscovite schist; and (c) pitted chlorite schist.

are in general, more feldspathic than the Sulphur Creek suite.

Medium to dark grey tonalite to diorite are also common constituents of the Simpson Range suite. These rocks are invariably fine grained, equigranular, and biotite bearing (Fig. 7c). Locally, elongate biotite clots are suggestive of biotite pseudomorphs after hornblende. In outcrop, the compositionally mafic varieties of this suite of rocks are commonly homogeneous and locally layered (Fig. 7d).

On the regional scale of the Yukon-Tanana terrane, the Simpson Range plutonic suite includes felsic to intermediate plutons ranging in age from 357 Ma to 345 Ma (Mortensen, 1992; Piercey *et al.*, 2006). In southwest McQuesten area, plutons that have been assigned to this suite are presently undated, but are inferred to be Early Mississippian in age. Similar plutons in adjacent parts of Yukon-Tanana terrane to the northwest (Stewart River area; J.J. Ryan and S.P. Gordey, unpublished data; Ruks *et al.*, 2006; Mortensen, 1992)

and the southeast (Glenlyon area; Colpron *et al.*, 2006b) yield Mississippian ages ranging from ca. 357 Ma to ca. 343 Ma. However, preliminary U-Pb results from a foliated tonalite body on Coldspring Mountain indicate that some 'Simpson Range' rocks may actually be Permian in age (see below).

Sulphur Creek plutonic suite

Metaplutonic rocks assigned to the Sulphur Creek suite are primarily exposed in the northwestern part of the map area, between Mount Adami and the White Mountains (Fig. 2). They consist of monzogranites that are variably deformed, fine to medium grained, biotite bearing, and quartz and K-feldspar porphyritic to augen bearing (Fig. 8a). They commonly display a strong transposition foliation overprinted by up to two crenulations (Fig. 8b). Locally, metaplutonic rocks of the Sulphur Creek suite are porphyroclastic straight gneisses. In places, the Sulphur Creek suite is represented by fine-grained, homogeneous felsic gneiss with a sugary texture. Augen granites of the

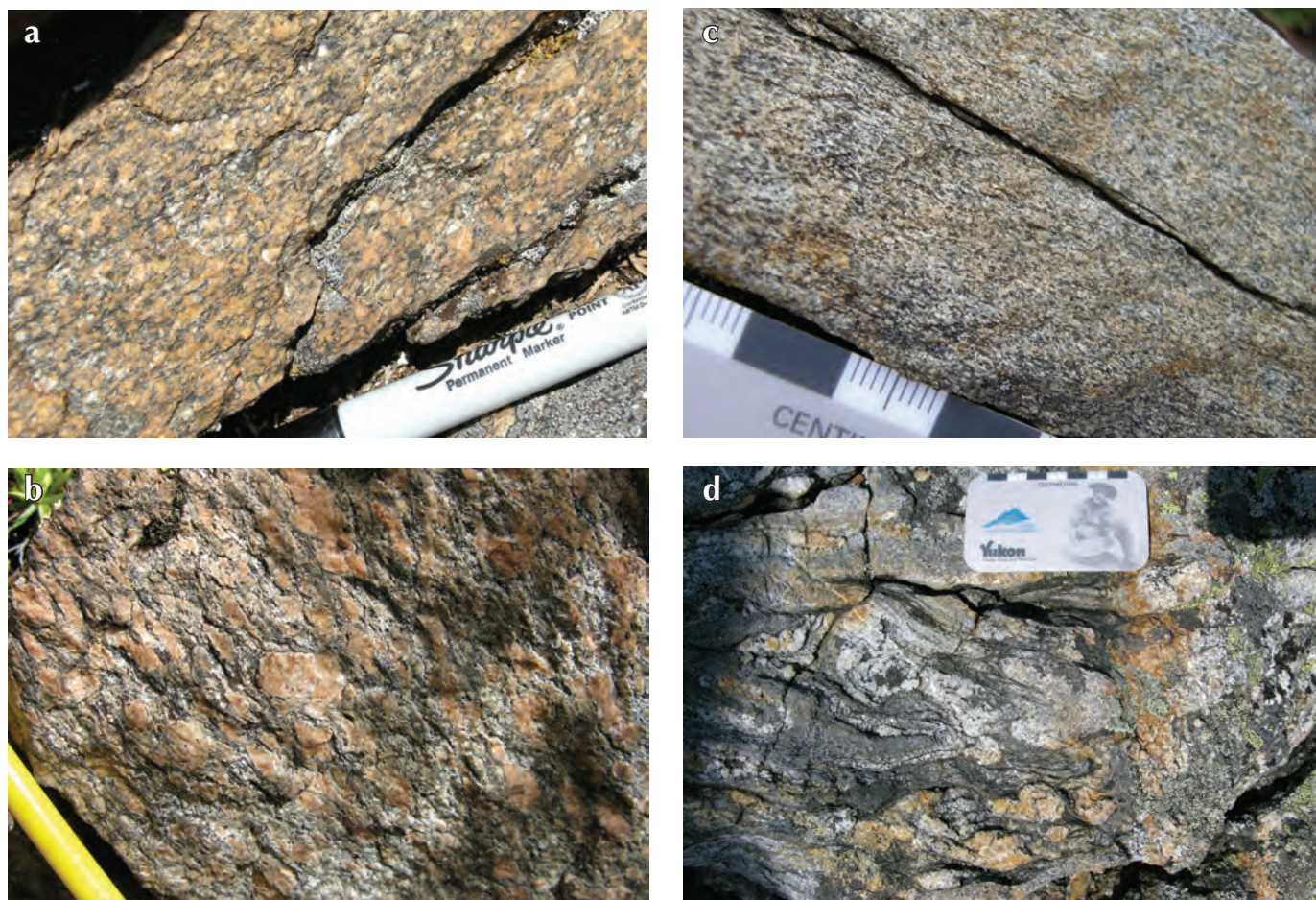


Figure 7. Representative lithologies of the Simpson Range plutonic suite: (a) pink monzogranite; (b) K-feldspar augen monzogranite; (c) fine-grained tonalite; and (d) layered diorite gneiss.

Sulphur Creek suite are spatially associated with felsic to intermediate schists of the Klondike assemblage (Fig. 2). As noted above, the distinction between metaplutonic rocks of the Sulphur Creek suite and felsic metavolcanic rocks is often difficult to discern, and may reflect variations in the degree of strain (Fig. 8b). The Sulphur Creek plutonic suite and Klondike assemblage range in age from 264 Ma to 252 Ma in the Klondike region to the northwest, and the Stewart River map sheet in general (Mortensen, 1990; Ruks *et al.*, 2006).

During 2009 field mapping, strongly foliated, fine-grained, hornblende-biotite tonalite to granodiorite that is exposed on Coldspring Mountain was assigned to the Simpson Range plutonic suite described above. However, preliminary U-Pb zircon dating suggests a Middle Permian age (N. Joyce, pers. comm., 2009), thereby casting doubt on how metaplutonic rocks in southwest McQuesten map

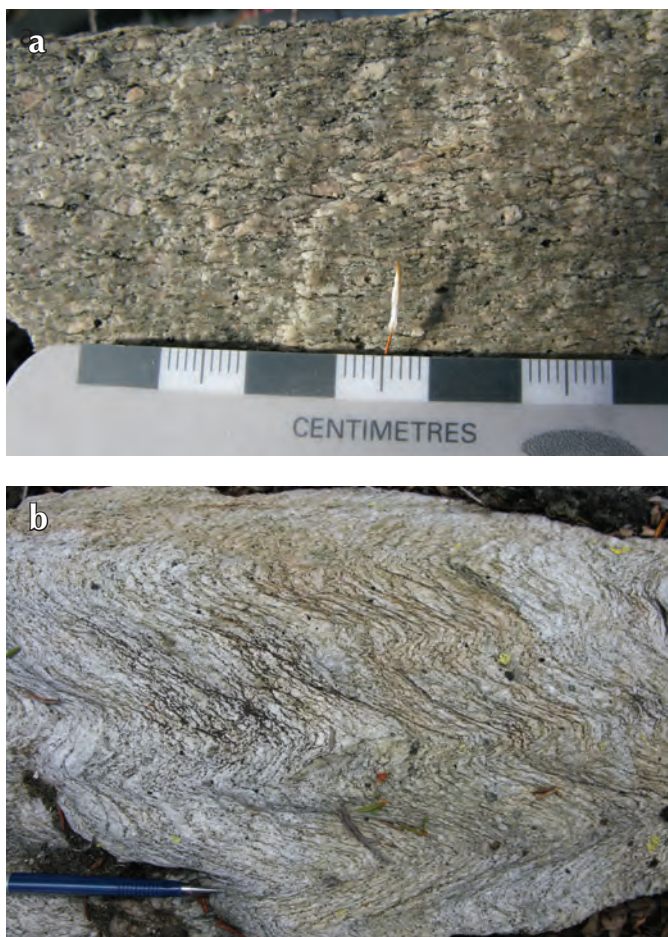


Figure 8. Representative lithologies of the Sulphur Creek plutonic suite: (a) quartz-feldspar augen granite; and (b) Klondike schist derived from plutonic quartz monzonite superposed by transposition foliation and crenulation.

area are classified through field descriptions alone. Additional geochronology of metaplutonic bodies in southwestern McQuesten area is necessary to discriminate between the Mississippian and Permian suites on the map.

Ultramafic rocks

Outcrops of ultramafic rocks can be found underlying the peaks of the White Mountains, as smaller exposures to the east, as well as isolated exposures associated with amphibolites north of Grand Valley Creek (Fig. 2). These rocks most commonly comprise fine-grained, massive and homogeneous, serpentinitized peridotite. In places, the ultramafic bodies occur as medium-grained, serpentinitized pyroxenite locally associated with coarse-grained garnet amphibolite (metagabbro). The degree to which rocks have been serpentinitized is variable, with the margins of individual bodies marked by fish-scale textured serpentinite. Proximal to the White Mountains, orientation of the serpentinite-hosted schistosity is consistent with that observed in the encompassing metamorphic rocks, dipping moderately to the west-southwest. The observed structural relationship suggests ultramafic bodies are not confined to klippe that sit structurally above Yukon-Tanana terrane rocks (Erdmer, 1982), but are instead structurally interleaved with them. It is plausible that the array of ultramafic bodies originally formed a continuous sheet that was emplaced prior to the onset of regional Permian deformation (Berman *et al.*, 2007).

ROCKS NORTHEAST OF WILLOW LAKE FAULT – REID LAKES COMPLEX

Northeast of the Willow Lake fault, rocks of the Yukon-Tanana terrane appear markedly different from those described above in that they are generally undeformed and weakly metamorphosed. The rocks on this side of the fault include intermediate to felsic intrusive rocks of the Reid Lakes batholith and, in the eastern limit of the map area, a sequence of intermediate to felsic volcanic and volcanoclastic rocks that are interpreted to be coeval with the main plutonic body (Fig. 2). Both the plutonic and extrusive rocks characteristically contain grey to blue smokey quartz phenocrysts.

Reid Lakes batholith

Much of the Reid Lakes batholith comprises a compositionally homogeneous, coarse-grained, massive, quartz-phyric, biotite monzogranite (Fig. 9a). The main granitic phase of the batholith is generally devoid of

solid-state deformation, except in close proximity to the Willow Lake fault where a weakly developed fabric is observed (Fig. 9b). At a locality near Willow Lake, the Reid Lakes granite displays a protomylonitic fabric that is defined by strung-out smokey quartz ribbons (Fig. 9c).

On Tonsure Mountain (Fig. 2), the granitic phase of the Reid Lakes batholith intrudes an earlier phase of coarse-grained, locally pegmatitic, hornblende gabbro (Fig. 9d).

As with the main granite phase, the gabbro is devoid of solid-state deformation fabrics. Coarse-grained, K-feldspar porphyritic granodiorite to quartz monzonite is common in the northeastern part of the batholith (Fig. 9e). This phase of the batholith commonly is characterized by the presence of hornblende and biotite.

Bostock (1964) originally assigned the granitic rocks of the Reid Lakes batholith to the Coast Intrusions and



Figure 9. Representative lithologies of the Reid Lakes plutonic complex: (a) quartz-phyric monzogranite typical of most of the batholith; (b) weakly foliated quartz-phyric monzogranite in proximity of the Willow Lake fault; (c) strongly foliated, ribbon quartz mylonite derived from Reid Lakes batholith near the Willow Lake fault; (d) coarse-grained gabbro on Tonsure Mountain; and (e) K-feldspar porphyritic, hornblende-bearing granodiorite phase, northeastern part of Reid Lakes batholith.

inferred their Jurassic and/or Cretaceous age. It is based on this original classification that the Reid Lakes batholith is currently assigned to the mid-Cretaceous period on the existing compilation map for Yukon (Gordey and Makepeace, 1999). However, K-Ar biotite ages from two Reid Lakes batholith samples collected along the Stewart River (Fig. 2, Hunt and Roddick, 1992) yielded a Permian to Triassic age. This led Colpron (2006) to postulate a Mississippian age for the batholith – a hypothesis that was recently confirmed with U-Pb zircon data obtained for two phases exposed along the North Klondike Highway, east of Willow Lake (Fig. 2), which yielded ages of 341.5 ± 0.7 Ma and 355.7 ± 0.9 Ma (Mortensen, 2009). Preliminary U-Pb results acquired for additional samples collected in this study confirm that the entire batholith is Early Mississippian in age (N. Joyce, pers. comm., 2009).

Reid Lakes volcanic succession

Exposures of volcanic and volcanoclastic rocks dominate the ridges between Reid Lakes and Willow Lake in the eastern portion of the map area (Fig. 2). Volcanic rocks include andesite to dacite flows, and rhyolite to rhyodacite porphyries (Fig. 10a). Volcanoclastic rocks include sandstone (Fig. 10b), conglomerate and breccia (Fig. 10c), and tuffaceous rocks. Near Stewart Crossing, the sequence also includes a quartz sandstone unit, with blue-grey quartz grains that are similar in appearance to quartz phenocrysts in the Reid Lakes batholith. The volcanic rocks are commonly massive and lack internal structures (Fig. 10a). They typically weather to a buff orange to grey colour. The volcanoclastic rocks locally preserve well-defined sedimentary structures such as parallel laminae and bedding that is commonly inclined to moderately dipping. Conglomerate and breccia are poorly sorted and composed of pebbles to cobbles of a variety

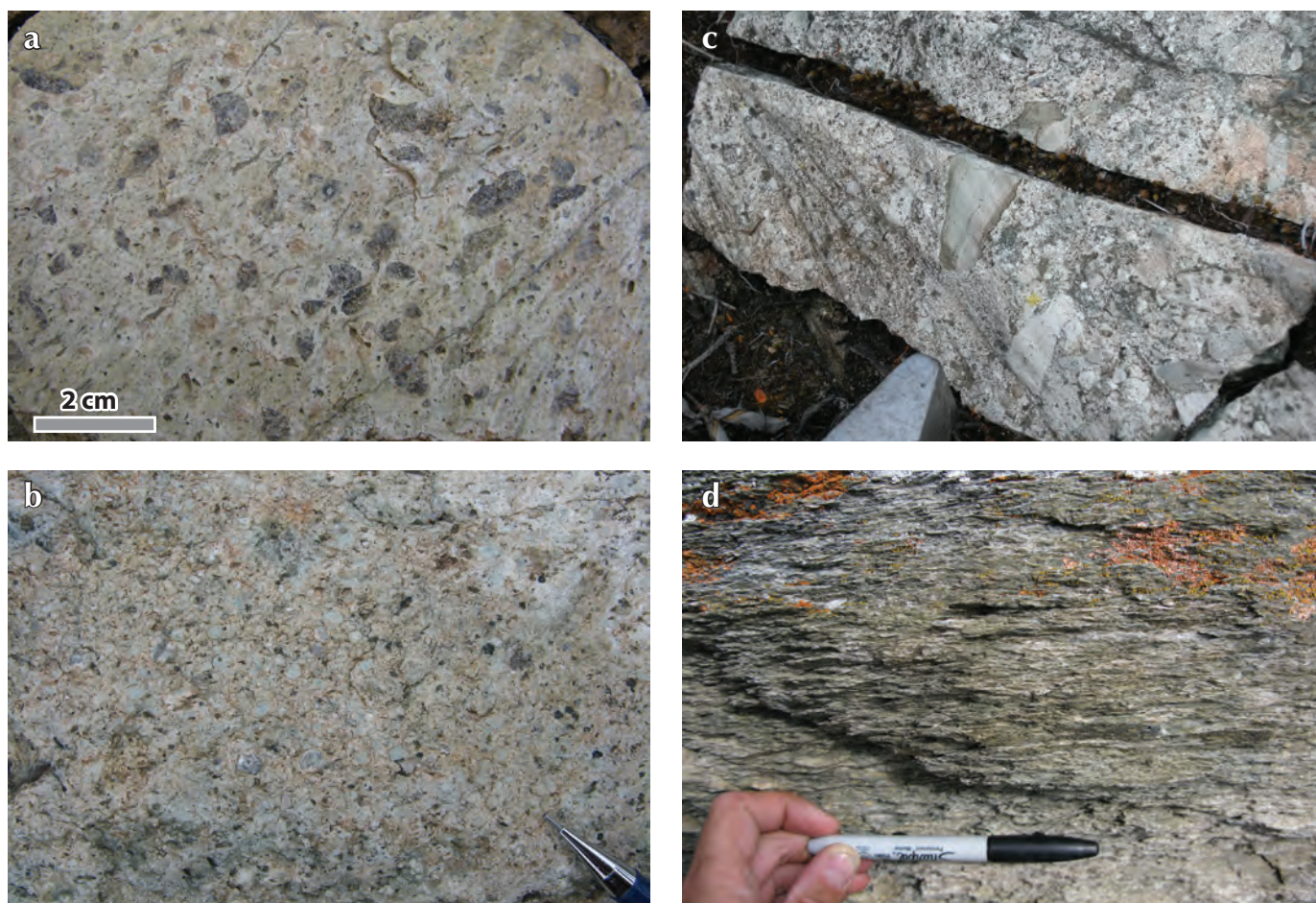


Figure 10. Representative lithologies of the Reid Lakes volcanic succession: (a) quartz-feldspar porphyritic volcanic flow; (b) quartz-hornblende-phyric hypabyssal intrusion; (c) volcanic breccia (scale is indicated by hammer point at bottom of the photo, which is up to 3 cm wide); and (d) strongly foliated intermediate volcanic rocks near the Willow Lake fault.

of felsic to intermediate volcanic and hypabyssal intrusive rocks, and less commonly, well-bedded tuffaceous rocks (Fig. 10c). Clasts in the volcanic conglomerate are generally of similar composition as nearby volcanic rocks, though exotic clasts of limestone and chert are also locally observed. As with the plutonic rocks of the batholith, the Reid Lakes volcanic sequence is generally devoid of solid-state deformation fabric, except in close proximity of the Willow Lake fault (Fig. 10d).

Bostock (1964) interpreted these rocks to be of Carboniferous(?) to Cretaceous age. Gordey and Makepeace (1999) defined the volcanoclastic rocks near Reid Lakes as Upper Triassic in age, and correlated volcanic rocks in the Willow Hills to the south with the mid-Cretaceous Mount Nansen Group. A distinguishing feature of the extrusive rocks described here is the presence of coarse, smokey quartz phenocrysts that resemble those observed in the main phase of the Reid Lakes batholith. It is this correlation that leads us to postulate a co-genetic relationship between the volcanic and plutonic rocks of the Reid Lakes batholith. Preliminary U-Pb zircon results also confirm this relationship and indicate an Early Mississippian age for the volcanic rocks (N. Joyce, pers. comm., 2009)

STIKINIA AND QUESNELLIA

The southern part of the map area is mainly underlain by rocks of Quesnellia and Stikinia. In the southeast, underlying the Pelly River valley, are Paleozoic metamorphic rocks that form the basement to Triassic rocks of Quesnellia in Glenlyon and Laberge map areas (Boswell assemblage; Colpron, 2006, 2010, in prep.). To the southwest, the Yukon River valley is underlain by Triassic volcanic rocks intruded by Early Jurassic granite plutons that could be of Quesnellian or Stikinian affinity.

BOSWELL ASSEMBLAGE – PALEOZOIC BASEMENT TO QUESNELLIA

Rocks on either sides of the Pelly River valley are assigned to the mid-Paleozoic Boswell assemblage of Quesnellia (Colpron, 2006). It includes intermediate metavolcanic rocks, amphibolite (\pm garnet), minor ultramafic rocks, and prominent marble bluffs south of the Pelly River. All are strongly foliated and recrystallized rocks that were subjected to high-grade (amphibolite facies?) metamorphism followed by overprinting at greenschist facies conditions. Their distinct lithological sequence, metamorphic history, and the discordance in structural

trends of the Boswell rocks set them apart from the metamorphic rocks of the Yukon-Tanana terrane to the north (Fig. 2).

The northernmost belt of the Boswell assemblage comprises a heterogeneous sequence of intermediate metavolcanic, metavolcanoclastic and metaplutonic rocks (Fig. 2). These rocks are typically light grey quartz-feldspar-biotite-muscovite schist that commonly show strong compositional layering of quartz-feldspar and mica-rich domains (Fig. 11a). This strong compositional heterogeneity is suggestive of volcanic and/or volcanoclastic protoliths compounded by a metamorphic segregation resulting from the development of a differentiated crenulation cleavage. Elsewhere along this belt, the rocks are more homogeneous, fine to medium grained, crystalline, and lack compositional layering. These rocks are compositionally similar to crystalline layers in the segregated schist. In places, they are clearly metaplutonic rocks of granodiorite to diorite compositions. Elsewhere, that distinction is difficult to establish in the field.

Metavolcanic rocks of intermediate composition are commonly intercalated with amphibolite that characterizes the Boswell assemblage to the south, along the shores of the Pelly River (Figs. 2, 11b). The medium to coarsely recrystallized amphibolite is overprinted by greenschist facies assemblages, and preserves strong compositional layering and evidence of high strain deformation (Fig. 11c). Garnet is locally preserved, but more commonly pseudomorphed by chlorite. At one locality, along the north shore of the Pelly River, serpentized pyroxenite cumulates occur at low structural level beneath garnet amphibolite.

Ridge tops south of the Pelly River are mainly underlain by marble of the Boswell assemblage. The marble is closely interrelated with amphibolite along the Pelly River (Fig. 11d), and amphibolite possibly underlies much of the unexposed recessive areas between carbonate ridges south of the river (Fig. 2). The marble is typically coarse grained (up to 6 mm) and beige to light medium grey. It locally contains dark grey, recrystallized chert nodules (Fig. 11e) and brecciated dark quartzite, presumably derived from chert. At the west end of this belt, a few outcrops of grey quartzite are intercalated with mafic metavolcanic rocks and carbonate.

Rocks of the Boswell assemblage can be traced for nearly 200 km to the southeast into the Glenlyon (105L) and Laberge (105E) map areas (Fig. 1). Along this trend, garnet

amphibolite and marble transition into low-grade chlorite schist and metabasalt near Little Salmon Lake (Colpron *et al.*, 2002, 2003), and well-preserved pillow basalts in southeastern parts of the Laberge map area (Simard, 2003; Simard and Devine, 2003). There, at its type section on Boswell Mountain, the Upper Devonian pillow basalt is unconformably overlain by Upper Triassic augite-phyric volcanic and volcanoclastic rocks that are typical of

Quesnellia (Simard, 2003; M. Colpron and R.-L. Simard, unpublished data). Felsic units associated with mafic rocks of the Boswell assemblage yield Late Devonian to Early Mississippian zircon ages in Glenlyon and Laberge areas (M. Colpron, unpublished data). A similar age is indicated by preliminary U-Pb zircon results for a foliated tonalite intruding amphibolite of the Boswell assemblage in the northern Carmacks area (N. Joyce, pers. comm., 2009). In

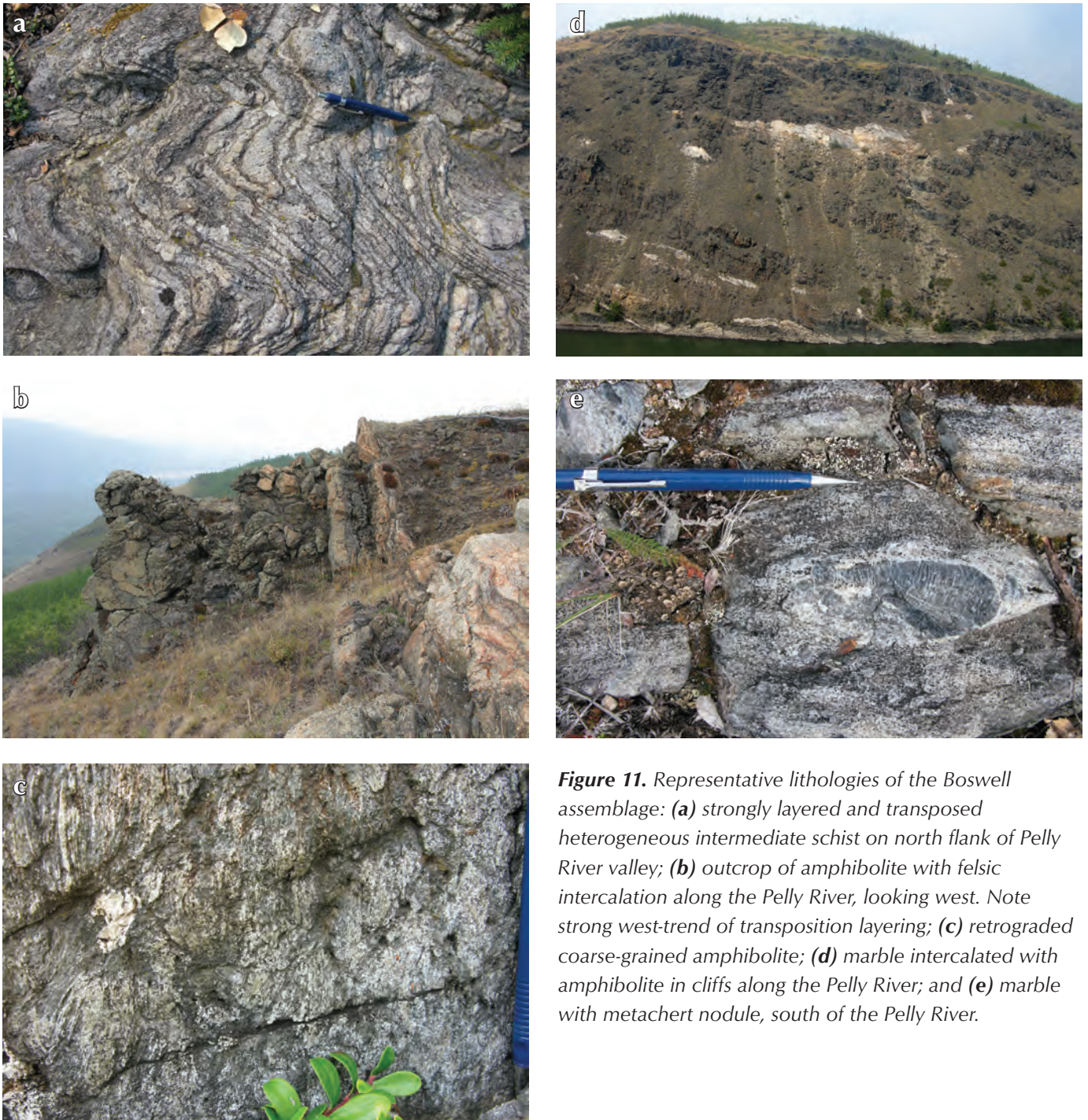


Figure 11. Representative lithologies of the Boswell assemblage: **(a)** strongly layered and transposed heterogeneous intermediate schist on north flank of Pelly River valley; **(b)** outcrop of amphibolite with felsic intercalation along the Pelly River, looking west. Note strong west-trend of transposition layering; **(c)** retrograded coarse-grained amphibolite; **(d)** marble intercalated with amphibolite in cliffs along the Pelly River; and **(e)** marble with metachert nodule, south of the Pelly River.

the Laberge map area, mafic rocks are overlain by a sedimentary sequence that includes Pennsylvanian limestone (Tempelman-Kluit, 1984, 2009; Simard, 2003). In Glenlyon, felsic metavolcanic and metaplutonic rocks also yield Pennsylvanian U-Pb ages (M. Colpron, unpublished data). Thus, it is possible that marble exposed in the northern Carmacks area (Fig. 2) are also Pennsylvanian in age.

TRIASSIC VOLCANIC ROCKS – STIKINIA OR QUESNELLIA?

The southwest corner of the map area is primarily underlain by volcanic and plutonic rocks of early Mesozoic age that could be part of either Stikinia or Quesnellia (Fig. 2). Augite-phyric andesitic to dacitic volcanic flows (Fig. 12a) and volcanoclastic rocks occur in a northwest-trending belt that roughly follows the north bank of the Yukon River (Fig. 2). The rocks can readily be

distinguished from adjacent Yukon-Tanana terrane rocks (see earlier descriptions) by the presence of primary augite phenocrysts that have been overprinted by a weakly to moderately developed cleavage and metamorphism at sub-greenschist to greenschist facies. These rocks resemble Upper Triassic volcanic rocks assigned to either the Povoas formation of the Lewes River Group (Stikinia), or the Semenof formation (Quesnellia), depending on which side of the Teslin fault they occur (Tempelman-Kluit, 1984, 2009; M. Colpron and R.-L. Simard, unpublished data).

EARLY JURASSIC AISHIHIK SUITE

Triassic augite-phyric volcanic rocks described in the previous section are intruded and bounded to the southwest by a biotite \pm hornblende granodiorite to monzogranite that is continuous with Early Jurassic granitoids exposed in the neighbouring Stewart River

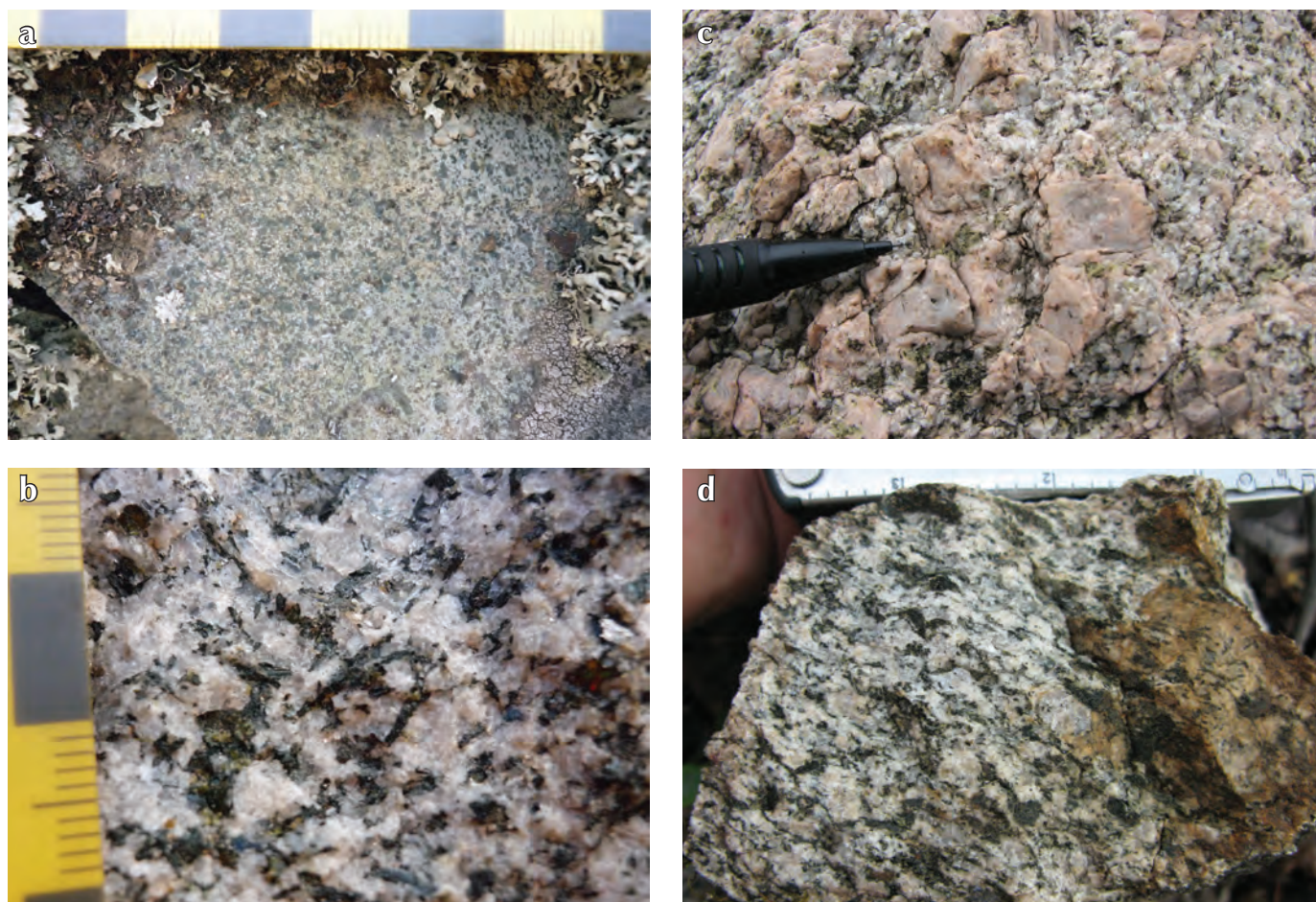


Figure 12. Representative photographs of Triassic and Jurassic rocks from northern Carmacks area. **(a)** Upper Triassic(?) augite-phyric volcanic rock of Stikinia or Quesnellia; **(b)** hornblende-biotite-epidote granodiorite, Early Jurassic Aishihik suite; **(c)** K-feldspar porphyritic biotite syenogranite, Aishihik suite; and **(d)** moderately foliated hornblende granodiorite of the Early Jurassic Aishihik suite.

(M.E. Villeneuve, unpublished data) and central Carmacks map areas (Breitsprecher and Mortensen, 2004). These Early Jurassic plutonic rocks form part of the Aishihik plutonic suite (Fig. 2). The granodiorite to monzogranite (locally quartz monzonite and quartz monzodiorite) phases are generally medium to coarse grained, equigranular, and have magmatic epidote which is indicative of crystallization at mid-crustal depths (Fig. 12b). K-feldspar porphyritic monzogranite is also common (Fig. 12c). Alteration of the granitoid is locally evidenced by chloritization of the mafic phases and epidote-filled fractures. Granitoids of the Aishihik suite are generally undeformed, but locally may have a well-developed solid-state foliation (Fig. 12d). This belt of plutonic rocks represents the northwest extension of the Minto pluton which hosts the high-grade Cu-Au Minto Mine approximately 10 km to the southeast.

POST-ACCRETIONARY ASSEMBLAGES

The youngest rocks in the southwest McQuesten-northern Carmacks map area include mid-Cretaceous granitoid plutons of the Whitehorse plutonic suite, and Upper Cretaceous and Quaternary volcanic rocks of the Carmacks and Selkirk groups, respectively. Emplacement of all these rocks postdates the regional deformation.

MID-CRETACEOUS WHITEHORSE PLUTONIC SUITE

A number of granite plutons intrude metamorphic rocks of the Yukon-Tanana terrane in the central part of the map area (Fig. 2). In outcrop, they are commonly pink to light grey, equigranular, biotite monzogranite to granodiorite (Fig. 13). Locally, plutons and dykes of this suite are syenogranitic in composition and contain K-feldspar phenocrysts. Though the timing of their emplacement has not been constrained in the map area, field observations suggest emplacement following regional deformation. The rocks themselves resemble granites of the mid-Cretaceous Whitehorse plutonic suite to the south, and are tentatively assigned to this suite.

UPPER CRETACEOUS CARMACKS GROUP

Rocks of the Upper Cretaceous Carmacks Group occur as scattered exposures throughout the southwest McQuesten-northern Carmacks area (Fig. 2). They generally form topographic features with positive relief and are well defined by patchy high magnetic anomalies in the new aeromagnetic data (Fig. 3). Exposures of the



Figure 13. Mid-Cretaceous biotite monzogranite of the Whitehorse plutonic suite.

Carmacks Group are likely to represent erosional remnants of what once formed an extensive volcanic cover. Though its contact with underlying rocks is generally not exposed, it is inferred to rest unconformably over all older rocks in the area (Fig. 2). In the southwest McQuesten and northern Carmacks areas, the Carmacks Group largely comprises dacite and rhyodacite, similar to those in the Stewart River area to the west (Bostock, 1942; Tempelman-Kluit, 1974; Ryan and Gordey, 2002; 2004; Gordey and Ryan, 2005), and minor brown to black basalt and basaltic andesite, that are more common to the southeast in Carmacks and Glenlyon areas (Bostock, 1936; Tempelman-Kluit, 1984, 2009; Colpron *et al.*, 2002). The intermediate volcanic rocks are commonly hornblende and/or plagioclase porphyritic (Fig. 14); the basalt is locally hornblende-phyric. Locally, flow banding



Figure 14. Homogeneous, grey-weathering, biotite-hornblende porphyritic dacite of the Upper Cretaceous Carmacks Group.

and flattened vesicles attest to the extrusive origins of these flows. They vary from a few metres to hundreds of metres in thickness. Both intermediate and mafic compositions have been dated by K-Ar and $^{40}\text{Ar}/^{39}\text{Ar}$ methods at ca. 70-65 Ma in the surrounding Stewart River and Carmacks area (Breitsprecher and Mortensen, 2004; J.J. Ryan and S.P. Gordey, unpublished data).

PLIOCENE-PLEISTOCENE SELKIRK VOLCANICS

Subaerial to subglacial mafic volcanic flows of the Selkirk volcanics occur as valley fill near Fort Selkirk, at Volcano Mountain, and along Rosebud Creek (Fig. 2). The young basalt lava flows and associated breccias are typically vesicular and fresh olivine-phyric basalt; they are expressed in the new aeromagnetic data by very strong positive anomalies that follow valleys (Fig. 3). The flows appear to have experienced little erosion, commonly preserving the volcanic geomorphology; this is spectacularly expressed at Volcano Mountain where a cinder cone, craters, lava domes and flows are well preserved (Fig. 15). Selkirk lavas form impressive palisades near the confluence of the Yukon and Pelly rivers (Jackson *et al.*, 2009) where they likely dammed the Yukon River on a number of occasions (Huscroft *et al.*, 2004). The Selkirk volcanics vary in composition from olivine nephelinite to basanite and alkaline olivine basalt (Francis and Ludden, 1990). A number of flows have been dated in the area and yield $^{40}\text{Ar}/^{39}\text{Ar}$ whole rock ages spanning ca. 3.25 Ma to <0.311 Ma. The youngest eruption took place at Volcano Mountain in the late Pleistocene (Nelson *et al.*, 2009; Huscroft *et al.*, 2004).

STRUCTURAL GEOLOGY

A variety of structural styles are observed in the southwest McQuesten-northern Carmacks area depending on the belt of rocks being mapped. The central belt of the

Yukon-Tanana terrane is characterized by at least two phases of isoclinal folding and development of transposition foliations. The main foliation observed in these rocks developed at upper greenschist to amphibolite facies conditions and may be representative of a second generation fabric; this is most obvious in metasiliciclastic rocks of the Snowcap assemblage (e.g., Fig 4c). Metaplutonic rocks of the Simpson Range and Sulphur Creek suites generally only exhibit this second regionally pervasive foliation that developed in the Late Permian (Berman *et al.*, 2007). This dominant foliation is itself deformed by two younger sets of open folds that are defined by an axial planar crenulation cleavage that likely developed during episodes of less pervasive Triassic and/or Jurassic deformation and metamorphism.

In the northeastern part of the map area, rocks of the Reid Lakes batholith and volcanic succession appear to have escaped the regional deformation recorded in the Yukon-Tanana terrane south of the Willow Lake fault (Fig. 2). Rocks of the Reid Lakes complex are only foliated in proximity to the fault and only show limited evidence for metamorphism in the form of local chloritization of mafic minerals. The Willow Lake fault is well defined in the aeromagnetic data where it corresponds to a magnetic low and truncation of anomalies (Fig. 3). Although the kinematics of the Willow Lake fault is unknown, the juxtaposition of undeformed, high-level Reid Lakes rocks next to intensely deformed and metamorphosed, mid-crustal level rocks of the Snowcap and Klondike assemblages to the south, suggests an important vertical component of displacement along this fault.

To the south, rocks of the Boswell assemblage are also affected by two phases of tight isoclinal folding. In sharp contrast to the northwest-trending structures observed in the Yukon-Tanana terrane rocks to the north, structures

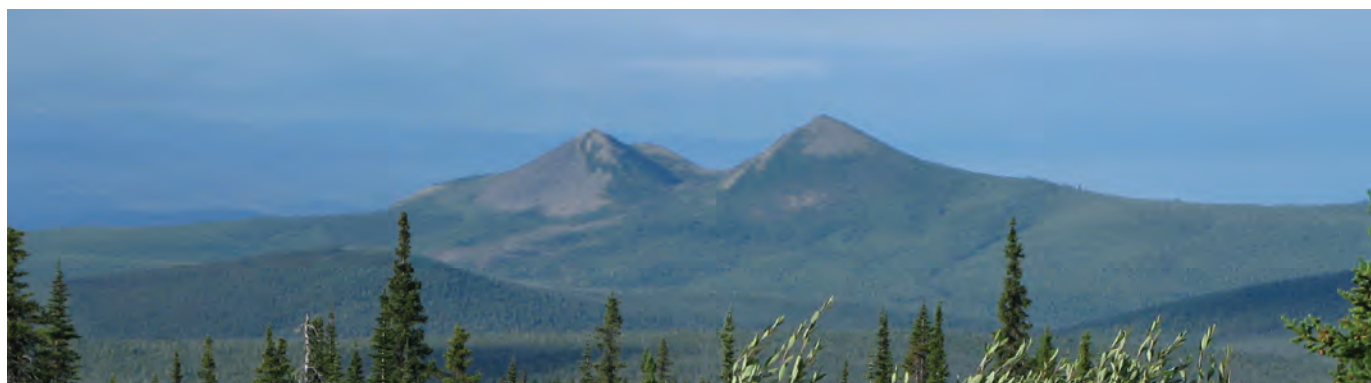


Figure 15. Looking southwest at Volcano Mountain, underlain by Quaternary basalt of the Selkirk volcanics.

within the Boswell assemblage trend east-west. This discontinuity is likely marked by a fault that is nowhere exposed in the map area, but is well delineated in the geophysical data by an east-trending low that extends eastward from Mount Watson (Figs. 2, 3). To the southeast, in the Glenlyon map area, a similar structure juxtaposes rocks of the Snowcap assemblage over amphibolite and marble of the Boswell assemblage (Colpron *et al.*, 2002). There, the Needlerock thrust is well exposed at one locality where fabric relationships indicate a top-to-the-south sense of displacement (Colpron *et al.*, 2003). A similar interpretation is considered for the fault bounding the Boswell assemblage in the northern Carmacks area (Fig. 2).

To the southwest, in the vicinity of Mount Walters, the Paleozoic Boswell assemblage has been juxtaposed with Triassic augite-phyric volcanic rocks along a dextral strike-slip fault. This structure is also well defined in the aeromagnetic data (Fig. 3) and can be traced northwestward beyond Volcano Mountain to Grand Valley Creek and the Mount Adami area where it splays out into a number of smaller faults (Fig. 2). This fault could be the northern extension of the Teslin fault system, which juxtaposes the Quesnellia and Cache Creek terranes, potentially recording ~125 km of Late Cretaceous dextral displacement near the Yukon-British Columbia boundary (Gabrielse *et al.*, 2006). Though it appears as a prominent structure in seismic sections (Cook *et al.*, 2004; Colpron *et al.*, 2007) in Yukon, displacement along the Teslin fault appears to wane progressively to the northwest into the area just east of Carmacks where the fault is entirely contained within Jurassic rocks of the Laberge Group. It is unclear whether the fault near Mount Walters in southwest McQuesten-northern Carmacks area is the continuation of the Teslin fault proper (Colpron *et al.*, 2007), or one of its many splays.

Another dextral strike-slip fault is inferred to separate metamorphic rocks of the Finlayson assemblage (east of the Klondike Highway) from undeformed rocks of the Reid Lakes complex (Fig. 2). This structure may form another splay of the Teslin system that separates the Reid Lakes complex from similar unstrained, quartz-phyric granite of the Tatlain batholith situated approximately 30 km to the south in the Glenlyon map area (Colpron *et al.*, 2002, 2003, 2006b). This fault is apparently truncated by the Tintina fault (Fig. 2).

The Tintina fault marks the northeast boundary of the map area. It is well defined in the aeromagnetic data and is

marked by one of the most prominent topographic lineaments in the northern Cordillera. The Tintina fault has a well-constrained dextral displacement of ~425 km since the Eocene, and up to 490 km since the Late Cretaceous (Gabrielse *et al.*, 2006). Restoration of this displacement juxtaposes the McQuesten area with part of the Finlayson Lake area of southeastern Yukon (Fig. 1), where relatively unstrained Mississippian rocks have also been documented (Murphy *et al.*, 2006).

MINERAL POTENTIAL

The southwest McQuesten-northern Carmacks area is an under-explored region that is situated at the juncture of many important mineral belts (Fig. 16). The region only has a few active mineral claims and a handful of occurrences reported in the Yukon MINFILE (http://www.geology.gov.yk.ca/databases_gis.html). Despite the limited activity, the rocks exposed in the project area do share many attributes with rocks observed in nearby prospective areas of the Dawson Range mineral belt, the recently discovered White Gold property to the west (Yukon MINFILE 115O 011-013, 165-166), and the producing Minto Mine to the south (Yukon MINFILE 115I 021-022; Fig. 16). Limited accessibility and geoscience information, compounded by the complex Quaternary history of the region, are all factors that have likely hindered exploration in the southwest McQuesten area. Thus, an objective of this project is to improve our geological understanding of the area and to provide new exploration tools (e.g., high-resolution aeromagnetic data) to assist in evaluating the mineral prospectivity of the area.

The Yukon-Tanana terrane hosts significant syngenetic sulphide deposits in the Finlayson Lake district of southeastern Yukon (Fig. 1; Hunt, 2002). There, much of the sulphide mineralization is associated with Upper Devonian to Lower Mississippian felsic metavolcanic rocks (e.g., Wolverine and Kudz Ze Kayah mineral deposits, Yukon MINFILE 105G 072 and 105G 117, respectively). Additional occurrences are associated with Upper Devonian (Fyre, Yukon MINFILE 105G 034) and Early Permian (Ice, Yukon MINFILE 105G 118) mafic metavolcanic rocks (Hunt, 2002). In most cases, many of the mineral occurrences developed in a back-arc environment within the Yukon-Tanana terrane. On the southwest side of the Tintina fault, in the Stewart River (Gordey and Ryan, 2005; S.J. Piercey and J.J. Ryan, unpublished data) and Glenlyon regions (Colpron *et al.*, 2003, 2006b), Yukon-Tanana rocks are dominated by

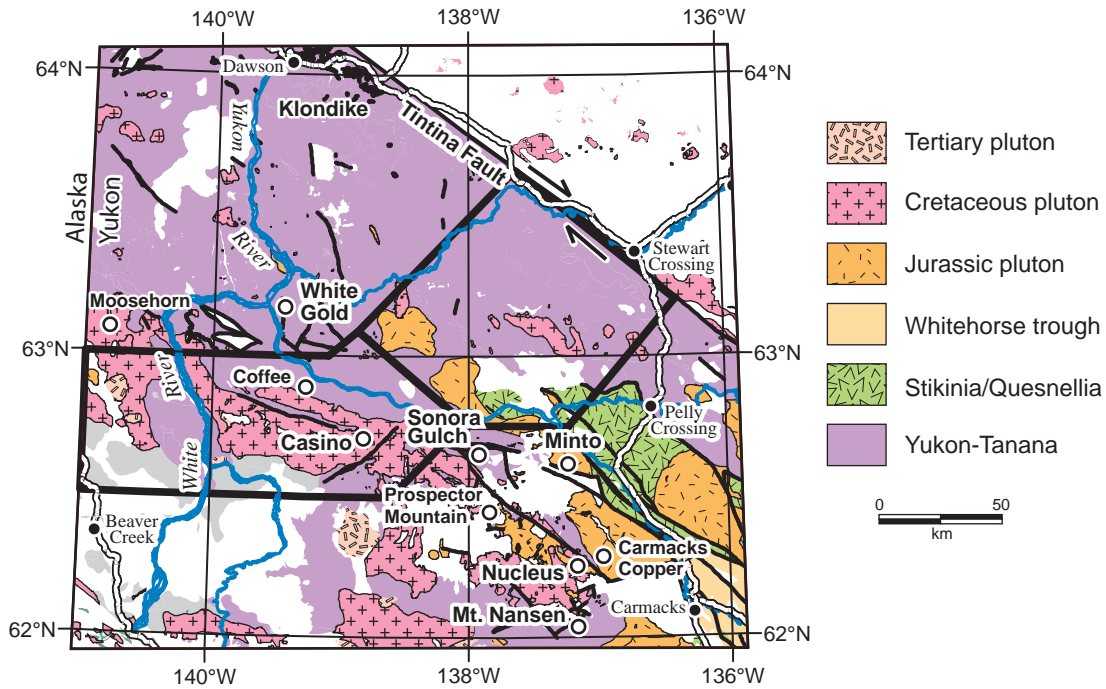


Figure 16. Location of southwest McQuesten-northern Carmacks area with respect to major mineral occurrences of the Dawson Range mineral belt in west-central Yukon. Black outlines illustrate area of detailed aeromagnetic surveys in southwest McQuesten (Kiss and Coyle, 2009 a-r) and northern Stevenson Ridge (Kiss and Coyle, 2009 s-af).

mafic to intermediate metavolcanic and metaplutonic rocks that are representative of an arc environment (Piercey *et al.*, 2006), and thus less prospective for syngenetic sulphide occurrences. In Stewart River, the Lucky Joe occurrence (Yukon MINFILE 115O 051) is probably an Early Mississippian, intrusion-related skarn or porphyry-style occurrence that developed in this arc setting (J. Peter and R. Presnell, pers. comm.).

In the southwest McQuesten area, the Yukon-Tanana terrane is dominated by metasedimentary rocks of the Snowcap assemblage with proportionally fewer metavolcanic rocks that appear limited in their prospectivity for massive sulphide deposits. Most of the metavolcanic rocks are mafic schists and amphibolite of unknown age and protolith. Their geochemical characterization will assist in evaluating their tectonic environment and prospectivity.

North of the Willow Lake fault, rocks of the Reid Lakes complex were emplaced at high levels in the crust and remained so for much of their history. An Early Mississippian age for this assemblage suggests they may be related to the Simpson Range plutonic suite – the suite with which the Lucky Joe prospect to the west is

associated. At the Lucky Joe property, probable intrusion-related mineralization is overprinted by penetrative deformation and metamorphism, thus complicating exploration. In contrast, the well-preserved, high-level magmatic rocks of the Reid Lakes complex appear to have experienced little post-emplacement deformation and should perhaps be evaluated for their porphyry or epithermal mineralization potential.

Rocks of the Sulphur Creek suite and Klondike assemblage are associated with the source region for the renowned Klondike placer gold fields situated northwest of the McQuesten area (Fig. 16). These rocks are typically strongly altered, as indicated by high concentration of micas, and are commonly laced with quartz veins and pyrite. The unusual alteration of the Klondike assemblage may be the result of synmagmatic hydrothermal alteration that was later overprinted by regional amphibolite facies metamorphism. These rocks may be prospective for vein-hosted gold.

Granodiorite to monzogranite of the Early Jurassic Aishihik plutonic suite in the southwest part of the map area represents the northwest extension of the Minto pluton, which is host to the high-grade Cu-Au deposit of the

Minto Mine. This belt of rocks is currently the focus of most of the exploration activities in the map area. Due to forest fire activity in 2009, our evaluation of the belt was limited during the field season, but will be the focus of further mapping in 2010.

Finally, the southwest McQuesten-northern Carmacks area is northeast of the Dawson Range mineral belt which is known for its wealth of Cretaceous Cu-Au deposits, including the recent discovery at White Gold and auriferous gold veins of the Moosehorn Range (Yukon MINFILE 115N 024; Fig. 16). A series of small, post-tectonic plutons in southwest McQuesten are inferred to be part of the mid-Cretaceous Whitehorse plutonic suite and should be evaluated for their intrusion-related gold potential.

SUMMARY

Bedrock mapping of the southwest McQuesten-northern Carmacks area has confirmed that most of the area is underlain by rocks of the Yukon-Tanana terrane (Fig. 2). In the centre of the map area, metasedimentary and metavolcanic rocks are correlated with the Snowcap and Klondike assemblages of Yukon-Tanana, whereas the metaplutonic rocks are attributed to the Early Mississippian Simpson Range and Permian Sulphur Creek suites. Northeast of the Willow Lake fault, undeformed plutonic and volcanic rocks of the Reid Lakes complex are also part of the Yukon-Tanana terrane. They were previously interpreted to be of Cretaceous age, but recent U-Pb geochronology has demonstrated an Early Mississippian age for the complex. Juxtaposition along the Willow Lake fault of the high-level Reid Lakes volcano-plutonic complex to the north, against mid-crustal metamorphic rocks of the Snowcap and Klondike assemblages to the south, implies a significant component of vertical displacement along the fault. The southern part of the map area is underlain by mid-Paleozoic to early Mesozoic rocks of Quesnellia and/or Stikinia. The map area is dissected by a series of faults that we infer to be dextral strike-slip faults related to the Teslin fault system. The southwest McQuesten-northern Carmacks area is an under-explored region that shares many attributes with nearby, highly prospective areas of the Dawson Range, White Gold and Carmacks/Minto districts.

ACKNOWLEDGEMENTS

Bedrock mapping of southwest McQuesten and northern Carmacks map areas in 2009 was funded by Natural Resources Canada's Geomapping for Energy and Minerals (GEM) program, and the Yukon Geological Survey. We thank Joyia Chakungal, Witold Ciolkiewicz, Dan Gibson, Nicolai Goepfel, Shawn Hood, Melanie Kelman, Ellie Knight, Kristy Long, John Mayer, Shaun O'Connor, Kirsten Rasmussen, Dave Schneider and Reid Staples for assistance with mapping and various aspects of maintaining the field camp. The Quaternary team including Jeff Bond, Panya Lipovsky, Riley Gibson and Samantha Darling are thanked for field camaraderie, sharing of logistics, and scientific discussions. Nancy Joyce is thanked for visiting the field, and for providing fast turn around on preliminary geochronology. A great deal of gratitude goes to Steve Williams for providing us with his invaluable GIS expertise and digital data management. We appreciate the ongoing collaboration with Nathan Hayward in analysing the potential field data for the area, and improving the quality of our mapping.

We greatly appreciate the generosity of the Bradleys (Dale, Sue and Hugh) for allowing us to camp at the Pelly River Farm, a tradition that was initiated in the 1930s when Hugh Bostock operated out of this location with his horse-party. We are indebted to them for assisting us in so many ways, and for supplying fresh water and farmed goods. We thank Prism Helicopters for supplying a great Hughes 500D, and pilots Yoshio Nishimura and Hal Marsden for safe flight services, and flight engineer Graham Ducommun for keeping the machine in fine working order. To the Aurora Geosciences team, our thanks is extended to Bob Yonker for overseeing camp construction and demobilization, Gord Ruby for managing camp, and Phil Jackson for overseeing the operations from Whitehorse. We thank Ken Cohoe and Core Expediting for transporting our fuel and gear. A special thanks goes out to Eileen McKie for her excellent culinary services and top notch first aid attendance. We were honoured by Selkirk First Nation elder, Peter Isaac's visit to our camp, and for sharing his wonderful memories of the work he did with Hugh Bostock when the area was mapped for the first time. Finally, we thank Joyia Chakungal for a thoughtful review.

REFERENCES

- Abbott, J.G., 2005. Yukon Geoscience Needs: Results of the third Yukon Geoscience planning workshop. Yukon Geological Survey, Open File 2005-4, 55 p.
- Berman, R.G., Ryan, J.J., Gordey, S.P. and Villeneuve, M., 2007. Permian to Cretaceous polymetamorphic evolution of the Stewart River region, Yukon-Tanana terrane, Yukon, Canada: P-T evolution linked with *in situ* SHRIMP monazite geochronology. *Journal of metamorphic Geology*, vol. 25, p. 803-827.
- Bond, J.D. and Lipovsky, P.S., 2010 (this volume). Pre-Reid surficial geology investigations in southwest McQuesten map area (115P). *In: Yukon Exploration and Geology 2009*, K.E. MacFarlane, L.H. Weston and L.R. Blackburn (eds.), Yukon Geological Survey, p. 103-117.
- Bostock, H.S., 1936. Carmacks district, Yukon. Geological Survey of Canada, Memoir 189, 67 p.
- Bostock, H.S., 1942. Ogilvie, Yukon Territory. Geological Survey of Canada, Map 711A, scale 1:253,440.
- Bostock, H.S., 1964. Geology, McQuesten, Yukon Territory. Geological Survey of Canada, Map 1143A, scale 1:253,440.
- Breitsprecher, K. and Mortensen, J.K., 2004. Yukonage 2004: A database of isotopic age determinations for rock units from Yukon Territory, Canada. Yukon Geological Survey, CD-ROM.
- Colpron, M., 2006. Tectonic assemblage map of Yukon-Tanana and related terranes in Yukon and northern British Columbia (1:1 000 000 scale). Yukon Geological Survey, Open File 2006-1.
- Colpron, M., 2010 (in press). Geological compilation of Whitehorse trough. Yukon Geological Survey, scale 1:250 000.
- Colpron, M. and Nelson, J.L. (eds.), 2006. Paleozoic Evolution and Metallogeny of Pericratonic Terranes at the Ancient Pacific Margin of North America, Canadian and Alaskan Cordillera. Geological Association of Canada, Special Paper 45, 523 p.
- Colpron, M., Nelson, J.L. and Murphy, D.C., 2006a. A tectonostratigraphic framework for the pericratonic terranes of the northern Cordillera. *In: Paleozoic Evolution and Metallogeny of Pericratonic Terranes at the Ancient Pacific Margin of North America*, Canadian and Alaskan Cordillera, M. Colpron and J.L. Nelson (eds.), Geological Association of Canada, Special Paper 45, p. 1-23.
- Colpron, M., Gordey, S.P., Lowey, G.W., White, D. and Piercey, S.J., 2007. Geology of the northern Whitehorse trough, Yukon (NTS 105E/12, 13, and parts of 11 and 14; 105L/4 and parts of 3 and 5; parts of 115H/9 and 16; 115I/1 and part of 8) (1:150 000 scale). Yukon Geological Survey, Open File 2007-6.
- Colpron, M., Mortensen, J.K., Gehrels, G.E. and Villeneuve, M.E., 2006b. Basement complex, Carboniferous magmatism and Paleozoic deformation in Yukon-Tanana terrane of central Yukon: Field, geochemical and geochronological constraints from Glenlyon map area. *In: Paleozoic Evolution and Metallogeny of Pericratonic Terranes at the Ancient Pacific Margin of North America*, Canadian and Alaskan Cordillera, M. Colpron and J.L. Nelson (eds.), Geological Association of Canada, Special Paper 45, p. 131-151.
- Colpron, M., Murphy, D.C., Nelson, J.L., Roots, C.F., Gladwin, K., Gordey, S.P. and Abbott, J.G., 2003. Yukon Targeted Geoscience Initiative, Part 1: Results of accelerated bedrock mapping in Glenlyon (105L/1-7, 11-14) and northeast Carmacks (115I/9,16) areas, central Yukon. *In: Yukon Exploration and Geology 2002*, D.S. Emond and L.L. Lewis (eds.), Exploration and Geological Services Division, Yukon Region, Indian and Northern Affairs Canada, p. 85-108.
- Colpron, M., Murphy, D.C., Nelson, J.L., Roots, C.F., Gladwin, K., Gordey, S.P., Abbott, G. and Lipovsky, P.S., 2002. Preliminary geological map of Glenlyon (105L/1-7, 11-14) and northeast Carmacks (115I/9,16) areas, Yukon Territory (1:125 000 scale). Exploration and Geological Services Division, Yukon Region, Indian and Northern Affairs Canada, Open File 2002-9; Geological Survey of Canada, Open File 1457.
- Cook, F.A., Clowes, R.M., Snyder, D.B., van der Velden, A.J., Hall, K.W., Erdmer, P. and Evenchick, C.A., 2004. Precambrian crust beneath the Mesozoic northern Canadian Cordillera discovered by Lithoprobe seismic reflection profiling. *Tectonics*, vol. 23, TC2010, doi: 10.1029/2002TC001412.

- Erdmer, P., 1982. Nature and significance of the metamorphic minerals and structures of cataclastic allochthonous rocks in the White Mountains, Last Peak and Fire Lake areas, Yukon Territory. Unpublished PhD thesis, Queen's University, Kingston, Ontario, Canada, 254 p.
- Francis, D. and Ludden, J., 1990. The mantle source for olivine nephelinite, basanite and alkaline olivine basalt at Fort Selkirk, Yukon, Canada. *Journal of Petrology*, vol. 31, p. 371-400.
- Gabrielse, H., Murphy, D.C. and Mortensen, J.K., 2006. Cretaceous and Cenozoic dextral orogen-parallel displacements, magmatism and paleogeography, north-central Canadian Cordillera. *In: Paleogeography of the North American Cordillera: Evidence For and Against Large-Scale Displacements*, J.W. Haggart, J.W.H. Monger and R.J. Enkin (eds.), Geological Association of Canada, Special Paper 46, p. 255-276.
- Gordey, S.P. and Makepeace, A.J., 1999. Yukon digital geology. Exploration and Geological Services Division, Yukon, Indian and Northern Affairs Canada, Open File 1999-1(D); Geological Survey of Canada, Open File D3826, scale 1:1 000 000.
- Gordey, S.P. and Ryan, J.J., 2005. Geology, Stewart River area (115N, 115O and part of 115J), Yukon Territory. Geological Survey of Canada, Open File 4970, scale 1:250 000.
- Hunt, J.A., 2002. Volcanic-associated massive sulphide (VMS) mineralization in the Yukon-Tanana Terrane and coeval strata of the North American miogeocline, in the Yukon and adjacent areas. Exploration and Geological Services Division, Yukon Region, Indian and Northern Affairs Canada, Bulletin 12, 107 p.
- Hunt, P.A. and Roddick, J.C., 1992. A compilation of K-Ar ages: Report 21. *In: Radiogenic Age and Isotopic Studies, Report 5*, Geological Survey of Canada, Paper 91-2, p. 207-261.
- Huscroft, C.A., Ward, B.C., Barendregt, R.W., Jackson, L.E., Jr. and Opdyke, N.D., 2004. Pleistocene volcanic damming of Yukon River and the maximum age of the Reid Glaciation, west-central Yukon. *Canadian Journal of Earth Sciences*, vol. 41, p. 151-164.
- Jackson, L.E., Jr., Froese, D.G., Huscroft, C.A., Nelson, F.E., Westgate, J.A., Telka, A.M., Shimamura, K. and Rotheisler, P.N., 2009. Surficial geology and late Cenozoic history of the Stewart River and northern Stevenson Ridge map areas, west-central Yukon Territory. Geological Survey of Canada, Open File 6059, 414 p.
- Kiss, F. and Coyle, M., 2009a. Residual total magnetic field, McQuesten Aeromagnetic Survey, NTS 115I/13 and 115I/14, Yukon. Geological Survey of Canada, Open File 6106; Yukon Geological Survey, Open File 2009-4, scale 1:50 000.
- Kiss, F. and Coyle, M., 2009b. First vertical derivative of the magnetic field, McQuesten Aeromagnetic Survey, NTS 115I/13 and 115I/14, Yukon. Geological Survey of Canada, Open File 6107; Yukon Geological Survey, Open File 2009-5, scale 1:50 000.
- Kiss, F. and Coyle, M., 2009c. Residual total magnetic field, McQuesten Aeromagnetic Survey, NTS 115I/15, Yukon. Geological Survey of Canada, Open File 6108; Yukon Geological Survey, Open File 2009-6, scale 1:50 000.
- Kiss, F. and Coyle, M., 2009d. First vertical derivative of the magnetic field, McQuesten Aeromagnetic Survey, NTS 115I/15, Yukon. Geological Survey of Canada, Open File 6109; Yukon Geological Survey, Open File 2009-7, scale 1:50 000.
- Kiss, F. and Coyle, M., 2009e. Residual total magnetic field, McQuesten Aeromagnetic Survey, NTS 115J/16 and part of 115J/15, Yukon. Geological Survey of Canada, Open File 6110; Yukon Geological Survey, Open File 2009-8, scale 1:50 000.
- Kiss, F. and Coyle, M., 2009f. First vertical derivative of the magnetic field, McQuesten Aeromagnetic Survey, NTS 115J/16 and part of 115J/15, Yukon. Geological Survey of Canada, Open File 6111; Yukon Geological Survey, Open File 2009-9, scale 1:50 000.
- Kiss, F. and Coyle, M., 2009g. Residual total magnetic field, McQuesten Aeromagnetic Survey, NTS 115O/1 and 115O/2, Yukon. Geological Survey of Canada, Open File 6112; Yukon Geological Survey, Open File 2009-10, scale 1:50 000.
- Kiss, F. and Coyle, M., 2009h. First vertical derivative of the magnetic field, McQuesten Aeromagnetic Survey, NTS 115O/1 and 115O/2, Yukon. Geological Survey of Canada, Open File 6113; Yukon Geological Survey, Open File 2009-11, scale 1:50 000.

- Kiss, F. and Coyle, M., 2009i. Residual total magnetic field, McQuesten Aeromagnetic Survey, NTS 115P/5, 115O/8 and part of 115O/7, Yukon. Geological Survey of Canada, Open File 6114; Yukon Geological Survey, Open File 2009-12, scale 1:50 000.
- Kiss, F. and Coyle, M., 2009j. First vertical derivative of the magnetic field, McQuesten Aeromagnetic Survey, NTS 115P/5, 115O/8 and part of 115O/7, Yukon. Geological Survey of Canada, Open File 6115; Yukon Geological Survey, Open File 2009-13, scale 1:50 000.
- Kiss, F. and Coyle, M., 2009k. Residual total magnetic field, McQuesten Aeromagnetic Survey, NTS 115P/2 and part of 115P/1, Yukon. Geological Survey of Canada, Open File 6116; Yukon Geological Survey, Open File 2009-14, scale 1:50 000.
- Kiss, F. and Coyle, M., 2009l. First vertical derivative of the magnetic field, McQuesten Aeromagnetic Survey, NTS 115P/2 and part of 115P/1, Yukon. Geological Survey of Canada, Open File 6117; Yukon Geological Survey, Open File 2009-15, scale 1:50 000.
- Kiss, F. and Coyle, M., 2009m. Residual total magnetic field, McQuesten Aeromagnetic Survey, NTS 115P/3 and 115P/4, Yukon. Geological Survey of Canada, Open File 6118; Yukon Geological Survey, Open File 2009-16, scale 1:50 000.
- Kiss, F. and Coyle, M., 2009n. First vertical derivative of the magnetic field, McQuesten Aeromagnetic Survey, NTS 115P/3 and 115P/4, Yukon. Geological Survey of Canada, Open File 6119; Yukon Geological Survey, Open File 2009-17, scale 1:50 000.
- Kiss, F. and Coyle, M., 2009o. Residual total magnetic field, McQuesten Aeromagnetic Survey, NTS 115P/6 and 115P/7, Yukon. Geological Survey of Canada, Open File 6120; Yukon Geological Survey, Open File 2009-18, scale 1:50 000.
- Kiss, F. and Coyle, M., 2009p. First vertical derivative of the magnetic field, McQuesten Aeromagnetic Survey, NTS 115P/6 and 115P/7, Yukon. Geological Survey of Canada, Open File 6121; Yukon Geological Survey, Open File 2009-19, scale 1:50 000.
- Kiss, F. and Coyle, M., 2009q. Residual total magnetic field, McQuesten Aeromagnetic Survey, NTS 115P/11 and 115P/12, Yukon. Geological Survey of Canada, Open File 6122; Yukon Geological Survey, Open File 2009-20, scale 1:50 000.
- Kiss, F. and Coyle, M., 2009r. First vertical derivative of the magnetic field, McQuesten Aeromagnetic Survey, NTS 115P/11 and 115P/12, Yukon. Geological Survey of Canada, Open File 6123; Yukon Geological Survey, Open File 2009-21, scale 1:50 000.
- Kiss, F. and Coyle, M., 2009s. Residual total magnetic field, Northern Stevenson Ridge Aeromagnetic Survey, NTS 115 J/9 and 115 J/10, Yukon. Geological Survey of Canada, Open File 6254; Yukon Geological Survey, Open File 2009-28, scale 1:50 000.
- Kiss, F. and Coyle, M., 2009t. First vertical derivative of the magnetic field, Northern Stevenson Ridge Aeromagnetic Survey, NTS 115 J/9 and 115 J/10, Yukon. Geological Survey of Canada, Open File 6255; Yukon Geological Survey, Open File 2009-29, scale 1:50 000.
- Kiss, F. and Coyle, M., 2009u. Residual total magnetic field, Northern Stevenson Ridge Aeromagnetic Survey, NTS 115 J/11 and 115 J/12, Yukon. Geological Survey of Canada, Open File 6256; Yukon Geological Survey, Open File 2009-30, scale 1:50 000.
- Kiss, F. and Coyle, M., 2009v. First vertical derivative of the magnetic field, Northern Stevenson Ridge Aeromagnetic Survey, NTS 115 J/11 and 115 J/12, Yukon. Geological Survey of Canada, Open File 6257; Yukon Geological Survey, Open File 2009-31, scale 1:50 000.
- Kiss, F. and Coyle, M., 2009w. Residual total magnetic field, Northern Stevenson Ridge Aeromagnetic Survey, NTS 115 J/13 and 115 J/14, Yukon. Geological Survey of Canada, Open File 6258; Yukon Geological Survey, Open File 2009-32, scale 1:50 000.
- Kiss, F. and Coyle, M., 2009x. First vertical derivative of the magnetic field, Northern Stevenson Ridge Aeromagnetic Survey, NTS 115 J/13 and 115 J/14, Yukon. Geological Survey of Canada, Open File 6259; Yukon Geological Survey, Open File 2009-33, scale 1:50 000.
- Kiss, F. and Coyle, M., 2009y. Residual total magnetic field, Northern Stevenson Ridge Aeromagnetic Survey, NTS 115 J/15 and 115 J/16, Yukon. Geological Survey of Canada, Open File 6260; Yukon Geological Survey, Open File 2009-34, scale 1:50 000.
- Kiss, F. and Coyle, M., 2009z. First vertical derivative of the magnetic field, Northern Stevenson Ridge Aeromagnetic Survey, NTS 115 J/15 and 115 J/16, Yukon. Geological Survey of Canada, Open File 6261; Yukon Geological Survey, Open File 2009-35, scale 1:50 000.

- Kiss, F. and Coyle, M., 2009aa. Residual total magnetic field, Northern Stevenson Ridge Aeromagnetic Survey, NTS 115 K/9 and 115 K/10, Yukon. Geological Survey of Canada, Open File 6262; Yukon Geological Survey, Open File 2009-36, scale 1:50 000.
- Kiss, F. and Coyle, M., 2009ab. First vertical derivative of the magnetic field, Northern Stevenson Ridge Aeromagnetic Survey, NTS 115 K/9 and 115 K/10, Yukon. Geological Survey of Canada, Open File 6263; Yukon Geological Survey, Open File 2009-37, scale 1:50 000.
- Kiss, F. and Coyle, M., 2009ac. Residual total magnetic field, Northern Stevenson Ridge Aeromagnetic Survey, NTS 115 K/15 and 115 K/16, Yukon. Geological Survey of Canada, Open File 6264; Yukon Geological Survey, Open File 2009-38, scale 1:50 000.
- Kiss, F. and Coyle, M., 2009ad. First vertical derivative of the magnetic field, Northern Stevenson Ridge Aeromagnetic Survey, NTS 115 K/15 and 115 K/16, Yukon. Geological Survey of Canada, Open File 6265; Yukon Geological Survey, Open File 2009-39, scale 1:50 000.
- Kiss, F. and Coyle, M., 2009ae. Residual total magnetic field, Northern Stevenson Ridge Aeromagnetic Survey, NTS 115 O/1, 115 O/2 and part of 115 O/3, Yukon. Geological Survey of Canada, Open File 6266; Yukon Geological Survey, Open File 2009-40, scale 1:50 000.
- Kiss, F. and Coyle, M., 2009af. First vertical derivative of the magnetic field, Northern Stevenson Ridge Aeromagnetic Survey, NTS 115 O/1, 115 O/2 and part of 115 O/3, Yukon. Geological Survey of Canada, Open File 6267; Yukon Geological Survey, Open File 2009-41, scale 1:50 000.
- Mortensen, J.K., 1990. Geology and U-Pb geochronology of the Klondike District, west-central Yukon. *Canadian Journal of Earth Sciences*, vol. 27, p. 903-914.
- Mortensen, J.K., 1992. Pre-Mid-Mesozoic tectonic evolution of the Yukon-Tanana terrane, Yukon and Alaska. *Tectonics*, vol. 11, p. 836-853.
- Mortensen, J.K., 2009. U-Pb age and geochemical studies of Mississippian and Cretaceous plutonic rocks in south-central McQuesten map area, Yukon. *In: Yukon Exploration and Geology 2008*, L.H. Weston, L.R. Blackburn and L.L. Lewis (eds.), Yukon Geological Survey, p. 187-194.
- Murphy, D.C., Mortensen, J.K., Piercey, S.J., Orchard, M.J. and Gehrels, G.E., 2006. Mid-Paleozoic to early Mesozoic tectonostratigraphic evolution of Yukon-Tanana and Slide Mountain terranes and affiliated overlap assemblages, Finlayson Lake massive sulphide district, southeastern Yukon. *In: Paleozoic Evolution and Metallogeny of Pericratonic Terranes at the Ancient Pacific Margin of North America*, Canadian and Alaskan Cordillera, M. Colpron and J.L. Nelson (eds.), Geological Association of Canada, Special Paper 45, p. 75-105.
- Nelson, F.E., Barendregt, R.W. and Villeneuve, M., 2009. Stratigraphy of the Fort Selkirk Volcanogenic Complex in central Yukon and its paleoclimatic significance: Ar/Ar and paleomagnetic data. *Canadian Journal of Earth Sciences*, vol. 46, p. 381-401.
- Nelson, J.L. and Colpron, M., 2007. Tectonics and metallogeny of the Canadian and Alaskan Cordillera, 1.8 Ga to present. *In: Mineral Deposits of Canada: A Synthesis of Major Deposit Types, District Metallogeny, the Evolution of Geological Provinces, and Exploration Methods*, W.D. Goodfellow (ed.), Mineral Deposits Division, Geological Association of Canada, Special Publication 5, p. 755-791.
- Nelson, J.L. and Friedman, R.M., 2004. Superimposed Quesnel (late Paleozoic-Jurassic) and Yukon-Tanana (Devonian-Mississippian) arc assemblages, Cassiar Mountains, northern British Columbia: field, U-Pb and igneous petrochemical evidence. *Canadian Journal of Earth Sciences*, vol. 41, p. 1201-1235.
- Piercey, S.J. and Colpron, M., 2009. Composition and provenance of the Snowcap assemblage, basement to the Yukon-Tanana terrane, northern Cordillera: Implications for Cordilleran crustal growth. *Geosphere*, vol. 5, p. 439-464, doi: 10.1130/GES00505.1.
- Piercey, S.J., Nelson, J.L., Colpron, M., Dusel-Bacon, C., Roots, C.F. and Simard, R.-L., 2006. Paleozoic magmatism and crustal recycling along the ancient Pacific margin of North America, northern Cordillera. *In: Paleozoic Evolution and Metallogeny of Pericratonic Terranes at the Ancient Pacific Margin of North America*, Canadian and Alaskan Cordillera, M. Colpron and J.L. Nelson (eds.), Geological Association of Canada, Special Paper 45, p. 281-322.

- Ruks, T.W., Piercey, S.J., Ryan, J.J., Villeneuve, M.E. and Creaser, R.A., 2006. Mid- to late Paleozoic K-feldspar augen granitoids of the Yukon-Tanana Terrane, Yukon, Canada: Implications for crustal growth and tectonic evolution of the northern Cordillera. *Geological Society of America Bulletin*, vol. 118, p. 1212–1231.
- Ryan, J.J. and Gordey, S.P., 2002. Bedrock geology of Yukon-Tanana terrane in southern Stewart River map area, Yukon Territory. *Geological Survey of Canada, Current Research 2002-A1*, 11 p.
- Ryan, J.J., Gordey, S.P., Glombick, P., Piercey, S.J. and Villeneuve, M.E., 2003. Update on bedrock geological mapping of Yukon-Tanana terrane in southern Stewart River map area, Yukon Territory. *Geological Survey of Canada, Current Research 2003-A9*, 7 p.
- Ryan, J.J. and Gordey, S.P., 2004. Geology, Stewart River area (Parts of 115 N/1,2,7,8 and 115 O/2-12), Yukon Territory. *Geological Survey of Canada, Open File 4641*, scale 1:100 000.
- Schroeter, T.G. (ed.), 1995. *Porphyry Deposits of the Northwestern Cordillera*. Canadian Institute of Mining, Metallurgy and Petroleum, Special Volume 46, 888 p.
- Simard, R.-L., 2003. Geological map of southern Semenof Hills (part of NTS 105E/1,7,8), south-central Yukon (1:50 000 scale). Yukon Geological Survey, Open File 2003-12.
- Simard, R.-L. and Devine, F., 2003. Preliminary geology of the southern Semenof Hills, central Yukon (105E/1,7,8). *In: Yukon Exploration and Geology 2002*, D.S. Emond and L.L. Lewis (eds.), Exploration and Geological Services Division, Yukon Region, Indian and Northern Affairs Canada, p. 213-222.
- Tempelman-Kluit, D.J., 1974. Reconnaissance geology of Aishihik Lake, Snag and part of Stewart River map-areas, west-central Yukon. *Geological Survey of Canada, Paper 73-41*, 97 p.
- Tempelman-Kluit, D.J., 1984. Geology, Laberge (105E) and Carmacks (105I), Yukon Territory. *Geological Survey of Canada, Open File 1101*, scale 1:250 000.
- Tempelman-Kluit, D.J., 2009. Geology of Carmacks and Laberge map areas, central Yukon: Incomplete draft manuscript on stratigraphy, structure and its early interpretation (ca. 1986). *Geological Survey of Canada, Open File 5982*, 399 p.
- Yukon MINFILE 2009 - A database of mineral occurrences. Yukon Geological Survey, <http://www.geology.gov.yk.ca/databases_gis.html>.

Major- and trace-element composition of platinum group minerals and their inclusions from several Yukon placers

Yana Fedortchouk¹

Department of Earth Sciences, Dalhousie University, Halifax, Canada

William LeBarge²

Yukon Geological Survey, Whitehorse, Yukon, Canada

Andrei Yu Barkov

Department of Earth and Planetary Sciences, McGill University, Montreal, Canada

Luca Fedele and Robert J. Bodnar

Department of Geosciences, Virginia Tech, Blacksburg, USA

Fedortchouk, Y., LeBarge, W., Barkov, A.Y., Fedele, L. and Bodnar, R.J., 2010. Major- and trace-element composition of platinum group minerals and their inclusions from several Yukon placers. *In: Yukon Exploration and Geology 2009*, K.E. MacFarlane, L.H. Weston and L.R. Blackburn (eds.), Yukon Geological Survey, p. 185-196.

ABSTRACT

Occurrences of placer platinum-group minerals (PGM) were reported in several gold placer deposits in Yukon. The source rock and the type of platinum mineralization are not known for these localities. We investigated five grains of Pt-Fe alloy from Burwash Creek (map area 115G and F), one grain from Scroggie Creek (map area 115O and N) and one grain from Wolverine Creek (map area 105C and D). Results of multiple electron microprobe analysis display elevated levels of Pd, Rh, Ir and Cu in these Pt-Fe alloy grains. The grains host micro-inclusions of various species of PGMs and silicate-melt inclusions with diopside, albite and sodic-calcic amphiboles. Trace element composition of the silicate inclusions determined using laser ablation ICP-MS shows a notable enrichment in large ion lithophile elements. We infer that the reported association of PGM and the trace element composition of silicate-melt inclusions observed in the studied grains are likely derived from a subduction-related Alaskan-type mineralization.

¹yana@dal.ca

²bill.lebarge@gov.yk.ca

INTRODUCTION

Many gold placer deposits in Yukon historically report placer occurrences of platinum-group minerals (PGM). Only very few of these occurrences were confirmed analytically, while the source rocks of the placer PGMs is not well known. Platinum mineralization can be associated with several types of mafic and ultramafic intrusive rocks, including Alpine-type peridotites or ophiolites, subduction-related Alaskan-type complexes and continental mafic-ultramafic intrusive rocks, such as Triassic Kluane sills, which are associated with continental rifting events. The Alaskan-type, concentrically zoned ultramafic-mafic complexes, are a recognized source of placer platinum. For example, ~20 tonnes of platinum derived from Alaskan-type source rocks was recovered from placer deposits of Goodnews Bay, Alaska (Tolstykh *et al.*, 2002). Potential relationships with Alaskan-type complexes are inferred for a number of placer occurrences of PGM, documented in Canada (Nixon *et al.*, 1990; Cabri *et al.*, 1996; Barkov *et al.*, 2005, 2008a,b). These species of PGM are dominantly alloys of the platinum-group elements (PGE). On the other hand, Kluane sills forming a 'Kluane-belt' in southwestern Yukon, host Ni-Cu-PGE mineralization including the Wellgreen deposit (Hulbert, 1997; Barkov *et al.*, 2002) and may also supply PGM grains into the adjacent creeks. Possible fragments of other mafic rocks related to continental rifting events were reported in other parts of Yukon (Johnston *et al.*, 2007).

Pt-Fe alloy is the most common type of placer PGM. Its geochemistry and composition of the inclusion suite can shed light on the origin of PGM-host magmas. The present paper documents the first confirmed occurrence of placer grains of Pt-Fe alloy in Burwash Creek and reports a detailed mineralogical and geochemical study of Pt-Fe alloy grains from Burwash, Scroggie and Wolverine creeks in southern-central Yukon. Our objectives are (1) to characterize compositional variations, extents of solid-solutions and minor element abundance present in these placer grains of Pt-Fe alloy, based on the results of electron microprobe analysis (EMP); (2) to characterize the PGMs found as inclusions in Pt-Fe alloy grains; (3) to examine the compositions of silicate melt inclusions in Pt-Fe alloy grains, their mineralogical composition and patterns of trace element concentrations based on the results of laser ablation (LA) ICP-MS; and (4) to identify a potential provenance for these placer grains of PGM.

SAMPLE LOCATIONS

This study uses five PGM grains from a gold placer deposit in Burwash Creek, one grain from Scroggie Creek and one grain from Wolverine Creek (Fig. 1). Burwash Creek is situated in the Kluane area in southeastern Yukon, where placer gold was discovered in the 1920s. The Burwash stream is a tributary of the Kluane River. No occurrences of PGM were previously reported from Au-bearing placers in this locality. For this study we used grains donated to the Yukon Geological Survey (YGS) from the estate of placer inspector George Gilbert and grains obtained by W. LeBarge from placer miner Steve Johnson in 2008. The Kluane area is located along the eastern margin of Wrangellia (Fig. 1) and to the west of the Denali fault. The Triassic Kluane sill-like subvolcanic mafic-ultramafic intrusive rocks with Ni-Cu-PGE mineralization serve as magma-conduits for the overlying basalts of the Nikolai Group (Hulbert, 1997). In addition, fragments of oceanic-type serpentinized peridotites, possibly representing the basement of Wrangellia, are known along the Denali fault zone (Mezger, 2000). Detrital chromites, with a composition corresponding to an ophiolitic source, have been recorded in Burwash Creek (Fedortchouk and LeBarge, 2008).

Scroggie Creek (Fig. 1) cuts through rocks of the Yukon-Tanana terrane in central Yukon. It is located in the proximity of Pyroxene Mountain, the best-known example of an Alaskan-type complex in Yukon (Hart *et al.*, 2001). Fragments of oceanic Alpine-type peridotites incorporated into the Yukon-Tanana terrane assemblage are also present in the drainage area of Scroggie Creek.

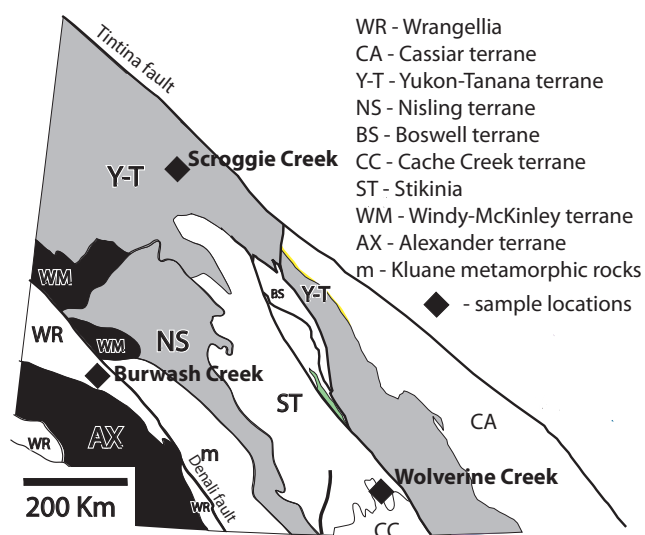


Figure 1. Regional terrane and sample location map.

Wolverine Creek is located in the southern part of Yukon. It cuts through rocks of the Cache Creek terrane (Fig. 1) consisting of Mississippian to lower Jurassic oceanic volcanic rocks with fragments of Alpine-type peridotites. The Alpine-type peridotites contain associated chromite lenses, which may host PGE mineralization. However, ultramafic intrusive rocks with features distinct from the Alpine-type peridotites have been reported from the Cache Creek terrane and may represent Alaskan-type complexes (Hart *et al.*, 2001).

ANALYTICAL METHODS

Compositions of the host Pt-Fe alloys and some larger PGM phases in micro-inclusions were analysed using the electron microprobe (EMP) in wavelength-dispersion spectrometry mode (WDS) with a JEOL JXA-8900 instrument (McGill University), at 20 kV and 30 nA, using a finely focused beam (2 μm) and on-line correction procedures. Pure metals (Os, Ir, Ru, Rh, Pt, Pd, Fe and Ni) and PtAs_2 , FeS_2 , CuFeS_2 and Bi_2Te_3 were used as standards. The $\text{L}\alpha$ line was applied for Ir, Pt, Rh, Ru, Te and Cu, the $\text{M}\alpha$ line for Os, the $\text{L}\beta$ line for Pd and As, and the $\text{K}\alpha$ line for Fe, Ni and S. All possible peak-overlaps between the X-ray emission lines employed were checked and corrected. Compositions of PGM micro-inclusions and individual phases of PGM and silicate micro-inclusions were examined using a Hitachi S-4700 FEG Field Emission Scanning Electron Microscope (FE SEM) at the Institute for Research in Materials, Dalhousie University, equipped with an energy-dispersion spectrometer (SEM-EDS) and a set of well-characterized standards. The obtained results of EDS and WDS analysis are in good agreement with each other.

One placer grain of Pt-Fe alloy from Burwash Creek contained four silicate melt inclusions, which are considered to be primary and represent the melt trapped in the PGM during growth. The inclusions contain multiple crystals, or daughter minerals, which is characteristic of melt inclusions that have cooled relatively slowly after trapping (Bodnar and Student, 2006). The grain was mounted in epoxy and polished to expose the inclusions. The composition of the individual mineral phases in each inclusion was examined using EDS analysis on FE-SEM. As the inclusions in an opaque Pt-Fe alloy have to be exposed by polishing prior to the analysis, they could not be homogenized to obtain the composition of the whole inclusion by EMP analysis. As a result, individual phases were analysed using EDS-SEM analysis

and an assumed SiO_2 content of 50 wt% — a realistic estimate for mafic magmas. This estimate was used as an internal standard for the LA ICP-MS analysis. For this reason, the absolute values of the element concentrations obtained by LA ICP-MS analysis are only accurate to approximately $\pm 10\%$, while the relative concentrations and ratios of the elements are determined with high precision. LA ICP-MS analysis were conducted at Virginia Tech using an Agilent 7500ce quadrupole ICP-MS and a Lambda Physik GeoLas 193 nm Excimer laser ablation system with He gas flow. NIST 610 glass, used as an external standard, was analysed twice, before and after the analysis. The laser spot size was adjusted to the largest possible size, to include the maximum amount of the inclusion material but avoiding the host phase. The time-resolved LA ICP-MS data were reduced using AMS analytical software (Mutchler *et al.*, 2008).

MINERALOGY OF PGM

HOST PT-FE ALLOY

Seven placer grains of Pt-Fe alloy (0.5 to 2 mm in size) from Burwash, Scroggie and Wolverine creeks were examined and analysed (Table 1, Fig. 2). The polished sections of five of these grains had exposed micro-inclusions (typically 10-20 μm thick) of various phases of PGM and silicate inclusions and are described below (Fig. 3). Compositional variation in all seven grains of Pt-Fe alloy were examined from the centre to the margins, along EMP profiles with 15 to 30 data points each (Fig. 2). In the Wolverine grain, the analyses were collected along two profiles (WN-1 and WN-2; Fig. 2; Table 1). The observed levels of solid solution in all seven grains typically decrease: Pd (0.49-5.84, mean 2.38 wt%) > Rh (1.05-1.94, mean 1.50 wt%) > Ir (<0.2 to 6.91, mean 1.33 wt%) > Cu (0.17-1.19, mean 0.62 wt%) > Os (<0.1 to 0.90, mean 0.40 wt%) and > Ni (<0.06 to 0.12, mean 0.05 wt%). Concentrations of Ru are low in all of these placer grains (Table 1), ranging from the lower limit of detection (<0.03 wt%; WDS) to 0.11, with a mean value of <0.03 wt% Ru. In contrast, the maximum content of Pd is notably high (5.8 wt%), although higher concentrations, up to 11 wt% Pd, were documented in a Pt-(Pd)-Fe alloy from Arch Creek, Yukon (Barkov *et al.*, 2008b). The ratio $\Sigma\text{PGE}/(\text{Fe}+\text{Cu}+\text{Ni})$ varies from 2.5 to 5.7, implying a compositional gap between Pt_3Fe , corresponding to stoichiometry of the mineral isoferroplatinum, and a Pt-Fe alloy richer in Pt (Fig. 2a). In Ir-Rh-Pd compositional space, the composition of the seven Pt-Fe alloy grains plot along

Table 1. Representative compositions of Pt-Fe alloy placer grains from three placers. All analyses are the average of 15-30 point analysis. SC = Scroggie, BR = Burwash, WN = Wolverine.

	SC-1	BR-1	BR-2	BR-3	BR06-1	BR06-2	WN-1
wt%							
Fe	4.99	7.33	4.85	7.24	5.00	4.69	9.03
Rh	0.45	1.31	1.71	1.42	1.12	1.83	1.24
S	0.02	0.03	0.02	0.02	0.03	0.03	0.05
Cu	0.33	0.97	0.31	1.00	0.39	0.49	0.91
Pt	88.90	85.13	85.46	85.72	87.74	91.03	85.46
Pd	2.80	0.75	5.64	1.03	3.60	0.58	0.37
Te	0.02	0.01	0.01	0.01	0.01	0.01	0.01
Ir	0.94	3.21	0.43	2.43	0.86	0.06	2.28
Ru	0.00	0.00	0.09	0.00	0.00	0.01	0.00
Ni	0.05	0.01	0.10	0.04	0.05	0.02	0.12
Os	1.00	0.12	0.33	0.09	0.70	0.74	0.21
Total	99.63	98.97	99.06	99.12	99.65	99.60	99.76
Atomic proportions							
Fe	15.04	21.48	14.29	20.78	14.87	14.27	24.99
Rh	0.73	2.13	2.74	2.22	1.81	3.02	1.86
S	0.12	0.14	0.13	0.12	0.13	0.15	0.23
Cu	0.86	2.55	0.79	2.53	1.02	1.30	2.20
Pt	76.75	69.75	72.09	70.44	74.82	79.36	67.73
Pd	4.44	0.92	8.72	1.55	5.63	0.92	0.53
Te	0.02	0.01	0.02	0.01	0.02	0.01	0.02
Ir	0.82	2.81	0.37	2.02	0.75	0.05	1.85
Ru	0.00	0.00	0.14	0.00	0.00	0.02	0.00
Ni	0.14	0.03	0.28	0.10	0.15	0.06	0.33
Os	0.89	0.05	0.29	0.08	0.61	0.66	0.17
Total	100.00	100.00	100.00	100.00	100.00	100.00	100.00

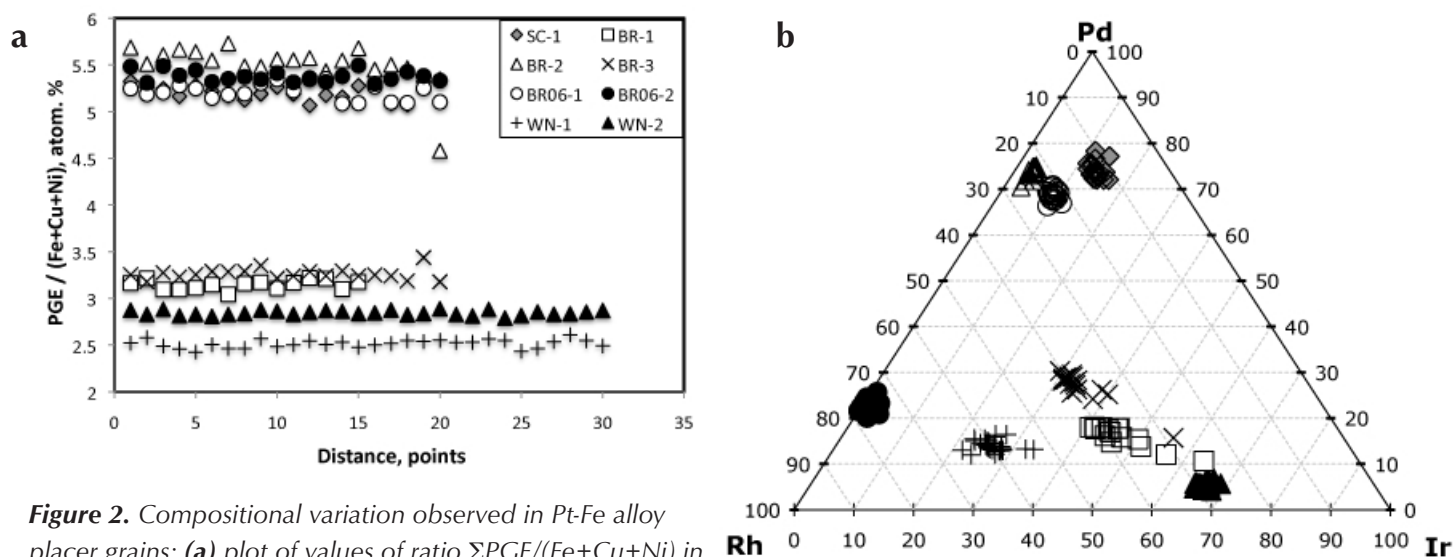


Figure 2. Compositional variation observed in Pt-Fe alloy placer grains: (a) plot of values of ratio $\Sigma\text{PGE}/(\text{Fe}+\text{Cu}+\text{Ni})$ in the compositional profiles through the grains (15-30 data points from each grains); (b) Ir-Rh-Pd diagram (atom %).

the Ir-Rh and Rh-Pd joins (Fig. 2b). Also the grains with $\Sigma\text{PGE}/(\text{Fe}+\text{Cu}+\text{Ni}) < 3.5$ have similar Ir-enrichment trends and the grains with $\Sigma\text{PGE}/(\text{Fe}+\text{Cu}+\text{Ni}) > 5$ plot along the Rh-Pd join (Fig. 2b). Composition of the host PGM grains correlate with the composition of micro-inclusions. The Ir-rich grain BR-3 contains Ir-rich inclusions of bowieite and the more Pd-enriched grain BR-2 contains inclusions with Pd-rich phases (miassite and vasilite; Table 2).

PGM INCLUSIONS

Five placer grains of Pt-Fe alloy contain micro-inclusions that were exposed during polishing. Composition of these inclusions was studied using the EDS mode on the SEM, and some larger inclusions were analysed using the WDS

mode on the EMP (Table 2). The description of the identified phases is given below.

PGMs from the micro-inclusions in the placer grains of Pt-Fe alloy from Burwash Creek:

Members of the bowieite Rh_2S_3 – kashinite Ir_2S_3 series.

Bowieite is relatively common in the analysed inclusions. Two observed compositional varieties are: Pt-rich (poor in Ir) and Ir-rich (analysis 1, Table 2). Bowieite and kashinite are isostructural and the existence of a solid-solution series between these end members is not unusual (Desborough and Criddle, 1984; Begizov *et al.*, 1985). The incorporation of Pt is much less common. The phase

Table 2. Composition of micro-inclusions of platinum group minerals in grains of Pt-Fe alloy from several placers in Yukon.

No.	1	2	3	4	5	6	7	8	9
wt%									
Fe	0.05	0.02	1.29	0.04	0.04	0.61	2.04	0.34	18.24
Rh	29.90	0.00	3.76	2.30	0.98	1.91	2.06	0.95	0.71
S	25.65	11.41	25.76	34.41	37.27	0.01	0.02	0.00	0.05
Cu	0.01	1.77	0.00	0.01	0.03	0.06	0.13	0.00	0.88
Pt	0.60	2.07	0.89	0.65	0.59	14.12	23.63	2.35	72.01
Pd	0.05	84.69	0.14	0.04	0.05	0.05	0.09	0.11	0.30
Te	0.01	0.00	0.00	0.00	0.02	0.02	0.02	0.01	0.02
Ir	42.51	0.11	11.06	2.17	0.95	51.69	48.44	14.92	0.01
Ru	0.01	0.00	1.36	37.43	53.43	0.71	0.44	2.14	0.00
Ni	0.01	0.12	0.02	0.00	0.01	0.03	0.04	0.01	0.14
Os	0.03	0.03	51.05	21.35	5.27	29.28	22.17	78.65	0.12
Total	98.97	100.23	96.76	98.46	98.65	98.57	99.14	99.57	93.56
Atomic proportions									
Fe	0.07	0.03	1.88	0.04	0.04	2.03	5.93	1.12	43.06
Rh	22.04	0.00	2.98	1.42	0.55	3.47	3.67	1.70	0.91
S	60.69	29.81	65.44	67.32	66.88	0.04	0.08	0.00	0.19
Cu	0.01	2.34	0.00	0.01	0.03	0.18	0.34	0.00	1.81
Pt	0.23	0.89	0.37	0.21	0.17	13.48	20.15	2.20	48.65
Pd	0.04	66.69	0.11	0.03	0.03	0.08	0.14	0.20	0.38
Te	0.01	0.00	0.00	0.00	0.01	0.02	0.03	0.01	0.02
Ir	16.78	0.05	4.69	0.71	0.29	50.34	46.88	14.34	0.01
Ru	0.01	0.00	1.10	23.02	30.40	1.32	0.81	3.90	0.00
Ni	0.02	0.17	0.03	0.00	0.01	0.09	0.11	0.02	0.31
Os	0.01	0.01	21.86	7.21	1.60	28.81	21.77	76.38	0.08
Total	100.00	100.00	100.00	100.00	100.00	100.00	100.00	100.00	100.00

Note: 1 - inclusion of bowieite - kashinite in BR-3 grain 2 - vasilite matrix in micro-inclusion from BR-2
 3 - erlichmanite from WN-1 4,5 - laurite from WN-1 6,7 - iridium from WN-1 8 - osmium from WN-1
 9 - Pt-Fe alloy from WN-1

'Pt₂S₃' was previously reported in experiments in the Pt-S system (Grønvold *et al.*, 1960) and may require special conditions to stabilize the 'Pt₂S₃' component.

Miassite (Rh, Pt, Pd)₁₇S₁₅. Miassite forms euhedral grains in a few micro-inclusions. Its composition corresponds to Rh₁₇S₁₅ (cubic, Pm3m) with minor Pd and Pt, a phase that exists in the Rh-S and Fe-Rh-S systems (Okamoto, 1992; Makovicky *et al.*, 2002).

Cooperite PtS. The EMP data show some deviation of the few PtS micro-inclusions from an ideal stoichiometry of cooperite, giving a composition of Pt_{0.9}S_{1.1}. This observed minor nonstoichiometry may represent a compositional feature (*cf.*, synthetic analog of cooperite, PtS_{1.1}, Grønvold *et al.*, 1960).

Isoferroplatinum (or Fe-rich platinum). Ideally Pt₃Fe (cubic, Pm3m) typically contains 25 to 35 atom % Fe. The related Pt-Fe alloy phase is Fe-rich platinum (20-50 atom % Fe) or "native Pt" (Fe < 20 atom % and Pt > 80 atom %). Compositions of some inclusions in the Pt-Fe alloy placer grains correspond to a Pt₃Fe-type alloy, which has stoichiometry of isoferroplatinum, or an Fe-rich platinum.

Vasilite (Pd, Cu, Pt)₁₆S₇. Pd-(Cu-) rich sulfide forms a matrix in the micro-inclusion in Fig. 3a. Its composition is most consistent with atomic proportions of vasilite, Pd₁₆S₇ (analysis 2, Table 2). It has elevated levels of Cu (1.9 wt% or 0.6 apfu (atoms per formula unit) and Te-content below the detection limit of WDS analysis (<0.06 wt%). A similar Cu-bearing and poor in Te phase, related to vasilite, was described in the Pustaya River placer deposit associated with an Alaskan-type complex, Kamchatka, Russia, by Tolstykh *et al.* (2000).

Pt-Pd-Ni-Cu alloy (Pd-rich platinum). Inclusions of a Pt-dominant alloy were found in vasilite matrix in the inclusion in Figure 3a. Their analyses show unusually high Pd, Ni and Cu, and low Fe (minor concentrations of S, ascribed to contamination by a sulfide phase, were omitted in these results). The three analysed inclusions give the following ranges (expressed in wt%): Pd 20.8-27.7, Ni 2.5-3.1, Cu 2.7-3.2 and Fe 0.7-1.0; or in terms of atom %: Pt_{47.7-52.8}Pd_{29.3-37.9}Ni_{6.3-8.0}Cu_{6.1-7.5}. Values of ΣPGE/(Fe + Cu + Ni) vary from 4.5 to 5.9. We note that the maximum value in this range (5.9) is close to the maximum of 5.7 observed for Pt-Fe alloy placer grains. This correspondence implies that these alloy phases, the host and inclusions, have attained equilibrium in the distribution of PGE and base metals.

Keithconnite Pd₂₀Te₇ (or Pd_{3-x}Te; 0.14 < x < 0.43). Pd-rich telluride forms tiny grains in the matrix of vasilite in the inclusion in Figure 3a. It has the composition: Pd 71.71, Pt 0.63, Te 27.66, for a total of 100.0 wt%, which corresponds to (Pd_{3.01}Pt_{0.01})_{Σ3.02}Te_{0.97} or to (Pd_{20.3}Pt_{0.1})_{Σ20.4}Te_{6.6}, calculated on the basis of a total of 4 apfu and 27 apfu, respectively.

Unnamed Pd₁₁Te₂S₂ (?). An unusual phase of Pd-rich sulfotelluride (?) occurs as tiny grains in the inclusion shown in Figure 3a. The composition of the analysed phase is (SEM-EDS): Pd 73.65, Pt 1.28, Au 1.37, Te 19.83 and S 3.87, for a total of 100.0 wt%; the formula is (Pd_{10.57}Au_{0.11}Pt_{0.10})_{Σ10.78}Te_{2.37}S_{1.84} (basis: Σ=15 apfu).

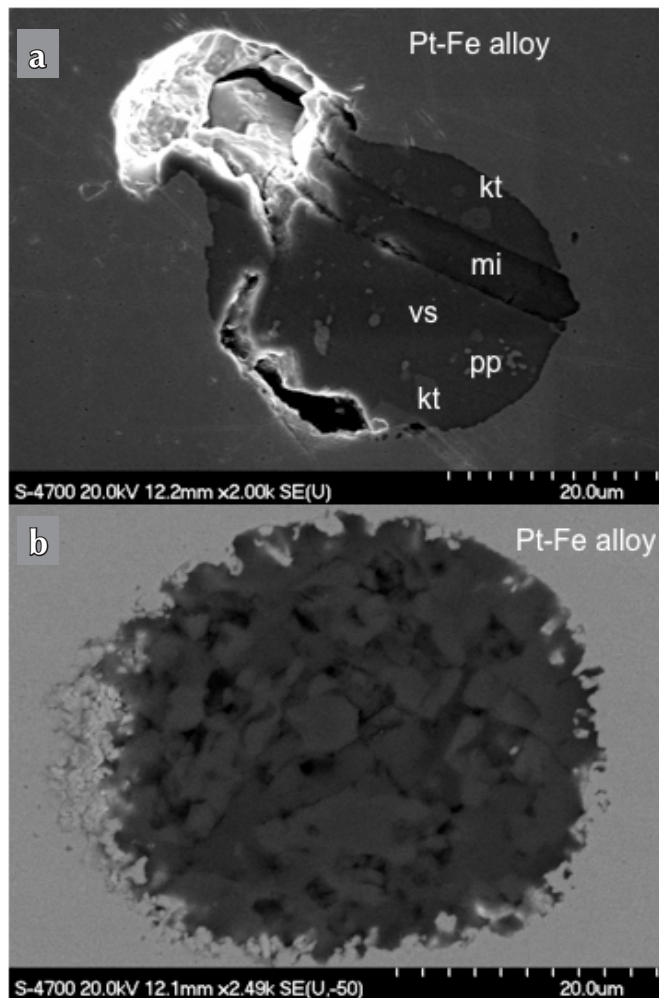


Figure 3. Examples of micro-inclusions in Pt-Fe alloy placer grains with (a) PGM and (b) silicates.

mi = miassite (Rh,Pt,Pd)₁₇S₁₅, vs = vasilite (Pd,Cu,Pt)₁₆S₇
kt = keithconnite (Pd₂₀Te₇), pp = Pd-rich platinum.

PGMs from the micro-inclusions in the Pt-Fe alloy placer grain from Wolverine Creek:

Erlichmanite OsS₂. An inclusion of erlichmanite was found in the grain from Wolverine Creek (analysis 3, Table 2). It has high iridium (11.06 wt%) and elevated Rh and Ru (3.76 and 1.36 wt%, respectively).

Laurite RuS₂. Inclusions of laurite were found in the same grain (analysis 4, 5, Table 2). The two analysed inclusions show elevated content of Os (21.4 and 5.3 wt%) and Rh (2.3 and 0.98 wt%).

Iridium (Ir, Os, Ru, Pt) and Osmium (Os, Ir). Inclusions of iridium and osmium are found in the Wolverine grain (analysis 6, 7, 8, Table 2). The iridium inclusion has elevated Os (up to 29.3 wt%), Pt (up to 23.6 wt%) and Rh (~2 wt%). The osmium inclusion has 14.9 wt% Ir, 2.35 wt% Pt and 2.14 wt% Ru.

SILICATE MINERALS

One placer grain of Pt-Fe alloy from Burwash Creek contains four silicate micro-inclusions (10 – 40 µm in diameter) with various silicate phases (Fig. 3b). The silicates form euhedral and subhedral grains with length up to 10 µm. Using EDS-SEM analysis we have identified clinopyroxene, Cl-bearing amphibole and plagioclase in these inclusions. All phases were too small for WDS-EMP analysis. The clinopyroxene phase is a diopside, which varies in composition from high to moderately rich in Mg: Ca_{47.1}Mg_{48.0}Fe_{4.9} (mg# 90.7; *i.e.*, [Mg:(Mg + Fe²⁺)]); Ca_{47.5}Mg_{43.9}Fe_{8.6} (mg# 83.6); and Ca_{45.7}Mg_{37.5}Fe_{16.8} (mg# 69.0). The calculated formulae, Ca_{0.84}(Mg_{0.85}^[6]Al_{0.15}Fe_{0.09})_{Σ1.09}Si_{1.99}O₆, Ca_{0.84}(Mg_{0.77}Fe_{0.15}^[6]Al_{0.15}Mn_{0.01})_{Σ1.08}(Si_{1.99}Al_{0.01})₂O₆, and (Ca_{0.85}Na_{0.06})_{Σ0.91}(Mg_{0.69}Fe_{0.31}^[6]Al_{0.10})_{Σ1.10}(Si_{1.92}Al_{0.08})₂O₆ suggest the presence of elevated values of ^[6]Al.

Sodic-calcic amphiboles (0.6 and 1.1 Na apfu) are relatively enriched in Cl (0.72 and 1.17 wt%, or 0.17 and 0.36 Cl apfu, respectively). Similar inclusions of sodic-calcic amphibole, but notably richer in Cl, were observed in the placer grains of a Pt-Fe alloy from Florence Creek, Yukon (Barkov *et al.*, 2008b). Plagioclase in our inclusions from a Pt-Fe grain from Burwash Creek, is albite-enriched in anorthite component: Ab₆₀An_{35.1}Or_{4.8} and Ab_{57.5}An_{39.9}Or_{2.6}. Interestingly, a nearly pure albite (Ab_{97.8}) occurs as an inclusion in Pt-Fe alloy at Florence Creek, Yukon (Barkov *et al.*, 2008b).

TRACE ELEMENT COMPOSITIONS OF SILICATE-MELT INCLUSIONS

Trace element compositions of the four inclusions of silicate melt were determined using LA ICP-MS. Two inclusions are located closer to the margin of the grain and two are in the interior part of the Pt-Fe alloy host grain. Mineralogical and chemical composition of all four inclusions is identical (Fig. 4; Table 3). Concentrations of light and heavy rare earth elements (LREE and HREE) normalized to the chondritic abundances (McDonough and Sun, 1995) show a slightly negative slope for REE (Fig. 4a). The slope of the REE pattern is not steep with the ratio of La/Lu ~3 and a well-developed Eu minimum. Depletion in HREE, if present, is very minor indicating a garnet-absent mantle source for the magmas. The multi-element 'spider-diagram' (Fig. 4b) shows significant decoupling between the two important groups of

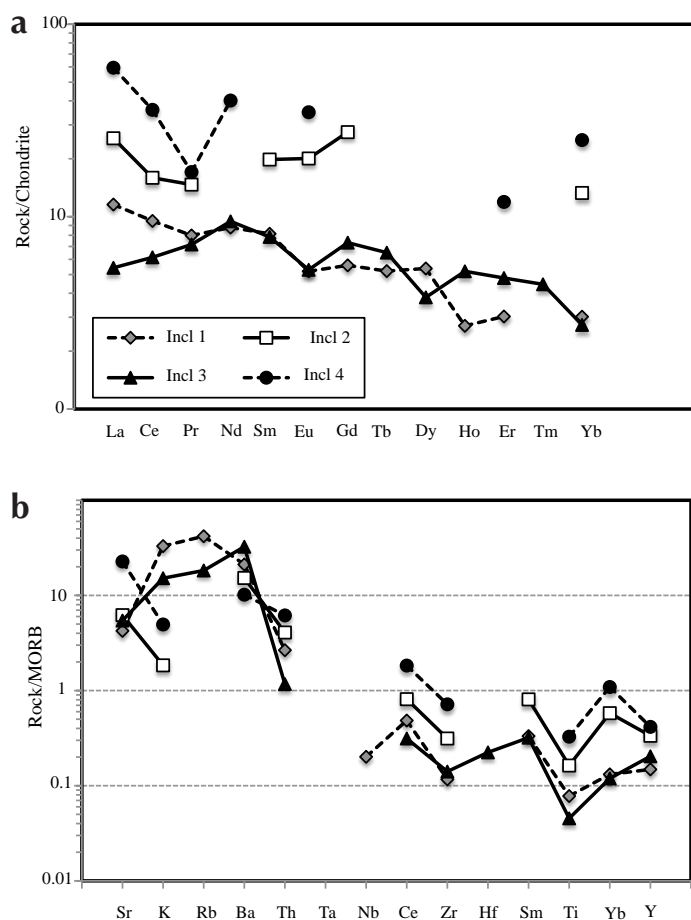


Figure 4. Composition of silicate melt micro-inclusions in a host Pt-Fe alloy placer grain: (a) chondrite normalized (McDonough and Sun, 1995) REE and (b) N-MORB normalized (Hofmann, 1988; Hart, 1999) LIL and HFS abundances.

incompatible elements. The large ion lithophile elements (LIL), Sr, K, Rb and Ba are enriched and behave differently than the high field strength elements (HFS), Th – Y, which show much lower concentrations (Fig. 4b). Another important feature on this diagram is the large negative trough at Nb and Ti. The Nb trough shown for inclusion 1 is even larger for the other three inclusions, which have Nb concentrations below the detection limit (Table 3).

DISCUSSION

POSSIBLE PROVENANCE OF PLACER GRAINS OF PT-FE ALLOY

In all three localities studied, there are three types of possible source-rocks for the detrital grains of Pt-Fe alloy: oceanic Alpine-type peridotites or ophiolites, subduction-related Alaskan-type complexes and continental mafic-

Table 3. Average major- and trace-element composition of four melt inclusions (Incl 1-4) from BR06-2 (LOD - limit of detection).

	Incl 1	LOD	Incl 2	LOD	Incl 3	LOD	Incl 4	LOD
LA ICP-MS, wt%								
Si	23.37		23.37		23.37		23.37	
Na	2.09		1.04		1.68		0.58	
Mg	3.35		6.00		5.01		1.10	
Al	9.78		4.95		6.57		16.47	
K	3.17		0.16		1.34		0.44	
Ca	4.82		12.41		9.88		18.50	
Ti	0.10		0.26		0.07		0.53	
Mn	0.10		0.19		0.18		0.15	
Fe	1.83		11.65		4.52		22.01	
LA ICP-MS, ppm								
Rb	57.65	1.04		7.50	23.06	1.08		20.79
Sr	453.05	0.11	702.44	0.82	616.55	0.11	2574.14	2.49
Y	5.49	0.16	11.99	1.04	7.30	0.18	14.87	2.79
Zr	11.54	0.17	32.69	1.37	14.68	0.14	74.70	2.93
Nb	0.70	0.27		2.01		0.29		5.87
Ba	268.12	0.07	211.45	0.35	450.23	0.06	141.09	1.39
La	2.81	0.10	6.06	0.56	1.28	0.11	14.09	1.88
Ce	5.88	0.04	9.75	0.50	3.76	0.04	21.98	0.91
Pr	0.74	0.07	1.36	0.53	0.67	0.08	1.58	1.43
Nd	4.07	0.68		4.90	4.41	0.71	18.75	12.87
Sm	1.39	0.29	3.03	2.48	1.20	0.35		6.89
Eu	0.28	0.10	1.16	0.72	0.31	0.11	2.02	1.76
Gd	1.17	0.35	5.42	2.13	1.44	0.40		6.41
Tb	0.21	0.09		0.84	0.24	0.11		2.10
Dy	1.17	0.46		3.69	0.97	0.61		9.53
Ho	0.18	0.05		0.58	0.28	0.06		1.53
Er	0.51	0.15		1.02	0.79	0.15	1.97	1.57
Tm		0.08		0.75	0.11	0.10		1.78
Yb	0.58	0.16	2.26	1.62	0.47	0.13	4.25	2.32
Lu		0.35		2.53		0.36		6.70
Hf	0.32	0.23		1.76	0.67	0.28		4.24
Ta		0.08		0.48		0.06		1.54
Th	0.54	0.05	0.76	0.37	0.22	0.07	1.15	0.96

ultramafic intrusions of 'Kluane-type' sills. Compositions of the Pt-Fe alloy grains from the three localities studied here, and the previously studied PGM grains from Florence Creek (Barkov *et al.*, 2008b) are similar, and show an enrichment in Cu, Ir, Rh and Pd, and strong depletion in Ru (Tables 1, 2), indicating that they may have been derived from a similar type of source rock. These compositional characteristics do not agree with derivation from an ophiolite-type source but rather point to an Alaskan-type source.

In general, compositions of PGM present as inclusions in Pt-Fe alloy placer grains cannot provide distinctive mineralogical criteria to recognize their provenance. For example, Rh-Ir sulfides can occur in association with a podiform chromitite (Malitch *et al.*, 2001), a layered intrusion (Oberthür *et al.*, 2004), or with an Alaskan-type complex (Stanley *et al.*, 2005). Also, PGM may experience significant re-equilibration upon cooling of the host intrusion and their composition may be notably changed in the presence of fluids. Nevertheless, the observed assemblage of PGM in the analysed inclusions at Burwash rather corresponds to Alaskan-type mineralization. Indeed, the same association of bowieite-kashinite, miassite, vasilite, cooperite and keithconnite was documented in inclusions in grains of isoferroplatinum-type alloy from a placer of the Miass River, in the Urals (Britvin *et al.*, 2001). Alaskan-type complexes are the recognized source of placer platinum in this region. Furthermore, these types of Rh-Ir sulfides were first discovered in association with Alaskan-type complexes: bowieite in Alaska (Desborough and Criddle, 1984), and kashinite and miassite in the Urals (Begizov *et al.*, 1985; Britvin *et al.*, 2001). Phases corresponding to the composition of vasilite were reported in association with Pt-Fe alloy from Alaskan-type complexes of the Kamchatka-Koryak belt (Rudashevsky and Zhdanov 1983; Tolstykh *et al.*, 2000).

The other possible type of source rock is continental mafic-ultramafic intrusions associated with continental rifting. The Kluane mafic-ultramafic sill-like intrusions developed in the drainage area of Burwash Creek correspond to this type of mafic intrusion. The Quill Creek complex hosts a number of occurrences of Ni-Cu-PGE mineralization, including the Wellgreen deposit, which is economically important and adjoins the Burwash property to the west (Cabri *et al.*, 1993; Hulbert 1997). Fragments of other mafic intrusive rocks, likely formed in continental rifting settings, were identified in other areas of the Cordilleran part of Yukon (Johnston *et al.*, 2007). However, the Wellgreen deposit is characterized by a very

small grain size for most of the PGMs, which are principally Pd-(Pt)-Ni-rich antimonite and bismuthotellurides. PGE alloy minerals are very rare in this deposit and in related deposits (Cabri *et al.*, 1993; Barkov *et al.*, 2002). Thus, the Kluane-type source appears to be less likely.

The mg# of inclusions of diopside, in the Pt-Fe alloy detrital grains, attains a maximum of 90.7, which is high and consistent with high-magnesian compositions of their lode source-rocks. These inclusions are notably enriched in octahedrally coordinated Al. Content of ⁶Al in pyroxene increases with increasing pressure (e.g., Aoki and Kushiro, 1968). Thus, these inclusions of diopside presumably crystallized under high-pressure conditions, similar to inclusions of omphacite-rich clinopyroxene hosted by grains of Pt-Fe alloy from Nizhniy Tagil, which is a 'classic' Alaskan-Uralian-type complex in the Urals, Russia (*cf.*, Johan, 2006). In addition, the observed inclusions of Na-(Cl)-rich amphibole and of albite-rich plagioclase, documented at Burwash, are similar to inclusions of a Na-rich amphibole and sodic plagioclase in nuggets of Fe-bearing platinum, likely derived from an Alaskan-type complex in Papua New Guinea (Johan *et al.*, 2000). The occurrence of sodic-calcic amphiboles enriched in Cl and associated with Pt-Fe alloy implies the presence of fluid phase in the system.

TECTONIC SETTING BASED ON TRACE ELEMENT GEOCHEMISTRY

Concentrations of trace elements in silicate melt are determined by the nature of the mantle source undergoing partial melting to produce mafic magma, and the processes of magma differentiation, crystallization and contamination. Patterns of REE and other groups of incompatible elements (LIL and HFS) vary greatly in different tectonic environments and their ratios are commonly used as indicators of the tectonic environment of magma generation. In this study, the three main candidates for the type of source rock for the Pt-Fe alloy placer grains belong to very different tectonic settings. The ophiolites or Alpine-type peridotites are products of magmatism at mid-ocean ridges; continental mafic-ultramafic complexes and small bodies, such as Kluane sills, are the result of continental rifting; and Alaskan-type complexes represent subduction zone magmatism present in arc environments.

Ophiolites and oceanic peridotites are characterized by a positive or slightly negative slope of REE. Plagioclase fractional crystallization resulting in the development of a

Eu minimum in REE patterns is rare. These magmas are equally depleted in all the incompatible elements and show similar behavior of LIL and HFS. Such behavior of LIL and HFS is very different from the significant decoupling between these two groups of incompatible elements observed in our samples. The large LIL/HFS ratio of silicate inclusions hosted in Pt-Fe alloy from Burwash Creek can be used to rule out ophiolites or Alpine-type peridotites as the source of the placer platinum. This is also supported by the complex patterns of REE in the studied inclusions. The pattern of high LIL/HFS ratio is a distinctive feature of subduction zone magmas due to the much higher mobility of LIL in aqueous fluids involved in magma generation at subduction zones. To some extent, decoupling between LIL and HFS may also be present in magmas generated during continental rifting, such as the Klauane sills, due to the contribution of fluids in the mantle source region undergoing melting. However, the extremely high LIL/HFS ratio, of over two orders of magnitude, is in better agreement with a subduction-related Alaskan-type complex as the source of the placer platinum. This is also supported by the presence of a negative trough for Nb that is characteristic of arc magmatism, low Ti and the complex patterns of REE typical for magmas derived from the mantle wedge above the subduction zone with the complex depletion and enrichment history. The trace element ratios in the silicate inclusions suggest that the source of the Pt-Fe alloy placer grains in Burwash Creek is not ophiolite-type or oceanic peridotites. These data cannot undeniably distinguish between the Klauane sills and fragments of an Alaskan-type complex, but are much more consistent with an Alaskan-type complex to be the source of this Pt-Fe alloy. The similarity between this grain and the other PGMs from Burwash, Scroggie, Wolverine and Florence Creeks suggests that Alaskan-type intrusions are the best candidates to be the source of PGM in all these creeks.

ACKNOWLEDGMENTS

This study was made possible with financial support from the Yukon Geological Survey, which is gratefully acknowledged. We thank Lang Shi for his technical assistance with electron-microprobe analysis. Patricia Scallion is thanked for the help with SEM work and the Institute for Research in Materials for the access to the FE-SEM, funded by the Canada Foundation for Innovation.

REFERENCES

- Aoki, K. and Kushiro, I., 1968. Some clinopyroxenes from ultramafic inclusions in Dreiser Weiher, Eifel. *Contributions to Mineralogy and Petrology*, vol. 18, no. 4, p. 326-337.
- Barkov, A.Y., Fleet, M.E., Nixon, G.T. and Levson, V.M., 2005. Platinum-group minerals from five placer deposits in British Columbia, Canada. *The Canadian Mineralogist*, vol. 43, no. 5, p. 1687-1710.
- Barkov, A.Y., Laflamme, J.H.G., Cabri, L.J. and Martin, R.F., 2002. Platinum-group minerals from the Wellgreen Ni-Cu-PGE deposit, Yukon, Canada. *The Canadian Mineralogist*, vol. 40, no. 2, p. 651-669.
- Barkov, A.Y., Martin, R.F., Fleet, M.E., Nixon, G.T. and Levson, V.M., 2008a. New data on associations of platinum-group minerals in placer deposits of British Columbia, Canada. *Mineralogy and Petrology*, vol. 92, p. 9-29.
- Barkov, A.Y., Martin, R.F., LeBarge, W. and Fedortchouk, Y., 2008b. Grains of Pt-Fe alloy and inclusions in a Pt-Fe alloy from Florence Creek, Yukon, Canada: evidence for a mobility of Os in a Na-H₂O-Cl-rich fluid. *The Canadian Mineralogist*, vol. 46, no. 2, p. 343-360.
- Begizov, V.D., Zavyalov, E.N. and Rudashevskii, N.S., 1985. Kashinite (Ir, Rh)₂S₃ - a new sulfide of iridium and rhodium. *Zapiski Vsesouznogo Mineralogicheskogo Obshchestva*, vol. 114, p. 617-622 (in Russian).
- Bodnar, R.J. and Student, J.J., 2006. Melt inclusions in plutonic rocks: Petrography and microthermometry. *In: Melt Inclusions in Plutonic Rocks*, J.D. Webster (ed.), Mineralogical Association of Canada, Short Course, vol. 36, p. 1-26.
- Britvin, S.N., Rudashevskii, N.S., Bogdanova, A.N. and Shcherbachev, D.K., 2001. Miassite Rh₁₇S₁₅ - a new mineral from a placer of the Miass River, Urals. *Zapiski Vserossijskogo Mineralogicheskogo Obshchestva*, vol. 130, p. 41-45 (in Russian).
- Cabri, L.J., Hulbert, L.J., Laflamme, J.H.G., Lastra, R., Sie, S.H., Ryan, C.G. and Campbell, J.L., 1993. Process mineralogy of samples from the Wellgreen Cu-Ni-Pt-Pd deposit, Yukon. *Exploration and Mining Geology*, vol. 2, no. 2, p. 105-119.

- Cabri, L.J., Harris, D.C. and Weiser, T.W., 1996. Mineralogy and distribution of platinum-group mineral (PGM) placer deposits of the world. *Exploration and Mining Geology*, vol. 5, p. 73-167.
- Desborough, G.A. and Criddle, A.J., 1984. Boweite; a new rhodium-iridium-platinum sulfide in platinum-alloy nuggets, Goodnews Bay, Alaska. *The Canadian Mineralogist*, vol. 22, no. 4, p. 543-552.
- Fedortchouk, Y. and LeBarge, W., 2008. Sources of placer platinum in Yukon: provenance study from detrital minerals. *Canadian Journal of Earth Sciences*, vol. 45, no. 8, p. 879–896.
- Grønvold, F., Haraldsen, H. and Kjekshus, A., 1960. On the sulfides, selenides, and tellurides of platinum. *Acta Chemica Scandinavica*, vol. 14, no. 9, p. 1879-1893.
- Hulbert, L.J., 1997. Geology and metallogeny of the Klauane mafic-ultramafic belt, Yukon Territory, Canada: eastern Wrangellia – a new Ni-Cu-PGE metallogenic terrane. *Geological Survey of Canada, Bulletin 506*, 265 p.
- Hart, S.R., Blusztajn, J., Dick, H.J.B., Meyer, P.S. and Muehlenbachs, K., 1999. The fingerprint of seawater circulation in a 500-meter section of ocean crust gabbros. *Geochimica et Cosmochimica Acta*, vol. 63, p. 4059-4080.
- Hart, C.J.R., Burke, M. and Stronghill, G., 2001. Yukon Platinum Occurrences and Potential. *Exploration and Geological Services Division, Indian and Northern Affairs Canada, Yukon Region, Open File 2001-2*, 1:1 000 000-scale map and report, 12 p.
- Hofmann, A.W., 1988. Chemical differentiation of the Earth: the relationship between mantle, continental crust, and oceanic crust. *Earth and Planetary Science Letters*, vol. 90, p. 297-314.
- Johan Z., 2006. Platinum-group minerals from placers related to the Nizhni Tagil (Middle Urals, Russia) Uralian-Alaskan-type ultramafic complex: ore-mineralogy and study of silicate inclusions in (Pt, Fe) alloys. *Mineralogy and Petrology*, vol. 87, p. 1-30.
- Johan, Z., Slansky, E. and Kelly, D.A., 2000. Platinum nuggets from the Kompiam area, Enga Province, Papua New Guinea: evidence for an Alaskan-type complex. *Mineralogy and Petrology*, vol. 68, p. 159-176.
- Johnston S.T., Canil D. and Heaman, L.H., 2007. Perian exhumation of the Buffalo Pitts orogenic peridotite massif, northern Cordillera, Yukon. *Canadian Journal of Earth Sciences*, vol. 44, no. 3, p. 275-286.
- Makovicky, E., Makovicky, M. and Rose-Hansen, J., 2002. The system Fe-Rh-S at 900° and 500°C. *The Canadian Mineralogist*, vol. 40, p. 519-526.
- Malitch, K.N., Melcher, F. and Mühlhans, H., 2001. Palladium and gold mineralization in podiform chromitite at Kraubath, Austria. *Mineralogy and Petrology*, vol. 73, no. 4, p. 247-277
- McDonough, W.F. and Sun, S.-S., 1995. Composition of the Earth. *Chemical Geology*, vol. 120, p. 223-253.
- Mezger, J.E., 2000. 'Alpine-type' ultramafic rocks of the Klauane metamorphic assemblage, southwest Yukon: Oceanic crust fragments of a late Mesozoic back-arc basin along the northern Coast Belt. *In: Yukon Exploration and Geology 1999*, D.S. Emond and L.H. Weston (eds.), *Exploration and Geological Services Division, Yukon Region, Indian and Northern Affairs Canada*, p. 127-138.
- Mutchler, S.R., Fedele, L. and Bodnar, R.J., 2008. Analysis Management System (AMS) for reduction of laser ablation ICP-MS data. *In: Laser Ablation ICP-MS in the Earth Sciences: Current Practices and Outstanding Issues*, P. Sylvester (ed.), *Mineralogical Association of Canada, Short Course volume 40*, p. 318-327.
- Nixon, G.T., Cabri, L.J. and Laflamme, J.H.G., 1990. Platinum-group-element mineralization in lode and placer deposits associated with the Tulameen Alaskan-type complex, British Columbia. *The Canadian Mineralogist*, vol. 28, no. 3, p. 503-535.
- Oberthür, T., Melcher, F., Gast, L., Wöhr, C. and Lodziak, J., 2004. Detrital platinum-group minerals in rivers draining the eastern Bushveld complex, South Africa. *The Canadian Mineralogist*, vol. 42, no. 2, p. 563-582.
- Okamoto, H., 1992. Rh-S (Rhodium-Sulfur). *Journal of Phase Equilibria*, vol. 13, no. 1, p. 108-109.
- Rudashevsky, N.S. and Zhdanov, V.V., 1983. Accessory platinum mineralization of a mafic-ultramafic intrusion in Kamchatka. *Bull. Moscow Soc. Naturalists, Geology Department* vol. 58, no. 5, p. 49-59 (in Russian).

Stanley, C.J., Criddle, A.J., Spratt, J., Roberts, A.C., Szymanski, J.T. and Welch, M.D., 2005. Kingstoneite, (Rh, Ir, Pt) $3S_4$, a new mineral species from Yubdo, Ethiopia. *Mineralogical Magazine*, vol. 69, no. 4, p. 447-453.

Tolstykh, N.D., Foley, J.Y., Sidorov, E.G. and Laajoki, K.V.O., 2002. Composition of the platinum-group minerals in the Salmon River placer deposit, Goodnews Bay, Alaska. *The Canadian Mineralogist*, vol. 40, no. 2, p. 463-471.

Tolstykh, N.D., Sidorov, E.G., Laajoki, K.V.O., Krivenko, A.P. and Podlipskiy, M., 2000. The association of platinum-group minerals in placers of the Pustaya River, Kamchatka, Russia. *The Canadian Mineralogist*, vol. 38, no. 5, p. 1251-1264.

Preliminary Quaternary geology of Coal River area (NTS 95D), Yukon

*Kristen Kennedy*¹
Yukon Geological Survey

Kennedy, K., 2010. Preliminary Quaternary geology of Coal River area (NTS 95D), Yukon. *In: Yukon Exploration and Geology 2009*, K.E. MacFarlane, L.H. Weston and L.R. Blackburn (eds.), Yukon Geological Survey, p. 197-212.

ABSTRACT

Quaternary geology investigations in the Coal River map sheet (NTS 95D) during the 2009 field season focused on characterizing surficial materials and their distributions, with attention to the eastern half of the map sheet which has not been previously mapped. Moraine deposits are relatively thin in valley bottoms (<2 m) and become thinner and more intensely colluviated on upland surfaces. Streamlined glacial landforms and till plains are pronounced in the southern half of the map sheet. Surficial deposits are limited in many east-trending meltwater canyons, and in the northeastern corner of the map sheet.

The map area was glaciated most recently by the Cordilleran Ice Sheet, which advanced from the south and west. Meltwater from montane glaciers and the Laurentide Ice Sheet in adjacent map sheets likely contributed to extensive glaciolacustrine, glaciofluvial and glaciodeltaic deposits in north-trending valleys that were dammed by the Cordilleran Ice Sheet.

¹kristen.kennedy@gov.yk.ca

INTRODUCTION

The Coal River project in southeast Yukon is a collaborative effort between the Geological Survey of Canada (GSC) and the Yukon Geological Survey (YGS) under the Government of Canada's Geomapping for Energy and Minerals (GEM) program. The Coal River map sheet (Fig. 1; NTS 95D) was selected for mapping because it is considered to have high mineral potential and is under-explored both scientifically and economically. Furthermore, surficial geological mapping has not been completed for the east half of 95D, and existing maps for the west half lack field-based observations and descriptive documentation. The goals of the Coal River GEM project are to provide a revised 1:250 000-scale bedrock

geological map (Pigage *et al.*, in prep), an aeromagnetic map of the adjacent Yukon part of the Flat River map sheet (NTS 95E), and new surficial geological mapping for the previously unmapped east half of Coal River map sheet.

Preliminary investigations of the surficial geology of the Coal River map sheet (NTS 95D) have resulted in a broad characterization of the distribution of surficial materials. This paper outlines new observations of glacial geomorphology and provides stratigraphic controls on the regional surficial geology. From these observations, an interpretation of the regional glacial history will be proposed.

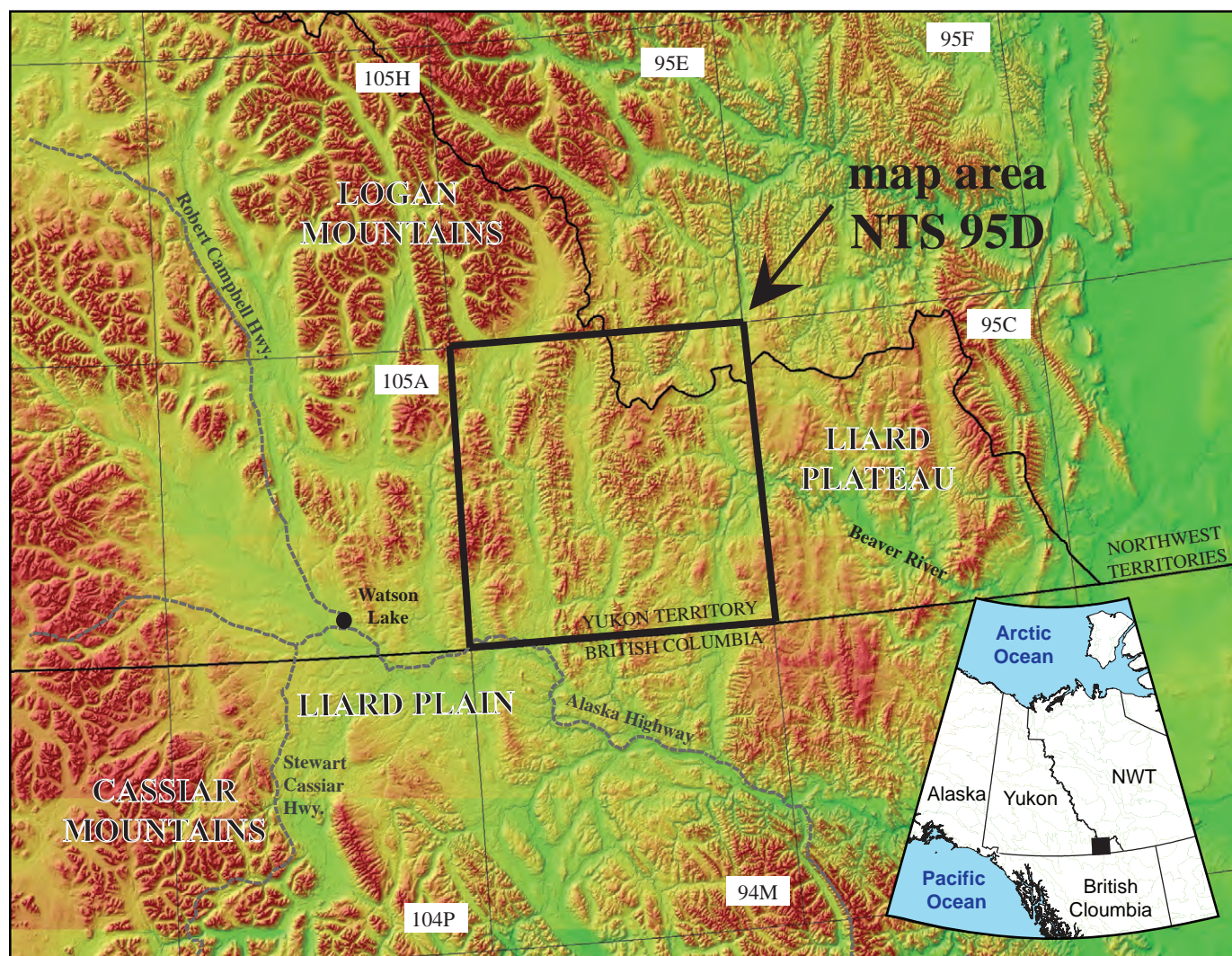


Figure 1. Coal River map sheet (NTS 95D) is located in southeast Yukon and includes part of southwest Northwest Territories.

REGIONAL SETTING

The Coal River map sheet is located in southeast Yukon and includes part of southwest Northwest Territories (Fig. 1). The map sheet is predominantly within the Hyland Highland ecoregion (Fig. 2), an elevated area higher than neighbouring plains and plateaus, but lacking the high summits of mountains or ranges (Smith *et al.*, 2004). The highest elevations in the ecoregion are on the Yukon Territory-Northwest Territories border, and between the West Coal and upper Rock rivers at ~1900 m a.s.l.; local relief is generally between 300 m and 750 m a.s.l. The physiography of the Coal River map sheet is characterized by three broad, near-parallel, north-trending valleys extending the length of the map sheet (Fig. 3).

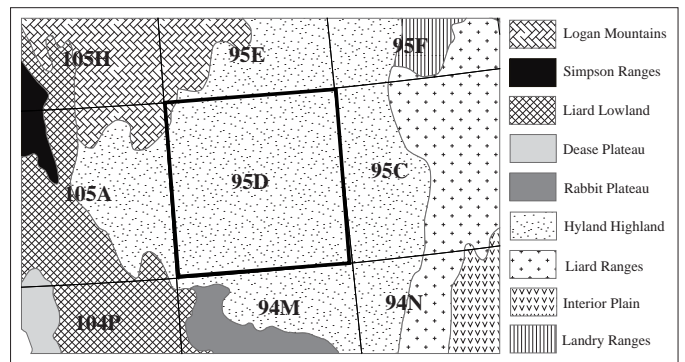
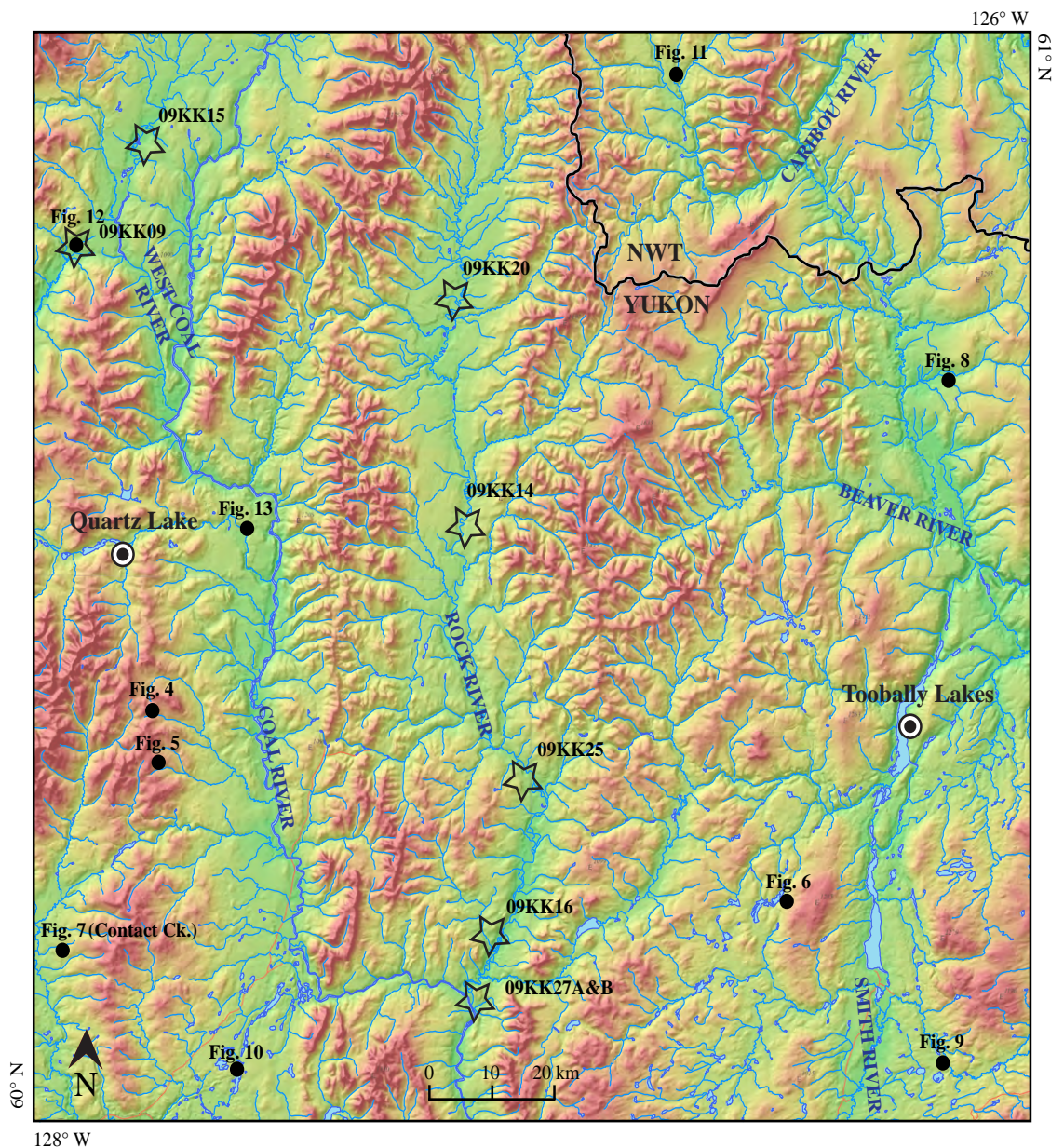


Figure 2. Physiographic regions of the Coal River map sheet and surrounding area. Map area (95D) falls almost entirely within the Hyland Highland physiographic region (regions from Smith *et al.*, 2004).

Figure 3. Hillshade and DEM (Digital Elevation Model) image of the Coal River map sheet. The West Coal River and Coal River valleys are oriented north-south in the western map area. The Rock River valley is in the centre of the map sheet and joins the Coal River near the southern margin of the map area. The Caribou, Beaver and Smith rivers, along with the Toobally Lakes, occupy the eastern north-trending valley in the map area. Stratigraphic sections presented in the paper are indicated with stars, and camp locations are identified with a circle.



The Coal River originates in the northwest corner of the map sheet and flows south; it has only two minor eastward deviations during its course, which are incised into bedrock. The broad valley in the centre of the map sheet is occupied by the Rock River, which flows south throughout its course. The Rock River frequently exposes bedrock along its banks, including Tertiary deposits, suggesting the valley is a pre-glacial feature, and that its modern drainage route has not changed significantly during the Pleistocene. The valleys of the Rock and Coal rivers are the largest in the map area, and contain the most extensive glacial deposits.

The north-trending valley on the eastern edge of the map sheet is host to three modern drainages: the Smith River draining south, the Caribou River draining north, and the Beaver River draining east. The paleoflow direction of Tertiary fluvial gravel deposits preserved ~150 m above the modern Beaver River suggest pre-glacial drainage of the east Coal River map sheet was to the east (Pigage, 2009). Modern drainage in the Coal River map sheet is predominantly south into the Liard River, and ultimately into the Mackenzie River and Arctic Ocean.

Underlying the unconsolidated sediments in the Coal River map area is a thick sequence of slope, basin, platform and clastic shelf sedimentary and volcanic rocks that range in age from late Proterozoic to Triassic (Pigage *et al.*, in prep).

SURFICIAL GEOLOGY

PREVIOUS WORK

Previous surficial geological mapping of the Coal River map sheet (NTS 95D) is limited to the west half of the sheet, and was mapped between 1978 and 1981 by Klassen (1983) at a scale of 1:250 000. This mapping also included the Watson Lake (NTS 105A) and Wolf Lake (NTS 105B) map sheets to the west (Klassen and Morison, 1982a; Klassen and Morison, 1982b). No ground-truthing locations are noted on Klassen's map for 95D West.

Detailed surficial geological mapping was completed from 1999 to 2001 in the La Biche River map sheet (NTS 95C; Fig. 1). This mapping resulted in seven 1:50 000-scale maps (Smith, 2002a,b; Smith, 2003a,b,c,d; Smith, 2004b); one 1:100 000-scale map (Smith, 2004a); a revised ice-flow map (Duk-Rodkin and Smith, 2002); and a report outlining early findings (Smith, 2000). Most notably, Smith (2000) demonstrated that the Laurentide Ice Sheet

advanced further west than previously thought, and coalesced with the Cordilleran Ice Sheet along its western margin. Ice flow directions and meltwater channels in the study area were mapped by Duk-Rodkin (1999) as part of a Yukon-wide glacial limits map.

The Quaternary history of the Coal River map sheet is largely undocumented. South of the map sheet, the Liard Plain (Fig. 1) is thought to have been a major conduit of Cordilleran ice during multiple Pleistocene glaciations (Ryder and Maynard, 1991). The Cordilleran Ice Sheet in this region was likely composed of coalescent valley and piedmont glaciers, which may have thickened enough to over-top ridges and divides, but likely always remained somewhat constrained by topography (Klassen, 1987). Ice advancing southeast across the Liard Plain is thought to have diverted northward into the three main valleys of the Coal River map sheet (Klassen, 1987) and ultimately inundated even the highest points in the map area, establishing southwest to northeast ice flow during glacial maximum (Duk-Rodkin, 1999).

A lengthy Quaternary and Tertiary record was described by Klassen (1987) in the Watson Lake map sheet (105A) where four distinct till units are interbedded with four non-glacial units that include basalt and organic horizons. The till units represent glaciations beginning in the early Pleistocene, with the uppermost till recording glaciation during the late Wisconsinan (Klassen, 1987). The evidence of multiple glaciations fits well with regional reconstructions of repeated northern Cordilleran glaciations throughout the Pleistocene (Jackson *et al.*, 1991; Ryder and Maynard, 1991).

The Coal River map area is situated near the eastern limit of the Cordilleran Ice Sheet and is immediately west of the Laurentide Ice Sheet limit, which reached its maximum position in the adjacent map sheet (95C; Smith, 2000). Regional east-flowing streams that were diverted by the westward-advancing Laurentide Ice Sheet were likely rerouted into the Coal River map sheet. Early advances of both ice sheets may have been valley-constrained and limited to low elevations; however, a mutual buttressing upon coalescence would have allowed the ice sheets to thicken and attain glacial maximum distributions that likely covered all but the highest peaks in the region (I.R. Smith, pers. comm.).

SURFICIAL GEOLOGY

The distribution of surficial materials in the map area can be broadly divided into highland, upland and valley-

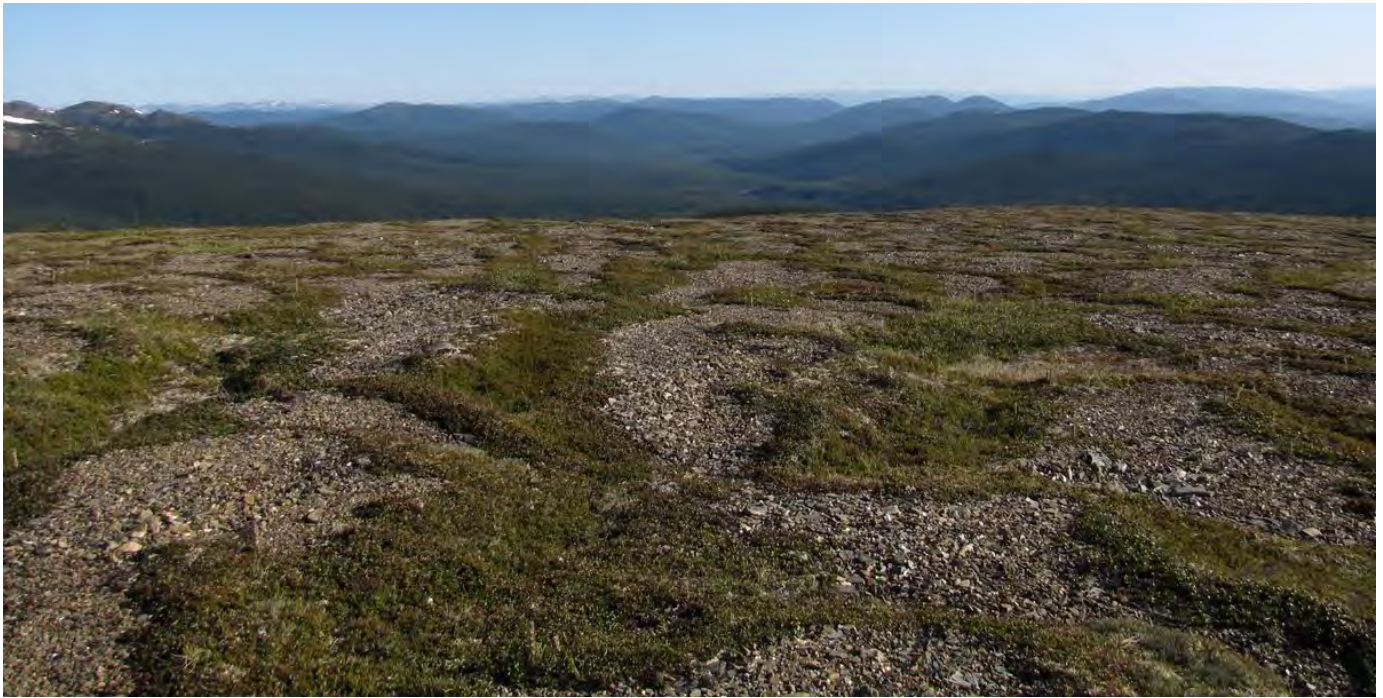


Figure 4. Periglacial and colluvial processes are common on high-elevation surfaces that are covered in thin till and weathered bedrock. Here, on an upland surface near Quartz Lake, cryoturbation has sorted the weathered bedrock colluvium and soil creep has modified the hummocks into linear mounds.

bottom units. The high rugged topography in the northern part of the map sheet is characterized by cirque development on north-facing aspects, and thin accumulations of weathered bedrock. Other than cirques and limited moraine deposition on cirque floors, evidence of glaciation is rare in this region.

Upland units in lower terrain, which characterizes most of the map sheet, are typically thin veneers of glacial diamict and weathered bedrock. Bedrock is at, or near, surface in most areas above tree line. Colluvial processes such as soil creep, solifluction and slope wash are common at high elevations above tree line (Fig. 4). Upland surfaces, particularly those in the southern part of the map sheet, are scoured and sculpted by glaciation. These surfaces contain streamlined landforms indicating regional ice flow to the northeast, and localized flow directions ranging from north to east (Fig. 5). Colluvial processes are minimized where surface materials are stabilized by the dense forest cover, which is typical of the Coal River map area. On average, the elevation of tree line is ~1400 m a.s.l.

Mid-elevation (~1000-1400 m a.s.l.), forested slopes are covered in mixed colluvial and glacial diamicts that are characterized by predominantly sharp, angular, pebble-

cobble clasts with a minor component (~15%) of well-rounded clasts. Matrices are dominantly silty, and contain variable sand and clay fractions. Where there are relatively thin moraine deposits and limited erosion, flights of lateral meltwater channels flanking mid-elevation slopes are the most distinctive evidence of glaciation in the uplands of the Coal River map sheet (Fig. 6). The channels are predominantly erosional features, but also form linear depressions where colluvial and organic deposits accumulate to greater thicknesses than on the surrounding slopes.

Valley-bottom geomorphology is characterized by thick glacial, glaciolacustrine and glaciofluvial deposits. The nature of the valley-bottom geomorphology can be separated into two distinct regions based on landforms. In the southern part of the map sheet, the valley-bottom geomorphology is characterized by bedrock-cored drumlins, or drumlinoid features, glaciofluvial terraces, deltas, eskers, kames and meltwater channels (Figs. 7, 8, 9). Hummocky and ablation moraine, and crevasse-fill type deposits associated with glacier recession are abundant in the southwestern corner of the map sheet (Fig. 10).



Figure 5. Chatter marks (circled) and striations preserved on polished bedrock surfaces indicate ice flow directions. Compass diameter is ~6 cm and black arm points in direction of ice flow (~004°).



Figure 6. Lateral meltwater channels are common features on heavily forested mid-elevation slopes. Meltwater channels flowed to the north (bottom left of photo), indicating the ice margin was retreating to the south (top right of photo).

Alternatively, valley bottoms in the central, eastern and northern parts of the map area lack distinct ice-contact glacial recession features. Instead, they are primarily blanketed by glaciolacustrine and glaciofluvial deposits. Deltas, terraces and streamlined glacial features in the Beaver River and Toobally Lakes areas provide evidence of glaciation and glacial lakes in the south and central parts of the primary north-trending valley in the eastern map area. However, very little evidence for glaciation exists in the northern extension of the valley, where the



Figure 7. Light-coloured, sinuous ridges in the foreground are eskers in the Contact Creek (Fig. 3) area in the southwest part of the map sheet. These deposits typically contain sand and gravel. Trees on valley floor are ~20-30 m high.



Figure 8. Glaciofluvial delta formed at the outlet of a small meltwater channel in a west-flowing tributary to the Beaver River (Fig. 3). These deposits often consist of well-sorted sand, and mixed sand and gravel. Dashed black line marks the front edge of the delta surface.

Caribou River occupies a deeply incised bedrock canyon (Fig. 3). Bedrock (strath) terraces are common in this part of the map sheet and provide evidence of high-energy fluvial erosion (Fig. 11).

The Coal and Rock river valleys (Fig. 3), along with many of their tributaries, are filled with thick glaciolacustrine clay, silt and sand deposits (Fig. 12). Ice-rich clay, often located near the bottom of exposures, is prone to slope

Figure 9. Streamlined landforms in the southeast part of the map area indicate ice flow from the southwest to the northeast. (National Air Photo Library (NAPL) A28344-106).

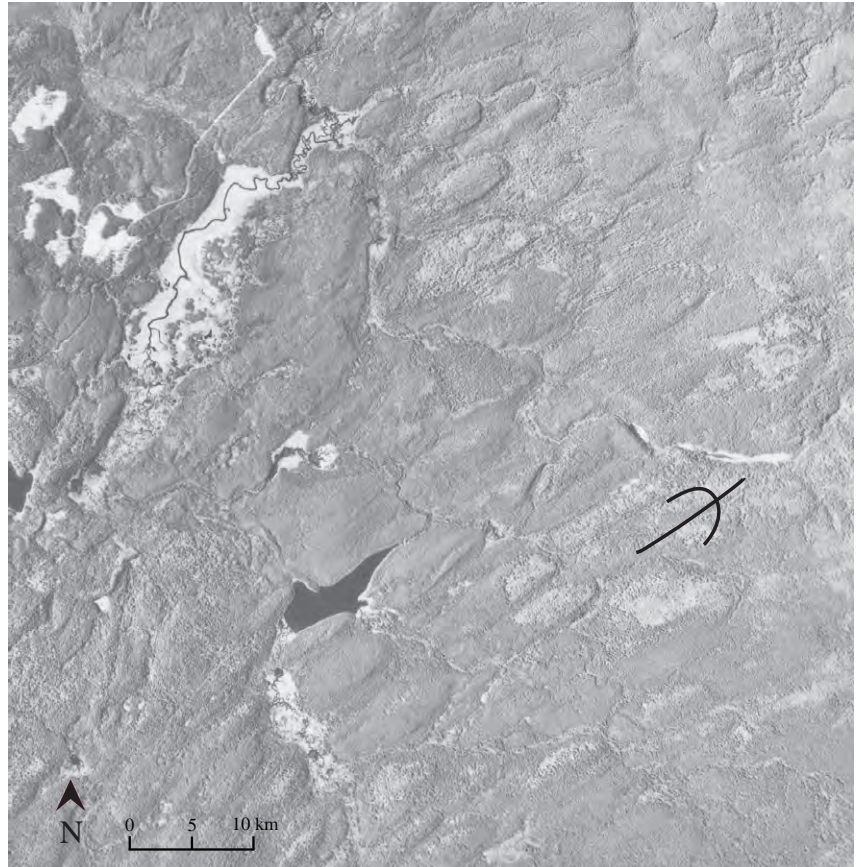


Figure 10. Recessional moraine deposits in the southwest part of the map area are likely formed in part by buried ice and moraine deposited during retreat of the ice front. (NAPL A28344-52).

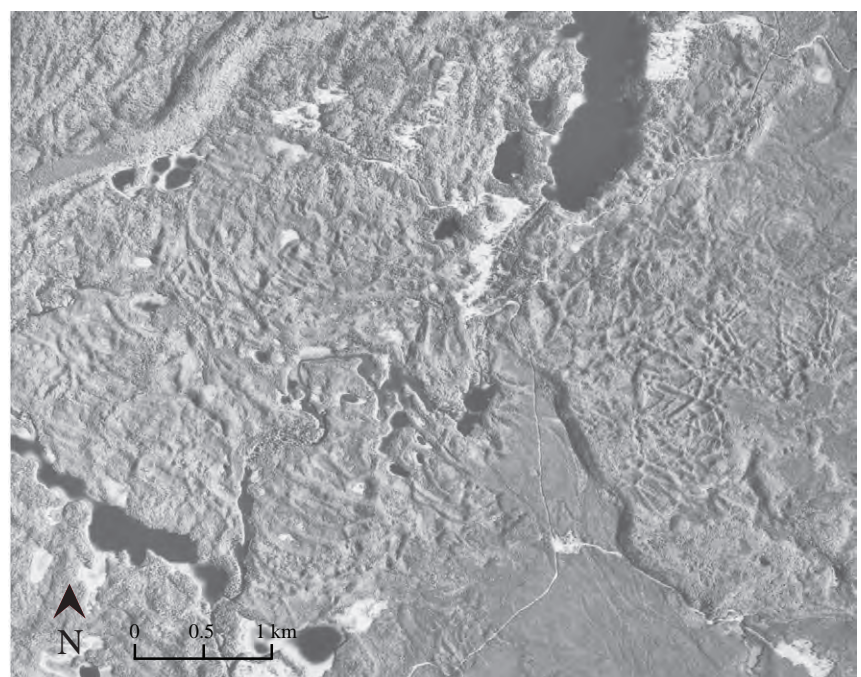




Figure 11. Bedrock, or strath terrace on the Caribou River in the northeast corner of the map sheet. Outlined area (t) represents the bedrock erosion surface. Modern stream flow is from right to left in the photo.

failure when exposed to fluvial erosion. Glacial lake sequences are frequently capped by coarser grained (sand, pebbles and cobbles) glaciofluvial deposits, and represent glacial lake drainage and subsequent re-establishment of fluvial regimes. The surface expressions of these deposits are relatively flat to gently inclined plains, terraces and deltas. Modern streams have incised through much of the glacial deposition in the Coal and Rock river valleys, reaching bedrock in some locations.

Deeply incised, east-flowing meltwater channels, and associated glaciofluvial deltas at their outlets, are distinctive landforms of the Coal River map sheet (Fig. 13). These meltwater canyons dissect the regional north-trending ridges at regular intervals across the map sheet (Fig. 14). The channels are generally 10-15 km long, but some channels extend to as much as 50 km in length. These meltwater channels form box-shaped canyons that are predominantly erosional features, but in many cases contain extensive accumulations of organic deposits on their channel floors. The primary depositional feature associated with the meltwater channels are large, terraced deltas that formed where the channels debauch into a north-trending valley (Fig. 13).



Figure 12. Thick glaciolacustrine deposits in the West Coal River valley. Section is ~30 m high and its stratigraphy is presented in Figure 14 (09KK09). Massive clay at the bottom of the section is ice-rich and prone to slope failure when exposed.

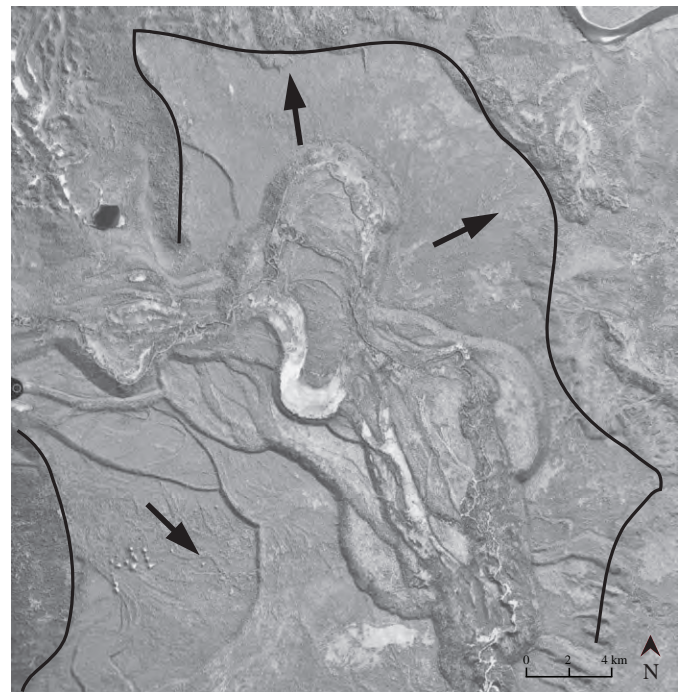


Figure 13. Large delta at the mouth of an east-flowing meltwater channel in the Coal River valley (NAPL A28425-35). Outside edge of the delta is outlined, and flow direction is indicated with arrows.

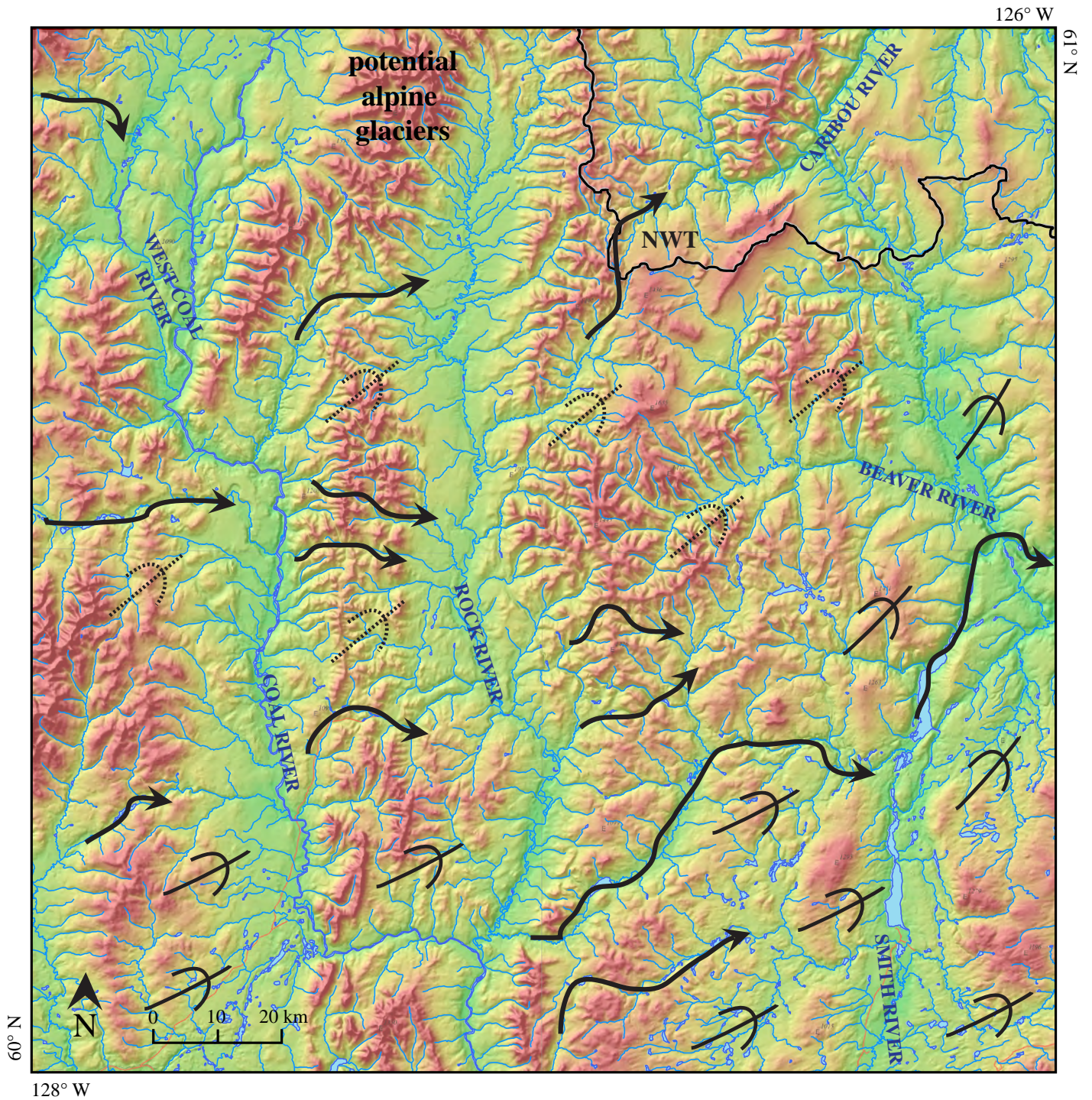


Figure 14. East-flowing meltwater channels dissect the north-trending ridges of the Coal River map area at regular intervals. Arrows indicate major meltwater channels, and streamlined symbols represent ice-flow directions across the southern part of the map sheet. Dashed streamlined symbols are inferred ice-flow directions.

STRATIGRAPHY

Stratigraphic sections are illustrated in Figure 15 for the West Coal, Coal and Rock rivers. The locations of the sections are indicated on Figure 3.

09KK15

Section 09KK15 comprises ~40 m of gravel, sand, silt and clay (Fig. 15). The lowermost unit is an ~8-m-thick sequence of highly oxidized, well-sorted, centimetre-sized pebble gravel and crossbedded sand that is unique to the map area. It is overlain by an ~30-m sequence that grades from massive sand, to interbedded sand and cross-stratified silt and clay, to massive clay, and finally back to interbedded cross-stratified sand with silt and clay. The uppermost unit in the exposure is a thin (~2 m) sandy gravel unit with an erosive lower contact.

The highly oxidized fluvial sediments at the bottom of the 09KK15 exposure are interpreted as a pre-glacial fluvial deposit. The overall gradually fining-up stratigraphy of section 09KK15 is interpreted as representing sedimentation from an increasing distal source, or deposition into a deepening lake. Drainage of the lake would have initiated deposition of the uppermost glaciofluvial unit.

09KK09

The stratigraphy at section 09KK09 is largely inverted from that at 09KK15. A thick (~10 m) silty clay unit grades up to a silty sand, and finally into massive to weakly bedded sand at the top of the exposure (see also Figure 12). One thin horizon of cobbles was observed between the silty sand and massive sand units. The lower oxidized unit of section 09KK15 was not observed at the 09KK09 exposure.

The stratigraphy at section 09KK09 is interpreted to represent the progradation of a delta in the West Coal River valley. The delta was likely fed by a meltwater channel flowing from the west. The thin cobble horizon may record shifting channel patterns, or a periodic high-energy flow event. Stratigraphic exposures on the West Coal River provide evidence for extended glaciolacustrine sedimentation in the upper Coal River valley. The fine-grained textures of glaciolacustrine sediments, along with the absence of observed dropstones or other ice-rafted debris, suggest the ice front blocking the regional drainage was at a considerable distance from the West Coal River area.

09KK27A

Two exposures on the lower Coal River, occurring only 100 m apart, have distinctly different stratigraphy. Section 09KK27A is comprised of ~15 m of interbedded silty clay, and silty fine sand. This unit has an erosional upper contact and is overlain by an ~3-m-thick, moderately to well-sorted pebble-cobble gravel unit.

The fine sand, silt and clay comprising the bulk of the 09KK27A exposure is similar to exposures on the West Coal River, and is interpreted as glaciolacustrine deposition. Similar to the sections to the north, the 09KK27A section is also capped by a thin gravel deposit interpreted as post-lacustrine glaciofluvial deposition.

09KK27B

Exposure 09KK27B is located approximately 100 m downstream of section 09KK27A and can be divided into a lower, ~16-m-thick diamict unit, and an upper, ~4-m-thick diamict unit. The lower diamict is well indurated, contains striated, boulder-sized clasts, and has a matrix of silt and clay with minor sand. In contrast, the upper diamict lacks very large boulders (all <1 m in diameter), is less cohesive, contains isolated lenses of sorted sand and gravel, and has a matrix dominated by sand with a lesser component of silt and minor clay.

The lower diamict at section 09KK27B is interpreted as till, while the overlying upper diamict is interpreted as a melt-out, or colluviated till. The juxtaposition of two very different stratigraphic profiles in close proximity makes interpretations of their depositional environments difficult. The lower Coal River exposures have been interpreted as representing a moraine ridge (09KK27B) with later, glaciolacustrine deposits (09KK27A) abutting the moraine margin.

09KK20

Unlike the West Coal River sections, the upper Rock River sections (09KK20 and 09KK14) both contain diamict units. In section 09KK20, the lower, dark grey to almost black, well-indurated diamict is ~9 m thick and has a silty clay matrix (~75%) with a maximum clast size of ~25 cm. The underlying unit of interbedded silty clay and sand display disrupted and faulted bedding planes, indicative of glacio-tectonism.

The upper, tan diamict at exposure 09KK20 is ~4-5 m thick, and has a sharp lower contact with the underlying sand and gravel. The matrix (~40%) is composed

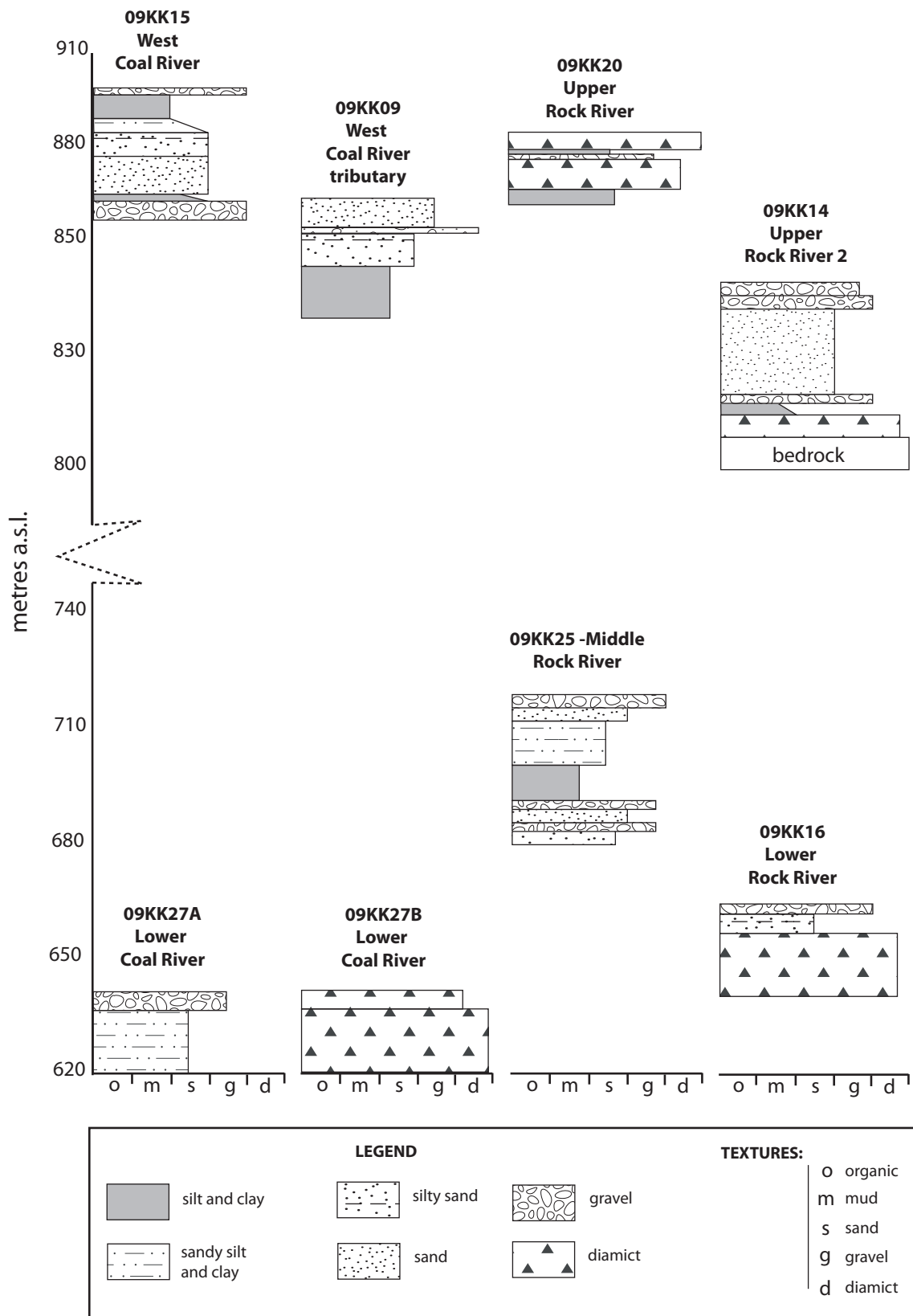


Figure 15. Stratigraphic logs of sections on the West Coal, Coal and Rock rivers. Unit textures are presented on the x-axis. Lithologies are represented by fill patterns.

predominantly of silt, and clasts are well rounded with a maximum diameter of ~80 cm.

The uppermost Rock River exposure is unusual in that it preserves significant thicknesses of glacial diamict. The dark, fine-grained lower diamict at 09KK20 is interpreted as till, while the genesis of the upper diamict is uncertain. The upper diamict either represents a different glacial depositional event, or post-glacial reworking of hillslope moraine into the valley bottom.

09KK14

At section 09KK14, ~3 m of matrix-dominated, clay-rich diamict is overlain by a thick package of sand, silt, clay and gravel. The diamict is poorly exposed and overlies bedrock. This is the only section where the underlying bedrock contact was observed.

The diamict unit overlying bedrock at section 09KK14 is interpreted as a till. Fine-grained sediments overlying the diamict are interpreted as glaciolacustrine and glaciofluvial deposits associated with glacial recession.

09KK25

Section 09KK25 consists predominantly of fluvial, or glaciofluvial and glaciolacustrine sediments, without any diamict units. The lower sand and gravel units (~15 m thick) have sedimentary structures indicating northerly, or up-valley paleo-flow (compared to modern southward flow); these units are overlain by ~2 m of massive silt with well-developed compression jointing (Fig. 16). The silt unit has a sharp, conformable contact with an overlying unit of interbedded massive grey clay and thinly laminated fine grey sandy-silt that becomes increasingly clay rich over its ~5 m exposure. This fine-grained grey unit grades upward into a tan-coloured, ripple cross-laminated silty-sand with flow structures that are parallel to present-day flow direction (to the south). The uppermost unit is a sand and gravel deposit with a lower erosive contact and south-trending flow structures.

The north-flow directions (opposite to present-day flow) on the lowest sand and gravel units at section 09KK25 are interpreted as ice-proximal glaciofluvial deposits from a southward-retreating ice front. Loading and compression features in the overlying silt unit suggest this unit represents abrupt deposition and equally abrupt drainage of a small lake or pond in the proglacial environment. Following drainage, the weight of the saturated silt itself could be responsible for forming the compression fractures in this unit. The thick package of fine-grained



Figure 16. Compression jointing formed in a silt unit of section 09KK25. Ice axe is 75 cm tall.

sand, silt and clay overlying the compressed silt unit is interpreted as glaciolacustrine sedimentation. The reverse (coarsening-up) grading of this unit is interpreted as the progradation of a sediment source. The section is capped with a coarse, pebble-cobble unit interpreted as glaciofluvial sedimentation following drainage of a glacial lake. The entire sequence was likely formed in a highly dynamic proglacial environment characterized by sudden shifts in drainage and meltwater input.

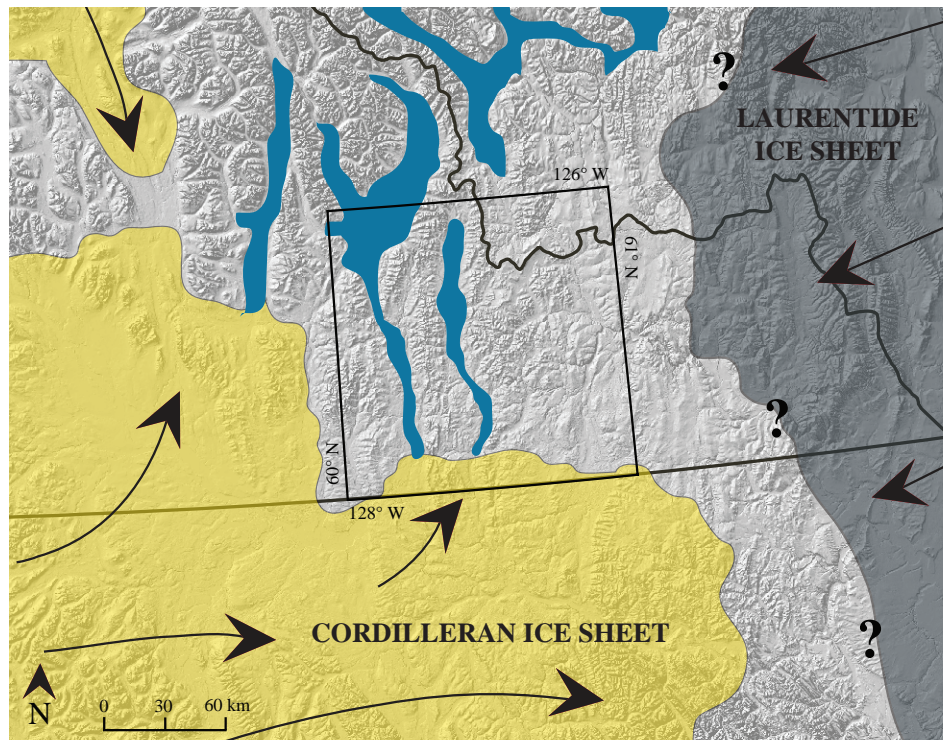
09KK16

The lowermost exposure on the Rock River (09KK16) is similar to the lower Coal River exposures and comprises ~15-20 m of diamict overlain by sand and gravel. The tan-weathered, silt-rich diamict is ~40% subrounded, pebble to cobble-sized clasts with a maximum diameter of ~30 cm. The overlying massive to weakly bedded sand has a gradational contact with the uppermost imbricated, clast-supported, pebble-cobble gravel. Imbrication indicates southward flow, *i.e.*, parallel to modern-day flow. The sequence of diamict and overlying sand and gravel at section 09KK16 is interpreted as a till with overlying recessional glaciofluvial sedimentation.

DISCUSSION

The surficial geology of the Coal River map sheet reflects the history of glaciation in southeastern Yukon. The pre-glacial landscape of north-trending valleys and uplands has been altered by east-flowing meltwater channel incision, by erosion and deposition by proglacial

Figure 17. Early in the Cordilleran Ice Sheet advance, glacial lakes were probably impounded in south-flowing valleys in the Coal River map sheet (outlined). The Laurentide Ice Sheet had probably already advanced near its maximum limit at that time.



lakes and streams, and by the movement of glaciers across the landscape. Predicting the distribution of surficial materials relies on accurately reconstructing the processes that created the post-glacial landscape. While the observations presented here are only preliminary, they suggest a number of potentially new interpretations for the glacial history of the Coal River map sheet.

GLACIAL ADVANCE

The advance of Cordilleran glaciers from the Cassiar Mountains into the map area was probably in the form of a piedmont glacier flowing southeast across the Liard Plain (Klassen, 1987). Early in the advance phase of glaciation, sublobes of the main piedmont glacier advanced north into regional south-flowing drainages and created proglacial lakes (Fig. 17). Until the Cordilleran Ice Sheet advanced sufficiently to meet the Laurentide Ice Sheet, free drainage to the east likely persisted. Advance-phase proglacial lakes may have overtopped regional divides and incised meltwater channels to establish northern drainage at this time.

As the Laurentide Ice Sheet advanced westward toward the Coal River map sheet, east-flowing drainages were probably diverted west into unglaciated regions. It is possible that diverted Laurentide meltwater flowed south into the Coal River map sheet and was responsible for the

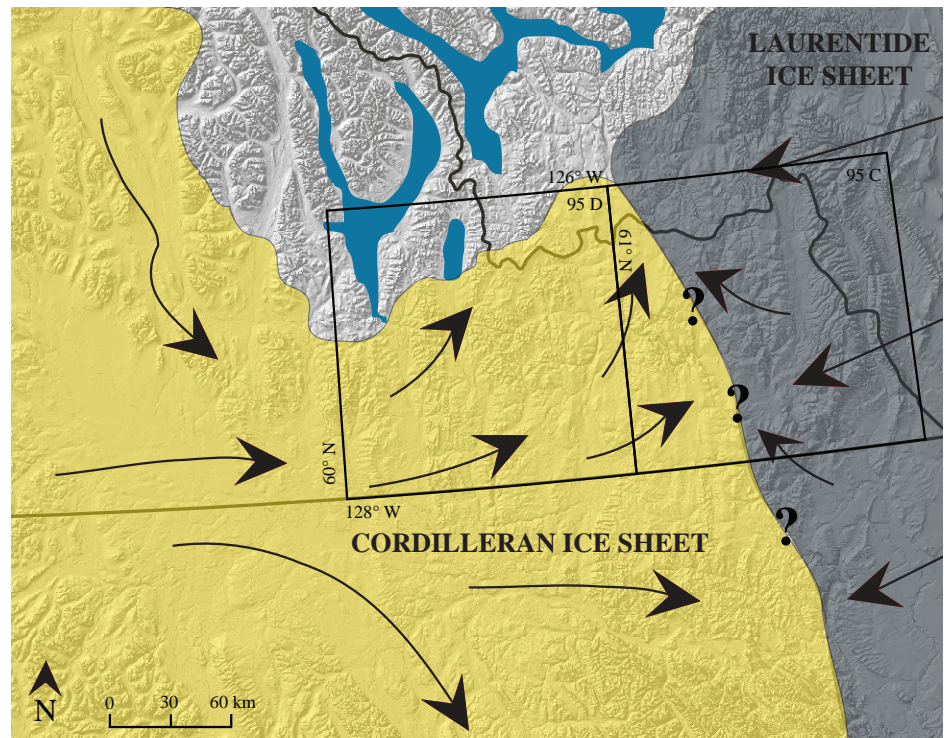
extensive erosion in the eastern Caribou River and Toobally Lakes valleys.

GLACIAL MAXIMUM

While the Cordilleran glacial advance was valley-constrained, striations on bedrock along high ridges in the map area suggest the ice eventually thickened sufficiently to overtop topographical highs and establish an east-northeast flow direction. Only one general ice-flow direction from glacial maximum was recorded in the map area, despite other evidence that the region has been glaciated repeatedly during the Pleistocene. This suggests that all advances occurred with the same pattern of growth and maximum flow, or that only one, or a few very similar, glaciations were extensive enough to overtop regional divides. If the latter case is true, the striations found at higher elevations may be artifacts of an early or mid-Pleistocene glaciation, as the most recent Cordilleran advance in Yukon was the least extensive of Pleistocene glaciations (Jackson, 1991).

Cirque landforms developed on north-facing slopes in the northern part of the map sheet provide evidence of montane glaciation. Many cirques are weakly developed and lack the neo-glacial moraines and rock glaciers common to higher regions to the north (e.g., Dyke, 1990). This implies that many of the cirques were formed during

Figure 18. Potential glacial maximum extent in the Coal River map sheet (outlined). The location where the Cordilleran and Laurentide ice sheets converged is approximate (adapted from Smith, 2000); however, ice-flow indicators from both ice sheets divert northward, just east of the Coal River map sheet.



pre-late Wisconsinan glaciation(s) that were more conducive to alpine glacier growth in this region. The two distinct diamict units on the upper Rock River (09KK20) are not preserved elsewhere in the map area, and may represent montane ice advances limited to the northern part of the Rock River valley.

The possibility exists that some of the higher topographic regions in the north-central and northwest corner of the map sheet remained unglaciated during Cordilleran glacial advances (Fig. 18). Klassen (1987) initially suggested an ice-free region in the northwest corner of the map sheet based on thick lacustrine sediments and more dissected surfaces without the distinct glacial features evident in the south. The stratigraphy from the West Coal River supports this hypothesis, and it is possible that alpine glaciers originating in the few high cirques in the region were limited in extent since glacial deposits were not observed in the valley bottoms. Similar dissected surfaces without obvious glacial features are found in the high ridges between the Caribou and Rock rivers, suggesting these areas may have remained unglaciated throughout the Pleistocene. Unglaciated regions typically preserve important paleo-ecological records, and further investigation is required to determine potential in the Coal River map sheet for glacial refugia.

Smith (2000) suggests that the Laurentide Ice Sheet advanced at least to the middle of the La Biche River map area (95C; Fig. 18) during its late-Wisconsinan advance, but no clear limit was mapped. Because the late-Wisconsinan advance was the most extensive of the Laurentide glaciations, it has the highest potential to have extended near, or into, the Coal River map sheet. Geomorphic evidence east of Coal River (Smith, 2000) places the Laurentide Ice Sheet into the area before the Cordilleran Ice Sheet advanced, but the advance lacks chronological controls. It is assumed that both ice sheets were present in southeast Yukon during the late-Wisconsinan glacial maximum, and that the Laurentide Ice Sheet began to retreat earlier than the Cordilleran Ice Sheet.

GLACIAL RETREAT

Deglaciation of the Coal River map sheet produced extensive glaciolacustrine and glaciofluvial deposits. As ice retreated south and westward out of the map area, glacial lakes formed in the Coal, Rock, Smith and Beaver river valleys. Eastern drainages became ice-free before western drainages, and the deep meltwater canyons (Fig. 14) within the map area were likely successively incised as these meltwater routes became available. As the meltwater channels became active, the large deltas at

the mouths of many channels were deposited (e.g., Fig. 13).

Evidence of ice-front retreat is recorded in the southwestern corner of the map area, where the ice sheet was pulling back from the edge of the Hyland Plateau to the lower elevation Liard Plain. Abundant moraine, eskers, kettled and hummocky landforms reflect large volumes of meltwater and buried ice left by the ice sheet as it retreated west (Fig. 10). This is the only area in the map sheet with abundant features of glacier retreat, and clearly reflects a different style of deglaciation than that which occurred in other regions of the map area. The deposits may record a minor readvance or slowing of active retreat, allowing glacier ice to be buried under thick blankets of debris.

IMPLICATIONS FOR FUTURE DEVELOPMENT

The glacial history and distribution of surficial materials in the Coal River map area has a number of important implications for future development in the region. The distribution of both stable (sand and gravel) and unstable (silt and clay) surficial materials will be important for regional development and land use planning. Thick massive clay deposits in the Coal and Rock river valleys always contain some amount of ground ice and are prone to catastrophic slope failures when the ice melts. However, massive clay deposits are nearly always stratigraphically below well-drained glaciofluvial sand and gravel. Provided the ice-rich clay deposits are not exposed, the ground surface should remain stable. The many flat terraces in the Coal and Rock river valleys provide ideal surfaces for infrastructure development.

Prospecting in the Coal River map sheet should take into account the complex drainage history of the map area. Meltwater channels between drainage divides obscure the distribution and provenance of heavy minerals and stream sediments. Geochemical signatures from the western map sheet are expected to be present at least as far east as the Beaver River in 95C (Fig. 1).

Thin moraine deposits and unidirectional ice flow/dispersion trains can facilitate mineral exploration on high and mid-elevation slopes in the map area. Northern cirques affected by local glaciation are an exception and need to be examined on an individual basis. At low elevations in the map area, up-valley advancing ice, and thick fine-grained deposits have the potential to make drift prospecting considerably more complicated. Prospectors should keep in mind that the glaciofluvial deposits at

surface in the north-trending valleys are far-travelled and likely do not reflect underlying, or exclusively upstream, bedrock sources.

CONCLUSIONS

Glacial meltwater impoundment and drainage are major landscape-forming events in the Coal River map area. These processes have resulted in abrupt drainage diversions, thick accumulations of potentially unstable clay deposits and abundant, flat, gravel-rich terrace surfaces. Environments proximal to the edges of ice sheets are sensitive barometers of changes in ice sheet-climate dynamics, and can record regional climate changes on a local scale. The ice-proximal environments in southeast Yukon lack chronologies or paleoenvironmental descriptions.

Unresolved questions about the Coal River map area include the extent and chronology of Cordilleran and nearby Laurentide glaciations, the effect buttressing and subsequent debuttressing would have had on the Cordilleran Ice Sheet in the Coal River map area, and the potential existence and extent of glacial refugia.

Continuing investigations of the surficial geology and Quaternary history of the Coal River map sheet will include mapping of ice-flow patterns and drainage routes (in 2010), the production of new surficial geology maps for the east half of 95D (in 2012), and updated surficial geology maps for the west half of 95D (in 2013).

ACKNOWLEDGEMENTS

Funding for this project was provided by the Yukon Geological Survey and the Geological Survey of Canada's Geomapping for Energy and Minerals (GEM) program. Able assistance in the field was provided by Martina Bezzola, Casey Cardinal, Gavin Clarkson and Kristy Long. Casey Cardinal also assisted with drafting some of the figures provided in this manuscript. Lee Pigage collected and shared alpine striation data that has been a valuable contribution to this study. Charlie Roots is thanked for his generosity in planning, running and sharing what turned out to be a successful and productive field camp. A review by Jeff Bond resulted in a greatly improved manuscript and his many valuable contributions are acknowledged.

REFERENCES

- Duk-Rodkin, A., 1999. Glacial Limits Map of Yukon, Yukon Geological Survey, Geoscience Map, 1999-2; GSC Open File 3694, scale 1:1 000 000.
- Duk-Rodkin, A. and Smith, I.R., 2002. Glacial limits, La Biche River (NTS 95C), west of sixth meridian, Yukon Territory. Geological Survey of Canada, Open File 3814, 1 map sheet, scale 1:250 000.
- Dyke, A.S., 1990. Quaternary geology of the Frances Lake map area, Yukon and Northwest Territories. Geological Survey of Canada Memoir, 426, 39 p.
- Jackson, L.E., Jr., Ward, B., Duk-Rodkin, A. and Hughes, O.L., 1991. The last Cordilleran Ice Sheet in southern Yukon Territory. *Géographie physique et Quaternaire*, vol. 45, p. 341-354.
- Klassen, R.W., 1987. The Tertiary Pleistocene stratigraphy of the Liard Plain, southeastern Yukon Territory. Geological Survey of Canada Paper 86-17, 16 p.
- Klassen, R.W., 1983. Surficial geology, Coal River (west-half) Yukon Territory. Geological Survey of Canada Map 13-1982, scale 1:250 000.
- Klassen, R.W. and Morison, S.R., 1982a. Surficial geology, Watson Lake, Yukon Territory. Geological Survey of Canada Map 21-1981, scale 1:250 000.
- Klassen, R.W. and Morison, S.R., 1982b. Surficial geology, Wolf Lake, Yukon Territory. Geological Survey of Canada Map 14-1982, scale 1:250 000.
- Pigage, L.C., 2009. Bedrock geology of NTS 95C/5 (Pool Creek) and NTS 95D/8 map sheets, southeast Yukon. Yukon Geological Survey, Bulletin 16, 150 p.
- Ryder, J.M. and Maynard, D., 1991. The Cordilleran Ice Sheet in northern British Columbia. *Géographie physique et Quaternaire*, vol. 45, p. 355-363.
- Smith, C.A.S., Meikle, J.C. and Roots, C.F. (editors), 2004. Ecoregions of the Yukon Territory: Biophysical properties of Yukon landscapes. Agriculture and Agri-Food Canada, PARC Technical Bulletin No. 04-01, Summerland, British Columbia, 313 p.
- Smith, I.R., 2000. Preliminary report on surficial geology investigations of La Biche River map area, southeast Yukon Territory. Geological Survey of Canada, Current Research 2000-B3, 9 p.
- Smith, I.R., 2002a. Surficial geology, Mount Martin (NTS 95 C/1), Yukon Territory-Northwest Territories-British Columbia. Geological Survey of Canada, Open File 4260, 1 map sheet, scale 1:50 000.
- Smith, I.R., 2002b. Surficial geology, Mount Merrill (NTS 95 C/2) Yukon Territory - British Columbia. Geological Survey of Canada, Open File 4324; 1 map sheet, scale 1:50 000.
- Smith, I.R., 2003a. Surficial geology, Brown Lake (NTS 95 C/7), Yukon Territory. Geological Survey of Canada, Open File 1771, 1 map sheet, scale 1:50 000.
- Smith, I.R., 2003b. Surficial geology, Babiche Mountain (NTS 95 C/8), Yukon Territory - Northwest Territories. Geological Survey of Canada, Open File 1558, 1 map sheet, scale 1:50 000.
- Smith, I.R., 2003c. Surficial geology, Chinkeh Creek (NTS 95 C/9), Northwest Territories - Yukon Territory. Geological Survey of Canada, Open File 16151, scale 1:50 000.
- Smith, I.R., 2003d. Surficial geology, Etanda Lakes (NTS 95 C/16), Northwest Territories - Yukon Territory. Geological Survey of Canada, Open File 1671, 1 map sheet, scale 1:50 000.
- Smith, I.R., 2004a. Surficial geology, La Biche River (southwest), (NTS 95 C/3/4/5/6) Yukon Territory - British Columbia. Geological Survey of Canada, Open File 4680, 1 map sheet, scale 1:100 000.
- Smith, I.R., 2004b. Surficial geology, Tika Creek (NTS 95 C/10), Yukon Territory - British Columbia. Geological Survey of Canada, Open File 4702, 1 map sheet, scale 1:50 000.

Ar-Ar geochronology and Pb isotopic constraints on the origin of the Rau gold-rich carbonate replacement deposit, central Yukon

Scott Kingston¹, James K. Mortensen² and Janet Gabites

Pacific Centre for Isotopic and Geochemical Research, University of British Columbia

Matt Dumala

Archer, Cathro & Associates (1981), Ltd.

Kingston, S., Mortensen, J.K., Dumala, M. and Gabites, J.E., 2010. Ar-Ar geochronology and Pb isotopic constraints on the origin of the Rau gold-rich carbonate replacement deposit, central Yukon. *In: Yukon Exploration and Geology 2009*, K.E. MacFarlane, L.H. Weston and L.R. Blackburn (eds.), Yukon Geological Survey, p. 213-222.

ABSTRACT

The Rau deposit in central Yukon is a gold-rich carbonate replacement deposit hosted in mid-Paleozoic carbonate rocks of the Mackenzie Platform in the footwall of the Dawson thrust. Gold-bearing sulphide mineralization is peripheral to a zone of hornfels and local tungsten-bearing skarn that is associated with several small bodies of granitic aplite and pegmatite that have yielded $^{40}\text{Ar}/^{39}\text{Ar}$ muscovite ages of 62.3 ± 0.7 Ma, 62.4 ± 1.8 Ma and 59.1 ± 2.0 Ma. These intrusions are geochemically different and slightly younger than the 65.2 ± 2.0 Ma McQuesten plutonic suite farther to the south. Most Pb isotopic analyses of sulphides from the Rau deposit cluster within compositions of igneous feldspars from the associated intrusions; however, some analyses fall on a trend toward more radiogenic compositions that were determined for the host carbonate rocks. The data are consistent with the Rau sulphide mineralization being genetically related to the early Paleocene felsic intrusions, and forming peripheral to more proximal zones of hornfelsing and tungsten-bearing skarns.

¹spk@dccnet.com

²jmortensen@eos.ubc.ca

INTRODUCTION

Gold-rich carbonate replacement mineralization recently discovered by ATAC Resources Ltd. at the Rau property in west-central Yukon (Fig. 1) is an excellent example of a relatively poorly understood style of mineral deposit. Presently, similar mineralization is only known at the Ketzka deposit in south-central Yukon (Fig. 1; Fonseca, 1998) and a small number of other occurrences elsewhere in the North American Cordillera.

An investigation of the character, age and origin of gold mineralization at the Rau occurrence was undertaken as a BSc thesis by Kingston (2009). The work focused on the analysis of drill core from two 2008 diamond drillholes (08-Rau-11 and 08-Rau-18). Results from $^{40}\text{Ar}/^{39}\text{Ar}$ dating and Pb isotopic studies that were carried out as part of that study are included in the following report, as well as the implications of these results for the age and genesis of gold mineralization at the Rau occurrence.

GEOLOGY OF THE RAU PROPERTY

The Rau property is located approximately 100 km northeast of Mayo (Fig. 1). The geology of the study area is depicted in simplified form in Figure 2 (Abbott, 1990; unpublished data ATAC Resources Ltd., <http://www.atacresources.com/s/home.asp>). Initial work on the property focused on small zones of W (\pm Au) skarn and hornfelsing associated with a small granitic stock (the Rackla pluton) and associated dykes in the eastern part of the property (Fig. 2; Panton, 2008). Subsequent work on the property in 2008 led to the discovery of the Tiger zone,

Figure 2. Simplified geology of the eastern portion of the Rau property (based on unpublished geological mapping by ATAC Resources Ltd. geologists).

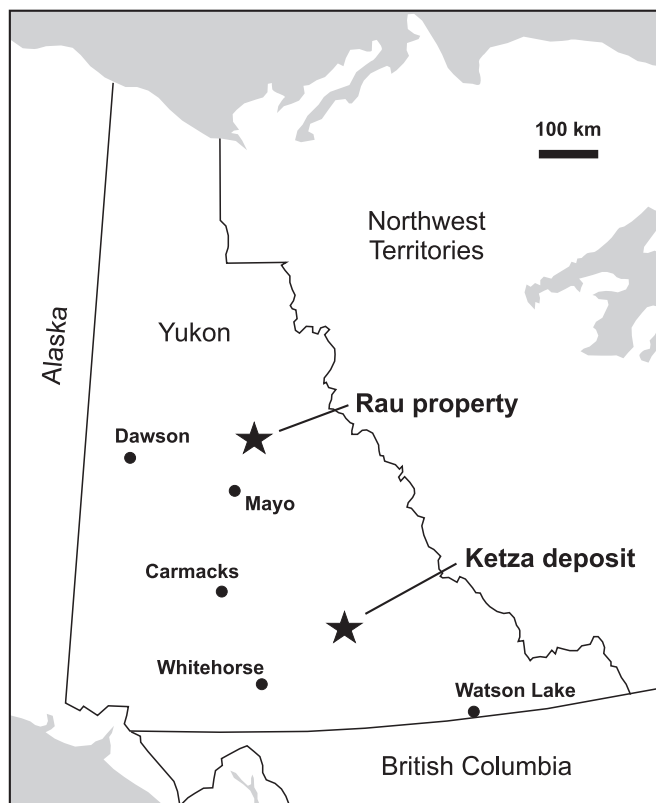
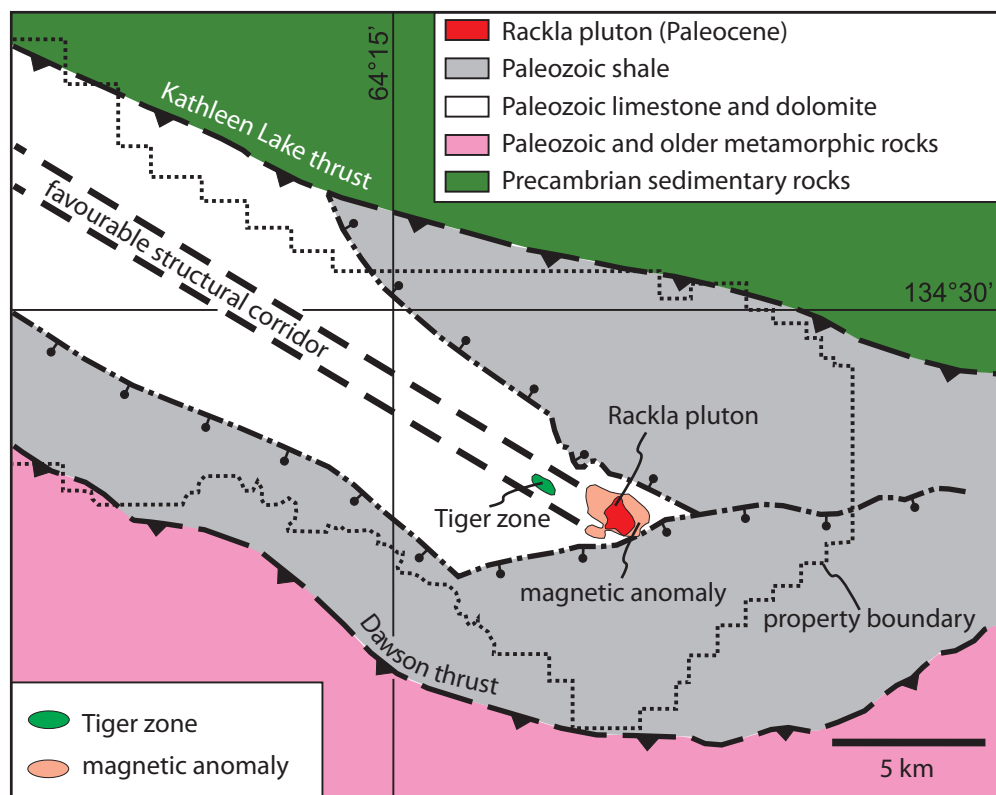


Figure 1. Location of the Rau property and the Ketzka River gold-bearing carbonate replacement deposit.



which comprises Au-bearing carbonate replacement mineralization farther to the west of the zone of hornfelsing and skarn development that is directly associated with the Rackla pluton. A substantial portion of the Tiger zone has been strongly oxidized and all or most of the primary sulphide minerals have been replaced by iron oxides and hydroxides.

Tungsten and gold-bearing skarns, and the gold-bearing replacement-style mineralization of the Tiger Zone, are hosted mainly by carbonate rocks of the Devonian Bouvette Formation (Morrow, 1999), which makes up part of a southwest-dipping panel of mid-Paleozoic strata that is bounded between the Dawson thrust above and the Kathleen Lake thrust below (Fig. 2). The Bouvette Formation, in the vicinity of the Tiger zone, comprises medium grey to buff-weathering limestone and tan to pale grey dolomite. 'Zebra texture' is locally developed within the carbonate; this texture is commonly also observed in the vicinity of Mississippi Valley-type (MVT) Pb-Zn deposits elsewhere in the northern Cordillera (e.g., Paradis and Nelson, 2007). Volcanic and volcanoclastic rocks are interlayered with the carbonates in the vicinity of the Tiger zone, including a layer up to 20 m thick that occurs in the immediate hangingwall of the mineralized zone. It is unclear what role, if any, these volcanic units played in the genesis of the mineralization. They contain abundant fine-grained biotite, which could, in part, be a product of hydrothermal alteration; however, the biotite is commonly weakly aligned, suggesting that it crystallized (or was recrystallized) during regional deformation.

Sulphide mineralization in the Tiger zone includes massive to semi-massive replacement of the host carbonate by fine to coarse-grained sulphides, as well as irregular sulphide veins. Sulphides present in the two 2008 drillholes in the Tiger zone that were examined in this study, comprise mainly pyrite with lesser pyrrhotite and arsenopyrite, and rare sphalerite, chalcopyrite and bismuthenite. Sulphide mineralization encountered during 2009 drilling in the Tiger zone was typically more arsenopyrite rich than that observed in the 2008 drillholes; arsenopyrite is present at equivalent or greater levels than pyrite, accompanied by minor pyrrhotite, bismuthinite and scheelite, and rare sphalerite and chalcopyrite. A number of other gold occurrences and anomalies have been identified by company geologists along strike to the northwest from the Tiger zone, within a belt referred to as the 'favourable structural corridor' (Fig. 2).

The Rackla pluton is approximately 1 km in diameter at the present level of exposure; however, an extensive magnetic anomaly that encompasses and surrounds the pluton has been delimited by aeromagnetic surveys of the property by ATAC Resources (<http://www.atacresources.com/s/home.asp>) and may suggest that the stock is considerably larger in the subsurface (Fig. 2). Exposure of the pluton is generally poor; however, Panton (2008) describes it as primarily coarse-grained biotite-muscovite granite with finer grained aplitic phases common near the margins that contain local garnet, tourmaline and fluorite. Mirolitic cavities are common, suggesting a relatively high level of emplacement. Small dykes and sills, within the area of hornfelsing to the west of the pluton, range from aplite to pegmatite, and commonly contain tourmaline and garnet (Panton, 2008). Biotite-garnet, tremolite and actinolite skarn that developed west of the Rackla pluton contain sporadic values of W, Cu and Au.

AGE AND LITHOGEOCHEMISTRY OF INTRUSIVE ROCKS ON THE RAU PROPERTY

The felsic composition and mineralogy of intrusive rocks of the Rackla pluton and associated dykes and sills suggest that they are peraluminous magmas produced through crustal melting. Previous attempts to date the Rackla pluton using U-Pb dating of zircons (Mortensen and Abbott, unpublished data, 1991) indicated a minimum emplacement age of ~61 Ma, and this age, in addition to the geographic location of the Rackla pluton, led to the initial inference that the Rackla pluton and associated intrusions in the vicinity were related to the 65.2 ± 2.0 Ma McQuesten plutonic suite that occurs in an east-trending belt approximately 50 km south of the Rau occurrence (Murphy, 1997).

In this study, we used $^{40}\text{Ar}/^{39}\text{Ar}$ step-heating methods to date muscovite from three samples of muscovite-bearing aplite and pegmatite from small intrusive bodies. These intrusive bodies are northwest of the Rackla pluton and occur within the zone of strong hornfelsing where there is locally developed tungsten skarn mineralization. Analyses were completed at the Pacific Centre for Isotopic and Geochemical Research (PCIGR) laboratories at the University of British Columbia, using methods as described by Mortensen *et al.* (in press). Age spectra for the three samples are shown in Figure 3a-c and analytical data is listed in Table 1. The three ages overlap at a two-sigma level; however, we consider the best age for

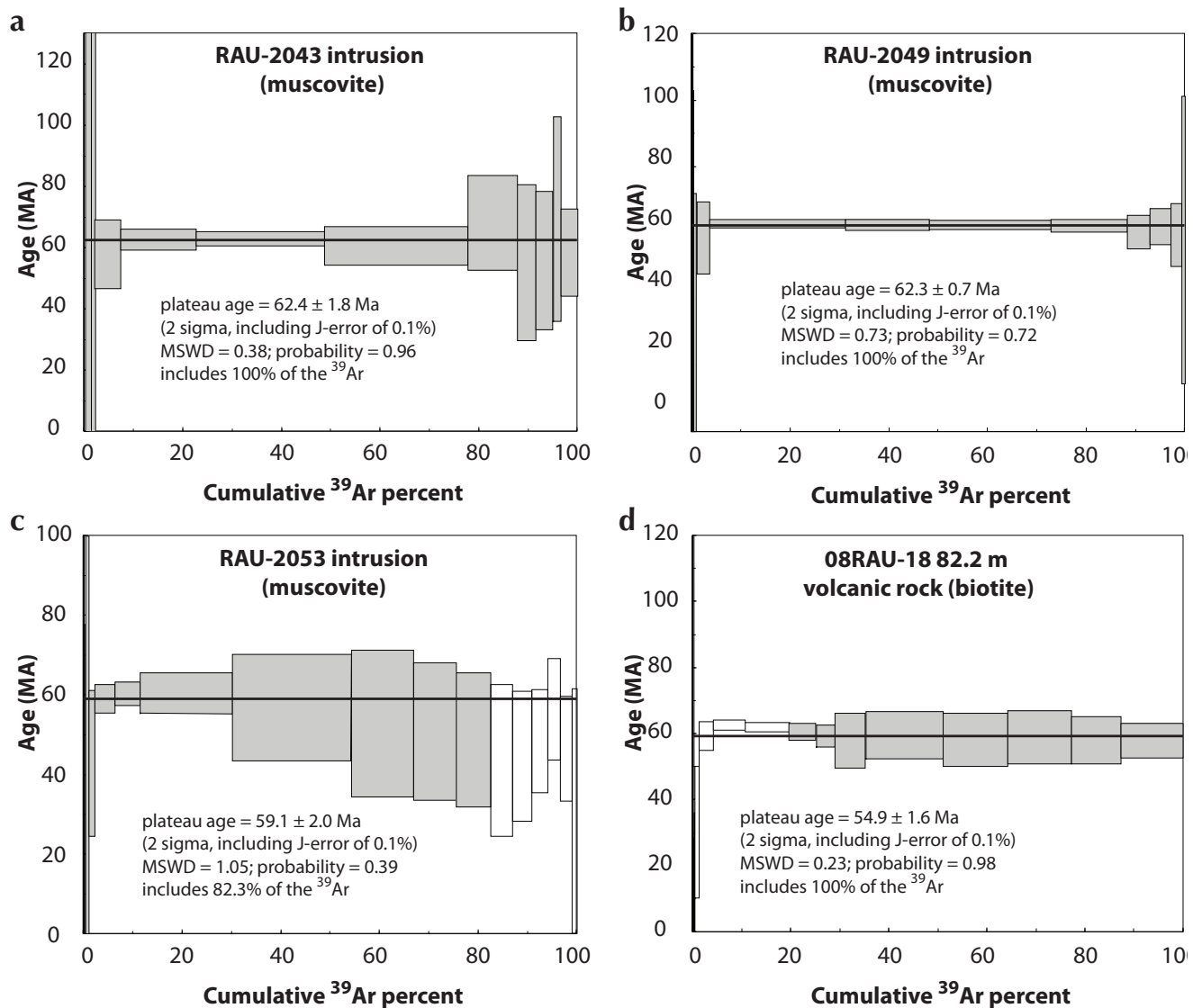


Figure 3. $^{40}\text{Ar}/^{39}\text{Ar}$ dating results from intrusive and volcanic rocks on the Rau property. Shaded analyses were used in calculation of the plateau ages; MSWD = mean square of the weighted deviates.

the magmatism to be given by a weighted average of the two oldest and most precise age determinations, at 62.3 ± 0.6 Ma. This result is in good agreement with a recent U-Pb zircon age of 62.9 Ma for the Rackla pluton (V. Bennett, pers. comm.). Together, the new $^{40}\text{Ar}/^{39}\text{Ar}$ and U-Pb ages for the Rackla pluton and associated dykes in the vicinity, indicate that intrusive rocks on the Rau property are early Paleocene in age; this represents a slightly younger pulse of magmatism than that represented by the latest Cretaceous to earliest Paleocene McQuesten plutonic suite to the south.

Major, trace and rare earth element analyses were reported by Panton (2008) for two fine to medium-grained samples from granitic dykes within the main zone of hornfelsing adjacent to the western margin of the Rackla pluton (Fig. 2). Geochemical analyses of the Rackla pluton itself are not available. The dyke compositions are plotted on total alkali vs. SiO_2 and Rb vs. Yb+Ta diagrams (after Le Bas *et al.*, 1986) in Figure 4. Five analyses of McQuesten suite intrusions are included on the plots for comparison (data from Murphy, 1997). The Rau dykes overlap with part of the range of McQuesten suite in terms of major elemental compositions (Fig. 4a). On the Pearce *et al.* (1984)

Table 1. $^{40}\text{Ar}/^{39}\text{Ar}$ analytical results for micas from intrusive and volcanic rocks from the Rau property.

Laser Power (watts)	^{39}Ar (cum. %)	Age (Ma)	Error (2 sigma)	^{40}Ar (rad.) (%)	^{39}Ar (%)	K/Ca	Error (2 sigma)
Rau-2043 (muscovite)							
2	0.057	437.19	679	81.750	0.057	0.75	1.22
2.2	1.267	40.04	151	5.713	1.210	7.73	9.01
2.4	2.158	67.11	112	16.245	0.892	0.87	0.23
2.7	7.284	57.93	11.14	43.161	5.125	2.91	0.63
3	22.579	62.59	3.29	64.922	15.296	98.89	135.21
3.3	48.661	62.90	2.34	78.465	26.082	167.02	170.33
3.6	77.798	60.56	6.28	73.373	29.137	143.53	70.75
3.9	87.761	68.05	15.41	65.748	9.963	67.06	62.84
4.2	91.586	55.07	25.41	42.125	3.825	19.42	34.48
4.6	95.049	55.75	22.49	50.332	3.463	21.87	17.90
5.1	96.810	69.37	33.30	49.743	1.760	9.89	6.12
5.7	100.000	58.45	14.22	56.890	3.190	24.01	22.23
Rau-2049 (muscovite)							
2	0.018	-324.67	1605	-7.905	0.018	135.30	140808
2.2	0.117	-127.94	294	-15.426	0.099	1.02	1.59
2.4	0.335	-22.88	126	-2.325	0.217	2.56	4.15
2.7	0.909	12.45	59.27	1.969	0.574	7.94	13.71
3	3.597	58.49	10.82	58.840	2.688	1391.39	758588
3.3	31.105	62.67	1.21	94.825	27.508	229.53	288.48
3.6	48.235	62.40	1.64	96.081	17.131	822.02	4206.45
3.9	72.963	62.27	1.28	97.302	24.728	983.93	4110.63
4.2	88.358	62.04	1.84	96.498	15.394	293.38	590.51
4.5	92.881	60.10	5.05	91.192	4.523	152.70	634.11
4.9	97.145	61.74	5.43	93.514	4.264	36.97	35.72
5.3	99.468	59.32	9.45	87.877	2.323	43.86	127.82
5.8	100.000	57.85	43.22	66.066	0.532	388.73	28716
Rau-2053 (muscovite)							
2	0.006	-138.70	586	-23.147	0.006	-0.17	0.29
2.2	0.093	-34.66	112	-4.323	0.086	-2.73	3.75
2.4	0.299	-117.41	105	-13.564	0.207	-39.55	276.49
2.7	1.015	0.04	100	0.009	0.715	2.43	0.39
3	2.252	42.76	18.25	24.129	1.237	-38.82	67.37
3.3	6.229	58.97	3.50	69.803	3.977	77.28	65.23
3.6	11.320	60.15	2.93	62.324	5.091	167.14	399.08
3.9	30.188	60.34	5.11	74.649	18.868	93.29	35.62
4.2	54.266	56.71	13.34	63.310	24.078	89.52	36.35
4.3	66.922	52.85	18.35	53.237	12.656	52.84	28.68
4.4	75.675	50.80	17.16	51.146	8.753	145.02	129.41
4.6	82.587	48.69	16.80	49.249	6.912	42.80	13.85
4.9	86.961	43.62	19.01	41.826	4.375	34.54	26.55
5.2	90.928	44.56	16.21	46.047	3.966	92.94	179.69
5.6	94.120	48.40	12.95	46.069	3.192	73.38	70.50
6	96.635	56.25	12.70	52.156	2.515	216.49	939.03
6.5	99.089	46.47	13.14	44.991	2.454	56.33	75.12
7	100.000	27.86	33.70	19.307	0.911	191.17	2261.86
Rau-08-18 82.2a (biotite)							
2	-0.001	2845.46	2121	100.000	-0.001	-0.03	0.05
2.2	0.063	-53.21	61.60	-22.910	0.064	-12.68	80.80
2.4	0.183	-9.70	38.33	-4.594	0.120	3.93	3.38
2.7	0.381	-13.63	49.77	-5.759	0.197	6.48	7.98
3	1.203	30.17	19.87	22.296	0.823	6.18	2.14
3.3	4.114	59.23	4.39	74.213	2.910	7.69	0.91
3.6	10.646	62.51	1.56	89.919	6.533	22.92	3.97
3.9	19.567	61.80	1.37	90.119	8.921	33.89	5.49
4.2	25.024	60.40	2.42	83.252	5.456	35.03	13.59
4.5	28.960	59.15	3.28	74.511	3.936	32.38	10.64
4.9	35.114	57.77	8.23	63.186	6.154	15.13	3.30
5.3	50.940	59.38	7.16	67.595	15.827	24.27	3.33
5.7	64.237	57.93	8.01	64.841	13.296	18.09	1.90
6	77.145	58.83	8.00	65.916	12.909	14.85	2.18
6.3	87.280	57.87	7.13	65.514	10.135	11.01	0.94
7	100.000	57.71	5.16	69.923	12.720	3.70	0.23

discriminant plot shown in Figure 4b, the McQuesten suite intrusions fall either within the “volcanic arc granite” or “syncollisional granite” fields, whereas the Rau dykes fall in the “within-plate granite” field. Although the available analyses are from dykes in the Rau area and not from the Rackla pluton itself, the lithogeochemical evidence suggests that intrusions in the Rau area may not be directly related to the McQuesten plutonic suite.

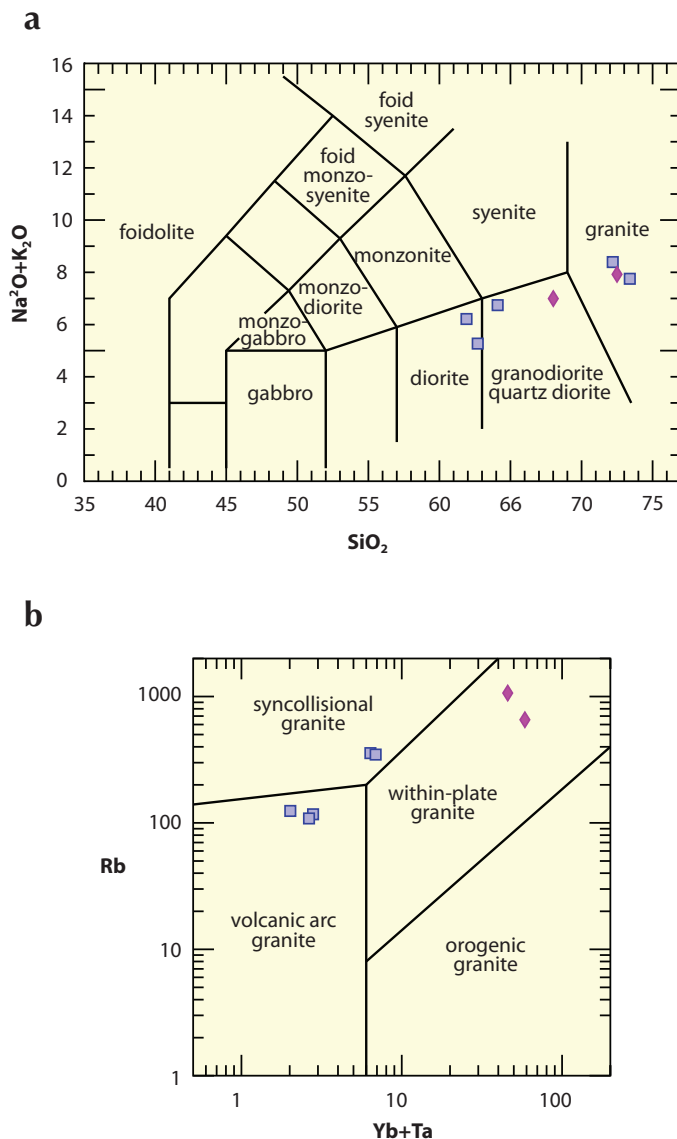


Figure 4. Geochemistry of felsic dykes on the Rau property (diamonds) in comparison to the McQuesten plutonic suite (squares; from Murphy, 1997).

OTHER DATING STUDIES

Biotite from within one of the volcanic/volcaniclastic units was separated and dated using $^{40}\text{Ar}/^{39}\text{Ar}$ methods. A plateau age of 59.4 ± 1.6 Ma was obtained from the sample (Fig. 3d). The significance of this age is uncertain; it may reflect either cooling following the emplacement of the Rackla pluton, or a slightly younger thermal event.

LEAD ISOTOPE STUDIES

Lead isotopes can be used to constrain the source(s) of metals contained within a mineral deposit (e.g., Tosdal *et al.*, 1999). This approach is particularly valuable when one is able to directly measure the isotopic composition of potential reservoirs from which metals contained within a deposit might have been derived.

In the case of the Rau sulphide mineralization, there are three potential reservoirs in the immediate vicinity of the mineralization that could potentially have contributed Pb to the deposit: 1) the host carbonate rocks; 2) the volcanic/volcaniclastic rock units that are spatially closely associated with at least some of the mineralization; and 3) felsic intrusive rocks adjacent to the mineralization.

In order to assess the contribution of Pb (and by inference, the other contained metals) from the three potential reservoirs, and to determine whether other unidentified sources might have played a role in the genesis of the mineralization, we measured the Pb isotopic compositions of several representative samples. These samples included K-feldspar separated from four discrete felsic dykes within the main zone of hornfelsing and tungsten skarn development west of the Rackla pluton; two samples of the host carbonates distal from any sulphide mineralization; one sample of unaltered volcaniclastic rock; and a total of 17 samples of pyrite, representing the range of styles of mineralization present in the two 2008 drillholes that we studied. Analytical data are listed in Table 2 and are plotted on a conventional $^{207}\text{Pb}/^{204}\text{Pb}$ vs. $^{206}\text{Pb}/^{204}\text{Pb}$ diagram in Figure 5a, and a $^{208}\text{Pb}/^{206}\text{Pb}$ vs. $^{207}\text{Pb}/^{206}\text{Pb}$ diagram in Figure 5b. Also shown for comparison are isotopic compositions of K-feldspars from both the 92-94 Ma Tombstone and the 65.2 ± 2.0 Ma McQuesten plutonic suites, and a field of Pb isotopic compositions of galenas from veins in the Keno Hill Mining District. The “shale curve” of Godwin *et al.* (1982), which closely approximates the Pb isotopic evolution of the North American miogeocline in the northern Cordillera, is shown for reference.

Table 2. Lead isotopic compositions of sulphide, whole rock (wr) and feldspar samples from the Rau property.

Sample	Mineral	$^{206}\text{Pb}/^{204}\text{Pb}$	Error	$^{207}\text{Pb}/^{204}\text{Pb}$	Error	$^{208}\text{Pb}/^{204}\text{Pb}$	Error	$^{207}\text{Pb}/^{206}\text{Pb}$	Error	$^{208}\text{Pb}/^{206}\text{Pb}$	Error
Rau 5	pyrite	19.868	0.10	15.693	0.10	40.101	0.12	0.7898	0.05	2.0184	0.05
Rau 7	pyrite	20.014	0.04	15.729	0.05	40.491	0.07	0.7859	0.04	2.0232	0.03
Rau 11	pyrite	20.233	0.03	15.757	0.04	40.574	0.06	0.7788	0.04	2.0053	0.03
Rau 19	pyrite	20.037	0.05	15.736	0.05	40.421	0.08	0.7854	0.04	2.0173	0.04
Rau 6	pyrite	20.031	0.28	15.647	0.17	40.018	0.36	0.7812	0.22	1.9978	0.22
Rau 9	pyrite	19.665	0.09	15.596	0.10	39.784	0.11	0.7931	0.04	2.0231	0.04
Rau 10	pyrite	20.144	0.04	15.768	0.05	40.392	0.07	0.7828	0.04	2.0052	0.03
Rau 11	pyrite	19.969	0.11	15.739	0.08	40.333	0.14	0.7882	0.09	2.0197	0.08
Rau 12	pyrite	19.854	0.04	15.699	0.05	40.173	0.07	0.7907	0.04	2.0234	0.03
Rau 14	pyrite	19.962	0.08	15.769	0.09	40.209	0.10	0.7900	0.04	2.0143	0.03
Rau 15	pyrite	20.020	0.03	15.714	0.05	40.434	0.07	0.7849	0.04	2.0197	0.03
Rau 16	pyrite	21.046	0.87	15.940	0.83	38.510	0.93	0.7574	0.25	1.8298	0.33
Rau 17	pyrite	19.588	0.08	15.710	0.09	39.826	0.10	0.8020	0.04	2.0332	0.03
Rau 18	pyrite	19.871	0.13	15.845	0.12	40.248	0.14	0.7974	0.06	2.0255	0.04
Rau 23	pyrite	19.105	0.03	15.635	0.05	38.976	0.06	0.8183	0.04	2.0401	0.03
Rau 21	pyrite	19.997	0.06	15.729	0.05	40.306	0.09	0.7866	0.06	2.0156	0.04
Rau 22	pyrite	20.329	0.52	15.808	0.49	40.915	0.55	0.7776	0.19	2.0126	0.15
Rau 1	carbonate wr	20.627	0.10	15.791	0.10	40.507	0.12	0.7656	0.06	1.9638	0.04
Rau 2	carbonate wr	20.316	0.44	15.695	0.43	40.259	0.44	0.7726	0.06	1.9816	0.04
Rau 3	volcanic wr	19.958	0.16	15.911	0.16	39.751	0.18	0.7972	0.05	1.9918	0.05
Rau 20	feldspar	19.945	0.04	15.767	0.05	40.189	0.08	0.7905	0.04	2.0150	0.05
Rau 45	feldspar	19.821	0.03	15.711	0.04	40.037	0.06	0.7927	0.04	2.0200	0.03
Rau 49	feldspar	19.797	0.03	15.697	0.05	40.028	0.07	0.7929	0.04	2.0220	0.03
Rau 53	feldspar	19.768	0.17	15.676	0.15	40.136	0.18	0.7930	0.09	2.0303	0.05

Results normalized using a fractionation factor of 0.12% based on multiple analyses of NBS981 standard lead, and the values in Thirlwall (2000). Errors are reported at the 2-sigma level.

Several observations can be made from the Pb isotopic data array. The isotopic compositions of feldspars in the Rau dykes fall in a tight cluster that is much more radiogenic than corresponding clusters for the McQuesten suite intrusions, indicating very different sources for the magmas. The measured isotopic compositions of most of the sulphides that were analysed plot relatively close to the compositions measured for feldspar from felsic dykes on the Rau property. Some of the Rau sulphide analyses trend towards the compositions of the host carbonates, which yield substantially more radiogenic compositions than the Rau intrusions themselves. A few of the Rau sulphide analyses trend towards somewhat less radiogenic compositions than those of the Rau feldspars. The single isotopic analysis of the volcanic rocks on the Rau property plots well away from the array of compositions for Rau feldspars and the carbonate host rocks (Fig. 5).

Taken together, the Pb isotopic data strongly suggest that most metals in all of the various styles of sulphide mineralization present within the two 2008 Rau drillholes that were examined in this study represent variable mixtures with most Pb derived from the Rau felsic intrusions (or more probably a larger associated intrusive body at depth) and a lesser component from the host carbonates. The small number of sulphide analyses that are less radiogenic in composition than the Rau intrusion feldspars indicate that some other less radiogenic reservoir also contributed metals to some of the deposit. The volcanic rocks on the property did not appear to have contributed any significant amount of metal to the mineralization.

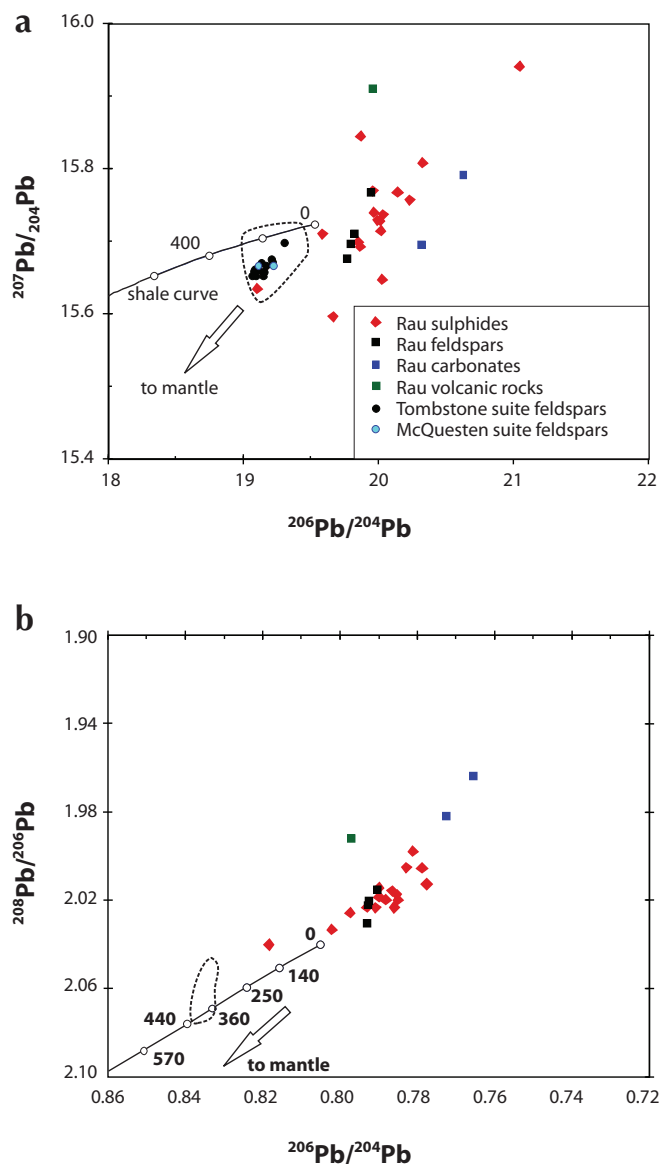


Figure 5. Lead isotopic compositions of sulphide minerals, igneous feldspars and country rock at the Rau property. The “shale curve” of Godwin *et al.* (1982) is shown for reference. Lead isotopic compositions of Tombstone and McQuesten suite intrusions (black and blue circles, Figure 5a) and galenas from Keno Hill (area outlined by dashed line, Figs. 5a and 5b) are from Mortensen (unpublished data).

DISCUSSION

Although the genesis of base metal carbonate replacement deposits is reasonably well understood (e.g., Nelson, 2005), the nature and origin of the much less common gold-rich carbonate replacement mineralization such as that in the Tiger zone on the Rau property are still poorly understood. Fonseca (1998) inferred, but could not directly prove, that the Ketz River gold-rich manto deposit in south-central Yukon (Fig. 1) was part of an intrusion-centered, gold base-metal system. The only other example of a gold-rich carbonate replacement deposit in the northern Cordillera is the Mosquito Creek gold deposit in the Wells-Barkerville camp in the Cariboo Gold District of east-central British Columbia (e.g., Alldrick, 1983; Rhys *et al.*, 2009), and there is no evidence for any association with intrusive rocks at that deposit. Although the Ketz River and Mosquito Creek deposits are the only other gold-rich carbonate replacement deposits that have ever been studied in any detail, it appears that there is no consistent genetic association between this style of mineralization and intrusions.

Results of the present study shed new light on some aspects of the Rau occurrence; however, many questions still remain concerning the genesis of this exciting new gold discovery. Two main conclusions arising from the present study bear on the genesis of gold mineralization on the Rau property and exploration for similar styles of mineralization elsewhere in this part of Yukon.

Firstly, the Pb isotopic data strongly suggest that sulphide mineralization in the Tiger zone that was sampled in the two 2008 drillholes that were examined for this study is genetically related to the early Paleocene Rackla pluton and related dykes and sills (and possibly a larger associated intrusion at depth). This is consistent with the presence of both gold and tungsten in skarns in a more proximal relationship with the Rackla pluton, and suggests a possible metallogenic zonation developed concentrically outwards from the central stock, as described elsewhere in the world by Sillitoe and Bonham (1990). It is recommended that additional Pb isotopic analyses be carried out on the more arsenopyrite-rich sulphide mineralization discovered in the Tiger zone during 2009 drilling in order to determine whether this style of mineralization is also related to the Rau intrusions, or represents a different, and possibly unrelated, mineralizing event.

Secondly, the Rackla pluton and related dykes and sills are distinct from the McQuesten plutonic suite in terms of age (early Paleocene as opposed to latest Cretaceous-earliest Paleocene), geochemistry and geographic location. Both the McQuesten suite and the Rackla pluton and related dykes and sills are inferred to be products of crustal melting; however, the two sets of intrusions yield tightly clustered, but very different Pb isotopic compositions, indicating that the magmas were not derived by melting of the same source rocks. Very little mineralization of any kind is known to be associated with the McQuesten suite intrusions (Murphy, 1997), and we suggest that potential for Rau-type gold mineralization associated with the McQuesten suite intrusions is unlikely.

ACKNOWLEDGEMENTS

We thank ATAC Resources Ltd., for access to drill core and confidential company reports related to the Rau property, and for funding the analytical work described in this paper. The paper was improved by a critical review by Venessa Bennett.

REFERENCES

- Abbott, J.G., 1990. Geological map of Mt. Westman map area (106D/1). Exploration and Geological Services Division, Yukon Region, Indian and Northern Affairs Canada, Open File Map 1990-1, 1:50 000 scale.
- Alldrick, D.J., 1983. The Mosquito Creek mine, Cariboo gold belt (93H/4). British Columbia Ministry of Energy, Mines and Petroleum Resources, Geological Fieldwork 1982, Paper 1983-1, p. 99-112.
- Fonseca, A., 1998. Origin of carbonate hosted gold rich carbonate replacement deposits and related mineralization styles in the Ketz River deposit, Yukon Territory. Unpublished MSc thesis, University of British Columbia, Vancouver, British Columbia, 37 p.
- Godwin, C.I. and Sinclair, A.J., 1982. Average lead isotope growth curves for shale-hosted zinc-lead deposits, Canadian Cordillera. *Economic Geology*, vol. 77, p. 675-690.
- Kingston, S.P., 2009. Nature and origin of gold-rich carbonate-replacement deposits at the Rau occurrence, central Yukon. Unpublished BSc thesis, University of British Columbia, Vancouver, British Columbia, 56 p.
- Lebas, M.J., Lemaitre, R.W., Streckeisen, A. and Zanettin, B., 1986. A chemical classification of volcanic rocks based on the total alkali-silica diagram. *Journal of Petrology*, vol. 27, p. 745-750.
- Morrow, D.W., 1999. Lower Paleozoic stratigraphy of northern Yukon Territory and northwestern District of Mackenzie. Geological Survey of Canada, Bulletin 538, 202 p.
- Mortensen, J.K., Craw, D., MacKenzie, D.J., Gabites, J.E. and Ullrich, T., in press. Age and origin of orogenic gold mineralization in the Otago Schist Belt, South Island, New Zealand: Constraints from lead isotopic and $^{40}\text{Ar}/^{39}\text{Ar}$ dating studies. *Economic Geology*.
- Murphy, D.C., 1997. Geology of the McQuesten River Region, northern McQuesten and Mayo map areas, Yukon Territory (115P/14, 15, 16; 105M/13, 14). Exploration and Geological Services Division, Yukon Region, Indian and Northern Affairs Canada, Bulletin 6, 122 p.
- Nelson, J.L., 2005. Polymetallic mantos Ag-Pb-Zn. BC Mineral Deposit Profiles, <<http://www.em.gov.bc.ca/Mining/Geosurv/MetallicMinerals/MineralDepositProfiles/PROFILES/J01.htm>> [access date 2008].
- Panton, B., 2008. A deposit model for mineralization at the Rau property, Yukon Territory. Unpublished BSc thesis, University of British Columbia, Vancouver, British Columbia, 57 p.
- Paradis, S. and Nelson, J.L., 2007. Metallogeny of the Robb Lake carbonate-hosted zinc-lead district, northeastern British Columbia. In: *Mineral Deposits of Canada: A Synthesis of Major Deposit-Types, District Metallogeny, the Evolution of Geological Provinces, and Exploration Methods*. W.D. Goodfellow (ed.), Geological Association of Canada, Mineral Deposits Division, Special Publication No. 5, p. 633-654.
- Pearce, J.A., Harris, B.W. and Tindle, A.G., 1984. Trace element discrimination diagrams for the tectonic interpretation of granitic rocks. *Journal of Petrology*, vol. 25, p. 956-983.
- Rhys, D.A., Mortensen, J.K. and Ross, K., 2009. Investigations of orogenic gold deposits in the Cariboo gold district, east central British Columbia (parts of NTS 093A, H): progress report. In: *Geoscience BC Summary of Activities 2008*, Geoscience BC, Report 2009-1, p. 49-74.

Sillitoe, R.H. and Bonham, H.F. Jr., 1990. Sediment-hosted gold deposits: distal products of magmatic-hydrothermal systems. *Geology*, vol. 18, p. 157-161.

Thirwall, M.F., 2000. Inter-laboratory and other errors in Pb isotope analyses investigated using a $^{207}\text{Pb}/^{204}\text{Pb}$ double spike. *Chemical Geology*, vol. 163, p. 299-322.

Tosdal, R.M., Wooden, J.L. and Bouse, R.M., 1999. Pb isotopes, ore deposits, and metallogenic terranes. *In: Reviews in Economic Geology*, D.D. Lambert and J. Ruiz (eds.), vol. 12. p. 1-28.

Evaluation of titanite as an indicator mineral for tungsten-skarn mineralization

Robert Linnen¹

Department of Earth and Environmental Sciences, University of Waterloo

Xudong Che²

*State Key Laboratory for Mineral Deposits Research,
School of Earth Sciences and Engineering, Nanjing University*

Linnen, R. and Che, X., 2010. Evaluation of titanite as an indicator mineral for tungsten-skarn mineralization. *In: Yukon Exploration and Geology 2009*, K.E. MacFarlane, L.H. Weston and L.R. Blackburn (eds.), Yukon Geological Survey, p. 223-228.

ABSTRACT

One of the challenges in exploring for skarn mineralization is that barren skarn may not give any indication that mineralization is close by. The purpose of the present study is to evaluate titanite as an indicator mineral for tungsten-skarn mineralization. Titanite from samples of scheelite mineralization from the Risby, Ray Gulch and Mactung deposits was analysed by electron microprobe. The titanite is fluorine-rich and some grains contain anomalous tin, but in most grains metal concentrations are at or below the detection limits of the microprobe (~20-50 ppm). Future work is planned to analyze titanite by LA ICP-MS to determine, in particular, the W-Mo-Sn contents to further evaluate the use of titanite as an indicator mineral for W skarn exploration.

¹Waterloo, Ontario Canada, N2L 3G1, rlinnen@uwaterloo.ca

²Nanjing 210093, China

INTRODUCTION

Tungsten skarns have long been an important deposit type in Yukon, but exploration for these deposits is challenging because barren skarns may lie metres or even centimetres from strongly mineralized skarn. A potential solution to this problem is to use an indicator mineral, *i.e.*, a mineral that indicates that the skarn system is mineralized even though a particular sample or drill core intersection is not. Indicator minerals may be used as vectors for mineralization, at the deposit scale as well as for regional exploration. An ideal indicator mineral should: 1) be resistant to chemical weathering; 2) have a high enough density so that it is concentrated in sediments and can be separated from stream sediment or soil samples, and; 3) have high concentrations of elements that are uniquely associated with mineralization. Preferably the indicator element and the commodity of interest are the same, *i.e.*, W for W skarn deposits, but this is not the case for diamond exploration and thus it is not a necessity.

The most suitable indicator minerals for W deposits are likely to be titanium-rich minerals, notably titanite, rutile and ilmenite. This is because the ionic radii of W and Ti are similar: in six-fold coordination the ionic radius of Ti^{4+} is 0.605 Å, whereas W^{4+} , W^{5+} and W^{6+} are 0.66, 0.62 and 0.60 Å, respectively (Shannon, 1976). Other elements that substitute for Ti^{4+} are Nb^{5+} and Ta^{5+} , both with an ionic radius of 0.64 Å, Sn^{4+} , 0.69 Å, Zr^{4+} , 0.72 Å and Sb^{5+} , 0.60 Å. Rutile has long been considered to have potential as an indicator mineral (Williams and Cesbron, 1977) and has been the focus of recent studies (e.g., Scott and Radford, 2007), but because of the calcareous host rocks in skarn deposits titanite is generally the main titanium phase.

High concentrations of various high field strength elements have been observed in titanite from a number of different environments. Complete solid solution has been observed between titanite [$CaTiSiO_5$] and malayaite [$CaSnSiO_5$] (Takenouchi, 1971) and thus it is not surprising that high concentrations of Sn can be present in titanite. For example, titanite from the Mt. Lindsay Sn-W skarn contains up to 9.26% SnO_2 (Kwak, 1983). Titanites from this deposit also contain 1300 ppm WO_3 , although the tungsten contents are variable and range down to below the detection limit for the electron microprobe. Elsewhere, up to 3.7% Ta_2O_5 and 6.5% Nb_2O_5 have been observed in titanite from a Manitoba pegmatite (Groat *et al.*, 1985). Highly evolved alkaline rock can also contain high concentrations of Nb_2O_5 (up to 7.3%), ZrO_2 (up to 2.8%)

and REE_2O_3 (up to 3.9%) (Hode Vuorinen and Halenius, 2005). Consistent with these observations are the experiments of Tiepolo *et al.* (2002) and Prowatke and Klemme (2005) which show that Y, REE, Nb, Ta and Zr all partition strongly in favour of titanite over a coexisting melt (W data are lacking). As a result magmatic titanite, even from barren intrusions, can contain hundreds to several thousand ppm Nb (Piccoli *et al.*, 2000; Hoskin *et al.*, 2000).

OVERVIEW OF THE DEPOSITS INVESTIGATED

Samples from three tungsten skarn deposits were collected in the summer of 2008. Samples from the Risby deposit were obtained from the YGS core library; eight samples were taken from drillholes 80-40 and 80-41. The Ray Gulch deposit was also sampled from cores stored at the YGS core library; 14 samples were taken from drillholes 80-46, 80-51, 80-53, 80-54, 80-57, 80-58, 80-60 and 80-61. In the summer of 2008, samples from the Mactung deposit were collected by Lara Lewis from surface exposures of the upper and lower skarn zones. Two other deposits of note, but not examined in this preliminary study, are the Cantung tungsten skarn, located in the Northwest Territories at the Yukon border and the Logtung (Northern Dancer) W-Mo stockwork deposit (Fig. 1).

The Risby deposit is located southwest of the Tintina fault in the Cassiar Terrane. The mineralization is hosted by limestones of the Lower Cambrian Rosella assemblage, associated with a mid-Cretaceous quartz monzonite pluton of the Cassiar Suite (Yukon MINFILE 105F 034). The most recent grade and tonnage estimate for the deposit is 8.5 Mt of 0.475% WO_3 (Desautels, 2009). The Ray Gulch deposit contains 5.31 Mt of 0.39% WO_3 (Yukon MINFILE 106D 027). The mineralization is associated with the mid-Cretaceous Dublin Gulch intrusion and is hosted by Neoproterozoic to Early Cambrian Hyland Group metasedimentary rocks (Brown *et al.*, 2002). The deposit occurs within a hornfelsed roof pendant. Tungsten grade is proportional to the pyroxene content of the skarn and the pyroxene is iron-rich (*op. cit.*). The Mactung deposit contains 33.029 Mt of 0.88% WO_3 (MINFILE 105O 002). It is associated with an Upper Cretaceous quartz monzonite stock that intruded lower Paleozoic carbonate rocks (Dick and Hodgson, 1982). The mineralization is associated with pyroxene skarn, particularly where pyrrhotite is also abundant.

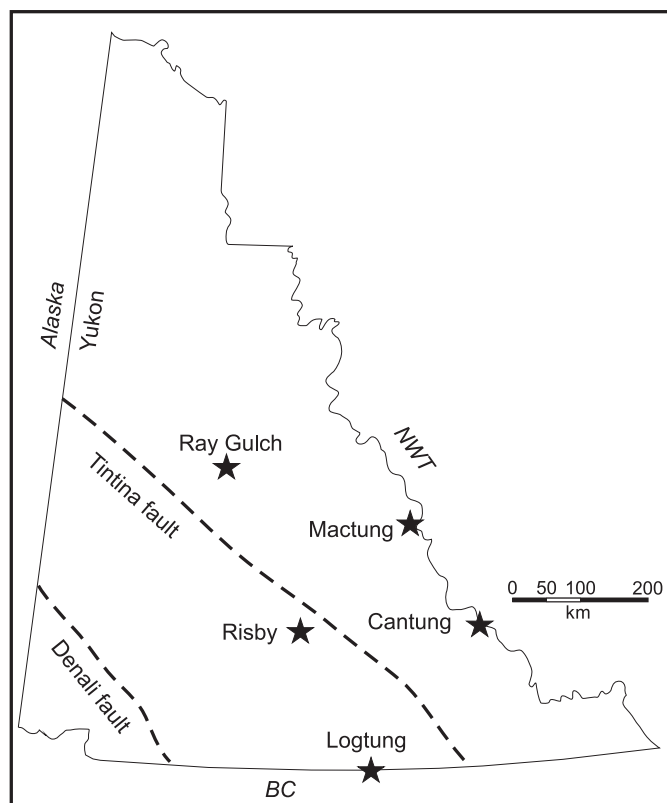


Figure 1. Location of tungsten deposits in the Yukon and adjacent portions of the Northwest Territories.

In all three of these deposits, tungsten mineralization occurs as disseminated scheelite in garnet-clinopyroxene-pyrrhotite skarn. Titanite is also an accessory phase in each of these deposits and forms part of the prograde, anhydrous skarn assemblage. This titanite is subhedral to euhedral, typically 200 μm to 1 mm across (Fig. 2a). The occurrence of titanite in the associated igneous rocks is less clear. In some cases, titanite is euhedral and is intergrown with other magmatic phases, yet even in these cases hydrothermal minerals are typically close by and it is possible that titanite is also a secondary phase in these rocks (Fig. 2b).

ANALYTICAL RESULTS

Titanite from both skarn and igneous samples were analysed on a Cameca SX50 electron microprobe at the University of Toronto. The operating conditions were 20 kV, 65 nA, a 1 μm beam size and counting times ranged from 20 to 60 seconds. Elements analysed were SiO_2 , TiO_2 , Al_2O_3 , Fe_2O_3 , CaO , F , MnO , ZrO_2 , Nb_2O_5 , Y_2O_3 , Ce_2O_3 , Ta_2O_5 , WO_3 , MoO_3 , SnO_2 and Yb_2O_3 . The

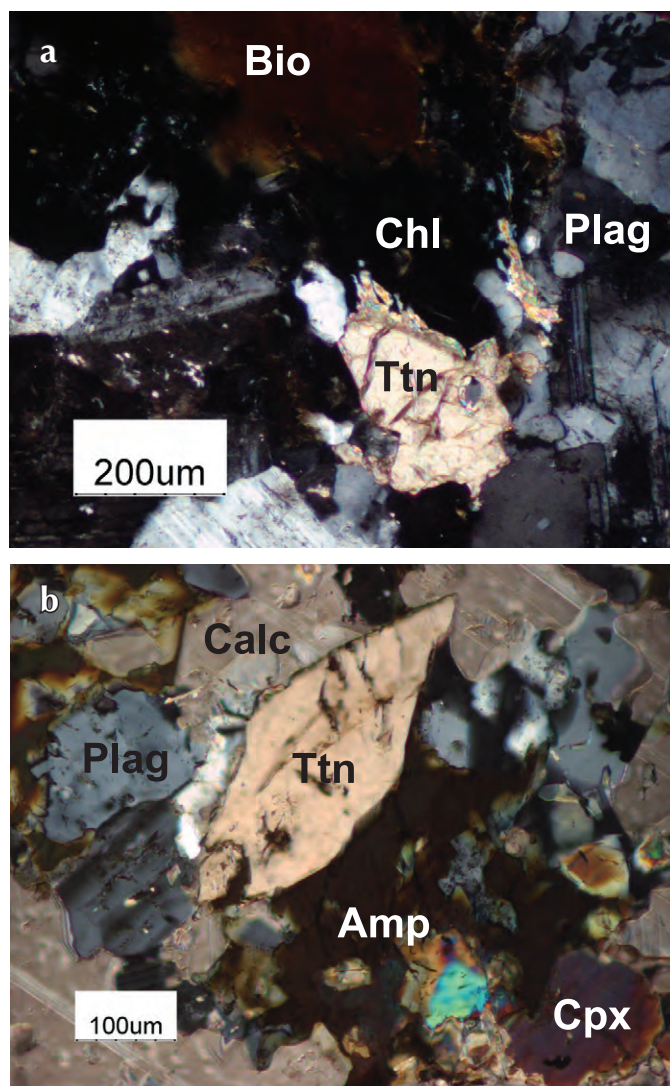


Figure 2. Photomicrographs of titanite from the Ray Gulch deposit (a) from associated granodiorite intrusion (b) from scheelite-bearing skarn. The abbreviations are Amp = amphibole, Bio = biotite, Calc = calcite, Cpx = clinopyroxene, Chl = chlorite, Plag = plagioclase and Ttn = titanite.

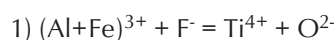
detection limits for the trace elements range from 20 to 50 ppm. Average and maximum values of the most useful elements are reported in Table 1. Of particular note are the fluorine contents of skarn titanite, which have averages that range from 1.25 to 1.72 wt% F (Table 1). To date, the only titanites from igneous rocks that have been analysed are from Ray Gulch, but these have distinctly lower F contents in comparison to the associated skarn. Skarn titanite can contain thousands of ppm of REE, Zr and Nb, but considering that these elements are

Table 1. Average and maximum trace element contents in titanite. Analyses where the average or maximum value is less than the detection limit is denoted by '-'.

Deposit	F avg	F max	ZrO ₂ avg	ZrO ₂ max	Nb ₂ O ₅ avg	Nb ₂ O ₅ max	Y ₂ O ₃ avg	Y ₂ O ₃ max	Ce ₂ O ₃ avg	Ce ₂ O ₃ max
Risby skarn	1.46	3.17	0.10	0.32	-	0.10	0.11	0.29	0.06	0.31
Ray Gulch skarn	1.25	1.53	0.27	0.92	-	d.l.	0.19	0.44	0.08	0.18
Ray Gulch igneous	0.75	1.04	0.09	0.59	-	1.64	0.39	2.31	0.12	0.43
Mactung skarn	1.72	1.89	0.05	0.07	-	0.07	0.42	0.47	-	-
Deposit	Ta ₂ O ₅ avg	Ta ₂ O ₅ max	WO ₃ avg	WO ₃ max	SnO ₂ avg	SnO ₂ max	Yb ₂ O ₃ avg	Yb ₂ O ₃ max		
Risby skarn	-	0.07	-	0.07	0.06	0.20	-	-		
Ray Gulch skarn	-	0.05	-	0.06	0.09	0.18	-	-		
Ray Gulch igneous	-	0.50	-	0.04	0.03	0.13	-	-		
Mactung skarn	-	0.09	-	-	0.27	0.32	-	-		

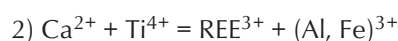
compatible in this phase, these values are not particularly high. The Sn contents are also not extraordinarily high, but these values are nevertheless anomalous and the Sn content of titanite may have potential as an indicator for W skarn. Tungsten is below the detection limit of most analyses, but a maximum of 700 ppm WO₃ was observed.

The substitution mechanisms for titanite are examined in Figure 3. The stoichiometry of titanite was calculated assuming five equivalent oxygen atoms per formula unit and all iron as Fe³⁺. Figure 3a shows a negative correlation between titanium and all of the elements that substitute in the titanium site. However, this does not show which coupled substitution mechanisms are important. Figure 3b shows Al + Fe³⁺ versus F. If the substitution reaction is



then the data on Figure 3b should have a slope of 1.0. There are two apparent trends on this diagram; the lower trend does have a slope of approximately 1.0, but an upper trend is also apparent. A possible explanation could be that the iron is actually ferrous instead of ferric, but a similar diagram results if Al is plotted against F. Two separate trends are also observed when Fe is plotted against Sn+Nb+Ta, the elements of economic interest that are above the detection limit (Fig. 3c). The strong negative correlation between Ti and F (Fig. 3d) indicates that the substitution is dominantly by reaction 1, however the scatter must be caused by another reaction. A

potential explanation could include coupled substitution involving the Ca site, such as



This exchange should result in a slope of -1 on Figure 3e and the data on this figure do vary with a slope of nearly -1.

DISCUSSION AND FUTURE WORK

The titanites from skarn deposits in the Yukon display substitution mechanisms similar to what have been observed elsewhere. With more data it should be possible to distinguish skarn from igneous sources, although the major elements will not discriminate barren from mineralized systems. The most promising indicator element is Sn, but its abundance in most of the samples is near the detection limit of the electron microprobe. Consequently, future analyses will be carried out using laser ablation ICP-MS, so that accurate data on metal concentrations at the ppm level, particularly for W, can be determined.

ACKNOWLEDGEMENTS

We are grateful for the assistance provided by Lara Lewis in sampling from the core library and in obtaining samples from the Mactung deposit. We also benefited from discussion with Lee Groat and Allison Brand on different aspects of tungsten skarns.

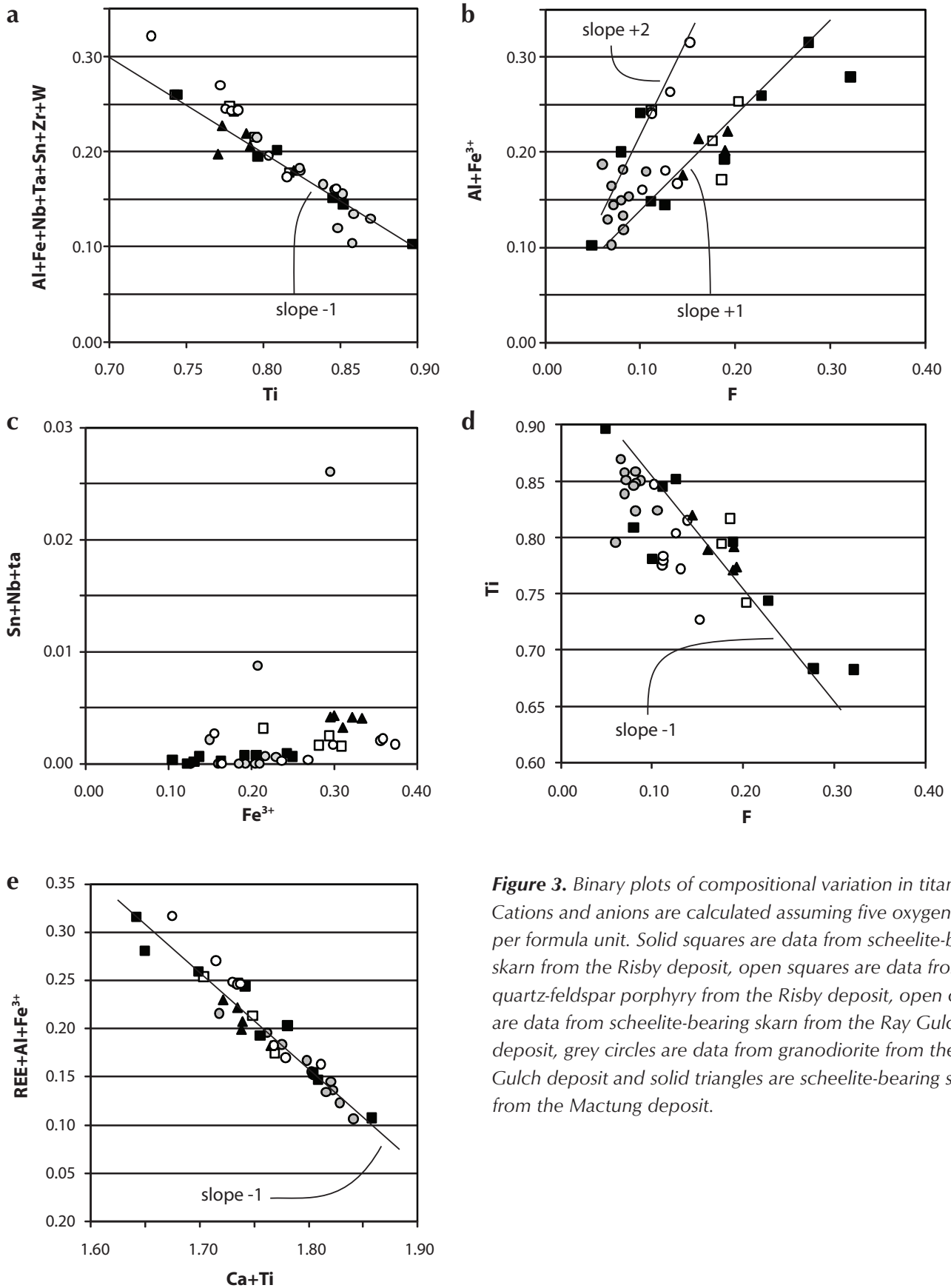


Figure 3. Binary plots of compositional variation in titanite. Cations and anions are calculated assuming five oxygen atoms per formula unit. Solid squares are data from scheelite-bearing skarn from the Risby deposit, open squares are data from quartz-feldspar porphyry from the Risby deposit, open circles are data from scheelite-bearing skarn from the Ray Gulch deposit and grey circles are data from granodiorite from the Ray Gulch deposit and solid triangles are scheelite-bearing skarn from the Mactung deposit.

REFERENCES

- Brown, V.S., Baker, T. and Stephens, J.R., 2002. Ray Gulch tungsten skarn, Dublin Gulch, central Yukon: Gold-tungsten relationships in intrusion-related ore systems and implications for gold exploration. *In*: Yukon Exploration and Geology 2001, D.S. Emond, L.H. Weston and L.L. Lewis (eds.), Exploration and Geological Services Division, Yukon Region, Indian and Northern Affairs Canada, p. 259-268.
- Desautels, P., 2009. Risby deposit, Yukon, Technical Report Update. Unpublished Playfair Mining Ltd. Report. 35 p. <http://www.playfairmining.com/i/pdf/2009_Playfair_Risby_Resource.pdf>
- Dick, L.A. and Hodgson, C.J., 1982. The MacTung W-Cu(Zn) contact metasomatic and related deposits of the northeastern Canadian Cordillera. *Economic Geology*, vol. 77, no. 4, p. 845-867.
- Groat L.A., Carter, R.T., Hawthorne F.C. and Ercit T.S., 1985. Tantalum niobium titanite from the Irgon claim, southeastern Manitoba. *The Canadian Mineralogist*, vol. 23, no. 4, p. 569-571.
- Hode Vuorinen, J. and Halenius, U., 2005. Nb-, Zr- and LREE-rich titanite from the Alnö alkaline complex: Crystal chemistry and its importance as a petrogenetic indicator. *Lithos*, vol. 83, p. 128-142.
- Hoskin P.W.O., Kinny P.D., Wyborn D. and Chappell B.W., 2000. Identifying accessory mineral saturation during differentiation in granitoid magmas: An integrated approach. *Journal of Petrology*, vol. 41, no. 9, p. 1365-1396.
- Kwak, T.A.P., 1983. The geology and geochemistry of the zoned, Sn-W-F-Be skarns at Mt. Lindsay, Tasmania, Australia. *Economic Geology*, vol. 78, no. 7, p. 1440-1465.
- Piccoli P., Candela P.A. and Rivers M., 2000. Interpreting magmatic processes from accessory phases: titanite - a small-scale recorder of large-scale processes. *In*: 4th Hutton Symposium, Transactions of the Royal Society of Edinburgh, B. Barbarin, W.E. Stephens, B. Bonin, J.-L. Bouchez, D.B. Clarke, M. Cuney and H. Martin (eds.), *Earth Science*, vol. 91, p. 257-267.
- Prowatke S. and Klemme S., 2005. Effect of melt composition on the partitioning of trace elements between titanite and silicate melt. *Geochimica et Cosmochimica Acta*, vol. 69, issue 3, p. 695-709.
- Shannon R.D., 1976. Revised effective ionic radii and systematic studies of interatomic distances in halides and chalcogenides. *Acta Crystallographica*, vol. A32, p. 751-767.
- Scott, K.M. and Radford, N.W., 2007. Rutile compositions at the Big Bell Au deposit as a guide for exploration. *Geochemistry: Exploration, Environment, Analysis*, vol. 7, no. 4, p. 353-361.
- Takenouchi, S., 1971. Hydrothermal synthesis and consideration of the genesis of malayaite. *Mineralium Deposita*, vol. 6, no. 4, p. 335-347.
- Tiepolo M., Oberti R. and Vannucci R., 2002. Trace-element incorporation in titanite: constraints from experimentally determined solid/liquid partition coefficients. *Chemical Geology*, vol. 191, p. 105-119.
- Williams S. A. and Cesbron F. P., 1977. Rutile and apatite: Useful prospecting guides for porphyry copper deposits. *Mineralogical Magazine*, vol. 41, p. 288-292.
- Yukon MINFILE, 2009 - A database of mineral occurrences. Yukon Geological Survey <http://www.geology.gov.yk.ca/databases_gis.html>.

Pressure-depth relationships of the Roop Lakes Stock and Keno Hill Ag-Pb-Zn veins

*Greg Lynch*¹

Consulting Geologist, Calgary Alberta

Lynch, G., 2010. Pressure-depth relationships of the Roop Lakes Stock and Keno Hill Ag-Pb-Zn veins. *In: Yukon Exploration and Geology 2009*, K.E. MacFarlane, L.H. Weston and L.R. Blackburn (eds.), Yukon Geological Survey, p. 229-235.

ABSTRACT

Key mineral assemblages help determine pressure, temperature and depth of emplacement for mineralized veins of the Keno Hill district, as well as for local Cretaceous pluton emplacement. New electron microprobe analyses are presented on samples collected in the field, enabling further characterization of the hydrothermal and plutonic regimes. Staurolite-garnet-albite-biotite schist along the margins of the Cretaceous Roop Lakes stock record contact metamorphic conditions, averaging 518°C and 3450 bar. To the west, hydrothermal veins of the Keno Hill district containing pyrite-pyrrhotite-sphalerite-arsenopyrite, indicate hydrothermal conditions of approximately 400°C and 1500 bar. Lithostatic conditions for the pluton, and likely hydrostatic conditions for the veins, are interpreted to indicate a similar depth of emplacement for the two systems, near 10-13 km below the surface.

¹tglynch@telusplanet.net

INTRODUCTION

The Roop Lakes stock (Roots, 1997; also known as the Mayo Lake pluton, Boyle 1965; Green, 1971) is the largest exposed granitic body of the Tombstone Plutonic Suite. It occurs at the eastern extremity of the west-trending string of plutons spanning 220 km across central Yukon. The stock is elliptical in shape, measuring 8 km wide and 20 km long (Fig. 1). The granitic body features a coarse porphyritic core and a medium to fine-grained margin. As with many of the plutons from the Tombstone Suite (e.g., Poulsen *et al.*, 1997), the Roop Lakes stock has a well-developed contact metamorphic aureole, overprinting the tectonic fabric. Contact metamorphic minerals such as andalusite and staurolite place upper and lower limits, respectively, on pressure (e.g., Lynch, 1989a,b). However, acquisition of new electron microprobe data on selected minerals, combined with mineral equilibrium data and software (TWEEQ, Berman 1991), allow for a quantitative determination of pressure and temperature. Similarly, in the veins of the Keno Hill district (Fig. 1), the key assemblage of sphalerite-pyrite-pyrrhotite-arsenopyrite is a useful barometer/thermometer as described from other districts by Lynch and Mengel

(1995) and Lentz (2002). Although sphalerite and pyrite are widespread, pyrrhotite is restricted to the central portion of the vein system between Keno Hill and Galena Hill, and is one of the diagnostic minerals in the definition of separate broad mineral zones (Lynch, 1989a,b). Previous determinations of pressures for the vein systems were made from CO₂-bearing fluid inclusions (Lynch, 1989b), and temperatures have been established from fluid inclusions, as well as from tetrahedrite composition (Sack *et al.*, 2003). These data provide a basis for comparison with the results presented here. Although methods for determining temperature in vein systems are relatively common, the means for pressure determinations are rare, and the assemblage of coexisting sphalerite-pyrite-pyrrhotite-arsenopyrite provides an opportunity to determine pressure and temperature. Furthermore, establishing pressures for the Mayo Lake Pluton and the Keno Hill vein system will contribute to investigating possible links between pluton emplacement and hydrothermal circulation. To this end, a basic understanding of the differences between hydrostatic and lithostatic pressure-depth relationships are required, and presented in the discussion.

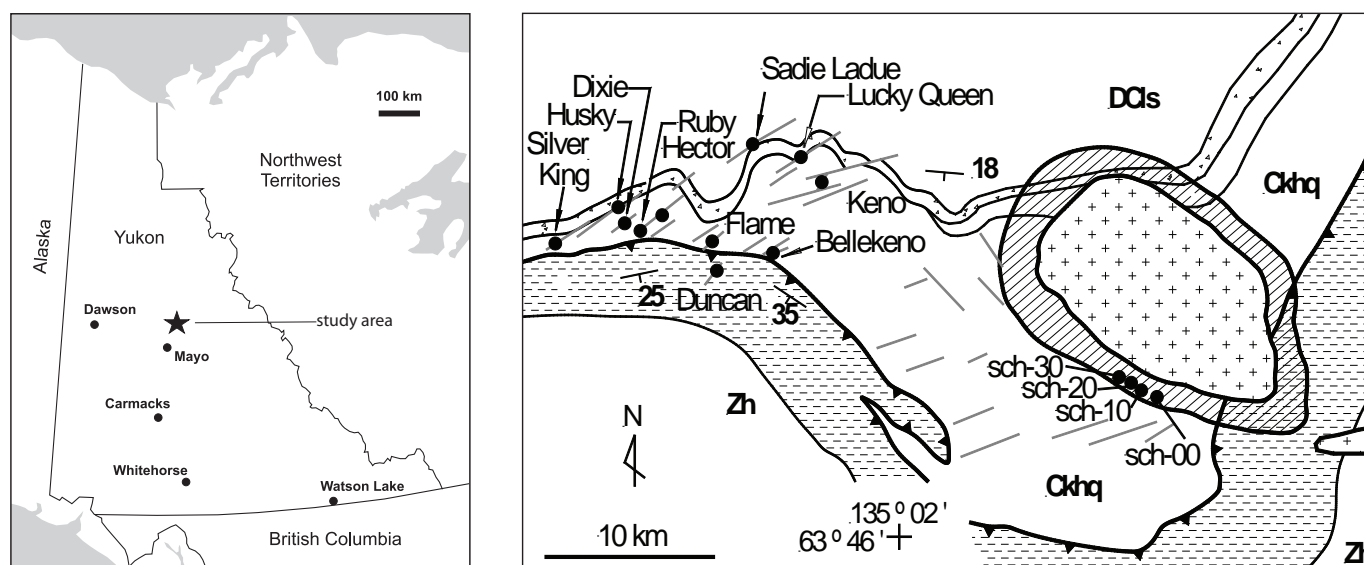


Figure 1. Location map of sample sites from the Keno Hill district and from the margin of Roop Lakes stock. Thick grey lines are fracture systems and fault planes containing hydrothermal assemblages and mineralization. Stratigraphy includes the Devonian-Carboniferous Lower Schist unit (DCIs); the graphitic Keno Hill Quartzite of Carboniferous age (Ckhq); as well as Neoproterozoic to Cambrian units of the Hyland Group (Zh) including the Upper Schist unit patterned with the horizontal dashed motif. Units dip moderately to the south and the Robert Service thrust bounds the top of the Keno Hill Quartzite. The Late Cretaceous Roop Lakes granitic pluton is a prominent crosscutting feature to the east and has a well-developed contact metamorphic aureole, shown here with the diagonal ruled pattern.

GEOLOGIC SETTING

Comprehensive descriptions of the regional geologic setting are contained in bulletin form by Murphy (1997) and Roots (1997), each of which include an extensive bibliography of previous work. The veins in both the Keno Hill district and the Roop Lakes stock crosscut, and are largely contained within, the Mississippian Keno Hill Quartzite unit (KHQ), which extends east-west for approximately 220 km along the northern edge of the Selwyn Basin (Tempelman-Kluit, 1970; Mortensen and Thompson, 1990; Gordey and Anderson, 1993). The region has been affected by late Jurassic to middle Cretaceous deformation, metamorphism and igneous activity (Roots, 1997). Strata dip generally south as a result of northerly thrusting (Murphy, 1997). The KHQ may be as much as 1 km thick where affected by imbrication and structural thickening. Lithologically the KHQ includes dark graphitic quartzite, calcareous quartzite, schist, graphitic phyllite and minor limestone, as well as tuffaceous metavolcanic rocks (Roots, 1997; Lynch, 2006). Granitic bodies of the Tombstone Plutonic Suite (e.g., Anderson, 1987) intrude the KHQ and include the Roop Lakes stock, which has been dated at 92.8 ± 0.5 Ma (Roots, 1997).

Mineralized veins of the Keno Hill district are described in a GSC Bulletin by Boyle (1965), and in a thesis by Lynch (1989b). Veins are controlled by a district-wide series of northeast-trending fractures and faults contained primarily, but not uniquely, within the KHQ and Triassic diorite sills.

CONTACT METAMORPHISM

Contact metamorphism forms a broad halo around the Roop Lakes stock, extending for as much as 1-2 km beyond the contact exposed at surface. Mineral growths associated with contact metamorphism are more strongly expressed in schist and graphitic schist units between quartzite beds of the KHQ. Contact metamorphism is zoned away from the stock and is also influenced by host lithology. Sillimanite-schist occurs in immediate contact with the chilled margin of the stock comprising medium to fine-grained equigranular granodiorite. Sillimanite occurs in medium-grained bundles with fine prismatic needles aligned along the rock fabric. The rock is light coloured and bleached of graphite. In contrast to this, andalusite-schist is black and graphitic, occurring further outboard from the stock. Andalusite is coarse grained; crystals are randomly oriented and the porphyroblasts give the rock a distinct knobby texture. Alkali-rich bedded

units, on the other hand, contain a more diverse mineralogical assemblage featuring garnet-staurolite schist with associated plagioclase, biotite and muscovite. Traces of ilmenite are also present. Micas are medium to coarse and have a weak preferential orientation, whereas garnet and staurolite porphyroblasts clearly overgrow the older rock fabric and appear to be largely post-kinematic with regards to deformation.

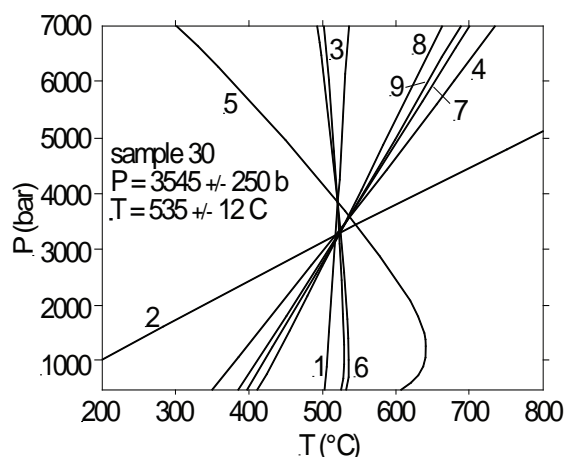
Staurolite-garnet schist was sampled at four different locations along the southwest margin of the stock for petrographic and electron microprobe analysis. Mineralogical data are presented in Table 1. The assemblage of garnet-staurolite-plagioclase-biotite-muscovite-quartz is ideal for metamorphic pressure-temperature determinations. Mineral equilibria data and software from Berman (1991; TWEEQ) was used to establish converging pressure-temperature intercepts for three independent reactions within the available mineral assemblage (Fig. 2). Results are shown in Figures 2 and 3. Pressure is estimated at between 2950-3830 bar, averaging 3440 ± 470 bar. Temperature is estimated at between 505° and 540°C , averaging $518^\circ \pm 22^\circ\text{C}$. These results occur near the upper stability limit of co-existing andalusite-sillimanite.

HYDROTHERMAL VEINS

In the Keno Hill district, mineralized veins are dominated by galena-sphalerite-tetrahedrite-pyrite, in a gangue of siderite and quartz. A number of accessory minerals are present and assemblages change, as well as the mineral compositions, according to position in the district (Lynch, 1989a,b). The full paragenesis is described in Boyle (1965) and Lynch (1989a,b). Pyrrhotite is an accessory mineral, which is restricted to the central portion of the regionally zoned hydrothermal system, including the Duncan, Flame and Moth veins situated between Keno Hill and Galena Hill. The presence of pyrrhotite defines the central mineral zone. Here, pyrrhotite is closely intergrown with the dominant sulphide assemblage of galena-sphalerite-pyrite-tetrahedrite, in addition to common arsenopyrite (Fig. 4). In general, pyrite and pyrrhotite may occur together under ideal conditions of temperature and sulphur fugacity. However, pyrrhotite is preferentially developed at higher temperatures, or when the sulphur content of mineralizing fluids diminishes. In the presence of pyrite and pyrrhotite, the iron content of sphalerite is pressure-dependant (e.g., Scott, 1983; Lynch and Mengel, 1995), whereas the As content of arsenopyrite is dependant on

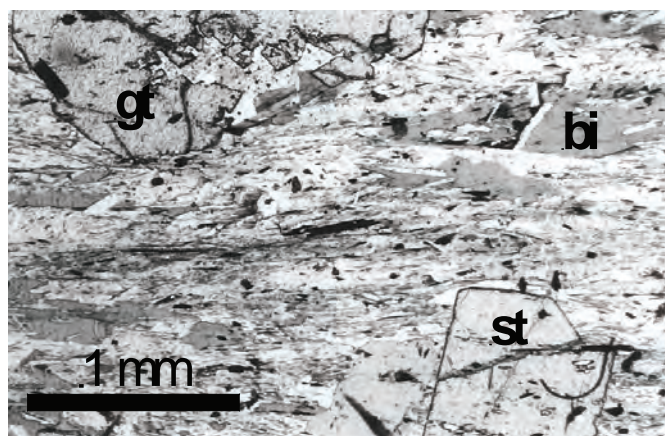
Table 1. Electron-microprobe data from metamorphic aureole. Values in wt%, averaged from five or more determinations.

SAMPLE	SiO ₂	TiO ₂	Al ₂ O ₃	FeO	MnO	MgO	CaO	Na ₂ O	K ₂ O	BAO	SRO	TOTAL
biotite-00	33.80	1.48	18.45	21.31	0.03	8.23	0.19	0.18	8.45	0.09	-	92.81
biotite-10	33.52	1.53	18.35	20.92	0.04	8.45	0.03	0.18	9.22	0.15	-	92.99
biotite-20	33.53	1.53	18.16	20.87	0.03	8.29	0.04	0.13	9.06	0.13	-	92.38
biotite-30	33.57	1.47	18.15	21.45	0.04	8.27	0.04	0.12	9.17	0.12	-	93.00
muscovite-00	45.63	0.27	33.92	1.17	0.00	0.72	0.04	1.12	9.76	0.27	-	93.18
muscovite-10	45.93	0.42	33.71	1.13	0.02	0.76	0.03	1.15	9.72	0.25	-	93.43
muscovite-20	45.65	0.25	33.36	1.16	0.04	0.75	0.02	1.15	9.75	0.34	-	92.79
muscovite-30	44.83	0.23	34.78	0.99	0.03	0.40	0.03	1.46	9.51	0.32	-	92.79
staurolite-00	33.37	1.46	18.16	21.45	0.03	8.51	0.16	0.11	8.47	0.16	-	92.55
staurolite-10	26.99	0.56	51.68	14.13	0.06	1.35	0.02	0.00	0.01	0.07	-	95.26
staurolite-20	27.27	0.51	51.79	14.04	0.10	1.36	0.02	0.00	0.00	0.05	-	95.63
staurolite-30	41.59	0.23	30.28	6.35	0.02	2.71	0.03	0.80	8.11	0.17	-	90.53
plagioclase-00	59.87	-	24.12	0.20	-	-	6.06	7.99	0.13	0.09	0.11	98.57
plagioclase-10	59.14	-	25.14	0.08	-	-	6.98	7.44	0.14	0.13	0.26	99.32
plagioclase-20	60.97	-	23.99	0.21	-	-	5.51	8.24	0.07	0.12	0.14	99.26
plagioclase-30	58.36	-	25.14	0.28	-	-	7.13	7.21	0.13	0.12	0.07	98.46
garnet-00	37.17	0.06	20.58	34.61	5.03	1.42	2.42	0.00	0.00	-	-	101.30
garnet-10	36.70	0.05	20.46	35.09	4.31	1.51	2.39	0.01	0.00	-	-	100.54
garnet-20	36.84	0.06	20.42	35.36	3.85	1.55	2.38	0.01	0.00	-	-	100.52
garnet-30	36.84	0.07	20.34	34.92	4.18	1.50	2.44	0.01	0.00	-	-	100.34
ilmenite-10	1.16	50.96	1.32	45.62	0.77	0.41	0.07	-	-	-	-	100.66
ilmenite-20	0.57	52.35	0.66	46.00	0.27	0.15	0.04	-	-	-	-	100.37
ilmenite-30	1.98	49.91	1.27	46.08	0.69	0.39	0.17	-	-	-	-	100.79



- 1): Alm + Phl = Py + Ann
- 2): Gr + Ms + Py = Phl + 3 An
- 3): 31 Py + 23 Ms + 8 Ann + 12 H₂O = 31 Phl + 48 aQz + 6 St
- 4): Ms + Gr + Alm = Ann + 3 An
- 5): 23 Ms + 31 Alm + 12 H₂O = 23 Ann + 48 aQz + 6 St
- 6): 23 Py + 23 Ms + 8 Alm + 12 H₂O = 23 Phl + 48 aQz + 6 St
- 7): 6 St + 48 aQz + 8 Ms + 31 Gr = 8 Ann + 93 An + 12 H₂O
- 8): 23 Gr + 8 Phl + 48 aQz + 6 St = 8 Py + 69 An + 8 Ann + 12 H₂O
- 9): 6 St + 48 aQz + 23 Gr = 8 Alm + 69 An + 12 H₂O

Figure 2. Example of pressure-temperature determination for staurolite-garnet schist in metamorphic halo of the Roop Lakes pluton. Series of equations here comprise three independent reactions, with best estimate equilibria indicating a pressure of 3514 ± 230 bar and $533^\circ \pm 11^\circ\text{C}$. Determinations were made using TWEEQ software and thermodynamic database of Berman (1991). Photomicrograph in plane polarized light displays staurolite and garnet porphyroblasts surrounded by, and overgrowing, a matrix of quartz, biotite and muscovite, with minor plagioclase. Reaction mineral abbreviations from Berman (1991).



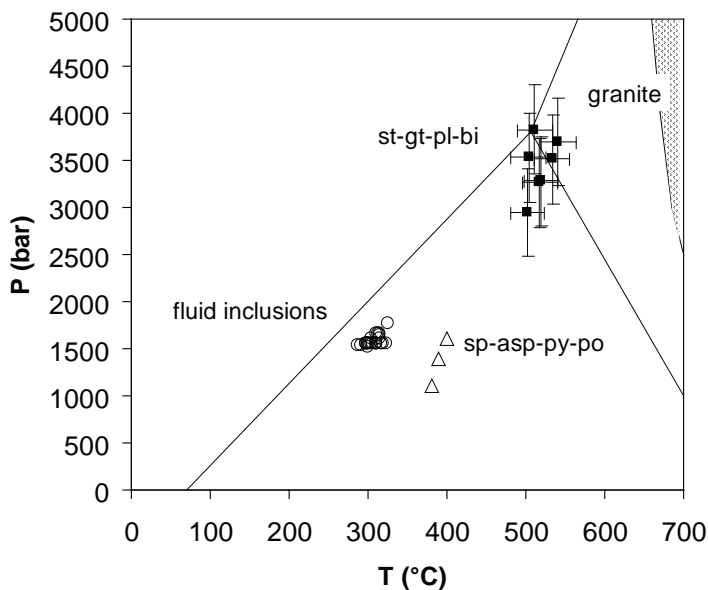


Figure 3. Pressure-temperature plot of data from Keno Hill district and metamorphic halo along margin of Roop Lakes pluton; staurolite-garnet schist (black squares) determinations occupy higher pressure and temperature domain approaching granite solidus; fluid inclusion determinations from paragenetically early vein quartz in the mining district (Lynch, 1989), shown as open circles; coexisting pyrite-pyrrhotite-sphalerite-arsenopyrite shown as open triangles. py = pyrite, sp = sphalerite, gt = garnet, asp = arsenopyrite, po = pyrrhotite.

temperature (Sharp *et al.*, 1985). A total of 156 spots on sphalerite were analysed in three samples, averaging 18.2 mole % FeS at Flame and Moth and 19.0 mole % FeS at Duncan (Fig. 5). These values translate to pressures of approximately 1.1 and 1.6 kilobar, respectively. Arsenopyrite thermometry from these samples is reported in Sack *et al.* (2003), indicating temperatures between 389° and 408°C (Fig. 5).

DISCUSSION AND CONCLUSIONS

This paper provides the first quantitative determinations of pressure and temperature for contact metamorphism along the Roop Lakes stock specifically, or for plutons of the Tombstone Suite in general. Pressure and temperature determinations on the other hand, have been made for mineralized veins using fluid inclusion techniques (Lynch, 1989b), as well as from tetrahedrite composition (Sack *et al.*, 2003). Results from veins and metamorphism are plotted together on the pressure-temperature graph of Figure 3. Fluid inclusion pressure determinations were obtained only from quartz which is early in the vein paragenesis relative to vein carbonate minerals. Quartz fluid-inclusion pressures overlap those from the sphalerite barometer, which together span 1100-1800 bar. Arsenopyrite temperatures are similar to those from tetrahedrite determinations (Sack *et al.*, 2003), which at near 400°C, are significantly higher than temperature

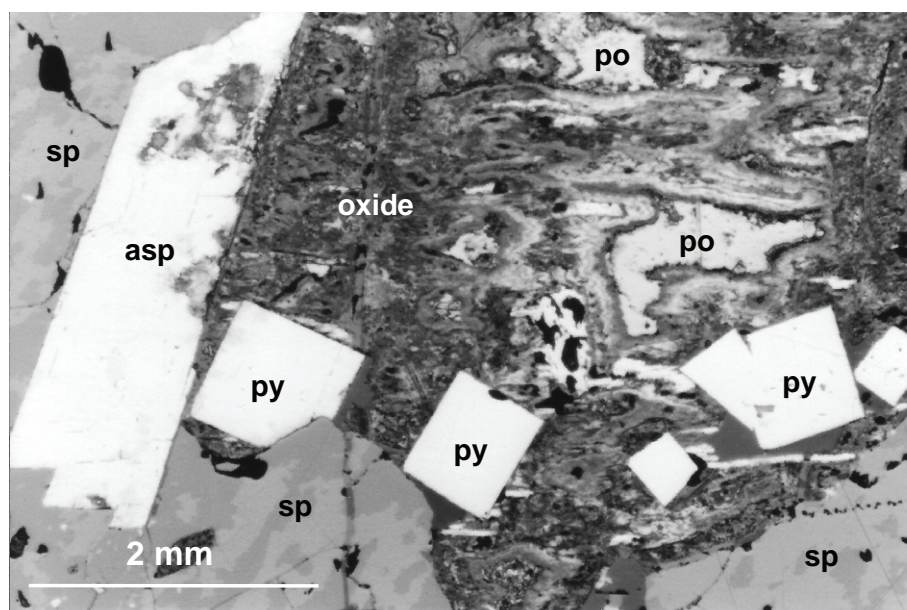


Figure 4. Reflected-light petrographic photograph of co-existing pyrite (py), sphalerite (sp), arsenopyrite (asp) and pyrrhotite (po); proportion of pyrrhotite is oxidized (oxide).

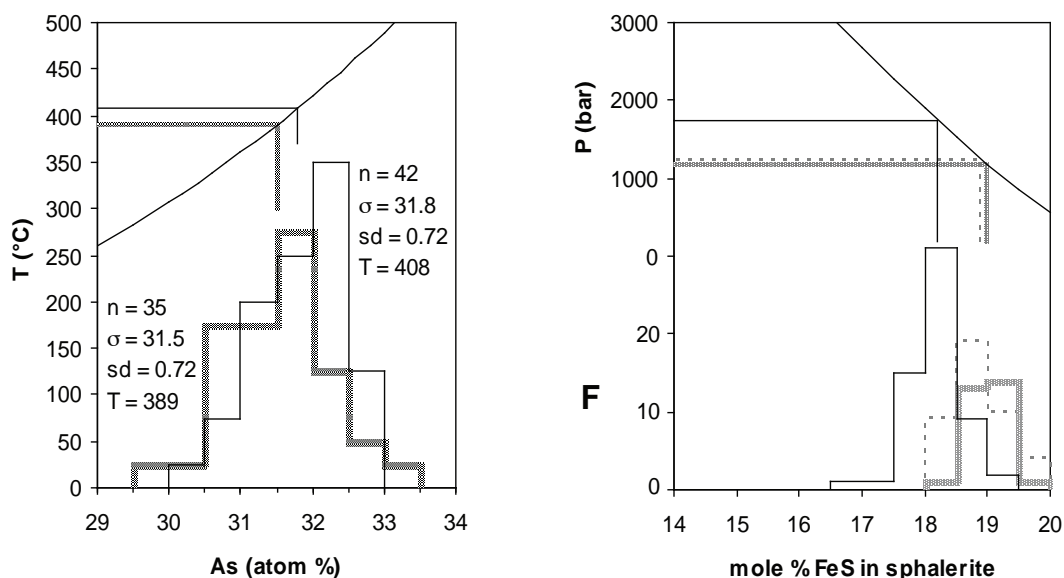


Figure 5. Histogram of microprobe analyses for arsenopyrite and sphalerite from Flame-Moth and Duncan veins in central Keno Hill district, from samples with co-existing sphalerite-arsenopyrite-pyrite-pyrrhotite.

determinations from fluid inclusions within quartz (Fig. 3) which are nearer to 300°C. Pressure and temperature determinations from contact metamorphism are significantly higher, near 3440 bar and 518°C.

Although there is a large difference between the absolute pressure of contact metamorphism and the pressure of the hydrothermal veins, there is no discrepancy once converted to depth, while taking into account differences in lithostatic versus hydrostatic gradients. Contact metamorphism occurs under lithostatic conditions whereas hydrothermal circulation takes place largely under hydrostatic conditions. At similar depths, hydrostatic pressures and lithostatic pressures are separated by a factor of three, approximately. Metamorphic minerals support the weight of the rock column, whereas hydrothermal fluids in pore space or along an open fault system support the weight of the water column. Observations from deep boreholes at several locations worldwide indicate that hydrostatic pore pressures typically persist to depths of as much as 12 km in the upper crust (Zoback and Townend, 2001). Transient overpressures in hydrothermal systems may increase up to a maximum of approximately 80% of the lithostatic pressure, at which point brecciation and pressure release will occur. However, hydrothermal pressures more typically approximate 37% of lithostatic pressure. Taking into account coexisting hydrostatic and lithostatic

conditions, the depth for the Roop Lakes stock and the veins of the Keno Hill district during sphalerite precipitation is estimated at approximately 10-13 km (Fig. 6).

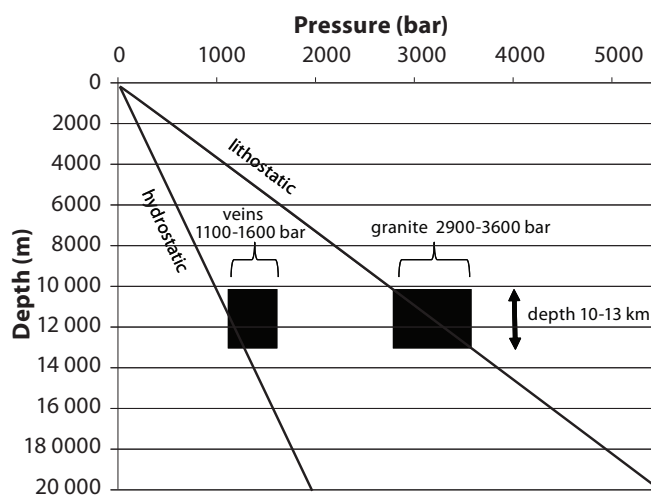


Figure 6. Interpreted pressure-depth plot for hydrostatic and lithostatic profiles for veins and metamorphism in Keno Hill district and Roop Lakes stock.

ACKNOWLEDGEMENTS

Support during early work (1985 to 1987) at Keno Hill was received from the Northern Affairs Program, and more recently, in 2005 from the Yukon Mining Incentives Program, to which I am grateful. Review and editing from Teresa Lynch and Karen MacFarlane are acknowledged.

REFERENCES

- Anderson, R.G., 1987. Plutonic rocks in the Dawson map area, Yukon Territory. *In: Current Research*, Geological Survey of Canada Paper 87-1A, p. 689-697.
- Berman, R.G., 1991. Thermobarometry using multi-equilibrium calculations: a new technique, with petrological applications. *Canadian Mineralogist* 29, p. 833-855.
- Boyle, R.W., 1965. Geology, Geochemistry and Origin, Lead-zinc-silver Deposits, Keno Hill-Galena Hill, Yukon Territory. Geological Survey of Canada, Bulletin 111.
- Gordey, S.P. and Anderson, R.G., 1993. Evolution of the Northern Cordilleran miogeocline, Nahanni map area (105I), Yukon and Northwest Territories. Geological Survey of Canada, Memoir 428, 214 p.
- Green, L.H., 1971. Geology of Mayo Lake, Scougale Creek and McQuesten Lake map areas, Yukon Territory (105M/15, 106D/2, 106 D/3). Geological Survey of Canada Memoir 357, 72 p.
- Lentz, D.R., 2002. Sphalerite and arsenopyrite at the Brunswick No. 12 massive-sulfide deposit, Bathurst camp, New Brunswick : constraints on P-T evolution. *The Canadian Mineralogist*, vol. 40, no. 1, p. 19-31.
- Lynch, J.V.G., 1989a. Large-scale hydrothermal zoning reflected in the tetrahedrite-freibergite solid solution, Keno Hill Ag-Pb-Zn district, Yukon. *The Canadian Mineralogist*, vol. 27, p. 383-400.
- Lynch, J.V.G., 1989b. Hydrothermal zoning in the Keno Hill Ag-Pb-Zn vein system: a study in structural geology, mineralogy, fluid inclusions and stable isotope geochemistry. PhD thesis, University of Alberta, Edmonton, Alberta, 219 pages.
- Lynch, 2006. Sediment-hosted disseminated gold occurrence, northeast Mayo Lake area. *In: Yukon Exploration and Geology 2005*, D.S. Emond, G.D. Bradshaw, L.L. Lewis and L.H. Weston (eds.), Yukon Geological Survey, p. 327-339.
- Lynch, G. and Mengel, F., 1995. Metamorphism of arsenopyrite-pyrite-sphalerite-pyrrhotite lenses, western Cape Breton Island, Canada. *The Canadian Mineralogist*, vol. 33, no. 1, p. 105-114.
- Mortensen, J.K., and Thompson, R.I., 1990. A U-Pb zircon-baddeleyite age for a differentiated mafic sill in the Ogilvie Mountains, west-central Yukon Territory. *In: Radiogenic Age and Isotope Studies, Report 3*, Geological Survey of Canada Paper 89-2, p. 23-28.
- Murphy, D.C., 1997. Geology of the McQuesten River Region, Northern McQuesten and Mayo, Yukon Territory (115P/14, 15, 16; 105 M/13, 14). Exploration and Geological Services Division, Yukon, Indian and Northern Affairs Canada, Bulletin 6, 122 p.; includes five 1:50 000 maps.
- Poulsen, K.H., Mortensen, J.K. and Murphy, D.C., 1997. Styles of intrusion-related gold mineralization in the Dawson-Mayo area, Yukon Territory. *In: Geological Survey of Canada, Current Research 1997-A*, p. 1-10.
- Roots, C.F., 1997. Geology of the Mayo map area, Yukon Territory (105 M). Exploration and Geological Services Division, Yukon Region, Indian and Northern Affairs Canada, Bulletin 7, 82 p.
- Sack, R.O., Lynch, J.V.G. and Foit, F., Jr., 2003. Fahlore as a petrogenetic indicator: Keno Hill Ag-Pb-Zn District, Yukon, Canada. *Mineralogical Magazine*, vol. 67, no. 5, p. 1023-1038.
- Scott, S.D., 1983. Chemical behaviour of sphalerite and arsenopyrite in hydrothermal and metamorphic environments. *Mineralogical magazine*, vol. 47, p. 427-435.
- Sharp, Z.D., Essene, E.J. and Kelly, W.C., 1985. A re-examination of the arsenopyrite geothermometer; pressure considerations and applications to natural assemblages. *The Canadian Mineralogist*, vol. 23, p. 517-534.
- Tempelman-Kluit, D.J., 1970. Stratigraphy and structure of the "Keno Hill Quartzite" in Tombstone River, Upper Klondike River map areas, Yukon Territory (116 B/7, B/8). Geological Survey of Canada, Bulletin 180, 102 p.
- Zoback, M.D. and Townend, J., 2001. Implications of hydrostatic pore pressures and high crustal strength for the deformation of intraplate lithosphere. *Tectonophysics*, vol. 336, p. 19-30.

Upper Fifteenmile Group in the Ogilvie Mountains and correlations of early Neoproterozoic strata in the northern Cordillera

F.A. Macdonald¹

Department of Earth and Planetary Sciences, Harvard University

C.F. Roots²

Geological Survey of Canada

Macdonald, F.A. and Roots, C.F., 2010. Upper Fifteenmile Group in the Ogilvie Mountains and correlations of early Neoproterozoic strata in the northern Cordillera. *In: Yukon Exploration and Geology 2009*, K.E. MacFarlane, L.H. Weston and L.R. Blackburn (eds.), Yukon Geological Survey, p. 237-252.

ABSTRACT

An ~2-km-thick stratigraphic section measured through three consecutive shale-carbonate sequences documents the previously undescribed upper Fifteenmile Group in the Coal Creek inlier. These descriptions provide the basis for correlation with Proterozoic strata of adjacent inliers in eastern Alaska, as well as in the eastern Ogilvie Mountains.

The lowest unit contains interbedded limestone and mudstone with distinctive maroon-weathering layers. Similar strata are present in unit D of the Pinguicula Group exposed in the Hart River inlier. In that area however, the middle sequence containing massive dolostone, that is the most prominent unit of the upper Fifteenmile Group, is missing beneath an angular unconformity. The Callison Lake dolostone is above this surface and is lithologically indistinguishable from the uppermost, stromatolitic carbonate of the upper Fifteenmile Group. Both the middle and upper dolostone units are preceded by black shale, indicating abrupt transgressions. In contrast, the carbonate units contain abundant evidence of shallow water and periodic emergence. We interpret the upper Fifteenmile Group to comprise three shallowing-upward cycles in this area.

¹Cambridge MA 02138, USA, fmacdon@fas.harvard.edu

²c/o Yukon Geological Survey, charlie.roots@gov.yk.ca

INTRODUCTION

The Proterozoic record in northwestern Cordillera is gleaned from the study of erosional windows through the covering Phanerozoic platform strata (herein called inliers), augmented by sparse geophysical information and rare drillhole information. Fortunately, three inliers in western Yukon and eastern Alaska provide considerable exposure of Proterozoic strata, although structural complexity and depositional hiatuses pose formidable challenges in deciphering the record. Since early recognition of analogous sequences in the inliers (e.g., Gabrielse, 1972; Eisbacher, 1978; Young *et al.*, 1979), correlation of units, particularly those with stratabound mineral potential, has been a principal goal in mapping and stratigraphic analysis. Improved understanding of sequence relationships, isotopic dates from volcanic zircons, and minimum ages determined from detrital zircons, have refined these correlations.

The Coal Creek inlier, located north of Dawson, Yukon, is under-studied by comparison to other Proterozoic

sequences in northwestern Canada (Rainbird *et al.*, 1996; Long *et al.*, 2008; Fig. 1). Although regional-scale maps portray their distribution (Thompson *et al.*, 1994), the Fifteenmile Group strata overlying the Wernecke Supergroup lack a detailed description. This report contains information on the lithologic sequence of the 'upper' Fifteenmile Group in the western part of the Coal Creek inlier (Fig.1). It complements recent papers on the geochronology and chemostratigraphy of the 'upper' Fifteenmile Group (Macdonald *et al.*, 2010). An outline of some units of the 'lower' Fifteenmile Group, and their correlation, is found in Medig *et al.* (this volume).

REGIONAL SETTING

The Coal Creek inlier, a mountainous 35 km x 70 km area, consists of dominantly sedimentary strata (Wernecke Supergroup, Fifteenmile Group and Mount Harper Group; Fig. 1) that are unconformably overlain to the east, north and west by Cambrian and younger platformal carbonate rocks (Slats Creek, Bouvette and overlying formations),

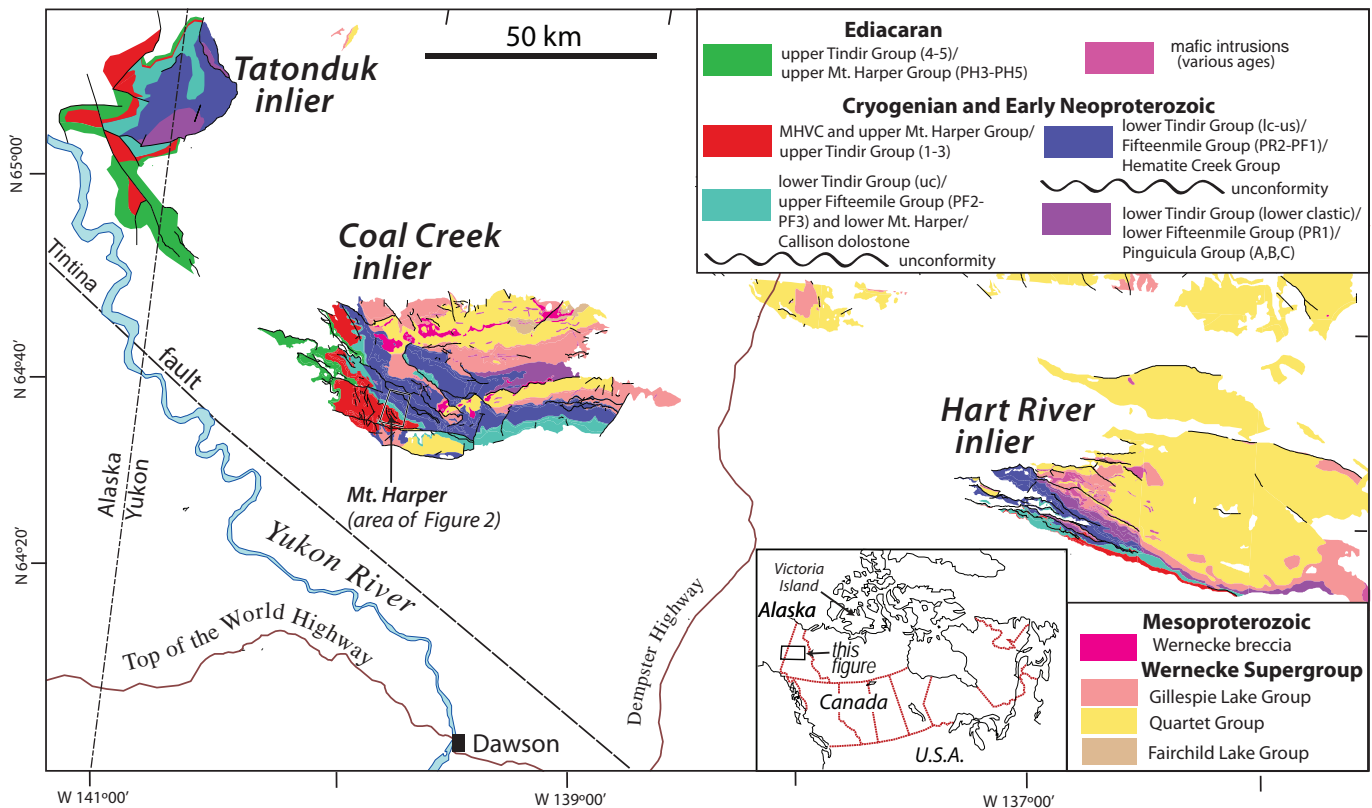


Figure 1. Distribution of Proterozoic rocks in west-central Yukon and adjacent Alaska. Modified from Gordey and Makepeace, 2003. Text in brackets represents unit designators by previous authors (see references listed on Figure 12; MHVC = Mount Harper volcanic complex).

and are truncated to the south by the Dawson fault. The older strata comprising the Fairchild Lake, Quartet and Gillespie Lake groups of the Wernecke Supergroup (e.g., Delaney, 1981; Thorkelson *et al.*, 2005) are exposed in variably tilted, fault-bounded blocks in the northern half of the outlier. Fifteenmile Group strata unconformably overlie these older units, and flank them mostly to the south and west. Overlying the Fifteenmile Group are conglomerate, bimodal volcanic rocks, diamictite and shale of the Mount Harper Group (Mustard and Roots, 1997).

FIFTEENMILE GROUP

Previous work on the Neoproterozoic strata of the Ogilvie Mountains was carried out during the course of regional mapping (Thompson *et al.*, 1987; Thompson *et al.*, 1994). The Fifteenmile Group (Roots and Thompson, 1992), named after Fifteenmile River, which drains the southern slope of the Ogilvie Mountains, was designated to distinguish these strata from those of the Tindir Group (Young, 1982), Pinguicula Group (Eisbacher, 1981; Thorkelson, 2000) and Mackenzie Mountains Supergroup (Gabrielse *et al.*, 1973). Recent geochronologic and chemostratigraphic studies on the Neoproterozoic rocks in the Coal Creek inlier have strengthened these correlations (Macdonald *et al.*, 2010; in press).

The Fifteenmile Group unconformably overlies rocks of the Wernecke Supergroup. It was separated into upper and lower subdivisions, and unit designations of the regional map by Thompson *et al.* (1994) are retained here, with the exception of the lowest unit, which we reassigned to PF1a (Fig. 2). The ‘lower’ Fifteenmile Group includes six map units (PR1a, PR1-PR5)³ which form alternating shale-dominated and dolostone-dominated successions (Thompson *et al.*, 1994). Direct age constraints on the lower Fifteenmile Group are lacking. Some units may be compared with strata in the Wernecke Mountains (e.g., Thorkelson *et al.*, 2005; Medig *et al.*, this volume). The ‘upper’ Fifteenmile Group consists of three thick packages of carbonate rocks separated by thinner siliciclastic units, with an interbedded argillite-dolostone sequence at the base (PF1a, PF1, PF2 and PF3; Thompson *et al.*, 1994). A tuff unit within the lower-most map unit of the upper Fifteenmile Group constrains the depositional

age to a maximum of 811.51 ± 0.25 Ma (Macdonald *et al.*, 2010; in press). A maximum age constraint on the upper Fifteenmile Group comes from a 717.43 ± 0.14 Ma quartzphyric rhyolite flow in the overlying Mount Harper volcanic complex (Macdonald *et al.*, 2010; in press).

LOWER CONTACT OF THE UPPER FIFTEENMILE GROUP

Stratigraphic relationships between the upper and lower Fifteenmile Group have been revised from the original interpretation of Thompson *et al.* (1994). The legend accompanying the open file maps by Thompson *et al.* (1994) indicates, below the upper Fifteenmile Group, a “disconformity, local angular unconformity over PR1”. In contradiction, the maps show PF1a in stratigraphic contact with PR5 (dominantly shale) and less commonly PR4 (dolostone breccia and dolostone). Thompson *et al.* (1994) interpreted the mafic sills, dykes, and the Wernecke Breccias, to have intruded the lower Fifteenmile Group, and that this intrusive event had ceased before deposition of the upper sediments. The presence of intrusive breccias in the lower Fifteenmile Group was subsequently disproved (Abbott, 1997; Thorkelson, 2000; Medig *et al.*, this volume). As in the Wernecke Mountains, only strata of the Wernecke Supergroup are intruded by these breccias, which formed at 1.6 Ga (Thorkelson *et al.*, 2005).

Our field observations suggest that the contact between PR5 and PF1a is conformable. Although an intrusive event has been disproved between the lower Fifteenmile and upper Fifteenmile strata, the separation between the shale-dominated (lower) and the carbonate-dominated (upper) parts is retained. Although gradational, the base of the upper Fifteenmile Group can be defined by the onset of widespread limestone deposition above PR5, in general accordance with Thompson *et al.* (1994; Fig. 2). However, this separation may be locally complicated by the presence of dolomite patch reefs within unit PR5.

MEASURED SECTION OF THE UPPER FIFTEENMILE GROUP

A composite section of the upper Fifteenmile Group was measured over three ridge-forming carbonate units separated by recessive shale units (Fig. 3; Table 1). The strata have a combined thickness of ~2 km and dip to the southwest (20° to 40°). The units are exposed with little change in thickness from Mount Harper eastward for 20 km along the southern edge of the Coal Creek inlier (Figs. 2, 3).

³All Coal Creek inlier units discussed in this paper are prefixed with a ‘P’ for Proterozoic following the convention of Thompson *et al.* (1994).

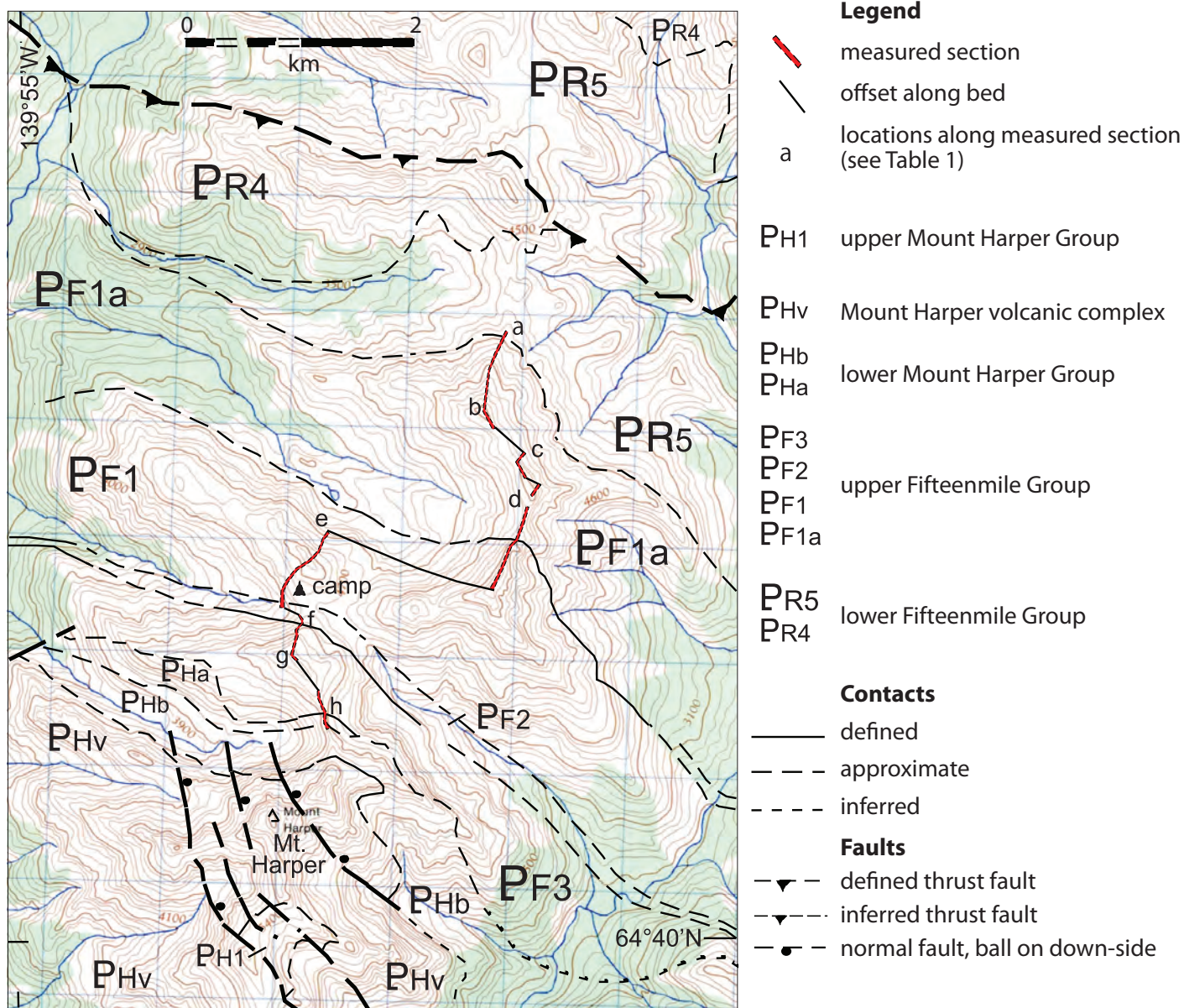


Figure 2. Distribution of geological units near Mount Harper with location of the measured section (line a-h), modified from Thompson et al. (1994). Letters correspond to endpoints along the composite stratigraphic section (see descriptions in Table 1 and Fig. 4).

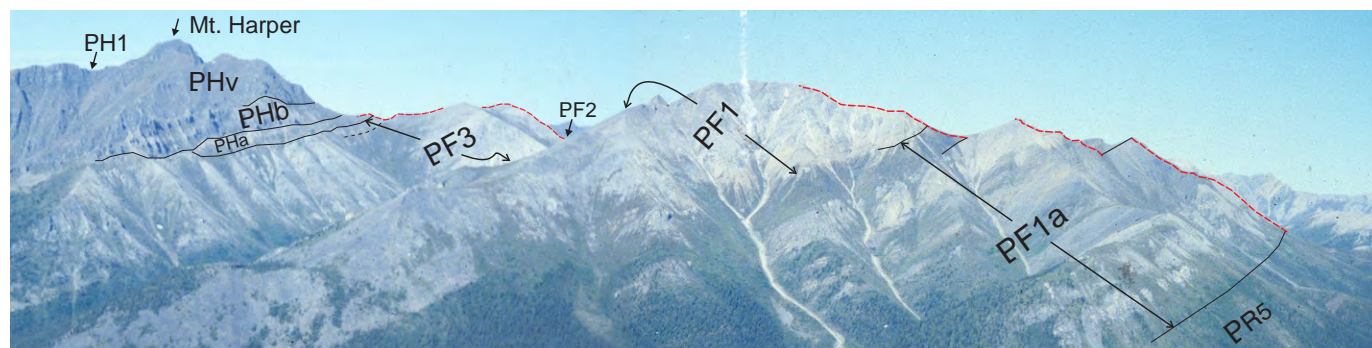


Figure 3. View northwestward of upper Fifteenmile Group strata. Field of view is 5 km.

Table 1. Locations of points along the measured composite stratigraphic section (Fig. 2) of the upper Fifteenmile Group (currently available topographic map 116B/12 (1971) is NAD 27, Zone 7W; contour intervals are 100 ft).

Site location	UTM_E	UTM_N	Description
a	555910	7176920	base of section on north-most spur; lowest limestone bed on south side of broad shale/siltstone saddle; elevation 4400'
b	555650	7176170	top of ridge; local highpoint; section continues south along crest
c	555985	7176030	section measurement offset to east-facing gully; elevation 5225'
d	556090	7175655	north end of saddle; black shale; elevation 5360'
e	554400	7175060	section measurement offset; start in north-facing gully; elevation 4360'
f	554180	7174350	top of weathered brown shale; base of carbonate in gully; elevation 4900'
g	554050	7174000	top of ridge; section continues along crest; elevation 5500'
h	554420	7173340	top of upper Fifteenmile/base of Lower Harper Group (see Mustard and Roots, 1997); saddle elevation 5100'

The lowest unit (PF1a) is 689 m thick. The second carbonate succession (PF1) is 611 m thick and is succeeded by the black shale interval (PF2) that is 111 m thick. The uppermost carbonate (PF3) is 338 m thick and overlain by polymictic conglomerate of the Lower Mount Harper Group (PHA; Mustard and Roots, 1997). The section is diagrammatically drawn in Figure 4.

In the stratigraphic measurement presented here we recognize five distinct facies that are associated with particular sedimentary environments. They include: 1) *rhythmite* - parallel-laminated carbonate mudstone, turbidite and debris flows deposited below storm wave-base in slope and basinal settings; 2) *ribbonite* - thin, wavy-bedded carbonate wackestone, siltstone and mudstone deposited deep in the sublittoral zone, above storm wave-base; 3) *stromatolites* - discrete columnar to rounded microbialites with >1 cm of synoptic relief that are commonly associated with edgewise conglomerates; 4) *grainstone* - a well-sorted, medium to thick-bedded carbonate sand with common crossbeds, deposited in the shallow sublittoral zone; and 5) *microbialaminite* - undulose and crinkly to fenestral lamination, with common intra-clast conglomerate and tepee structures, that formed subaerially in the littoral to super-littoral zone. In Figure 4, the terms *breccia* and *conglomerate* include the genetic terms of *debris flow*, *intra-clast breccia* and *edge-wise conglomerate*.

The base of the section was measured along a north-facing slope at the lowest carbonate bed above a broad saddle dominated by hackly dark brown-weathering mudstone (unit PR5; Fig.2). Evidence for an unconformity or thrust was not observed at the base of this unit.

Unit PF1a overlies PR5 and is dominantly limestone with ~15% dolostone, four sandstone beds 1-2 m thick, and several mudstone and breccia/conglomerate layers that are interpreted as debris flows, overlain by 65 m of black shale. The lowest 100 m of unit PF1a includes rhythmically bedded lime mudstone with local preservation of asymmetric ripples, and grades upward to ribbonite. Several units of metre-thick conglomerates, interpreted as debris flows, occur about 80 m above the base of the measured section. A 10-m covered interval obscures the stratigraphy immediately above the conglomerate units. The covered interval is believed to be black shale based on an overlying unit of limestone beds containing black chert nodules and lenses (Fig. 5). From 100 m to 190 m above the base of the measured section, light and medium grey-weathering zebra-textured dolostone (Vandeginste *et al.*, 2005) is exposed in several cliff bands. A medium-grained gabbro sill (2 m thick) occurs 190 m above the base of the measured section. Above the sill, dark grey-weathering limestone predominates, and beds increase in thickness with several rhythmite beds grading upward to ribbonite in metre-scale parasequences. A 20-m-thick, medium grey-weathering, platy limestone at 360 m in the section is succeeded by grainstone interbedded with rippled, nodular, organic-rich limestone. Molar tooth structures (James *et al.*, 1998) are a characteristic feature of the organic-rich limestone horizon at this location in the section and throughout the region (Fig. 6).

Between 409 m and 489 m above the base of the section, PF1a is characterized by alternating beige, green, grey and maroon-weathering marl, limestone and sandstone cycles that are 3 m to 5 m thick (Fig. 7). The colour and nodular

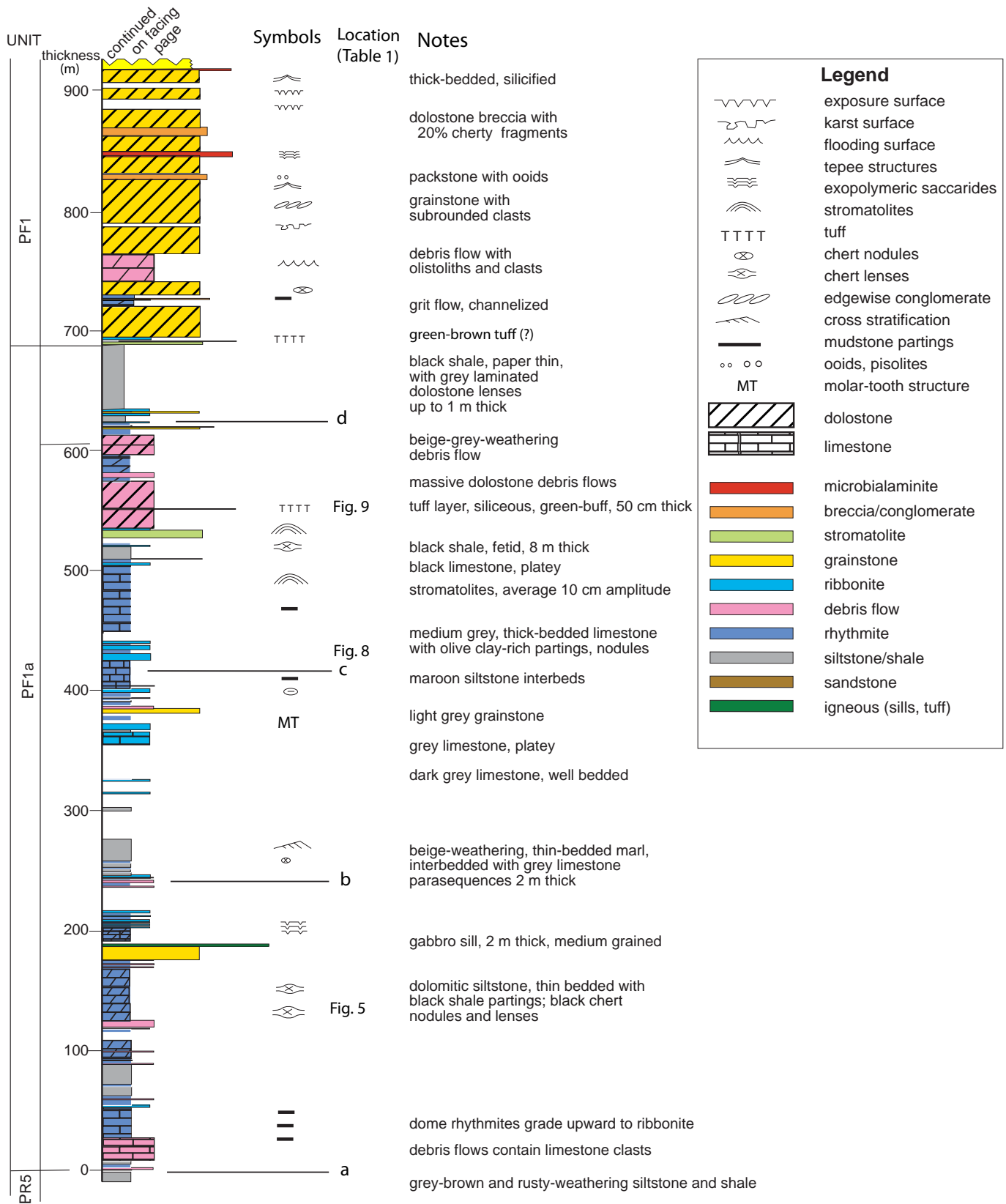


Figure 4. Diagrammatic stratigraphic section of upper Fifteenmile Group strata. Location column is keyed to Table 1 and figures.

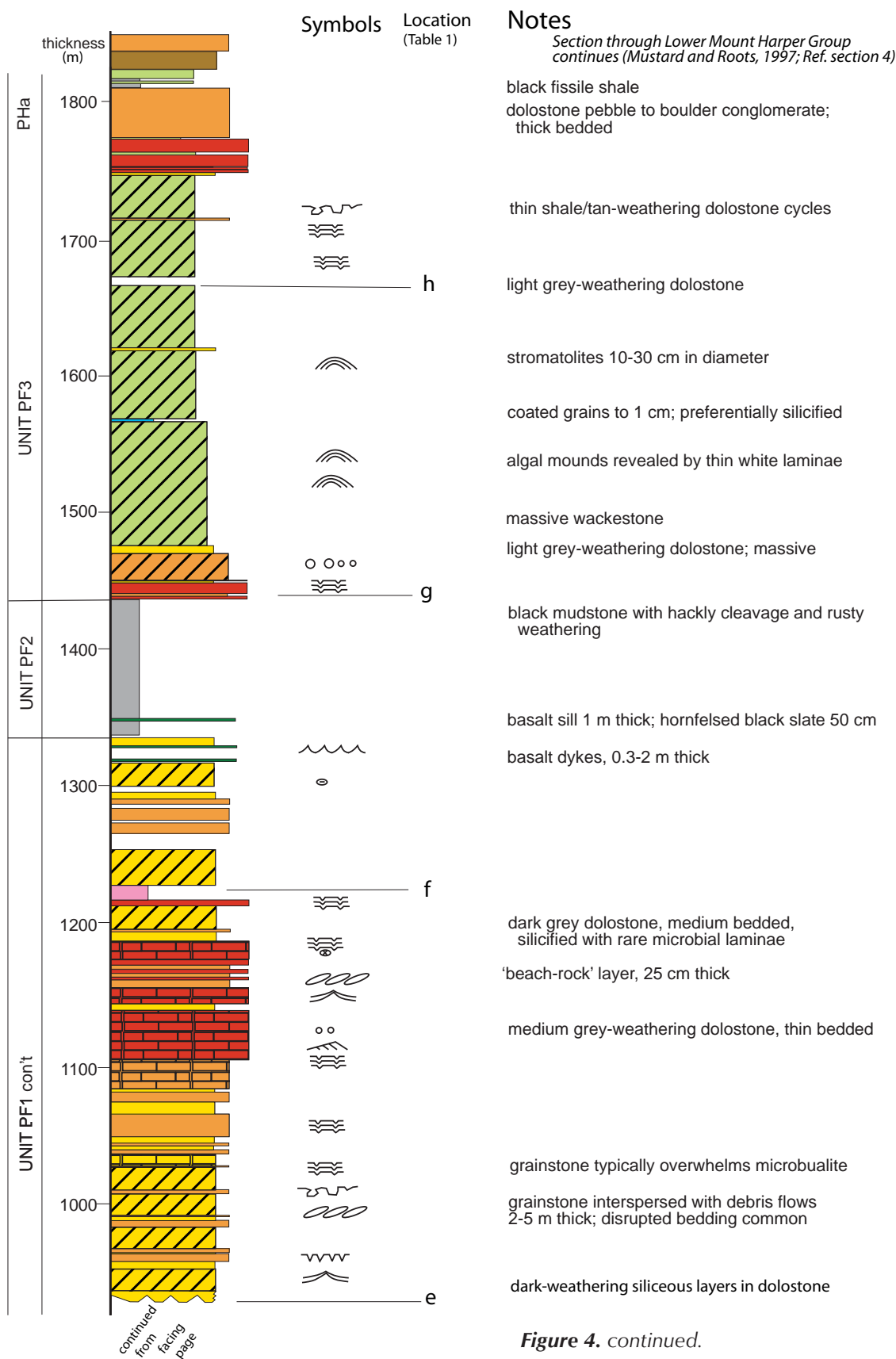


Figure 4. continued.

nature of these beds is distinctive and useful for regional correlation. Rhythmites are couplets of olive-coloured mudstone, intercalated with chert-nodular limestone (Fig. 8). The uppermost carbonate unit contains small



Figure 5. Chert nodules and swales in lime mudstone overlain by grey limestone; 132 m above the base of measured section.



Figure 6. Molar tooth structures in grey limestone of unit PF1a, 14 km north-northeast of Mount Harper (UTM 558000E 7186000N, elevation 4900').

branching stromatolites (2-5 cm in diameter) and has a humped upper surface overlain by pyritiferous black shale.

From 489 m to 560 m above the base of the section, exposure of PF1a is restricted to a ridge crest and includes grey-weathering limestone debris flows with minor carbonate beds containing black chert nodules. A light brown-weathering tuff horizon, situated 541.5 m above the base of the section, is 50 cm thick and occurs in a recessive gap between dolostone debris flows (Fig. 9a). It is cherty with faint brown streaks parallel to bedding. In thin section, the streaks define variations in the dust-sized particulate groundmass, and broken quartz grains (0.2 mm) are aligned with stratification (Fig. 9b). Zircon crystals were extracted from the tuff unit (Fig. 9c) and yielded a crystallization age of 811.51 ± 0.25 Ma (Macdonald *et al.*, in press).

Overlying the tuff unit is a thick interval of chaotically oriented blocks of centimetre-bedded rhythmite that are interpreted as debris flows. Above this, is a tan-weathering dolostone which is thinly interbedded with black shale. The top of unit PF1a consists of 65 m of black shale. Although monotonous, the shale exposed on the narrow ridge saddle, reveals at least three, beige-weathering lenses of dolostone with fenestral textures interpreted to be bioherms. The uppermost bioherm is draped by an unusual green-brown unit, ~25 cm thick. Although we interpreted this to be a volcanic tuff, it did not yield zircons.



Figure 7. View to the southeast of 80 m of well-layered upper part of unit PF1a (409-489 m above base of section). The brown-weathered intervals contain thin beds of maroon siltstone. Person circled for scale.



Figure 8. Rhythmites of limestone and lime mudstone, 461 m above base of section.

The surface expression of Unit PF1 (611 m thick) forms a dark grey, craggy-weathering mountain. The lower contact is sharp, with dolo-rhythmite beds conformably overlying the black shale of PF1a. The base of PF1 begins with three ~15-m-thick parasequences consisting of thin-bedded, flat-laminated dolo-rhythmite, succeeded by crossbedded grainstone. These parasequences are overlain by ~70 m of tabular clast breccia and graded grainstone beds, interpreted as mass flow deposits. The upper ~600 m of unit PF1 is dominated by dolomitized grainstone and microbialaminite and contains common crossbedding, cements and porous ‘tufa’ structures. Evidence for sub-

aerial exposure is extensive in the form of tepee structures, intra-clast breccia, and silica encrustations. Mafic dykes are common near the top of the unit, and have pilotaxitic and intersertal textures characteristic of lavas of the overlying Mount Harper volcanic complex (Mustard and Roots, 1997), less than 1 km to the south.

The contact between PF1 and PF2 is covered by colluvium and an alpine meadow; outcrops of PF2 are scant. The estimated 111 m thickness of PF2 is exaggerated by mafic sills which are resistant to erosion. Rusty-weathering shale and quartz sandstone are exposed at the contacts with the sills. On a ridge ~10 km northwest of the measured section, PF2 is well exposed, measuring 77 m in thickness. PF2 overlies a brecciated surface of PF1, and begins with up to 2 m of channelized, subrounded quartz gravel conglomerate in a sandy matrix. Overlying these beds is 17 m of green and red shale with dolomite lenses containing microbialite textures that are interpreted as bioherms. The bioherms are draped by an iron formation that is ~10 cm thick (Fig. 10). Above the multicoloured shale unit is an additional 60 m of black shale containing laterally discontinuous bioherms that can be distinguished by their peculiar waxy luster. Preliminary x-ray diffraction analyses indicate that this luster results from the presence of talc. In the absence of metamorphic alteration or mineral precursors, the talc appears to be detrital in origin.

Unit PF3 comprises a light grey to white-weathering limestone-dominated succession (311 m thick) overlain by dolostone and breccia (27 m thick). North of Mount Harper, the base of PF3 is indicated by an abrupt change from dark-coloured shale to microbial laminated dolostone, succeeded by massive, structureless breccia. Elsewhere in the study area this contact is gradational,

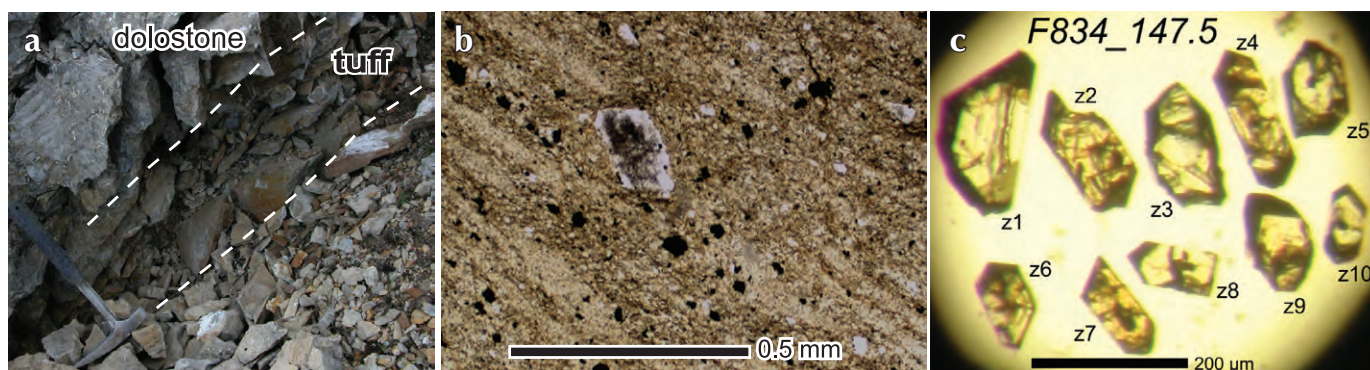


Figure 9. (a) Cherty tuff and overlying dolostone units, 562 m above base of section. (b) Photomicrograph (plane light) of tuff unit containing aligned quartz grains and opaque minerals (secondary pyrite?). (c) Zircon crystals separated from tuff unit (sample F837_147.5) for single-crystal ID-TIMS dating (Boise State University; data in Macdonald et al., in press).



Figure 10. Hematite and chert draped on laminated dolostone (tan and rust weathered) within unit PF2. This site is ~12 km north-northeast of Mount Harper. Rock hammer for scale. (UTM 0555753E 7185050N, elevation 5500').

with black talc beds draping *Jacutophyton* stromatolites. Continuing upwards in the section, the overlying 222-m-thick distinctive succession contains abundant domal stromatolites of two forms: 1) 2 to 3-mm-thick algal laminae forming hemispheres 15-25 cm across; and 2) branching forms characteristic of *Tungussia* (Fig. 11). The stromatolitic beds are typically 2-4 m thick and are intercalated with beds consisting of cm-sized, preferentially silicified, coated grains; these features have also been observed in the Callison Lake dolostone at the Hart River inlier (Abbott, 1997; 145 km east of Mount Harper).

The upper part of unit PF3 was measured along a ridge crest that has intermittent bedrock exposure. Many layers are clast-supported dolostone breccia containing algal-laminated limestone blocks, separated by silica-encrusted cavities that may represent a paleokarst surface (Mustard and Donaldson, 1990).

UPPER CONTACT OF THE UPPER FIFTEENMILE GROUP

The paleokarst at the top of unit PF3 is overlain by 19.5 m of black fissile shale, interbedded with tan-weathering, thin-bedded dolostone. We include these beds with the ~270-m-thick Lower Mount Harper Group on the northern flank of Mount Harper (see Mustard and Roots, 1997).



Figure 11. Stromatolite characteristic of Unit PF3 (Callison Lake dolostone) located at 1616 m above base of section.

These shale beds are overlain by a pebble to boulder conglomerate with rare dolomitic mudstone and wackestone horizons (unit PHb). Unit PHb is interpreted as subaerial alluvial fans that were likely sourced at a fault scarp 4 km south of the measured section. The proportion of carbonate lithologies in the conglomerate is inverse to the upper Fifteenmile Group stratigraphy, suggesting progressive downward denudation of the uplifted fault scarp (Mustard and Roots, 1997).

DISCUSSION

DEPOSITIONAL ENVIRONMENT

Three transgressive-regressive cycles constitute the upper Fifteenmile Group, however, they do not correlate with the existing map units to date. In the context of a sequence stratigraphic framework, if the top of the PR5 shale is included with PF1a in the first cycle, then the shaly top of unit PF1a forms the second cycle with PF1, and finally, PF2 and PF3 constitute the third cycle. Furthermore, it is nearly impossible to differentiate between transgressions resulting from subsidence of the shelf (block faulting, regional extension), global eustatic sea level rise, or geodynamic perturbations (e.g., Maloof *et al.*, 2006).

In the first cycle, the lowest carbonates of unit PF1a are characterized by rhythmite and ribbonite sequences that were deposited below, or near, storm wave-base. Sporadic preservation of wavy bedding and asymmetric ripples confirm the presence of bottom currents. These beds are succeeded by thin-bedded dolostone and grainstone, and contain occasional breccias that include imbricated tabular clasts, which are interpreted as debris flows. Stromatolites first appear 500 m above the base of the section. A high-stand tract is consistent with the successive thick-bedded limestone, marl and red-weathering siltstone layers. At least five debris flows near the top of this cycle exhibit large blocks of reef and algal-laminated carbonate, implying destruction of barrier or lagoonal deposits upslope. The tuff layer was deposited between two of these debris flow events.

The second cycle, the shale-carbonate cycle, begins with an ~70-m-thick black shale deposited below storm wave base. In the succeeding parasequences, rhythmites give way to crossbedded grainstone to packstone containing ooids and edgewise conglomerate, locally followed by emergence, causing breakdown and transport of carbonate crusts. Tepee structures, microbialites and porous tufa textures are indicative of a supra-littoral environment that periodically emerged. Silica encrustation further attests to the emergent, and possibly karstic, conditions in the upper part of the unit.

In the third cycle, shale is directly overlain by stromatolites. Stromatolite emergence is consistent with a marginal reef environment that extended as far as the Hart River inlier. With shelf subsidence, the reef continued to build to a thickness of more than 250 m. Subsequent sea level drop produced an emergent shelf that was exposed to karst dissolution and collapse. Burial beneath the Lower Mount Harper Group conglomerates resulted in preservation of the unit.

CORRELATION WITH ADJACENT INLIERS

The paucity of absolute time markers, an incomplete stratigraphic record, and the reality of lateral facies changes, has hindered attempts to correlate strata between the Proterozoic inliers of the northwestern Cordillera. Further complicating the issue is the stratigraphic nomenclature that is unique to each inlier, thereby limiting the inferences that can be made about the regional depositional and tectonic history. In Figure 12, we present a new correlation chart based on our litho and chemostratigraphic studies for each of the

inliers. Below, we discuss these correlations with respect to the upper Fifteenmile Group.

Tatonduk inlier

Proterozoic strata exposed near the Yukon-Alaska border (85 km northwest of Mount Harper; Fig. 1) are broadly divided into an upper and lower Tindir Group (Young, 1982). The purple mudstone and diamictite (unit 2; Fig. 12) at the base of the upper Tindir Group, which constitutes the Windermere Supergroup in this region, is likely correlative to unit PH1 of the upper Mount Harper Group (Fig. 12).

Lower Tindir strata underlie ridges separated by major faults, such that correlation of units across valleys is often uncertain. In recent mapping, four units have been recognized in the lower Tindir Group (Macdonald *et al.*, 2010) and include: i) a 'lower shale' unit; ii) a 350-m-thick 'lower carbonate' unit characterized by light grey quartzite with discontinuous stromatolitic bioherms (pCtq; Fig. 12); iii) an 'upper shale' unit (pCt_{sl}, pCt_s; Fig. 12) that includes minor sandstone and debris flows; and iv) an 'upper dolostone' unit (pCt_{ds}; Fig. 12) that is dominated by grainstone and breccia. The full thickness of these units is 1130 m. The 'upper shale' unit was previously mis-mapped and contains two shale-to-limestone sequences. The upper of these two sequences (pCt_{ds}; Fig. 12), consists of fissile shale with dolostone olistostromes (48 m thick) succeeded by dark grey limestone rhythmite with interbedded debris flows and black chert lenses. The lower carbonate unit (pCt_{sl}; Fig. 12) is lithologically similar to our unit PF1a. However, the exact correlations between the upper two units of the lower Tindir Group and units PF1 and PF3 of the upper Fifteenmile Group are unclear. Van Kooten *et al.* (1997) suggested the presence of an unconformity beneath the upper carbonate (pCt_{ds}). Although we have not observed this unconformity during our mapping, carbon isotope chemostratigraphy shows an abrupt change within the upper shale unit (Macdonald *et al.*, 2010). If the upper carbonate correlates with PF3 and the Callison Lake dolostone, the unconformity may truncate units PF1 and PF2 of the upper Fifteenmile Group.

Hart River inlier

In the Hart River inlier, Abbott (1997) defined six Pinguicula-correlative units unconformably overlain by the Callison Lake dolostone, a light grey-weathering, nearly massive unit (Fig. 12). From the base of the Pinguicula Group, the units include: PPA, PPB and PPC, and three

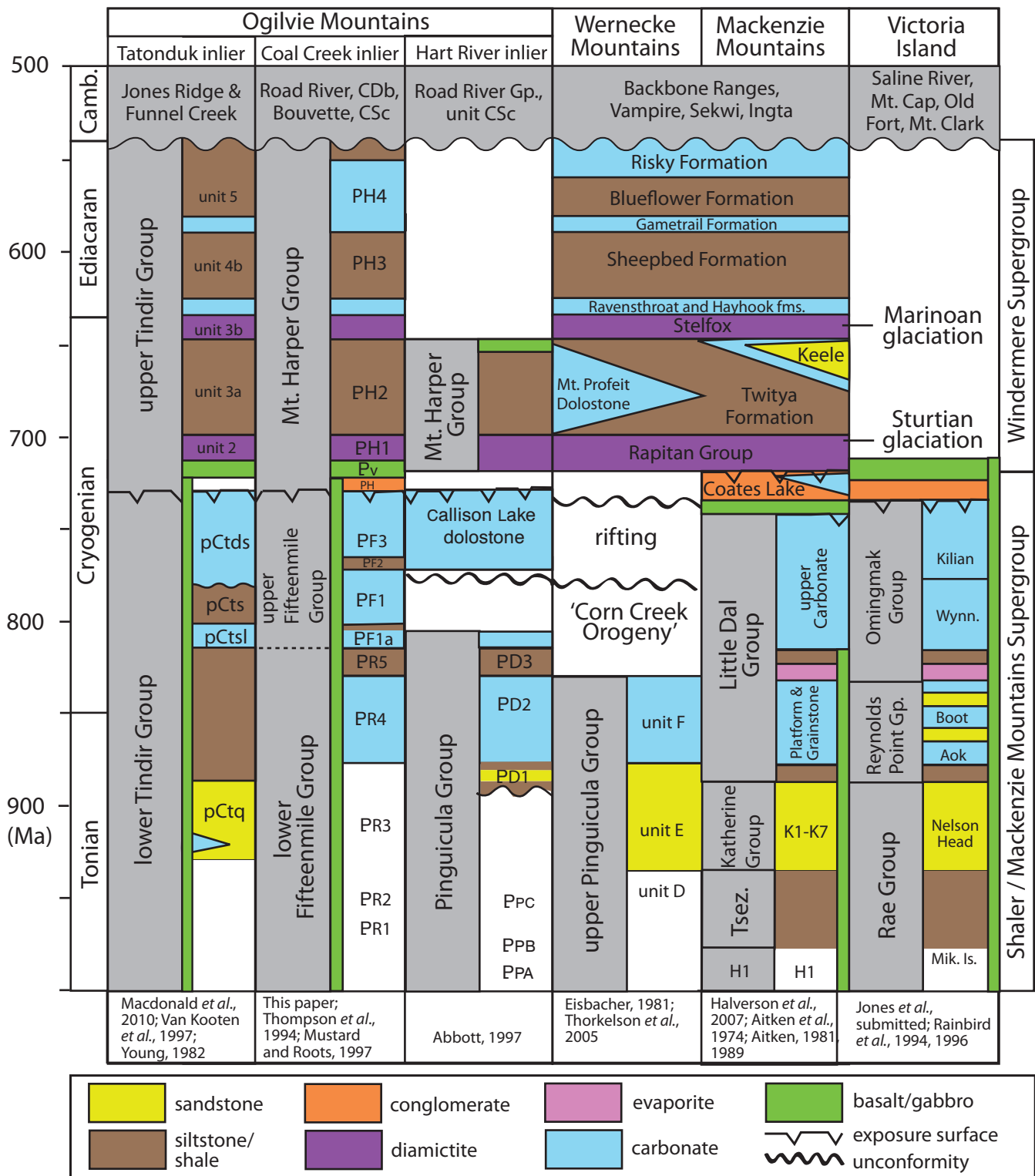


Figure 12. Strata correlative with Neoproterozoic upper Fifteenmile units in the Ogilvie Mountains (Tatonduk, Coal Creek and Hart River inliers), Wernecke Mountains, Mackenzie Mountains and Victoria Island.

discontinuous members of unit D (PD1 - brown shale; PD2 - thin-bedded brown limestone overlain by grey dolostone; and PD3 - brown sandstone and minor orange dolostone [Fig. 12]). A low-angle unconformity beneath the Callison Lake dolostone truncates unit PD3 progressively eastward across the Hart River inlier (see Fig. 13). The Callison Lake dolostone was correlated with Fifteenmile unit PF1 (Abbott, 1997; Thorkelson *et al.*, 2005).

We have examined the units above and below this unconformity. The Callison Lake dolostone is ~340 m thick, with delicate algal-laminated, stromatolitic and pisolitic textures preserved. The lowermost ~30 m of the Callison Lake dolostone consists of a black shale unit with a waxy luster. Together, these distinct facies of the Callison Lake dolostone display striking lithological similarities to units PF2 and PF3 of the upper Fifteenmile Group. The sedimentary rocks preserved beneath the unconformity include maroon shale and thin-bedded, orange-weathering dolostone, which resemble the middle interval of unit PF1a in the section north of Mount Harper.

We believe that the correlation of Callison Lake dolostone with PF1 is incorrect because the two units are lithologically and geochemically dissimilar (Macdonald *et al.*, 2010; in press). Instead, we recognize that strata absent beneath the unconformity would correlate with unit PF1. If the Callison Lake dolostone – Fifteenmile PF3 correlation is correct, then the unconformity cuts out strata equivalent to PF1. This is consistent with the basal PF2 contact observed ~10 km north of the measured section north of Mount Harper, where gravel lags are above an exposure surface at the top of PF1. An unconformity at this level matches the unconformity suggested by Van Kooten *et al.* (1997) in the Tatonduk inlier and provides a possible explanation for the absence of any obvious equivalent of PF1 in that region. Moreover, the unconformity beneath the Callison Lake dolostone may also explain the absence of *Pinguicula* units E and F (Eisbacher, 1981; later correlated with upper units of the Mackenzie Mountains Supergroup by Thorkelson *et al.*, 2005) in the Hart River inlier. Incursion of quartz-rich sediment from a continental-scale river system (Rainbird *et al.*, 1997) appears thickest in the Mackenzie Mountains (Katherine Group), with tongues thinning into the



Figure 13. Photo of the unconformity beneath the thick, grey Callison Lake dolostone, truncating orange- and brown-weathering beds of member PD3 (Abbott, 1997). Photo is looking southwest across the head of Marc Creek, Hart River inlier (64°34' 22.53"N 136°48'05.20"W, elevation 5500').

Wernecke Mountains (Pinguicula D and E, or Corn Creek lithofacies; Fig. 12). Alternatively, rather than being removed beneath the unconformity, the sandstone may not have extended to the western Ogilvie Mountains, with the possible exception of channelized bodies in the lower Fifteenmile Group and the lowermost unit of the lower Tindir Group (pCtq).

FUTURE WORK

Our stratigraphic studies to date within the inliers of the Yukon have led to more questions than answers. First-order questions include: What is the tectonic significance of the unconformity beneath the Callison Lake dolostone, and, to what extent has it confounded correlations? By better understanding the regional extent and nature of this surface, we will be able to establish correlations through the Proterozoic inliers of the Yukon with more confidence. Future mapping and stratigraphic studies aim to define formations within upper Fifteenmile Group, and extend these formation names to the other inliers in the Ogilvie Mountains, thereby replacing the informal and local map units. The resulting correlations will allow us to infer regional-scale lateral facies changes and learn more about the depositional environments and accommodation mechanisms recorded by Neoproterozoic strata in Yukon.

Reconnaissance work suggests that Pinguicula Group units A-D are equivalent to the lower Fifteenmile Group (Medig *et al.*, this volume) and a part of PF1a. These strata contain isolated stromatalite reefs similar to patch reefs in the basinal assemblage of the Little Dal Group (Turner *et al.*, 1997). Facies patterns in the lower Little Dal Group indicate a shallow-water area to the southeast (platform assemblage), and deep water with patch reefs to northwest (basinal assemblage) (Aitken, 1981). Further work is necessary to test these possible correlations and refine the geometries that evolved on the Proterozoic margin of northwest Laurentia.

CONCLUSIONS

Except for stratigraphic omissions beneath low-angle unconformities, time-correlative strata are exposed in the Tatonduk, Coal Creek and Hart River inliers, and eventually their nomenclatures should merge. The PF3 unit of the upper Fifteenmile Group should henceforth be called the Callison Lake dolostone.

The unconformity beneath Callison Lake dolostone in the Hart River inlier represents considerable erosion, or

non-deposition of units, equivalent to the Fifteenmile Group.

ACKNOWLEDGEMENTS

Trevor Petach and David Johnson (2008), and Justin Strauss and Sierra Petersen (2009) assisted with fieldwork. Trans North pilots and the Yukon Geological Survey provided field support. National Science Foundation and other grants to Paul Hoffman and Francis Macdonald made this research possible. Grant Abbott, Derek Thorkelson and Joyia Chakungal are acknowledged for their effort to bring clarity to this paper.

REFERENCES

- Abbott, J.G., 1997. Geology of the Upper Hart River area, eastern Ogilvie Mountains, Yukon Territory (116A/10, 116A/11). Exploration and Geological Services Division, Yukon Region, Indian and Northern Affairs Canada, Bulletin 9, 91 p.
- Aitken, J.D., 1981. Stratigraphy and sedimentology of the Upper Proterozoic Little Dal Group, Mackenzie Mountains, Northwest Territories. *In: Proterozoic Basins of Canada*, F.H.A. Campbell (ed.), Geological Survey of Canada, Paper 81-10, p. 47-71.
- Aitken, J.D., 1989. Uppermost Proterozoic formations in central Mackenzie Mountains, Northwest Territories. Geological Survey of Canada, Bulletin 368, 25 p.
- Aitken, J.D., Macqueen, R.W. and Usher, J.L., 1974. Reconnaissance studies of Proterozoic and Cambrian stratigraphy, lower Mackenzie River area, District of Mackenzie. Geological Survey of Canada, Paper 73-9, 173 p.
- Delaney, G.D., 1981. The mid-Proterozoic Wernecke Supergroup, Wernecke Mountains, Yukon Territory. *In: Proterozoic Basins of Canada*, F.H.A. Campbell (ed.), Geological Survey of Canada, Paper 81-10, p. 1-24.
- Eisbacher, G.H., 1978. Two major Proterozoic unconformities, northern Cordillera. *In: Current Research, Part A*, Geological Survey of Canada, Paper 78-1A, p. 53-58.
- Eisbacher, G.H., 1981. Sedimentary tectonics and glacial record in the Windermere Supergroup, Mackenzie Mountains, northwestern Canada. Geological Survey of Canada, Paper 80-27, 41 p.

- Gabrielse, H., 1972. Younger Precambrian of the Canadian Cordillera. *American Journal of Science*, vol. 272, p. 521-536.
- Gabrielse, H., Blusson, S.L. and Roddick, J.A., 1973. Flat River, Glacier Lake, and Wrigley Lake map area (95E, L,M), District of Mackenzie and Yukon Territory. Geological Survey of Canada, Memoir 366, 153 p.
- Gordey, S.P. and Makepeace, A.J., 2003. Yukon Digital Geology, version 2.0. Geological Survey of Canada, Open File 1749; Yukon Geological Survey, Open File 2003-9 (D).
- Halverson, G.P., Dudás, F.Ö., Maloof, A.C. and Bowring, S.A., 2007. Evolution of the $^{87}\text{Sr}/^{86}\text{Sr}$ composition of Neoproterozoic seawater. *Palaeogeography, Paleoclimatology, Palaeoecology*, vol. 256, p. 103-129.
- James, N.P., Narbonne, G.M. and Sherman, A.G., 1998. Molar-tooth carbonates: Shallow subtidal facies of the mid- to late Proterozoic. *Journal of Sedimentary Research*, vol. 68, no. 5, p. 716-722.
- Long, D.G.F., Rainbird, R.H., Turner, E.C. and MacNaughton, R.B., 2008. Early Neoproterozoic strata (Sequence B) of mainland northern Canada and Victoria and Banks islands: a contribution to the Geological Atlas of Northern Canadian Mainland Sedimentary basin. Geological Survey of Canada, Open File 5700, 24 p.
- Macdonald, F.A., Cohen, P.A., Dudás, F.Ö. and Schrag, D.P., 2010. Early Neoproterozoic scale microfossils in the Lower Tindir Group of Alaska and the Yukon Territory. *Geology*, vol. 38, no. 2, p. 143-146.
- Macdonald, F.A., Schmitz, M.D., Crowley, J.C., Roots, C.F., Jones, D.S., Maloof, A.C., Strauss, P.A., Cohen, P.A., Johnston, D.T. and Schrag, D.P., (in press). Calibrating the Cryogenian. *Science* (Feb. 2010).
- Maloof, A.C., Halverson, G.P., Kirschvink, J.L., Schrag, D.P., Weiss, B.P. and Hoffman, P.F., 2006. Combined paleomagnetic, isotopic, and stratigraphic evidence for true polar wander from the Neoproterozoic Akademikerbreen Group, Svalbard, Norway. *Geological Society of America Bulletin*, vol. 118, no. 9/10, p. 1099-1124.
- Medig, K.P., Thorkelson, D.J. and Dunlop, R.L., 2010 (this volume). The Proterozoic Pinguicula Group: stratigraphy, contact relations, and possible correlations. *In: Yukon Exploration and Geology 2009*, K.E. MacFarlane, L.H. Weston and L.R. Blackburn (eds.), Yukon Geological Survey, p. 265-278.
- Mustard, P.S. and Donaldson, J.A., 1990. Paleokarst breccias, calcretes, silcretes and fault talus breccias at the base of the upper Proterozoic "Windermere" strata, northern Canadian Cordillera. *Journal of Sedimentary Petrology*, vol. 60, no. 4, p. 525-539.
- Mustard, P.S. and Roots, C.F., 1997. Rift-related volcanism, sedimentation and tectonic setting of the Mount Harper Group, Ogilvie Mountains, Yukon Territory. Geological Survey of Canada, Bulletin 492, 92 p.
- Rainbird, R.H., Jefferson, C.W., Hildebrand, R.S. and Worth, J.K., 1994. The Shaler Supergroup and revision of Neoproterozoic stratigraphy in the Amundsen Basin, Northwest Territories. *In: Current Research, Part A*, Geological Survey of Canada, Paper 94-1A, p. 61-70.
- Rainbird, R.H., Jefferson, C.W. and Young, G.M., 1996. The early Neoproterozoic sedimentary Succession B of northwestern Laurentia: Correlations and paleogeographic significance. *Geological Society of America Bulletin*, vol. 108, no. 4, p. 454-470.
- Rainbird, R.H., McNicoll, V.J., Theriault, R.J., Heaman, L.H., Abbott, J.G., Long, D.G.F. and Thorkelson, D.J., 1997. Pan-continental river system draining Grenville orogen recorded by U-Pb and Sm-Nd geochronology of Neoproterozoic quartzite and mudrocks, northwestern Canada. *Journal of Geology*, vol. 105, p. 1-17.
- Roots, C.F. and Thompson, R.I., 1992. Long-lived basement weak zones and their role in extensional magmatism in the Ogilvie Mountains, Yukon Territory. *In: Basement Tectonics and Characterization of Ancient and Mesozoic Continental Margins – Proceedings of the 8th International Conference in Basement Tectonics (Butte Montana, 1988)*, M.J. Bartholomew, D.W. Hyndman, D.W. Mogk and R. Mason (eds.), Kluwer Academic Publishers, Dordrecht, The Netherlands, p. 359-372.
- Thompson, B., Mercier, E. and Roots, C., 1987. Extension and its influence on Canadian Cordilleran passive-margin evolution. *In: Continental Extensional Tectonics*, M.P. Coward, J.F. Dewey and P.L. Hancock (eds.), Geological Society Special Publication no. 28, p. 409-417.

- Thompson, R.I., Roots, C.F. and Mustard, P.S., 1994. Dawson map area. Geological Survey of Canada, Open File 2849, scale 1:50 000.
- Thorkelson, D.J., 2000. Geology and mineral occurrences of the Slats Creek, Fairchild Lake and "Delores Creek" areas, Wernecke Mountains (106D/16, 106C/13, 106C/14), Yukon Territory. Exploration and Geological Services Division, Yukon Region, Indian and Northern Affairs Canada, Bulletin 10, 73 p.
- Thorkelson, D.J., Abbott, J.G., Mortensen, J.K., Creaser, R.A., Villeneuve, M.E., McNicholl, V.J. and Layer, P.W., 2005. Early and Middle Proterozoic evolution of Yukon, Canada. *Canadian Journal of Earth Sciences*, vol. 42, p. 1045-1071.
- Turner, E.C., James, N.P. and Narbonne, G.M., 1997. Growth dynamics of Neoproterozoic calcimicrobial reefs, Mackenzie Mountains, northwest Canada. *Journal of Sedimentary Research*, vol. 67, p. 437-450.
- Van Kooten, G.K., Watts, A.B., Coogan, J., Mount, V.S., Swenson, R.F., Daggett, P.H., Clough, J.G., Roberts, C.T. and Bergman, S.C., 1997. Alaska Division of Geological and Geophysical Surveys, Report of Investigations 96-6A, 3 sheets, scale 1:125 000.
- Vandeginste, V., Swennen, R., Gleeson, S.A., Ellam, R.M., Osadetz, K. and Roure, F., 2005. Zebra dolomitization as a result of focused fluid flow in the Rocky Mountains Fold and Thrust Belt, Canada. *Sedimentology*, vol. 52, p. 1067-1095.
- Young, G.M., 1982. The late Proterozoic Tindir Group, east-central Alaska: Evolution of a continental margin. *Geological Society of America Bulletin*, vol. 93, p. 759-783.
- Young, G.M., Jefferson, C.W., Delaney, G.D. and Yeo, G.M., 1979. Middle and Late Proterozoic evolution of the northern Canadian Cordillera and Shield. *Geology*, vol. 7, p. 125-128.

Structural controls on hydrothermal gold mineralization in the White River area, Yukon

Doug MacKenzie and Dave Craw
Geology Department, University of Otago¹

MacKenzie, D.J. and Craw, D., 2010. Structural controls on hydrothermal gold mineralization in the White River area, Yukon. *In: Yukon Exploration and Geology 2009*, K.E. MacFarlane, L.H. Weston and L.R. Blackburn (eds.), Yukon Geological Survey, p. 253-263.

ABSTRACT

New mapping and drilling associated with gold exploration has elucidated the structural and lithological controls on hydrothermal gold systems in the White River area. The Paleozoic basement consists of a sequence of amphibolite facies clastic metasedimentary and meta-igneous rocks that host lower grade ultramafic rocks, some magmatically and some tectonically emplaced during the Late Triassic – Early Jurassic. Mapped ultramafic bodies show close congruence with published airborne magnetic anomalies. All of these rocks are cut by brittle normal faults and fractures, and dykes correlated with middle Cretaceous to early Tertiary extension-related intrusive rocks. Gold mineralization associated with these fractures is strongly controlled by host rock types. Two main rock types, felsic gneiss and quartzite, are preferentially fractured and hydrothermally altered. Other rock types are only weakly fractured and locally altered. In particular, ultramafic bodies and micaceous lithologies locally impeded fluid flow.

¹PO Box 56, Dunedin, New Zealand, doug.mackenzie@otago.ac.nz

INTRODUCTION

The discovery of new gold-bearing hydrothermal systems in the White River area of the central western Yukon, approximately 80 km south of the Klondike goldfield (Fig. 1), has generated a new rush of exploration activity in the region. Although the geology of the area has been mapped at 1:50 000 scale (Ryan and Gordey, 2001; 2004), little is known about the gold deposits and their relationship to the surrounding rocks.

Outcrop is generally poor and limited to a few exposures on the tops of ridges and in excised streams. Most of the area is forested and zones of anomalous gold were found initially by ridge and spur soil sampling. Since the discovery of these soil anomalies in 2007, the area has been the focus of an extensive and ongoing diamond drilling program by Underworld Resources Ltd.

This report outlines results of detailed structural mapping conducted in the White River area during the 2008 and 2009 field seasons. Due to poor outcrop, field mapping was aided by published aeromagnetic data (e.g., Shives *et al.*, 2002a,b) and augmented by the analysis of numerous drill core samples. This approach enabled us to determine a sequence of structural events that affected the underlying rocks and to deduce the relative timing of the gold mineralization event. We also describe the principal structural and lithological controls on mineralization. This research is part of an ongoing study supported by Underworld Resources Ltd.

REGIONAL GEOLOGY AND STRUCTURAL SETTING

The main basement lithologies in the Klondike - White River area (Fig. 1) are part of the Yukon-Tanana terrane and consist of schists and gneisses that were deformed and metamorphosed in the late Paleozoic (Mortensen, 1990, 1992, 1996; Mortensen *et al.*, 2007). The rocks range in grade from lower and upper greenschist facies in the Klondike area to amphibolite facies in the White River area. The rocks are pervasively foliated and contain at least two overprinting foliations (S_1 and S_2 of MacKenzie *et al.*, 2008a; S_T of Ryan and Gordey, 2004). The rocks were tectonically stacked along foliation-parallel thrust faults in the Early Jurassic (Mortensen, 1996) resulting in rock slices of differing metamorphic reconstitution being juxtaposed (MacKenzie *et al.*, 2008b). Slices of Triassic metasedimentary rocks and mafic and ultramafic rocks of the Slide Mountain terrane (Mortensen, 1990, 1996) were

incorporated into the thrust stack at this time. The regional-scale thrust faults are generally poorly exposed but are locally marked by lenses of sheared ultramafic rocks and serpentinite. Thrust imbrication resulted in local macroscopic semi-ductile folding and shearing, and the development of a crenulation cleavage in the rocks adjacent to thrusts. All of these metamorphic and thrust-related fabrics were then locally overprinted by m-scale semibrittle upright folds and associated angular kink folds and fractures (MacKenzie *et al.*, 2008a). By the mid-Cretaceous these compressional features were cut by post-metamorphic extensional structures that accompanied exhumation of the metamorphic pile. Felsic and mafic igneous rocks were intruded at this time, their emplacement controlled by coeval normal faults (Gabrielse and Yorath, 1991; Mortensen, 1996). Regional extension continued through the Cretaceous to the Eocene, when initiation of the Tintina fault (Fig. 1) resulted in ~450 km of strike-slip displacement (Gabrielse *et al.*, 2006). Minor regional uplift continued until the late Tertiary and erosion of basement led to concentration of gold-bearing gravels into numerous district-wide alluvial placer deposits (e.g., Lowey, 2006; LeBarge, 2007).

STRUCTURAL GEOLOGY

The basement rocks of the White River area (Figs. 1, 2) consist of an interlayered sequence (1-100 m) of amphibolite-facies quartzite, marble, hornblende gneiss, biotite gneiss (locally garnet-bearing) and felsic gneiss (locally containing millimetre to centimetre-scale K-feldspar augen). All of these lithologies contain a pervasive foliation (S_2) that is a composite feature, composed of at least one earlier metamorphic foliation (S_1) that was folded and reactivated by a second phase of ductile deformation during peak metamorphism (D_2 ; Table 1). This S_2 foliation is generally shallowly to moderately NE-dipping (30° to 50°) over most of the study area, except where locally steepened by later deformation (D_3 - D_5 ; Table 1).

The most prominent folds in the area are m-scale, late metamorphic, tight to isoclinal folds (Fig. 2b) that are best developed in and near semiductile deformation zones (D_3 ; Table 1). The axial planes of these folds (F_3) are generally shallowly dipping and subparallel to the regional S_2 foliation (Fig. 3a). Where D_3 deformation is most intense, crenulation cleavage, semi-ductile shears, fractures and breccia zones developed parallel to fold axial surfaces (Fig. 3b). Serpentinite bodies (1-50 m thick) are commonly associated with zones of strong D_3

deformation. Here they are tightly folded, sheared and metasomatically altered to greenschist facies minerals (e.g., chlorite, talc, actinolite; Fig. 4). Where folding has been intense, the hinges of tight F_3 crenulations define a new closely spaced S_3 fold-axial-surface cleavage (Fig. 4a,c,d). The serpentinites are commonly magnetic

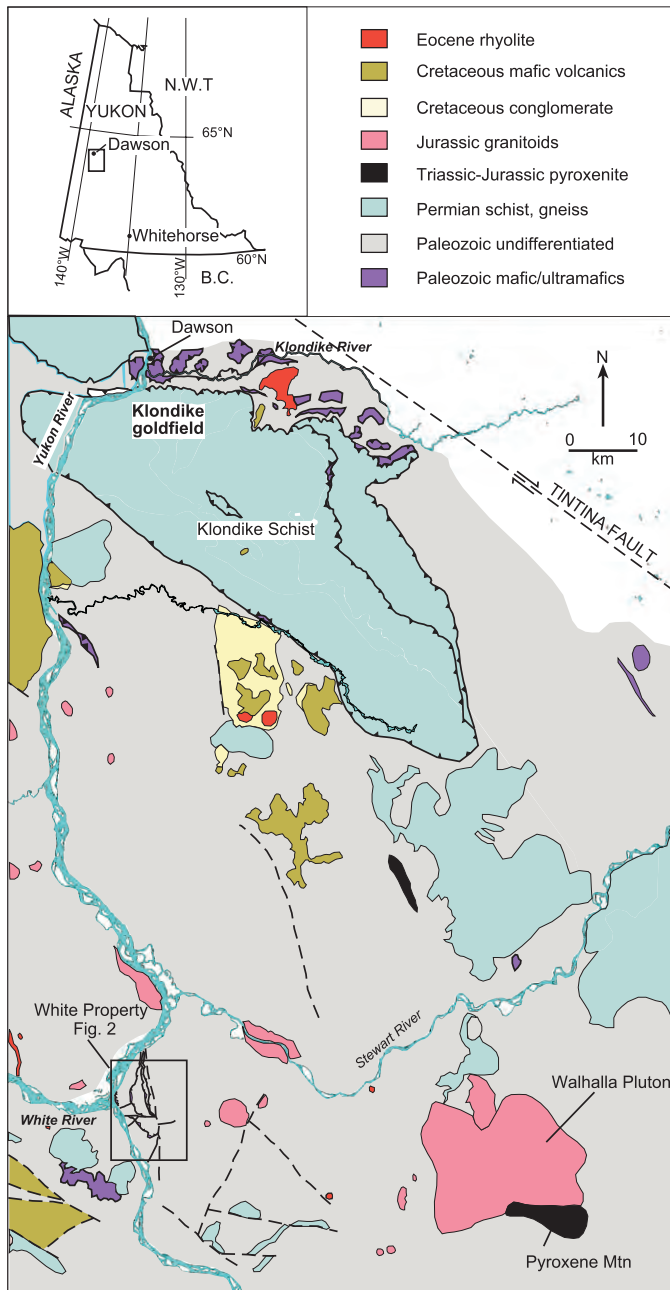


Figure 1. Geological map of the Klondike - White River area (modified after Ryan and Gordey, 2004 and MacKenzie et al., 2008a). Top inset map outlines the study area within the Yukon. The location of the White Property and Figure 2 are indicated lower left.

and locally contain up to 1-2% euhedral magnetite. Lensoid bodies of serpentinite form prominent magnetic highs and stand out from the surrounding gneiss sequence in aeromagnetic images (Fig. 5a). Some of the serpentinite bodies form lenses that pinch in and out along zones of strong F_3 folding and interpreted thrust faults (Fig. 5b).

A bimodal suite of pyroxenite and light-coloured felsic granitoid dykes and sills (1-20 m thick) intrude the gneiss sequence (Fig. 6a). These bodies are relatively massive, coarse-grained (pyroxenites locally contain cm-scale pyroxene crystals) and lack the S_2 metamorphic foliation. They are locally affected by D_3 structures, and in strong D_3 deformation zones, pyroxenite bodies form massive pods that are cut by shears and a new greenschist facies S_3 foliation, especially along their margins (Fig. 3c, 6b). These dykes and sills are petrographically similar to larger Late Triassic - Early Jurassic pyroxenite and granitoid intrusions that crop out 40-50 km east (e.g., Pyroxene Mountain and Walhalla Plutons; Fig. 1; J.K. Mortensen, unpublished data; Gordey and Ryan, 2005). Although they do not contain visible magnetite like the serpentinite rocks, the pyroxenite bodies are also coincident with prominent magnetic highs in the aeromagnetic images (Fig. 5a).

The D_3 structures are locally overprinted by rare semi-brittle folds, angular kinks and fractures (D_4 ; Table 1). F_4 folds and kinks are typically upright, at high angle to the S_2 foliation and have an associated axial surface fracture. These D_4 structures are weakly developed in the White River area (c.f., MacKenzie et al., 2007, 2008a); outcrops that show evidence for this phase of deformation are generally only sporadically distributed throughout the region.

The basement gneiss sequence and post-metamorphic ultramafic and felsic rocks are cut by a set of high-angle north and east-striking normal faults (Figs. 2a,b). These faults represent the youngest recognized deformation event in the White River area (D_5 ; Table 1) and cut across all earlier structures. The faults are generally poorly exposed in outcrop, but where intersected in drill core, they juxtapose different lithologic units in the gneiss sequence. The F_5 faults and fracture zones locally host felsic aphanitic dykes that are correlated with mid-Cretaceous to early Tertiary extension-related igneous activity (Gabrielse and Yorath, 1991; Mortensen, 1996). Several Mesozoic granitoid plutons (up to 2 km in diameter) crop out approximately 10 km east of the White River area (Fig. 1; Ryan and Gordey, 2001).

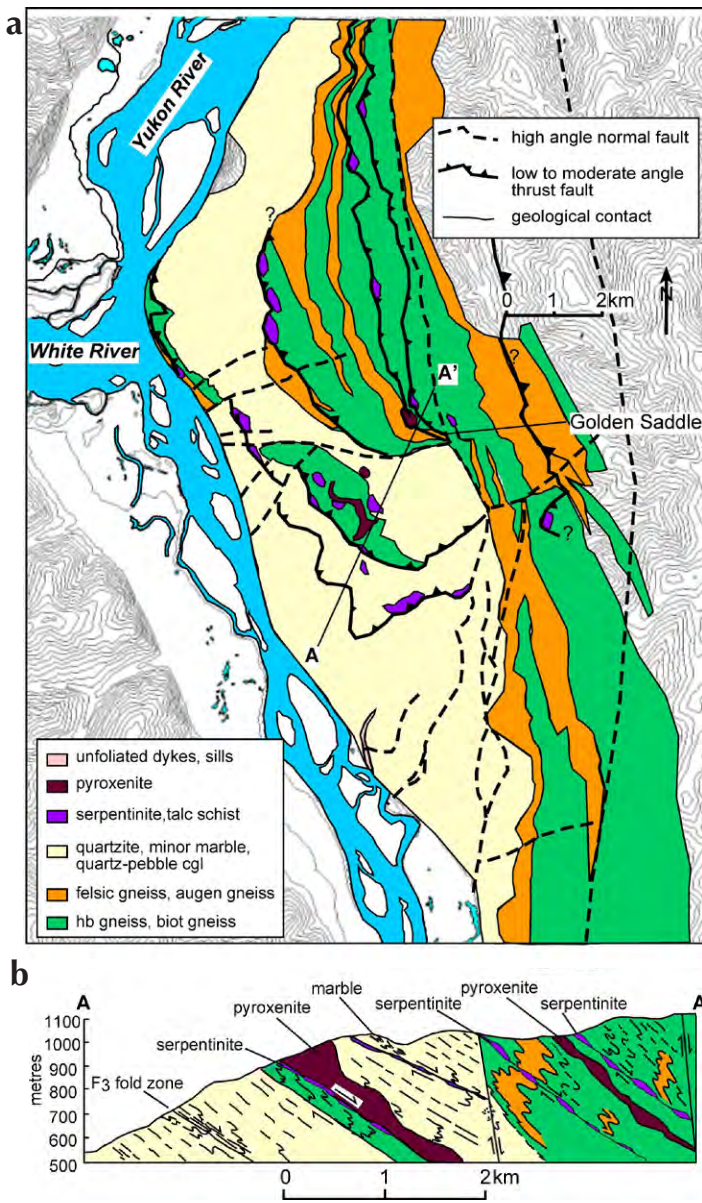


Figure 2. Geology of the White River area. (a) Geological map based in part on Ryan and Gordey (2004) and on detailed field mapping conducted by the authors and Underworld Resources personnel. (b) Northeast cross section through Golden Saddle (line A-A') showing the structural relationships between gneisses and post-metamorphic ultramafic bodies. cgl = conglomerate, hb = hornblende, biot = biotite.

Table 1. Summary of principal structural events relevant to gold mineralization in the White River area (modified after Berman et al., 2007).

Regional structural event	Structures	Alteration/mineralization	Age
D ₅	Steeply dipping normal faults, felsic dykes (m-scale)	Hydrothermal alteration and disseminated gold mineralization controlled by lithologic layering and steeply dipping fractures	Middle Cretaceous-early Tertiary
D ₄	Rare angular kink folds and upright warps; local veins along fold axial surfaces	Massive mm to m-scale white quartz veins controlled by fold axial surface fractures	Jurassic
D ₃	Ductile folds, shears and chloritic foliation, especially associated with ultramafic horizons and thrusts	Greenschist facies retrogression, mainly subparallel to S ₂	Jurassic
Bimodal pyroxenite and granitoid intrusion	Dykes and sills intruded into D ₃ deformation zones		Late Triassic-Early Jurassic
D ₂	Pervasive amphibolite facies foliation (S ₂), stretching lineation, rare isoclinal folds (F ₂)		Late Paleozoic
D ₁	rare S ₁ segregations preserved in intrafolial fold hinges, almost completely transposed by D ₂		Late Paleozoic

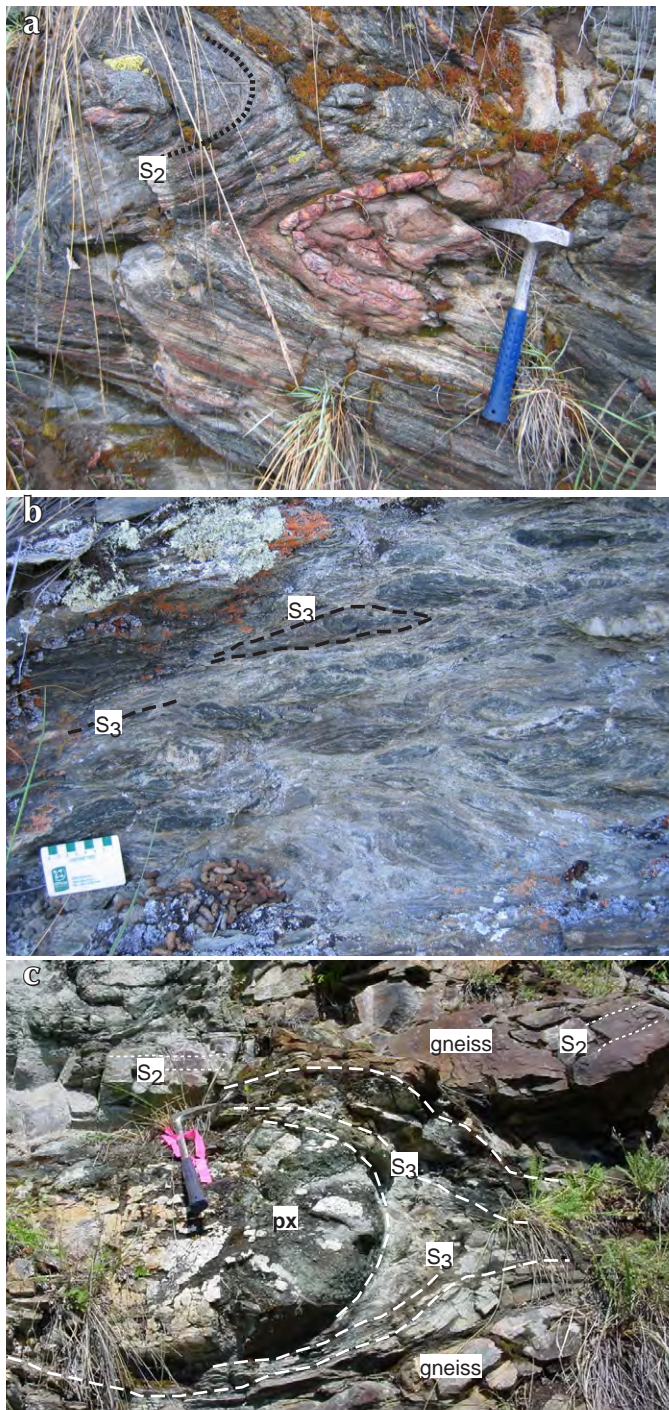


Figure 3. F_3 folds, ductile shears and S_3 foliation. (a) Outcrop of strongly folded biotite gneiss. Prominent S_2 foliation (black dashed line) is highly folded by F_3 folds. (b) Zone of ductile shearing in biotite gneiss. S_3 foliation (dashed lines) anastomoses around lenses of sheared gneiss. (c) S_3 foliation (long-dashed lines) cuts through an outcrop of biotite gneiss at an angle to S_2 (short-dashed lines) and anastomoses around a relatively massive pod of pyroxenite (px).

MINERALIZATION

Hydrothermal fluid flow and gold mineralization is controlled primarily by brittle normal faults that cut the metamorphic structures. However, there has been little emplacement of auriferous quartz veins along these faults and most of the gold occurs in altered rocks adjacent to the faults. Fluid penetration into the rock mass adjacent to the faults is controlled by fractures in brittle host rocks, especially brecciated zones (Fig. 7). These features are generally steeply dipping, subparallel to the normal faults. In addition, shears and foliation associated with F_3 folding facilitated penetration of fluids parallel to S_3 , which is typically shallow-dipping subparallel to S_2 (Fig. 2).

Hydrothermal alteration mineralogy is strongly controlled by host rock mineralogy. Felsic gneisses have an oxidized alteration assemblage, with abundant hematite and sericite (Fig. 7a-d). Hematite is most prominent in weakly altered rocks (Fig. 7b), and strongly altered rocks have hematite replaced by pyrite (Fig. 7c,d). Gold occurs in, and is closely associated with pyrite, and the highest gold grades occur in pyritic breccias (Fig. 7d). Quartzites have a reduced metamorphic assemblage, with accessory graphite and pyrrhotite (Fig. 7e). Hence, hydrothermal alteration is also reduced in these rocks and is dominated by recrystallization of graphite and pyrrhotite, with localized addition of arsenopyrite (Fig. 7f,g,h). Gold is enriched in arsenopyrite-bearing rocks, including those with stylonitic seams (Fig. 7f,g) and breccias (Fig. 7h). Late-stage pharmacosiderite (K-Fe-arsenate) occurs locally within mineralized rocks.

Biotite and hornblende gneisses, pyroxenites, and serpentinite horizons have deformed in more ductile manner than felsic gneisses and quartzites during normal faulting. Hence, fracture networks are poorly developed in these rock types and there has been little hydrothermal alteration and addition of gold. Pyroxenites have locally altered to fuchsite (Fig. 6c), and serpentinite bodies have non-penetrative fuchsite-talc-carbonate alteration (Fig. 4d). Both these ultramafic alteration processes involved formation of rutile and pyrite from pre-existing metallic minerals, and magnetite has decomposed. Hence, the minor hydrothermal alteration has decreased the magnetic signature of the ultramafic bodies that otherwise makes them mappable regionally (Fig. 5).



Figure 4. Altered serpentinite and biotite gneiss in drill core. **(a)** Contact between dark grey biotite gneiss and light green chlorite-altered serpentinite and talc-carbonate schist. S_2 foliations in biotite gneiss exhibit ductile folds from F_3 folding. Serpentinite and talc-carbonate schist are strongly crenulated. **(b)** Close-up of garnetiferous biotite schist with relatively planar S_2 foliation defined by green and black micaceous minerals (running top right to bottom left). **(c)** Close-up of talc carbonate schist (white) and chlorite (green). Crenulations in micaceous fabric define weak S_3 foliation. **(d)** Fuchsite-altered serpentinite with F_3 crenulations.

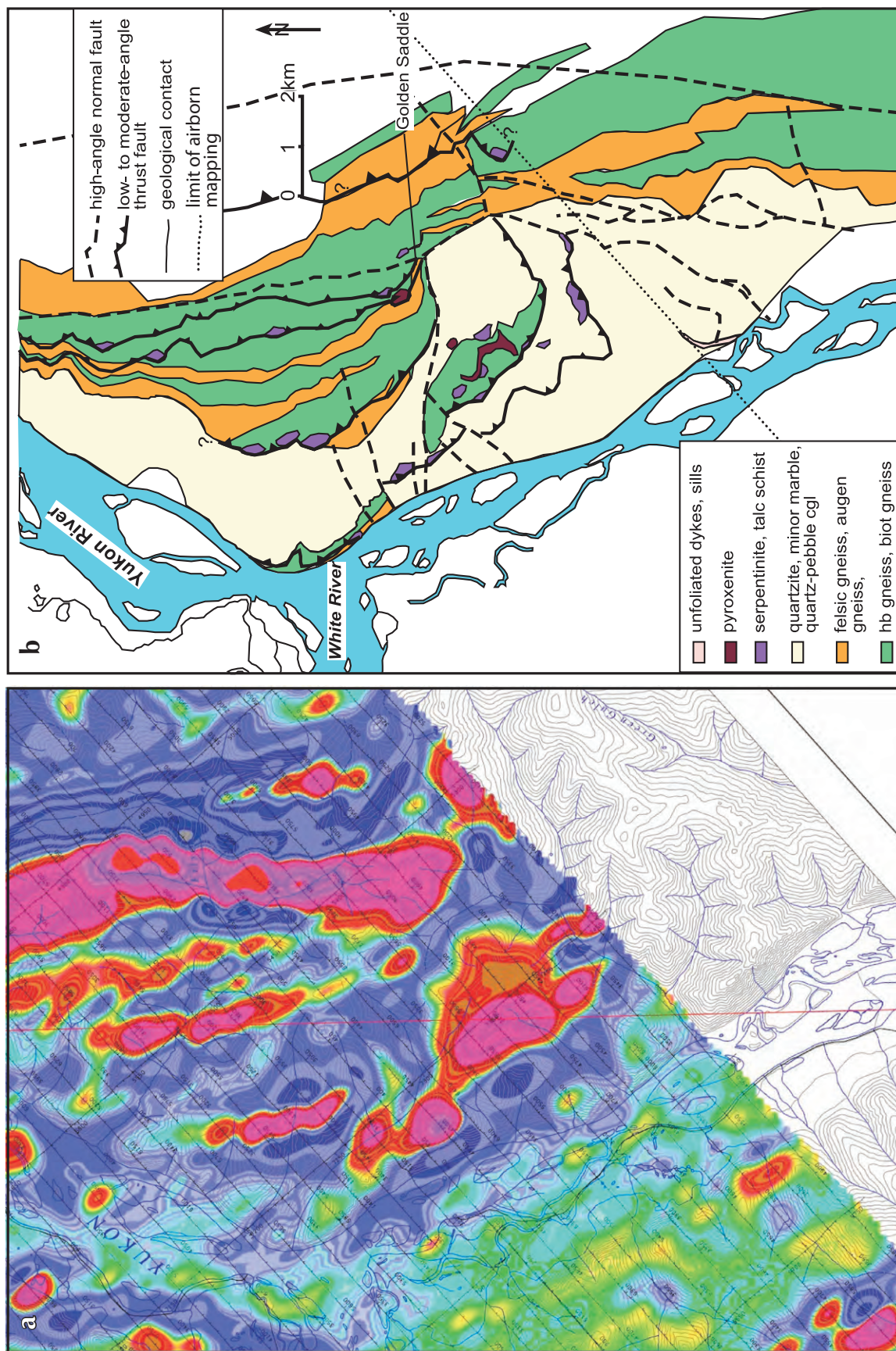


Figure 5. Comparison of airborne magnetic response with mapped geology in the White River area. **(a)** Magnetic first vertical derivative map (after Shives et al., 2002b). Magnetic highs (red, yellow, orange) show close congruence with mapped ultramafic bodies. **(b)** Geological map of the White River area as in Figure 1.

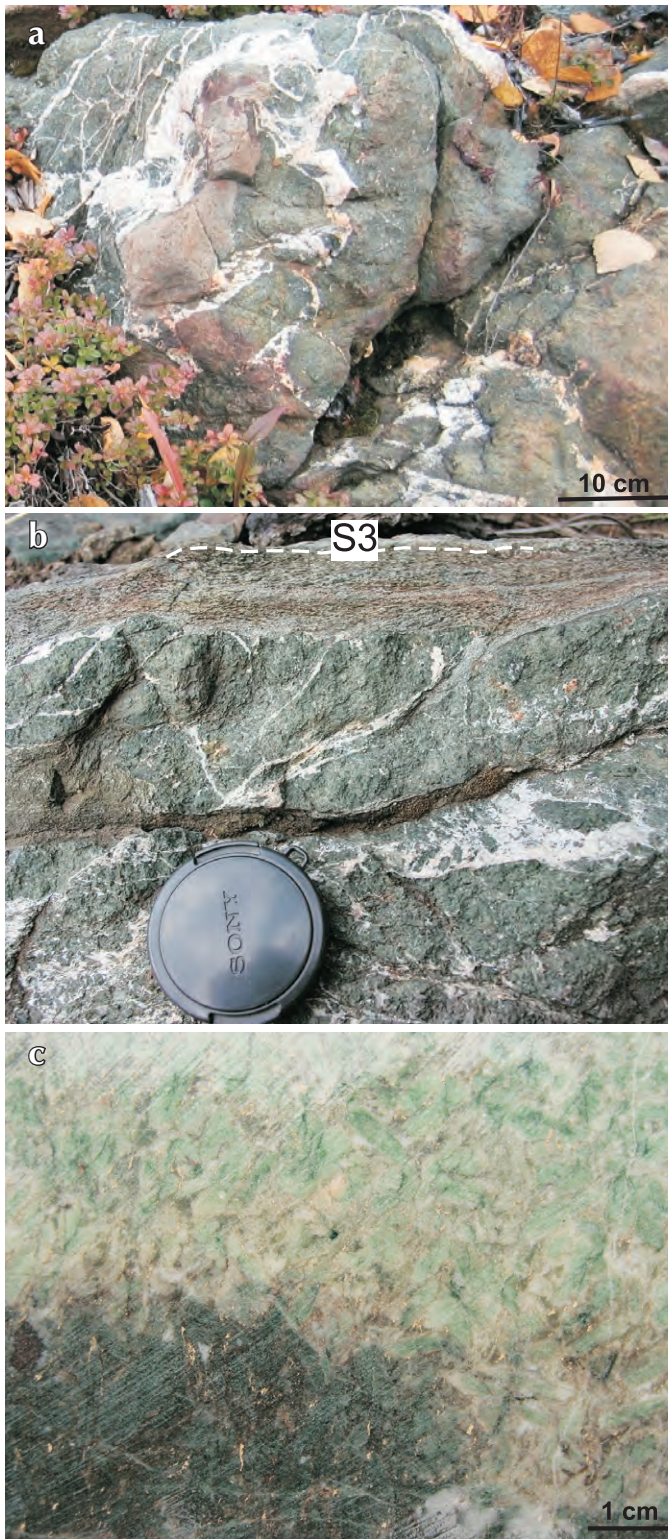
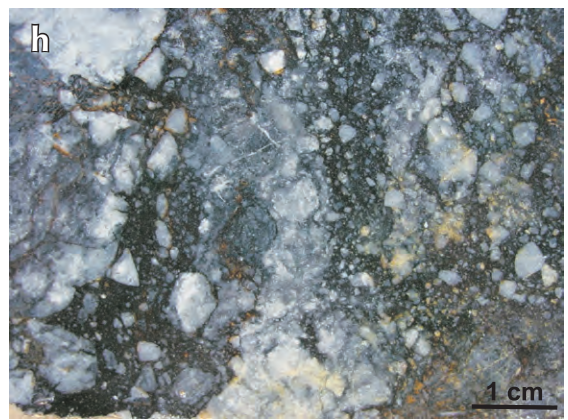
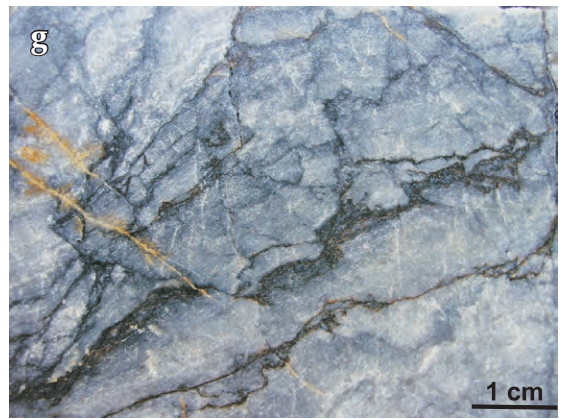
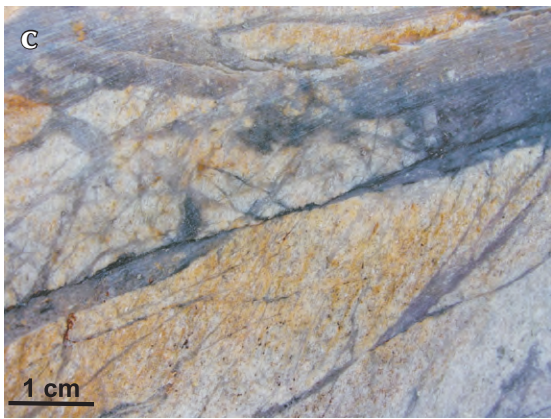
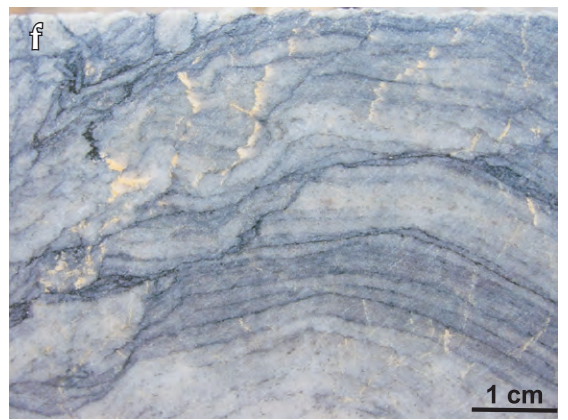
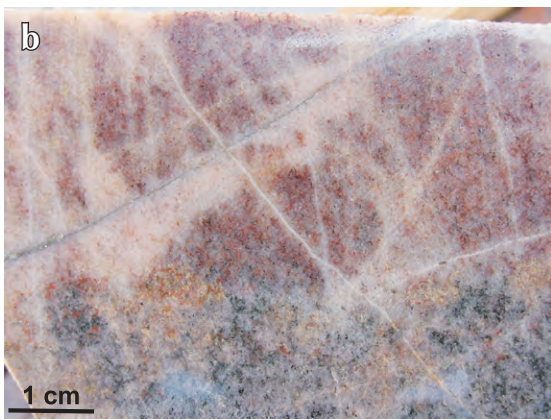
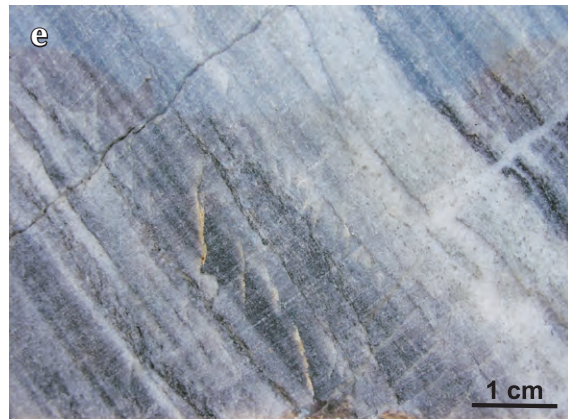
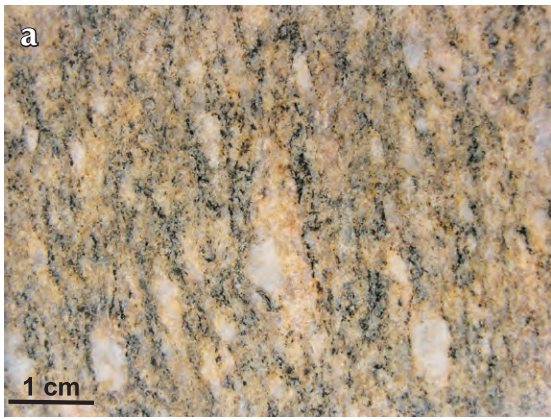


Figure 6. Pyroxenite intrusions. **(a)** Dark green coarse-grained pyroxenite (mm to cm-scale pyroxene crystals) and associated felsic veining (white) contains blocky inclusions of light grey biotite gneiss (left of centre). **(b)** Relatively massive pyroxenite and associated felsic veins (white) cut by S_3 foliation (white dashed line) on upper margin. **(c)** Boundary between altered fuchsite-bearing pyroxenite (light green) and unaltered pyroxenite (dark green) in drill core.

Figure 7. (next page) Drill core from Golden Saddle, showing the two main rock types that are fractured and altered in the White River area. **(a)** Felsic gneiss with prominent S_2 foliation defined by black biotite (running top to bottom) anastomosing around relict K-feldspar augen (white). **(b)** Weakly altered felsic gneiss with red hematite and yellow sericite alteration. Fine hydrothermal pyrite is disseminated in the alteration patches. White bleaching defines fracture-controlled silicification. **(c)** Highly fractured, sericitised (yellow) and silicified (white) felsic schist. Dark grey pyrite veins infill fractures. **(d)** Strongly silicified and sericitised felsic gneiss breccia infilled with quartz and pyrite. **(e)** Quartzite with prominent S_2 foliation defined by fine graphitic laminations (running top left to bottom right) cut by numerous brittle fractures and quartz veins. **(f)** Folded quartzite with S_2 foliation, defined by graphitic laminations, cut by dark stylolites and shears containing hydrothermal graphite and local arsenopyrite. **(g)** Quartzite with S_2 foliation almost completely disrupted by fractures, shears and incipient stylolite development. **(h)** Strongly silicified quartzite and quartz vein breccia infilled with quartz, pyrite and arsenopyrite.



DISCUSSION AND CONCLUSIONS

Two distinctly different types of ultramafic bodies have been emplaced into the amphibolite facies gneissic sequence in the White River area, and their magnetic signatures have been helpful for mapping the area. Sill-like pyroxenite bodies were intruded subparallel to the regional pervasive metamorphic foliation, and these bodies have been deformed by a localized greenschist facies foliation associated with tight recumbent folding and thrusting of that foliation. Serpentinite bodies have been emplaced by thrust faults into the gneisses, and these serpentinite bodies have also been affected by the greenschist facies fabric that formed in association with the thrust faults.

The gneissic rock mass and emplaced ultramafic bodies have been cut by moderately to steeply dipping brittle normal faults with northerly and easterly strikes. These faults formed in the Late Cretaceous or early Tertiary. The normal faults have disrupted the gneisses into structural blocks on the km-scale, and have juxtaposed distinctly different rock types. This disruption of rock types can be mapped in a general way using magnetic signatures of the enclosed ultramafic rocks.

The normal faults have acted as conduits for hydrothermal fluids that introduced gold to the White River area. There was little emplacement of quartz veins during this hydrothermal activity, and most mineralization is disseminated through the gneisses adjacent to the faults. Fluid flow was controlled by brittle fractures and breccias associated with the faults, and also by shallow-dipping shears associated with the greenschist facies folds and thrust faults.

Hydrothermal alteration was strongly controlled by rock types adjacent to the normal faults. Felsic gneisses and quartzites have the best-developed fracture systems, and are the principal hosts for introduced gold. Felsic gneisses have an oxidised alteration assemblage dominated by hematite and sericite, with later stage pyritic alteration that contains the highest gold grades. In contrast, quartzites, with metamorphic graphite and pyrrhotite, have a reduced alteration assemblage with recrystallized graphite and pyrrhotite and introduced arsenopyrite. Gold grades are highest in arsenic-rich rocks in quartzites. Other gneisses and the ultramafic rocks have had only limited hydrothermal interaction because of lack of fracturing, and gold addition has been minimal. Ultramafic rocks have localised fuchsitic alteration and associated decomposition of primary magnetite. Magnetite

decomposition affects the geophysical signature of these rocks, and this may be visible in detailed magnetic surveys.

ACKNOWLEDGEMENTS

Financial assistance for this research was provided by Underworld Resources Ltd., the University of Otago, and the NZ Foundation for Research, Science and Technology. Discussions with Adrian Fleming, Rob McLeod, Mike Cooley, Lamont Leatherman, Colin Brodie, Jodie Gibson and Hanne-Kristen Paulsen helped us to develop our ideas. The map in Figure 2 incorporates some aspects of an unpublished map by Chris Ash for Madalena Ventures Inc. 2005. A constructive review by Jim Mortensen helped improve the manuscript.

REFERENCES

- Berman, R.G., Ryan, J.J., Gordey, S.P. and Villeneuve, M. 2007. Permian to Cretaceous polymetamorphic evolution of the Stewart River region, Yukon-Tanana terrane, Yukon, Canada: P-T evolution linked with *in situ* SHRIMP monazite geochronology. *Journal of Metamorphic Geology*, vol. 25, p. 803-827.
- Gabrielse, H. and Yorath, C.J., 1991. Tectonic synthesis, Chapter 18. *In: Geology of the Cordilleran Orogen in Canada*, H. Gabrielse and C.J. Yorath (eds.), Geological Survey of Canada, Geology of Canada, vol. 4, p. 677-705. (also Geological Society of America, *The Geology of North America*, v. G-2)
- Gabrielse, H., Murphy, D.C. and Mortensen, J.K., 2006. Cretaceous and Cenozoic dextral orogen-parallel displacements, magmatism, and paleogeography, north-central Canadian Cordillera. *In: Paleogeography of the North American Cordillera: Evidence For and Against Large-Scale Displacements*, J.W. Haggart, R.J. Enkin and J.W.H. Monger (eds.), Geological Association of Canada, Special Paper 46, p. 255-276.
- Gordey, S.P. and Ryan, J.J., 2005. Geology map, Stewart River Area (115 N, 115-O and part of 115J), Yukon Territory. Geological Survey of Canada, Open File 4970, 1:250 000 scale.
- LeBarge, W.P., 2007. Yukon Placer Mining Industry, 2003-2006: An overview of placer activity and production. *In: Yukon Placer Mining Industry 2003-2006*, W.P. LeBarge and C.S. Welsh (compilers), Yukon Geological Survey, 235 p.

- Lowey, G.W., 2006. The origin and evolution of the Klondike goldfields, Yukon, Canada. *Ore Geology Reviews*, vol. 28, p. 431-450.
- MacKenzie, D.J., Craw, D.C., Mortensen, J.K. and Liverton, T., 2007. Structure of schist in the vicinity of the Klondike goldfield, Yukon. *In: Yukon Exploration and Geology 2006*, D.S. Emond, L.L. Lewis and L.H. Weston (eds.), Yukon Geological Survey, p. 197-212.
- MacKenzie, D.J., Craw, D. and Mortensen, J., 2008a. Structural controls on orogenic gold mineralization in the Klondike goldfield, Canada. *Mineralium Deposita*, vol. 43, p. 435-448.
- MacKenzie, D., Craw, D. and Mortensen, J.K., 2008b. Thrust slices and associated deformation in the Klondike goldfields, Yukon. *In: Yukon Exploration and Geology 2007*, D.S. Emond, L.R. Blackburn, R.P. Hill and L.H. Weston (eds.), Yukon Geological Survey, p. 199-213.
- Mortensen, J.K., 1990. Geology and U-Pb chronology of the Klondike District, west-central Yukon. *Canadian Journal of Earth Sciences*, vol. 27, p. 903-914.
- Mortensen J.K., 1992. Pre-mid-Mesozoic tectonic evolution of the Yukon-Tanana Terrane, Yukon and Alaska. *Tectonics*, vol. 11, p. 836-853.
- Mortensen, J.K., 1996. Geological compilation maps of the northern Stewart River map area, Klondike and Sixtymile Districts (115N/15, 16; 115O/13, 14; and parts of 115O/15, 16). Exploration and Geological Services Division, Yukon Region, Indian and Northern Affairs Canada, Open File 1996-1(G), 43 p.
- Mortensen, J.K., Beranek, L. and Murphy, D.C., 2007. Permo-Triassic Orogeny in the Northern Cordillera: Sonoma North? Geological Society of America, Abstracts with Programs, 103rd Annual Meeting, Cordilleran Section, Bellingham, WA, USA, Paper No. 28-5.
- Ryan, J.J. and Gordey, S.P., 2001. Geology of the Thistle Creek area, Yukon Territory (115-O/3). Geological Survey of Canada, Open File 3690, 1:50 000 scale.
- Ryan, J.J. and Gordey, S.P., 2004. Geology, Stewart River Area (Parts of 115 N/1,2,7,8 and 115-O/2-12), Yukon Territory. Geological Survey of Canada, Open File 4641, 1:100 000 scale.
- Shives, R.B.K., Carson, J.M., Ford, K.L., Holman, P.B., Gordey, S. and Abbott, G., 2002a. Magnetic Anomaly Map (Residual Total Field), Stewart River Area – 115O/6, 1:50 000 scale. Geological Survey of Canada, Open File 4307; Exploration and Geological Services Division, Yukon, Indian and Northern Affairs Canada, Open File 2002-13.
- Shives, R.B.K., Carson, J.M., Ford, K.L., Holman, P.B., Gordey, S. and Abbott, G., 2002b. Magnetic First Vertical Derivative Map Stewart River Area – 115O/6, 1:50 000 scale. Geological Survey of Canada, Open File 4307; Exploration and Geological Services Division, Yukon, Indian and Northern Affairs Canada, Open File 2002-13.

The Proterozoic Pinguicula Group: Stratigraphy, contact relationships and possible correlations

K.P.R. Medig¹, D.J. Thorkelson and R.L. Dunlop

Simon Fraser University

Medig, K.P.R., Thorkelson, D.J. and Dunlop, R.L., 2010. The Proterozoic Pinguicula Group: Stratigraphy, contact relationships and possible correlations. *In: Yukon Exploration and Geology 2009*, K.E. MacFarlane, L.H. Weston and L.R. Blackburn (eds.), Yukon Geological Survey, p. 265-278.

ABSTRACT

The Pinguicula Group is a Proterozoic succession of clastic and carbonate rocks exposed in the Wernecke Mountains of northern Yukon. The strata were deposited with angular unconformity on the Wernecke Supergroup following the Racklan orogeny and emplacement of the Hart River sills. Two contact relationships have been resolved in the 2009 field season. The first, a 1.38 Ga dyke previously thought to crosscut unit A, has instead been recognized to crosscut the underlying Wernecke Supergroup strata. This relationship is significant because it once again places the lower age limit of the Pinguicula Group into question and may reposition the Pinguicula Group within the history of geologic events. Secondly, the previously undefined contact relationship between units B and C has been identified as a gradational contact confirming the placement of unit C within the Pinguicula Group. In addition, preliminary data collected from the western Ogilvie Mountains draws similarities between units PR1 and PR2 of the lower Fifteenmile Group and units A, B and C of the Pinguicula Group. Although preliminary results from the 2009 field season have resolved some of the unknowns surrounding the Pinguicula Group, they have also raised more questions.

¹kmedig@alumni.sfu.ca

INTRODUCTION

The Proterozoic Pinguicula Group consists of clastic and carbonate rocks in the Wernecke Mountains of northern Yukon (Eisbacher, 1981). These strata were deposited with angular unconformity on the Wernecke Supergroup following contractional deformation and metamorphism during the Racklan orogeny (Eisbacher, 1978; Thorkelson, 2000). Previous work, summarized in Thorkelson *et al.* (2005), described the main characteristics of the group, but questions remained about its age, depositional environment, areal extent and relations with Proterozoic successions in adjacent inliers. Suggested correlations between the Pinguicula Group and strata in the Ogilvie Mountains (Abbott, 1997) had not been tested.

The Pinguicula Group *sensu stricto* is located in the Wernecke Mountains approximately 150 km north-northeast of Mayo along the Bonnet Plume River (map areas 106C/5, 106C/6, 106C/11, 106C/12, 106C/13 and 106C/14). Possible correlative strata are exposed in the eastern Ogilvie Mountains (map areas 116A/10 and A/11), approximately 140 km northeast of Dawson City, and in the western Ogilvie Mountains (map areas 116B/11, 116B/13 and 116B/14) approximately 90 km north of Dawson City. Field work in the summer of 2009 was carried out in the Wernecke and western Ogilvie mountains (Fig. 1).

This paper outlines field data collected in summer 2009 and preliminary interpretations of contact relationships and sedimentary environments. These data are part of a graduate degree project that aims to map and characterize the Pinguicula Group in the Wernecke Mountains and evaluate correlations with similar strata in the Ogilvie Mountains. Geochemical, isotopic and geochronological analyses will be completed on samples in the spring of 2010. Future work may include additional mapping and sampling in the Wernecke and Ogilvie mountains and related laboratory analyses. Locations given in this report by UTM coordinates are based on North American Datum (NAD) 1927.

PREVIOUS WORK

STRATIGRAPHIC NOMENCLATURE

Eisbacher (1981) defined the Pinguicula Group and divided it into six formations, termed units A through F. Subsequent work, completed by Thorkelson (2000), broke the Pinguicula Group into two successions

separated by a lacuna of ~380 million years. This division was based on field data suggesting that unit A is crosscut by a ca. 1380 Ma dyke, whereas units D-F are younger than ca. 1000 Ma (the age of a detrital muscovite population from unit D). The hiatus was placed between units C and D because comparable strata in the Hart River inlier are separated by an angular unconformity (Abbott, 1997; Thorkelson *et al.*, 2005). This configuration was supported by relations in the Wernecke inlier, where zones of coarse, sparry carbonate in unit C were thought to represent karst caverns that developed during an interval of subaerial exposure (Abbott, 1997; Thorkelson, 2000). On this basis, Thorkelson (2000) kept units A through C in the Pinguicula Group and assigned units D through F to a new succession termed the Hematite Creek Group. The Hematite Creek Group was subsequently correlated with parts of the Mackenzie Mountains Supergroup (Thorkelson *et al.*, 2003). The restriction of the Pinguicula Group to units A-C of Eisbacher (1981) is followed in this report.

STRATIGRAPHIC DESCRIPTIONS, THICKNESSES AND CONTACT RELATIONSHIPS

The initial stratigraphic descriptions of the Pinguicula Group by Eisbacher (1978, 1981) were modified appreciably by Thorkelson (2000) and Thorkelson *et al.* (2005). Eisbacher (1981) described the group as a succession of “basaltic flows overlain by laminated and flasered limestone (unit A) grading into laminated dolosiltite (unit B) followed by massive dolostone (unit C), black shale with limestone laminites and stromatolites (unit D), brown laminated quartzite and red dolomitic siltstone (unit E), and finally, thinly bedded particulate limestone (unit F).” In contrast, Thorkelson *et al.* (2005) portrayed the Pinguicula Group as a succession of “basal sandstones grading into green and maroon mudstones (unit A) which are gradationally overlain by orange-weathering micritic dolostones (unit B) that are in turn overlain by grey micritic carbonate (unit C).” Thorkelson (2000) was unable to locate the volcanic flows of unit A (termed the Kohse Creek volcanics by Eisbacher, 1981) and suggested that they do not exist.

Figure 1. (opposite page) Previously mapped extent of the Pinguicula Group in the Wernecke Mountains (Gordey and Makepeace, 2003; Thorkelson, 2000) and additional mapping completed during the 2009 field season.

LEGEND

STRATIFIED ROCKS

Neo-Proterozoic

Windermere Supergroup
SA Sayunei Formation

Meso to Neo-Proterozoic

Hematite Creek Group
HC Hematite Creek

Meso-Proterozoic

Pinguicula Group
Pc Unit C
Pb Unit B
Pa Unit A

Paleo-Proterozoic

Wernecke Supergroup
GL Gillespie Lake Group

INTRUSIVE ROCKS

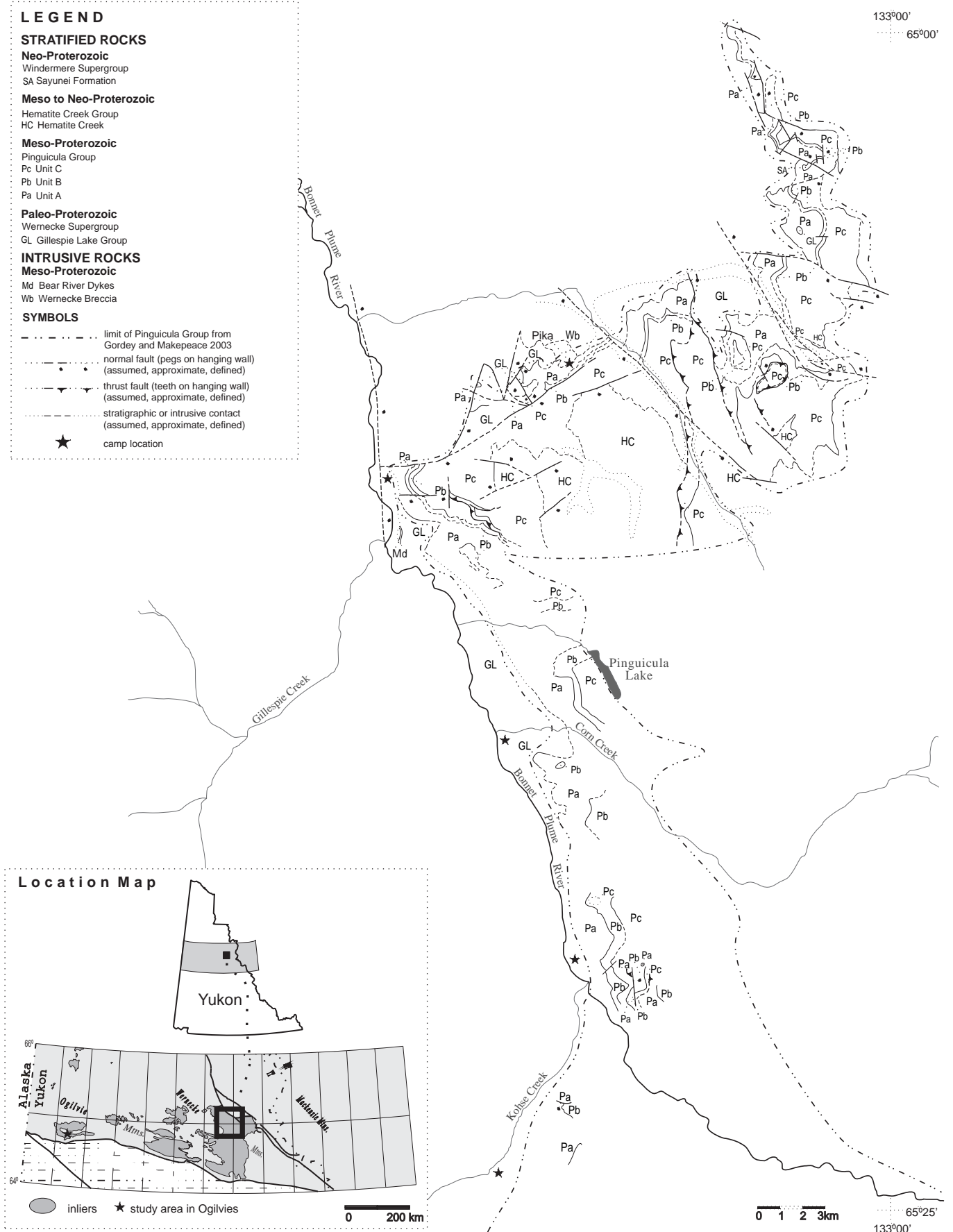
Meso-Proterozoic

Md Bear River Dykes
Wb Wernecke Breccia

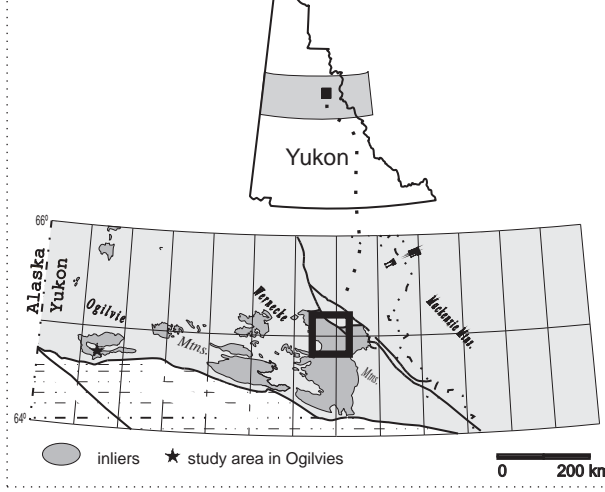
SYMBOLS

- limit of Pinguicula Group from Gordey and Makepeace 2003
- - - normal fault (pegs on hanging wall) (assumed, approximate, defined)
- - - thrust fault (teeth on hanging wall) (assumed, approximate, defined)
- - - stratigraphic or intrusive contact (assumed, approximate, defined)
- ★ camp location

133°00'
65°00'



Location Map



0 1 2 3km
65°25'
133°00'

In the Wernecke inlier, the Pinguicula Group unconformably overlies the Gillespie Lake and Quartet groups of the Wernecke Supergroup, and zones of Wernecke Breccia (Thorkelson, 2000). Similarly, in the Hart River inlier, a succession classified as Pinguicula Group overlies the Gillespie Lake Group, as well as the Hart River sills and basalts, with angular unconformity (Abbott, 1997; Thorkelson, 2000). The angular relationship between the two successions is considered to be mainly a result of the Racklan orogeny in the Wernecke Mountains and the correlative Fifteenmile orogeny in the Ogilvie Mountains (Brideau *et al.*, 2002).

Eisbacher (1981) estimated the thickness of the Pinguicula Group (formerly units A through F) in the Wernecke inlier near Pinguicula Lake at approximately 2300 m. More recent work provided an estimated thickness of the Pinguicula Group (units A through C) of 2720 m, thickening to approximately 3520 m in the south (map areas 106C/13 and 106C/14; Thorkelson, 2000). Unit A thickens southward in map area 106C/11, and units B and C decrease in thickness in the same area (Thorkelson, 2000). A measured section in the Hart River inlier provided a thickness of 1984 m for units A and B, and an estimated thickness for unit C of 250 m (Abbott, 1997).

AGE CONSTRAINTS AND DETRITAL ZIRCON PROVENANCE

The age of the Pinguicula Group was considered by Thorkelson *et al.* (2005) to be approximately 1380 Ma. In the Wernecke inlier, Thorkelson (2000) documented a dioritic intrusion crosscutting black shale identified as unit A. Igneous zircons from the diorite were dated at approximately 1380 Ma, and the diorite was assigned to the Hart River sills of Abbott (1997). As a result, the deposition of the base of the Pinguicula Group was constrained between 1380 Ma and 1590 Ma (the age of the underlying Wernecke Breccia in other locations; Thorkelson, 2000; Thorkelson *et al.*, 2005). New data that bear on this contact relationship will be discussed later in this paper. The Bear River dykes may constrain the end of deposition of the Pinguicula Group at more than 1270 Ma (Thorkelson, 2000).

In the eastern Ogilvie Mountains, strata that Abbott (1997) correlated with unit A of the Pinguicula Group overlie the Hart River sills and Hart River basalts. This relation contrasts with the interpretation that the Hart River sills crosscut unit A in the Wernecke Mountains, and suggests that the Pinguicula Group was deposited after emplacement of the Hart River volcanics, and is therefore

younger than 1380 Ma. To account for the contrasting pre- and post-1380 Ma timing relations, Thorkelson *et al.* (2005) considered that “basin formation and magmatism were broadly concurrent and locally diachronous.”

Detrital zircon ages for basal sandstone of Pinguicula Group unit A provide an indication of sandstone provenance. Using thermal ionization mass spectrometry (TIMS), U-Pb analyses plotted in two distinct clusters, with the youngest detrital zircon age plotting at 1841 Ma (Thorkelson *et al.*, 2005). The detrital ages reflect the ages of the source region and not the time of Pinguicula Group deposition. Detrital zircons probably originated from the Wernecke Supergroup or directly from Laurentian crystalline rocks (Thorkelson *et al.*, 2005).

CORRELATIVE STRATA IN ADJACENT MOUNTAIN RANGES AND SEQUENCE A, B, C CLASSIFICATION

Work completed in the late 1970s correlated units A through F of the Pinguicula Group, with the upper part of the Mackenzie Mountains Supergroup (Eisbacher, 1978; Young *et al.*, 1979). More recent work has led to correlation of units D through F (Hematite Creek Group of Thorkelson, (2000)) with the Mackenzie Mountains Supergroup (Thorkelson *et al.*, 2005; Fig. 2). Pinguicula Group units A through C have been correlated with the Dismal Lakes Group of the Coppermine Homocline (MacLean and Cook, 2004) and with units PR1 through PR4 in the lower Fifteenmile Group in the Ogilvie Mountains. Units A and B have been correlated with unit H1 in the Mackenzie Mountains (Rainbird *et al.*, 1996; Thorkelson *et al.*, 2005).

Young *et al.* (1979) divided the Proterozoic stratigraphy of northwestern Canada into unconformity-bounded Sequences A, B and C. The sequences were defined on the basis of ages and orogenic events with “Sequence A encompassing the oldest rocks in the Cordillera, Sequence B intermediate age rocks and Sequence C the youngest Proterozoic rocks” (Young *et al.*, 1979). The Pinguicula Group was originally classified as Sequence B and separated from the Wernecke Supergroup (Sequence A) by age and the Racklan orogeny. Based on ages obtained from the Hart River sills by Thorkelson *et al.* (2005), which were more closely aligned with the Wernecke Supergroup than the overlying Mackenzie Mountains Supergroup strata of Sequence B, the Pinguicula Group has since been moved from Sequence B to Sequence A. MacLean and Cook (2004) further subdivided Sequence A based on the analysis of

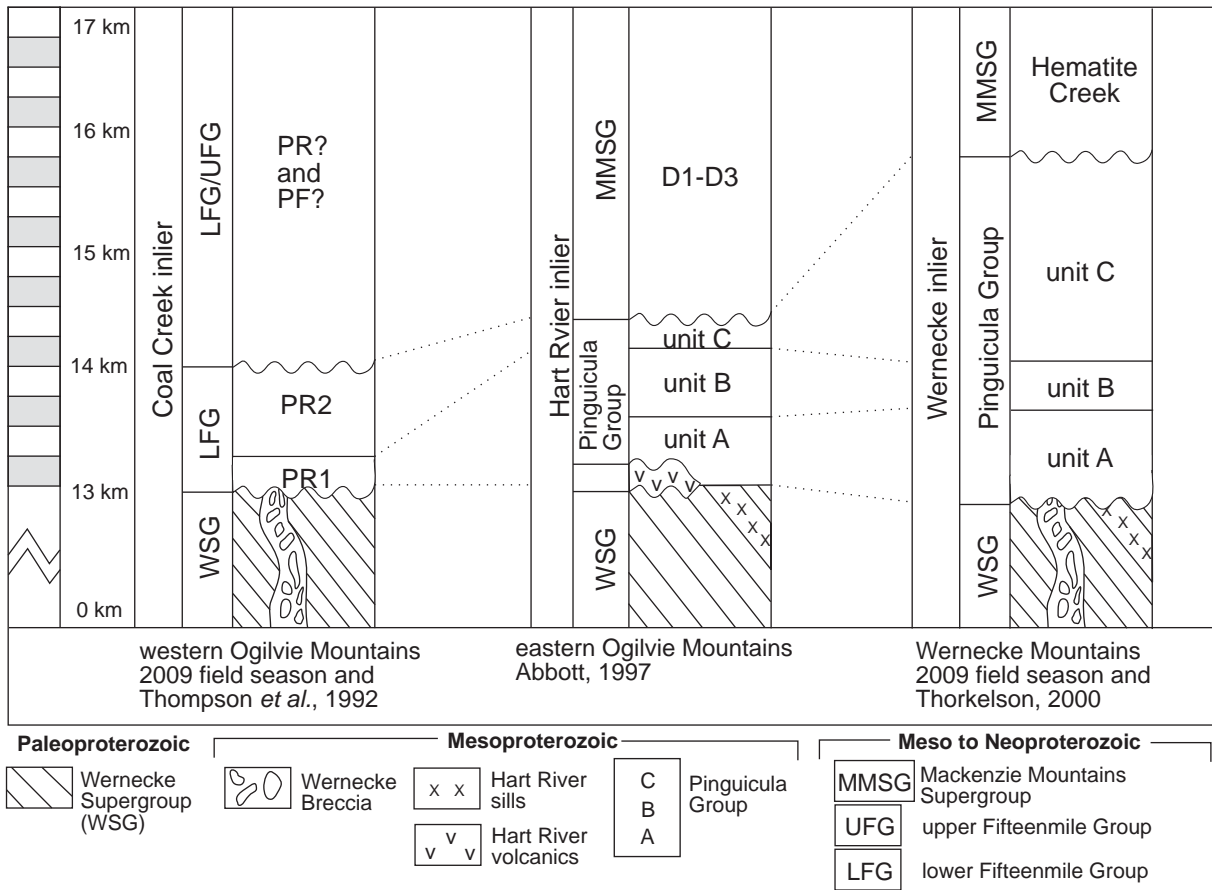


Figure 2. Strata correlative with Meso to Neoproterozoic Pinguicula units A, B and C in the eastern and western Ogilvie Mountains (Hart River and Coal Creek inliers; modified from Abbott, 1997).

reflection seismic data from across the western Northwest Territories, resulting in four units: A1, A2, A3 and A4. The oldest unit, A1, includes the Wernecke Supergroup, whereas the Pinguicula Group has been placed in unit A3 (MacLean and Cook, 2004). There are no strata equivalent to unit A2 in the Wernecke Mountains (MacLean and Cook, 2004), although the work of Furlanetto *et al.* (2009) implies that the Wernecke Supergroup is younger than previously thought, and may be part of Sequence A2.

DEPOSITIONAL ENVIRONMENTS

An interval of crustal stability, after deposition of the Wernecke Supergroup and contractional deformation of the Racklan orogeny, was followed by extension and emplacement of the Hart River sills (Thorkelson *et al.*, 2005). The Hart River sills likely represent an episode of rifting and crustal extension that in turn led to subsidence that allowed the deposition of the Pinguicula Group.

The Pinguicula Group was thought to have been deposited during a time of basin development with a “progression from a mid to deep-water shale basin (unit A), to a mid-water carbonate shelf (unit B), to a subtidal or intertidal carbonate bank (unit C)” (Thorkelson, 2000). Based on the thickness of the units, the basin was interpreted to deepen to the south (Thorkelson, 2000). Although the broader significance of Pinguicula basin formation has not been fully evaluated, it may reflect the separation of Laurentia from another continent (Thorkelson *et al.*, 2005).

2009 FIELD WORK

In the summer of 2009, five locations in the Wernecke Mountains (Fig. 1) and three locations in the Ogilvie Mountains were studied. The objectives of the field work were to measure stratigraphic thicknesses at selected locations, examine contact relationships, collect samples

for U-Pb geochronology, isotope and geochemical analyses, and record detailed lithologic descriptions. While in the Wernecke Mountains, camps were located at the Pika MINFILE occurrence (Yukon MINFILE, 106C 071) and several locations along the eastern side of the Bonnet Plume River and Kohse Creek. Camps in the Ogilvie Mountains were located near the headwaters of Fifteenmile Creek and Coal Creek.

Stratigraphic sections were measured at two locations in the Pinguicula Group in the Wernecke Mountains previously documented by Thorkelson (2000). A section through units A and B was measured near the Pika occurrence (UTM 573349E, 7190628N). A second section was measured farther south, adjacent to the Bonnet Plume River (UTM 563956E, 7185104N), and included units B and C.

STRATIGRAPHY

Unit A

Unit A of the Pinguicula Group unconformably overlies the Gillespie Lake and Quartet groups and the Wernecke Breccia of the Wernecke Supergroup. At its base, Pinguicula A is lithologically variable, consisting of mudstone, sandstone and conglomerate. Conglomerate and sandstone form layers and lenses in the mudstone, and are locally present at the base of the succession.

Figure 3. Centimetre-scale green-maroon mottling in mudstone of unit A at the Pika MINFILE occurrence (UTM 573381E, 7190576N).



Conglomerate clasts range from granule to boulder-sized (~50 cm in diameter) and are well-rounded to subrounded. Diverse clast types include yellow siltstone, green and black mudstone and distinctly red clasts with local specular hematite. The red clasts are prevalent in conglomerate overlying the Wernecke Breccia (e.g., Pika occurrence) and appear to be derived from it. Some conglomerate layers are well-sorted and matrix-supported, with clasts in a matrix of well-sorted, subangular granules and coarse quartz sand. In other areas, the conglomerate is well to moderately well sorted and the matrix is composed of subrounded, fine to medium quartz sand with specular hematite and pyrite altering to limonite.

Sandstone is orange to black-weathering, grey to white, and fine to medium-grained. It is massive to thin-bedded (1-2 cm) and laminated in some areas. The grains are well sorted, well rounded and consist of approximately 90% quartz. Adjacent to the Bonnet Plume River (UTM 573352E, 7167986N), the sandstone beds (approximately 10 cm thick) are interbedded with conglomerate and contain traces of pyrite that is locally weathered to limonite. Sandstone bed thicknesses at the Pika occurrence are 3 cm to 9 m (massive) and 18 m (laminated).

Above the basal strata, unit A consists of a succession of laminated mudstone. The mudstone is commonly cleaved, locally exhibiting pencil cleavage and in a few localities

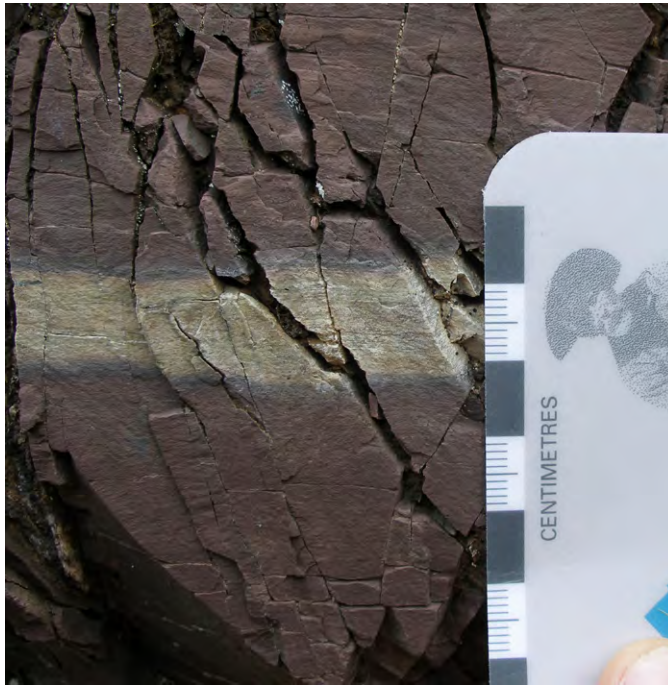


Figure 4. Possible ash beds in mudstone of unit A at the Pika occurrence (UTM 573343E, 7190633N). These centimetre-scale beds are less indurated than overlying and underlying beds.

the cleavage is crenulated (UTM 572959E, 7169440N). Near the Pika occurrence, the mudstone is dominantly maroon with green and grey interlayers. Although the maroon and green colours are broadly stratiform, some layers display both colours in a mottled pattern (Fig. 3). The mottling may be the product of diagenetic overprinting because it is independent of primary lamination. Toward the contact with unit B, the mudstone alternates between maroon and green, before changing to a slightly darker grey/black colour, and then returning to maroon just below the contact with unit B. In the southern part of map sheet 106C/14, the mudstone is grey to black and locally displays limonitic staining on fracture surfaces, interpreted as oxidation of diagenetic pyrite.

Upsection, toward the contact with unit B, unit A typically becomes slightly calcareous and contains calcareous nodules. The nodules are tabular to lenticular and typically deflect sedimentary laminae, forming a pinch-and-swell structure. Nodules are approximately 1-9 cm thick and tend to be concentrated in certain layers.



Figure 5. Unit B yellow/orange-weathering, maroon to green dolomudstone (UTM 573524E, 7190577N).

Possible tephra layers are present in laminated mudstone near the base of unit A, near the Pika occurrence. These light grey, slightly recessive layers are 0.1-5.5 cm thick (Fig. 4). Several samples were taken to determine their age and composition.

Unit B

Unit B gradationally overlies the increasingly calcareous mudstone beds of unit A and is dominated by yellow/orange-weathering, maroon to green dolomudstone (Fig. 5). At the base of unit B, a massive, quartz-silty carbonate grades into green to maroon, laminated dolomudstone. As with unit A, unit B alternates in colour between green and maroon. The boundary between units A and B is placed at the base of the yellow/orange-weathering dolomudstone of unit B.

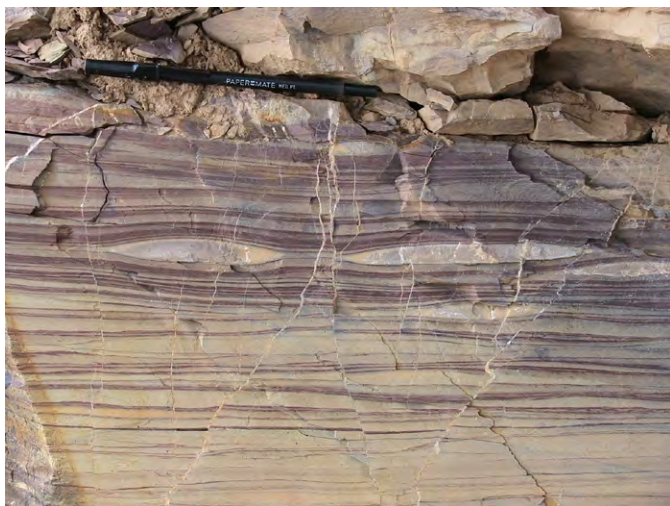


Figure 6. Carbonate lenses (approximately 2 cm thick and 10 cm long) in unit B at the Pika occurrence (UTM 573524E, 7190577N).



Figure 7. Carbonate lenses (approximately 3 cm thick and 10 cm long) that have undergone soft sediment deformation in unit B (UTM 564074E, 7185389N).

Features characteristic of unit B include carbonate nodules, flat-pebble conglomerate and possibly thin carbonate beds. Most of the nodules are in maroon, quartz-silty dolostone and are 2-5 cm thick and 5-10 cm long. Some are lenticular, whereas others are ellipsoidal (Figs. 6, 7). Others are tabular, with an approximate thickness of 1-5 cm and appear bedlike. The nodules, intraclasts and possible beds are grey-green on fresh surfaces, medium-grey on weathered surfaces and weather recessively relative to the host rock.

The flat-pebble conglomerate in unit B, above the Bonnet Plume River (UTM 564074E, 7185389N), consists of light grey or white dolostone clasts in maroon, quartz-silty dolostone. The conglomerate forms layers up to 2 m thick. Clasts range from <1 cm to 9 cm long and are approximately 1-2 cm thick (Fig. 8). Some of the pebbles appear to have undergone soft sediment deformation whereas others have maintained their tabular morphology. In one location (UTM 564074E, 7185389N), a section rich in flat-pebble conglomerate overlies 1 m carbonate beds and underlies pyrite-rich dolomudstone.

Unit C

Unit C is dominated by craggy and dark to medium-grey weathering, layered to massive grey dolostone. At the Bonnet Plume River section (UTM 563956E, 7185104N) the unit gradationally overlies unit B as the weathered colour grades from yellow to grey over an interval of approximately 7 m. The lower part of unit C consists of



Figure 8. Metre-scale beds of flat-pebble conglomerate that have undergone soft sediment deformation in unit B above the Bonnet Plume River (UTM 563956E, 7185104N). Clasts are 1-9 cm long and 1-2 cm thick.

carbonate layers, some of which contain shaly partings, interbedded with laminated grey siltstone. Most of the beds are 1-60 cm thick, but some are more massive, with thicknesses >60 cm. The dolostone in the lower part of unit C is typically fetid (on fresh surface), contains stylolites, and has pervasive carbonate veins.



Figure 9. Zebra dolostone of Unit C above the Bonnet Plume River (UTM 564124E, 7185044N).

Zebra dolostone (Fig. 9) becomes conspicuous several metres above the stylolites. White dolospar 'stripes' in darker primary dolostone define the texture. In separate horizons, chert nodules and brecciated dolostone with void-filling dolospar cement (Fig. 10) are also present.

The contact between units B and C was previously not well understood and thought to be unconformable (Thorkelson, 2000). Recent work in the area has shown that yellow-weathering dolostone of unit B grades upward to a grey-weathering, fetid dolostone of unit C.



Figure 10. Pervasive, late brecciation in thin-bedded dolostone; breccia interstices are filled with coarsely crystalline dolospar.

IGNEOUS INTRUSIONS

Diorite dykes crosscutting units A, B and C

Three diorite dykes that crosscut the Pinguicula Group were sampled. The first is an east-trending dyke hosted by units A, B and C at UTM 576862E, 7161598N. The second, a northwest-trending dyke, and the third, a northeast-trending dyke, crosscut unit A adjacent to Kohse Creek (UTM 572676E, 7150368N and UTM 572865E, 7150726N). Geochronological analyses will be undertaken to determine the minimum ages of the units cut by the dykes.

Re-evaluation of Hart River sills in unit A

The age of the Pinguicula Group in the Bonnet Plume River area was previously constrained by a relationship that is now called into question. The minimum age of the basal Pinguicula Group was provided by a dioritic Hart River sill, dated at 1380 Ma, that intrudes black siltstone (Thorkelson *et al.*, 2005). The siltstone was regarded by Thorkelson (2000) and Thorkelson *et al.* (2005) as part of unit A. Re-examination of this locality on either side of a small tributary of the Bonnet Plume River (UTM 574258E, 7159882N) has confirmed that diorite intrudes siltstone, but the siltstone does not appear to belong to unit A. The siltstone differs in detail from nearby black, laminated, sandy siltstone that clearly belongs to unit A (exposed up-section across a short covered interval) that is not crosscut by the diorite. The siltstone hosting the diorite is now considered to belong to either the Gillespie Lake Group or the Quartet Group of the Wernecke Supergroup, and to be unconformably overlain by unit A.

Differences between the graphitic siltstone intruded by the Hart River sills and the siltstone of unit A leading to this reclassification are as follows: the bedding is thicker in graphitic siltstone, as compared to unit A laminated siltstone; fracturing is widely spaced in the graphitic siltstone compared to more closely spaced fracturing in unit A; red weathering and pyrolusite pervade the graphitic siltstone, whereas unit A has neither red weathering nor pyrolusite staining; the orientation of bedding in the graphitic siltstone and unit A are dissimilar (strike differing by as much as 100° and dip 26°); crenulations are present in the graphitic siltstone but absent in unit A at that locality; and unit A is clearly not graphitic or as strongly indurated. For these reasons, the diorite dyke is tentatively considered to crosscut strata of the Wernecke Supergroup, rather than unit A. This hypothesis will be tested using geochemistry and isotopes.

This new crosscutting relationship resolves complications identified by Thorkelson *et al.* (2005) regarding discrepancies between the position of the Hart River sills in the Wernecke inlier. Because the Hart River sills have not been shown to crosscut unit A in the Wernecke inlier, locally diachronous basin formation and synchronous magmatism are not required.

SAMPLING

Sampling was undertaken for further characterization of the Pinguicula Group. Forty-two samples were collected in the Wernecke Mountains for petrographic, geochemical and/or isotopic analyses, and sixteen samples were collected for geochronological analysis (Fig. 11).

Detrital zircons will be extracted from sandstone for U-Pb geochronology. In addition, clasts from conglomerates will be sorted into lithologic groups and, where possible, dated using U-Pb zircon geochronology. This may provide insight into the possibility that strata were deposited, or that a terrane was obducted, between the time of Wernecke Supergroup deposition (<1640 Ma; Furlanetto *et al.*, 2009) and formation of the Pinguicula basin.

DEPOSITIONAL ENVIRONMENTS AND POST-DEPOSITIONAL TEXTURE FORMATION

The Pinguicula Group represents basinal to platformal sedimentation (Thorkelson, 2000). Deposition began after uplift and erosion of the Wernecke Supergroup. Following an interval of extension associated with the emplacement of the Hart River sills, subsidence and/or sea-level rise resulted in the deposition of deep-ocean sediment characteristic of unit A. The basin appears to have deepened to the south (map area 106C/11) where unit A becomes thicker and darker.

Flat-pebble conglomerate such as that in unit B is common in Proterozoic carbonate rocks. Another distinctive characteristic of the Pinguicula Group is the abundance of zebra textures. Zebra textures and stylolites form in deep subsurface environments where limestone is replaced by Mg-metasomatism at temperatures of up to 200°C (Merino *et al.*, 2006; Wallace *et al.*, 1994). This information suggests that zebra textures in unit C probably developed at depth, which is in contrast to interpretations made by Thorkelson (2000), who described zebra-textured clasts in an intraclast conglomerate in unit C and suggested that they formed “at or near the sediment surface, shortly after micritic deposition and prior to lithification.”

		limestone/dolostone	siltstone/mudstone	sandstone	conglomerate	intrusive diorite
PINGUICULA GROUP	unit C	<ul style="list-style-type: none"> ● KM09-8-2-1 ● KM09-8-1-5 ● KM09-8-1-4 ● KM09-8-1-3 ● KM09-8-1-2 				
	unit B	<ul style="list-style-type: none"> ● KM09-8-1-1 ● KM09-7-2-2 ● KM09-7-2-1 ● KM09-3-2-5 ● KM09-3-2-3 ● KM09-3-2-2 ● KM09-3-2-1 	◆ KM09-3-2-6			◆ KM09-11-1-1
	unit A		<ul style="list-style-type: none"> ◆ KM09-2-7-1 ◆ KM09-2-6-2 ◆ KM09-2-6-1 ◆ KM09-2-5-1 ◆ KM09-2-4-2 ◆ KM09-2-4-1 ◆ KM09-2-1-1 ◆ KM09-1-3-2 ★ KM09-1-3-1* ◆ KM09-12-4-1 ◆ KM09-12-3-1 ◆ KM09-12-2-1 ◆ KM09-11-2-1 ◆ KM09-10-4-1 ◆ KM09-3-1-1 ★ KM09-2-9-1* ◆ KM09-2-8-1 	<ul style="list-style-type: none"> ★ KM09-12-2-2 ★ KM09-10-3-1 ★ KM09-4-1-2 ★ KM09-1-4-2 ★ KM09-1-4-1 	<ul style="list-style-type: none"> ★ KM09-10-3-7 ★ KM09-10-3-3 ★ KM09-10-3-2 ★ KM09-10-3-6 ★ KM09-4-1-1 	<ul style="list-style-type: none"> ◆ KM09-11-6-2 ◆ KM09-11-6-1 ◆ KM09-11-7-3 ◆ KM09-10-6-1

● C, O and Sr isotopes ◆ Nd isotopes ★ U-Pb dating, detrital zircon ◆ U-Pb dating, zircon *possibly ash

Figure 11. Summary of samples collected from units A, B and C of the Pinguicula Group in the Wernecke Mountains. For anticipated analyses for each sample refer to symbol legend.

FIFTEENMILE GROUP IN OGILVIE MOUNTAINS

Work completed in the Fifteenmile Group in the Ogilvie Mountains focused on three locations previously mapped by Thompson *et al.* (1992). Traverses were completed along Fifteenmile Creek (UTM 579128E, 7183747N) to examine PR1 and PR2, and at the northern reaches of Coal Creek (UTM 552687E, 7186821N and UTM 549468E, 7188402N) to characterize PR3 through PR5. Field work at these locations focused on sampling, detailed rock descriptions and contact relationships. This information will be used to clarify the possible relationship between the Pinguicula and lower Fifteenmile groups.

Stratigraphy

Descriptions of the lower Fifteenmile Group, from the western Ogilvie Mountains, provided by Thompson *et al.* (1992) are as follows: PR1 comprises shale and silty dolostone with common dolostone olistoliths; PR2 is a medium to thick-bedded dolomitic mudstone, dolostone breccia, and massive, medium-crystalline dolostone; PR3 is a recessive-weathering, grey, medium-bedded dolostone with mudstone interbeds; PR4 is a brecciated, medium-grey oolitic packstone, with rare stromatolites; and PR5 comprises shale, pebbly mudstone, gritty mudstone, stromatolitic limestone and quartz sandstone.

Thompson *et al.* (1992) mapped the Wernecke Breccia as crosscutting siltstone (PR1 and locally PR5) of the lower Fifteenmile Group near Fifteenmile Creek (UTM 577590E, 7180979N). More recent field work, however, determined that the Wernecke Breccia underlies unit PR1 and is bleached and stained with malachite. Such features record an episode of subaerial exposure (Thorkelson, 2000) between deposition of the Wernecke Breccia and deposition of the lower Fifteenmile Group, and suggest that the Fifteenmile Group is younger than the Wernecke Breccia. Field investigation in 2009 confirmed this relationship: units PR1 and PR5 are not bleached and have not been affected by the emplacement of Wernecke Breccia.

The following observations of the lower Fifteenmile Group were made while traversing three sections in the 2009 field season. Unit PR1 comprises grey- and orange-weathering, black mudstone, with pencil cleavage, interbedded with grey to brown, very fine to coarse, silty sandstone beds approximately 10 cm thick. The clastic rocks are overlain by an orange-weathering, silty dolostone with bedding 1-5 cm thick. The light-grey-weathering dolostone of unit PR2 is bedded (layers

4-50 cm thick) and alternates between laminated beds and massive beds crosscut by an intense white veining with no distinct orientation. A second set of pink veins crosscuts both beds. Stylolites separate the beds and the rock is fetid. Another notable feature of unit PR2 is flat-pebble conglomerate with planar clasts 1-10 cm long. Unit PR3 comprises stromatolitic dolostone with stromatolites approximately 10 cm across and 30 cm high at the top of the unit, but 1-2 m in diameter lower in the unit. Subtle pink carbonate veins are present throughout the unit. Chert nodules and buff weathering are characteristic of unit PR4 dolostone. Unit PR5 is largely as described by Thompson *et al.* (1992), with the exception of desiccation cracks in the shale.

Sampling

Sixteen samples were collected for geochemical and isotopic analyses and six samples were collected for geochronological analysis. Two of the six samples collected for geochronological analyses are from fine-grained, green, diorite dykes (2-12 m wide): one crosscutting PR2 and another crosscutting PR5. Analytical results will be compared with those from the Pinguicula Group.

Correlations with Pinguicula Group

Correlations between the Pinguicula Group and the lower Fifteenmile Group are based on stratigraphic similarity to the two lower units of the lower Fifteenmile Group, and on similar contact relationships with the underlying Wernecke Supergroup. In contrast to the descriptions of Thompson *et al.* (1992), unit PR1 of the lower Fifteenmile Group unconformably overlies the Wernecke Breccia. This relationship is analogous to that in the Wernecke Mountains, where unit A of the Pinguicula Group unconformably overlies bleached Wernecke Breccia at the Pika occurrence. In addition, unit PR1 and units A and B of the Pinguicula Group have similar stratigraphic characteristics, including sandstones overlain by black and green siltstone and orange-weathering dolostone. Similarities can also be drawn between unit PR2 and Pinguicula Group unit C, which are both grey-weathering dolostones. The presence of stromatolites in unit PR3 but not in the Pinguicula Group makes such a correlation less plausible: unit PR3 is better equated with the Hematite Creek Group. Units PR4 and PR5 are dissimilar to the Pinguicula Group, but contain abundant shallow-water features such as ripple marks and mudcrack casts, and are

favourably correlated with strata of the Hematite Creek Group.

MINERALIZATION

Three styles of mineralization were identified during the field work. Two of the styles involve Cu enrichment and one involves Pb and possibly Ag enrichment. All may be worth consideration in mineral exploration programs.

One style of Cu enrichment is present in units that underlie the Pinguicula Group (Wernecke Supergroup and Wernecke Breccia), within a few metres of the sub-Pinguicula unconformity. This phenomenon was noted at three localities: two in the Ogilvie Mountains and one in the Wernecke Mountains. In the Wernecke Mountains, the Pika occurrence (UTM 572861E, 7191172N) was originally described by Thorkelson (2000) as supergene oxide mineralization within Wernecke Breccia and adjacent strata of the Wernecke Supergroup. The mineralization is expressed as malachite staining on fracture surfaces in bleached and crumbly rock that apparently formed during subaerial weathering, leaching and supergene mineralization prior to deposition of the Pinguicula Group.

In the Ogilvie Mountains, this style of mineralization is present beneath units PR1 and PR5 (UTM 552687E, 7186821N and UTM 549570E, 7188381N respectively) of the lower Fifteenmile Group (Thompson *et al.*, 1992). Beneath both units, underlying zones of Wernecke Breccia are bleached and fractured, and host local fracture-fillings of malachite. The prevalence of malachite-staining beneath the Pinguicula and lower Fifteenmile groups indicates that supergene enrichment of Wernecke Breccia-related Cu-mineralization is widespread in the Proterozoic inliers and locally augments pre-existing hypogene mineralization; such secondary enrichment may add economic value to underlying zones of Wernecke Breccia.

The second style of Cu mineralization is in unit A of the Pinguicula Group and is most prominent at a locality overlooking the Bonnet Plume River near the southeast corner of map area 106C/13 (UTM 563803E, 7184575N). The mineralization consists of malachite-staining on platy siltstone and nodules (0.5-2 cm diameter) of pyrite altered to limonite, with additional malachite-staining surrounding individual nodules.

The Pb and possibly Ag mineralization is in a set of veins that crosscut the Pinguicula Group 8 km south and 2 km west of the confluence of the Bonnet Plume River and

Kohse Creek (approximate UTM 572779E, 7150112N). The veins are approximately 2 m wide, highly weathered, and their original constituents have been largely converted to earthy encrustations and fracture-fillings of limonite, possibly anglesite and other minerals or mineraloids. Remnants of galena within the weathered vein material were noted in one of the veins. At depth, these veins probably contain greater abundances of the original vein minerals. Possible Ag mineralization in these veins is suggested by the presence of galena- and silver-bearing veins in the region (e.g., Yukon MINFILE, 106C 001, Kohse prospect).

CONCLUSIONS

Contacts between units A, B and C of the Pinguicula Group are gradational. The gradational contact between units A and B was previously suggested, but the nature of the contact between units B and C was not well understood. Firm documentation of a gradational contact between units B and C confirms that all units of the Pinguicula Group belong to a single, conformable succession.

The age of the Pinguicula Group may not be as old as previously considered by Thorkelson *et al.* (2005). A 1380 Ma dyke, previously thought to crosscut Pinguicula unit A, is now regarded as crosscutting only the Wernecke Supergroup. The contact relationship between the Pinguicula Group and the Hart River sills is now comparable to the relationship in the eastern Ogilvie documented by Abbott (1997), which shows the Pinguicula Group unconformably overlying the Hart River sills and possibly related volcanic strata. Elimination of the crosscutting relationship between the 1380 Ma intrusion and the Pinguicula Group means that the latter could be nearly as young as the overlying Hematite Creek Group, and may be more appropriately placed in Sequence B of Young *et al.* (1979), rather than Sequence A. Forthcoming age determinations on detrital minerals and crosscutting dykes may further constrain the age and affinity of the Pinguicula Group.

Correlations between the Pinguicula Group and strata in the adjacent western Ogilvie Mountains were revisited. At this stage, correlations between PR1 and PR2 of the lower Fifteenmile Group with units A, B and C of the Pinguicula Group seem most favourable. Additional work involving comparison of isotopic signatures and detrital mineral populations will serve to test this hypothesis.

Cu, Pb and possibly Ag mineral enrichments were identified in both the Wernecke and western Ogilvie mountains. Two styles of Cu enrichment were identified: one in the underlying Wernecke Supergroup and one in unit A of the Pinguicula Group. Lead, and possibly Ag enrichments, are present east of Kohse Creek, near the Kohse occurrence, in a series of veins that crosscut what is thought to be unit A of the Pinguicula Group.

ACKNOWLEDGEMENTS

Funding for this project was provided by the Yukon Geological Survey, NSTP and an NSERC grant to D. Thorkelson. Thanks to Alexander Nielsen for assistance in the field. We are grateful to Elizabeth Turner for a detailed critical review and to Grant Abbott, Charlie Roots and Francis Macdonald for additional review comments and discussions.

REFERENCES

- Abbott, G., 1997. Geology of the upper Hart River area eastern Ogilvie Mountains, Yukon Territory (116A/10, 11). Exploration and Geological Services Division, Yukon Region, Indian and Northern Affairs Canada Bulletin 9, 92 p.
- Brideau, M.-A., Thorkelson, D.J., Godin, L. and Laughton, J.R., 2002. Paleoproterozoic deformation of the Racklan orogeny, Slats Creek (106D/16) and Fairchild Lake (106C/13) map areas, Wernecke Mountains, Yukon. *In: Yukon Exploration and Geology 2001*, D.S. Emond, L.H. Weston and L.L. Lewis (eds.), Exploration and Geological Services Division, Yukon Region, Indian and Northern Affairs Canada, p. 65-72.
- Eisbacher, G.H., 1978. Two major Proterozoic unconformities, northern Cordillera. Geological Survey of Canada Current Research Paper 78-1A, p. 53-58.
- Eisbacher, G.H., 1981. Sedimentary tectonics and glacial record in the Windermere Supergroup, Mackenzie Mountains, northwestern Canada. Geological Survey of Canada 80-27, 40 p.
- Furlanetto, F., Thorkelson, D.J., Davis, W.J., Gibson, H.D., Rainbird, R.H. and Marshall, D.D., 2009. Preliminary results of detrital zircon geochronology, Wernecke Supergroup, Yukon. *In: Yukon Exploration and Geology 2008*, L.H. Weston, L.R. Blackburn and L.L. Lewis (eds.), Yukon Geological Survey, p. 125-135.
- Gordey, S.P. and Makepeace, A.J., 2003. Yukon Digital Geology, version 2.0; Geological Survey of Canada, Open File 1749; Yukon Geological Survey, Open File 2003-9 (D).
- MacLean, B.C. and Cook, D.G., 2004. Revisions to the Paleoproterozoic Sequence A, based on reflection seismic data across the western plains of the Northwest Territories, Canada. *Precambrian Research*, vol. 129, no. 3-4, p. 271-289.
- Merino, E., Canals, A. and Fletcher, R.C., 2006. Genesis of self-organized zebra textures in burial dolomites: Displacive veins, induced stress, and dolomitization. *Geologica Acta*, vol. 4, no. 3, p. 383-393.
- Rainbird, R.H., Jefferson, C.W. and Young, G.M., 1996. The early Neoproterozoic sedimentary succession B of northwestern Laurentia: Correlations and paleogeographic significance. *Geological Society of America Bulletin*, vol. 108, no. 4, p. 454-470.
- Thompson, R.I., Roots, C.F. and Mustard, P.S., 1992. Geology of Dawson map area (116B, C) (northeast of Tintina Trench). Geological Survey of Canada, Open File 2849, 13 sheets, scale 1:50 000.
- Thorkelson, D.J., 2000. Geology and mineral occurrences of the Slats Creek, Fairchild Lake and "Dolores Creek" areas, Wernecke Mountains (106D/16, 106C/13, 106C/14), Yukon Territory. Exploration and Geological Services Division, Yukon Region, Indian and Northern Affairs Canada, Bulletin 10, 73 p.
- Thorkelson, D.J., Abbott, J.G., Mortensen, J.K., Creaser, R.A., Villeneuve, M.E., McNicoll, V.J. and Layer, P.W., 2005. Early and Middle Proterozoic evolution of Yukon, Canada. *Canadian Journal of Earth Sciences*, vol. 42, no. 6, p. 1045-1071.
- Thorkelson, D.J., Laughton, J.R., Hunt, J.A. and Baker, T., 2003. Geology and mineral occurrences of the Quartet Lakes map area (NTS 106E/1), Wernecke and Mackenzie mountains, Yukon. *In: Yukon Exploration and Geology 2002*, D.S. Emond and L.L. Lewis (eds.). Exploration and Geological Services Division, Yukon Region, Indian and Northern Affairs Canada, p. 223-239.
- Wallace, M.W., Both, R.A., Ruano, S.M. and Hachali, P.F., 1994. Zebra textures from carbonate-hosted sulfide deposits; sheet cavity networks produced by fracture and solution enlargement. *Economic Geology*, vol. 89, no. 5, p. 1183-1191.

Young, G.M., Jefferson, C.W., Delaney, G.D. and Yeo, G.M., 1979. Middle and Late Proterozoic Evolution of the Northern Canadian Cordillera and Shield. *Geology*, vol. 7, no. 3, p. 125-128.

Yukon MINFILE 2009 – A database of mineral occurrences. Yukon Geological Survey, <http://www.geology.gov.yk.ca/databases_gis.html>.

Preliminary O-S isotopic compositions of Cretaceous granitoids in the Cassiar Platform and Selwyn Basin, Yukon and Northwest Territories

K.L. Rasmussen¹

Department of Earth and Ocean Sciences, University of British Columbia

G.B. Arehart²

Nevada Stable Isotope Laboratory, University of Nevada-Reno

Rasmussen, K.L. and Arehart, G.B., 2010. Preliminary O-S isotopic compositions of Cretaceous granitoids in the Cassiar Platform and Selwyn Basin, Yukon and Northwest Territories. *In: Yukon Exploration and Geology 2009*, K.E. MacFarlane, L.H. Weston and L.R. Blackburn (eds.), Yukon Geological Survey, p. 279-292.

ABSTRACT

A regional stable isotopic study of Cretaceous granitoids (109-90 Ma) emplaced into miogeoclinal Cassiar Platform and Selwyn Basin rocks was undertaken to provide new insights into the origin of several plutonic suites (Cassiar, Hyland, Tay River, Tungsten, Mayo and Tombstone). All of the intrusions have high positive $\delta^{18}\text{O}$ (+8.4 to +16.9‰). There is very little systematic variation in $\delta^{18}\text{O}$, indicating that the majority of the plutons assimilated significant amounts of, or were entirely derived from, crustal rocks. $\delta^{34}\text{S}$ typically ranges from +2.0 to +11‰ for all of the plutonic suites. This is consistent with derivation of the majority of sulphur from seawater sulphate, with some component of mantle or sedimentary (sulphide) sulphur evident in samples with the lowest $\delta^{34}\text{S}$. Future work, including comparison of these data with radiogenic isotopic data, will better define the specific roles that the crust and the mantle played in the petrogenesis of Cretaceous magmatism.

¹6339 Stores Road, Vancouver, British Columbia, Canada V6T 1Z4, krasmussen@eos.ubc.ca

²Department of Geological Sciences, MS-172, 1664 N. Virginia St., Reno, NV, USA 89557-0138

INTRODUCTION

Stable sulphur (S) and oxygen (O) isotopic compositions of granitoids can provide constraints on the magma source as well as extent and nature of crustal contaminants (e.g., Taylor and Sheppard, 1986). These stable isotope systems can be both more sensitive to crustal contamination and better indicators of magma generating processes than are radiogenic isotopic systems (Pb-Pb, Nd-Sm and Sr-Rb), therefore the stable isotopic compositions can provide more specific evidence for the nature and composition of source regions and contaminants (particularly crustal).

A regional sulfur and oxygen isotope study of intrusive rocks was undertaken in order to provide new insights into the origin of Cretaceous felsic magmatism in the northern Cordillera. Several plutonic suites have been characterized throughout the Selwyn Basin and Cassiar Platform regions in south central to eastern Yukon and the southwesternmost Northwest Territories (Fig. 1). Most of these suites are interpreted to be entirely derived from partial melting of underlying miogeoclinal

metasedimentary rocks of predominantly North American affinity, however some uncertainty remains as to the presence and amount of a mantle component that may have interacted with the intrusions (Mortensen *et al.*, 2000; Hart *et al.*, 2004a,b; Heffernan, 2004). We herein present a comprehensive S and O stable isotope dataset to determine what role melts sourced from the mantle may have had on the genesis of the different plutonic suites, which components of the crust may have contributed sulphur to the melts, and what clues into the underlying basement could be determined from the isotopic composition of the intrusions.

CRETACEOUS MAGMATISM IN THE CASSIAR PLATFORM AND SELWYN BASIN

Cretaceous intrusions emplaced into the Cassiar Platform and Selwyn Basin have been interpreted to be a result of collisional to post-collisional back-arc magmatism related to ongoing subduction along the western margin of North

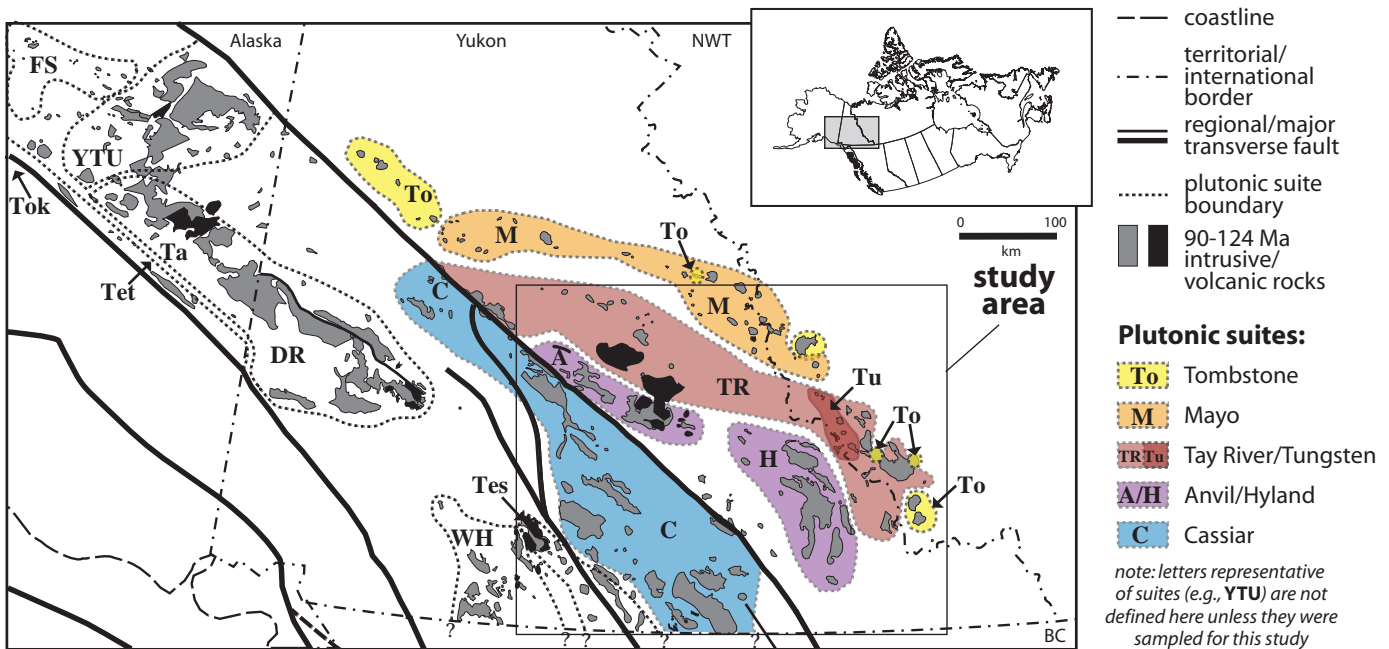


Figure 1. Location map (inset) and distribution map of Cretaceous igneous rocks emplaced into the autochthonous North American margin and Intermontane terranes in the northern Cordillera. The plutons are subdivided into the suites: Tok-Tet = Tok-Tetlin, FS = Fairbanks-Salcha, YTU = Yukon-Tanana Uplands, Ta-DR = Tanacross-Dawson Range, WH = Whitehorse, Tes = Teslin, C = Cassiar, TR = Tay River, A = Anvil, H = Hyland, Tu = Tungsten, To = Tombstone and M = Mayo. The study area is indicated by the box, and plutonic suites of interest are shaded. Intrusion polygons and regional structures are modified from Gordey and Makepeace (1999) and Nelson and Colpron (2007); outlines of plutonic suites are adapted from Mortensen *et al.* (2000), Hart *et al.* (2004a,b) and Rasmussen *et al.* (2007).

America. This aerially extensive magmatism (Fig. 1) is attributed to partial melting of the crust with late-enriched, mantle-derived melts contaminating the youngest plutonic suite(s). Based on geochronological, geochemical and radiogenic isotope similarities, there are two main groups of plutonic suites in the study area that are discussed here: (1) Cassiar, Hyland/Anvil and Tay River; and, (2) Tungsten, Mayo and Tombstone.

The Cassiar (approximately 115-99 Ma), Hyland/Anvil (109-95 Ma) and Tay River (99-96 Ma) suites comprise several belts in which many of the intrusions form large composite batholiths, and with the exception of the Cassiar suite (emplaced primarily into the Cassiar Platform), these plutonic suites are located northeast of the Tintina fault in rocks of the Selwyn Basin (Fig. 1). This aluminous and sub-alkalic magmatism consists primarily of biotite \pm hornblende or muscovite-bearing quartz monzodiorite, granodiorite and monzogranite with associated mafic enclaves and local felsic volcanism. This voluminous magmatism is interpreted to have formed in response to arc-continent collision to the west, either through partial melting of over-thickened continental crust driven by regional compression (Woodsworth *et al.*, 1991), decompression melting during orogenic collapse (Hart *et al.*, 2004a,b; Mair *et al.*, 2006), or decompression melting during movement along deep transpressional structures (Gabrielse *et al.*, 2006). Most of the larger intrusions are emplaced into, or near to, thick Proterozoic rift-related sedimentary packages largely eroded from crystalline Precambrian Shield (e.g., Boghossian *et al.*, 1996; Garzzone *et al.*, 1997; Patchett *et al.*, 1999) with thin overlying Paleozoic metasedimentary miogeoclinal (Cassiar Platform and Selwyn Basin) rocks (e.g., Cook *et al.*, 2004). Regardless of their exact petrogenesis, Cassiar, Hyland/Anvil and Tay River plutonic suites should have stable isotopic compositions consistent with derivation from the rift-related and miogeoclinal crustal rocks that are inferred to underlie much of the North American miogeocline (Cook *et al.*, 2004; Clowes *et al.*, 2005; Evenchick *et al.*, 2005).

The Tungsten (98-94 Ma), Mayo (96-93 Ma) and Tombstone (93-90 Ma) suites emplaced into the Selwyn Basin in central to eastern Yukon and southwestern Northwest Territories are the youngest and most inboard mid-Cretaceous magmatic rocks (Figs. 1, 2). These intrusions typically form very small to medium-sized circular plutons (e.g., <1 km to 10 km in diameter), lack the large batholiths that are characteristic of the older plutonic suites described above, and are frequently

associated with mafic dykes. The Tungsten suite typically comprises subalkalic and peraluminous biotite \pm muscovite \pm garnet monzogranitic to leucogranitic plugs, and is interpreted on the basis of mineralogy, geochemistry, and radiogenic isotopic data to have been derived entirely by crustal melting (Woodsworth *et al.*, 1991; Gordey and Anderson, 1993; Hart *et al.*, 2004a,b; Mair *et al.*, 2006). Similar to the Tungsten suite, sub-alkalic biotite \pm hornblende \pm clinopyroxene quartz monzonite to quartz monzodiorite to monzogranite Mayo suite intrusions also appear to have been primarily derived from partial melting of middle to upper crustal rocks, but there is also evidence for minor enriched-mantle melt contamination of these bodies (Hart *et al.*, 2004a,b). Weakly to strongly alkalic biotite \pm hornblende \pm clinopyroxene monzonite to monzogranite Tombstone Suite plutons, in contrast, include abundant intermediate and minor mafic components (e.g., enclaves, dykes) and have mineralogical, geochemical and radiogenic isotopic features that indicate at least some melt was derived from melting of an enriched or lithospheric mantle source (Mortensen *et al.*, 2000; Hart *et al.*, 2004a,b). These later plutonic suites are typically exposed in the Paleozoic miogeoclinal rocks overlying Proterozoic rift-related packages, and are interpreted to have been emplaced in a tensional post-collisional tectonic regime (Mair *et al.*, 2006).

Despite previous work on the origin of Cretaceous magmatism in the northern Cordillera, there are still many unknowns with respect to the nature and the source of the intrusions and associated mineralization. For example: what is the nature of the underlying crust, and which part(s) of it are undergoing partial melting? How much of a mantle melt component is present in each plutonic suite, and have any of the older plutonic suites interacted with mantle-derived melts? From where do the intrusions obtain their sulphur? Although these uncertainties are in part due to the felsic composition of most of the intrusions, much of the confusion regarding the origin of Cretaceous magmatism results from contradictory evidence. This stable isotope study aims to provide new insights into the petrogenesis of the Cretaceous plutonic suites emplaced into North American miogeoclinal rocks by addressing the questions above.

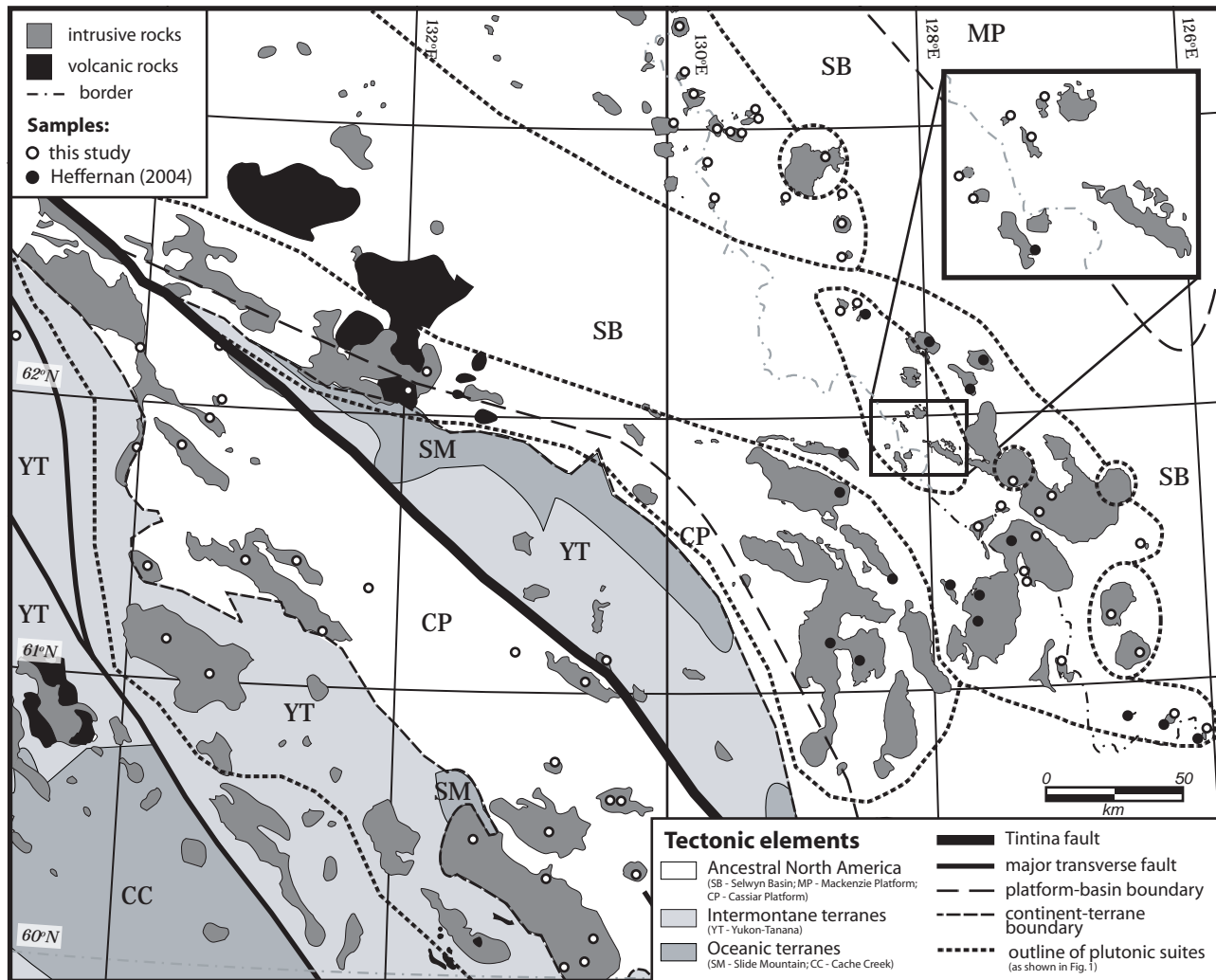


Figure 2. Detailed map of terranes and mid-Cretaceous intrusive and extrusive rocks exposed in the study area. Locations of samples collected for this study and from Heffernan (2004) are denoted by open and solid dots respectively. Plutonic suites of interest are outlined with a dashed line; refer to Figure 1 for the plutonic suite names. Map is modified from Gordey and Makepeace (1999) and Nelson and Colpron (2007).

STABLE ISOTOPE STUDY

Analyzing oxygen isotopic compositions ($\delta^{18}\text{O}$) allows us to distinguish between rocks that were derived solely from mantle material and rocks that were derived from, or heavily contaminated by, crustal material. Because oxygen is present in large quantities in virtually all rocks, it is relatively difficult to alter the primary $\delta^{18}\text{O}$ signature of a melt without significant assimilation of material of a distinctly different isotopic signature. Mantle-derived rocks have $\delta^{18}\text{O}$ of $\sim 6.0 \pm 0.5\text{‰}$ (Kyser, 1986), whereas most sedimentary rocks have higher values (e.g., $>8\text{‰}$; Taylor and Sheppard, 1986). Oxygen isotopic values from

plutons that are greater than $8\text{--}9.0\text{‰}$ would therefore indicate a significant crustal component to the melt. In contrast, hydrothermal water-rock interaction with meteoric waters (which have low $\delta^{18}\text{O}$) will act to lower the $\delta^{18}\text{O}$ signature of the rock. In many (but not all) cases, water-rock interaction is evident petrographically, thus samples for this study were selected to discriminate against hydrothermally altered rocks.

Sulfur isotopic compositions ($\delta^{34}\text{S}$) are particularly useful for detecting even small contributions of differing types of contaminants to a melt. Due to the relatively low concentrations of sulfur in igneous rocks, particularly in

felsic magmas, it takes very little assimilation of a sulphur-bearing material (e.g., pyritic shale, evaporates or stratiform barite) to alter $\delta^{34}\text{S}$ in a magma body. This makes sulphur a particularly sensitive tool for detecting not only the presence of contamination, but even different types of crustal contamination. However, this sensitivity may also complicate the interpretation of $\delta^{34}\text{S}$ data. Mantle-derived sulfur typically has a narrow and consistent range of $\delta^{34}\text{S}$ ($0 \pm 0.3\text{‰}$), whereas sedimentary sulfur has a very large range of $\delta^{34}\text{S}$ (-40 to $+40\text{‰}$). Goodfellow (2007) reports values for sedimentary sulfur (from syngenetic pyrite and barite) for the northern Cordillera that are typically $>10\text{‰}$.

ANALYTICAL METHODS

Eighty-seven representative samples with pre-existing radiogenic, geochemical and geochronological data of approximately 65 intrusive bodies in the Yukon and Northwest Territories were analyzed for sulfur and oxygen isotopic compositions. Eighteen of these samples were provided by S. Heffernan from samples used for an MSc thesis at UBC (Heffernan, 2004). Prior to crushing, hand samples were examined and sample material containing

quartz \pm sulphide-bearing veins or fractures were avoided to the best of our ability. However, minor hydrothermal alteration and its effects on the stable isotope systematics, although minimized, cannot be completely dismissed for all samples.

Oxygen

Quartz grains were handpicked from a light fraction of crushed and coarsely ground whole rock material that was processed on a Wilfley table. Quartz grain samples weighing approximately 1000 μg were sealed into tin cups; oxygen isotopes in quartz were analyzed using the high-temperature carbon reduction technique in which silicate oxygen is liberated by reaction with graphitic carbon to produce CO (Arehart and Poulson, 2006). The resultant CO is then introduced to the mass spectrometer in continuous-flow mode for isotopic analysis. Ten percent of the samples underwent duplicate analysis in order to monitor repeatability. Replicate analyses of standards NCSU, NBS-28 and ARQ indicated a precision of $\pm 0.2\text{‰}$, and $\delta^{18}\text{O}$ is reported relative to an NBS-28 value of $+9.6\text{‰}$. Data are presented in Table 1.

Table 1. Oxygen isotope data. Samples appended with “r” are replicate analyses and samples appended with “d” are duplicate analyses.

Sample ID	Pluton Name	Plutonic Suite	Weight (mg) / no. samples	$\delta^{13}\text{C}$	Raw $\delta^{18}\text{O}$	Corrected $\delta^{18}\text{O}$ / raw $\delta^{18}\text{O}$ st.dev.	Stretch corr	Reported $\delta^{18}\text{O}$
KR-05-198	Hole-in-the-Wall	Tombstone	987	20.91	21.35	14.49	2.79	14.0
KR-05-62	Mt. Christie	Tombstone	1023	21.28	22.04	14.31	2.61	13.9
KR-05-62_d	Mt. Christie	Tombstone	992	21.40	22.36	14.63	2.93	14.1
KR-05-97b	O’Grady	Tombstone	1030	21.46	22.80	15.07	3.37	14.5
CL-06-33	Dechen’La	Tombstone	992	20.88	20.72	13.32	1.62	13.0
CL-06-33_d	Dechen’La	Tombstone	1028	21.06	22.32	14.92	3.22	14.4
CL-06-34	Natla	Tombstone	1012	20.69	22.44	15.04	3.34	14.5
SH-99-011	Big Charlie	Tombstone	969	21.26	23.66	17.00	5.30	16.1
98-HAS-14	McLeod	Tombstone	998	20.20	19.71	12.10	0.40	12.0
KR-05-113	S. Nahanni	Mayo	1031	21.64	23.16	15.43	3.73	14.8
KR-05-130	C. Nahanni	Mayo	980	21.68	22.97	15.24	3.54	14.6
KR-05-136	N. Nahanni	Mayo	982	21.07	22.08	14.35	2.65	13.9
KR-05-68	Mt. Wilson	Mayo	990	21.44	23.54	15.81	4.11	15.1
CL-06-35	Logan	Mayo	1013	20.43	21.36	13.96	2.26	13.6
CL-06-36	Mt. Christie	Mayo	1022	20.85	21.59	13.86	2.16	13.5
CL-06-37	Christie Pass	Mayo	1021	21.18	22.52	14.79	3.09	14.3
CL-06-38	Ross River	Mayo	980	20.52	20.83	13.10	1.40	12.9
CL-06-39	Keele River	Mayo	979	20.62	21.49	13.76	2.06	13.4
CL-06-39_d	Keele River	Mayo	972	21.52	23.43	15.70	4.00	15.0
CL-06-40	Mile 222	Mayo	1025	21.60	22.83	15.10	3.40	14.5
KR-05-110	Cac	Tungsten	992	22.19	23.98	16.25	4.55	15.5

Table 1. continued.

Sample ID	Pluton Name	Plutonic Suite	Weight (mg) / no. samples	$\delta^{13}\text{C}$	Raw $\delta^{18}\text{O}$	Corrected $\delta^{18}\text{O}$ / raw $\delta^{18}\text{O}$ st.dev.	Stretch corr	Reported $\delta^{18}\text{O}$
KR-05-143	Rifle Range	Tungsten	1029	22.02	23.64	15.91	4.21	15.2
KR-05-148	Circular Stock	Tungsten	1019	21.83	22.63	14.90	3.20	14.3
KR-05-175	Lened	Tungsten	982	21.04	21.17	14.10	2.40	13.7
KR-05-175_d	Lened	Tungsten	997	20.75	20.48	13.46	1.76	13.2
KR-05-208	Little Hyland	Tungsten	990	20.47	20.28	13.46	1.76	13.2
KR-05-210	Nahanni Range Rd.	Tungsten	1028	20.57	20.14	13.36	1.66	13.1
KR-05-215	Mine Stock	Tungsten	1009	20.45	20.69	13.95	2.25	13.6
KR-05-215_d	Mine Stock	Tungsten	1020	20.66	21.30	14.60	2.90	14.1
KR-05-32	Ivo	Tungsten	995	22.51	24.60	16.87	5.17	16.0
SH-99-016	Tuna	Tungsten	974	20.44	20.54	12.93	1.23	12.7
98-Z-C-028	Rudi	Tungsten	1028	20.60	21.37	13.81	2.11	13.4
98-Z-C-028_d	Rudi	Tungsten	973	20.81	21.50	13.95	2.25	13.6
KR-05-08	Powers	Tay River	1021	23.05	25.01	17.28	5.58	16.3
KR-05-10	Jorgensen	Tay River	1039	22.90	22.05	15.23	3.53	14.6
KR-05-164	Hole-in-the-Wall	Tay River	1006	21.97	24.25	16.52	4.82	15.7
KR-05-191	Coal River	Tay River	1028	22.54	23.48	16.50	4.80	15.7
KR-05-194	Coal River	Tay River	1003	21.02	21.29	14.35	2.65	13.9
KR-05-196	Coal River	Tay River	981	20.51	18.60	11.70	0.00	11.7
KR-05-22	Roy	Tay River	1001	21.67	21.94	14.21	2.51	13.8
KR-05-26	Fish	Tay River	1048	23.05	24.69	17.95	6.25	16.9
KR-05-43	Park	Tay River	1003	21.68	21.27	13.54	1.84	13.2
SH-99-001	Shannon Creek	Tay River	982	20.49	19.18	12.52	0.82	12.4
SH-99-006	Coal River	Tay River	1023	20.66	18.32	11.70	0.00	11.7
SH-99-008	Coal River	Tay River	983	20.56	18.45	10.79	-0.91	10.9
SH-99-009	Coal River	Tay River	999	21.92	22.41	14.76	3.06	14.2
SH-99-013	Caesar Lakes	Tay River	1020	20.41	19.28	11.64	-0.06	11.7
SH-99-013_d	Caesar Lakes	Tay River	1004	20.55	19.38	11.76	0.06	11.7
98-HAS-02	Mt. Appler	Tay River	994	20.41	21.88	14.29	2.59	13.8
98-HAS-03	Faille	Tay River	987	20.85	21.14	13.94	2.24	13.6
98-HAS-06	Mulhulland	Tay River	994	20.87	20.70	13.57	1.87	13.3
98-HAS-07	Jorgensen	Tay River	978	20.70	19.32	12.28	0.58	12.2
98-HAS-07_d	Jorgensen	Tay River	1010	20.53	18.69	11.72	0.02	11.7
98-HAS-12	Patterson	Tay River	997	20.35	18.85	11.25	-0.45	11.3
98-HAS-12_d	Patterson	Tay River	1012	21.00	20.15	13.25	1.55	13.0
98-Z-12	Powers	Tay River	998	21.32	18.67	11.10	-0.60	11.2
SH-005	Mt. Billings	Hyland/Anvil	1005	20.39	15.18	7.75	-3.95	8.4
SH-011E	Mt. Billings	Hyland/Anvil	1011	20.65	19.18	11.90	0.20	11.9
SH-029	Tyers Pass	Hyland/Anvil	977	20.62	17.33	9.97	-1.73	10.3
SH-070	Anderson	Hyland/Anvil	991	20.79	20.88	13.37	1.67	13.1
07M-150	Carolyn/Orchay	Hyland/Anvil	1016	20.71	18.87	11.14	-0.56	11.2
07M-151	volcanic	South Fork	978	21.60	21.99	14.26	2.56	13.8
KR-07-01	Dycer Creek	Cassiar	977	21.00	21.10	13.37	1.67	13.1
KR-07-02	Quiet Lake	Cassiar	1013	21.44	22.68	14.95	3.25	14.4
KR-07-03	Quiet Lake	Cassiar	995	21.25	21.66	13.93	2.23	13.5
KR-07-04	Nisutlin	Cassiar	1027	22.03	23.93	16.20	4.50	15.4
KR-07-05	Nisutlin	Cassiar	1002	21.90	24.29	16.56	4.86	15.7

Table 1. continued.

Sample ID	Pluton Name	Plutonic Suite	Weight (mg) / no. samples	$\delta^{13}\text{C}$	Raw $\delta^{18}\text{O}$	Corrected $\delta^{18}\text{O}$ / raw $\delta^{18}\text{O}$ st.dev.	Stretch corr	Reported $\delta^{18}\text{O}$
KR-07-06	Nisutlin	Cassiar	986	21.21	21.19	13.46	1.76	13.2
KR-07-07	“Young”	Cassiar	985	22.00	23.94	16.21	4.51	15.4
KR-07-08	unnamed	Cassiar	1003	20.75	20.02	12.29	0.59	12.2
KR-07-09	Fox Mountain	Cassiar	1010	21.12	21.63	13.90	2.20	13.5
KR-07-10	Big Salmon	Cassiar	1000	20.45	19.55	11.82	0.12	11.8
KR-07-10_d	Big Salmon	Cassiar	984	20.41	19.81	12.08	0.38	12.0
KR-07-11	Glenlyon	Cassiar	985	21.01	23.07	15.34	3.64	14.7
KR-07-12	unnamed	Cassiar	995	21.01	22.19	14.46	2.76	14.0
KR-07-14	“Black Lake”	Cassiar	990	20.50	20.39	12.66	0.96	12.5
KR-07-15	Meister Lake	Cassiar	991	20.59	19.30	11.57	-0.13	11.6
07M-152	Battle Creek	Cassiar	1021	21.33	22.56	14.83	3.13	14.3
07M-153	Glenlyon	Cassiar	994	20.31	19.55	11.82	0.12	11.8
KR-07-16	Cassiar	Cassiar	998	20.42	20.02	12.29	0.59	12.2
KR-07-17	Cassiar	Cassiar	1005	19.84	19.14	11.41	-0.29	11.5
KR-07-18	Cassiar	Cassiar	987	20.40	20.88	13.15	1.45	12.9
KR-07-19	Marker Lake	Cassiar	1020	20.80	21.09	13.36	1.66	13.1
KR-07-20	Cabin Creek	Cassiar	1009	20.56	20.34	12.61	0.91	12.5
KR-07-21	Cabin Creek	Cassiar	998	20.84	19.84	12.11	0.41	12.0
KR-07-22	Cassiar	Cassiar	997	21.59	20.56	12.83	1.13	12.6
KR-07-23	Gravel Creek	Cassiar	1014	22.58	25.18	17.45	5.75	16.5
KR-07-24	Cassiar	Cassiar	1005	21.34	22.43	14.70	3.00	14.2
KR-07-13	“Square Lake”	unknown	1006	20.12	22.14	14.41	2.71	13.9
07M-154	Cornolio	unknown	971	20.62	20.36	12.63	0.93	12.5
07M-154_d	Cornolio	unknown	1011	21.42	22.20	14.47	2.77	14.0

Sulfur

Sulfur was extracted from whole rock powder using the Kiba method (Sasaki *et al.*, 1979) and ultimately precipitated as Ag_2S ; approximately 10% of the samples underwent a duplicate sulphide extraction. About 380 μg of silver sulphide was weighed into a tin cup with V_2O_5 (to aid oxidation), sealed, and then combusted in a high-temperature elemental analyzer oven to produce SO_2 , which was then introduced to the mass spectrometer in continuous-flow mode. Approximately 30% of the

samples, including half of the duplicated samples, also underwent replicate analysis in order to monitor repeatability in the unknown samples. GSL (sphalerite) and MIC (marcasite) standards of known isotopic composition were used to correct for the presence of $^{32}\text{S}^{16}\text{O}^{18}\text{O}$ (which has the same isotopic weight as $^{34}\text{S}^{16}\text{O}^{16}\text{O}$) and for machine drift. Typical analytical precision for these analyses is $\pm 0.3\text{‰}$ or better, and data are reported relative to the Vienna Canyon Diablo Troilite (VCDT) standard. Data are presented in Table 2.

Table 2. Sulphur isotope data with calculated wt% sulphur. *Italicized data are minimum estimates only due to either loss of material during sulphur extraction (wt% S), or a lack of sufficient sample material to obtain a peak height >1. Samples appended with “r” are replicate analyses and samples appended with “d” are duplicate analyses.*

Sample ID	Pluton Name	Plutonic Suite	Calc. S (wt%)	Peak Height (nA)	$\delta^{34}\text{S}_{\text{VCDT}}$ (‰)
KR-05-198	Hole-in-the-Wall	Tombstone	0.0018	2.07	2.92
KR-05-62	Mt. Christie	Tombstone	0.0244	2.87	9.27
KR-05-97	O’Grady	Tombstone	0.0061	2.24	8.40
KR-05-97b_r	O’Grady	Tombstone	0.0061	3.38	8.45
CL-06-33	Dechen’La	Tombstone	0.0033	1.97	8.79
CL-06-34	Natla	Tombstone	0.0026	2.37	11.24
SH-99-011	Big Charlie	Tombstone	0.0012	2.91	4.93
SH-99-011_r	Big Charlie	Tombstone	0.0012	2.69	5.35
98-HAS-14	McLeod	Tombstone	0.0008	3.14	5.85

Table 2. continued.

Sample ID	Pluton Name	Plutonic Suite	Calc. S (wt%)	Peak Height (nA)	$\delta^{34}\text{S}_{\text{VCDT}}$ (‰)
KR-05-113	S. Nahanni	Mayo	0.0029	2.57	13.30
KR-05-130	C. Nahanni	Mayo	0.0050	2.32	11.02
KR-05-136	N. Nahanni	Mayo	0.0195	2.57	11.04
KR-05-68	Mt. Wilson	Mayo	0.0156	2.57	7.42
KR-05-68_d	Mt. Wilson	Mayo	0.0237	2.66	7.85
KR-05-76	Pelly River	Mayo	0.0024	2.36	6.27
KR-05-77	Pelly-mafic dyke	Mayo	0.0251	2.40	7.77
KR-05-77_r	Pelly-mafic dyke	Mayo	0.0251	2.28	7.77
CL-06-35	Logan	Mayo	0.0028	1.75	12.57
CL-06-36	Mt. Christie	Mayo	0.0048	1.94	9.93
CL-06-37	Christie Pass	Mayo	0.0241	2.85	10.00
CL-06-37_d	Christie Pass	Mayo	0.0361	2.12	9.91
CL-06-37_dr	Christie Pass	Mayo	0.0361	2.13	9.90
CL-06-38	Ross River	Mayo	0.0057	1.61	11.00
CL-06-38_r	Ross River	Mayo	0.0057	1.58	10.91
CL-06-39	Keele River	Mayo	0.0062	1.12	8.16
CL-06-40	Mile 222	Mayo	0.0028	2.31	10.40
KR-05-110	Cac	Tungsten	0.0046	2.86	10.54
KR-05-110_r	Cac	Tungsten	0.0046	2.72	10.53
KR-05-143	Rifle Range	Tungsten	0.0035	2.13	7.29
KR-05-143_r	Rifle Range	Tungsten	0.0033	2.40	7.36
KR-05-143_d	Rifle Range	Tungsten	0.0033	2.45	7.35
KR-05-148	Circular Stock	Tungsten	0.0108	2.56	8.68
KR-05-175	Lened	Tungsten	0.0026	2.32	9.47
KR-05-207	East Tuna	Tungsten	0.0029	2.24	9.14
KR-05-208	Little Hyland	Tungsten	0.0012	1.89	9.02
KR-05-210	Nahanni Range Rd.	Tungsten	0.0007	2.09	9.75
KR-05-212	Cantung-felsic dyke	Tungsten	0.5447	2.51	8.62
KR-05-213	Cantung-mafic dyke	Tungsten	0.1042	3.34	4.56
KR-05-213_r	Cantung-mafic dyke	Tungsten	0.1042	3.80	4.60
KR-05-213_r	Cantung-mafic dyke	Tungsten	0.1042	1.86	3.97
KR-05-215	Mine Stock	Tungsten	0.0024	2.39	6.54
KR-05-215_r	Mine Stock	Tungsten	0.0024	2.31	6.53
KR-05-32	Ivo	Tungsten	0.0015	2.11	4.59
KR-05-32_r	Ivo	Tungsten	0.0015	2.25	4.58
SH-99-016	Tuna	Tungsten	0.0027	2.80	4.46
98-Z-C-028	Rudi	Tungsten	0.0006	0.66	6.82

Sample ID	Pluton Name	Plutonic Suite	Calc. S (wt%)	Peak Height (nA)	$\delta^{34}\text{S}_{\text{VCDT}}$ (‰)
KR-05-08	Powers	Tay River	0.0921	2.59	7.39
KR-05-08_r	Powers	Tay River	0.0921	2.54	7.30
KR-05-10	Jorgensen	Tay River	0.0120	2.31	4.23
KR-05-157	Roy-mafic dyke	Tay River	0.1504	3.73	11.13
KR-05-157_r	Roy-mafic dyke	Tay River	0.1504	1.75	10.97
KR-05-164	Hole-in-the-Wall	Tay River	0.0049	2.46	9.91
KR-05-191	Coal River	Tay River	0.0047	2.17	8.08
KR-05-194	Coal River	Tay River	0.0014	2.36	6.73
KR-05-196	Coal River	Tay River	0.0020	2.53	8.32
KR-05-22	Roy	Tay River	0.0050	2.06	5.38
KR-05-26	Fish	Tay River	0.0039	2.35	3.93
KR-05-43	Park	Tay River	0.0051	2.65	3.94
SH-99-001	Shannon Creek	Tay River	0.0007	0.87	3.94
SH-99-006	Coal River	Tay River	0.0025	2.83	5.08
SH-99-006_r	Coal River	Tay River	0.0025	3.03	5.14
SH-99-008	Coal River	Tay River	0.0010	2.93	5.78
SH-99-009	Coal River	Tay River	0.0061	3.58	7.50
SH-99-013	Caesar Lakes	Tay River	0.0017	nd	nd
SH-99-013	Caesar Lakes	Tay River	nd	nd	nd
98-HAS-02	Mt. Appler	Tay River	0.0005	1.60	8.25
98-HAS-03	Faille	Tay River	0.0020	3.45	4.46
98-HAS-03_r	Faille	Tay River	0.0020	3.31	4.46
98-HAS-06	Mulhulland	Tay River	0.0011	3.01	7.41
98-HAS-07	Jorgensen	Tay River	0.0008	2.15	2.41
98-HAS-12	Patterson	Tay River	0.0058	3.42	9.21
98-HAS-12_r	Patterson	Tay River	0.0058	3.72	9.28
98-HAS-12_d	Patterson	Tay River	0.0113	1.48	9.30
98-HAS-12_dr	Patterson	Tay River	0.0113	3.10	9.58
98-Z-12	Powers	Tay River	0.0661	3.84	12.75
98-Z-12_r	Powers	Tay River	0.0661	2.05	12.36
SH-005	Mt. Billings	Hyland/Anvil	0.0010	2.56	8.51
SH-99-022	Mt Billings	Hyland/Anvil	0.0049	3.22	3.17
SH-011E	Mt. Billings	Hyland/Anvil	0.0132	3.37	13.57
SH-011E_r	Mt. Billings	Hyland/Anvil	0.0132	2.10	13.40
SH-029	Tyers Pass	Hyland/Anvil	0.0014	3.02	6.12

Table 2. continued.

Sample ID	Pluton Name	Plutonic Suite	Calc. S (wt%)	Peak Height (nA)	$\delta^{34}\text{S}_{\text{VCDT}}$ (‰)
SH-029_r	Tyers Pass	Hyland/Anvil	0.0014	3.07	6.05
SH-070	Anderson	Hyland/Anvil	0.0242	4.69	nd
SH-071_r	Anderson	Hyland/Anvil	0.0242	1.96	9.41
07M-150	Carolyn/Orchay	Hyland/Anvil	0.0010	1.70	8.86
07M-151	volcanic	South Fork	0.0031	2.15	10.24
KR-07-01	Dycer Creek	Cassiar	0.0016	3.06	7.31
KR-07-02	Quiet Lake	Cassiar	0.0010	0.53	9.04
KR-07-03	Quiet Lake	Cassiar	0.0003	0.19	4.39
KR-07-04	Nisutlin	Cassiar	0.0003	0.41	3.37
KR-07-05	Nisutlin	Cassiar	0.0010	0.63	10.12
KR-07-06	Nisutlin	Cassiar	0.0019	3.41	8.08
KR-07-07	“Young”	Cassiar	0.0062	3.40	8.68
KR-07-08	unnamed	Cassiar	0.0061	3.01	8.02
KR-07-08_d	unnamed	Cassiar	0.0063	2.97	8.02
KR-07-08_dr	unnamed	Cassiar	0.0063	2.84	8.02
KR-07-09	Fox Mountain	Cassiar	0.0013	2.69	9.63
KR-07-10	Big Salmon	Cassiar	0.0020	3.02	7.92
KR-07-10_r	Big Salmon	Cassiar	0.0020	2.85	7.96
KR-07-11	Glenlyon	Cassiar	0.0003	0.73	7.44
KR-07-12	unnamed	Cassiar	0.0007	0.54	8.37
KR-07-14	“Black Lake”	Cassiar	0.0011	2.75	10.23
KR-07-15	Meister Lake	Cassiar	0.0002	nd	nd
07M-152	Battle Creek	Cassiar	0.0066	2.89	9.31
07M-152_r	Battle Creek	Cassiar	0.0066	2.53	9.30
07M-153	Glenlyon	Cassiar	0.0036	2.14	9.08
KR-07-16	Cassiar	Cassiar	0.0005	2.82	4.45
KR-07-17	Cassiar	Cassiar	0.0012	3.17	8.00
KR-07-18	Cassiar	Cassiar	0.0009	2.04	8.35
KR-07-19	Marker Lake	Cassiar	0.0100	3.39	2.06
KR-07-19_d	Marker Lake	Cassiar	0.0113	3.06	2.03
KR-07-20	Cabin Creek	Cassiar	0.0008	2.98	5.14
KR-07-21	Cabin Creek	Cassiar	0.0011	2.68	6.00
KR-07-22	Cassiar	Cassiar	0.0035	3.58	8.58
KR-07-23	Gravel Creek	Cassiar	0.0004	0.23	5.70
KR-07-24	Cassiar	Cassiar	0.0012	2.72	3.86
KR-07-24_r	Cassiar	Cassiar	0.0012	2.95	3.84
KR-07-13	“Square Lake”	unkn	0.0004	0.93	0.78
07M-154	Cornolio	unkn	0.0008	1.29	3.46

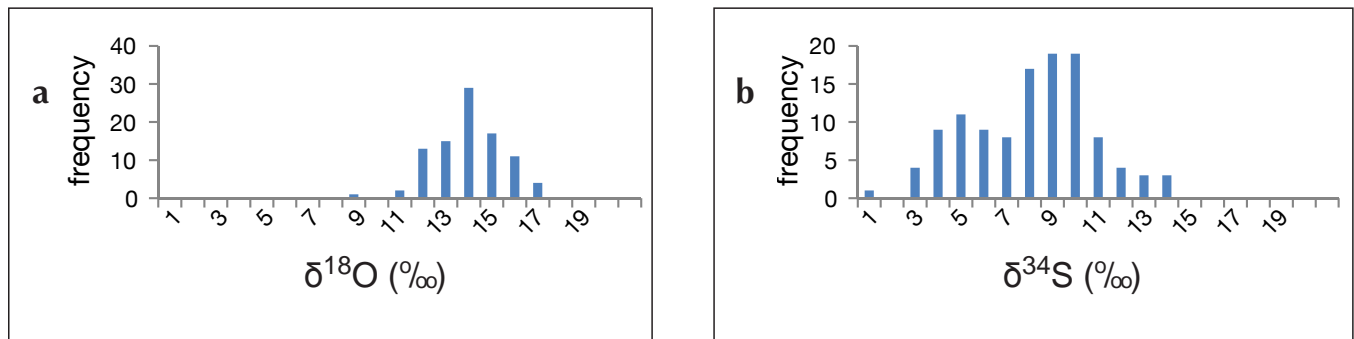


Figure 3. (a) Frequency plot for all $\delta^{18}\text{O}$ values. (b) Frequency plot for all $\delta^{34}\text{S}$ values.

RESULTS

Oxygen

All of the intrusions analyzed have a normal distribution of high positive $\delta^{18}\text{O}$, ranging from +8.4 to +16.9‰ (Table 1; Fig. 3a). There is very little systematic variation in the $\delta^{18}\text{O}$ across the study area, indicating that the majority of the rocks in the region were derived from, or significantly contaminated by, crustal materials (Fig. 4a). There is, however, a small group of lower $\delta^{18}\text{O}$ (+8.4 to +11.9‰) in

the southeastern part of the study area, or the ‘southeastern block’. Plutonic suites with the smallest range in $\delta^{18}\text{O}$ on the data summary plotted in Figure 5a (e.g., Tombstone, Mayo and Tungsten) were sampled from smaller geographic areas, therefore the increasing range of $\delta^{18}\text{O}$ from Tombstone to Tay River suite intrusions may be due more to regional variations in the basement, rather than intra-plutonic suite variation.

Sulfur

Throughout the study area, $\delta^{34}\text{S}$ ranges from +2.1‰ to +13.6‰ and contains two sub-populations (Table 1; Fig. 3b), although the majority of the intrusions have $\delta^{34}\text{S}$ values ranging from +6 to +10‰, which is suggestive of the influence of seawater sulphate. There is also a significant population of lower $\delta^{34}\text{S}$ ranging from +3‰ to +6‰ that is primarily concentrated in the southeast block (Fig. 4b); many of these isotopically 'lighter' sulphur samples correlate with lower $\delta^{18}\text{O}$. Furthermore, the highest $\delta^{34}\text{S}$ values appear to be concentrated in the northeastern part of the study area ('northeastern block') and are predominantly associated with small Mayo suite intrusions (Fig. 4b). From the data summary plot, it appears that from younger to older rocks (*i.e.*, Mayo through to Tay River suites), there is a general decrease in $\delta^{34}\text{S}$ (Fig. 5b).

DISCUSSION

SOURCE OF MELT

As most $\delta^{18}\text{O}$ isotopic compositions are well above +10‰, it is clear that all of the plutonic suites were derived, in significant portion, from crustal melts, or have assimilated a significant amount of crustal material. This effect is still evident in the Tombstone suite, which is interpreted to have at least some enriched mantle-derived component (*e.g.*, Hart *et al.*, 2004a,b). The generally lower $\delta^{18}\text{O}$ observed in the southeastern block may be reflecting either less input of middle to upper crustal material into the melt versus lower crustal rocks (of unknown composition), or melting of crustal material with slightly lower $\delta^{18}\text{O}$ due to compositional variations in the basement. Although globally most granitoids do not have $\delta^{18}\text{O} > 14\text{‰}$ in quartz even after extensive interaction

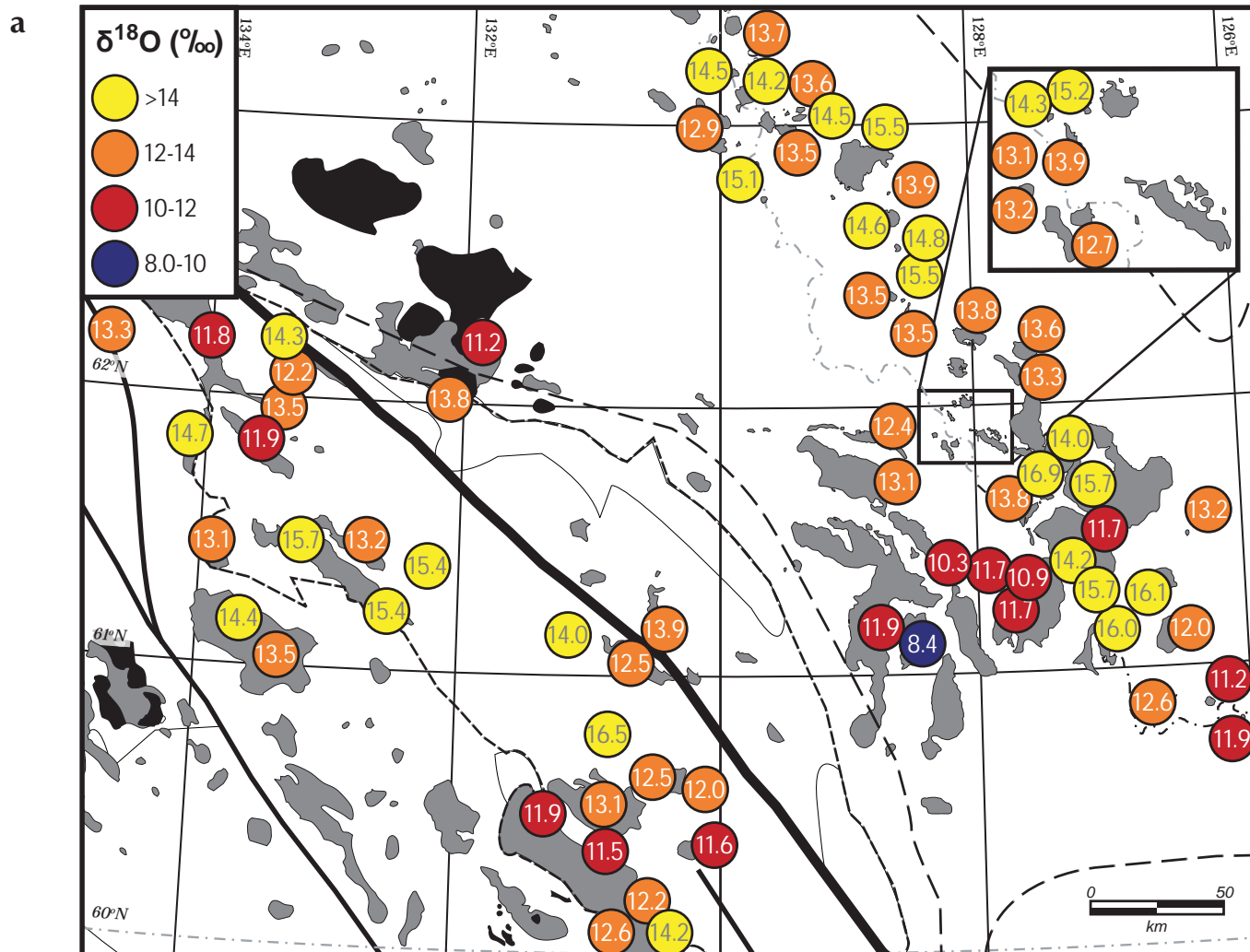


Figure 4. (a) Spatial distribution of $\delta^{18}\text{O}$ isotopic compositions. Line work as in Figures 1 and 2.

with the crust, many intrusions that were sampled for this study returned values of +14‰ to +16.9‰, which is probably indicative of primarily partial melting of pelitic rocks, or in some cases, incorporation of significant sedimentary material along plutonic margins (e.g., Taylor and Sheppard, 1986).

For the most part, $\delta^{34}\text{S}$ is greater than +6‰, particularly in the northeastern block in association with Mayo suite intrusions, and is generally typical of incorporation of seawater sulphate (e.g., evaporate lithologies), such as the Gypsum Formation of the Proterozoic Little Dal Group ($\delta^{34}\text{S} = +13.9\text{‰}$ to +17.6‰; Turner, 2009). There is, however, a second significant population of +3‰ to +6‰. These 'lighter' $\delta^{34}\text{S}$ values are predominantly from samples located in the southeastern block of the study area and could be a result of lesser amounts of the

seawater sulphur contaminant, but contamination from either mantle-derived, or sedimentary-derived (sulphide) sulphur is possible. Interestingly, this southeastern block is also correlative with particularly low ϵNd values (K.L. Rasmussen, unpublished data, 2009), which suggests that either the basement underlying the southeastern block may be isotopically more juvenile, or that mantle-derived material has been incorporated into all plutonic suites in this area. The general decrease in $\delta^{34}\text{S}$ with increasing age (Fig. 5b) might indicate decreasing interaction with crustal material in general in the older plutonic suites, or perhaps some input from mantle-derived melts; this is contrary to current models of mid-Cretaceous magmatism in the region where geochemistry, mineralogy and radiogenic isotopic compositions indicate that the younger intrusions are more likely to have

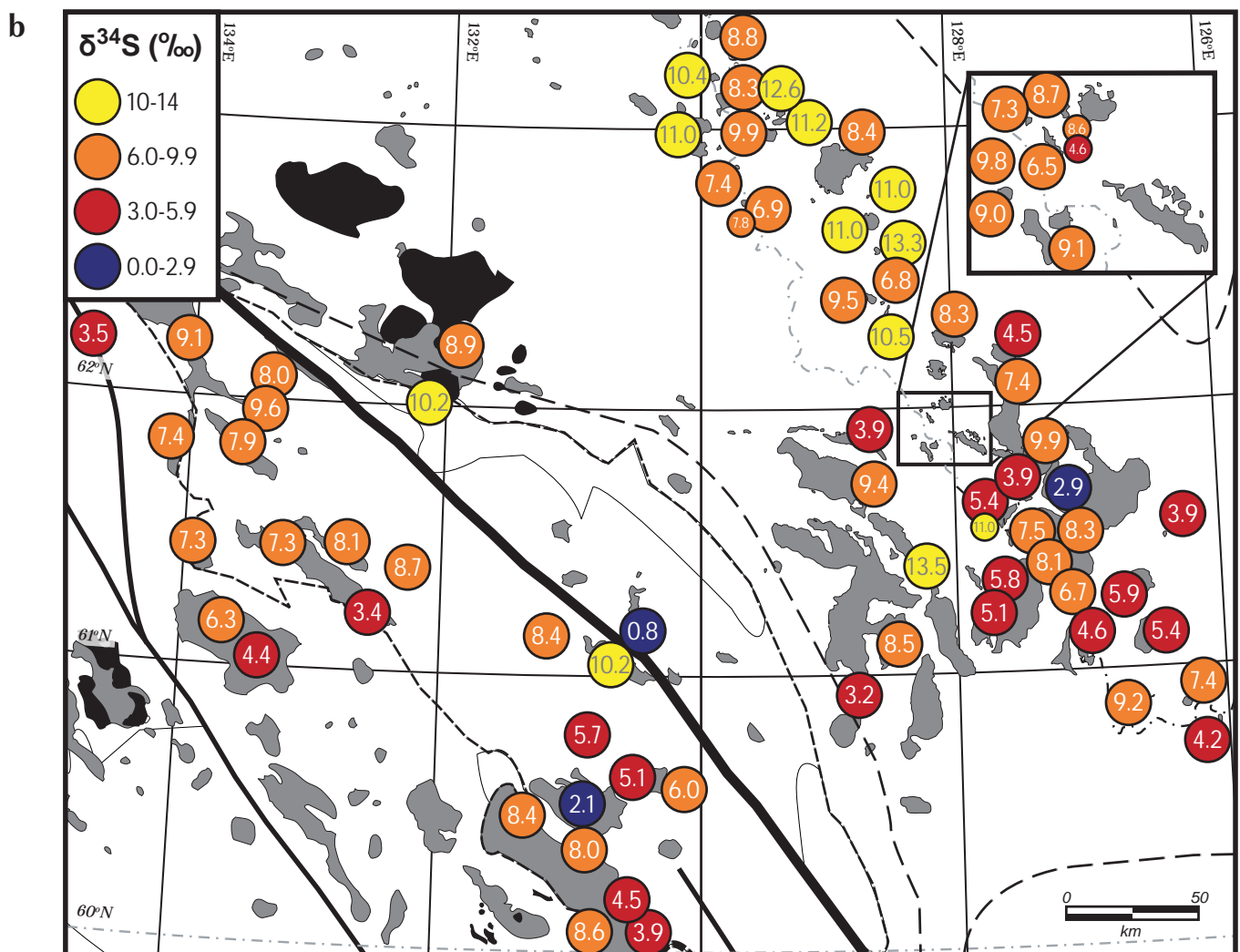


Figure 4. (b) Spatial distribution of $\delta^{34}\text{S}$ isotopic compositions. Line work as in Figures 1 and 2.

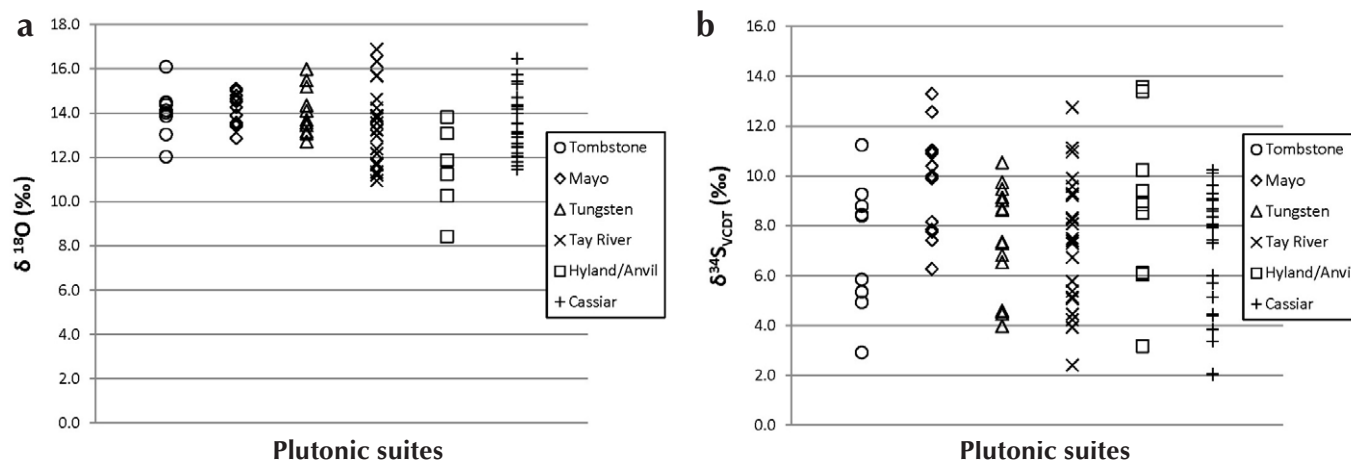


Figure 5. Summary plots of all stable isotopic data, subdivided by plutonic suite: (a) $\delta^{18}\text{O}$; (b) $\delta^{34}\text{S}$.

incorporated some mantle-derived material (e.g., Hart *et al.*, 2004a,b). Further work such as comparison of $\delta^{34}\text{S}$ with radiogenic isotopic data (e.g., Sm-Nd, Rb-Sr) is required to resolve the uncertainties of granite melt sources.

REGIONAL VARIATIONS AND IMPLICATIONS FOR THE NATURE OF THE BASEMENT

The Cassiar plutonic suite was emplaced southwest of the Tintina fault and largely within the Cassiar Platform: an offshore carbonate platform that was deposited from at least the latest Proterozoic through to the Devonian (e.g., Cecile and Morrow, 1997). After restoration of 400-430 km of primarily Cenozoic dextral offset along the Tintina fault (Gabrielse *et al.*, 2006), the Cassiar plutonic suite is essentially the coeval and along-strike southern equivalent of magmatism in the Selwyn Basin. The Cassiar Platform was deposited originally as a marginal plateau along an upper plate margin, or a continental rifted margin with a sub-crustal detachment (related to mid- to late Proterozoic rifting; Hansen *et al.*, 1993; Cecile *et al.*, 1997). Conversely, the magmatism examined northeast of the Tintina fault in the Selwyn Basin has been interpreted by the same authors to have been emplaced within a lower plate margin, or a continental rifted margin with a shallow crustal detachment overlain by highly rotated normal fault blocks. This geometry of the rifted margin has been used to explain the difference in width of mid-Cretaceous magmatism in the Selwyn Basin, as much as 250 km relative to magmatism in the Cassiar Platform, which was emplaced over a much narrower region (~100 km).

Overall, there are no significant variations in the stable isotope compositions between intrusions emplaced into the Selwyn Basin of the lower plate rifted margin (e.g., northeast of the Tintina fault) and those emplaced into the Cassiar Platform of the upper plate rifted margin (e.g., southwest of the Tintina fault). This suggests that the composition of the middle to upper crust, from which the granitic melts were likely derived, is reasonably homogenous for ~1700 km along the length of the ancient continental margin. However, intrusions in the southern part of the Selwyn Basin do have somewhat lower $\delta^{34}\text{S}$ and $\delta^{18}\text{O}$. Although pyritiferous shales may be responsible for lower $\delta^{34}\text{S}$, these would be expected to lead to higher $\delta^{18}\text{O}$ compositions. Therefore, the combination of sulphur and oxygen isotopic data are suggestive of the incorporation of melts that are not derived from a middle to upper crustal source. The correlation of these lighter stable isotopic values with more juvenile ϵNd values for this region (K.L. Rasmussen, unpublished data, 2009) further supports this inference for a second distinct melt source, such as the underlying mantle, or an unknown basement component (e.g., mafic/ultramafic lower crust). Cretaceous movement along deep transverse structures related to Proterozoic rifting is a possible mechanism that may have allowed for the ascension of such deeper melts.

ACKNOWLEDGEMENTS

The authors would like to thank Scott Heffernan for access to sample material from his MSc thesis project. Funding for this work was provided by the Yukon Geological Survey and by the Society of Economic Geologists. The authors are also grateful to Dr. Thomas Bissig for providing a critical review of this manuscript.

REFERENCES

- Arehart, G. and Poulson, S., 2006. Carbon reduction as a safe, simple, and rapid technique for $\delta^{18}\text{O}$ analysis of silicates and oxides. *In: Geological Society of America Abstracts with Programs*, vol. 38, no. 7, p. 486.
- Boghossian, N.D., Patchett, J.P., Ross, G.M. and Gehrels, G.E., 1996. Nd isotopes and the source of sediments in the miogeocline of the Canadian Cordillera. *The Journal of Geology*, vol. 104, p. 259-277.
- Cecile, M.P., Morrow, D.W. and Williams, G.K., 1997. Early Paleozoic (Cambrian to Early Devonian) tectonic framework, Canadian Cordillera. *Bulletin of Canadian Petroleum Geology*, vol. 45, p. 54-74.
- Clowes, R.M., Hammer, P.T.C., Viejo, G.F. and Welford, J.K., 2005. Lithospheric structure in northwestern Canada from LITHOPROBE seismic refraction and related studies: A synthesis. *Canadian Journal of Earth Sciences*, vol. 42, p. 1277-1293.
- Cook, F.A. and Erdmer, P., 2004. An 1800 km cross section of the lithosphere through the northwestern North American plate: lessons from 4.0 billion years of Earth's history. *Canadian Journal of Earth Science*, vol. 42, p. 1295-1311.
- Evenchick, C.A., Gabrielse, H. and Snyder, D., 2005. Crustal structure and lithology of the northern Canadian cordillera: alternative interpretations of SNORCLE seismic reflection lines 2a and 2b. *Canadian Journal of Earth Sciences*, vol. 42, p. 1149-1161.
- Gabrielse, H., Murphy, D.C. and Mortensen, J.K., 2006. Cretaceous and Cenozoic dextral orogen-parallel displacements, magmatism, and paleogeography, north-central Canadian Cordillera. *In: Paleogeography of the North American Cordillera: Evidence For and Against Large-Scale Displacements*, J.W. Haggart, R.J. Enkin and J.W.H. Monger (eds.), Geological Association of Canada, Special Paper 46, p. 255-276.
- Garziona, C.N., Patchett, P.J., Ross, G.M. and Nelson, J.A., 1997. Provenance of Paleozoic sedimentary rocks in the Canadian cordilleran miogeocline: A Nd isotopic study. *Canadian Journal of Earth Sciences*, vol. 34, p. 1603-1618.
- Goodfellow, W.D., 2007. Metallogeny of the Selwyn Basin. *In: Mineral Resources of Canada: A Synthesis of Major Deposit-types, District Metallogeny, the Evolution of Geological Provinces, and Exploration Methods*, W.D. Goodfellow (ed.), Geological Survey of Canada and Mineral Deposits Division of the Geological Association of Canada Special Publication, p. 553-580.
- Gordey, S.P. and Anderson, R.L., 1993. Evolution of the northern cordilleran miogeocline, Nahanni map area (1051), Yukon and Northwest Territories. *Geological Survey of Canada, Memoir 428*, 214 p.
- Gordey, S.P. and Makepeace, A.J., 1999. Yukon digital geology. S.P. Gordey and A.J. Makepeace (compilers), Geological Survey of Canada, Open File D3826, and Exploration and Geological Services Division, Yukon Region, Indian and Northern Affairs Canada, Open File 1999-1(D).
- Hansen, V.L., Goodge, J.W., Keep, M. and Oliver, D.H., 1993. Asymmetric rift interpretation of the western North American margin. *Geology*, vol. 21, p. 1067-1070.
- Hart, C.J.R., Goldfarb, R.J., Lewis, L.L. and Mair, J.L., 2004a. The northern cordilleran mid-Cretaceous plutonic province: ilmenite/magnetite-series granitoids and intrusion-related mineralization. *Resource Geology*, vol. 54, p. 253-280.
- Hart, C.J.R., Mair, J.L., Goldfarb, R.J. and Groves, D.I., 2004b. Source and redox controls on metallogenic variations in intrusion-related ore systems, Tombstone-Tungsten Belt, Yukon Territory, Canada. *Transactions of the Royal Society of Edinburgh: Earth Sciences*, vol. 95, p. 339-356.
- Heffernan, R.S., 2004. Temporal, geochemical, isotopic and metallogenic studies of mid-Cretaceous magmatism in the Tintina Gold Province, southeastern Yukon and southwestern Northwest Territories, Canada. Unpublished MSc thesis, University of British Columbia, Vancouver, British Columbia, 83 p.
- Kyser, K., 1986. Stable Isotope Variations in the Mantle. *In: Stable Isotopes in High Temperature Geological Processes*, J.W. Valley, H.P. Taylor Jr. and J.R. O'Neil (eds.), *Reviews in Mineralogy*, vol. 16, p. 141-162.

- Mair, J.L., Hart, C.J.R. and Stephens, J.R., 2006. Deformation history of the northwestern Selwyn Basin, Yukon, Canada: implications for orogen evolution and mid-Cretaceous magmatism. *GSA Bulletin*, vol. 118, p. 304-323.
- Mortensen, J.K., Hart, C.J.R., Murphy, D.C. and Heffernan, S., 2000. Temporal evolution of Early and mid-Cretaceous magmatism in the Tintina Gold Belt. *In: The Tintina Gold Belt: Concepts, Exploration and Discoveries*, J. Jambor (ed.), British Columbia and Yukon Chamber of Mines, Special Volume 2, p. 49-57.
- Nelson, J. and Colpron, M., 2007. Tectonics and metallogeny of the British Columbia, Yukon and Alaska Cordillera, 1.8 Ga to present. *In: Mineral Resources of Canada: A Synthesis of Major Deposit-types, District Metallogeny, the Evolution of Geological Provinces, and Exploration Methods*, W.D. Goodfellow (ed.), Geological Survey of Canada and Mineral Deposits Division of the Geological Association of Canada Special Publication, p. 755-792.
- Patchett, P.J., Roth, M.A., Canale, B.S., de Freitas, T.A., Harrison, J.C., Embry, A.F. and Ross, G.M., 1999. Nd isotopes, geochemistry, and constraints on sources of sediments in the Franklinian mobile belt, Arctic Canada. *GSA Bulletin*, vol. 111, p. 578-589.
- Rasmussen, K.L., Mortensen, J.K., Falck, H. and Ullrich, T.D., 2007. The potential for intrusion-related mineralization within the South Nahanni River MERA area, Selwyn and Mackenzie mountains, Northwest Territories. *In: Mineral and energy resource assessment of the Greater Nahanni Ecosystem under consideration for the expansion of the Nahanni National Park Reserve, Northwest Territories*, D.F. Wright, D. Lemkow and J.R. Harris (eds.), Geological Survey of Canada, Open File 5344, 557 p.
- Sasaki A., Arikawa Y. and Folinsbee R.E., 1979. Kiba reagent method of sulfur extraction applied to isotopic work. *Bulletin of the Geological Survey of Japan*, vol. 30, p. 241-245.
- Taylor, H.P., Jr. and Shepard, S.M.F., 1986. Igneous Rocks I: Processes of isotopic fractionation and isotope systematics. *In: Stable Isotopes in High Temperature Geological Processes*, J.W. Valley, H.P. Taylor Jr. and J.R. O'Neil (eds.), *Reviews in Mineralogy*, vol. 16, p. 227-269.
- Turner, E.C., 2009. Lithostratigraphy and stable isotope values of the early Neoproterozoic Gypsum formation (Little Dal Group, Mackenzie Mountains Supergroup), NWT. Northwest Territories Geoscience Office, NWT Open File Report 2009-002, 26 p.
- Woodsworth, G.J., Anderson, R.G. and Armstrong, R.L., 1991. Plutonic regimes. *In: Geology of the Cordilleran Orogen in Canada*, H. Gabrielse and C.J. Yorath (eds.), *GSC Geology of Canada*, no. 4, p. 491-531.

Soil reconnaissance of the Fort Selkirk volcanic field, Yukon (115I/13 and 14)

Paul Sanborn¹

University of Northern British Columbia

Sanborn, P., 2010. Soil reconnaissance of the Fort Selkirk volcanic field, Yukon (115I/13 and 14). *In: Yukon Exploration and Geology 2009*, K.E. MacFarlane, L.H. Weston and L.R. Blackburn (eds.), Yukon Geological Survey, p. 293-304.

ABSTRACT

Valley-filling basalts of the Selkirk Volcanics north and west of the Pelly River-Yukon River confluence, range in age from early Pleistocene to Holocene. Soils formed on the older surfaces have complex parent materials reflecting early Pleistocene glaciation and significant loess accumulation. A diamicton overlying the early Pleistocene basalt is covered by up to 1 m or more of calcareous loess, and shows no field evidence of weathering or soil formation. Middle Pleistocene basalt has a similar depth of loess cover and appears fresh and unweathered. Lava flows originating on the south side of the Volcano Mountain cinder cone display vegetation ranging from discontinuous lichen and moss cover to white spruce-aspens forest. Soil profile development varies correspondingly from almost nil to reddish-brown Brunisolic soils with ~30 cm of B horizon, depending on substrate age and/or the presence of lapilli deposits overlying the flows.

¹sanborn@unbc.ca

INTRODUCTION

The Fort Selkirk volcanic field in central Yukon has been active for more than four million years (Jackson *et al.*, 2008). Previous research has documented the history and products of its eruptive activity and interactions with glaciations and the Yukon River (Francis and Ludden, 1990; Jackson and Stevens, 1992; Jackson *et al.*, 1996; Trupia and Nicholls, 1996; Jackson, 2000; Huscroft *et al.*, 2004; Nelson *et al.*, 2009). These studies have not examined soil development on volcanic deposits despite the availability of radiometric dates that could potentially constrain the ages of volcanic soil parent materials. Although pedologists have begun to study Yukon soils formed on weathered bedrock (Bond and Sanborn, 2006; Smith *et al.*, 2009), none of this research has involved basalts and related volcanic rocks.

Logistics support provided by the Yukon Geological Survey in July, 2009, enabled a first reconnaissance of the soils of the Fort Selkirk area. This field report presents the key observations resulting from this initial work and suggests potential follow-up studies.

STUDY AREA

Although basaltic rocks of the Selkirk Volcanics occur both south and north of the Pelly-Yukon confluence, this study was only able to examine the latter area (Fig. 1) where three age groupings of lava flows have been delineated (for the thick basalt sequences exposed along the north side of the Yukon River, only the ages of the uppermost units are cited here).

Early Pleistocene basalt flows outcrop along the Pelly River upstream of its confluence with the Yukon River and extend along the north bank of the Yukon River to approximately 6 km downstream of Fort Selkirk (Fig. 1). The uppermost of these flows is dated at 1.36 ± 0.04 Ma (Nelson *et al.*, 2009) in a section with discontinuous till at the top. The latter is considered to have been deposited by a pre-Reid glaciation, consistent with an earlier report that the lava flow surface is "mantled with undulating drift deposits" northwest of Fort Selkirk and is striated near the Pelly River (Bostock, 1966).

A Middle Pleistocene flow centred on Black Creek (Fig. 1) was identified by Huscroft *et al.* (2004), who provided a $^{40}\text{Ar}/^{39}\text{Ar}$ age of 311 ± 32 ka, which has recently been recalculated as 441 ± 76 ka (L.E. Jackson, writ. comm., 2009). Downstream of Black Creek, this flow is partially overlain by gravels correlated with the Reid (penultimate)

Glaciation, but its surface is otherwise devoid of erratics and other evidence of glacial overriding (Huscroft *et al.*, 2004). Based on new paleomagnetic evidence (Nelson *et al.*, 2009), the Reid glacial advance did not reach the Pelly-Yukon confluence (L.E. Jackson, writ. comm., 2009). The western limit of the most recent (McConnell) advance of the Cordilleran ice sheet is more than 50 km to the east (Duk-Rodkin, 2001). Surficial geology mapping indicates that both the Early and Middle Pleistocene flows in the study area are extensively covered by aeolian deposits (Jackson, 1997).

The youngest lava flows occur immediately north and south of Volcano Mountain (Fig. 1). Based on surface expression and vegetation cover, Jackson and Stevens (1992) infer three relative ages of flows south of Volcano Mountain and two to the north. Indirect limiting ages for the most recent flows are provided by radiocarbon dates from basal sediments in lava-dammed Leech Lake (ca. 4200 BP) and Caitlin Pond (ca. 7300 BP; Fig. 1). Jackson and Stevens (1992) also noted the presence of a lapilli blanket locally exceeding 0.5 m in thickness over the lava flow in the valley of Grand Valley Creek. The prominent cleft that bisects Volcano Mountain and the associated landslides north and south of the cinder cone are presumably created by this Holocene activity. Although the most extensive lava flows at Volcano Mountain are apparently Holocene, older volcanic surfaces may exist in the vicinity, notably at 'Ancient Volcano Mountain' approximately 2 km to the west. In addition, Nelson *et al.* (2009) suggests that flows higher up on Volcano Mountain could be old enough to belong to the Matuyama Reversed Chron (*i.e.*, >0.78 Ma).

Previous studies document compositional differences between the basaltic lavas in the study area. The Volcano Mountain flows have a nephelinite (low silica) composition, while the Early and Middle Pleistocene flows are alkaline olivine basalts (high silica; Francis and Ludden, 1990; Nelson *et al.*, 2009). It is unclear whether such differences are large enough to influence the direction and rate of soil-forming processes. Non-volcanic geomorphic processes such as glacial erosion and deposition and contributions of aeolian materials could be much stronger influences on soil parent material composition.

Any comparison of soil formation on the three age groupings of lava flows in the study area needs to consider potential elevation-related differences in climate. The Early and Middle Pleistocene lava flows along the Yukon River lie almost entirely below 600 m

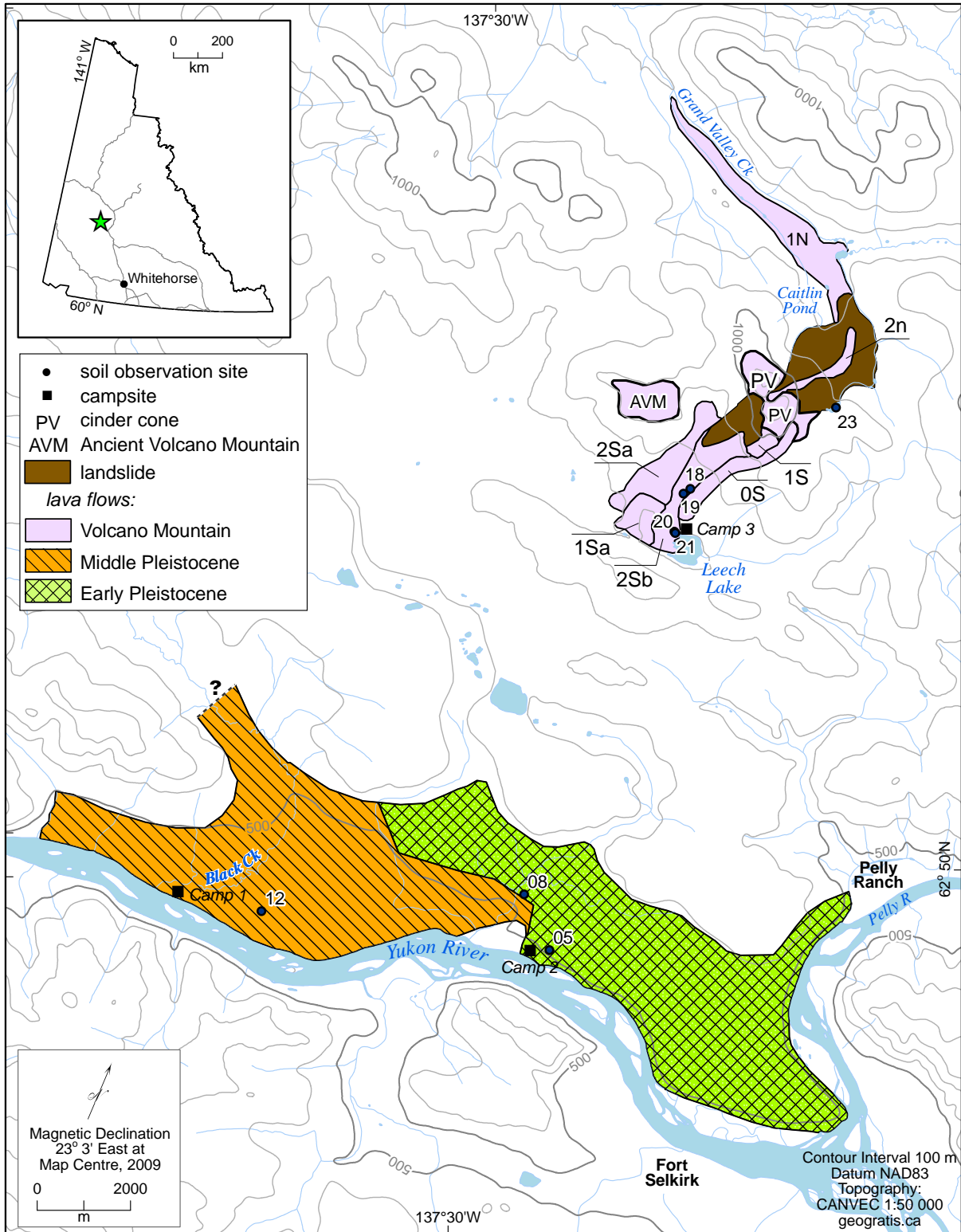


Figure 1. Lava flows and soil study sites, northern portion of the Fort Selkirk volcanic field. Nomenclature and boundaries for units near Volcano Mountain are taken from Jackson and Stevens (1992). The extents of Middle and Early Pleistocene lava flows immediately north of the Yukon River are based on much smaller-scale mapping by Huscroft et al. (2004) and Nelson et al. (2009).

elevation (Fig. 1). Long-term records from the nearby weather station at Pelly Ranch (elevation 454 m) indicate a cold, dry climate, with mean annual temperature of -3.9°C and mean annual precipitation of 310 mm (Environment Canada online climate data http://climate.weatheroffice.ec.gc.ca/climate_normals/index_e.html [accessed November 15, 2009]). The younger lava flows near Volcano Mountain occur at higher elevations (700-1000+ m), so temperatures should be correspondingly lower.

At this high latitude – almost 63°N – slope aspect has an important influence on microclimate, permafrost distribution and vegetation patterns. The very gently sloping Early and Middle Pleistocene lava flows along the Yukon River have a generally south- to southwest-facing aspect, and the significant proportion of trembling aspen (*Populus tremuloides*) in the forest cover suggested that permafrost is absent (Perala, 1990) over much of these landforms. The flows originating on the south flank of Volcano Mountain have a pronounced southwest-facing slope aspect and should have a warmer microclimate than those on the north side of the mountain. Permafrost distribution in the study area has not been examined, but Jackson and Stevens (1992) did report a permafrost occurrence in the lapilli deposit in the valley of Grand Valley Creek.

METHODS

Field work was conducted on each of the three age groups of lava flows. Ground traverses involved checks with hand-augering to assess the thickness of surficial deposits and a limited number of soil pits on representative landscape positions. Soil description terminology is according to Expert Committee on Soil Survey (1983) and Green *et al.* (1993). Presence of carbonates was assessed in the field by reaction with 10% HCl. Soil horizon nomenclature (Table 1) and provisional soil classifications (Soil Classification Working Group, 1998) are assigned based on field observations. Soil reaction was measured in 0.01 M CaCl₂ (Carter and Gregorich, 2008) with an Orion 550A pH meter and combination electrode. Laboratory analyses for other properties (e.g., carbon, particle-size distribution) are pending and results may alter these designations.

Table 1. Selected notation for soil horizons (Green *et al.*, 1993; Soil Classification Working Group, 1998).

Organic horizons
L – fresh or slightly decomposed plant litter (e.g., leaves, needles, twigs)
F – moderately decomposed organic matter
m – abundant fungi present
H – humified (strongly decomposed) organic matter
h – very few if any recognizable plant residues
Mineral horizons
A – uppermost horizon(s) (not always present)
e – bleached in appearance
h – enriched in organic matter
B – middle horizon(s)
m – moderate degree of modification of parent material
BC – transitional horizon between B and C
C – original mineral parent material with only slight modification of chemical and/or physical properties
ca – enriched in secondary carbonates
k – containing primary (inherited) carbonates
R – consolidated bedrock
Additional modifiers applied to A, B or C horizons
u – disrupted or mixed by physical or biological processes (e.g., treethrow)
j – indicates weak expression of the property that precedes it
II, III, IV – Roman numeral prefix identifies materials differing significantly in geological origin or texture
1, 2, 3 – Numeric suffix identifies horizon subdivision

FIELD OBSERVATIONS

EARLY PLEISTOCENE LAVA FLOWS

Although basalts form prominent cliffs along the Yukon River, bedrock is not encountered within 1 m of the surface in any of the five soil pits excavated on level to gently sloping sites near Camp 1. At site Y09-05 (Fig. 1), approximately 50 cm of predominantly silty Bm horizon, free of coarse fragments, overlie a dark-coloured sandy loam matrix-supported diamicton containing numerous basalt cobbles (Figs. 2, 3; Table 2). Secondary carbonate is abundant in a 15-25 cm thick horizon that appears to be a mixture of these two materials. The diamicton is moderately calcareous, and appears fresh and

unweathered, as do the basalt cobbles in this material; there is no indication of a buried paleosol. While the upper silty material is most likely loess, the origin of the diamicton is unclear, but the overwhelming predominance of basalt coarse fragments suggests a local source.

Elsewhere on this landform, the uppermost 40-100 cm of soil profiles appear similar in colour and texture to the Bm horizons noted at Y09-05. Although diamicton was not encountered at the other examined sites, materials

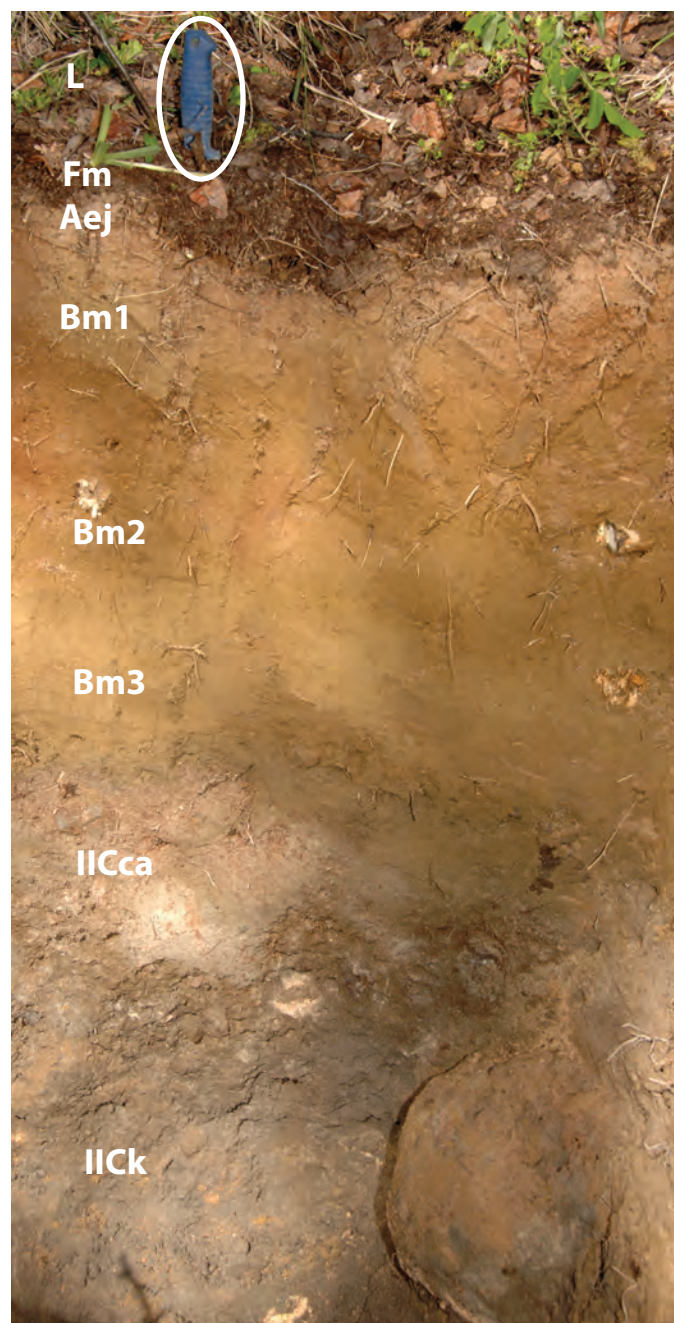


Figure 2. Eluviated Eutric Brunisol at site Y09-05. Knife handle (circled; see Table 2) for scale is 11 cm long.

Table 2. Description of Eluviated Eutric Brunisol at site Y09-05 (62°48'54.1"N, 137°27'42.9"W).

Horizon	Depth (cm)	Description
L	4-3	Deciduous leaf litter; abrupt, smooth boundary; 1 cm thick; pH 5.50.
Fm	3-0	Black (7.5YR 2.5/2 m); partially decomposed organic matter; moderate, non-compact matted; loose; abundant fungal mycelia; abundant very fine roots; abrupt, wavy boundary; 2-4 cm thick; pH 6.19.
Aej	0-4	Brown (7.5YR 5/3 m); silt loam; weak, fine, subangular blocky; very friable; abundant, very fine and fine, and plentiful, medium and coarse roots; clear, wavy boundary; 2-5 cm thick; pH 4.63.
Bm1	4-25	Dark yellowish brown (10YR 4/4 m), brown (7.5YR 4/4 m); silt loam; moderate, fine and medium platy; very friable; abundant, very fine and fine, and plentiful, medium and coarse roots; gradual, irregular boundary; 15-25 cm thick; pH 5.90.
Bm2	25-45	Brown (10YR 4/3 m); silt loam; moderate, fine and medium platy; very friable; plentiful, very fine and fine roots; clear, wavy boundary; 18-25 cm thick; pH 6.36.
Bm3	45-52	Olive brown (2.5Y 4/3 m); loamy sand; single grain; very friable; few, very fine and fine roots; abrupt, irregular boundary; 5-12 cm thick; pH 7.26.
IICca	52-70	Dark greyish brown (2.5Y 4/2 m), pale yellow (2.5Y 7/3 m); silt loam; weak, medium platy; friable; plentiful, very fine and fine roots (concentrated in upper 10 cm of horizon); 20% gravels and 10% cobbles, subrounded and subangular; strongly effervescent; streaked and spotted, many fine and medium secondary carbonates in matrix, with 1-2 mm thick carbonate coatings on undersides of most coarse fragments; gradual, wavy boundary; 15-25 cm thick; pH 7.80.
IICk	70-105+	Very dark grey (2.5Y 3/1 m); sandy loam; massive; friable; few, very fine and fine roots; 20% gravels and 10% cobbles, subrounded and subangular; moderately effervescent; pH 7.76.



Figure 3. Basalt cobbles collected from diamicton at site Y09-05. Light-coloured surfaces of some cobbles are secondary carbonate coatings (arrows).

become sandier at depth, perhaps indicating fluvial deposits as at site Y09-08 on a terrace above a small unnamed stream (Fig. 1).

Based on the measured pH values and the shallow depth to carbonates, all of these soils are provisionally classified as Orthic Eutric Brunisols, indicating that pH values are above 5.5 within some part or all of the uppermost 25 cm of the B horizon (Soil Classification Working Group, 1998).

MIDDLE PLEISTOCENE LAVA FLOWS

Eight soil inspections were made east of the confluence of Black Creek and the Yukon River. This lava flow displays 1-2 m of relief, with a gently undulating surface expression. On the local high points, basalt occasionally outcrops or is often within 20-30 cm of the surface, covered by silty aeolian material with no coarse fragments other than occasional angular fragments of the underlying basalt. Where this silty material is thicker (up to 1 m or more), secondary carbonates are usually encountered at ~50 cm depth. The pH values are high enough for soils to be classified as Eutric Brunisols (Table 3).

Contacts with the underlying basalt are usually abrupt, or with a thin transitional zone of basalt fragments mixed with calcareous fines derived from the aeolian materials above, as at site Y09-12 (Fig. 4; Table 3). The bedrock is hard, dark-coloured, and shows no evidence of formation of weathering rinds, or accumulation of weathering products, or translocated clay in fractures or other voids. Consistent with previous work (Huscroft *et al.*, 2004), no evidence of erratics on the soil surface, or glacial till overlying the bedrock is found.

Table 3. Description of Orthic Eutric Brunisol at site Y09-12 (62°49'13.1"N, 137°34'59.9"W).

Horizon	Depth (cm)	Description
L	5-4	Deciduous leaf litter (aspen); 1 cm thick; pH 5.50.
Fm	4-0	Dark brown (7.5YR 3/2 m); partially decomposed organic matter; moderate, non-compact matted; friable; felty; abundant fungal mycelia; abundant very fine, fine and medium roots; abrupt, wavy boundary; 3-5 cm thick; pH 5.65.
Bmu1	0-30	Brown (7.5YR 4/3 m), yellowish brown (10YR 5/4 m); silt loam; weak, fine and medium platy; very friable; plentiful very fine, fine, medium and coarse roots; clear, broken boundary; 20-35 cm thick; pH 6.30.
Bmu2	30-50	Olive brown (2.5YR 4/4 m); silt loam; moderate, fine and medium subangular blocky; friable; plentiful very fine, fine, and medium roots; clear, smooth boundary; 10-35 cm thick; pH 7.10.
Cca	50-90	Greyish brown (2.5Y 5/2 m); silt loam; moderate, fine and medium subangular blocky; friable; plentiful, very fine and fine roots; strongly effervescent; common, fine, streaked and spotted, random and irregular, friable, grey (10YR 6/1 m) secondary carbonates; clear, wavy boundary; 35-45 cm thick; pH 7.90.
II Cca	90-105	Olive brown (2.5 Y 4/3 m); very fine sandy loam; massive; friable; few, very fine and fine roots; 10% angular and subangular gravels, 30% angular and subangular cobbles (all are basalt); strongly effervescent; many, medium, spotted, irregular, friable, light yellowish brown (10YR 6/4 m) secondary carbonates; pH 7.97
R	105+	Basalt bedrock.

VOLCANO MOUNTAIN LAVA FLOWS

Although a traverse was made from the summit (1239 m) of Volcano Mountain easterly to a small drained pond at site Y09-23, detailed soil inspections were restricted to the flows on the south side of the cinder cone (Fig. 1). Two inspection sites are near the terminus of the sparsely vegetated flow designated as 2Sb by Jackson and Stevens (1992). Site Y09-20 is typical of much of the southern portion of this landform, with only lichens and mosses partially covering an angular, blocky surface of the lava

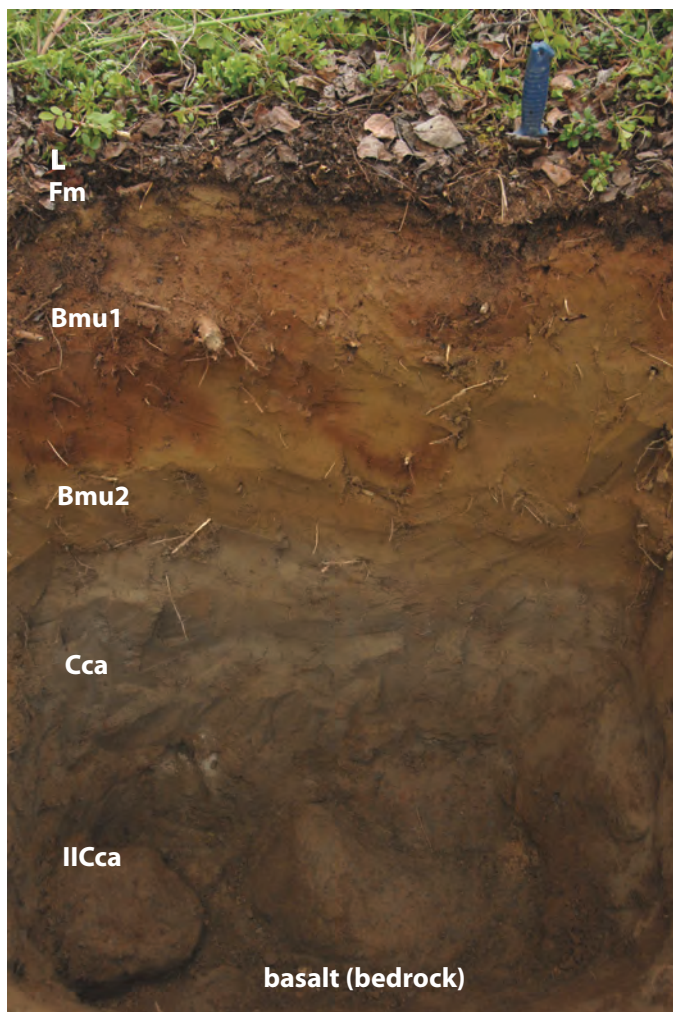


Figure 4. Orthic Eutric Brunisol soil at site Y09-12.

flow (Fig. 5). Underneath this cover, little or no soil has accumulated (Fig. 6) despite the estimated age of ca. 4200 BP for this flow. Occasional linear depressions up to 1 m deep in the flow surface serve as more efficient traps for organic detritus and may have clumps of paper birch (*Betula papyrifera*) or aspen (Fig. 7). For example, at Y09-21 these microsites have thicknesses of organic matter that can equal or exceed that of the mineral soil (Fig. 8; Table 4). Based on the thickness of the organic horizons, and the fragmental character of the contact with the underlying basalt, this soil would be classified as a Hemic Folisol. This type of organic soil, consisting of a forest floor resting directly on intact or fragmented bedrock, is unusual in Yukon; most documented occurrences are in coastal British Columbia (Fox *et al.*, 1987).



Figure 5. Site view of Y09-20 on Holocene lava flow.



Figure 6. Close-up view of basalt flow surface at Y09-20; lichen removed to show limited accumulation of organic matter and mineral soil.



Figure 7. Basalt flow surface with linear depression occupied by paper birch and aspen and with localized thicker accumulation of organic matter and mineral soil.

Table 4. Description of Hemic Folisol at Site Y09-21 (62°53'45.3"N, 137°24'56.6"W).

Horizon	Depth (cm)	Description
L	15-10	Birch leaf litter; pH 4.72.
Fm	10-5	Very dark brown (7.5YR 2.5/2 m); partially decomposed organic matter; moderate, non-compact matted; friable; felty; abundant mycelia; abundant very fine, fine and medium roots; pH 4.18.
Hh	5-0	Black (7.5YR 2.5/1 m); granular; friable; abundant, very fine, fine and medium roots; pH 4.49.
Bm	0-15	Dark yellowish brown (10YR 4/4 m); silt loam; abundant, very fine, fine and medium roots; 80% angular basalt fragments; abrupt, irregular boundary; pH 4.96.
R	15+	Basalt bedrock.

Farther north, we examined two sites near the eastern edge of flow 2Sb (Fig. 1). At site Y09-19, a sloping surface (10% slope, southwest aspect) has stronger vegetation and soil development than at the two previous sites, with about 20% canopy cover by black and white spruce (*Picea mariana*, *P. glauca*) and aspen, and a continuous moss and lichen groundcover. Fragmentation of the basalt enables digging with hand tools to >30 cm, and the uppermost portion of the Bm horizon has a noticeably silty texture, suggesting incorporation of some aeolian materials (Fig. 9; Table 5). Abundant roots are still present at the bottom of this shallow excavation, and along with fungal mycelia form mat-like arrays over the rock fragment surfaces (Fig. 10).

Only a short distance to the northeast, a denser vegetation cover indicates a possible transition to an older landform. The soil at this site (Y09-18) is strikingly different, with much thicker forest floors (15 vs. 6 cm) and B horizons forming in lapilli overlying basalt (Fig. 11; Table 6). This surface may correspond to the OS flow designated by Jackson and Stevens (1992), although the occurrence of lapilli on this feature is not previously reported. Since the lapilli deposit is absent at site Y09-19, it presumably predates the 2Sb flow. Although the soil at Y09-19 would therefore be older than at Y09-18, mineral horizon pH values are higher in the former (Tables 5, 6), perhaps reflecting a greater aeolian contribution to the B horizon.



Figure 8. Hemic Folisol at site Y09-21 formed under paper birch and scattered shrubs.



Figure 9. Orthic Dystric Brunisol at site Y09-19.

Table 5. Description of Orthic Dystric Brunisol at Site Y09-19 (62°54'12.6"N, 137°24'46.6"W).

Horizon	Depth (cm)	Description
L	6-5	Lichen and moss with intermingled spruce needle litter; abrupt, wavy boundary; 1 cm thick.
Fm	5-0	Very dark greyish brown (10YR 3/2 m); partially decomposed organic matter; strong, non-compact matted; friable; abundant mycelia; abundant very fine, fine, medium and coarse roots; abrupt, wavy boundary; 3-7 cm thick; pH 4.94.
Bm1	0-8	Brown (10YR 5/3 m); silt loam; weak, fine subangular blocky; very friable; abundant, very fine, fine and medium roots; 80% angular basalt fragments (40% gravel, 40% cobbles); clear, wavy boundary; 5-10 cm thick; pH 4.33.
Bm2	8-35	Brown (7.5YR 4/4 m); sandy loam; single grain; very friable; abundant, very fine, fine and medium roots; 80% angular basalt fragments (40% gravel, 40% cobbles); abrupt, irregular boundary; 15-30 cm thick; pH 5.07.
R	35+	Basalt bedrock.



Figure 10. Close-up view of basalt fragments from B horizon of soil at Y09-19, showing fine roots and fungal mycelia forming mats over rock surfaces.

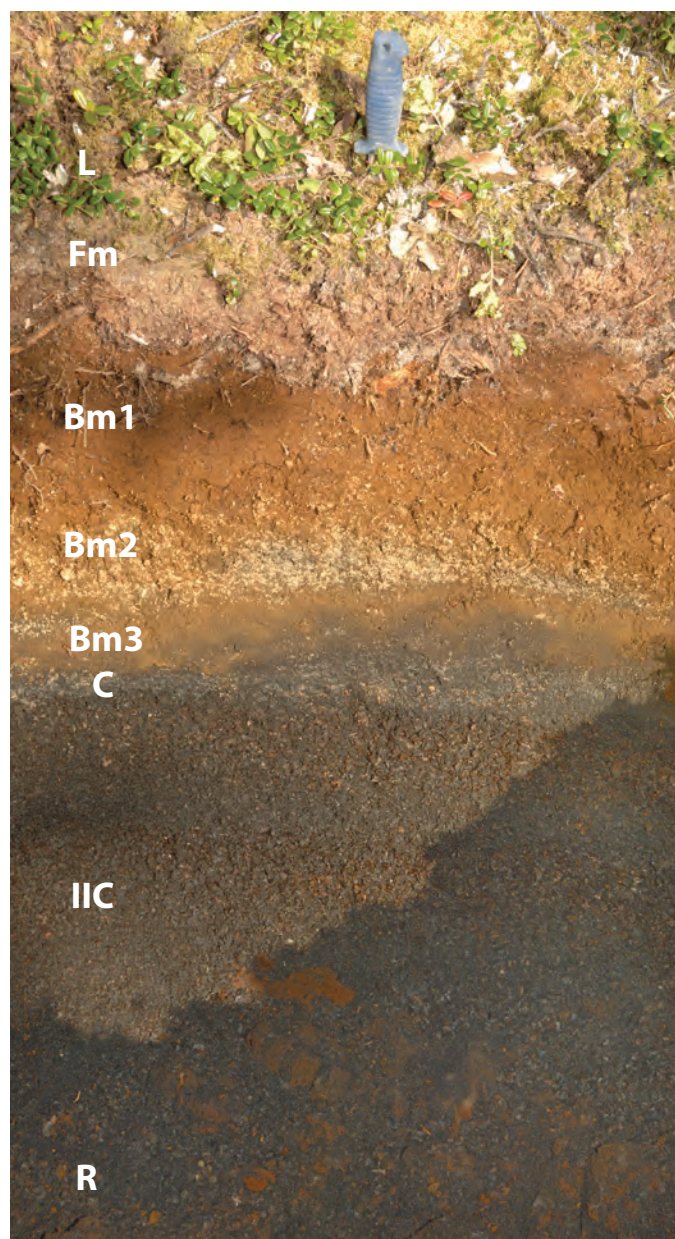


Figure 11. Orthic Eutric Brunisol soil at site Y09-18.

DISCUSSION AND RECOMMENDATIONS FOR FUTURE RESEARCH

Although the basaltic lava flows in the Fort Selkirk volcanic field span a large age range, geological events – glacial advances, loess deposition – have prevented the soils on these surfaces from comprising a true chronosequence, *i.e.*, differing only in age, but otherwise subjected to the same ecological, climatic and

Table 6. Description of Orthic Eutric Brunisol at Site Y09-18 (62°54'16.1"N, 137°24'36.6"W)

Horizon	Depth (cm)	Description
L	15-13	Feathermoss with intermingled spruce needle litter; abrupt, wavy boundary; 2-4 cm thick.
Fm	13-0	Very dark brown (7.5YR 2.5/2 m); partially decomposed organic matter; moderate, non-compact matted; friable; felty and fibrous; abundant mycelia; abundant very fine, fine and medium roots; abrupt, wavy boundary; 10-15 cm thick; pH 4.31.
Bm1	0-15	Dark brown (7.5YR 3/4 m); sandy loam; weak, fine subangular blocky; very friable; plentiful very fine, fine and medium roots; 20% angular gravel (lapilli); clear, wavy boundary; 9-17 cm thick; pH 5.88.
Bm2	15-22	Dark yellowish brown (10YR 4/4 m); sandy loam; single grain; very friable; plentiful very fine and fine roots; 80% angular gravel (lapilli); abrupt, smooth boundary; 5-10 cm thick; pH 6.24.
Bm3	22-26	Dark brown (10YR 3/3 m); sandy loam; weak, fine subangular blocky; very friable; few very fine and fine roots; abrupt, wavy boundary; 3-7 cm thick; pH 6.06.
C	26-32	Black (2.5 Y 2.5/1 m); sand; single grain; very friable; few very fine roots; abrupt, smooth boundary; 2-7 cm thick; pH 6.37.
IIC	32-72	Black (10YR 2/1 m); sand; single grain; loose; >95% angular gravel (lapilli); abrupt, wavy boundary; 35-45 cm thick; pH 6.54.
R	72+	Basalt bedrock.

topographic influences. Nevertheless, this fascinating area provides conditions that may facilitate a number of follow-up studies of both pedological and ecological processes.

The observations of the Early and Middle Pleistocene lava flows are restricted to limited areas near their southern edges, so any general interpretations must be made cautiously. Diamicton of uncertain origin is encountered (site Y09-05) on the Early Pleistocene flow, but there is no evidence of previous soil formation in this material below the loess veneer. This is unexpected, because Early

Pleistocene glacial deposits elsewhere in central Yukon, including within the Carmacks (1151) map sheet, display strong soil development characterized by thick reddish-brown B horizons with significant clay accumulations (Tarnocai and Smith, 1989; Jackson, 2000). Similarly, on the Middle Pleistocene lava flow, the loess-basalt contacts are abrupt and the bedrock appears fresh and unweathered. In both situations, the loess is strongly calcareous and has been decalcified to depths of about 40-50 cm, suggesting that it is of the same age on both surfaces, and presumably deposited during the McConnell glaciation. The lack of soil development on the underlying materials is striking and unexpected, particularly given the subdued topography which should favour preservation of older soils. Perhaps loess accumulations of equal or greater thickness, with similarly high carbonate content, have persisted on these surfaces throughout much of the Pleistocene, serving to isolate the underlying materials from pedogenesis. Additional observations should be made farther north, away from the Yukon River, to determine if this pattern of limited soil formation is indeed typical on these landforms.

The most interesting area for potential follow-up work is around Volcano Mountain. The virtual absence of soils and vascular plant cover on the Holocene flow immediately west of Leech Lake is a graphic demonstration of the slow rate of primary succession in this climate. However, climate may not be the paramount factor, as shown by similarly slow rates of soil formation on Holocene basalts in the Craters of the Moon lava field in southern Idaho (Vaughan and McDaniel, 2009). Lava morphological types are shown to exert a strong influence on soil formation, with much slower accumulation of organic detritus and soil mineral material on the highly fractured, blocky surfaces of a'a-type flows. Although the lapilli at site Y09-18 may be older than the adjacent lava flow at Y09-19, the more strongly coloured solum formed on this material may also reflect the influence of its finer particle size in promoting weathering and plant colonization. Since basalts are generally devoid of quartz, it may be possible to quantify the aeolian contribution to soils formed on these volcanic surfaces.

Observations made on this trip were restricted by time, but it would be worth examining the Holocene flows at Volcano Mountain more carefully to assess the gradients of primary succession and soil formation at their margins. Detrital organic matter fluxes (e.g., wind-blown leaf litter) should diminish rapidly with distance from the flow margin, and these conditions may enable field studies of

successional pathways. Since the Holocene flows occur across a considerable elevation range, the assemblage of surfaces at Volcano Mountain may provide a matrix of age and elevation combinations that would be useful in ecological research. With additional dating control, the sequence of flows around Volcano Mountain could be a valuable addition to comparative studies of succession and soil formation on basaltic materials at other sites in the Cordillera, such as the Nass River flows, Nazko Cone in the Anahim volcanic belt, and the Wells Gray area of east-central British Columbia.

ACKNOWLEDGEMENTS

Helicopter and camp support contributed by the Yukon Geological Survey and facilitated by Jeff Bond made this work possible. Lionel Jackson Jr., (Geological Survey of Canada) provided helpful advice and reviewed a draft of this article. Diligent (and musical!) field assistance was provided by Ekaterina Daviel (UNBC), Nancy Alexander prepared Figure 1, and NSERC supported this research through a Discovery Grant to Paul Sanborn.

REFERENCES

- Bond, J.D. and Sanborn, P.T., 2006. Morphology and geochemistry of soils formed on colluviated weathered bedrock: Case studies from unglaciated upland slopes in west-central Yukon. Yukon Geological Survey, Open File 2006-19, 70 p.
- Bostock, H.S., 1966. Notes on glaciation in the Central Yukon Territory. Geological Survey of Canada, Paper 65-36.
- Carter, M.R. and Gregorich, E.G. (eds.), 2008. Soil Sampling and Methods of Analysis (2nd ed.). Canadian Society of Soil Science, CRC Press, Boca Raton, FL, 1224 p.
- Duk-Rodkin, A., 2001. Glacial limits, Carmacks, west of sixth meridian, Yukon Territory. Geological Survey of Canada, Open File 3805, 1:250 000 scale.
- Environment Canada, 2009. National Climate Data and Information Archive, <http://climate.weatheroffice.ec.gc.ca/climate_normals/index_e.html> [accessed November 15, 2009].

- Expert Committee on Soil Survey, 1983. Manual for Describing Soils in the Field. LRRRI Contribution No. 82-52. Research Branch, Agriculture Canada, 175 p. <http://sis.agr.gc.ca/cansis/publications/manuals/describing_soils.html> [accessed November 15, 2009].
- Fox, C.A., Trowbridge, R. and Tarnocai, C., 1987. Classification, macromorphology and chemical characteristics of folisols from British Columbia. *Canadian Journal of Soil Science*, vol. 67, no. 4, p. 765-778.
- Francis, D. and Ludden, J., 1990. The mantle source for olivine nephelinite, basanite, and alkaline olivine basalt at Fort Selkirk, Yukon, Canada. *Journal of Petrology*, vol. 31, p. 371-400.
- Green, R.N., Trowbridge, R.L. and Klinka, K., 1993. Towards a taxonomic classification of humus forms. *Forest Science Monograph*, vol. 29, p. 1-48.
- Huscroft, C.A., Ward, B.C., Barendregt, R.W., Jackson, L.E., Jr. and Opdyke, N.D., 2004. Pleistocene volcanic damming of Yukon River and the maximum age of the Reid Glaciation, west-central Yukon. *Canadian Journal of Earth Sciences*, vol. 41, no. 2, p. 151-164.
- Jackson, L.E., Jr., 1997. Surficial geology, Victoria Rock, Yukon Territory. Geological Survey of Canada, Map no. 1877A, 1:100 000 scale.
- Jackson, L.E., Jr., 2000. Quaternary geology of the Carmacks map area, Yukon Territory. Geological Survey of Canada, Bulletin 539, 74 p.
- Jackson, L.E., Jr., Barendregt, R.W., Baker, J. and Irving, E., 1996. Early Pleistocene volcanism and glaciation in central Yukon: a new chronology from field studies and paleomagnetism. *Canadian Journal of Earth Sciences*, vol. 33, p. 904-916.
- Jackson, L.E., Jr., Huscroft, C.A., Ward, B.C. and Villeneuve, M., 2008. Age of volcanism of the Wolverine volcanic center, west-central Yukon Territory, Canada and its implications for the history of Yukon River. *EOS Transactions AGU*, vol. 89, no. 53, Fall Meeting Supplement, Abstract V41D-2110.
- Jackson, L.E., Jr. and Stevens, W., 1992. A recent eruptive history of Volcano Mountain, Yukon Territory. *In: Current Research, Part A, Cordillera and Pacific*. Geological Survey of Canada, Paper no. 92-01A, p. 33-39.
- Nelson, F.E., Barendregt, R.W. and Villeneuve, M., 2009. Stratigraphy of the Fort Selkirk Volcanogenic Complex in central Yukon and its paleoclimatic significance: Ar/Ar and paleomagnetic data. *Canadian Journal of Earth Sciences*, vol. 46, no. 5, p. 381-401.
- Perala, D.A., 1990. *Populus tremuloides Michx.* Quaking aspen. *In: Silvics of North America: Volume 2, Hardwoods*, R.M. Burns and B.H. Honkala, technical coordinators. Agriculture Handbook 654. Washington, DC: US Department of Agriculture, Forest Service, p. 555-569.
- Smith, C.A.S., Sanborn, P.T., Bond, J.D. and Frank, G., 2009. Genesis of Turbic Cryosols on north-facing slopes in a dissected, unglaciated landscape, west-central Yukon Territory. *Canadian Journal of Soil Science*, vol. 89, p. 611-622.
- Soil Classification Working Group, 1998. The Canadian System of Soil Classification, 3rd ed. Publication 1646. Research Branch, Agriculture and Agri-Food Canada, 187 p. <<http://sis.agr.gc.ca/cansis/taxa/cssc3/index.html>> [accessed November 15, 2009].
- Tarnocai, C. and Smith, C.A.S., 1989. Micromorphology and development of some central Yukon paleosols. *Geoderma*, vol. 45, p. 145-162.
- Trupia, S. and Nicholls, J., 1996. Petrology of Recent lava flows, Volcano Mountain, Yukon Territory, Canada. *Lithos*, vol. 37, no. 1, p. 61-78.
- Vaughan, K.L. and McDaniel, P.A., 2009. Organic soils on basaltic lava flows in a cool, arid environment. *Soil Science Society of America Journal*, vol. 73, no. 5, p. 1510-1518.

Observations of polymetallic Ag-Pb-Zn (\pm Au \pm In) mineralization at the Eagle and Fisher vein-faults, airborne total field magnetics and identification of Tombstone age-equivalent aplite dykes in the Galena Hill area, Keno City, Yukon

Dave Tupper¹

Mega Precious Metals Inc.

Venessa Bennett²

Yukon Geological Survey

Tupper, D. and Bennett, V., 2010. Observations of polymetallic Ag-Pb-Zn (\pm Au \pm In) mineralization at the Eagle and Fisher vein-faults, airborne total field magnetics and identification of Tombstone age-equivalent aplite dykes in the Galena Hill area, Keno City, Yukon. *In: Yukon Exploration and Geology 2009*, K.E. MacFarlane, L.H. Weston and L.R. Blackburn (eds.), Yukon Geological Survey, p. 305-330.

ABSTRACT

We present a new dataset from the Eagle exploration project, completed in 2009 on the lesser explored southeast slopes of Galena Hill in the Keno Hill silver camp. The Keno Hill silver camp is hosted in Neoproterozoic and Paleozoic sedimentary rocks of the Selwyn Basin that were subsequently intruded by the Cretaceous Tombstone Plutonic Suite. Although a genetic association is documented between the Tombstone plutons and Au-As mineralization regionally, the genesis and age of the Keno Ag-Pb-Zn mineralization remains poorly understood.

Mineralization studied from the Eagle project area, while modally dominated by indium-rich sphalerite, was introduced in at least three distinct phases. A low-amplitude aeromagnetic high occurs at the southeast end of Galena Hill and is suggestive of a buried intrusion. Two new U-Pb age dates of ca. 93 Ma have been determined for aplite dykes, indicating the presence of Tombstone Suite intrusions within the Eagle property.

¹dt.pgeo@gmail.com

²venessa.bennett@gov.yk.ca

INTRODUCTION

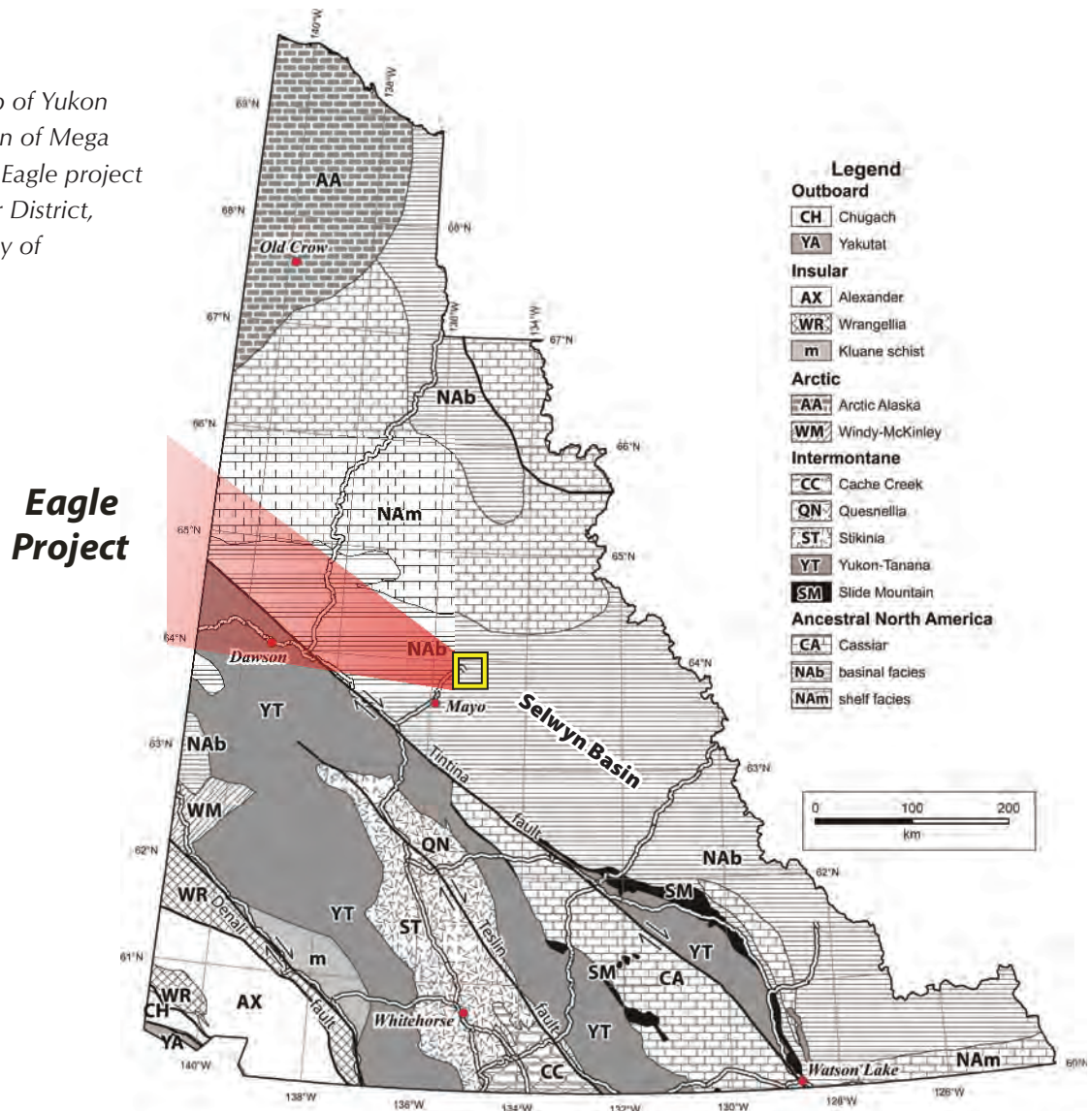
The Eagle Silver project of Mega Precious Metals Inc. (MPI; previously Mega Silver Corp.), is located on the southeast slope of Galena Hill in the Keno Hill silver camp, north-central Yukon (Figs. 1, 2). Total claim disposition comprises the Fisher, Eagle, Spiderman, Blue and One properties (Fig. 2). Exploration efforts by MPI during the past two years have focused on identifying economic extensions of both the Eagle and Fisher polymetallic vein-faults.

The mines of the Keno Hill silver camp, which included up to 35 different sites, produced a total 6 656 t (214 million ounces) of silver, 80% of which was extracted from veins located on the north slopes of Galena Hill (Cathro, 2006). Up to 45% of the total silver production

was from the Hector-Calumet Mine alone, located on Galena Hill. The primary ore milled was galena-tetrahedrite-sphalerite-rich and averaged 1374 g/t (41.0 oz/ton) silver.

Although a genetic association between the mid-Cretaceous plutons of the Tombstone Suite and Au-As and W mineralization in the region (e.g., Scheelite Dome and Dublin Gulch) is well documented, the genesis and age of the Keno Ag-Pb-Zn mineralization remains poorly constrained. Lynch (1989) considered the Roop Lakes pluton, a member of the Tombstone Suite, to be the heat source linked to the concentration of the Keno Hill Ag-Pb-Zn mineralization, but not the source of the metals. Duncan Creek and its tributaries, parts of which drain the Eagle Silver project area (Fig. 2), have also produced a reported total of 15.5 million grams (49 416 oz) of Au

Figure 1. Terrane map of Yukon illustrating the location of Mega Precious Metals Inc.'s Eagle project within the Keno Silver District, Selwyn Basin (courtesy of M. Colpron).



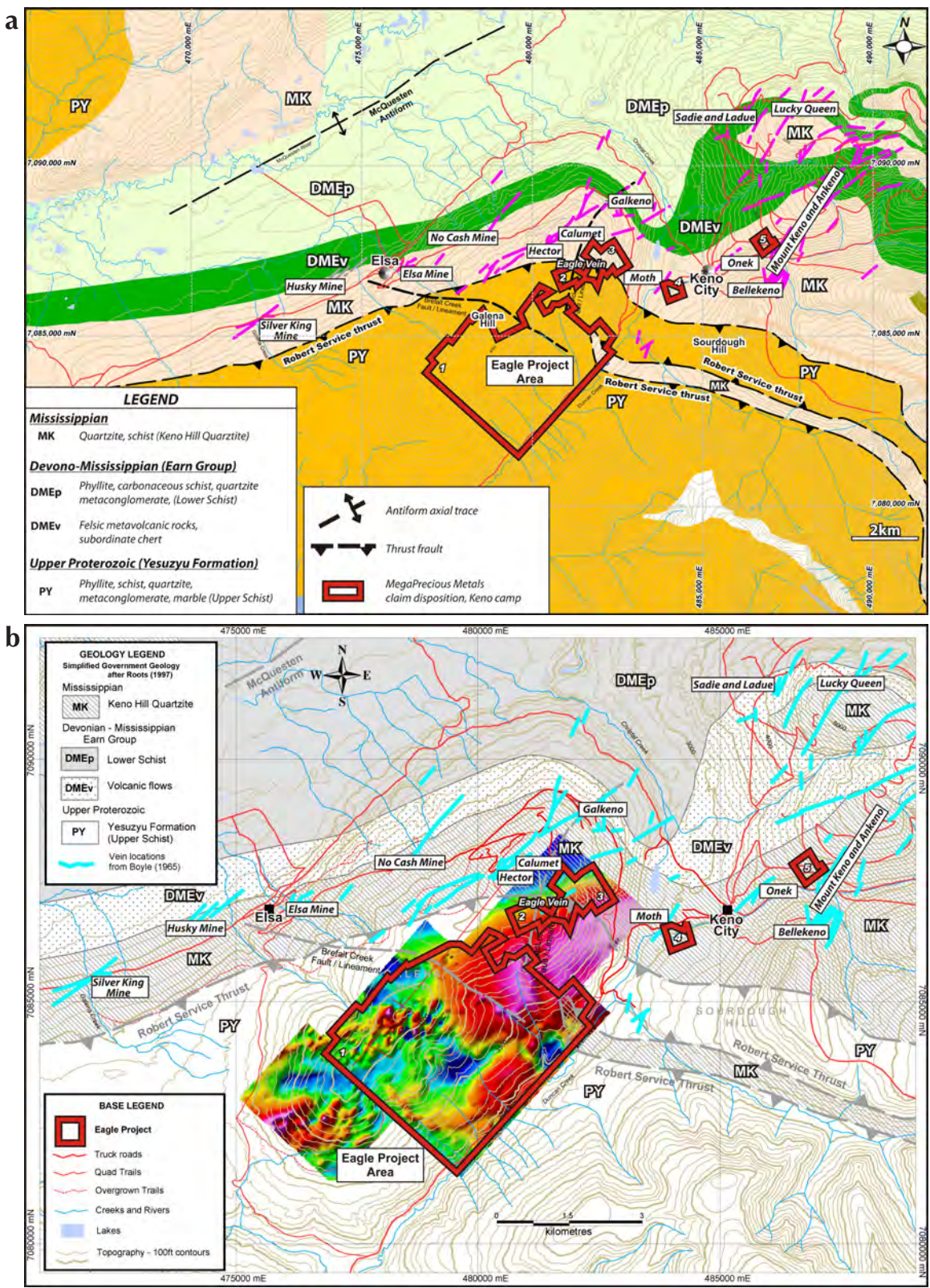


Figure 2. (a) Geological map of Keno Hill camp illustrating the distribution of Ag-Pb-Zn properties and historic mines. The location of Mega Precious Metals Inc.'s claim disposition is outlined in red. Claim blocks labeled 1 - 5 represent Fisher, Eagle, Spiderman, Blue and One properties respectively. (b) Total magnetic intensity map acquired for Mega Precious claims superimposed on Keno Hill camp geological map.

from 1898 to 2006 (LeBarge, 2007), indicating important bedrock reserves of Au exist within the Keno Hill silver camp.

In 2009, the Eagle Silver project was the focus of 4022 m of NTW diamond drilling targeting the Eagle Vein, a strong, steep southeast-dipping, vein-fault hosted within interbedded quartzite and phyllitic schist of the locally defined Keno Hill Quartzite. Vein intercepts of Ag-Pb-Zn-rich mineralization at Eagle and Fisher provide key petrographic observations that assist in the understanding of ore mineral paragenesis in this region of the Keno Hill silver camp. Mineralization observed in drill core from the Eagle Vein, although modally dominated by sphalerite, show at least three phases of mineralization including: (i) an early Au-enriched pyrite-marcasite-sphalerite \pm cassiterite \pm arsenopyrite phase associated with quartz-siderite gangue; (ii) an intermediate Ag-enriched galena \pm

chalcopyrite-pyrite \pm stannite phase with overprinting late-stage siderite to cubic pyrite veining; and (iii) a late-stage, moderately Au-enriched pyrite \pm arsenopyrite \pm pyrrohotite \pm cassiterite phase of mineralization that clearly overprints pre-existing Ag-Pb-Zn mineralization. Analytical results also indicate that the Eagle Vein includes potentially economic concentrations of indium with weighted average intercepts from hole D09-EE-07 containing over 3.1 m (from 217.8 to 220.9 m) of 3.55 g/t Au, 787.7 g/t Ag, 4.46% Pb, 18.68% Zn and 168.52 g/t In.

An aeromagnetic survey flown over the property provides additional information relevant to the question of its genesis. An elongate, low-amplitude aeromagnetic high occurs at lower elevations on the southeast end of Galena Hill and is unique within the Keno Hill silver camp (Figs. 2, 3). The geometrical expression of the anomaly is suggestive of a buried pluton, the margins of which

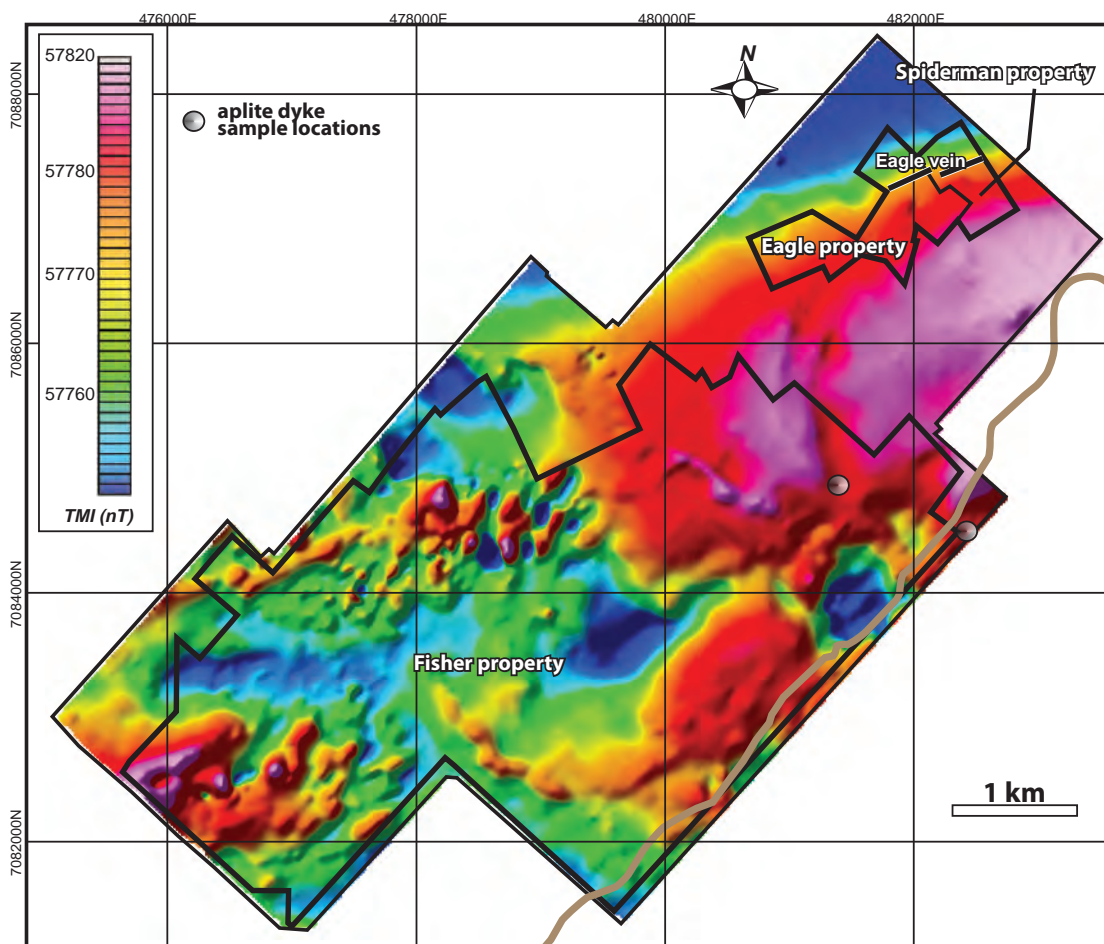


Figure 3. Total magnetic field intensity map of Mega Precious Metals Inc.'s claim block, showing the locations of the Eagle, Fisher and Spiderman claims on edges of low-amplitude magnetic high. U-Pb geochronology sample locations marked.

coincide with two proximal fault zones which separate the Eagle Vein from the prolific silver veins on the north slopes of Galena Hill (*i.e.*, Hector and Calumet). The age of this inferred intrusion is unknown; however, two new U-Pb dates on peripheral aplite dykes with similar texture and chemistry sampled from (i) within the Fisher fault zone, adjacent to the magnetic high, and (ii) to the south along Duncan Creek, are ca. 93 Ma, affirming the presence of Tombstone-age magmatism in the area.

REGIONAL GEOLOGY

The bedrock geology of the Keno Hill and surrounding Mayo area has been reported by Bostock (1947), Boyle (1956, 1957, 1965), McTaggart (1960), Kindle (1962), Watson (1986), Murphy (1997) and Roots (1997). The mineralogy and paragenesis of the Keno Hill silver base-metal veins have been discussed most extensively by Boyle (1956, 1957, 1965). Contributions have also been made by Franzen (1979), Lynch (1989; 2003), and Watson (1986). U-Pb geochronological data for intrusions in the area are reported in Roots (1997) and Murphy (1997). Sinclair *et al.* (1980), provided a K-Ar date for the mineralization from sericite of 90 Ma.

The Keno Hill camp is located within the Selwyn Basin of the northern Canadian Cordillera (Fig. 1). An informal tripartite stratigraphic subdivision has been applied to the highly deformed rocks of the camp during its protracted history; more recent work has shown that the succession is imbricated as well as highly deformed (Murphy, 1997; Roots, 1997; Fig. 2). The stratigraphically and structurally lowest informal unit of the camp is the 'lower schist' which is the local expression of the Devonian to Mississippian Earn Group (Fig. 2). In this area, the Earn Group comprises greenish-white, siliceous, chloritic-phyllitic schist (felsic metavolcanic), carbonaceous phyllite and minor quartzite horizons (Murphy, 1997). The Earn Group/'lower schist' is overlain by the Keno Hill Quartzite of Mississippian age (Mortensen and Thompson, 1990), a massive, clean, grey quartzite intercalated with lesser carbonaceous schist/phyllite. The structurally highest unit, the 'upper schist', is a composite unit disrupted by a cryptic regional thrust fault. The lower part of the 'upper schist' that directly overlies the Keno Hill Quartzite, comprises carbonaceous schist/phyllite, thin quartzite, and rare chloritic and quartz-sericite phyllite/schist of felsic metavolcanic protolith; all of the above is intercalated with dolomitic carbonate (Murphy, 1997; Roots, 1997; hereafter, the 'metavolcanic member'). The

upper part of the 'upper schist' comprises quartz-mica schist, impure quartzite, muscovite-chlorite phyllite, grit, minor limestone and rare graphitic schist (Boyle, 1965; PY; Fig. 2); these rocks have now been correlated with the Yusezyu Formation of the Late Proterozoic to Cambrian Hyland Group. Tempelman-Kluit (1970) and Thompson (1995) recognized the older-over-younger relationship and placed the Robert Service thrust between the two parts of the 'upper schist'. The Earn Group, Keno Hill Quartzite and the lower part of the 'upper schist' were intruded by a number of Triassic (Mortensen and Thompson, 1990) gabbro sills that are historically referred to as greenstones; these typically exhibit a discontinuous, lenticular shape due to post-intrusion deformation (Murphy, 1997; Roots, 1997).

All lithological units in the Keno Hill area are isoclinally folded at a variety of scales, are significantly internally thrust imbricated, and have undergone greenschist-facies metamorphism (McTaggart, 1960; Roots, 1997). These structures are part of the Tombstone strain zone of Murphy (1997), the hanging-wall shear zone above the Tombstone thrust which places the deformed and metamorphosed Keno Hill succession to the northwest above less highly deformed strata, which is as young as Upper Jurassic. The Robert Service thrust is deformed within the Tombstone strain zone, attesting to its older age, and all structures are folded by the southwest-plunging McQuesten antiform (Murphy, 1997; Roots, 1997; Mair *et al.*, 2006).

All stratigraphic units of the region have been intruded by a post-deformation suite of granodiorite to quartz monzonite related to the Early to Late Cretaceous-age Tombstone Plutonic Suite. Medium-grained granodiorite of the Roop Lakes stock is located 20 km to the east and has a U-Pb titanite age of 92.8 ± 0.5 Ma (Roots, 1997). Intrusions of the ca. 63 – 69 Ma McQuesten Suite are also recognized in the region, where their emplacement locally exploited the existing structural weakness in the axis of the McQuesten antiform (Murphy, 1997).

The Elsa-Keno mining camp has been a major worldwide producer of silver from a series of sulphide-rich veins or vein-faults forming in dilational zones along east-northeast-striking, southeast-dipping, sinistral-oblique normal faults. Productive veins occur dominantly within the Keno Hill Quartzite, and to a lesser extent, in the underlying 'lower schist', although the host structures do extend up across the Robert Service thrust and into the structurally overlying Yusezyu Formation. Principal ore minerals include galena, sphalerite and tetrahedrite with

siderite and/or quartz as gangue material (Boyle, 1965). Cross-oriented vein faults, roughly perpendicular to the dominant structures, offset the mineralized structures (Boyle, 1965).

PROPERTY GEOLOGY

The southern slope of Galena Hill in the Eagle project area is underlain by the west-northwest-striking, moderate south-southwest-dipping structural succession of isoclinally folded/imbricated and unaltered to strongly altered Keno Hill Quartzite, the 'metavolcanic member' and Yusezyu Formation. The Keno Hill Quartzite is exposed only in the most northeastern part of the project area (Fig. 4). The surface traces of the contacts with the Yusezyu Formation trend west-northwesterly across the gentle upper slopes of Galena Hill to the north.

The Keno Hill Quartzite is generally siliceous and has a variable thickness of 1-20 m. The unit is tan to pale grey, massive to laminated quartzite and medium to dark grey graphitic quartzite with centimetre to metre-scale, schistose graphitic partings, seams and interbeds. The Yusezyu Formation is a variable package of 1 to 10 m-thick horizons of grey schistose graphitic quartzite, dark grey graphitic schist, phyllitic schist and minor brown biotite schist, and pale grey marble. Green to pale green chlorite \pm sericite \pm talc schist of the 'metavolcanic member' occurs interspersed throughout all rock types within the zone between Keno Hill Quartzite and Yusezyu Formation.

Metagabbro lenses are intercalated with the Keno Hill Quartzite and the 'upper schist' contact zone where they vary from 0.5 m to 30 m in thickness and occur as competent green, variably foliated, sill-like bodies. They are calcareous, host trace amounts of chalcopyrite and commonly exhibit feldspar porphyry textures; the composition of these sill-like bodies are best described as foliated amphibolite (Boyle, 1965; Le Couteur, 2009). Greenstone units observed in the project area vary from weakly to intensely foliated and are characterized by pervasive chloritization, sausseritization and silicification.

Fine-grained, unfoliated grey-white, equigranular albite-quartz-muscovite-bearing aplitic dykes or sills were mapped just off the property to the southeast on Duncan Creek and in drill core (D09-EF-05) along the trace of the Fisher Creek fault on the Fisher property (Figs. 3, 4). Both localities were sampled for U-Pb geochronology.

The Eagle Vein trends 057°/60° southeast and has been traced laterally in outcrop and drillholes for up to 900 m along a southwest trend from the east boundary of the project area, as well as down dip for over 500 m (Fig. 4).

The McLeod-Fisher fault is a major structure that extends west-southwest from the Galkeno Mine, before arcing to the south into the Eagle project area along the trace of Fisher Creek (Fig. 4). Boyle (1957) shows that the McLeod fault, which is considered to post-date the Robert Service thrust, is a continuation of the McLeod Vein (azimuth 025°/60° southeast) at the Galkeno Mine. The McLeod-Fisher fault dips southeast to east-southeast and exhibits apparent left-lateral movement that structurally isolates the project area from the prolific silver-rich veins on the north slopes of Galena Hill. Additionally, the McLeod-Fisher fault is coincident with linear topographic features and linear aeromagnetic features interpreted from 2008 airborne total magnetics and magnetic tilt derivative survey plots completed by CMG Airborne (Figs. 3, 4). A second coincident topographic and geophysical lineament extends northwesterly from the headwaters of Duncan Creek, along the west tributary of Fisher Creek and over Galena Hill to align with the right-lateral Brefalt Creek cross-fault in the area of the Elsa Mine (Fig. 2). Right-lateral offsets in geology suggest that a similar north-trending, west-dipping structure extends north through the headwaters of Hinton Creek.

GEOCHEMICAL AND GEOPHYSICAL SURVEYS

Geochemical soil surveys completed in 2006 and 2008 by Mega Precious repeated historic surveys and delineated Pb-Zn-Ag-As anomalies that parallel the Eagle Vein system and the McLeod-Fisher fault (Figs. 4, 5). A 2008 geochemical soil survey on the Spiderman property defined a 450 m Ag-Pb-Zn anomaly extending east along strike from the Eagle Vein (Pb = 56 ppm and 4036 ppm). A second, east-trending, lower threshold (56 ppm to 122 ppm Pb) soil anomaly was also identified down slope to the south. Drilling in 2009 confirmed the presence of the Eagle vein-fault extending to the northeast, and also suggested that the source of the second anomaly to the south is associated with weakly mineralized chloritic schist and/or gabbro sill at approximately 100 m depth in the hangingwall to the Eagle Vein.

A 610 line-km airborne magnetic survey was completed for the entire Eagle Silver project area during 2008

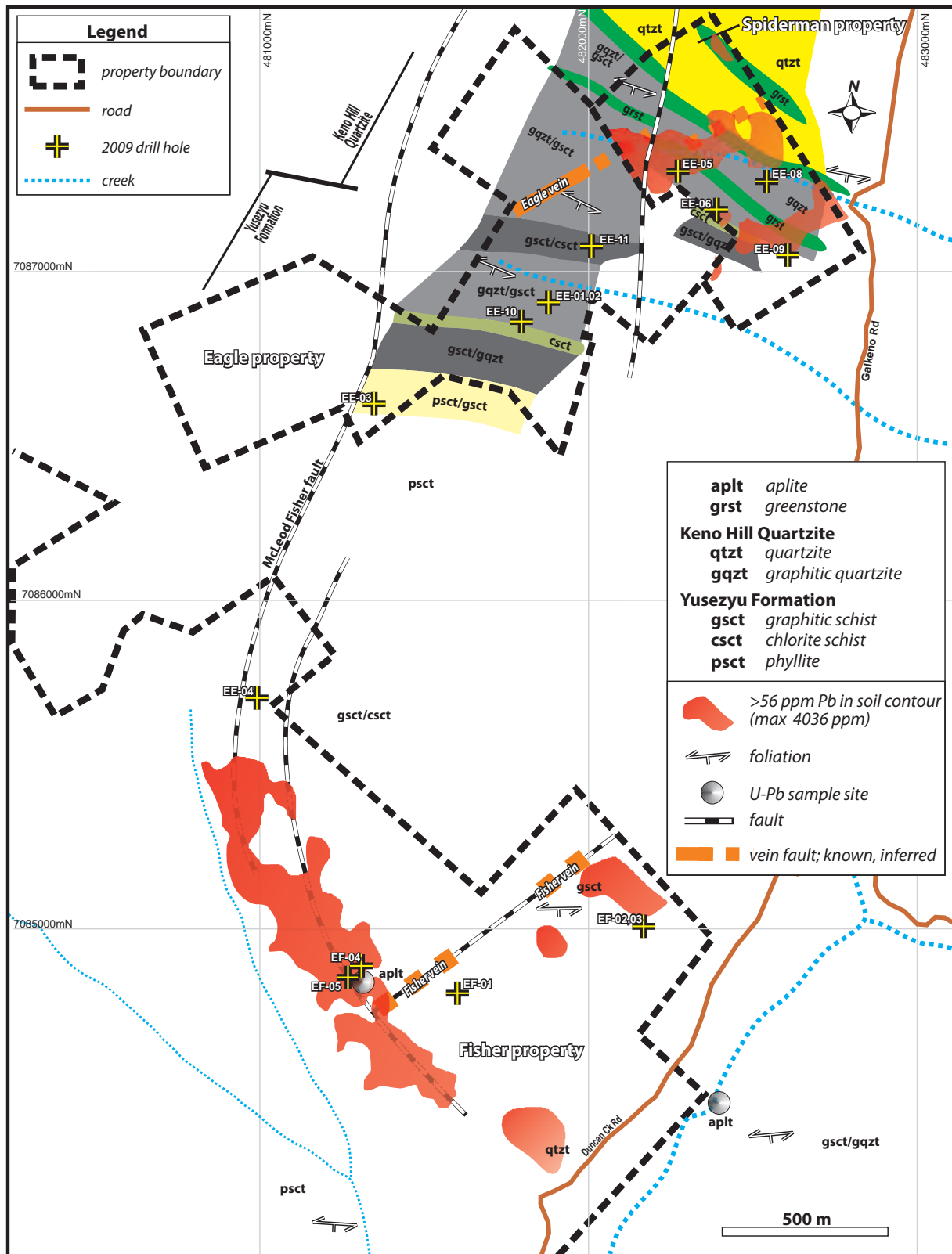
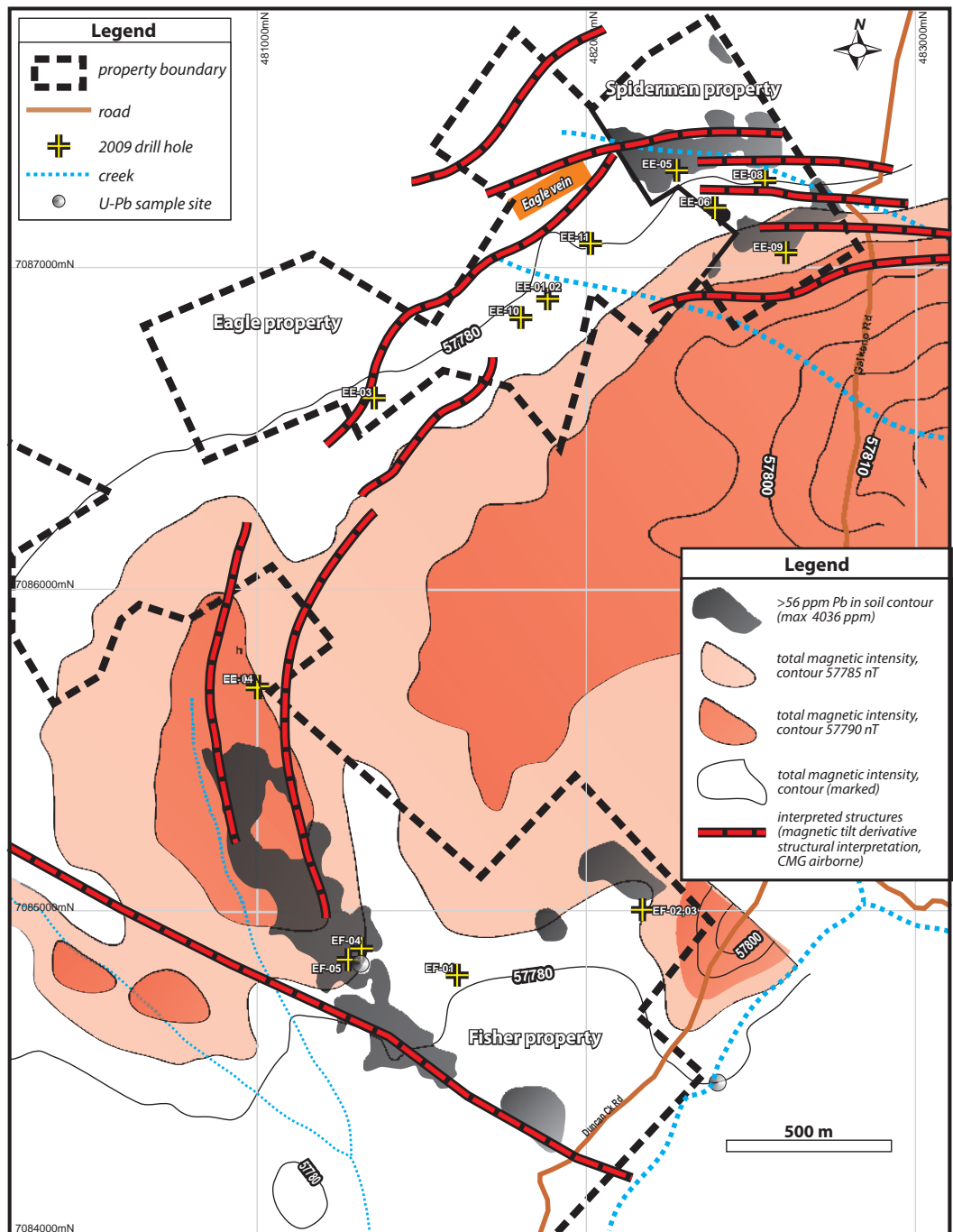


Figure 4. Property-scale geological map for the Eagle project. The Eagle and Fisher veins, Pb-soil geochemical anomalies (>56 ppm) and U-Pb geochronology sample locations are marked.

Figure 5. Integrated Pb-soil geochemistry, simplified total magnetic field data and interpreted structures for the Eagle, Spiderman and parts of the Fisher properties. Surface projection of Eagle Vein and U-Pb geochronology samples are indicated.



(Figs. 2b, 3, 5). Although resolution of the total field magnetic intensity anomaly is low (57707 to 57820 nT, TMI), the data indicate the presence of a west-southwest-trending, low-amplitude, elongate anomaly located immediately south of the Eagle Vein that may represent a buried intrusion. An arcing magnetic low extending through the main body of the anomaly is roughly coincident with the northward trend of the McLeod-Fisher

linear, suggestive of magnetic destruction along a fault system. Linear features identified from magnetic tilt derivative analysis of the data suggest a number of arcuate structures that could be related to the interpreted buried intrusion (Scriven, 2008; Fig. 5).

MINERALIZATION

GENERAL OBSERVATIONS AND VEIN MORPHOLOGIES

The Eagle Vein represents the most significant mineral occurrence within the Eagle project area, with minor mineralization occurring within the Fisher fault zone. The Eagle occurrence is described by Boyle (1965) as being composed of two ladder vein-fault structures mineralized with siderite, quartz, massive pyrite, galena, sphalerite, arsenopyrite, freibergite, limonite and manganese oxides. Recent work confirms this, although no freibergite was observed, and the mineralogy is dominated by sphalerite-pyrite-marcasite. A variety of vein styles have been observed at Eagle (Fig. 6) and, apart from the sphalerite-dominant mineralogy, are generally consistent with classifications described by Watson (1986), including:

- i. simple veins (D09-EE-07 and trench exposures) consisting of discontinuous bands and lenses of sulphides, with minor wall-rock brecciation present (Fig. 6a and b);
- ii. breccia zones of matrix-supported (siderite-quartz-sulphide), angular to rounded quartzite breccia (D09-EE-02; Fig. 6c);
- iii. sheeted zones of large angular blocks of country rock with gouge zones of siderite and massive sulphides (D09-EE-01 and -11);
- iv. greenstone-hosted, narrow irregular veins of siderite and sphalerite occurring between parallel vein-faults (D09-EE-02, Fig. 6d);
- v. zones of sheeted, narrow siderite stringer veins sub-parallel to the main vein structure, occurring within the vein-fault hangingwall (D09-EE-01, -09 and -11); and
- vi. rare foliaform siderite-sphalerite-pyrite mineralization occurring subparallel to parallel to the main foliation plane within the schistose host rocks (Fig. 6e).

ORE MINERAL PARAGENESIS

Boyle (1965) outlines three principal paragenetic stages of ore mineralization associated with the formation of the Keno Hill Ag-Pb-Zn veins, including:

Stage 1: small quartz-carbonate stringers;

Stage 2: camp-wide quartz-pyrite-arsenopyrite-gold lenses developed in vein-faults; and

Stage 3: extensive series of vein-faults mineralized with siderite-pyrite-sphalerite-galena-freibergite lodes and minor quartz.

Macroscopic and petrographic observations (LeCoutour, 2009) of important mineralized vein intercepts from the Eagle Vein are broadly consistent with Boyle's (1965) sequence of silver and base-metal mineralization; however, mineralization occurring within the Eagle Vein is unique due to the ubiquitous breakdown of Stages 1 – 3 mineralization and subsequent replacement by prismatic pyrite-arsenopyrite-pyrrhotite, which is locally enriched in Au. Three main stages of mineralization are recognized for the Eagle Vein ore, including:

- (i) early Au-enriched pyrite-marcasite ± sphalerite ± cassiterite ± arsenopyrite phase associated with a quartz-siderite gangue (Fig. 7a; 339 g/t Au);
- (ii) intermediate Ag-enriched galena ± chalcopyrite-pyrite ± stannite mineralization which crosscuts early-phase sphalerite-siderite-marcasite and subsequently is crosscut by late-stage secondary siderite to cubic pyrite veining (Figs. 6, 7a-c); and
- (iii) late-stage, moderately Au-enriched pyrite ± arsenopyrite ± pyrrhotite ± cassiterite phase of mineralization that clearly overprints pre-existing Ag-Pb-Zn mineralization (Fig. 8).

INDIUM MINERALIZATION

Iron-rich sphalerite in the Eagle Vein is highly enriched in indium where it is intergrown within the crystal lattice of coarse-grained sphalerite, combining with copper to replace zinc. High-grade zinc intercepts assayed 13.06% Zn and 182.80 g/t In over 10.9 m (e.g., D09-EE-07, 210.5 to 221.4 m). No data are available from other veins in the region to suggest any zonation in indium levels of sphalerite; however, Boyle (1965) reports enrichment in indium in quartz-sericite schist in the camp. It is notable that the Eagle Vein occurs in the 'metavolcanic member' above the Keno Hill Quartzite where the sericite schists are particularly abundant.

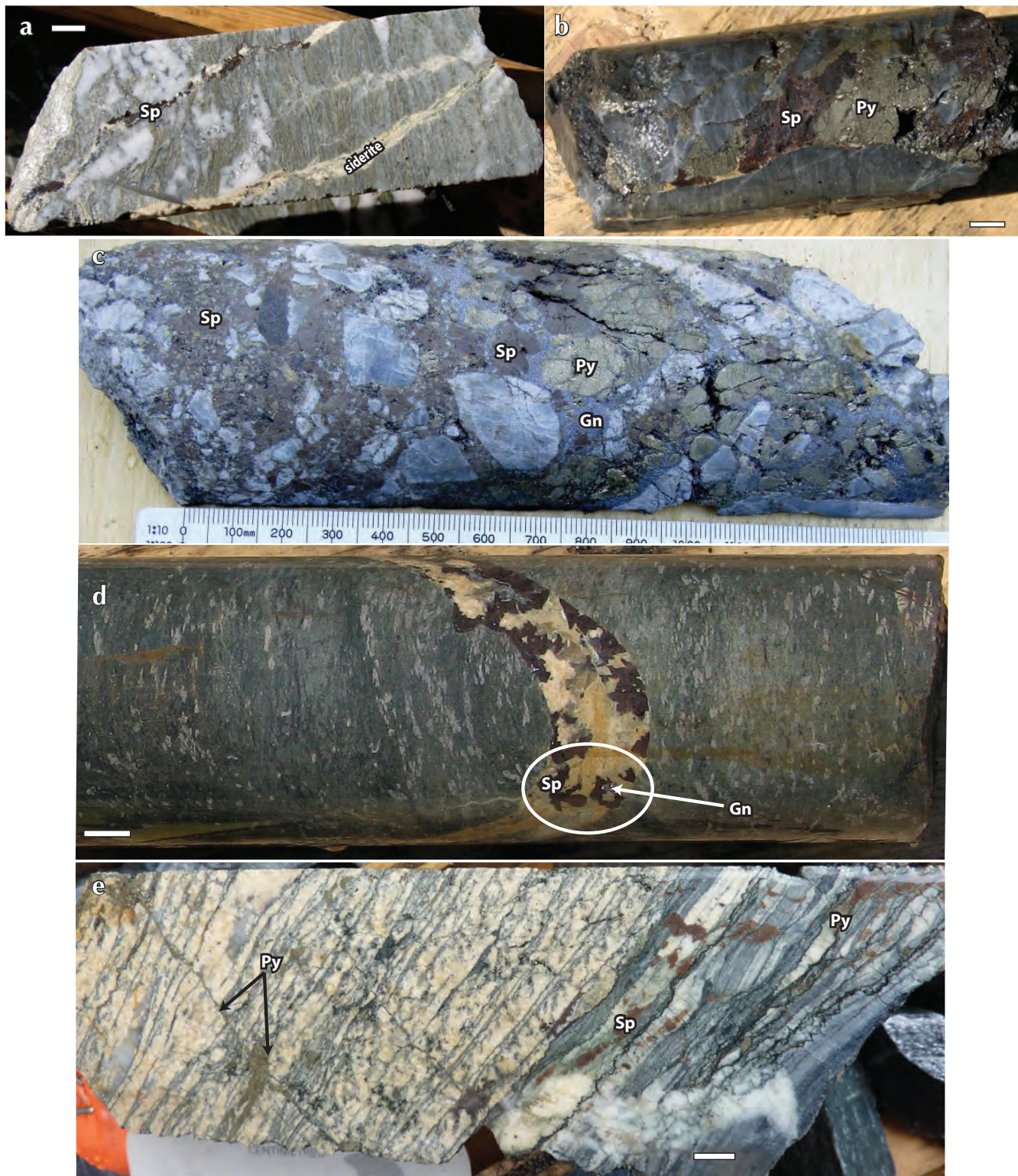


Figure 6. Representative styles of base-metal vein mineralization from the Eagle and Fischer veins: **(a)** siderite-sphalerite vein crosscutting sericite-chlorite schist (D09-EE-01); **(b)** sphalerite-pyrite vein crosscutting massive quartzite (D09-EE-01); **(c)** sphalerite-galena-pyrite mineralization in breccia matrix, Fischer vein (D09-EE-02); **(d)** siderite-sphalerite ± galena vein crosscutting greenstone; and **(e)** foliaform siderite-sphalerite mineralization within quartz-sericite schist (D09-EE-03). Siderite-sphalerite mineralization crosscut by late, oblique pyrite vein. Sp = sphalerite, Gn = galena, Py = pyrite. Scale bars represent 1 cm.

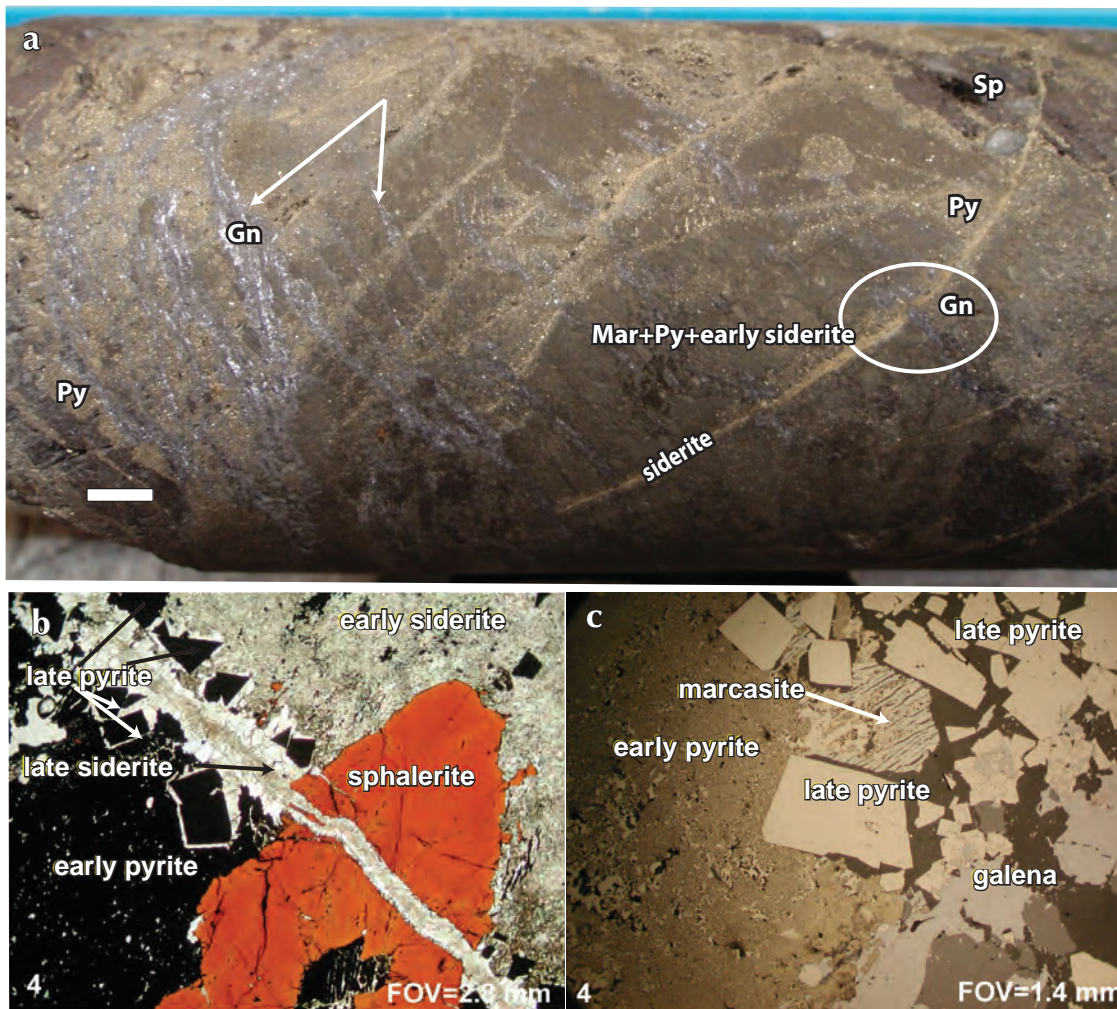


Figure 7. (a) Early-stage polymetallic mineralization, Eagle Vein (339 g/t Au from 273.3-273.7 m, D09-EE-02). Note: Galena veins are latest phase of mineralization present. Scale bar represents 1 cm. (b) Early-phase sphalerite + siderite overprinted by siderite + cubic pyrite. (c) Early-phase pyrite + marcasite overprinted by (i) cubic pyrite (\pm siderite 2) and (ii) latest stage galena. Photomicrographs from LeCoutour (2009). Sp = sphalerite, Gn = galena, Py = pyrite, Mar = marcasite.

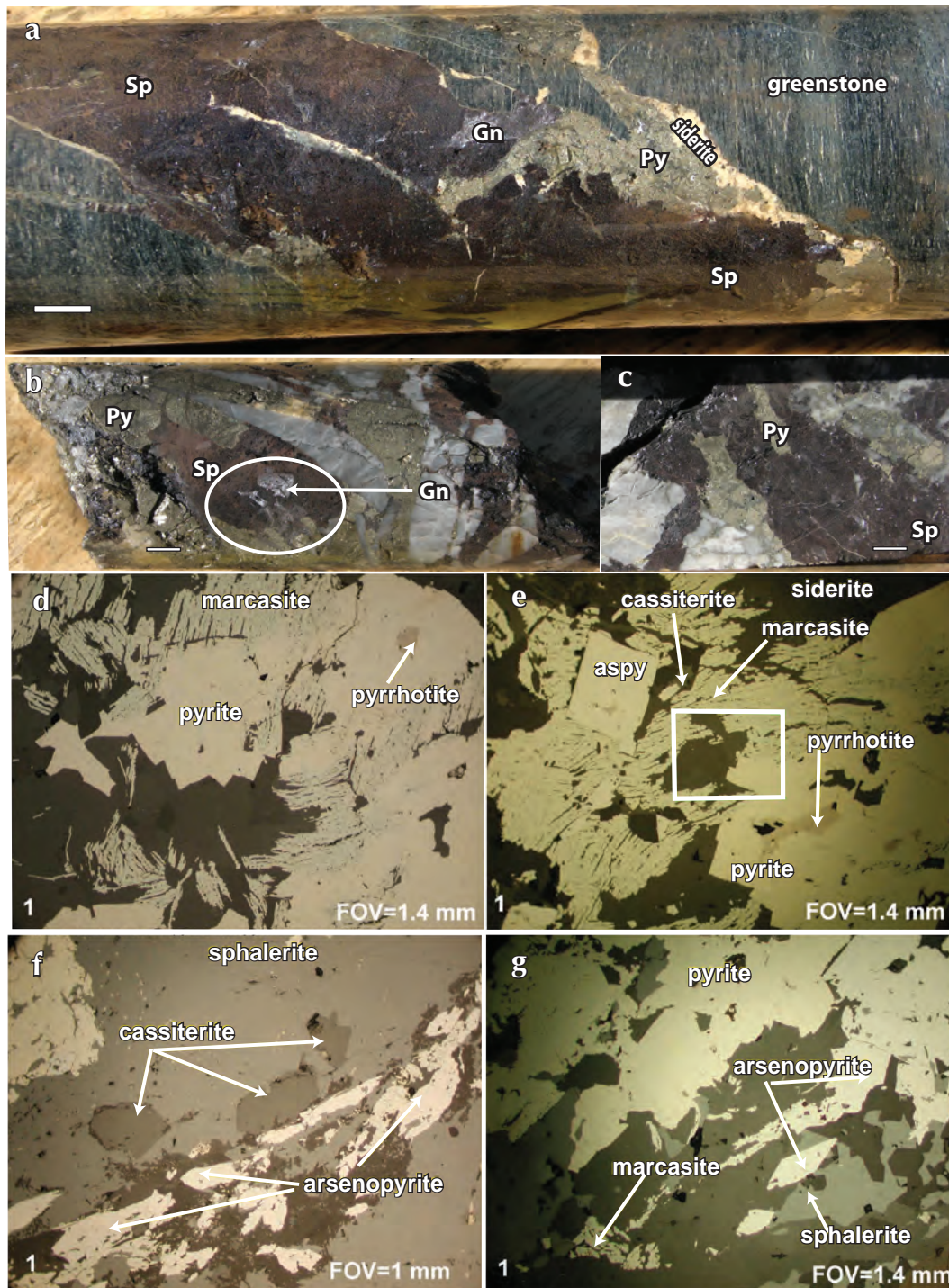


Figure 8. (a) Sphalerite-siderite \pm galena overprinted by pyrite in a vein crosscutting highly foliated greenstone, Eagle Vein (D09-EE-01); (b) sphalerite-galena infilling brecciated Keno Hill Quartzite and overprinted by late-stage pyrite, and (c) coarse-grained sphalerite replaced by secondary pyrite \pm pyrrhotite. Reflected-light photomicrographs of sulphide textures within D09-EE-01, Eagle Vein. Scale bars represent 1 cm. (d) Early-phase marcasite overprinted by cubic pyrite intergrown with pyrrhotite; (e) early-phase marcasite-siderite overprinted by secondary prismatic arsenopyrite-cassiterite and cubic pyrite intergrown with pyrrhotite; (f) early-phase sphalerite overprinted by arsenopyrite \pm cassiterite; and (g) late rhomboidal arsenopyrite-cubic pyrite overprinting early-phase marcasite intergrown with sphalerite. Photomicrographs from LeCoutour (2009). Field of view (FOV) marked. Sp = sphalerite, Gn = galena, Py = pyrite.

SKARN/REPLACEMENT MINERALIZATION

Late-stage arsenopyrite-pyrite-gold skarn/replacement mineralization was encountered at depth within the Eagle Vein system (Fig. 9; D09-EE-01). The host lithology is a strongly deformed, brown sericite schist that is replaced

by up to 45% coarse euhedral arsenopyrite and paramagnetic pyrite (Fig. 9b-d). The section assayed 1.23 g/t gold and was of interest as it was a new style of mineralization not encountered elsewhere on the property. Importantly, immediately above the

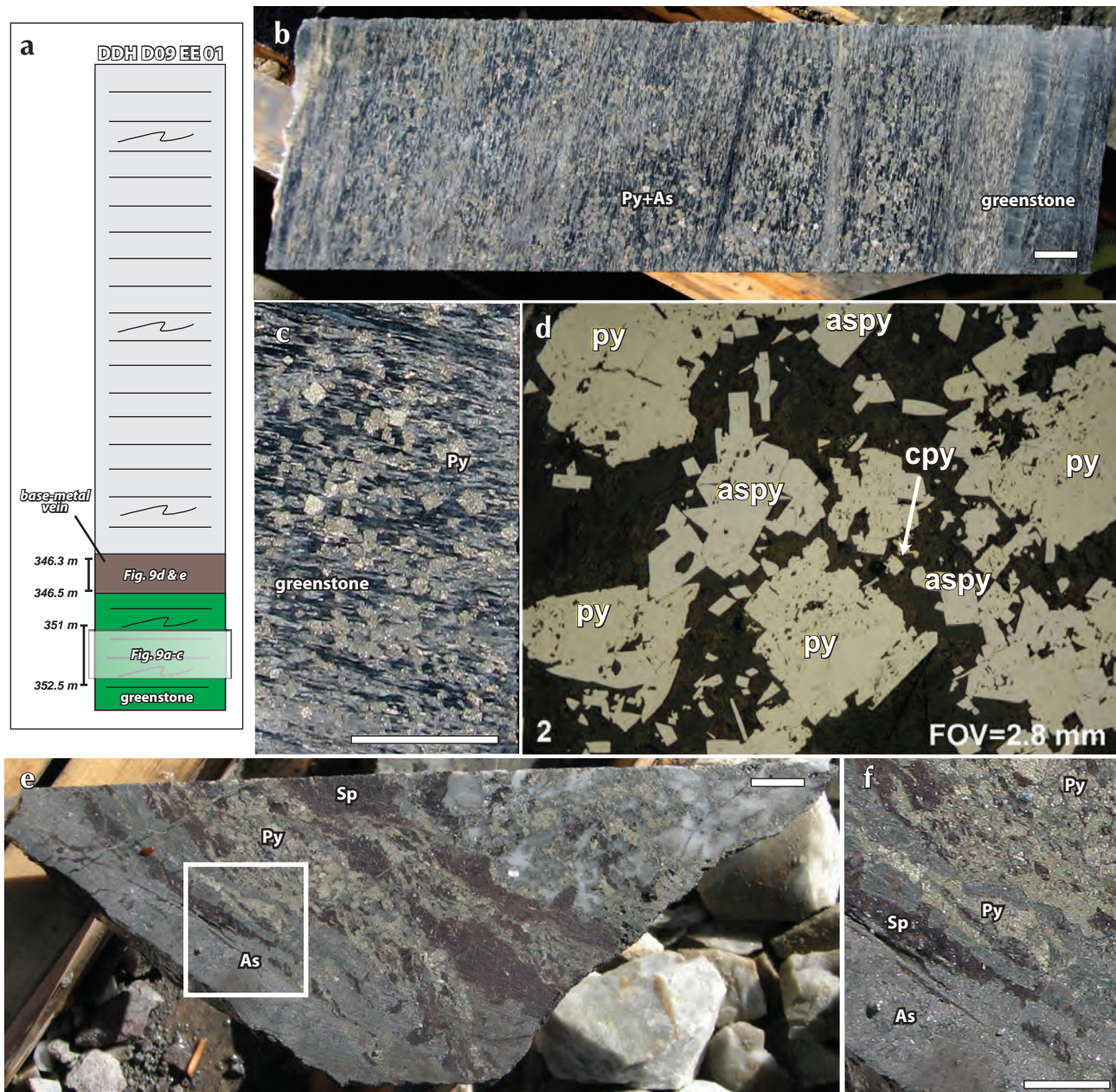


Figure 9. (a) Schematic diagram illustrating mineralization at lower levels of D09-EE-01, 346.3 m to 352.5 m; (b) and (c) late post-deformational skarn/replacement-style mineralization overprinting highly foliated greenstone (1.2 g/t Au and 3841 ppm As; 351-352.5 m, D09-EE-01). (d) Reflected-light photomicrograph of gold-bearing late pyrite-arsenopyrite overprinting greenstone; field of view (FOV) marked; photomicrograph from LeCoutour (2009); (e) and (f) base-metal vein immediately overlying skarn/replacement pyrite-arsenopyrite mineralized zone. Early-phase sphalerite overprinted by pyrite and arsenopyrite (0.99 g/t gold and 6684 ppm As; 346.3-349.9 m, D09-EE-01). Scale bars represent 1 cm. Asp = arsenopyrite, Sp = sphalerite, Py = pyrite.

replacement-style mineralized zone, more typical Ag-Pb-Zn mineralized veining occurred, which was characterized by early-phase sphalerite-siderite mineralization which is partially to completely replaced by pyrite-arsenopyrite (Fig. 9a, e and f). Assay results from this interval show elevations in Au and As, similar to the underlying replacement/skarn mineralized horizon, suggesting a genetic link between the Au-As mineralization in both horizons. The overprinting relationships are significant as they imply that the low-grade Au-As replacement/skarn-like mineralization, which is more typical of Tombstone intrusion-related Au-forming events in the region (e.g., Gold Dome), overprints the Keno Hill Ag-Pb-Zn mineralizing event, which itself post-dates an early-stage strongly Au-enriched mineralizing episode.

GEOCHRONOLOGY

Two aplite dykes were located within the Eagle project area during surface mapping along Duncan Creek and drilling of the Fisher Vein. Both dykes were sampled for U-Pb dating to constrain the age of magmatism occurring within the Eagle Silver project area. Data collection using Laser Ablation Microprobe Inductively Coupled Plasma Mass Spectrometry (LAM ICP-MS) techniques was completed in the Earth Sciences Department and the INCO Innovation Centre at Memorial University, St. Johns, Newfoundland. A detailed outline of the methodology is given in Bennett and Tubrett (this volume). Due to the prevalence of xenocrystic zircon within each of the dyke's zircon populations, an inherited zircon study was also completed for each sample. Analytical techniques to characterize the zircon populations included standard optical microscopy and backscattered electron (BSE) imaging and cathodoluminescence (CL) image analysis in order to permit greater understanding of zircon zoning and growth history. Image analysis was completed on all zircon grains selected ($n = 20 - 80$ depending on yield). Field relationships and zircon zonation styles are briefly described for each sample before reporting the U-Pb isotopic results. Final interpreted crystallization ages are based on calculation of concordia ages from individual U-Pb isotopic analyses that have a probability of concordance greater than 0.20 (see Bennett and Tubrett, this volume for more information on data treatment). Weighted-mean $^{206}\text{Pb}/^{238}\text{U}$ ages are also reported to remain consistent with current U-Pb geochronology reporting trends. Uncertainties reported for all calculated ages and plotted on associated concordia and weighted

mean diagrams are at the 2σ uncertainty level, unless stated otherwise. Final age calculations include U decay-constant uncertainties which are plotted graphically on concordia plots. Concordia and weighted mean $^{206}\text{Pb}/^{238}\text{U}$ ages were calculated as per Ludwig (1999). The concordia age that includes U decay-constant uncertainties is considered the best estimate of the crystallization age of a sample. Where a concordia age has a mean square of weighted deviates (MSWD) >1.5 , the weighted mean $^{206}\text{Pb}/^{238}\text{U}$ age is considered the best estimate of the crystallization age. Magmatic rims were analysed using a $10\ \mu\text{m}$ -diameter line raster. All inherited zircon analyses were completed using the standard $40 \times 40\ \mu\text{m}$ box raster (see Bennett and Tubrett, this volume). Uranium and Th concentration data and Th/U ratios were also calculated for each sample and are reported in Appendices 1 - 4.

FISHER VEIN APLITE (D09-EF-05)

During drill testing of the Fisher fault zone, an $\sim 3\ \text{m}$ (apparent width) aplitic dyke with brecciated upper and lower contacts was intersected from 36.0 m to 39.3 m depth in D09-EF-05 (Fig. 10a). The aplitic dyke has a fine-grained, saccharoidal texture and consists of subequal amounts of quartz and feldspar and approximately 20% - 25% biotite and muscovite. Weak to moderate chlorite-epidote alteration is pervasive throughout the intrusive unit where intersected in D09-EF-05.

Approximately 55 zircon grains of poor to moderate quality were liberated from the aplitic dyke sampled from the Fisher fault zone (Fig. 10c). Inherited zircon, in the form of both visible cores and grains with widely varying optical features (e.g., grain shape, colour and inclusions), makes up the majority of zircons present in this sample. The grains selected for analysis were grossly subdivided into: (i) subrounded to rounded zircons varying from dark pink turbid grains to translucent, inclusion-free grains; and, (ii) elongate, sub-prismatic grains with thin, inclusion-free, translucent rims. One prismatic and translucent needle fragment was also identified and selected for analysis.

Backscattered electron (BSE) and cathodoluminescence (CL) image analyses were completed on all zircon grains sampled. Representative images are given in Figure 11. Image analysis supports the initial interpretation based on optical criteria that the greater majority of zircons represent an inherited population. No single uniform zonation style was recognized amongst the inherited grains suggesting multiple sources for the inherited zircon (Fig. 10b). Importantly, four zircon rims were

characterized by very bright BSE and CL responses, suggestive of high U and/or Hf concentrations (Fig. 11a). Where rim development was more significant, oscillatory zoning is observed (Fig. 11a-iii). Similarity of BSE/CL responses of these rims and occurrences of rim oscillatory zoning (where better developed) suggests that new magmatic zircon growth associated with the aplitic magma was restricted to rim development on favourable inherited nuclei.

Four analyses were collected from the rims described above (Appendix 1). A concordia age calculated from these rim analyses yielded an age of 93.6 ± 1.4 Ma (MSWD = 2.7) and a weighted mean $^{206}\text{Pb}/^{238}\text{U}$ age of 93.3 ± 1.4 Ma (MSWD = 0.78; Fig. 12a and b). Concentration data calculated from magmatic rim analyses ranges from 3243 ppm to 4874 ppm U and 85 ppm to 131 ppm Th (Appendix 1) and demonstrates the U-rich nature of the magmatic rims. Twenty-two zircon cores were analysed to assess sources of inheritance

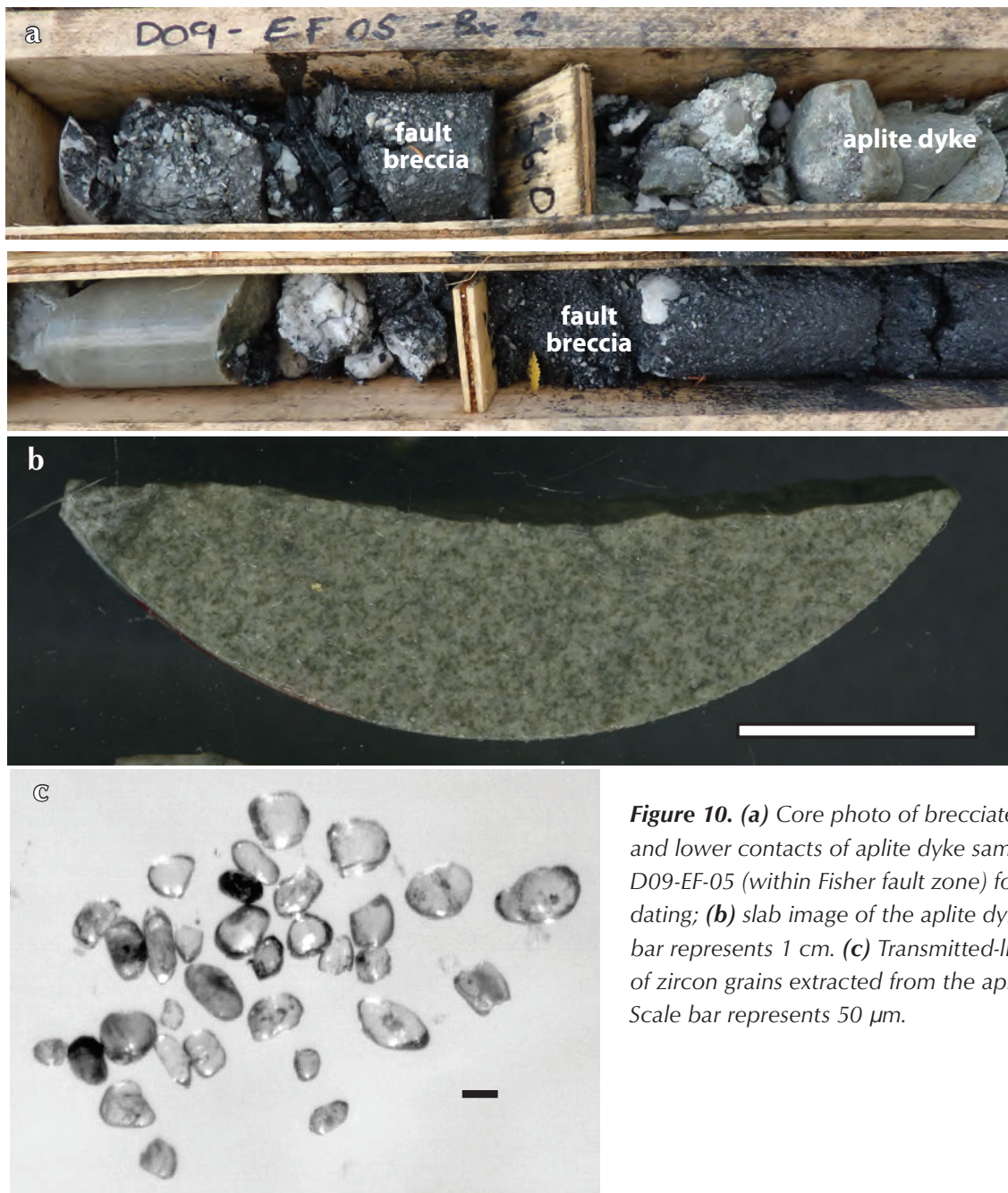


Figure 10. (a) Core photo of brecciated upper and lower contacts of aplite dyke sampled from D09-EF-05 (within Fisher fault zone) for U-Pb age dating; (b) slab image of the aplite dyke. Scale bar represents 1 cm. (c) Transmitted-light images of zircon grains extracted from the aplite dyke. Scale bar represents 50 μm.

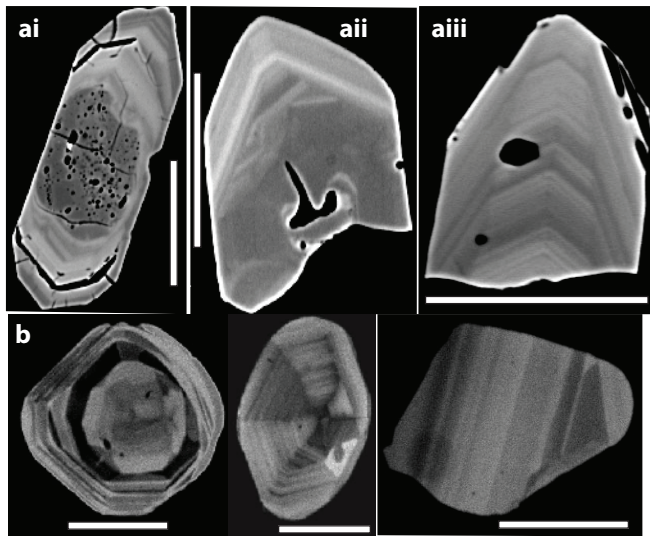


Figure 11. (a) BSE images of magmatic zircon extracted from aplite dyke sampled from D09-EF-05. Magmatic zircon occurs as overgrowths on xenocrystic cores (11ai and aii) or as fine-grained needles or needle tips (11aiii); (b) CL images of inherited zircon grains. All scale bars represent 50 μm . BSE = backscattered electron, CL = cathodoluminescence.

within the aplite sample (Appendix 2). Several inherited populations are recognized in the sample, which range in age from ca. 405 Ma to 2805 Ma within important Mesoproterozoic (ca. 1000 Ma, 1255 Ma, 1380 Ma, 1410 Ma and 1580 Ma), Paleoproterozoic (1720 Ma, 1750 Ma, 1905 Ma, 1955 Ma and 2005 Ma) and Neoproterozoic (2555 Ma, 2660 Ma and 2805 Ma; Figs. 12c and 13a). Th/U ratios calculated for all analyses clearly illustrate the difference between magmatic and inherited zircon chemistry (Fig. 13b).

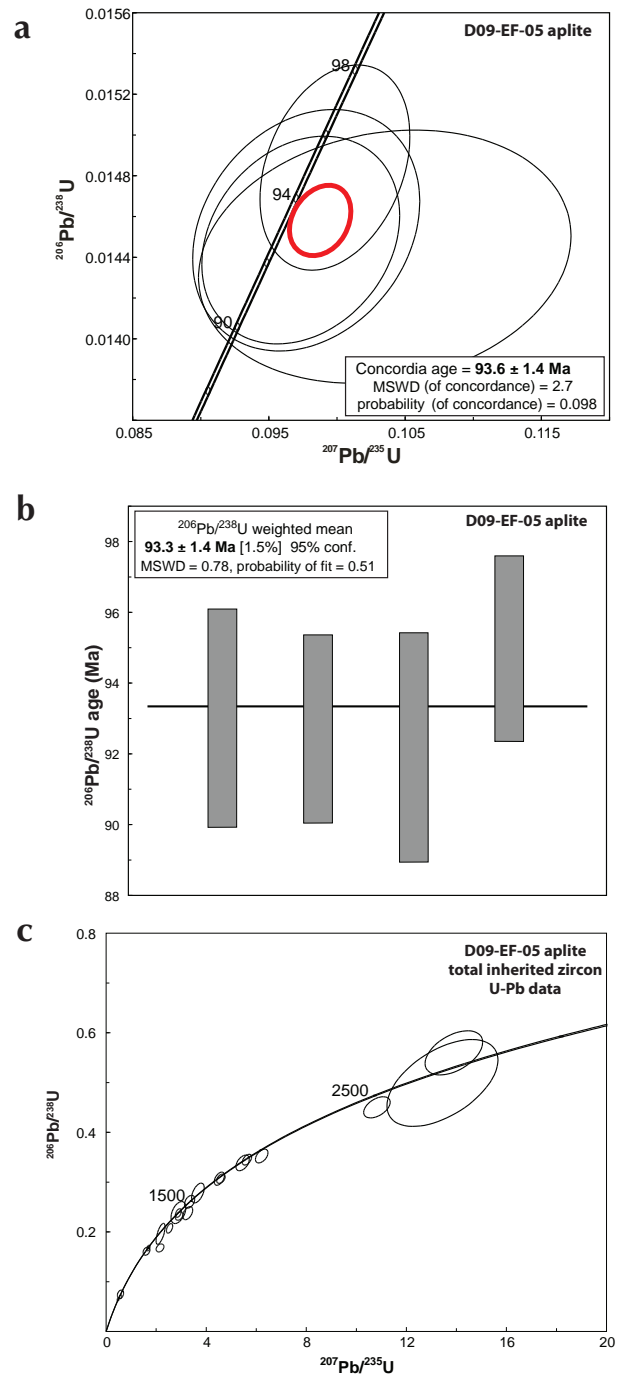


Figure 12. (a) Concordia diagram for U-Pb LAM ICP-MS analyses of magmatic zircon from aplite dyke, D09-EF-05. (b) Plot of weighted mean $^{206}\text{Pb}/^{238}\text{U}$ ages of magmatic zircon from aplite dyke, D09-EF-05. (c) Concordia diagram for U-Pb LAM ICP-MS analyses of inherited zircon from aplite dyke, D09-EF-05. Notes: 1. On all diagrams MSWD = mean square of the weighted deviates. 2. On all U-Pb concordia diagrams, data point error ellipses represent 2σ error and 2σ uranium decay constant errors are included in final age calculation. 3. On all weighted mean $^{206}\text{Pb}/^{238}\text{U}$ diagrams, box heights represent 2σ .

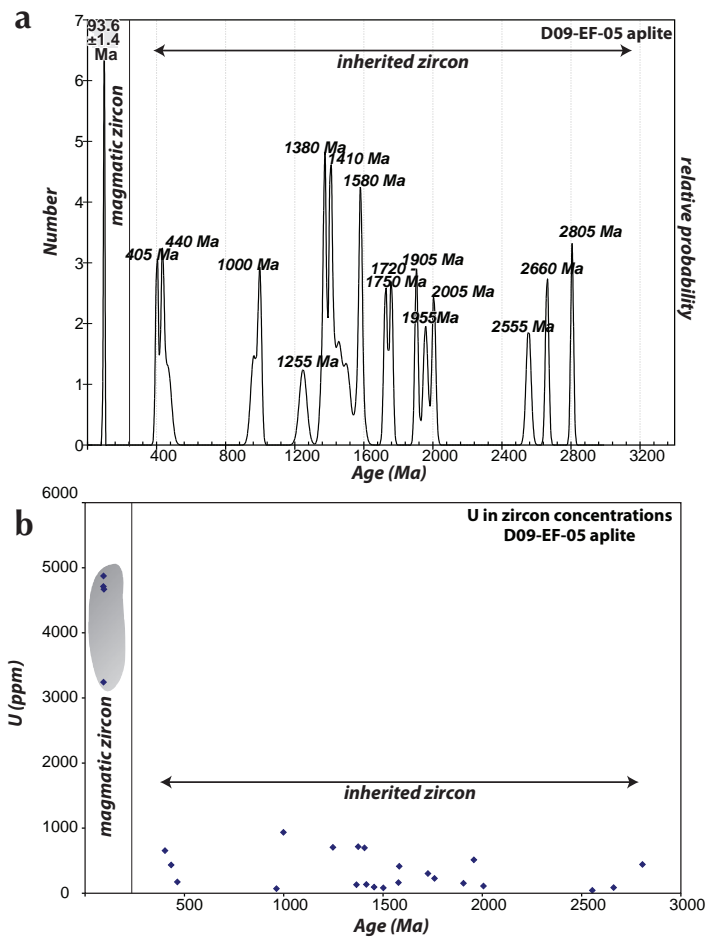


Figure 13. (a) Cumulative probability diagram illustrating the distribution of inherited zircon populations in aplite dyke sampled from D09-EF-05. Crystallization age plotted for reference. (b) U concentration vs. age for all zircon populations within the aplite dyke. Magmatic zircon is distinctive in high U concentrations when compared to the inherited populations (≤ 1000 ppm).

DUNCAN CREEK APLITE

A second aplitic dyke of similar texture and mineralogy to that observed in D09-EF-05 was mapped at surface on the northeast side of Duncan Creek where it intrudes graphitic schist and laminated quartzite of the 'upper schist' (482495E 7084445N; Figs. 3-5; Fig. 14a and b). The dyke is approximately east-trending and dips south, and is concordant to locally discordant to the prevailing foliation within the host 'upper schist'.

The sample yielded abundant zircons of highly variable quality which appeared similar in appearance to zircon populations in the aplitic dyke sampled from the Fisher fault zone. A greater zircon yield allowed for improved optical subdivision of the zircon populations into three main populations including: (i) irregular grains with core and rim zircon growth; (ii) subrounded to sub-prismatic zircon varying from dark pink turbid grains to translucent, inclusion-free grains; and (iii) a minor population of translucent, prismatic needles (Figs. 14c - e).

Backscattered electron and CL imaging of zircons selected from all three populations indicates that inherited zircon populations dominate (Fig. 15), as was the case for the aplite dyke sampled within the Fisher fault zone. Magmatic zircon occurs as bright BSE/CL rims, and more rarely as oscillatory zoned needles (Fig. 15a).

Eleven analyses were collected from rims and needles described above (Appendix 3). A concordia age calculated from magmatic zircon yielded an age of 93.6 ± 0.9 Ma (MSWD = 0.34) and a weighted mean $^{206}\text{Pb}/^{238}\text{U}$ age of 93.5 ± 1.2 Ma (MSWD = 1.3; Fig. 16a,b). These ages are virtually identical to those determined for the aplite dyke occurring within the Fisher fault zone. Concentration data calculated from magmatic zircon vary from 612 ppm to 8502 ppm U and 54 ppm to 1248 ppm Th (Appendix 3). Forty-two zircon cores were analysed to assess sources of inheritance within the aplite sample (Fig. 16c; Appendix 4). Inherited populations range in age from ca. 265 Ma to 2660 Ma. Four concordant points for the youngest inherited zircon population yield a concordia age of 266 ± 3.8 Ma (MSWD = 0.65; Fig. 16d). Other inherited ages in the Duncan Creek aplite are similar to those determined for the Fisher fault aplite. Important inherited populations are Silurian (ca. 430 Ma), Mesoproterozoic (ca. 1010 Ma, 1160 Ma and 1350 Ma), Paleoproterozoic (1630 Ma, 1700 Ma, 1760 Ma, 1870 Ma and 1920 Ma) and Neoproterozoic (2640 Ma and 2660 Ma; Figs. 16c and 17a). Th/U ratios calculated for all analyses illustrate the difference between magmatic and inherited zircon chemistry (Fig. 17b).



Figure 14. (a) U-Pb sampling locality for Duncan Creek aplite; (b) slab image of Duncan Creek aplite sampled for U-Pb analysis; transmitted-light images of (c) overgrowth zircon population; (d) rounded and milled, light to dark pink zircon population; and (e) zircon needle population. Scale bars represent 50 μm .

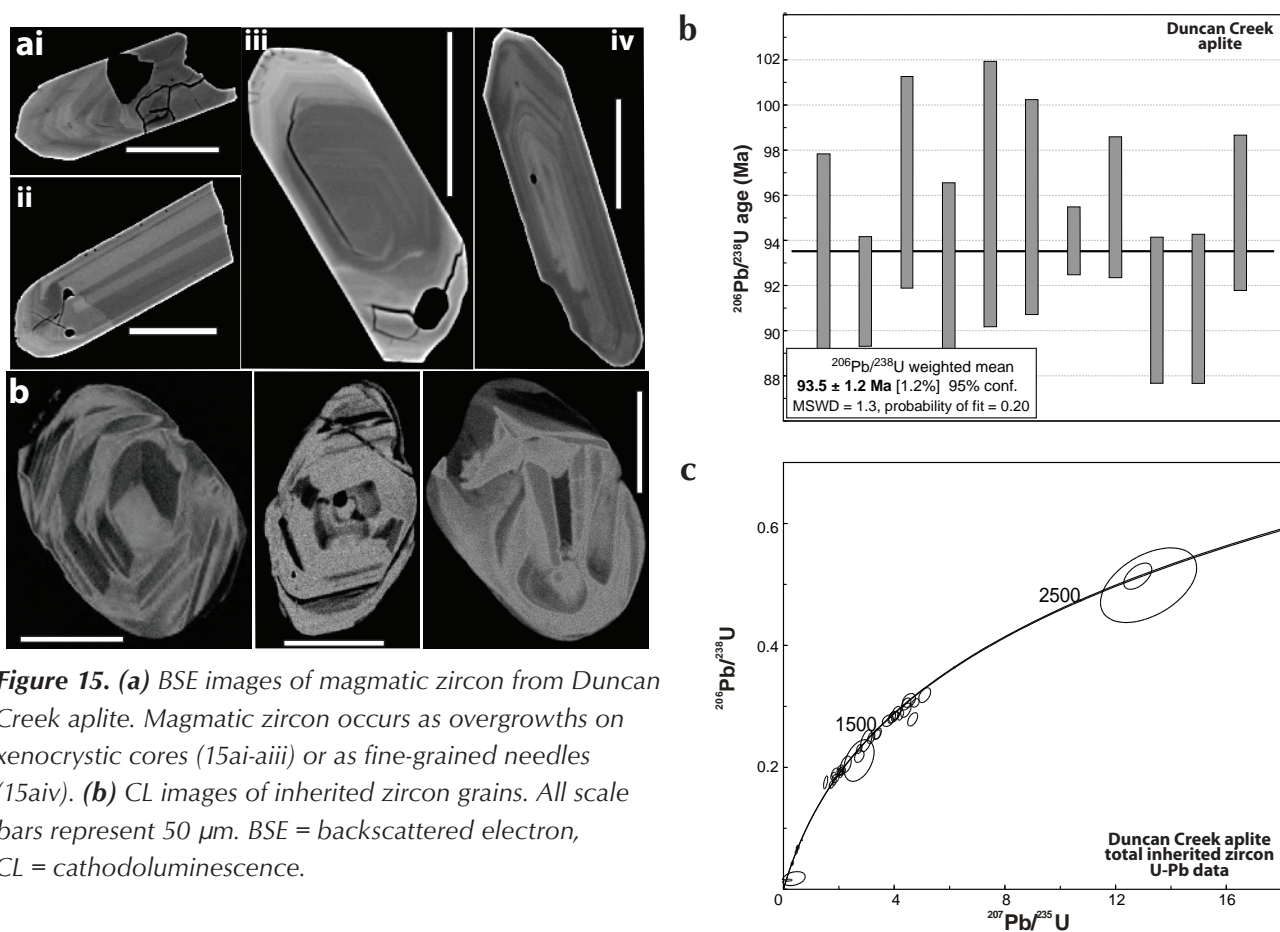


Figure 15. (a) BSE images of magmatic zircon from Duncan Creek aplite. Magmatic zircon occurs as overgrowths on xenocrystic cores (15ai-aiii) or as fine-grained needles (15aiv). (b) CL images of inherited zircon grains. All scale bars represent 50 μm. BSE = backscattered electron, CL = cathodoluminescence.

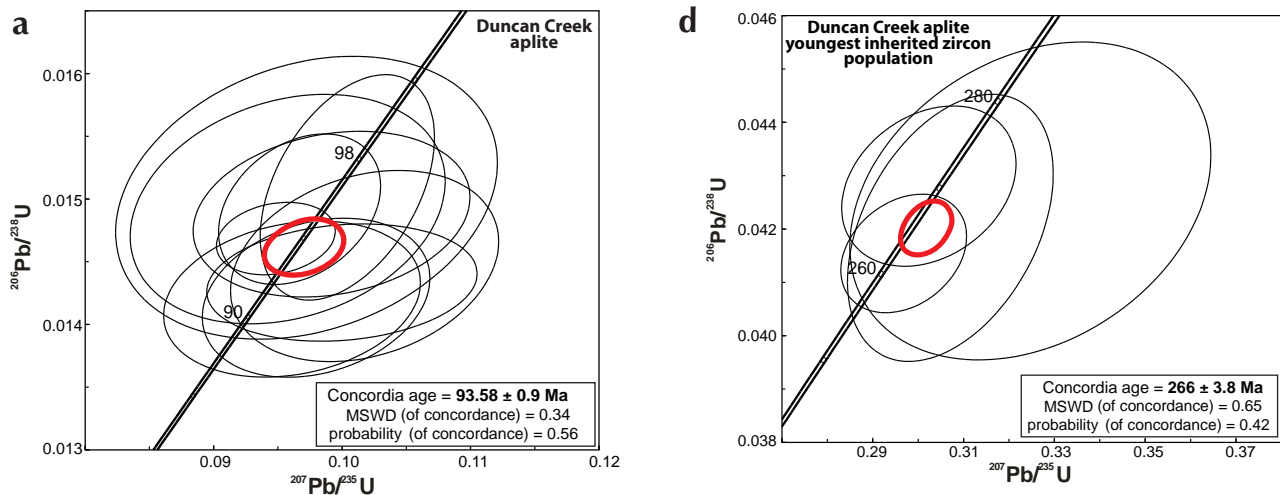


Figure 16. (a) Concordia diagram for U-Pb LAM ICP-MS analyses of magmatic zircon from Duncan Creek aplite. Individual analyses with probability of concordance less than 0.2 are not included in final data calculations. (b) Plot of weighted-mean $^{206}\text{Pb}/^{238}\text{U}$ ages with probability of concordance greater than 0.20. (c) Concordia diagram for U-Pb LAM ICP-MS analyses of inherited zircon from Duncan Creek aplite. (d) Concordia diagram for U-Pb LAM ICP-MS analyses of youngest inherited zircon population (ca. 266 Ma).

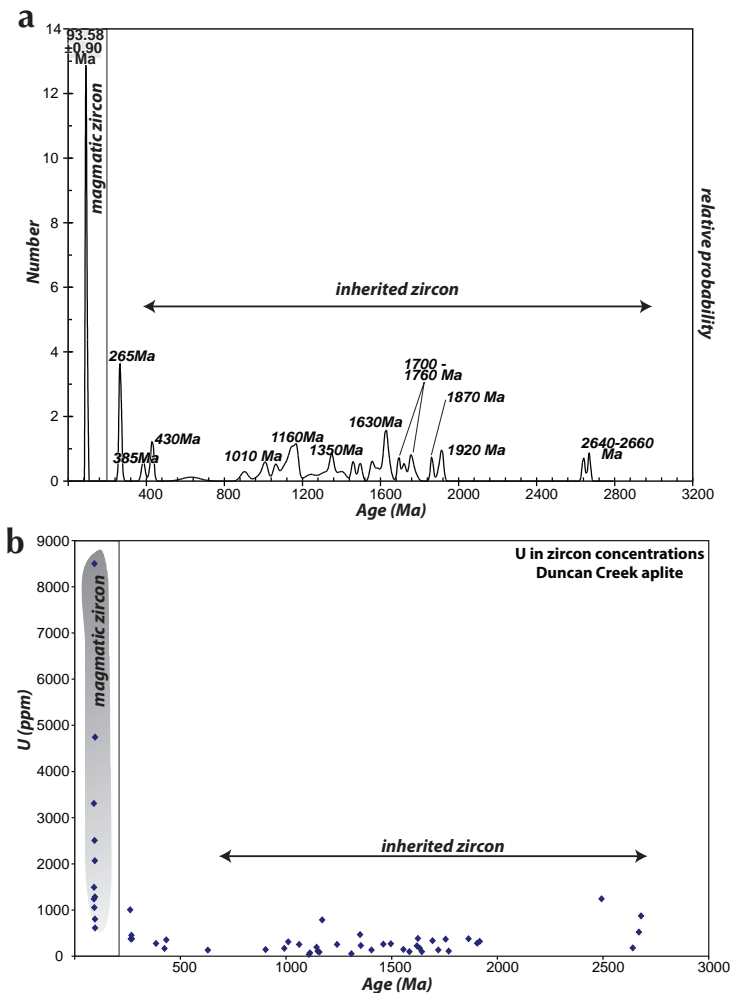


Figure 17. (a) Cumulative-probability diagram illustrating the age distribution of inherited zircon populations within Duncan Creek aplite. Crystallization age plotted for reference and comparison to youngest inherited population. (b) U concentration vs. age for all zircon populations from the Duncan Creek aplite. Magmatic zircon is distinctive in high U concentrations when compared to the inherited populations (<1000 ppm).

CONCLUSION

The integrated geological, geochemical, geophysical and geochronological datasets reported in this study for the Eagle Silver project highlight the presence of Tombstone-age intrusions and related structures that are more proximal to the Keno Hill silver veins than the Roop Lakes stock. Early-phase Ag-Pb-Zn mineralizing events recognized in the Eagle and Fisher veins are consistent with the polymetallic mineralization occurring in the historic adjacent veins and have an early bonanza-grade Au-enriched pyrite-marcasite-sphalerite \pm cassiterite \pm arsenopyrite phase associated with a quartz-siderite gangue (such as occurs at the Homestake occurrence); this phase of mineralization is overprinted by the more common sphalerite-galena-siderite veining. Petrographic evidence points to a complex paragenetic sequence during this intermediate stage of mineralization and also to the presence of at least two phases of siderite, pyrite and sphalerite mineralization. The prevalence of sphalerite over galena within the Eagle Vein may also directly reflect the elevated indium concentrations occurring within the Eagle Vein. The Eagle Vein is unique with respect to the occurrence of ubiquitous late-stage pyrite-pyrrhotite-arsenopyrite mineralization associated with low-grade gold concentrations, which occurs as replacement/skarn-like mineralization of weakly calcareous 'upper schist' host lithologies, and which also overprints earlier stage Ag-Pb-Zn mineralized veins. This style and grade of mineralization is more typical of Tombstone-age Au-As-W mineralization occurring elsewhere in the region (e.g., Gold Dome, Dublin Gulch). The presence of ca. 93 Ma aplite dykes that occur at the periphery of an elongate, low-amplitude aeromagnetic high at the southeast end of Galena Hill is unique in the Keno Hill silver camp. The geometry of the anomaly is suggestive of a large buried intrusion that is bounded by several arcuate fault structures, including the McLeod-Fisher fault.

Collectively, the coincidence of ca. 93 Ma Tombstone-age intrusive bodies, unique late-stage mineralization and overprinting, low-grade Au-As mineralization within Ag-Pb-Zn veins and vein-faults occurring at the margins of, or within the defined extents of, a large, low-amplitude total magnetic intensity anomaly, in addition to Au-As replacement/skarn-like mineralization occurring at depth within the Eagle Vein fault system, imply that Tombstone-age intrusions postdate the prolific Keno Hill Ag-Pb-Zn mineralizing event, at least within the confines of the Eagle Silver project area.

ACKNOWLEDGEMENTS

Thank you to Mike Padula of Victoria Gold Corporation, Avino Silver and Gold Mines Ltd. and Mega Precious Metals Inc. for funding assistance for the analytical work. We thank Pam King, Earth Sciences Department, Memorial University and Michael Tubrett and Michael Schaeffer for access and assistance in the MafIIC analytical facility. Thank you to Don Murphy who reviewed and improved an earlier draft of the manuscript.

REFERENCES

- Archer, A.R., 1979. Report on the recommended exploration, Keno Hill district. Internal report, Canada Tungsten Mining Corporation Ltd.
- Beaudoin, G. and Sangster, D.E., 1992. A descriptive model for silver-lead-zinc veins in clastic metasedimentary terranes. *Economic Geology*, vol. 87, p. 1005-1021.
- Becker, T.C., 2000. Assessment report describing prospecting, geological mapping, and soil geochemistry on the Fisher property. Assessment Report 09414, prepared for Expatriate Resources Ltd. by Archer, Cathro & Associates (1981) Ltd., 10 p.
- Bennett, V. and Tubrett, M., 2010 (this volume). U-Pb isotopic age dating by LAM ICP-MS, INCO Innovation Centre, Memorial University: Sample preparation methodology and analytical techniques. *In: Yukon Exploration and Geology 2009*, K.E. MacFarlane, L.H. Weston and L.R. Blackburn (eds.), Yukon Geological Survey, p.47-55.
- Bostock, H.S., 1947. Mayo, Yukon Territory. Geological Survey of Canada, Map 890A, scale 1:253,440.
- Boyle, R.W., 1957. Geology and Geochemistry of the Silver Lead Zinc Deposits of Galena Hill, Yukon Territory. Geological Survey of Canada, Paper 57-1.
- Boyle, R.W., 1965. Geology, geochemistry and origin of the lead-zinc-silver deposits of the Keno Hill-Galena Hill area, Yukon Territory. Geological Survey of Canada, Bulletin 111, 302 p.
- Boyle, R.W., 1979. The geochemistry of gold and its deposits. Geological Survey of Canada, Bulletin 280, 584 p.
- Boyle, R.W., Wanless, R.K. and Stevens, R.D., 1970. Sulfur isotope investigation of the lead-zinc-silver-cadmium deposits of the Keno Hill-Galena Hill area, Yukon, Canada. *Economic Geology*, vol. 65, p. 1-10.
- Carmichael, A.D., Jr., 1957. United Keno Hill Mines. *In: Structural Geology of Canadian Ore Deposits, Congress Volume*, G. Gilbert, (ed.), Canadian Institute of Mining and Metallurgy, Geology Division, p. 66-77.
- Cathro, R.J., 2006. Great mining camps of Canada: Announcing a new series. *Geoscience Canada*, vol. 33, no. 2, p. 56-59.
- Cockfield, W.E., 1921. Silver-lead deposits of the Keno Hill area, Mayo District, Yukon. Geological Survey of Canada, Summary Report, 1920, Part A, p. 1-6.
- Franzen, J.P., 1979. Metal-ratio zonation in the Keno Hill District. Unpublished paper presented at the Seventh Geoscience Forum, Whitehorse, Yukon.
- Keller, D., Sedlacek, J., Doerksen, G., Ghaffari, H. and Lister, D., 2008. Bellekeno Technical Report, Keno Hill Mining District, Yukon. Alexco Resource Corp., June 30, SRK Consulting (Canada) Inc., 2008 <http://sedar.com/CheckCode.do;jsessionid=00005vE9Z_pRgPlvakhLU6NAaju:-1> [accessed December 7, 2009].
- Kindle, E.D., 1962. Geology, Keno Hill. Geological Survey of Canada, Map 1105A, scale 1:63,360.
- Lebarge, W.R., Bond, J.D. and Hein, F.J., 2002. Placer gold deposits of the Mayo area, central Yukon. Exploration and Geological Services Division, Yukon Region, Indian and Northern Affairs Canada, Bulletin 13, 209 p.
- LeBarge, W.P. (compiler), 2007. Yukon Placer Database 2007 - Geology and Mining Activity of Placer Occurrences. Yukon Geological Survey, CD-ROM.
- Le Couter, P.C., 2009. Petrographic report on seven samples from the Eagle project, Galena Hill, Yukon. Unpublished internal report for MegaPrecious Metals.
- Ludwig, K.R., 1999. User's manual for Isoplot/Ex, version 2.06: a geochronological toolkit for Microsoft Excel. Berkeley Geochronological Center, Special Publication No. 1a, 49 p.
- Lynch, J.V.G., 1989. Large-scale hydrothermal zoning reflected in the tetrahedrite-freibergite solid solution, Keno Hill Ag-Pb-Zn district, Yukon. *Canadian Mineralogist*, vol. 27, p. 383-400.

- Mair, J.L., Hart, C.J.R. and Stephens, J.R., 2006. Deformation history of the northwestern Selwyn Basin, Yukon, Canada: implications for orogen evolution and mid-Cretaceous magmatism. *Geological Society of America Bulletin*, vol. 118, p. 304-323.
- McTaggart, K.C., 1960. The geology of Keno and Galena Hills, Yukon Territory. *Geological Survey of Canada Bulletin* 58, 37 p.
- Mortensen, J.K. and Thompson, R.I., 1990. A U-Pb zircon-baddeleyite age for a differentiated mafic sill in the Ogilvie Mountains, west-central Yukon Territory. *In: Radiogenic Age and Isotopic Studies, Report 3, Geological Survey of Canada, Paper 89-2, p. 23-28.*
- Murphy, D.C., 1997. Geology of the McQuesten River region, northern McQuesten and Mayo map areas, Yukon Territory (115P/14, 15, 16; 105M/13, 14). Exploration and Geological Services Division, Yukon Region, Indian and Northern Affairs Canada, *Bulletin* 6, 112 p.
- Nelson, J. and Colpron, M., 2007. Tectonics and metallogeny of the British Columbia, Yukon, and Alaskan Cordillera, 1.8 Ga to the present. *In: Mineral Deposits of Canada: A Synthesis of Major Deposit-Types, District Metallogeny, the Evolution of Geological Provinces, and Exploration Methods*, W.D. Goodfellow (ed.), Geological Association of Canada, Mineral Deposits Division, Special Publication No. 5, p. 755-791.
- Philpot, M.D., 1980. Geological and geochemical report; Bry mineral claims. Yukon Assessment Report 090545, prepared for Canada Tungsten Mining Corporation Ltd. by Bema Industries Ltd., 10 p.
- Roots, C.F. and Murphy, D.C., 1992. New developments in the geology of Mayo map area, Yukon Territory. *In: Current Research, Part A, Geological Survey of Canada, Paper 92-1A, p. 163-171.*
- Roots, C.F., 1997. Geology of the Mayo Map area, Yukon Territory (105M). Exploration and Geological Services Division, Yukon Region, Indian and Northern Affairs Canada, *Bulletin* 7, 82 p.
- Sack, R.O., Lynch, J.V.G. and Foit, E., Jr., 2003. Fahlore as a petrogenetic indicator, Keno Hill Ag-Pb-Zn district, Yukon, Canada. *Mineralogical Magazine*, vol. 67, p. 1023-1038.
- Scott, J. and Tupper, D.W., 2008. Mechanical trenching, rock, soil and stream sediment geochemical Assessment Report, Fisher 1-67 Claims. Unpublished assessment report.
- Scriven, S., 2008. Report on a helicopter-borne magnetic gradiometer and VLF-EM, Fisher-Man Project. Unpublished internal report for MegaPrecious Metals.
- Sinclair, A.J., Tessari, O.J. and Harakal, J.E., 1980. Age of Ag-Pb-Zn mineralization, Keno Hill-Galena Hill area, Yukon Territory. *Canadian Journal of Earth Sciences*, vol. 17, p. 1100-1103.
- Tempelman-Kluit, D.J., 1970. The stratigraphy and structure of the "Keno Hill Quartzite"; in Tombstone River – Upper Klondike River map areas, Yukon Territory. *Geological Survey of Canada, Bulletin* 180, 102 p.
- Tessari, O.J., 1979. Model ages and applied whole rock geochemistry of Ag-Pb-Zn veins, Keno Hill – Galena Hill mining camp, Yukon Territory. Unpublished MSc Thesis, University of British Columbia, Vancouver, British Columbia.
- Thompson, R.I., Roots, C.F. and Mustard, P.S., 1990. Repeated Proterozoic passive margin extension influences Late Cretaceous folding and thrusting in southern Ogilvie Mountains, Yukon. *In: Geological Association of Canada/Mineralogical Association of Canada, Program with Abstracts*, vol. 15, p. A131.
- Thompson, R.I., 1995. Geological compilation (1:250 000) map of the Dawson map area (116B, C; northeast of the Tintina Trench). *Geological Survey of Canada, Open File* 3223.
- Watson, K.W., 1986. Ag-lead-zinc deposits of the Keno Hill – Galena Hill area, Yukon Territory. *Yukon Geology*, vol. 1, p. 83-88.

Appendix 1. LAM ICP-MS U-Pb isotopic analyses of magmatic zircons from aplite dyke, D09-EF-05.

Analysis	Measured isotopic ratios					Calculated ages					Th ppm	U ppm	Ratio Th/U	
	$^{207}\text{Pb}/^{235}\text{U}$ 1 σ err.	$^{206}\text{Pb}/^{238}\text{U}$ 1 σ err.	Rho	$^{207}\text{Pb}/^{206}\text{Pb}$ 1 σ err.	$^{207}\text{Pb}/^{235}\text{U}$ Ma	$^{206}\text{Pb}/^{238}\text{U}$ Ma	1 σ err. Ma	Conc. age (Ma)	2 σ err. Ma	MSWD of conc.				Prob.
oc16a84	0.0977	0.0034	0.0145	0.0002	0.2391	0.0508	0.0017	95	3	0.28	0.60	108	3243	0.03
oc16b16	0.0973	0.0030	0.0145	0.0002	0.2359	0.0491	0.0017	94	3	0.34	0.56	117	4874	0.02
oc16b17	0.1035	0.0056	0.0144	0.0003	0.1634	0.0537	0.0014	100	5	2.31	0.13	131	4712	0.03
oc16b19	0.0998	0.0022	0.0148	0.0002	0.3079	0.0497	0.0012	97	2	0.64	0.42	85	4669	0.02

Appendix 2. LAM ICP-MS U-Pb isotopic analyses of inherited zircons from aplite dyke, D09-EF-05.

Inherited zircon	Measured isotopic ratios					Calculated ages								Th ppm	U ppm	Ratio Th/U		
	$^{207}\text{Pb}/^{235}\text{U}$ 1 σ err.	$^{206}\text{Pb}/^{238}\text{U}$ 1 σ err.	Rho	$^{207}\text{Pb}/^{206}\text{Pb}$ 1 σ err.	$^{207}\text{Pb}/^{235}\text{U}$ 1 σ err.	$^{206}\text{Pb}/^{238}\text{U}$ 1 σ err.	$^{207}\text{Pb}/^{206}\text{Pb}$ 1 σ err.	U-Pb/ Pb-Pb age	Conc. age	2 σ err.	MSWD of conc.	Prob. of conc.						
oc16a73	2.1544	0.0633	0.1677	0.0033	0.3365	0.0937	0.0010	1166	20	1000	18	1502	21	67	1058	33	52.53	0.00
oc16a74	1.6897	0.0267	0.1675	0.0024	0.4546	0.0724	0.0004	1005	10	998	13	998	10	100	1003	19	0.26	0.61
oc16a75	0.5736	0.0220	0.0696	0.0016	0.2948	0.0599	0.0007	460	14	434	9	601	26	72	440	18	3.29	0.07
oc16a76	0.4802	0.0158	0.0644	0.0014	0.3220	0.0559	0.0004	398	11	402	8	447	17	90	401	15	0.13	0.72
oc16a77	13.4434	0.9066	0.4991	0.0356	0.5296	0.1976	0.0010	2711	64	2610	153	2806	8	93	2718	126	0.61	0.44
oc16a78	3.6684	0.1032	0.2781	0.0081	0.5177	0.0975	0.0011	1565	22	1582	41	1578	20	100	1565	45	0.24	0.63
oc16a79	4.5878	0.0692	0.3068	0.0038	0.4100	0.1076	0.0006	1747	13	1725	19	1759	10	98	1743	24	1.54	0.22
oc16a80	3.2641	0.0801	0.2377	0.0054	0.4643	0.0978	0.0005	1473	19	1375	28	1582	9	87	1454	38	14.57	0.00
oc16a81	2.8885	0.0483	0.2379	0.0036	0.4516	0.0877	0.0004	1379	13	1376	19	1375	8	100	1378	24	0.03	0.85
oc16a82	2.1770	0.0736	0.1961	0.0087	0.6541	0.0821	0.0009	1174	24	1154	47	1248	22	92	1176	46	0.30	0.59
oc16a83	4.5247	0.0835	0.3068	0.0054	0.4761	0.1057	0.0006	1736	15	1725	27	1726	10	100	1735	31	0.20	0.65
oc16a105	13.8985	0.4698	0.5596	0.0181	0.4793	0.1809	0.0010	2743	32	2865	75	2661	9	108	2739	64	3.37	0.07
oc16a109	10.8234	0.2183	0.4502	0.0087	0.4793	0.1697	0.0014	2508	19	2396	39	2554	14	94	2507	38	11.01	0.00
oc16a110	1.6131	0.0545	0.1612	0.0033	0.3034	0.0740	0.0010	975	21	964	18	1042	28	92	968	32	0.25	0.62
oc16a111	2.9213	0.0594	0.2317	0.0035	0.3664	0.0896	0.0007	1387	15	1344	18	1416	15	95	1370	28	5.32	0.02
oc16a112	3.3361	0.0831	0.2605	0.0053	0.4083	0.0914	0.0008	1490	19	1492	27	1455	18	103	1490	37	0.01	0.92
oc16a113	2.5353	0.0509	0.2071	0.0039	0.4743	0.0891	0.0004	1282	15	1213	21	1407	8	86	1268	29	13.05	0.00
oc16a114	6.2176	0.1031	0.3523	0.0056	0.4824	0.1234	0.0007	2007	15	1945	27	2006	11	97	2004	29	6.85	0.01
oc16a115	2.8896	0.1220	0.2388	0.0090	0.4483	0.0873	0.0007	1379	32	1380	47	1366	16	101	1379	62	0.00	0.98
oc16a116	5.4548	0.1098	0.3385	0.0064	0.4714	0.1166	0.0006	1894	17	1879	31	1905	9	99	1893	34	0.27	0.60
oc16a117	0.5745	0.0507	0.0747	0.0034	0.2610	0.0591	0.0008	461	33	464	21	572	31	81	464	39	0.01	0.92
oc16b18	5.6304	0.0760	0.3451	0.0044	0.4772	0.1201	0.0009	1921	12	1911	21	1958	14	98	1920	23	0.26	0.61

Appendix 3. LAM ICP-MS U-Pb isotopic analyses of magmatic zircons from Duncan Creek aplite.

Analysis	Measured isotopic ratios				Calculated ages										
	$^{207}\text{Pb}/^{235}\text{U}$ 1 σ err.	$^{206}\text{Pb}/^{238}\text{U}$ 1 σ err.	Rho	$^{207}\text{Pb}/^{206}\text{Pb}$ 1 σ err.	$^{207}\text{Pb}/^{235}\text{U}$ Ma	1 σ err. Ma	$^{206}\text{Pb}/^{238}\text{U}$ Ma	1 σ err. Ma	Conc. age (Ma)	2 σ err. Ma	MSWD of conc.	Prob. of conc.	Th ppm	U ppm	Ratio Th/U
oc16b20	0.1098	0.0025	0.5098	0.0561	105.8	2.3	93.5	2.2	99	4	31.16	0.00	179	8502	0.02
oc16b23	0.1000	0.0043	0.1548	0.0515	96.8	4.0	91.7	1.2	92	2	1.60	0.21	542	1493	0.36
oc16b24	0.1004	0.0028	0.4408	0.0493	97.2	2.6	96.6	2.3	97	4	0.05	0.82	110	4743	0.02
oc16b26	0.1018	0.0043	0.2567	0.0519	98.4	3.9	92.6	2.0	93	4	2.18	0.14	301	1053	0.29
oc16b27	0.0972	0.0061	0.2457	0.0480	94.2	5.6	96.0	2.9	96	6	0.10	0.75	335	612	0.55
oc16b28	0.0958	0.0050	0.2394	0.0484	92.9	4.6	95.5	2.4	95	5	0.31	0.58	258	805	0.32
oc16b29	0.0948	0.0019	0.2013	0.0479	92.0	1.8	94.0	0.7	94	1	1.26	0.26	1248	2507	0.50
oc16b30	0.0967	0.0026	0.3080	0.0487	93.7	2.4	95.5	1.6	95	3	0.53	0.47	508	1284	0.40
oc16b31	0.0961	0.0041	0.2103	0.0498	93.2	3.8	90.9	1.6	91	3	0.36	0.55	504	1240	0.41
oc16b33	0.0980	0.0036	0.2465	0.0510	94.9	3.3	91.0	1.6	91	3	1.38	0.24	54	3307	0.02
oc16b34	0.0992	0.0044	0.2042	0.0491	96.0	4.1	95.2	1.7	95	3	0.04	0.84	76	2067	0.04

Appendix 4. LAM ICP-MS U-Pb isotopic analyses of inherited zircons, Duncan Creek aplite.

Inherited zircon	Measured isotopic ratios					Calculated ages													
	$^{207}\text{Pb}/^{235}\text{U}$ 1 σ err.	$^{206}\text{Pb}/^{238}\text{U}$ 1 σ err.	Rho	$^{207}\text{Pb}/^{206}\text{Pb}$ 1 σ err.	$^{207}\text{Pb}/^{235}\text{U}$ 1 σ err.	$^{206}\text{Pb}/^{238}\text{U}$ 1 σ err.	$^{207}\text{Pb}/^{206}\text{Pb}$ 1 σ err.	U-Pb/ Pb-Pb age	2 σ err.	MSWD of conc.	Prob. of conc.	Th ppm	U ppm	Ratio Th/U					
oc16b35	0.2968	0.0057	0.2865	0.0530	0.0010	0.264	4	262	3	331	42	79	263	5	0.11	0.73	322	1005	0.32
oc16b36	2.1128	0.0497	0.3040	0.0818	0.0011	1153	16	1142	15	1241	27	92	1147	25	0.33	0.56	56	255	0.22
oc16b37	0.3071	0.0093	0.4038	0.0532	0.0019	272	7	265	6	338	80	78	268	11	0.78	0.38	205	374	0.55
oc16b38	0.3024	0.0078	0.2763	0.0521	0.0017	268	6	270	4	290	76	93	270	7	0.10	0.75	202	374	0.54
oc16a21	2.7375	0.0703	0.3602	0.0847	0.0011	1339	19	1271	21	1309	24	97	1309	34	8.54	0.00	25	54	0.46
oc16a22	2.9909	0.0853	0.5278	0.0890	0.0009	1405	22	1406	38	1404	20	100	1405	43	0.00	0.98	46	136	0.34
oc16a23	4.6668	0.0742	0.5061	0.1174	0.0005	1761	13	1585	23	1917	8	83	1746	27	82.80	0.00	58	321	0.18
oc16a24	4.4203	0.0762	0.4828	0.1074	0.0006	1716	14	1660	24	1755	10	95	1711	28	6.93	0.01	119	368	0.32
oc16a25	5.1025	0.0869	0.4597	0.1166	0.0007	1837	14	1782	24	1904	11	94	1831	29	6.24	0.01	240	283	0.85
oc16a26	4.5344	0.0956	0.3563	0.1082	0.0009	1737	18	1740	23	1769	16	98	1738	32	0.01	0.93	44	111	0.39
oc16a27	4.4312	0.0697	0.4203	0.1053	0.0006	1718	13	1711	20	1720	10	99	1717	25	0.14	0.70	94	135	0.70
oc16a28	1.8904	0.0606	0.2733	0.0765	0.0011	1078	21	1125	18	1109	28	102	1106	31	4.03	0.04	34	40	0.85
oc16a29	1.5232	0.0309	0.6177	0.0722	0.0009	940	12	1042	24	991	26	105	931	25	28.06	0.00	55	170	0.32
oc16a30	1.8787	0.0496	0.2893	0.0767	0.0008	1074	17	1078	15	1113	20	97	1076	26	0.04	0.83	26	73	0.36
oc16a31	13.1906	0.7100	0.4657	0.1818	0.0007	2693	51	2609	108	2669	6	98	2693	102	0.80	0.37	218	522	0.42
oc16a32	1.8419	0.0276	0.4481	0.0748	0.0004	1061	10	1046	13	1062	12	99	1057	19	1.34	0.25	14	256	0.05
oc16a33	3.9167	0.0549	0.4832	0.1000	0.0005	1617	11	1598	19	1624	8	98	1616	23	1.25	0.26	272	386	0.71
oc16a34	2.7288	0.2228	0.4037	0.0867	0.0010	1336	61	1235	74	1354	22	91	1299	113	1.83	0.18	83	232	0.36
oc16a34	0.7709	0.2531	0.2674	0.0607	0.0013	580	145	546	92	630	45	87	553	173	0.05	0.82	47	131	0.36
oc16a40	4.2369	0.0431	0.5713	0.1038	0.0004	1681	8	1618	17	1693	7	96	1684	17	21.65	0.00	66	337	0.20
oc16a41	12.7988	0.2071	0.5297	0.1787	0.0008	2665	15	2672	37	2641	7	101	2665	30	0.04	0.84	165	181	0.91
oc16a42	3.3650	0.0561	0.3860	0.0964	0.0005	1496	13	1458	17	1556	10	94	1484	24	5.15	0.02	52	148	0.35
oc16a43	3.1670	0.0540	0.4475	0.0916	0.0004	1449	13	1430	20	1460	9	98	1446	26	1.13	0.29	47	261	0.18
oc16a44	0.5152	0.0218	0.2786	0.0565	0.0008	422	15	425	10	474	30	90	424	18	0.04	0.84	68	167	0.40
oc16a45	0.1500	0.0670	0.0475	0.1830	0.0069	142	59	96	4	2680	62	4	96	8	0.58	0.45	116	873	0.13
oc16a46	0.5135	0.0113	0.3329	0.0554	0.0005	421	8	433	6	430	21	101	429	11	2.36	0.12	223	354	0.63
oc16a47	0.3247	0.0162	0.2861	0.0539	0.0007	286	12	268	8	368	30	73	272	14	1.82	0.18	90	452	0.20

continued on next page

Appendix 4. continued

Inherited zircon	Measured isotopic ratios					Calculated ages									
	$^{207}\text{Pb}/^{235}\text{U}$ 1 σ err.	$^{206}\text{Pb}/^{238}\text{U}$ 1 σ err.	Rho	$^{207}\text{Pb}/^{206}\text{Pb}$ 1 σ err.	$^{207}\text{Pb}/^{235}\text{U}$ 1 σ err.	$^{206}\text{Pb}/^{238}\text{U}$ 1 σ err.	$^{207}\text{Pb}/^{206}\text{Pb}$ 1 σ err.	U-Pb/ Pb-Pb age	Conc. age	2 σ err.	MSWD of conc.	Prob. of conc.	Th ppm	U ppm	Ratio Th/U
oc16a48	0.3715	0.1699	0.2932	0.1636	0.0032	321	126	4	107	59	2.43	0.12	38	1241	0.03
oc16a49	2.0841	0.0306	0.4719	0.0790	0.0004	1144	10	96	1139	19	3.54	0.06	246	787	0.31
oc16a50	4.7652	0.0561	0.3963	0.1140	0.0005	1779	10	92	1765	19	18.95	0.00	22	377	0.06
oc16a51	4.0743	0.0678	0.4551	0.0997	0.0008	1649	14	101	1648	27	0.35	0.55	77	227	0.34
oc16a52	3.9675	0.0673	0.3926	0.1010	0.0007	1628	14	98	1622	26	1.48	0.22	35	99	0.36
oc16a57	4.0333	0.0540	0.4376	0.1004	0.0006	1641	11	99	1636	21	4.07	0.04	114	174	0.66
oc16a58	4.4666	0.0169	0.3285	0.0563	0.0006	389	12	83	386	16	0.11	0.73	117	277	0.42
oc16a59	1.8066	0.0398	0.3050	0.0691	0.0006	1048	14	122	1074	22	9.41	0.00	97	145	0.67
oc16a60	1.7363	0.0341	0.3687	0.0729	0.0005	1022	13	101	1021	22	0.01	0.91	94	312	0.30
oc16a61	2.0503	0.0374	0.3908	0.0779	0.0006	1132	12	99	1134	22	0.11	0.74	48	196	0.25
oc16a62	2.0541	0.0489	0.3694	0.0784	0.0007	1134	16	99	1140	28	0.76	0.38	29	90	0.33
oc16a63	3.4034	0.0541	0.4536	0.0934	0.0005	1505	12	98	1499	24	5.15	0.02	69	271	0.25
oc16a64	2.2555	0.0792	0.3902	0.0781	0.0008	1198	25	104	1199	45	0.00	0.96	52	109	0.48
oc16a65	2.7373	0.0412	0.4401	0.0865	0.0004	1339	11	99	1338	22	0.04	0.83	171	468	0.37
oc16a66	3.7721	0.0823	0.3236	0.0978	0.0008	1587	18	99	1581	30	0.38	0.54	46	99	0.47